Downloaded from orbit.dtu.dk on: Apr 29, 2024

DTU Library

Full Scale Measurements of the Hydro-Elastic Response of Large Container Ships for Decision Support

Andersen, Ingrid Marie Vincent

Publication date:
2014

Document Version
Publisher's PDF, also known as Version of record

Link back to DTU Orbit

Citation (APA):
Andersen, I. M. V. (2014). *Full Scale Measurements of the Hydro-Elastic Response of Large Container Ships for Decision Support*. Technical University of Denmark. DCAMM Special Report No. S166

General rights
Copyright and moral rights for the publications made accessible in the public portal are retained by the authors and/or other copyright owners and it is a condition of accessing publications that users recognise and abide by the legal requirements associated with these rights.

- Users may download and print one copy of any publication from the public portal for the purpose of private study or research.
- You may not further distribute the material or use it for any profit-making activity or commercial gain
- You may freely distribute the URL identifying the publication in the public portal

If you believe that this document breaches copyright please contact us providing details, and we will remove access to the work immediately and investigate your claim.

Full Scale Measurements of the Hydro-Elastic Response of Large Container Ships for Decision Support

PhD Thesis

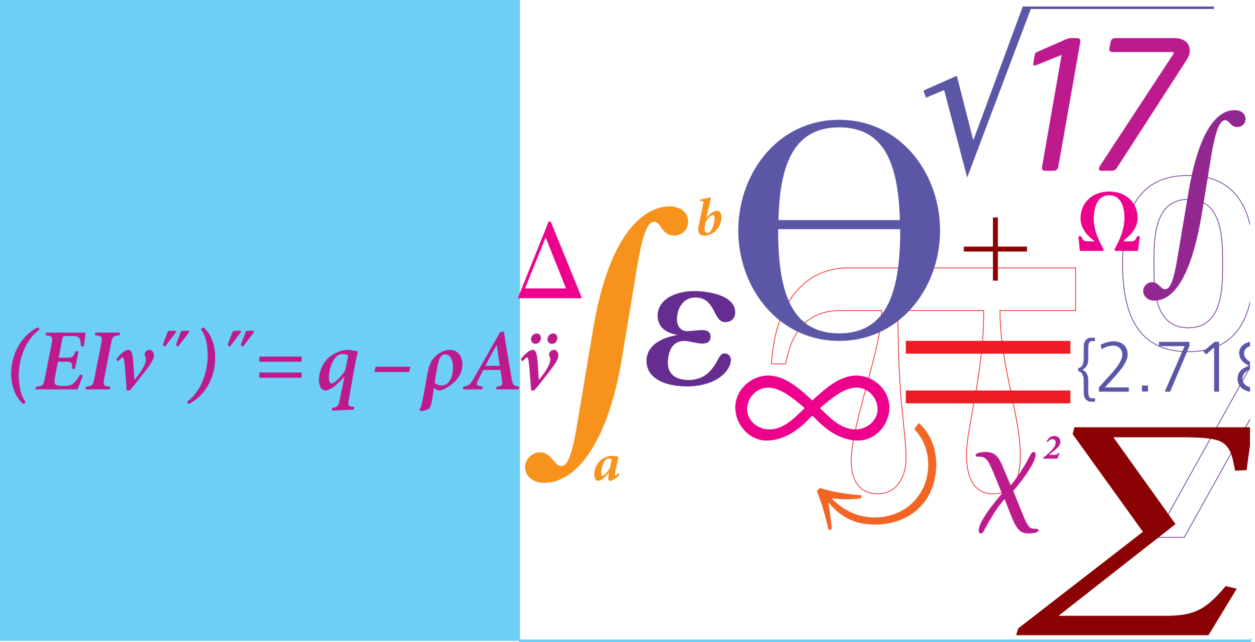
$(EIv'')'' = q - \rho A\ddot{v}$
Δ
$\int_a^b$
ε
Θ
$\sqrt{17}$
Ω
∞
$\{2.718$
χ^2
Σ

Ingrid Marie Vincent Andersen
DCAMM Special Report No. S166
April 2014

DTU Mechanical Engineering
Department of Mechanical Engineering

Full Scale Measurements of the Hydro-Elastic Response of Large Container Ships for Decision Support

Ingrid Marie Vincent Andersen
DTU Mechanical Engineering
Nils Koppels Alle, building 403
DK-2800 Kgs. Lyngby
Denmark

Preface

This thesis is submitted as a partial fulfilment of the requirements for acquiring a PhD degree at the Department of Mechanical Engineering, Section for Fluid Mechanical, Coastal and Maritime Engineering at the Technical University of Denmark. The study has been carried out during the period from 1 November 2010 to 30 April 2014 including 6 months of leave, and has been supervised by Professor Jørgen Juncher Jensen and Associate Professor Ulrik Dam Nielsen.

First and foremost I wish to express my sincere gratitude to professor Jørgen Juncher Jensen. During the past 3,5 years he has shown tremendous enthusiasm and interest in my work. He was always prepared for discussions and for answering my questions early morning, late night, in weekends and even during holidays from the Australian outback, and there was always a positive answer to any question. He has been outstanding and, without a doubt, the best PhD supervisor I could have wished for. Thanks to co-supervisor Ulrik Dam Nielsen for sharing his insight into the field of estimating the sea state from the motions of advancing ships and for his thoroughness in the help and support as well as for motivation, inspiration and support and for good times on travels and conferences abroad. Also thanks to the colleagues at the Section for Fluid Mechanics, Coastal and Maritime Engineering, particularly Sopheak Seng and Najmeh Montazeri, for discussions and assistance and to professor emeritus Preben Terndrup Pedersen for his valuable help, insight and feedback. Thanks to Søren Vinther Hansen for pleasant office company, talks and friendship.

The work was supported financially by the Technical University of Denmark, the EU FP7 project no. 234146 *Tools for Ultra Large Container Ships* (TULCS) and the Danish Maritime Fund. The financial support for this project is greatly acknowledged and a special thank in this respect goes to Carsten Melchiors, administrator of the Danish Maritime Fund, for personal support, enthusiasm and interest in the work through the entire project period.

In total, I spent about 2 months with the Maritime Advisory group of DNV GL in Høvik, Norway. I wish to thank Head of Section Erik Mathias Sørhaug for welcoming me to DNV GL and, in particular, to thank Dr Gaute Storhaug for sharing his tremendous knowledge on springing and whipping stresses in ships and very valuable full scale measurements with me without any reservations. From the DNV GL office in Hamburg Jan Oberhagemann, Adrian Kahl and Paul Anding were very helpful and insightful and seamlessly provided valuable full-scale data. Also thanks to Sonja and Thor Erik Jægersborg in Blommenholm

for their hospitality.

The Maritime Research Institute Netherlands (MARIN) was a TULCS project partner and the full scale data from this project has kindly been provided by Jos Konig, Eric Wictor and Marcus Schiere. I am very thankful for their immense helpfulness in providing the requested data and for their readiness and positive attitude in answering my endless row of questions - also after the TULCS project ended.

The crew on board CMA CGM RIGOLETTO was very helpful at several occasions. Special thanks to Francois Louis Marie Robic and Gregoire Wencesla Guitard for their time and help during my visit on board the vessel. Also thanks to the hydrodynamics team at Bureau Veritas associated with the TULCS project, where particularly Šime Malenica and Quentin Derbanne provided useful information and good discussions during the project.

Sara Knudsen and Palle Andersen from Structural Vibration Solutions A/S in Aalborg, Denmark, kindly provided a license and very efficient support for the ARTeMIS software for Operational Modal Analysis, and their help is very appreciated.

Sincere thanks to assistant professor Ying Min Low at Nanyang Technological University in Singapore for valuable discussions regarding the application of his spectral method for fatigue damage estimation on ocean going ships. Thanks to René Taudal from Copenhagen Business School for very interesting discussions across academic boundaries. A special thank goes across the globe to professor Giles Thomas from Australian Maritime College, University of Tasmania for encouragement at a critical point in time.

Thanks to my dear father for giving me tool sets, self-assembly kits and engineering books for Christmas instead of dolls, for always being inspiring, enthusiastic and supportive and for feeding my interests within natural science and engineering from early childhood. Thanks to my mother and sister for their immense help babysitting little Maja. Thanks to my family and friends for love and support.

I feel extremely privileged with the freedom, opportunities and responsibilities I have been given during my time as a PhD student at the Technical University of Denmark and I wish to thank everybody who was involved in making it a truly enjoyable time.

Ingrid Marie Vincent Andersen
30 April 2014

Executive Summary

The overall topic of this thesis is decision support for operation of ships and several aspects are covered herein. However, the main focus is on the wave-induced hydro-elastic response of large container ships and its implications on the structural response.

The analyses are based mainly on full scale measurements from four container ships of 4,400 TEU, 8,600 TEU, 9,400 TEU and 14,000 TEU Primarily, strains measured near the deck amidships are used. Furthermore, measurements of motions and the encountered sea state are available for one of the ships. The smallest ship is in operation on the North Atlantic, while the three largest ships are operated on the Europe - Asia route.

In the design rules of the classification societies for container ships the minimum design sagging bending moment amidships is larger than the hogging bending moment. Due to their design (full midship section and slender bow and stern sections) and their normal cargo loading condition, container ships are typically operated in a still-water hogging condition (tension in deck and compression in the bottom structure). The wave-induced bending moment is added to the still-water bending moment, which, together with the smaller design hogging bending moment, generally makes the wave-induced hogging bending moment more critical than the sagging bending moment in the operation of container ships.

As container ships of today become larger, their natural vibration frequencies become lower and approach the typical encounter frequency with the waves. Together with the relatively high design speed and often pronounced bow flare this makes large container ship more sensitive to slamming and, consequently, the effects of wave-induced hull girder vibrations. From full scale strain measurements of individual, measured hull girder responses in the four container ships, the wave-induced hull girder vibrations are found to increase the vertical bending moment amidships by 100% or more. From the full scale measurements the amplification, due to the hull girder flexibility, is found to be largest for the 8,600 TEU and the 9,400 TEU ships, but, in addition to ship size, speed and bow flare angle are also believed to be important factors contributing to the hull girder vibrations.

The hull girder vibrational response is found to be dominated by the 2-node vertical bending mode. No torsional vibrations are found but torsion may, however, still be a concern for ultra large container ships. The damping of the 2-node vertical bending mode is estimated from full scale measurements for the four ships to 1.3-2.5% of the critical

damping. No effect of ship size on the damping is identified.

In some cases the hogging bending moment is more amplified by the effect of the hull girder flexibility than the sagging bending moment. No general trend in the amplification of the response is found from the full scale measurements. In some cases, the rigid-body hogging bending moment, found from full scale measurements and model tests, is considerably larger than the corresponding sagging bending moment. Generally, the difference between the design sagging and hogging bending moments is not reflected in the full scale measurements considered here.

The extreme value of the vertical hogging bending moment, as estimated from full scale measurements, is investigated using the peak-over-threshold method for different periods. The tails of the peak distributions for the four different ships are found to be very different from case to case. The irregularity of the tail behaviour makes it difficult to determine an appropriate extreme value distribution for the hogging bending moment. The Gumbel distribution is believed to be the appropriate extreme value distribution, but it may be necessary to fit other types of extreme value distributions to the largest peaks.

From the full scale measurements it is difficult to assess the influence of operational parameters (ship speed, heading relative to the waves and wave height) on the extreme response because these data are not readily available in all cases. Model tests indicate that bow-quartering sea may induce larger structural loads on the ship than direct head sea and that the amplification of the response due to the hull girder flexibility is largest in bow-quartering waves. However, this fact is not necessarily reflected in the behaviour of ship masters who seemingly tend to prefer bow-quartering sea to head sea when encountering adverse weather.

Numerical design tools are widely used in ship design, but may not be able to fully capture the effect of the hull girder flexibility and are here found to significantly underestimate the effect compared to model tests and full scale measurements. Hence, full scale measurements from ships are highly valuable in the evaluation of existing designs and may reveal effects that cannot be assessed numerically.

For decision support, accurate knowledge of the encountered sea state parameters (wave height, period and relative wave direction) is crucial. One means to estimate the on-site sea state from an advancing ship is to use the wave buoy analogy, i.e. use the motions of the ship and the associated motion transfer functions to derive the sea state parameters. The method is promising but needs further refinement before it can be implemented in decision support systems on board ships.

Fatigue damage is estimated from full scale strain measurements from two of the container ships with focus on the assessment of the influence of the wave-induced high-frequency hull girder vibrations. In several cases, the high-frequency contribution to the fatigue damage is dominating the estimated fatigue damage. Spectral formulations for estimating fatigue damage from bi-modal processes are explored and found to yield results fairly similar to the outcome of classical fatigue damage estimation from rainflow counting. However, in a few cases higher fatigue damage rates were estimated from rainflow counting than from narrow-band approximations.

In summary and only considering larger container ships, the new and original contributions of the thesis are believed to be:

- From full scale measurements the hull girder vibrational response is generally found to be dominated by the 2-node vertical bending mode even when the ship is sailing in oblique seas.
- The vertical bending moment in hogging and sagging is amplified considerably by the effect of the hull girder flexibility and the wave-induced hull girder vibrations are found capable of increasing the vertical wave bending moment amidships by 100% or more.
- The vertical hogging bending moment can be as critical as the sagging bending moment in design.
- From comparison of models tests and numerical methods, it seems that the numerical methods are not capable of fully capturing the effect of hull girder flexibility seen in model tests.
- The peak-over-threshold method is found to be the most useful method for extreme value prediction of the vertical bending moment in combination with an appropriate asymptotic extreme value distribution.

Contents

Preface **3**

Executive Summary **5**

Contents **12**

1 Introduction **13**
- 1.1 Introduction and Motivation . . . 13
- 1.2 Objectives and Scope . . . 15

2 Measurements from Ships **19**
- 2.1 Introduction . . . 19
- 2.2 Coordinate System . . . 19
- 2.3 The 9,400 TEU Container Ship . . . 20
- 2.4 The 8,600 TEU Container Ship . . . 26
- 2.5 The 14,000 TEU Container Ship . . . 28
- 2.6 The 4,400 TEU Container Ship . . . 28
- 2.7 Faults and Uncertainties . . . 29

3 Sea State Estimation **31**
- 3.1 Introduction . . . 31
- 3.2 Visual Observations . . . 32
- 3.3 Meteorological Models . . . 32
- 3.4 Satellite Measurements . . . 32
- 3.5 Directional Wave Radars . . . 32
- 3.6 Down-Looking Wave Radar . . . 33
- 3.7 Wave Buoys . . . 33
- 3.8 Wave Buoy Analogy . . . 34
- 3.9 Discussion and Conclusions . . . 41

4 Ship Response Prediction using Full Scale Measurements **43**
- 4.1 Introduction . . . 43
- 4.2 Conditional Processes . . . 44
- 4.3 Autoregressive Predictor . . . 47
- 4.4 Sinusoidal Decomposition . . . 47
- 4.5 Comparisons with Measurements . . . 48

4.6 Discussion and Conclusions . . . 53

5 Hydro-Elastic Response of Container Ships 54

5.1 Introduction . . . 54

5.2 Hull Girder Flexibility . . . 57

6 Fatigue Damage Estimation from Full Scale Measurements 64

6.1 Introduction . . . 64

6.2 Fatigue Life . . . 65

6.3 Data and Filtering . . . 66

6.4 Fatigue Damage Estimation Methods . . . 68

6.5 Results . . . 74

6.6 Use of the Envelope Processes in Fatigue Damage Estimation . . . 76

6.7 Discussion . . . 77

6.8 Conclusions . . . 81

7 Influence of the Hull Girder Flexibility 83

7.1 Introduction . . . 83

7.2 Linear Time-Domain Strip-Theory . . . 84

7.3 Non-Linear Time-Domain Strip-Theory . . . 85

7.4 Hydro-Elastic Equations of Motion . . . 85

7.5 The Conditional Wave . . . 85

7.6 Vertical Bending Moment in the Conditional Wave . . . 87

7.7 Statistical Properties . . . 88

7.8 Comparison of Non-Linear Strip-Theory with Model Tests in Regular Waves 90

7.9 Discussion and Conclusions . . . 91

8 Measurements of Large Hull Girder Stresses in Container Ships 93

8.1 Introduction . . . 93

8.2 9,400 TEU Container Ship, 02 October 2011 . . . 93

8.3 9,400 TEU Container Ship, 12 August 2011 . . . 102

8.4 9,400 TEU Container Ship, 17 December 2011 . . . 103

8.5 8,600 TEU Container Ship, 17 November 2010 . . . 104

8.6 8,600 TEU Container Ship, 30 December 2011 . . . 105

8.7 14,000 TEU Container Ship, 29 September 2011 . . . 106

8.8 14,000 TEU Container Ship, 21 July 2011 . . . 107

8.9 4,400 TEU Container Ship, 02 November 2007 . . . 108

8.10 4,400 TEU Container Ship, 01 July 2008 . . . 109

8.11 Torsional Vibrations . . . 110

8.12 Discussion and Conclusions . . . 112

9 Extreme Value Prediction of the Vertical Bending Moment 114

9.1 Introduction . . . 114

9.2 Design Wave Loads . . . 115

9.3 9,400 TEU Container Ship, 02 October 2011 . . . 116
9.4 9,400 TEU Container Ship, 12 August 2011 . . . 132
9.5 9,400 TEU Container Ship, 17 December 2011 . . . 134
9.6 8,600 TEU Container Ship, 17 November 2010 . . . 136
9.7 8,600 TEU Container Ship, 30 December 2011 . . . 140
9.8 14,000 TEU Container Ship, 29 September 2011 . . . 143
9.9 14,000 TEU Container Ship, 21 July 2011 . . . 145
9.10 4,400 TEU Container Ship, 02 November 2007, 11-13 hours . . . 147
9.11 4,400 TEU Container Ship, 02 November 2007, 16-18 hours . . . 150
9.12 4,400 TEU Container Ship, 01 July 2008 . . . 152
9.13 Clustering and De-Clustering of Peaks . . . 155
9.14 Discussion and Conclusions . . . 157

10 Estimation of the Hull Girder Hydro-Elastic Behaviour 163
10.1 Introduction . . . 163
10.2 Hermite Transform based on Skewness and Standard Deviation . . . 163
10.3 Whipping Response Estimation . . . 164
10.4 Conclusions . . . 167

11 Model Tests with 9,400 TEU Container Ship 168
11.1 Introduction . . . 168
11.2 Significant Wave Height of 6.5 m . . . 169
11.3 Significant Wave Height of 9.5 m . . . 171
11.4 Discussion and Conclusions . . . 175

12 Extreme Hydro-Elastic Response of Container Ships 177
12.1 Introduction . . . 177
12.2 Response of Large Container Ships . . . 177
12.3 Hull Girder Ultimate Strength . . . 183

13 Data-Based Decision Support for Ship Operations 187
13.1 Data . . . 187
13.2 On-Board Decision Support . . . 188
13.3 On-Shore Decision Support . . . 192

14 Conclusions and Recommendations for Future Work 195
14.1 Sea State Estimation and Response Prediction . . . 195
14.2 Fatigue Damage Estimation . . . 196
14.3 Extreme Hydro-Elastic Response of Container Ships . . . 197

Bibliography 200

List of Figures 208

List of Tables 238

Appendix A Measurements from Ships 243
A.1 9,400 TEU Container Ship 243
A.2 8,600 TEU Container Ship 278
A.3 14,000 TEU Container Ship 285

Appendix B Specification and Illustrations of Measurement Equipment 287
B.1 9,400 TEU Container Ship 287
B.2 8,600 TEU Container Ship 298

Appendix C Estimated Fatigue Damage 300
C.1 9,400 TEU Container Ship 300
C.2 8,600 TEU Container Ship 312
C.3 Fatigue Damage Estimation using a Combination of a Stationary Gaussian Process and a Non-Gaussian Transient Process 333

Appendix D Measurements of Large Hull Girder Stresses 338
D.1 9,400 TEU Container Ship, 02 October 2011 338
D.2 9,400 TEU Container Ship, 12 August 2011 339
D.3 9,400 TEU Container Ship, 17 December 2011 340
D.4 8,600 TEU Container Ship, 17 November 2010 343
D.5 8,600 TEU Container Ship, 30 December 2011 344
D.6 14,000 TEU Container Ship, 29 September 2011 347
D.7 14,000 TEU Container Ship, 21 July 2011 348
D.8 4,400 TEU Container Ship, 02 November 2007, 11-13 hours 349
D.9 4,400 TEU Container Ship, 02 November 2007, 16-18 hours 350
D.10 4,400 TEU Container Ship, 01 July 2008 352
D.11 High-Frequency Vibrations 354

Appendix E Extreme Value Prediction 356
E.1 9,400 TEU Container Ship, 02 October 2011 356
E.2 9,400 TEU Container Ship, 12 August 2011 361
E.3 9,400 TEU Container Ship, 17 December 2011 365
E.4 8,600 TEU Container Ship, 17 November 2010 369
E.5 8,600 TEU Container Ship, 30 December 2011 373
E.6 14,000 TEU Container Ship, 29 September 2011 377
E.7 14,000 TEU Container Ship, 21 July 2011 382
E.8 4,400 TEU Container Ship, 02 November 2007, 11-13 hours 386
E.9 4,400 TEU Container Ship, 02 November 2007, 16-18 hours 390
E.10 4,400 TEU Container Ship, 01 July 2008 394
E.11 ACER Output Example 398

Appendix F Model Tests 400
F.1 $H_s = 6.5$ m 400
F.2 $H_s = 9.5$ m 403

Appendix G Basic Equations **409**
G.1 Dynamic Response of Flexible Hulls 409
G.2 The Gamma Function 410
G.3 Probability Distribution Functions 410
G.4 From Order Statistics to the Gumbel Distribution 410

Chapter 1

Introduction

1.1 Introduction and Motivation

In the present years, container ships are increasing in size and today's ultra large container ships built and on order have a capacity above 18,000 TEU. They are up to 400 metres long and, despite high fuel costs, still being designed to relatively high operating speeds in excess of 20 knots. An ultra large container ship is shown in Figure 1.1. In particular, the increase in length has an implication on the structural behaviour of the large container ships. They tend to become structurally ”softer” with lower hull natural frequencies and the result could be increased sensitivity to vertical and horizontal bending loads as well as torsional loads. The consequence is that the global hydro-elastic structural responses, particularly springing and whipping, could become as critical an issue in container ship design and operation as the rigid-body structural response. The rigid-body response is traditionally thoroughly assessed at the design stage, but hydro-elastic effects are not directly taken into account in the current design rules of the classification societies.

MAERSK LINE
Scandlines

Figure 1.1: *18,000 TEU container ship MAJESTIC MÆRSK.*

Fortunately, accidents related to structural failure of large container ships are rare, but the total loss of the 8,100 TEU container ship MOL COMFORT in 2013 due to structural collapse of the hull girder has sparked some concern related to the design of the large container ships. The particular ship was only five years old at the time of the incident and hydro-elastic effects may have played a role in the hull girder collapse. The present thesis, however, does not have any relation to this accident or the subsequent investigation of it.

The EU project TULCS (Tools for Ultra Large Container Ships)[1] was concerned with the influence of the hydro-elastic structural responses, such as springing and whipping, in large container ships and their implications on design and the project was finalised in 2012. One of the aims of the TULCS project was to develop tools and methodologies for efficient and safe design of ultra large container ships taking the hydro-elastic effects into account. The project combined numerical methods, model tests and full scale measurements through the following work packages:

WP 2 - End-user requirements
WP 3 - Global quasi-static wave loading and responses
WP 4 - Global hydro-elastic wave loading and responses
WP 5 - Local hydrodynamic loading and responses
WP 6 - Model tests
WP 7 - Full scale measurements
WP 8 - Overall technical coordination and integration

The project partners in the TULCS project were Bureau Veritas, Maritime Research Institute Netherlands (MARIN), CMA CGM, CEHIPAR, Ecole Centrale Marseille, the Technical University Delft, University of Zagreb, University of East Anglia, SIRENHA, WIKKI, HydrOcean, Brze Vise Bolje and the Technical University of Denmark. Additionally, Hyundai Heavy Industries was an associated partner. The analyses carried out in the present thesis primarily utilise the data produced for the WP 6 and WP 7 (model tests and full scale measurements) of the TULCS project.

The term "decision support system" is a broad term describing data and computer-based information systems capable of providing support to decision makers at various organisational levels. In relation to ship operations, decision support can be given to the crew on board the vessel or to the crew in the land-based part of the organisation to aid when complex decisions are to be made.

High fuel prices and operating expenses, low freight rates and fierce competition in the shipping industry mean that ship operations these years are continuously optimised and run closer to the margins - both in a technical and an economical sense. Savings are obtained through performance improvements and optimisation of the operation, and even incremental operational savings can be economically worthwhile to pursue. On the crewing side savings are achieved by employing cheaper and often less skilled on-board crew and technically, ships are generally designed and built to prescribed minimum standards.

Safety of the ship, cargo and crew is permanently of great concern for the shipping industry, regardless of the state of the market, due to the large costs typically associated with accidents involving ships. The maritime industry is asset heavy; ships represent large investments and they are expensive to maintain and repair. The economical risk of a wrong decision is large regardless if the consequence is an accident or a poor investment. More national and international legislation and reporting requirements are enforced on the shipping industry these years and in the years to come which further increase the general complexity of ship operations.

---

[1] `http://www.fsb.unizg.hr/tulcs`

Today, the amount of information available as support for decisions is increasing rapidly and data from ships is more easily obtained than ever. Increased number of sensors on board ships, increased automation and automatic logging of data mean that huge amounts of operational data can be generated. In addition, extended information connectivity between ship and shore means that the data more easily can be transferred to shore and used for decision support on land.

Because of the complexity in the decision process and increased amounts of data available there is a fundamental need for decision support to aid the correct decision and to minimise cost and risk. The time horizon for decision support can range from seconds to years depending on the decision to be made. Very quick decisions (of the order of seconds) could be required on board ships in relation to e.g. crane operations on offshore supply vessels or helicopter landings on board a navy ship. Long-term decisions in the order of years could e.g. be a shipowner's considerations regarding investments in new ship designs or retrofitting of existing ships. In between could be decisions related to e.g. ship route and maintenance planning. On-board decision support systems are becoming more widely used on board ships for operator guidance with respect to optimising the operation and ensuring safety.

On board, decision support based on measured data can be given with respect to fuel efficiency or safety, including route planning, optimum speed, trim and draught, ship stability, hull girder loads and avoidance of undesirable ship responses such as e.g. parametric roll. When sailing an ultra large, flexible container ship through harsh weather the operational conditions, namely the ship speed, wave height and heading relative to the waves are of great importance to the ship responses, and local and global structural loads. Contrarily to classical critical ship responses as e.g. roll, large structural loads on a ship may be more difficult to perceive for the ship master and an on-board decision support to ship masters with regards to safe speed and heading in adverse weather may serve to reduce extreme hull girder loads.

1.2 Objectives and Scope

In the present thesis decision support for ship operations implies support provided to the decision makers on board a ship or in the land-based part of the shipping organisation making decisions related to operation of existing ships and/or design of new ships. The thesis primarily deals with analysis of full scale measurements and tools used for on-board decision support for safe operation and design of large container ships. The thesis focuses almost exclusively on the wave-induced global structural ship responses from a combined theoretical and empirical viewpoint. The emphasis is on the extreme, whipping-induced loads, and springing is not explicitly considered in the thesis.

The present thesis is a monograph which partly reproduces and expands upon the six publications Andersen and Jensen, 2014, Andersen and Jensen, 2012, Andersen et al., 2013, Andersen and Jensen, 2013, Andersen and Storhaug, 2012 and Nielsen et al., 2013. Reference to the publications is made at the beginning of the respective chapters.

For decision support systems reliable input data is essential to produce a useful output. Chapter 2 describes the input data used in this thesis. Full scale measurements from four different container ships form the basis of the analyses carried out in the subsequent chapters, and data from the different ships are used in different chapters. Most data used in the thesis originates from the TULCS project case ship; a 9,400 TEU container ship, and the three other container ships are of sizes 4,400 TEU, 8,600 TEU, and 14,000 TEU. Additionally, model test results using a flexible model of the 9,400 TEU container ships are described. All the studied full scale data is automatically logged from sensors on board and no use of manually logged data has been made. Sensor faults and measurement uncertainties can influence the performance of a decision support system negatively and must be properly taken care of before the data is utilised for decision support. Data uncertainties are briefly assessed in Chapter 2, but data fault detection falls outside the scope of this thesis.

The prediction and forecasting of risks of undesired events like, e.g., large motion amplitudes, in a medium-term (1-3 hours) period require an accurate knowledge of the sea state in the local geographical area of the ship. Knowledge of the encountered sea state is also essential for carrying out more long-term performance monitoring of ships where fuel efficiency, fouling, resistance, etc., are of concern. Chapter 3 describes different methods for determining the statistics of the sea state for use in decision support systems. Using the ship as a wave buoy is one concept with several advantages as it uses relatively cheap motion sensors to derive an estimate of the encountered sea state at the exact location of the ship. The concept is based on measured responses of the ship combined with the associated linear transfer functions. In order to be applicable in decision support systems the method must be robust. Moreover, it should preferably be able to dynamically select the most appropriate combination of ship responses for the wave estimation in all operational conditions and take the uncertainties of the measured responses and the transfer functions into account in the estimate.

For advanced ship operations such as crane operations, helicopter landings, etc. very short-term response forecasting of the order of 5-15 seconds can, theoretically, be carried out based on measured global ship responses without any prior knowledge of sea state or transfer functions. A method for doing so is described in Chapter 4.

Hydro-elasticity can play an important role for the structural response of large container ships. It is believed that the hydro-elastic effects and the effect of hull girder flexibility are capable of significantly amplifying the hull girder stresses and thus contribute to fatigue damage as well as to the extreme hull girder loading in container ships. For this reason a large share of the thesis (Chapters 5-12) deals with the hydro-elastic structural response of container ships and the focus is on the wave-induced hogging bending moment. The influence of the hull girder flexibility on the wave-induced vertical bending moment is of interest at the design stage, and Chapter 5 serves as an introduction to the remaining part of the thesis. The mode shape, the natural frequency and the damping of particularly the vertical 2-node bending mode are of interest for the numerical estimation of the hull girder flexibility and are assessed in Chapter 5.

Fatigue damage in ships is generally believed to be influenced by the hull girder vibrations. Fatigue damage rates can be estimated from strain measurements in the time or in the frequency-domain, but the estimation method must be able to properly take the effect of hull girder vibrations into account. The vibration contribution to he fatigue damage is addressed in Chapter 6. For on-board decision support, fatigue damage rates must be estimated real-time and the estimation may be carried out most efficiently in the frequency-domain. Thus, different spectral methods, which are computationally fast, are investigated and compared to the outcome of the estimation in the time-domain. The overall effect of the hull girder vibrations on the estimated fatigue damage is assessed for the 9,400 TEU and the 8,600 TEU ships, but no attempt to assess the accumulated fatigue damage during the total life time of the ships is made.

The influence of hull girder flexibility can be assessed at the design stage using a simple and fast approach based on non-linear strip-theory. In combination with a flexible beam model the influence of the hull girder flexibility on a prescribed sagging and hogging bending moment in a conditional wave is investigated in Chapter 7, where results from the First Order Reliability Method are compared to those of Monte Carlo Simulations as well as to model tests for the 9,400 TEU ship.

Full scale measurements of hull girder stresses are available from four different container ships and provide valuable insight to the behaviour of large container ships in waves. The main objective is to assess the importance of the hydro-elastic effects on the extreme wave-induced vertical bending moment amidships. The influence of the high-frequency vibrations induced by e.g. slamming events is assessed in Chapter 8.

Longer time series of 2-3 hours of the measured stress from the four ships form the basis of prediction of the extreme response and the influence of hull girder flexibility on the extreme response in Chapter 9. Based on stress measurements forecasting of future critical responses such as a large vertical hogging bending moment amidships could be provided in a decision support system. For this prediction the extreme value distribution of the considered response must be known or determined. The Gumbel distribution is believed to be the appropriate extreme value distribution for the extreme wave-induced vertical bending moment in ships. In Chapter 9 the extreme value predictions of the largest response in three hours is explored using primarily the Gumbel distribution in combination with the peak-over-threshold method. Issues regarding the choice of a proper threshold level are discussed together with influence of statistically correlated peaks.

The hydro-elastic behaviour of the hull girder is assessed in Chapter 10 using simple approximations and the measured rigid-body statistical properties and closed-form expressions. The estimation from the simple methods are compared to the results from the First Order Reliability Method in Chapter 7 and the results derived from the full scale measurements from the 9,400 TEU ship.

For the 9,400 TEU container ship model tests with a flexible model in irregular waves were carried out as part of the TULCS project focusing on the extreme response. The model tests are described in Chapter 11 and serve as a good basis for comparison with the full scale measurements analysed in Chapters 8 and 9. From the model tests information about the effect of ship speed, relative heading and wave height on the largest responses can be obtained more easily than from full scale measurements. The results related to extreme hydro-elastic loads in container ships are compared and discussed in Chapter 12.

Although all of the analyses carried out in the theses are based on full scale measurements from container ships, the studied methods could be applied to other ship types as well. By the end of the thesis the view is expanded to include the use of the measured data from ships in other kinds of decision support systems in general. Chapter 13 gives an outline of the use data from ships in decision support on board ships and in the land-based part of the organisation to create value at different organisational levels.

A main part of the analyses in the thesis rely on the WAFO toolbox (Brodtkorb et al., 2011). The WAFO package contains routines for computation of the statistical properties of waves and other load sequences. It also contains tools for fatigue damage estimation and for extreme value analysis.

Chapter 2

Measurements from Ships

The analyses carried out in subsequent chapters of the thesis are based on full scale measurements and model tests of container ships. This chapter describes the ships, the equipment installed on board, the data logging procedures and outlines a few of the challenges in collecting data from ships.

2.1 Introduction

The main part of the studied data originates from a 9,400 TEU container ship used as the case ship in the TULCS project. In addition, DNV GL has kindly provided data for three other container ships of 8,600 TEU, 14,000 TEU and 4,400 TEU. All post-processing procedures, such as filtering of the data are described in the subsequent chapters.

The measurements from the four ships have also been used in other studies investigating e.g. fatigue damage and extreme loads. These studies are used as reference and for comparison. In some cases, the installation set-up has been described in earlier publications and those are given as reference here.

2.2 Coordinate System

Throughout the thesis a right-hand Cartesian coordinate system in accordance with Figure 2.1 is used. The origin is defined relative to the aft perpendicular (AP), the baseline (keel) and the centreline as illustrated.

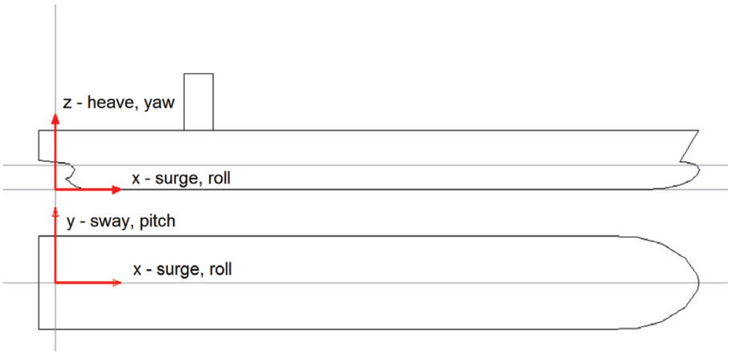

Figure 2.1: *Definition of the coordinate system.*

2.3 The 9,400 TEU Container Ship

The vessel was built in 2006 by Hyundai Heavy Industries in Korea and is owned and operated by CMA CGM. A sister ship is pictured in Figure 2.2.

Figure 2.2: *Sister ship of the TULCS case ship. Photo by CMA CGM.*

The ship previously served as the case ship for the joint industry project Lashing@Sea[1]. For the TULCS project additional measurement equipment was installed on board. Bigger ships have entered into operation since the initiation of the TULCS project, and today a 9,400 TEU ship cannot really be considered an ultra large container ship. However, the ship is of sufficient size to provide useful data for the analyses carried out in relation to hydro-elastic effects in ultra large container ships. The ship has a bow flare angle of about 45 deg (determined in accordance with Det Norske Veritas, 2013a). Its primary data and main dimensions are listed in Table 2.1.

As described in the following the ship is equipped with motion sensors, strain gauges and several systems for estimating the sea state. Furthermore, hindcast sea state data is available for relevant periods of the ship's operation.

During the TULCS project the ship traded on a route between the North Sea in Europe and the Sea of China. From the full data set, comprising a couple of years of measure-

---

[1] `http://www.dft.gov.uk/mca/19717-20-tm---executive_summary.pdf`

Deadweight	113,000 ton
GT	99,500 ton
L_{oa}	349.0 m
L_{pp}	333.4 m
Rule length	329.7 m
Beam	42.8 m
Max draught	14.5 m
Speed	25.4 knots

Table 2.1: *Principal dimensions for the 9,400 TEU container ship.*

ments, five 24-hour data periods, all recorded during 2011, were available for the present study. The data sets were chosen from the main criteria of all sensors being on-line at the same time, reasonably constant navigational conditions (speed, course, draft, etc.) and moderate to rough sea conditions.

The measurements from the 9,400 TEU ship are illustrated in Appendix A.1 and the illustration and specifications of the equipment installed on board are given in Appendix B.1. Analyses of the data from the 9,400 TEU ship appear in Chapters 3, 4, 5, 6, 7, 8, 9, 10 and 11.

2.3.1 *Navigational information*

The navigational data from the ship (position, heading, course, speed, water depth, wind and current information) is obtained from the existing Electronic Chart Display and Information System (ECDIS) on the bridge. See also Table A.1 in Appendix A.1.2 for information of the measured parameters. The ship's compass heading is from the gyro compass. Compass heading, course over ground and wind direction are given in traditional compass rose style with 0 deg being north. Wind speed and direction are not corrected for the speed and heading of the ship. The sea current direction and speed are measured relative to the ship speed and heading.

2.3.2 *Directional wave radar*

Sea state information is obtained from the Wave Monitoring System II (WaMoS II)[2]. To avoid interference with the existing radars, compass and communication antennas on board the WaMoS radar antenna was installed on top the wheelhouse deck as illustrated in Appendix B.1, Figure B.1 and B.2 about 45 m above sea level and with a viewing angle of 260 deg. The wiring diagram is illustrated in Figure B.3.

The raw radar images are processed real-time by a separate on-board computer on the bridge. The PC is installed with the WinWaMoS software and controls the antenna, treats the raw data images, analyses data and determines the sea state statistical parameters, which are displayed and stored. The sea state parameters are fitted with a Jonswap spectrum. According to Fresser, 2011 the system is capable of detecting wave lengths between 15-600 m and wave periods between 4-20 seconds. The statistics are displayed on the PC along with estimated wave spectrum and ECDIS data as shown in Figure 2.3. The data processing flowchart is illustrated in Figure B.4 and the working principle of the directional wave radar is further described in Chapter 3 concerning sea state estimation.

---

[2] `http://www.oceanwaves.de`

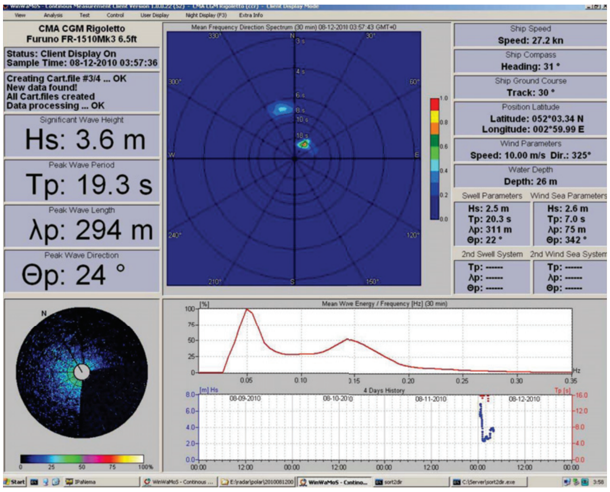

CMA CGM Rigoletto
Furuno FR-1510Mk3 6.5ft

Status: Client Display On
Sample Time: 08-12-2010 03:57:36

Creating Cart.file #3/4 ... OK
New data found!
All Cart.files created
Data processing ... OK

Significant Wave Height: Hs: 3.6 m
Peak Wave Period: Tp: 19.3 s
Peak Wave Length: λp: 294 m
Peak Wave Direction: Θp: 24 °

Ship Speed: Speed: 27.2 kn
Ship Compass: Heading: 31 °
Ship Ground Course: Track: 30 °
Position Latitude: Latitude: 052°03.34 N Longitude: 002°59.99 E
Wind Parameters: Speed: 10.00 m/s Dir.: 325°
Water Depth: Depth: 26 m

Swell Parameters: Hs: 2.5 m Tp: 20.3 s λp: 311 m Θp: 22 °
Wind Sea Parameters: Hs: 2.6 m Tp: 7.0 s λp: 75 m Θp: 342 °
2nd Swell System: Tp: ------ λp: ------ Θp: ------
2nd Wind Sea System: Tp: ------ λp: ------ Θp: ------

View
Analysis
Test
Control
User Display
Night Display (F3)
Extra Info
Mean Frequency Direction Spectrum (30 min) 08-12-2010 03:57:43 GMT+0
N
S
W
E
30°
60°
120°
150°
210°
240°
300°
330°
3 s
4 s
6 s
8 s
10 s
18 s
1.0
0.8
0.6
0.4
0.2
0.0
Mean Wave Energy / Frequency [Hz] (30 min)
[%]
100
75
50
25
0
0.05
0.10
0.15
0.20
0.25
0.30
0.35
Hz
4 Days History
[m] Hs
Tp [s]
08-09-2010
08-10-2010
08-11-2010
08-12-2010

Figure 2.3: Example of the display on the WaMoS PC screen on board the 9,400 TEU container ship. Illustration from Fresser, 2011.

The WaMoS system logs the sea state parameters every 5 minutes averaged over 20 minutes. For the TULCS project WaMoS provides the data given in Table A.2 in Appendix A.1 where the recorded wave parameters are also presented. The swell and the wind generated components are separated by WaMoS based on the estimated peak period, T_p. For the analysis in the TULCS project this value is set to 10 s, i.e. for T_p smaller than 10 s the sea state is assumed to be wind driven and if T_p is larger than 10 s the system is considered to be swell driven. The wave direction relative to the ship can be derived from the WaMoS system in combination with the ECDIS data.

2.3.3 *Down-looking wave radar*

The WaMoS radar system is supplemented by a WaveGuide System by the Dutch company Radac. The system is installed in the bow of the ship and consists of two radar sensors located as illustrated in Figure B.5 about 17 m above sea level. The port side sensor is illustrated in Figure B.6. The Radac system measures the distance between the device and the sea surface and includes a motion sensor which measures the acceleration at the position of the particular radar. The system performs a double-integration of the acceleration signal to obtain the absolute wave elevation which is logged at 20 Hz. It is noted, that only the wave elevation can be obtained; the relative heading is not known and the wave period can only be determined in the encounter domain.

2.3.4 *Hindcast wave data*

For the 9,400 TEU ship hindcast data was provided by Deutscher Wetterdienst on request for the relevant GPS positions on the considered voyage parts. Data is available for the wind speed and direction, the current speed and direction and the height, period and direction of the wind driven sea and the swell component. The hindcast data for wind and waves is given in Appendix A.1.3.

2.3.5 *Accelerations*

Accelerations on board are measured with 11 six-degrees-of-freedom accelerometers measuring the vertical, horizontal and rotational accelerations. The detailed specifications of the accelerometers are given in Figure B.8. The sampling rate is 20 Hz. The sensors are located on board the ship as illustrated in Figure 2.4. Only measurements from the two accelerometers in the bow (frame 154) are utilised throughout this study and their coordinates are given in Table 2.2. The definitions of the ship motions and sign conventions are listed in Table B.1.

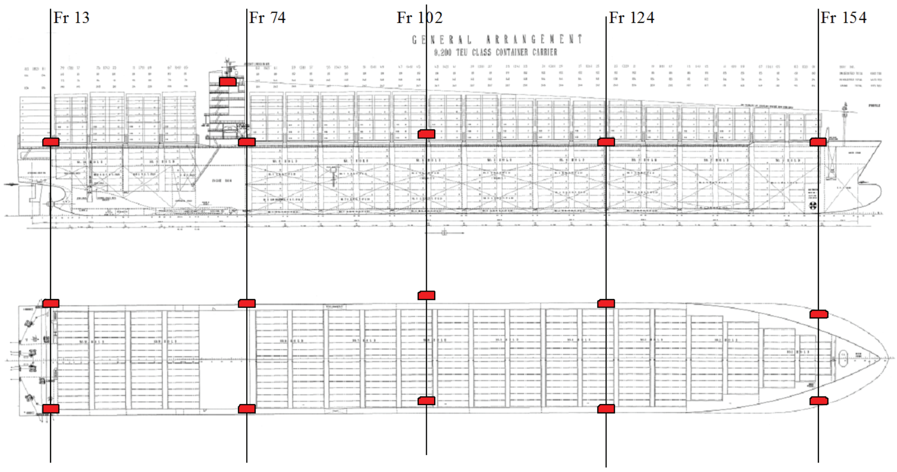

Figure 2.4: *Acceleration sensor set-up on board the 9,400 TEU container ship. Illustration from Koning, 2007.*

	x-coordinate	**y-coordinate**	**z-coordinate**
Accelerometer SB frame 154	318.10 m	-13.99 m	24.0 m
Accelerometer PS frame 154	318.10 m	13.99 m	24.0 m

Table 2.2: *Location of the accelerometers mounted in the bow of the 9,400 TEU ship.*

2.3.6 *Hull girder loads*

In order to measure the hull girder loads the ship is equipped with five sets of long-base strain gauges in hold 8 and 6 (frame 74-75 and 101-102) as illustrated in Figure 2.5.

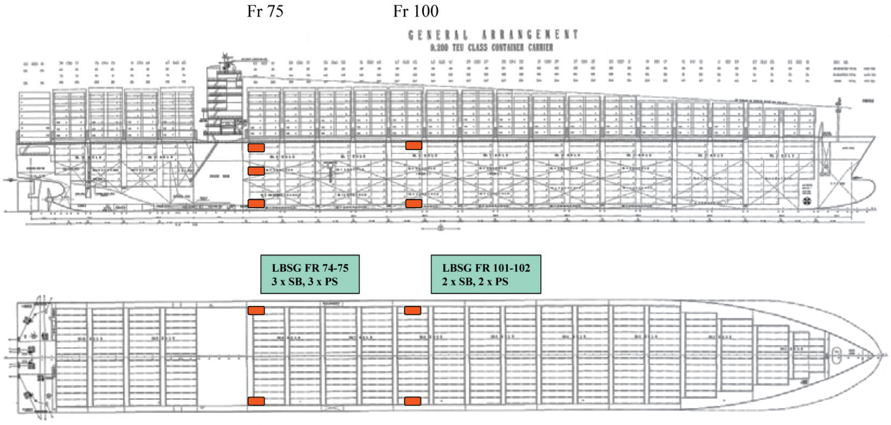

Figure 2.5: *Position of the strain gauges on board the 9,400 TEU container ship. Illustration from Koning, 2007.*

The principle of the long-base strain gauge is that the displacement is measured over a 2,000 mm steel rod, see Figure B.9. The rod is made of steel with the same thermal expansion factor as the ship structure to avoid the influence of temperature differences. The dynamic range is ± 5 mm and the sample rate of the strain gauge measurements is 20 Hz. The specifications of the strain gauges are given in Figure B.10. Only measurements from the set of strain gauges amidships (frame 102) are utilised in this study. Their location is in the passageway close to the deck amidships as illustrated in Figure B.11 and the coordinates are given in Table 2.3. The strain gauge in port side is pictured in Figure B.12.

	x-coordinate	**y-coordinate**	**z-coordinate**
Strain gauge SB frame 102	167.20 m	-19.25 m	25.70 m
Strain gauge PS frame 102	167.20 m	19.25 m	25.70 m

Table 2.3: *Location of long-base strain gauges at frame 102 (amidships) in ship local coordinate system.*

The strain gauges measure microstrain i.e. the deformation of the steel rod comprising the strain gauge. The strain is converted into stress using a modulus of elasticity of 210 GPa corresponding to normal ship building steel. Compressive strain is negative and thus a hogging condition yields positive strain values while the sagging condition yields negative values for the strain gauges in the deck. The strain gauge measurements contain contributions from horizontal and vertical bending as well as torsion, and it is not immediately possible to distinguish the contributions.

Eight strain gauges are installed in the bow of the ship to obtain an indication of the pressure loads in the bow flare area during slamming events. The strain gauges (four in each side) are of the Wheatstone bridge-type (see Figure B.13) and located at the mid longitudinal between the second deck and the first stringer. This is the highest section in the bow flare which is longitudinally stiffened and the location is also close to the part with largest flare angle as illustrated in Figure B.14.

2.3.7 *Model tests*

As part of the TULCS project (WP 6) model tests were carried out with a segmented, flexible model of the 9,400 TEU ship, see Figure 2.6, in the model basin at Canal de Experiencias Hidrodinámical de el Pardo (CEHIPAR), Madrid, Spain. The model is about 4.5 m long which gives a scale of 1:80. The CEHIPAR model basin is rectangular (150 m x 30 m) with a wave generator (consisting of individually controlled flaps of 0.50 m wide with a hinge depth of 3.0 m) on the short side.

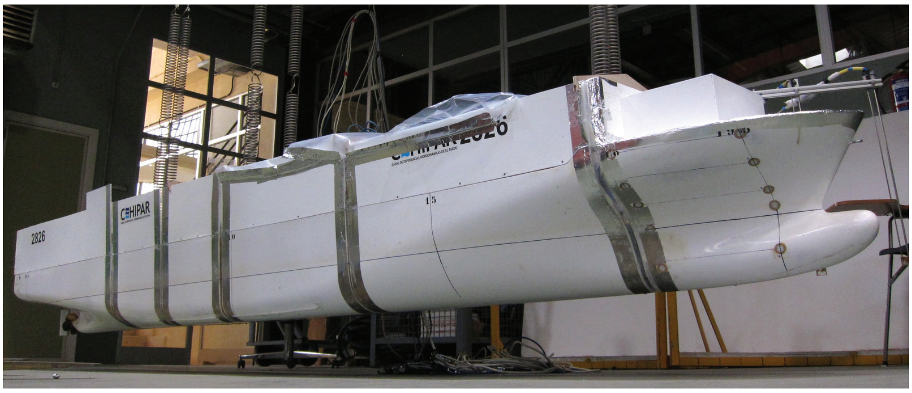

Figure 2.6: *Flexible ship model at CEHIPAR. Photo by Camille Fresser.*

The model consists of six segments held together by a flexible aluminium backbone beam. The beam is designed to represent the fundamental mode shapes of the lowest four eigenmodes of the full scale ship in the pure torsion mode, combined torsion, horizontal bending modes and the vertical bending mode. The model is extensively instrumented with strain gauges, accelerometers and pressure gauges for validation of the seakeeping codes and hydro-elastic models developed within the TULCS project for both the rigid and flexible modes and to provide data for verification of springing and whipping in the related work packages.

The model is self-propelled and the tests were carried out in regular and irregular waves in head and oblique seas. In this study, only the measurements from amidships are used. As shown in Table 2.3 the strain gauges amidships on the real ship are located at $x = 167.2$ m. For the model, the cut amidships is located at $x = 160.8$ m. The measurements are scaled to full scale and the strain converted to the vertical bending moment by CEHIPAR.

2.3.8 *Data format and errors*

The data is logged on board on two different computers. One computer uses local Amsterdam time and the the other is set to UTC (Coordinated Universal Time). Thus, the two different sets of time series (accelerations, strains and Radac data and the navigational and wave radar data, respectively) are offset by 1 or 2 hours depending on the daylight savings time. This has been taken into account when fusing data from the two data sets.

Directional wave radars are generally inaccurate for the wave height estimate in particular, see e.g. Stredulinsky and Thornhill, 2011, while wave direction and period is believed to be more accurately estimated. For the TULCS data the over-estimation of H_s was concluded by SIRENHA to be largest at high sea states, and H_s in the 3-5 m range is thought to be the most reliable region. See also Chapter 3.

2.4 The 8,600 TEU Container Ship

The 8,600 TEU ship was originally selected by Det Norske Veritas for a measurement campaign focusing on springing and whipping because of the ship's large design speed of almost 29 knots and very large bow flare angle of 58 deg (determined according to Det Norske Veritas, 2013a). The ship was built in 2009 by Hyundai Heavy Industries and its principal dimensions are given in Table 2.4.

Deadweight	95,810 ton
GT	94,511 ton
L_{oa}	339.6 m
L_{pp}	322.6 m
Rule length	318.4 m
Beam	45.6 m
Max draught	14.5 m
Speed	28.6 knots
Block coefficient	0.621

Table 2.4: *Principal dimensions for the 8,600 TEU container ship.*

The ship is operated on the Asia - Europe route and the measurement campaign started in 2009 when the ship was built. The measurement system is described in e.g. Heggelund et al., 2011 and Mondher, 2012, but a brief description is also included here.

The measured data is illustrated in Appendix A.2 and information about the location of the measurement equipment is given in Appendix B.2. Data from the 8,600 TEU ship is used in Chapters 5, 6, 8 and 9.

2.4.1 *Navigational data and sea state*

Seven days with high hull girder strain levels were selected for the analyses. There are no sea state measurements available for the 8,600 TEU ship, but the wind speed and direction (when available) can be used to give a rough estimate of the sea state, cf. Barhoumi and Storhaug, 2013. The wind speed and direction are given relative to the ship and not corrected for ship speed and heading. GPS heading, course over ground, speed over ground, speed trough water, wind speed and wind direction are given in Appendix A.2.2 for the days when the information was available.

2.4.2 *Hull girder loads*

The measurement equipment is provided by the Norwegian company Light Structures which is one of the few providers of hull monitoring systems approved by DNV GL for the HMON class notation (see Det Norske Veritas, 2013b).

The strains are measured using fibre optic strain sensors mounted amidships in the deck in port and starboard side, respectively. They are uni-axial and measure strains in the longitudinal direction only. Their locations are given in Table 2.5.

	x-coordinate	**y-coordinate**	**z-coordinate**
Strain gauge SB	Amidships	-22.29 m	24.34 m
Strain gauge PS	Amidships	22.29 m	24.34 m

Table 2.5: *Location of the strain gauges on 8,600 TEU container ship.*

The sensors are located between frame 101 and 102. The location of the strain gauges amidships is illustrated in Appendix B.2, Figure B.15 showing the sensors on the starboard side of the vessel. Sensors are placed symmetrically on the port side of the vessel. The deck sensors are placed on the web of the stiffener as seen in Figure B.16. Tensile stress is positive.

2.4.3 *Data format and errors*

The data is stored on board in binary data files sampled at 42 Hz. Statistical files containing the 5 minute- and 30-minute statistics are extracted from the measurements and stored correspondingly. The statistical data contains the average, min, max, standard deviation, etc, depending on the response considered. The fatigue damage is estimated on-line using rainflow counting and the rainflow data is stored in the statistical files. In this thesis, the statistical files are only used to identify interesting time periods of high response levels. The maximum stress for 2010 and 2011 from the 30 minute statistical files can be found in Figures A.147 and A.148 in Appendix A.2. It is noted that the SB side sensor consistently give higher measured stresses than the PS sensor for reasons not known.

Every week the system overwrites old raw files (the time series sampled at 42 Hz) with new ones, so the complete set of time series is not available for the full measurement period due to lack of regular backup. For several of the days considered here the GPS and ship speed data, respectively, are missing. The wind sensor was out of operation most of the time of consideration.

2.5 The 14,000 TEU Container Ship

A limited data set from a container ship with a capacity of about 14,000 TEU was available for this study. The approximate main dimensions of the vessel are given in Table 2.6.

Length	366 m
Beam	51 m
Draught	16 m
Speed	24 knots

Table 2.6: *Principal dimensions for the 14,000 TEU container ship.*

The ship features a twin-island design where the bridge is located forward and the engine room aft of amidships. The ship is equipped with an on-board decision support system measuring global and local hull girder loads. For the 14,000 TEU ship the recorded data is illustrated in Appendix A.3 and data from the 14,000 TEU ship is used in Chapters 5, 8 and 9.

2.5.1 *Navigational data and sea state*

The position, heading, course, ship speed, wind speed and wind direction is logged every 10 minutes. The ship does not have a system for measuring the sea state installed. The position and navigational data is only available for one of the two days of operation considered here.

2.5.2 *Hull girder loads*

Strains are measured approximately amidships in the deck in port and starboard side. The data is logged at 50 Hz, but has not been continuously logged for storage capacity reasons. Responses exceeding prescribed levels trigger storage of all measurements. When an interesting event is detected the 900 seconds prior to the event are additionally stored.

2.6 The 4,400 TEU Container Ship

The smallest container ship is a 4,400 TEU Panamax ship, and the approximate main dimensions of the vessel are given in Table 2.7. The ship has a small bow flare angle compared to three larger container ships.

Deadweight	47,754 ton
L_{oa}	294.0 m
L_{pp}	281.0 m
Beam	32.3 m
Max draught	10.8 m
Speed	23 knots
Block coefficient	0.69

Table 2.7: *Principal dimensions for the 4,400 TEU container ship.*

The ship was built in 2003 and operates in a trade on the North Atlantic between Canada, UK, Germany and France cf. Storhaug and Moe, 2007. It has been equipped with a hull stress monitoring system supplied Light Structures which is in accordance with the DNV guidelines for hull monitoring systems, Det Norske Veritas, 2013b. Further information about the installed system can be found in Storhaug and Moe, 2007. The sea state information is derived from a directional wave radar supplied by the Norwegian manufacturer Miros, cf Mathisen et al., 2009.

Data from the 4,400 TEU ship is used in Chapters 5, 8 and 9.

2.7 Faults and Uncertainties

Data from ships can be collected from existing systems on board, such as the ECDIS system, the loading computer or from sensors installed for a specific purpose. Depending on the installations and sensors on board the ship, the number of parameters which are logged or possible to log vary from ship to ship, but some new ships have a large amount of sensors installed. For some sensors, the sampling frequency is high and large amounts of data can potentially be generated in short time.

Collecting and recording data on board ships is a challenging task and made further complicated and expensive by the fact that most ships are relatively far from the shore the majority of the time. Installation of the equipment must be timed when ships are in the dock or port and data must be transferred either continuously via costly and bandwidth limited satellite connections or stored on large hard drives until it can be sent to shore.

For all the ships considered here the monitoring is faulty at times. The most common problem is that not all measurement subsystems are on-line at the same time, i.e. motions and strains may be available, but the navigational data or the wave radar is off-line.

Sensor measurements themselves can be uncertain due to bad calibration, drift, temperature effects etc., but sensors can also fail completely. If the data is simply stored on board and only being transferred to shore at longer intervals faulty measurements can take a long time to be detected.

No standards exist about how to log and store data on board ships, and the four ships considered here all have different systems on board, different data formats and different sample rates.

Chapter 3

Sea State Estimation

This chapter describes different means to obtain statistical knowledge of the sea state encountered by a ship. The knowledge is fundamental input for on-board decision support systems, since all analyses as well as predictions of ship responses can be made more accurate and reliable with accurate information of the current sea state. Various means of estimating the sea state are described, partly based on (Nielsen et al., 2013). The wave buoy analogy is described and a conceptual method to select the appropriate ship responses for the sea state estimation using the wave buoy analogy is outlined (Andersen and Storhaug, 2012).

3.1 Introduction

There are several ways to utilise estimated wave parameters or a directional wave spectrum on board a ship, but obviously the accuracy will affect the usefulness of the estimate in the desired application. Knowledge of the on-site sea state is crucial with regards to e.g.:

- Evaluation of operational alternatives, in a given seaway, to select the safest speed and heading combination predicted by on-board decision support systems.
- Assessment of the wave resistance on the ship for performance monitoring for determining the optimum time for cleaning of the hull and propeller.
- Voyage reporting and evaluation.
- Input to operational profiles for specific trades and future ship designs.
- Analysis of ship response measurements of e.g. extreme loads as illustrated in Chapters 8 and 9.

As indicated, the use of a sea state estimation system can be linked to both safety aspects and economy of operation. Examples of safety aspects can be service restrictions. A vessel may be instructed to reduce speed or change course or, for e.g. offshore service vessels, discontinue an operation when the sea state exceeds a predefined limit. Examples of the economy aspects in operation, fuel consumption and maintenance could be to e.g. estimate the speed reduction due to waves in order to determine the speed in calm water and thereby the performance of the ship.

The estimation of sea states is associated with uncertainty to a smaller or larger degree. Ocean waves are by nature irregular, non-stationary, multi-directional, non-linear and influenced by wind, current and bottom bathymetry. Anything but an approximate statistical description of the sea state is not possible to give.

The sea state can be estimated using several fundamentally different methods yielding either the wave parameters (i.e. the wave height, period and direction relative to the ship) or a 2D or 3D directional wave spectrum. The means listed here is not an exhaustive summary of means to estimate the sea state on board a ship and some means are only described briefly to provide a general overview.

3.2 Visual Observations

At least in daylight, the sea state can be estimated from the ship by the crew on board. The wave height can be estimated visually. Except from swell, ocean waves are multi-directional, and hence the mean wave direction relative to the ship and the wave period are difficult to estimate visually from ships. Navigators are trained to estimate the sea state visually, and the result is often reported in the log book or sent to the shore in the noon report.

3.3 Meteorological Models

Like the weather, the sea state can also be forecasted by the meteorological models. Typical providers of weather forecasts are the national meteorological institutions. Weather and ocean forecasts are used as input by many on-board systems for route planning to select the optimum route to avoid adverse weather, to predict fuel consumption during a trip, etc. Sea state data can also be made available by these providers retrospectively as hindcast data.

3.4 Satellite Measurements

The wave height can be measured using altimeters installed on satellites. The satellites are located in orbits approximately 700-800 km above the surface of the Earth. The wave height is in the order of meters so the satellite measurements must be very accurate in order to provide a useful estimate of the wave parameters. Today, satellite measurements are not available real-time and this restrict their use for real-time decision support.

3.5 Directional Wave Radars

As described in Section 2.3 the wave environment around the ship can be estimated by a directional wave radar. The wave radar technology is based on an X-band (microwave spectrum) directional radar system. The wave radar scans the surface like a conventional radar and uses the backscatter of radar energy from the ocean surface to create images from which the wave properties are extracted by some associated software. The radar image is created from the wind-generated roughness (ripples) on the sea surface and not the actual waves. The accuracy is influenced by the surface roughness and if there is little wind the system will have difficulties in detecting the waves. The working principle of a directional wave radar for shipboard use is further described by e.g. Stredulinsky and Thornhill, 2011.

The directional wave radars are generally believed to be capable of estimating the wave direction and period quite accurately, while the estimate of the significant wave height can be more inaccurate, cf. e.g. Stredulinsky and Thornhill, 2011, since it relies on accurate calibration of the system. The motions and forward speed of a ship introduce extra uncertainties compared to using the directional wave radar from a fixed platform. In the available literature, the wave radars are generally thought to overestimate the wave height. For a 2,800 TEU vessel Storhaug and Heggelund, 2008 found that the wave radar overestimated the wave height in higher sea states. The overestimation was adjusted for by multiplying the measured wave heights with a factor of 0.7. For a the,400 TEU vessel the difference between wave buoys and wave radar measurements was smaller but still with some overestimation in lower sea states. During the TULCS project overestimation of the wave height was also observed for the wave radar installed on board the 9,400 TEU ship and was more pronounced for high sea states. A significant wave height of 3-5 m was thought to be the most reliable region for the directional wave radar on board the TULCS ship.

3.6 Down-Looking Wave Radar

As described in Section 2.3 the relative wave height can also be measured using radars aimed directly down at the sea surface. These are often mounted on the bow or bridge of the ships. The advantage of the system is that it ”sees” all waves, independently of wave length or, equivalently, wave frequency. However, in bad weather, where water spray is present in the air, the measurements can become inaccurate because the radar sees the spray in the air as the sea surface. Waves refracted from the ship’s bow and sides also affect the estimate. Otherwise, the system effectively measures the distance from the radar to the sea surface and must be combined with a motion sensor in order to compensate from the ship’s motion and derive the wave height. The system is not capable of estimating the relative wave direction. The estimation of the wave period can be obtained in the encounter domain from spectral analysis of the wave elevation signal. Using the ship speed and relative wave direction - if available - the wave period can be transformed into the ”true” frequency domain.

3.7 Wave Buoys

Wave buoys are used extensively by weather services and providers of ocean wave statistics. There exist different types of wave rider buoys and one is seen in Figure 3.1. Their common concept of functionality is that they measure the motions of the buoy using accelerometers and gyros. The directional wave spectrum is determined from combined use of motions of the buoy and its transfer functions (RAOs). Some buoys are battery powered and some a solar powered. Due to their long-term employment wave rider buoys are moored so unless the ship is close to a wave rider buoy it cannot be used for on-site estimation of the sea state. Smaller wave buys are availably for temporary employment for measurement campaigns e.g. in connection with sea trials as done by e.g. Nielsen and Stredulinsky, 2012 and Stredulinsky and Thornhill, 2011.

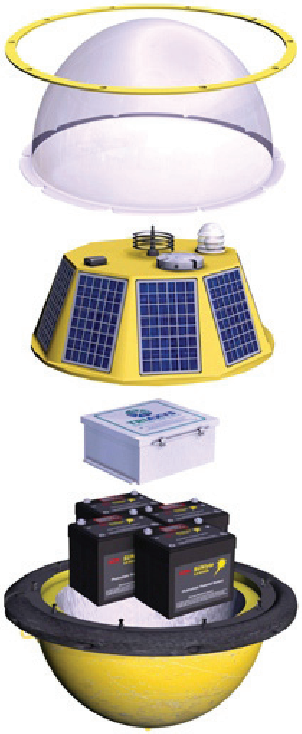

Figure 3.1: *A TRIAXYS^{TM}solar powered directional wave buoy.*

3.8 Wave Buoy Analogy

In the following, the wave buoy analogy is described. The basic concept of the method is to use the ship as a wave buoy and continuously compute the wave spectrum from the motions and transfer functions of the ship.

A thorough description of the method will not be given here. The wave buoy analogy has been developed and refined by e.g. Iseki and Terada, 2002, Tannuri et al., 2003, Nielsen, 2005, Nielsen, 2006, Pascoal et al., 2007 and Nielsen, 2008. The wave spectrum can be estimated using either a parametric or a non-parametric method. For both methods, the on-site directional wave spectrum is estimated based on the measured global responses of the ship and the linear complex-valued Response Amplitude Operators (RAOs) for the specific ship. The waves as well as the ship responses are considered being stationary, stochastic processes. Similar to the wave buoy more than one measured response is used in the estimation and a combination of three responses has been found to be the optimum. In order to determine the directional wave spectrum at least one response must have port/starboard asymmetry (e.g. roll or sway). Since measurements of more than three responses are generally available at the same time a proper choice of the optimal combination of three responses is essential and should preferably be made automatically based on the time series at hand. The selection procedure of the most suitable response combination for the wave spectrum estimation is described later in this section.

For any ship response, R, a complex-valued linear transfer function $\Phi(\omega)$ can be calculated as function of the wave frequency, ω (or the encounter frequency ω_e). This is normally done for a discrete number of relative heading angles χ. The RAOs must implicitly be calculated for each set of operational parameters (loading condition and speed). The theoretical relationship between the ship response frequency spectrum for the i'th response $S_{R,i}(\omega_e)$ and the wave power spectrum $E(\omega)$ is generally given by, e.g. Bhattacharyya, 1978:

$$S_{R,i}(\omega_e) = |\Phi_i(\omega)|^2 \, E(\omega) \left| \frac{\mathrm{d}\omega}{\mathrm{d}\omega_e} \right| \tag{3.1}$$

For the wave spectrum estimation the RAOs play an essential role and must thus be calculated as accurately as possible to yield realistic wave spectrum estimations. In a short-crested seaway where the wave spectral energy density is not only a function of frequency but also of direction the RAOs can be calculated as function of the wave direction relative to the ship's heading χ and thus Eq. (3.1) reads:

$$S_{R,i}(\omega_e) = \int_{-\pi}^{\pi} |\Phi_{R,i}(\omega,\chi)|^2 \, E(\omega,\chi) \left| \frac{\mathrm{d}\omega}{\mathrm{d}\omega_e} \right| d\chi \tag{3.2}$$

In matrix notation Eq. (3.2) can be written as:

$$\mathbf{b} = \mathbf{Af(x)} \tag{3.3}$$

where $\mathbf{f(x)}$ represents the unknown values of the wave spectrum $E(\omega,\chi)$ and the vector $\mathbf{b}$ contains the elements of the response spectra $S_{R,i}(\omega_e)$. The elements of the coefficient matrix $\mathbf{A}$ correspond to the products of the transfer functions in Eq. (3.2). In principle, Eq. (3.2) can be solved for $\mathbf{x}$ by minimising

$$\boldsymbol{\Upsilon}^2(\mathbf{x}) \equiv \|\mathbf{Af(x)\text{-}b}\|^2 \tag{3.4}$$

in a least squares sense, where $\| \cdot \|$ denotes the L_2 norm. Eq. (3.4) can then be solved using either parametric or non-parametric (Bayesian) modelling as described later.

The transfer functions can be calculated by the use of strip-theory or by more sophisticated 3D potential flow panel codes. Alternatively, the transfer functions can be derived from model tests. The response spectrum $S_{R,i}(\omega_e)$ as function of the ship's wave encounter frequency can e.g. be obtained from a time series of the response by the use of Fast Fourier Transformation (FFT) or Multivariable Autoregressive Modelling (MVAR) as described by Nielsen, 2005. The outcome of the FFT and thereby the wave estimation is sensitive to the choices of segmentation and window size and, since the selection of response signals must be able to run on-line, the spectral analysis must be carried out without any manual input of e.g. window size and hence MVAR can be favourable since in the latter procedure no manual input is needed. If purely using spectral energy density considerations in the estimation of sea state parameters as done by e.g. Montazeri and Nielsen, 2014 there is no need for smoothing functions since only the spectral moments of the response are utilised. Examples of the response spectra of the measured ship responses heave, sway, roll, pitch and the vertical bending moment amidships from the 9,400 TEU ship are given in Appendix A.1.4 together with the corresponding RAOs. The response spectra are derived from one hour of data from 02 October 2011 at 11:00 using FFT. All RAOs are calculated for a draft of 14.5 m and speed of 15 knots roughly corresponding to the operational conditions on 02 October 2011.

3.8.1 *Parametric modelling*

Using parametric modelling Eq. (3.4) can be solved directly as an optimisation problem where the directional wave spectrum $\mathbf{f(x)} \equiv E(\omega, \chi)$ is introduced as a parametrised wave spectrum. This can be uni-modal or multi-modal. Nielsen and Stredulinsky, 2012 used a 3-modal, five-parameter wave spectrum, which allows for estimation of mixed seas with swell and wind waves:

$$\begin{aligned} E(\omega,\chi) =& \sum_{i=1}^{3} E_i(\omega) G_i(\omega,\chi) \\ E_i(\omega) =& \frac{1}{4}\left(\frac{4\lambda_i+1}{4}\omega_{p,i}^4\right)^{\lambda_i} \frac{H_{s,i}^2}{\Gamma(\lambda_i)\omega^{4\lambda_i+1}} \times \\ & \exp\left[-\frac{4\lambda_i+1}{4}\left(\frac{\omega_{p,i}}{\omega}\right)^4\right] \\ G_i(\omega,\chi) =& A(s_i)\cos^{2s,i}\left(\frac{\chi-\chi_{mean,i}}{2}\right) \\ A(s) =& \frac{2^{2s-1}\Gamma^2(s+1)}{G\Gamma(2s+1)} \end{aligned} \tag{3.5}$$

In principle, any other type of parametrised wave spectrum can be used. In Eq. (3.5) $E_i(\omega)$ is a uni-directional (one-dimensional) wave spectrum with peak frequency $\omega_{p,i}$, significant wave height $H_{s,i}$ and shape parameter λ_i. $G_i(\omega, \chi)$ is the directional distribution function where χ_{mean} is the mean relative wave direction. $A(s)$ is a constant to secure normalisation using the Gamma function and the spreading parameter s. When inserting Eq. (3.5) into Eq. (3.4) one ends up with a non-linear optimisation problem which can e.g. be solved in Matlab by invoking the standard "fmincon" function. Examples of the outcome of the parametric modelling method are given for the 9,400 TEU ship for 12 August and 02 October 2011 based on 20 minutes of data in Figure 3.2 3.3 and for the response combination {sway, heave, pitch}.

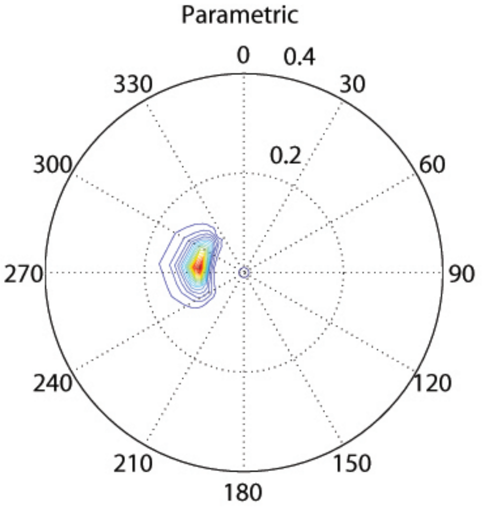

Figure 3.2: *Directional wave spectrum estimated using the parametric modelling on 12 August 2011 at 16 hours. Absolute ship heading is 0 deg.*

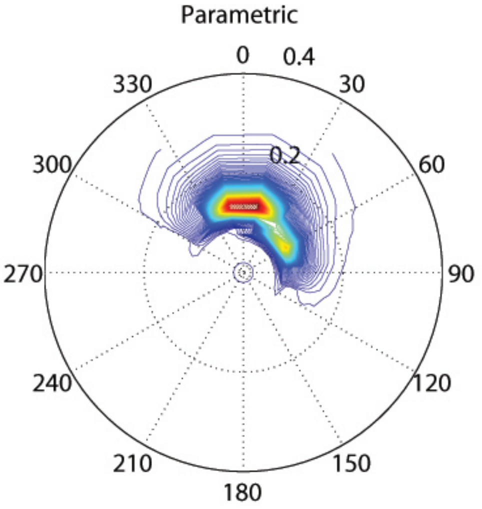

Figure 3.3: *Directional wave spectrum estimated using the parametric modelling on 02 October 2011 at 11 hours. Absolute ship heading is 0 deg.*

3.8.2 *Bayesian modelling*

When the wave spectrum is estimated by Bayesian modelling, each spectral component is solved for which makes the equation system Eq. (3.4) highly under-determined, or, in other words, unstable. However, a stable solution can be found by introducing prior information. The two assumptions introduced are 1) that the directional wave spectrum is changing smoothly with frequency and direction and 2) that the wave spectral energy goes towards zero for very high and very low wave frequencies. In the Bayesian approach the solution $\mathbf{x}$ is obtained by maximisation of the product of a likelihood function and the prior distributions. Details are found in Iseki and Terada, 2002, Nielsen, 2006 and Nielsen, 2008 and in principle any available prior information on e.g. the relative wave heading could be included in the procedure.

The computational effort for the two methods is comparable and they generally produce similar results. Examples of the outcome of the Bayesian modelling method are given for the 9,400 TEU ship for 12 August and 02 October 2011 based on 20 minutes of data in Figures 3.4 and 3.5 for the response combination {sway, heave, pitch}.

The agreement in this case is good for 12 August but, in this particular case, quite poor for 02 October for reasons not known.

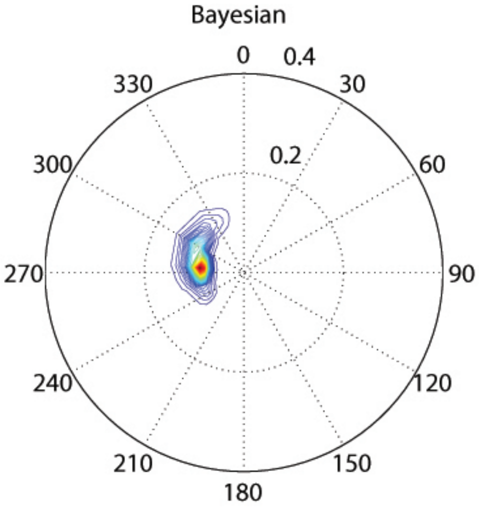

Figure 3.4: *Directional wave spectrum estimated using the Bayesian modelling on 12 August 2011 at 16 hours. Absolute ship heading is 0 deg.*

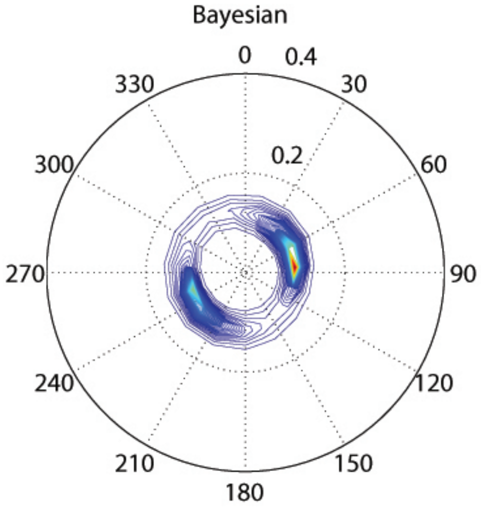

Figure 3.5: *Directional wave spectrum estimated using the Bayesian modelling on 02 October 2011 at 11 hours. Absolute ship heading is 0 deg.*

3.8.3 *Dynamic selection of ship responses for wave spectrum estimation*

Often, measurements of more than three ship responses are available for the sea state estimation. There is no general solution to the optimal choice of response combination for the wave buoy analogy and ideally, the combination should be automatically selected based on the operational and environmental circumstances encountered by the ship at any given time. Furthermore, the selection procedure could take into account the uncertainty of the RAO and measurement for each response in order to improve the reliability of the estimation. In the following, a conceptual procedure to carry out the response selection, taking the uncertainty associated with the RAO into account, is outlined. It is pointed out, that the procedure is conceptual and therefore no results are presented. Preliminary work was carried out by Nielsen et al., 2012.

Initially and before the full directional wave spectrum estimation is carried out, a parametric Pierson-Moskowitz (PM) spectrum could be estimated from each individual ship response. The estimation of the relative wave direction could also be carried out as an initial step as suggested in Nielsen and Iseki, 2012 in order to introduce prior information for the directional wave estimation described above. The one-directional PM spectrum as function of wave frequency, ω, depends on the significant wave height H_s and the mean wave period T_m:

$$E_{PM}(\omega, H_s, T_m) = 173 H_s^2 T_m (\omega T_m)^{-5} e^{-692(\omega T_m)^{-4}}$$

It is noted, that for the PM-spectrum $T_m = 1.087 T_z$, where T_z is the zero-upcrossing period. Taking into account that the amount of energy for each frequency theoretically must be equal on the left and right hand side of Eq. (3.1), an optimisation is carried out for each response by minimising the cost function proposed by Nielsen, 2005:

$$F = \int_0^\infty \left[E_{PM}(\omega)\Phi_i^2(\omega) \left| \frac{\mathrm{d}\omega}{\mathrm{d}\omega_e} \right| - S_i(\omega_e) \right]^2 \mathrm{d}\omega_e \tag{3.6}$$

where $S_i(\omega_e)$ is the response spectrum obtained from spectral analysis of the time series of the i'th response. For the i'th response the optimisation yields the significant wave height $H_{s,i}$ and zero-upcrossing period $T_{z,i}$. Constraints on H_s and T_z can be implemented and reasonable limits of the two parameters are the following:

$$\begin{aligned} 0 < H_s < 15 \text{ [m]} \\ 5 < T_z < 18 \text{ [s]} \end{aligned}$$

Furthermore, the condition, that waves can only have a certain steepness before they break, results in the following constraint, Jensen, 2001:

$$T_z > 8.1\sqrt{\frac{H_s}{g}}$$

where g is the acceleration of gravity. The zero'th spectral moment of the wave energy spectrum $E(\omega)$ is related to the significant wave height H_s:

$$m_0 = \int_0^\infty E(\omega)\mathrm{d}\omega = \left(\frac{H_s}{4}\right)^2 \tag{3.7}$$

By comparing the outcome (i.e. H_s and T_z) of the estimated PM spectrum derived from the time series of each ship response, the combination of three signals with the smallest difference, will be taken as the selected response combination. Similarly, the automatic response selection could be based on residuals as described by Nielsen et al., 2012 and, more recently, by Montazeri and Nielsen, 2014. Furthermore, one of the selected responses for the complete directional wave spectrum estimation must have an asymmetric frequency response function with respect to port/starboard entering waves as mentioned earlier.

The linear transfer functions can be determined using different methods of various degrees of complexity. Linear strip-theory is a computationally fast method, but the effect of reflection of waves by the ship hull is not accounted for in the strip-theory, and in some cases 3-dimensional, linear tools are better suited, although they, due to differences in computational method, often differ from each other, especially with forward speed. The user may also affect the results through the definition of mesh resolution and resolution of frequencies, and the cost of accuracy can be large CPU times.

The uncertainty associated with the RAO is not the same for each response. The roll motion has a non-linear, resonant behaviour and the non-linear viscous damping terms can be complicated to assess and linearise. Furthermore, the roll motion is sensitive to the location of the vertical centre of gravity, which varies with the loading condition. For the horizontal motions sway, surge and yaw no restoring term exists and the utilisation of those responses is furthermore complicated by the influence of the rudder and propeller. The vertical motions heave and pitch are the most straightforward motions to determine RAOs for. The transfer function for the vertical bending moment is also quite accurately determined, but pure vertical bending can be difficult to extract from measurements if torsion is present.

In order to improve the selection procedure the uncertainty associated with the transfer functions for the ship responses could be taken into account. It is assumed that the uncertainty of the RAO for the i'th response $\Phi_{0,i}$ calculated by e.g. strip-theory can be described by the deterministic factor $\epsilon_i(\omega)$, the standard deviation, determined from the uncertainty associated with the calculation of the RAO for the i'th response. Hence, the RAO, Φ_i, for the i'th response will be taken as:

$$\Phi_i(\omega_e) = \Phi_{0,i}(\omega_e)(1 + \epsilon_i u_i)$$

The variable u_i is a standard normal distributed variable. The uncertainty furthermore depends on the encounter angle between the ship and the waves, χ, but this consideration is not taken into account here. Thus Eq. (3.2) becomes:

$$\int_0^\infty S_{R,i}(\omega_e)\mathrm{d}\omega_e = \int_0^\infty |\Phi_i(\omega)|^2 E(\omega)\mathrm{d}\omega = (1 + \epsilon_i u_i)^2 \int_0^\infty |\Phi_{0,i}(\omega)|^2 E(\omega)\mathrm{d}\omega \tag{3.8}$$

A residual function for the i'th response becomes (cf. Eq. (3.8)):

$$G_i = (1 + \epsilon_i u_i)^2 \int_0^\infty \Phi_{0,i}^2(\omega)E_i(\omega)\left|\frac{\mathrm{d}\omega}{\mathrm{d}\omega_e}\right|\mathrm{d}\omega_e - \int_0^\infty S_{R,i}(\omega_e)\mathrm{d}\omega_e$$

where E_i is the parametrised wave spectrum estimated from the i'th response. Rearranging gives, according to Eq. (3.7):

$$m_{0,i} = (1 + \epsilon_i u_i)^2 \left(\frac{H_{s,0,i}}{4}\right)^2$$

where $H_{s,0,i}$ is the significant wave height determined from the i'th response from the minimisation of Eq. (3.6) using $\Phi_{0,i}$.

Thus, the uncertainty of the RAO is first taken into account after the estimation of the PM wave parameters is carried out by minimising F in Eq. (3.6). The key condition for the selection of three suitable ship responses is that the estimated wave parameters, e.g. H_s for the responses are as close as possible, ideally:

$$H_{s,i} = H_{s,j} = H_{s,k} \Longrightarrow m_{0,i} = m_{0,j} = m_{0,k}$$

which leads to

$$H_{s,0,i}(1 + \epsilon_i u_i) = H_{s,0,j}(1 + \epsilon_j u_j) = H_{s,0,k}(1 + \epsilon_k u_k)$$

For each combination of three response signals, i, j and k, a reliability index β can be defined. The selected response combination should thus be the one with the smallest value of β:

$$\beta = \sqrt{u_i^2 + u_j^2 + u_k^2}$$

conditional on:

$$J = (H_{s,i} - H_{s,j})^2 + (H_{s,i} - H_{s,k})^2 + (H_{s,j} - H_{s,k})^2 = 0$$

Thus the present "limit state" function J cannot be negative, but it is zero on the limit and positive elsewhere. The solution can be found using a standard optimisation routine or the First Order Reliability Method. Provided the uncertainties in the measurements can be quantified they can likewise be introduced in the selection procedure.

3.9 Discussion and Conclusions

In Nielsen et al., 2013 different means of sea state estimation from an advancing 9,400 TEU container ship are compared. The means are a directional wave radar, down-looking wave radar and the wave buoy analogy. The results of the sea state estimation carried out in Nielsen et al., 2013 are given in Appendix A.1.5. The agreement between the considered methods is reasonable. Particularly for the mean and peak wave periods, the measurements from the down-looking wave radar were found to be deviating the most. One possible explanation for the deviation in the estimated wave periods could be that the relative wave direction from the directional wave radar was used to transfer the measurements from the down-looking wave radar in the bow encounter domain to the "true" domain.

Hindcast data for the same time periods is also available and is given in Appendix A.1.3. It is not straight forward to compare the hindcast data with the sea state parameters measured on board. For the hindcast data there is a distinction between wind sea and swell which makes it difficult to compare with the significant wave height H_s from the on-board measurements. The directional wave radar also distinguishes between wind sea and swell but the distinction does not seem to be the same for the hindcast data. However, the addition of the wave heights from the wind sea and the swell from the hindcast data corresponds quite well to the significant wave height measured by the directional wave radar. Likewise, the wave periods are difficult to compare but there seems to be some agreement. For the wave period the agreement seems to be good when the wind driven sea dominates.

The wave buoy analogy described here relies on measurements of a number of ship responses and a pre-calculated database of RAOs for the same responses for different speeds, headings and loading conditions. Both the calculated and measured response level must be significant and for a small vessel this would be true for almost all sea states and responses. However, in relatively large seas the responses may be highly non-linear and the estimation is likely to be less accurate. For large vessels, the filtering effect means that low sea states typically do not produce significant response, and it will thus not be possible to accurately estimate the wave height. However, these low sea states may be of less interest, and the estimation may still be useful for higher sea states in relation to safety aspects and economy of operation. The same is true for low wave frequencies as illustrated in Figure 3.6. For large container ships sea states in the range of 3 to 7 m may be the most interesting range of wave heights to be able to estimate accurately, since extreme sea states are often avoided in the ships' route planning.

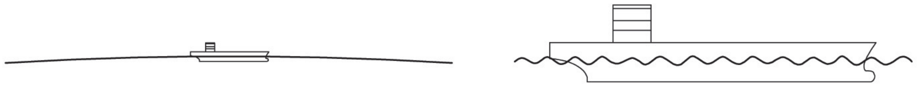

Figure 3.6: Lack of measurable ship response in very low and very high frequency waves. Figure courtesy of Nielsen, 2005.

The accuracy of a sea state estimate using the wave buoy analogy depends on the choice of responses, the accuracy of the transfer functions and the accuracy of the response measurements. This is also discussed by Iseki, 2012, who, similarly to the approach presented here, modelled the error in the transfer functions as Gaussian white noise and added an error matrix **C** composed of products of the response functions and the estimating error matrix to the coefficient matrix **A** in Eq. (3.3):

$$\mathbf{b} = (\mathbf{A}+\mathbf{C})\mathbf{f}(\mathbf{x}) \tag{3.9}$$

However, much work remains in order to determine the uncertainty related to each of the transfer functions $\epsilon_i(\omega)$ to be able assess the accuracy of the estimated wave spectrum.

The accuracy can in some cases be improved by fusing information from different means, e.g. motions and wave radar measurements as done by Stredulinsky and Thornhill, 2011, who fused the directional wave radar measurements with measured ship motions (heave and pitch) in order to improve the wave height estimation. Similarly, Kosleck, 2013 used radar images of the surface elevation for forecasting of the encountered sea states for the just-in-time prediction of an ocean wave field and associated ship motions.

Generally, relatively few ships are equipped with sea state estimation systems. The costs involved in the installation and maintenance of systems for sea state estimation is an important concern. Wave radars are expensive and need regular calibration to stay accurate. Motion sensors are relatively cheap and thus the wave buoy analogy involves less costs than the more hardware-heavy installations.

Chapter 4

Ship Response Prediction using Full Scale Measurements

This chapter is based on Andersen et al., 2013. The focus is on the real-time prediction accuracy of ship responses 5-15 seconds ahead of the measurements. Such results are less applicable in the operation of container ships but are important in e.g. loading/unloading operations at sea or helicopter landings on ships. In this chapter, data from the 9,400 TEU ship is used.

4.1 Introduction

Estimation of ship responses for the time $t > 0$ using the measured responses for $t \leq 0$ is important for various offshore operations as e.g. crane operations for shifting cargo between ships or mobile platforms and helicopter landings offshore. Today, numerous ship responses are often measured continuously during operation and the measurements are available real-time.

The memory effect in wave-induced hydrodynamic responses is usually quite small and of the order 30 seconds. Therefore, measurements older than this do not provide any useful deterministic information for prediction of future responses; neither can the predictions more than 30 seconds ahead in time be made better than what can be obtained by simply using statistical estimations under stationary conditions. The aim of the present study is evaluate conditional processes based on the autocorrelation function for the current stationary, stochastic condition together with real-time measured responses taken just prior to the current time. Hence, procedures needing off-line training like neural networks, principal or minor component analysis and autoregressive procedures are not dealt with here except for some comments regarding similarities with the conditional processes. An interesting discussion of the off-line training procedures can be found in Zhao et al. (2004).

The focus is thus on conditional processes, with some discussion on the auto-regressive predictor and sinusoidal decomposition. In all cases the ship response processes are assumed to be normal distributed stationary, stochastic processes.

4.2 Conditional Processes

Two different schemes are considered. In the first only the last measurement at $t = 0$ is used together with corresponding time derivatives of the response, whereas in the second scheme a number of measured response values at different times prior to $t = 0$ are applied without using time derivatives.

4.2.1 *Conditional process based on known current value*

Consider a normal distributed process $X(t)$ with the corresponding first and second derivative $\dot{X}(t)$ and $\ddot{X}(t)$. It is assumed that all three functions are known (measured or derived from measurements) at $t = 0$. Thereby, the associated conditional processes become normal distributed with the probability density functions:

$$\begin{aligned} p\left(x(t)\left|x(0)=x_0\right.\right) =& \varphi\left(x(t);\mu_0(t),s_0(t)\right), \\ p\left(x(t)\left|x(0)=x_0,\dot{x}(0)=\dot{x}_0\right.\right) =& \varphi\left(x(t);\mu_{00}(t),s_{00}(t)\right), \\ p\left(x(t)\left|x(0)=x_0,\dot{x}(0)=\dot{x}_0,\ddot{x}(0)=\ddot{x}_0\right.\right) =& \varphi\left(x(t);\mu_{000}(t),s_{000}(t)\right) \end{aligned} \tag{4.1}$$

Here, $\varphi\left(x;\mu,s\right)$ denotes the probability density function of a normal distributed variable:

$$\varphi\left(x;\mu,s\right) = \frac{1}{\sqrt{2\pi}s}\exp\left(-\frac{1}{2}\left(\frac{x-\mu}{s}\right)^2\right) \tag{4.2}$$

The conditional mean processes $\mu_0(t), \mu_{00}(t)$ and $\mu_{000}(t)$ in Eq. (4.1) become, respectively

$$\begin{aligned} \mu_0(t) =& E\left[X(t)\left|X(0)=x_0\right.\right] = x_0 r(t), \\ \mu_{00}(t) =& E\left[X(t)\left|X(0)=x_0,\dot{X}(0)=\dot{x}_0\right.\right] = x_0 r(t) + \dot{x}_0\sqrt{\frac{m_0}{m_2}}s(t), \\ \mu_{000}(t) =& E\left[X(t)\left|X(0)=x_0,\dot{X}(0)=\dot{x}_0,\ddot{X}(0)=\ddot{x}_0\right.\right] = \\ & x_0\frac{\alpha}{\alpha-1}\left(r(t)+\frac{1}{\alpha}u(t)\right) + \dot{x}_0\sqrt{\frac{m_0}{m_2}}s(t) + \ddot{x}_0\frac{m_0}{m_2}\frac{1}{\alpha-1}\left(r(t)+u(t)\right) \end{aligned} \tag{4.3}$$

depending on whether the measured response x_0 at $t = 0$ is used only or if the information of the time derivatives $\dot{x}_0$ and $\ddot{x}_0$ at $t = 0$ are included. Due to the normal distribution the most probable response for $t > 0$ becomes the same as the conditional mean process.

The variances of the three conditional processes, Eq. (4.1), become

$$\begin{aligned} s_0^2(t) &= m_0\left\{1-r^2\left(t\right)\right\} \\ s_{00}^2(t) &= m_0\left\{1-r^2\left(t\right)-s^2(t)\right\} \\ s_{000}^2(t) &= m_0\left\{1-r^2\left(t\right)-s^2(t)-\frac{\left(r(t)+u(t)\right)^2}{\alpha-1}\right\} \end{aligned} \tag{4.4}$$

The derivations of Eqs. (4.3)-(4.4) follow directly from the definition of the joint probability density function of dependent normal distributed variables. The first derivation of these results was given by Lindgren, 1970, but several alternative derivations have since been published. Note, that the actual measurements at $t = 0$ do not appear in the expressions in Eqs. (4.4) for the standard deviations $s_0(t), s_{00}(t)$ and $s_{000}(t)$.

In Eqs. (4.3)-(4.4) $r(t), s(t)$ and $u(t)$ are the normalised, time-dependent autocorrelation function $r(t)$ and its first, $s(t)$, and second, $u(t)$, time derivative:

$$\begin{aligned} r(t) &= \frac{1}{m_0} E\left[X(0)X(t)\right], \\ s(t) &= \frac{1}{\sqrt{m_0 m_2}} E\left[\dot{X}(0)X(t)\right] = -\sqrt{\frac{m_0}{m_2}}\dot{r}(t), \\ u(t) &= \frac{1}{m_2} E\left[\ddot{X}(0)X(t)\right] = \frac{m_0}{m_2}\ddot{r}(t) \end{aligned} \tag{4.5}$$

Here, these quantities are expressed in terms of their definition in the time domain, but the corresponding frequency domain definitions using the spectral density, $S(\omega)$, are straightforward.

The normalisations in Eqs. (4.3)-(4.5) make use of the spectral moments m_i of the motion response $X(t)$:

$$m_i = \int_0^\infty \omega^i S(\omega) d\omega \tag{4.6}$$

Furthermore, the bandwidth parameter

$$\alpha = \frac{m_0 m_4}{m_2^2} \tag{4.7}$$

is introduced. Note, that for broad-banded processes $m_4 \to \infty \Rightarrow \alpha \to \infty$. For such cases the inclusion of the second derivative, $\ddot{X}(0)$, does not add any information to the prediction. For the wave process itself this might happen, but ship responses and their first and second time derivatives will usually be more narrow-banded due to the filtering effect. However, as $r(t)$ and $u(t)$ are nearly equal but with opposite sign, the inclusion of the second derivative is only important if α is close to, but not equal to 1.

For an extremely narrow-banded process, $\alpha = 1$, with center frequency ϖ, the variance tends to zero and the response to the deterministic value

$$X(t) = x_0 \cos(\varpi t) + \frac{\dot{x}_0}{\varpi}\sin(\varpi t) \tag{4.8}$$

Numerical results for the standard deviations $s_0(t), s_{00}(t)$ and $s_{000}(t)$ for the vertical wave-induced bending stresses in the deck amidships will be shown later. Response predictions based on $\mu_0(t), \mu_{00}(t), \mu_{000}(t)$ will also be compared to measured time series.

4.2.2 *Conditional process based on a set of known values*

An alternative to conditioning on only the measured response value and its derivatives at $t = 0$ is to use measured values for a set of time values $0 > t_1 > t_2 > .. > t_n$ prior to $t = 0$. The corresponding conditional probability density function is normal distributed:

$$\begin{aligned} &p\left(x(t)\left|x(0)=x_0, x(t_1)=x_1, ..., , x(t_n)=x_n\right.\right)= \\ &\varphi\left(x(t); \mu_n(t), s_n(t)\right) \end{aligned} \tag{4.9}$$

As the influence of the knowledge of x diminishes with time t measured from $t = 0$, the results for $n = 1$ will be considered first:

$$\begin{aligned} &\mu_1(t) = E\left[X(t)|X(0)=x_0, X(t_1)=x_1\right] = \\ &\frac{\left[r(t)-r(t_1)r(t-t_1)\right]x_0+\left[r(t-t_1)-r(t)r(t_1)\right]x_1}{1-r^2(t_1)} \end{aligned} \tag{4.10}$$

and

$$s_1^2(t) = m_0\left[1-\frac{r^2(t-t_1)+r^2(t)-2r(t)r(t_1)r(t-t_1)}{1-r^2(t_1)}\right] \tag{4.11}$$

The autocorrelation function $r(t)$ is given by Eq. (4.5). It can be shown by a Taylor series expansion of both $r(t)$ and $x(t)$ that if $t_1 \to 0$, then Eqs. (4.10) - (4.11) reduce to $\mu_{00}(t)$ and $s_{00}(t)$ given in Eqs. (4.3) - (4.4).

If more terms are included, $n > 1$, the result simply becomes:

$$\begin{aligned} &\mu_n(t) = E\left[X(t)\left|X(0)=x_0, X(t_1)=x_1, ..., X(t_n)=x_n\right.\right] = \underline{r}^T(t)\underline{R}^{-1}\underline{x}, \\ &s_n^2(t) = m_0\left(1-\underline{r}^T(t)\underline{R}^{-1}\underline{r}(t)\right) \end{aligned} \tag{4.12}$$

in matrix notation with

$$\begin{aligned} \underline{r}(t) =& \left[r(t), r(t-t_1), r(t-t_2), ..., r(t-t_n)\right]^T, \\ \underline{x} =& \left[x_0, x_1, x_2, ..., x_n\right]^T, \\ \underline{R} =& \begin{bmatrix} 1 & r(t_1) & r(t_2) & ...... & r(t_n) \\ & 1 & r(t_2-t_1) & ...... & r(t_n-t_1) \\ & & 1 & ...... & r(t_n-t_2) \\ & & & ...... & \\ & & & & 1 \end{bmatrix} \end{aligned} \tag{4.13}$$

As previously, the standard deviation is independent of the actual measured values x_i. For $n = 1$ it is easy to show that Eqs. (4.12) - (4.13) yield Eqs. (4.10) - (4.11). For measurements taken under stationary stochastic conditions the autocorrelation matrix $\underline{R}$ does not change and therefore only needs to be calculated and inverted once. Furthermore, the autocorrelation vector, $\underline{r}(t)$, does not depend on the measured values and can therefore be re-used for each time step. Thus, the vector $\underline{y}(t)$

$$\underline{y}(t)^T \equiv \underline{r}(t)^T\underline{R}^{-1} \tag{4.14}$$

can be pre-calculated and used in each time step to determine the most probable future response:

$$\mu_n(t) = E\left[X(t)\left|X(0)=x_0, X(t_1)=x_1, ..., X(t_n)=x_n\right.\right] = \underline{y}(t)^T\underline{x} \tag{4.15}$$

4.3 Autoregressive Predictor

The discussion of the autoregressive (AR) predictor method will just focus on its relation to the conditional processes considered above. The Yule-Walker equations for the AR can be written in the present notation:

$$\begin{aligned}&\text{AR: } x(t) = \underline{a}(t)^T \underline{x};\; t > 0\\&\text{Yule-Walker: } \underline{a}(t) = \underline{R}^{-1}\underline{r}(t) \Rightarrow x(t) = \underline{r}(t)^T \underline{R}^{-1}\underline{x} = \mu_n(t)\end{aligned} \tag{4.16}$$

Thus, the two formulations are conceptually the same. However, in the AR the time step (i.e. t) is assumed to be just the next time step and not a continuous variable as in Eq. (4.12).

From the measurements, the autocorrelation, $r(t)$, can be estimated. An alternative is to base the prediction on off-line training. This is done by collecting N time series $\underline{x}_i = [x_0, x_1, x_2, ..., x_n]_i^T$; $i = 1, 2, .., N$ from the measurements in the beginning of a stationary stochastic period. For each of these time series the response $x_i(t);\; t > 0$ is determined with time t measured from the time where $(x_0)_i$ was measured. The error ε_i in each AR estimation is:

$$\epsilon_i = x_i(t) - \underline{a}^T \underline{x}_i; \quad i = 1, 2, .., N \tag{4.17}$$

or for all series

$$\begin{aligned}\underline{\varepsilon} &= [\varepsilon_1, \varepsilon_2, .., \varepsilon_n]^T = \underline{X}(t) - \left(\underline{a}^T \underline{X}\right)^T\\ \underline{X}(t) &= [x_1(t), x_2(t), ..., x_N(t)]^T\\ \underline{X} &= [\underline{x}_1, \underline{x}_2, ..., \underline{x}_N]\end{aligned} \tag{4.18}$$

A least square fit for $\underline{a}$ can be obtained by minimization of the error measure $\underline{\varepsilon}^T\underline{\varepsilon}$ with respect to $\underline{a}$:

$$\begin{aligned}\frac{d}{d\underline{a}}\left\{\underline{\varepsilon}^T\underline{\varepsilon}\right\} &= \frac{d}{d\underline{a}}\left\{\underline{X}(t)^T\underline{X}(t) - 2\underline{a}^T\underline{X}\underline{X}(t) + \underline{a}^T\underline{X}\underline{X}^T\underline{a}\right\}\\ &= -2\underline{X}\underline{X}(t) + 2\underline{X}\underline{X}^T\underline{a} = 0\end{aligned} \tag{4.19}$$

Thus, the best least square choice of the AR coefficients $\underline{a}$ becomes

$$\underline{a} = \underline{a}(t) = \left(\underline{X}\underline{X}^T\right)^{-1}\underline{X}\underline{X}(t) \tag{4.20}$$

stressing again that $\underline{a}$ is a function of the time step used.

4.4 Sinusoidal Decomposition

In this method, Chung et al., 1990, the response $x(t);\; t > 0$ is estimated assuming the following form of the response:

$$\mu_s(t) \equiv x(t) = \underline{b}(t)^T \underline{x};\; t > 0 \tag{4.21}$$

where

$$\underline{b}(t) = [b_{1s}\sin(\omega_1 t), b_{1c}\cos(\omega_1 t), .., b_{nc}\cos(\omega_n t)]^T \tag{4.22}$$

The frequency range and increments chosen $[\omega_1, \omega_2, ..., \omega_n]$ must obviously reflect the spectral content of the response.

The coefficients b_{is} and b_{ic}; $i = 1, 2, ..., n$ can be estimated by off-line training in the same way as for AR by collecting N time series $\underline{x}_i = [x_0, x_1, x_2, ..., x_n]_i^T$; $i = 1, 2, .., N$ from the measurements in the beginning of a stationary stochastic period. For each of these time series the response $x_i(t)$; $t > 0$ is determined with time t measured from the time where $(x_0)_i$ was measured. The error ε_i in each estimation is:

$$\varepsilon_i = x_i(t) - \underline{b}(t)^T \underline{x}_i; \quad i = 1, 2, .., N \tag{4.23}$$

or for all series

$$\begin{aligned} \underline{\varepsilon} &= [\varepsilon_1, \varepsilon_2, .., \varepsilon_n]^T = \underline{X}(t) - \left(\underline{b}(t)^T \underline{X}\right)^T \\ \underline{X}(t) &= [x_1(t), x_2(t), ..., x_N(t)]^T \\ \underline{X} &= [\underline{x}_1, \underline{x}_2, ..., \underline{x}_N] \end{aligned} \tag{4.24}$$

A least square fit for $\underline{b}(t)$ can be obtained by minimization of the error measure $\underline{\varepsilon}^T \underline{\varepsilon}$ with respect to $\underline{b}(t)$ in the same way as for the AR, Eq. (4.19), and the result becomes

$$\underline{b}(t) = \left(\underline{X}\underline{X}^T\right)^{-1} \underline{X}\underline{X}(t) \tag{4.25}$$

Finally, the coefficients b_{is}, b_{ic} are obtained by dividing the components in $\underline{b}(t)$ with the corresponding sine or cosine term. As the least square estimation depends on t it is, as in the AR, most convenient to choose a fixed value of t. The similarities between the AR and sinusoidal decompositions have previously been shown by e.g. From et al., 2011.

The variance follows directly from the error measure:

$$s_s^2(t) = \underline{\varepsilon}^T \underline{\varepsilon} = m_0 - \left(\underline{b}(t)^T \underline{x}\right)^2 \tag{4.26}$$

with $\underline{b}(t)$ given by Eq. (4.25).

4.5 Comparisons with Measurements

The measured data from a 9,400 TEU container ship, see Chapter 2.3, is used for the comparison in this chapter. Basically, any available time series could have been used, e.g. vertical acceleration, roll or heave, but here strain was used because the data was easily available. Strain measurements from 02 October 2011, where the ship was sailing through a storm, are used. The mean of the port and starboard signal is used and the mean value is set to zero.

4.5.1 *Variance estimations*

The normalised autocorrelation function *r(t)* and its time derivatives *s(t)* and *u(t)*, Eqs. (4.5), are shown in Figure 4.1 as derived from the measurements. The signal has been filtered to remove noise and high frequency vibration components as well as components with a period higher than 50 seconds, as these components are not important for the present study. The filtering process is further described in Chapter 6.

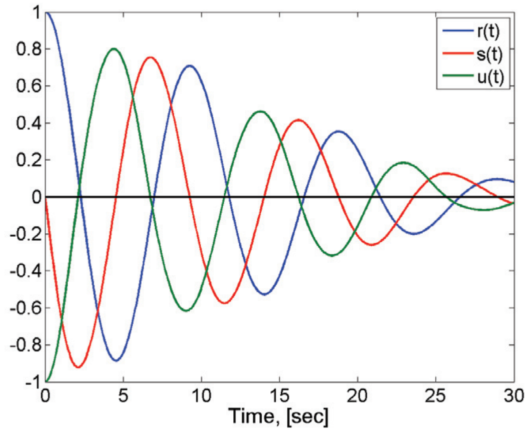

Figure 4.1: *Normalised autocorrelation function r(t) and its time derivative s(t) and u(t) for the measured stress.*

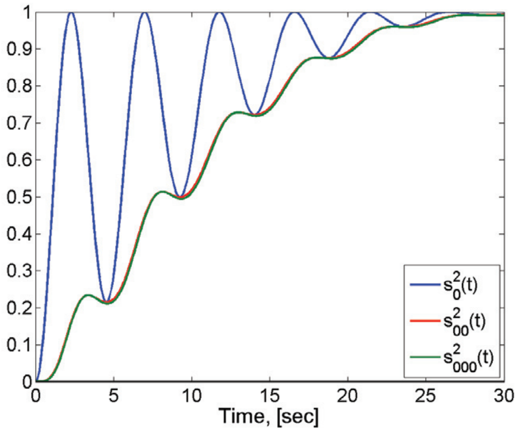

Figure 4.2: *Normalised variances $s_0^2(t), s_{00}^2(t), s_{000}^2(t)$ of the conditional processes for the measured stress, Eq. (4.4).*

It is clearly seen from the autocorrelation function that the memory time is about 30 seconds implying that measurements older than 30 seconds are not useful for response predictions. Consequently, response predictions more than 30 seconds ahead cannot be improved by conditioning the response on measured data.

The normalised variances, Eqs. (4.4), are shown in Figure 4.2 and obviously, the inclusion of information on the derivative *s(t)* reduces the variance quite significantly as compared to the reduction using information of the response alone. However, additional information of the second derivative, *u(t)*, does not add much reduction to the variances except for narrow-banded processes, where α, Eq. (4.7), is close to 1. Here, α is found to be 3.0. Generally, the inclusion of information about *r(t)* and *s(t)* yields a rather smooth reduction of the unconditional variance in the range from 0 to 30 seconds. The zero-upcrossing period of the response is 8.8 s, corresponding well with the variations shown in Figure 4.1 and 4.2. Thus, any influence of past values has vanished from the response after approximately three times the zero-upcrossing period.

Figure 4.3 shows the variance $s_1^2(t)$ for four different values of the time lag t_1. If the time lag is larger than 10 seconds, it does not reduce the standard deviation, whereas for smaller values its effect is closer to the effect obtained by inclusion of the first derivative, Eq. (4.4), i.e. $s_1^2(t) \rightarrow s_{00}^2(t)$ for $t_1 \rightarrow 0$. It can also be noted from Figure 4.3 that the reduction in variance is not monotonically decreasing with increasing time lag t_1. For instance, the reduction using $t_1 = 7$ s is larger than for $t_1 = 5$ seconds.

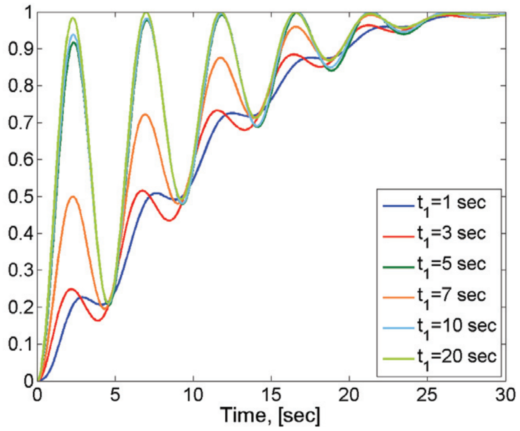

Figure 4.3: *Normalized variances $s_1^2(t)$; t_1= 1, 3, 5, 7, 10 and 20 seconds determined for the conditional process for the measured stresses, Eq. (4.11).*

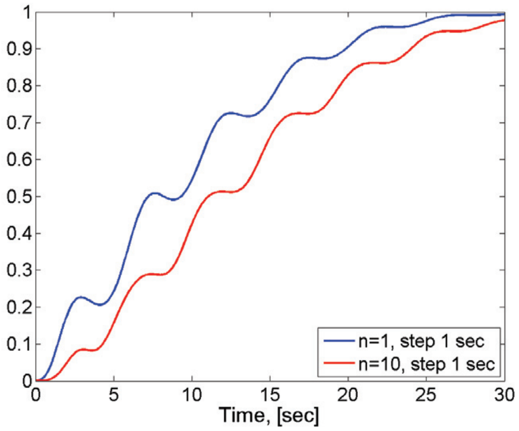

Figure 4.4: *Normalised variances $s_n^2(t)$ for $n = 1$ and $n = 10$ with constant time step $t_i - t_{i+1} = 1$ s, determined for the conditional process for the measured stresses, Eqs. (4.12)-(4.13).*

If the response prediction is made conditional on more than one measured value, the variance can be reduced as shown in Figure 4.4. Here, a constant time step of 1 second between the measured values $x_0, x_1.., x_n$ applied in the conditioning is used, and the figure shows that going from two terms (at $t = 0$ and $t_1 = -1$ s, i.e. n = 1) to eleven terms (at $t = 0$ and $t_1 = -1$ s, $t_2 = -2$ s, $t_{10} = -10$ s, i.e. $n = 10$) reduces the variance to some extent.

The same result will be obtained by the autoregressive predictor (AR) method based on the Yule-Walker formulations as discussed in the previous section.

For the sinusoidal decomposition method the variance can be estimated by Eq. (4.26). However, as it needs off-line training, Eq. (4.25), it will not be considered further in this study as it will be more difficult to implement in an on-board decision support system.

4.5.2 *Comparison with measured stress responses*

The conditional mean processes, Eqs. (4.3), (4.10) and (4.15) are shown in Figure 4.5-4.12 together with the measured response. The time difference in the measurements between each figure is 5 seconds and the time axis shown is from 10 seconds before $t = 0$ to 30 seconds after. Some observations are:

- Estimations based on $\mu_0(t)$, Eqs. (4.3), are not useful.
- Estimations based on $\mu_{00}(t)$ and $\mu_{000}(t)$, Eqs. (4.3), give in general good results for the first 3-5 seconds The inclusion of the second derivative, $\mu_{000}(t)$, only marginally improve the predictions.

- Estimations based on $\mu_1(t)$, Eqs. (4.10), give predictions not as good as those from $\mu_{00}(t)$.
- Estimations based on $\mu_n(t)$, Eqs. (4.12), (4.15), i.e. using measured points spaced 1 second and taken from the last 10 seconds of the measured signal are generally far better than the other predictions and give fair predictions typically up to 5-10 seconds ahead of the current time.

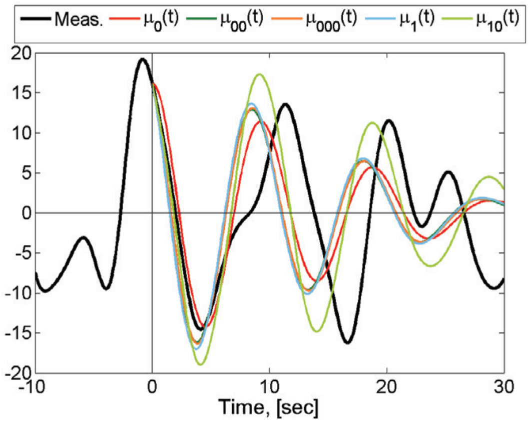

Figure 4.5: *Measurements and conditional mean responses.*

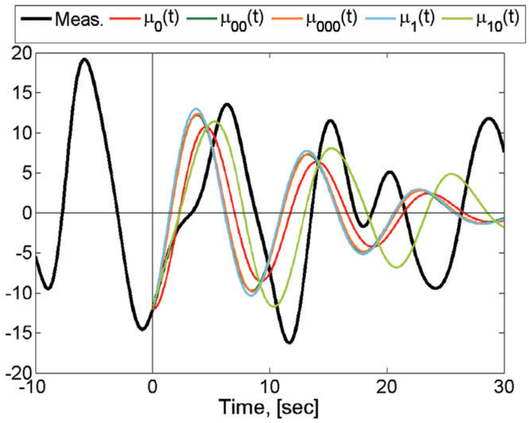

Figure 4.6: *Measurements and conditional mean responses.*

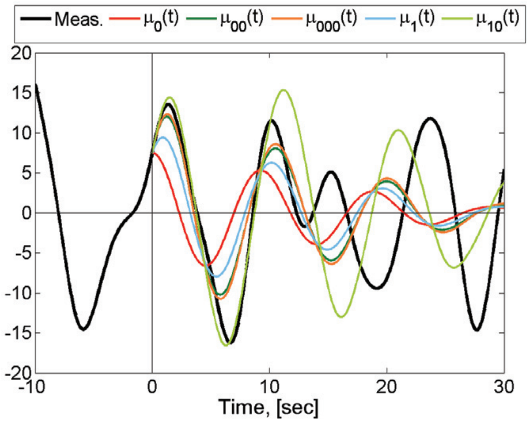

Figure 4.7: *Measurements and conditional mean responses.*

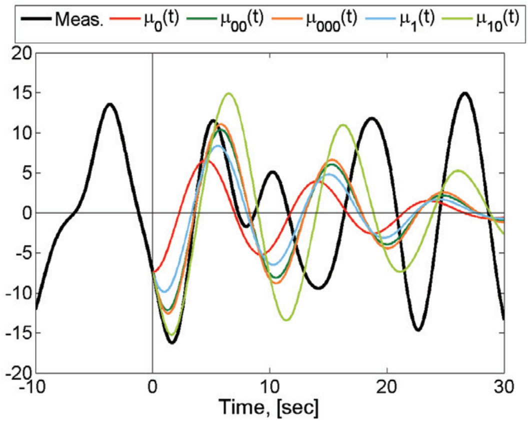

Figure 4.8: *Measurements and conditional mean responses.*

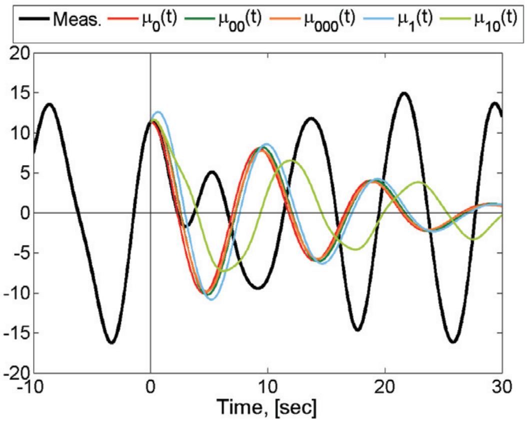

Figure 4.9: *Measurements and conditional mean responses.*

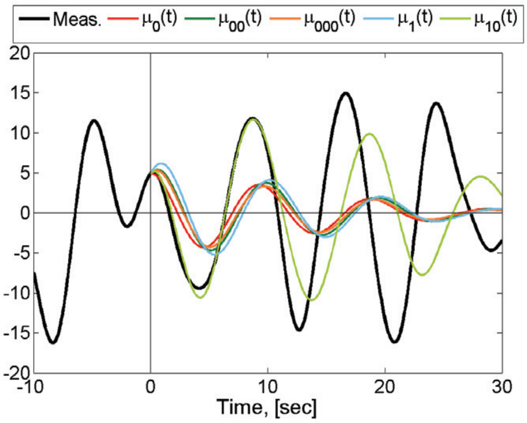

Figure 4.10: *Measurements and conditional mean responses.*

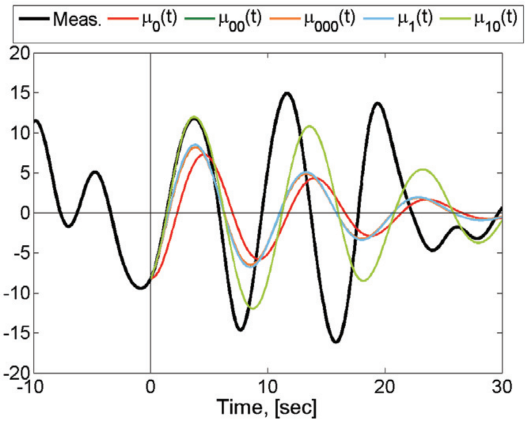

Figure 4.11: *Measurements and conditional mean responses.*

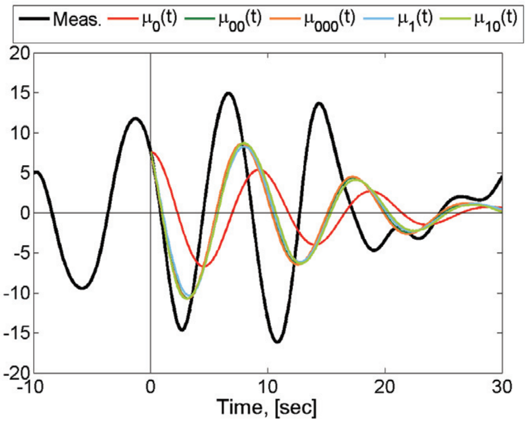

Figure 4.12: *Measurements and conditional mean responses.*

4.6 Discussion and Conclusions

Various procedures for estimation of ship responses in waves covering the next 1-30 seconds ahead in time have been described and evaluated by comparison with full scale measurements of hull girder stresses. A procedure based on 11 measured points spaced 1 second, covering the last 10 seconds of the instantaneous measured signal seems generally able to give fair predictions up to 5-15 seconds ahead of the current time.

Figure 4.13: *Subsea support vessel with heave compensated crane. Photo by Maersk Supply Service.*

This procedure can easily be implemented in a decision support system and provide the master information about the ship responses to be expected the next 5-15 seconds. This can be useful for e.g. loading and offloading operations at sea, helicopter landings, ship-to-ship operations in general, and for e.g., motion control of floating offshore units. Obviously, the use for such information on board a container ship is somewhat limited. More work should be carried out applying the procedure to other, more broad banded response types such as e.g. the roll response for other ship types.

Another approach for just-in-time prediction of ship responses is described by Kosleck, 2013. The method is based on analysis of images of the surrounding wave field in order to extract the wave trains to be immediately encountered by the ship or the offshore structure. The responses can subsequently be predicted based using e.g. linear transfer functions.

Chapter 5

Hydro-Elastic Response of Container Ships

Part of this chapter is published in Andersen and Jensen, 2014, but here estimates of the natural frequency for the 2-node vertical bending mode and the associated damping is included for all four container vessels using Operational Modal Analysis (OMA).

5.1 Introduction

During recent years, the length of the largest container ships has increased to about 400 m. With increasing length, the natural hull girder frequency is reduced making the large container ships potentially more sensitive to wave-induced vibration. With operation speeds in excess of 20 knots the natural vibration frequency of the hull approaches the range of typical wave encounter frequencies. The importance of the hull girder vibrations is a concern regarding fatigue as well as the extreme wave-induced bending moment. Hydro-elastic effects are difficult to account for and are not directly taken into account in the classification societies' current design rules for container ships. It can be a concern if the current design values for the wave-induced bending moment for container ships are too low due to partial negligence of hydro-elastic effects and the aim of the following chapters is to assess these hydro-elastic effects.

A ship sailing in a seaway is subject to wave-induced random excitations of the hull. The hull becomes excited at two main frequencies: The wave encounter frequency and at the higher 2-node vertical bending natural frequency of the hull. The high-frequency (HF) response obviously occurs simultaneously with the wave-frequency (WF) response as illustrated in e.g. Figure 5.1, and the HF vibration part is superimposed onto the WF part and thus adds to the total load cycle.

The design of container ships features large hatch openings and high tensile strength steel which, together with the increased length, act to reduce the hull stiffness. Another particular design feature of container vessels is the pronounced bow flare which allows more cargo to be carried on deck, but also makes the ships more vulnerable to slamming loads. A sketch of the body plan of the 9,400 TEU container ship with a bow flare angle of

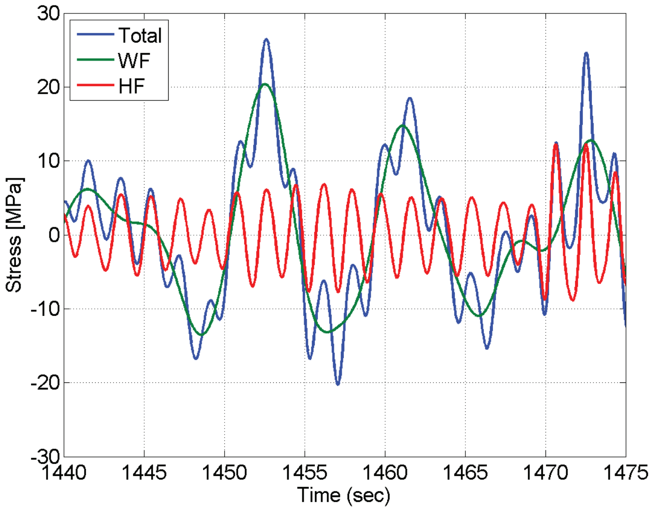

Figure 5.1: *Total, wave-frequency and high-frequency ship hull stress response in the deck amidships. Example from the 9,400 TEU container ship.*

around 45 deg can be seen in Figure 5.2.

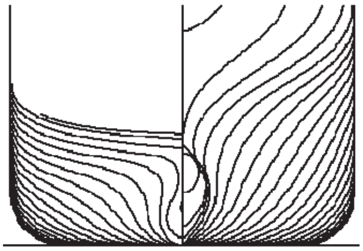

Figure 5.2: *Body plan of the 9,400 TEU container ship. Illustration courtesy of the TULCS project.*

Whipping is a short, transient response following a large impulsive load, typically a slamming impact. The whipping response is excited at the hull girder natural frequency and decays due to the damping in the structure and due to friction between the containers in addition to the hydrodynamic damping. Whipping events can be identified from the high-pass filtered time series of e.g. stress time history as illustrated in Figure 5.3 where the whipping is clearly seen as transient, damped responses.

Springing is a continuous smaller-amplitude resonance phenomenon at the ship's 2-node vertical hull girder natural frequency.

Whipping and springing can contribute to the possible failure of the ship structure in two ways: Yielding and buckling due to increased extreme loads and fatigue damage related to repeated oscillatory loads, respectively. On the extreme load side, the hydro-elastic response in container ships can contribute significantly to the maximum amplitudes of the hull girder loads and can be as critical an issue in the ship design and operation as

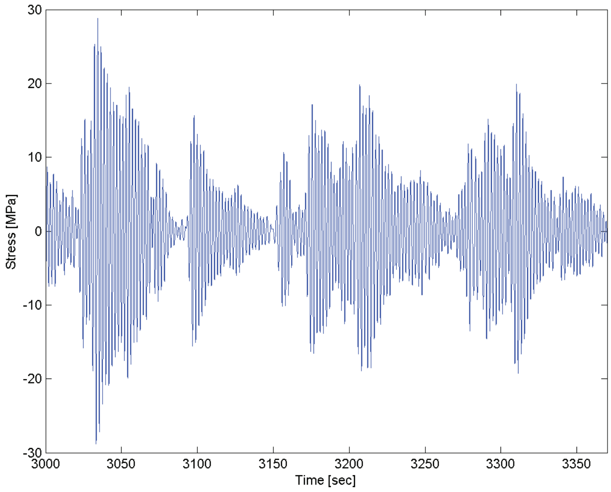

Figure 5.3: *High-pass filtered stress signal amidships for a container ship sailing in bow-quartering sea illustrating a series of transient slamming/whipping events. Full scale measurements from the 9,400 TEU container ship.*

the rigid-body wave-induced bending moments as will be shown in Chapter 8 and 9.

Slamming loads on ships with forward speed are difficult to predict numerically due to the complexity of treating quasi-static and dynamic responses under linear, non-linear and impulsive wave loads simultaneously, see e.g. Malenica and Derbanne, 2012. The fluid-structure interaction can be modelled using 3D boundary element or CFD codes coupled with finite element tools as the state-of-the-art procedures, but direct calculation in the time domain is computationally very heavy, see e.g. Seng et al., 2012, Oberhagemann et al., 2012 and Seng and Jensen, 2013, especially in stochastic seas.

Hydro-elastic response of ships has been studied extensively by different means, see e.g. Storhaug and Moe, 2007 and Storhaug et al., 2007 who focus on analysis of full scale measurements of strains and structural vibrations from vessels operating in harsh environments. Significant contribution to the expected fatigue damage was found as well as to the extreme stress peaks from the high-frequency vibrations in both hogging and sagging. Storhaug et al., 2007 conclude that the vibration-induced fatigue damage is of similar order of magnitude as the wave-frequency induced damage for the ore carrier considered.

Although mainly dealing with the fatigue damage when assessing the influence of whipping Okada et al., 2006 also investigated the additional stresses due to whipping on the long-term distribution of vertical bending stresses and concluded that much more attention should be paid to whipping stresses. A simple procedure for prediction of extreme vibration-induced hull girder loads in container ships outlined in Jensen et al., 2009 shows good agreement with the measurements carried out by Okada et al., 2006.

Senjanović et al., 2008 investigated the flexibility of a large container ship using a fairly complex mathematical beam model and a 3D finite element analysis. Impulsive loads were not directly assessed, but it was concluded that whipping caused by impulsive loads is important to consider.

The global hydro-elastic structural responses, i.e. whipping and springing, are important issues in the container ship design and operation. These hydro-elastic responses are described in the following and this chapter briefly outlines the basic theory of ship hydro-elasticity. A description of the dynamic response of a ship considered as a Bernoulli-Euler beam is given, and the emphasis here is on the 2-node vertical bending mode. However, in the numerical analysis the more general Timoshenko beam is used.

5.2 Hull Girder Flexibility

In the following, an introduction to the fundamental equations for Bernoulli-Euler beams under dynamic loads is given. The governing equation for the vertical deflection, $w(x,t)$, of a Bernoulli-Euler beam as function of location x and time t is:

$$(EI(x)w''(x,t))'' = p(x,t) - m(x)\ddot{w}(x,t) \tag{5.1}$$

where

$$\dot{()} = \frac{\partial}{\partial t} \quad \text{and} \quad ()' = \frac{\partial}{\partial x} \tag{5.2}$$

Furthermore, $EI(x)$ is the bending rigidity, $m(x)$ the mass per unit length including the added mass of water. Superposition of modes can be used to describe the deflection of the beam. Each deformation mode is characterised by an eigenfunction associated with a natural frequency. Here, only one term, the 2-node vertical bending mode, is included. The 2-node vertical bending mode illustrated in Figure 5.4 is found to be the most important mode when considering wave-induced vibrations. This assumption will be justified from analysis of full scale measurements in Chapter 8.

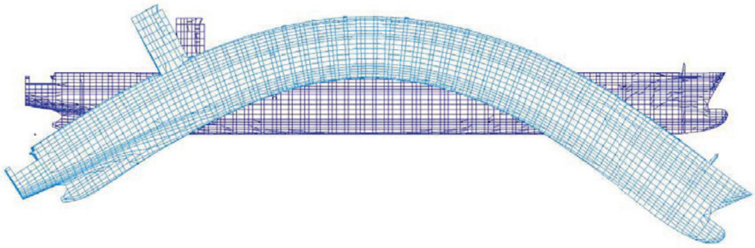

Figure 5.4: *The 2-node vertical bending mode of the 9,400 TEU container ship. Illustration courtesy of the TULCS project, WP.4.*

Assuming that the deflection of the hull can be described solely by the 2-node mode shape implies:

$$w(x,t) = \nu_2(x)u(t) \tag{5.3}$$

The 2-node mode shape $\nu_2(x)$ and the corresponding natural frequency ω_2 can be determined by setting $p = 0$ in Eq. (5.1) together with $w(x,t) = \nu_2(x)\cos(\omega_2 t)$ which yields the eigenvalue problem:

$$(EI(x)\nu_2''(x))'' - \omega_2^2 m(x)\nu_2(x) = 0, \quad 0 \leq x \leq L \tag{5.4}$$

with the boundary conditions at the free ends: $\nu_2'' = \nu_2''' = 0$ for $x = 0, L$ where L is the ship length. The solution to the eigenvalue problem in Eq. (5.4) yields corresponding values of $\nu_2(x)$ and ω_2.

The general solution to Eq. (5.1) can be found by inserting Eq. (5.3) in Eq. (5.1), multiplying with $\nu_2(x)$ and integrating over L:

$$u(t)\int_0^L (EI(x)\nu_2''(x))''\nu_2(x)\mathrm{d}x = \int_0^L p(x,t)\nu_2(x)\mathrm{d}x - \ddot{u}(t)\int_0^L m(x)\nu_2^2(x)\mathrm{d}x \tag{5.5}$$

By using Eq. (5.4) on the left hand side of Eq. (5.5) one gets:

$$\omega_2^2 M_2 u(t) = \int_0^L p(x,t)\nu_2(x)\mathrm{d}x - M_2\ddot{u}(t) \tag{5.6}$$

where M_2 is the modal mass:

$$M_2 = \int_0^L m(x)\nu_2^2(x)\mathrm{d}x \tag{5.7}$$

By dividing with M_2 and introducing

$$P_2(t) = \int_0^L p(x,t)\nu_2(x)\mathrm{d}x$$

Eq. (5.6) can be written as:

$$\ddot{u}(t) + \omega_2^2 u(t) = \frac{1}{M_2}P_2(t)$$

Finally, an empirical damping term can be added to get the resulting expression:

$$\ddot{u}(t) + 2\xi\omega_2\dot{u}(t) + \omega_2^2 u(t) = \frac{1}{M_2}P_2(t) \tag{5.8}$$

Eq. (5.8) determines the time variation of the hull girder response given a slamming load $p(x,t)$ and will be used in Chapter 8 in the validation study of the full scale measurements from the 9,400 TEU ship.

5.2.1 *2-node natural frequency and damping*

The dry and wet natural frequencies for the 9,400 TEU ship for vertical bending as determined by Bureau Veritas in connection with the TULCS project are given in Table 5.1. The calculated wet natural frequencies, which include the hydrodynamic damping, can be confirmed from full scale measurements as seen in Figure 5.5 and 5.6 where the 2-node natural vertical vibration frequency of the ship is seen at about 0.48 Hz ≈ 2 s.

The 3-node vertical vibration frequency can be identified from the semi-logarithmic plot in Figure 5.6 and is also in agreement with the calculated values in Table 5.1, but the energy content of the response at this frequency is of insignificant magnitude compared to the 2-node vibration.

Vertical bending 2-node, dry	0.67 Hz
Vertical bending 2-node, wet	0.47 Hz
Vertical bending 3-node, dry	1.38 Hz
Vertical bending 3-node, wet	0.98 Hz

Table 5.1: *Calculated dry and wet natural frequencies of the 9,400 TEU container ship. From (Kapsenberg et al., 2010).*

As the ratio between the dry and wet 2-node natural frequency is close to $\sqrt{2}$ cf. Table 5.1, the the added mass of water is nearly equal to the displacement of the present vessel, but this also holds quite generally.

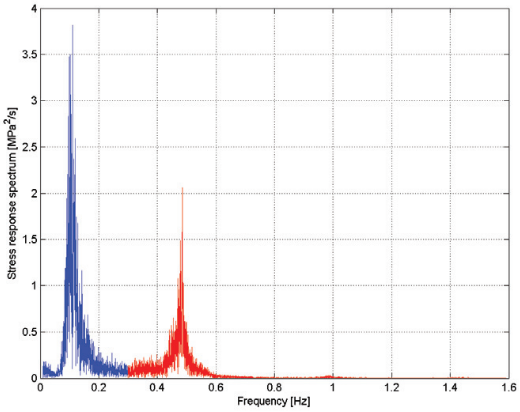

Figure 5.5: *FFT of stress time history (one hour) from 9,400 TEU container ship in rough sea on 02 October 2011. The vibration at the 2-node vertical mode is seen at about 0.48 Hz.*

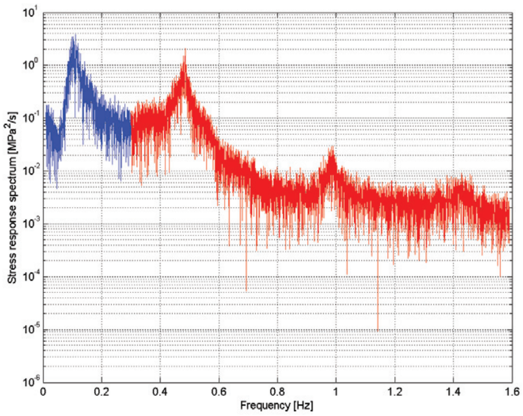

Figure 5.6: *FFT of stress time history (one hour) in semi-logarithmic plot from 9400 TEU container ship in rough sea on 02 October 2011. The vibration at the 2-node vertical mode is seen at about 0.48 Hz and the 3-node vertical vibration frequency can be identified at about 0.99 Hz. FFT of the same time series as in Figure 5.5.*

The natural frequency varies with the operational conditions. It is most influenced by the loading condition and mass distribution on board the ship, but also varies with speed, water depth and sea state.

While the 2-node natural frequency is relatively straightforward to determine from full scale measurements, it is more cumbersome to estimate the damping. The structural damping is higher for container ships than for other ship types due to the friction between the containers and in the lashing system, and thus the damping for large container ships is also thought to be higher than for small container ships. The damping is difficult to accurately assess, but it is low and of the order of 1-3% of critical damping cf. e.g. Storhaug and Moe, 2007.

For ship models the damping can be determined using hammer or shaker tests, which are more difficult to apply in full scale. For real ships, the damping estimate can be based on analysis of full scale data, i.e. measurements of the ship response in waves. Storhaug et al., 2003 describe two methods for estimation of the damping ratio from full scale measurements. The linear analysis is based on the equation of vertical deflection for the hull in Eq. (5.8). In the linear analysis the modal deflection is proportional to the measured stress or accelerations, so measurements of both can be used for the damping estimation. When considering the FFT, only the resonance part is considered (the second peak in Figure 5.5). The damping parameter ξ is obtained by fitting the power function for the expected decay of the FFT spectrum to the measurements. The non-linear method for estimating the damping described by Storhaug et al., 2003 takes into account the contributions from non-linear viscous effects. As the scope of this work is not damping estimation these methods will not be described further, but reference is given to Storhaug et al., 2003, Storhaug, 2007 and Rüdinger, 2002.

Here, the damping is estimated using operational modal analysis (OMA). The commercial software ARTeMIS (Ambient Response Testing and Modal Identification Software) by Structural Vibration Solutions[1] is used. The software can identify the natural frequencies, damping ratios of different modes of a given structure based on measured data from the structure under excitation where there is no information describing the excitation source. This can be bridges, buildings or ships in waves. For reference see e.g. Döhler et al., 2012 for application of the software on a Ro-Ro cargo ship. A screen dump of the software is seen in Figure 5.7.

Motion or strain measurements can be used for the damping estimate. Here, measurements of the vertical acceleration in the bow is used for the 9,400 TEU ship and for the other three ships the strains measured in the deck amidships are used. Using the strain measurements for the 9,400 TEU ship instead of the vertical accelerations measurements give virtual the same estimate of the damping of the 2-node mode. The longest available time series are used and information of the length of the time series is also included in the tables below. The estimated natural frequency for 2-node vertical bending and the associated damping is given in Tables 5.2-5.5 for each ship.

As seen, both natural frequency and damping varies for the time series considered but are all within the expected range. For the 14,000 TEU ship the variation between the estimates from the two different time series are the greatest. As mentioned, the natural frequency varies with operational parameters such as speed, water depth and sea state as well as with the loading condition. The variation of the ship natural frequency

---

[1] `http://www.svibs.com/products/ARTeMIS_Modal.aspx`

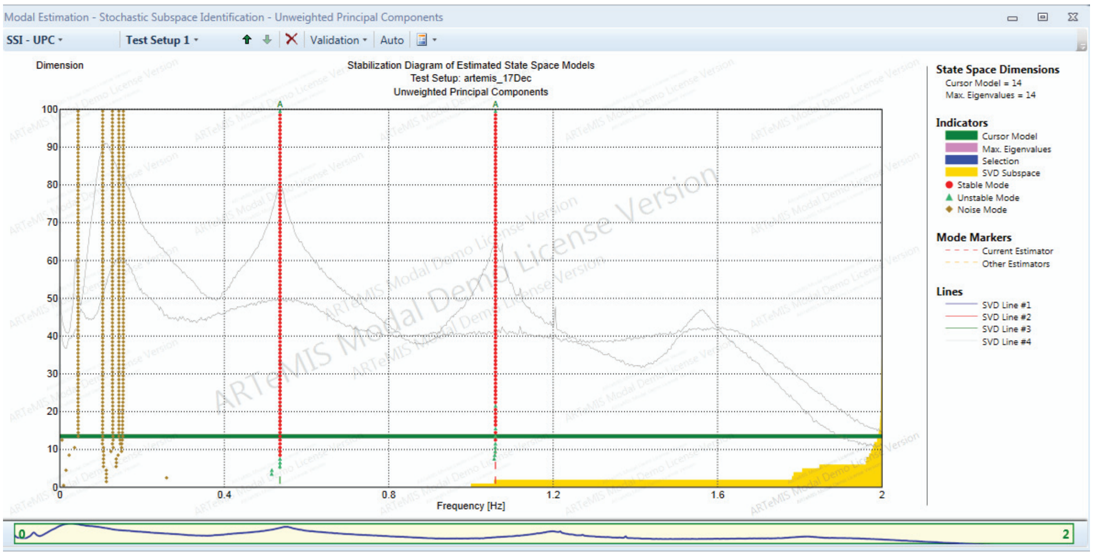
Modal Estimation - Stochastic Subspace Identification - Unweighted Principal Components
SSI - UPC
Test Setup 1
Validation
Auto
Dimension
Stabilization Diagram of Estimated State Space Models
Test Setup: artemis_17Dec
Unweighted Principal Components
100
90
80
70
60
50
40
30
20
10
0
0
0.4
0.8
1.2
1.6
2
Frequency [Hz]
State Space Dimensions
Cursor Model = 14
Max. Eigenvalues = 14
Indicators
Cursor Model
Max. Eigenvalues
Selection
SVD Subspace
Stable Mode
Unstable Mode
Noise Mode
Mode Markers
Current Estimator
Other Estimators
Lines
SVD Line #1
SVD Line #2
SVD Line #3
SVD Line #4
ARTeMIS Modal Demo License Version
0
2

Figure 5.7: *Screendump from ARTeMIS for estimating of modal parameters with indication of two stable modes (2 and 3-node vertical bending).*

Date	ω_2 [Hz]	ξ [%]	s_ξ [%]	Time
12 Aug 2011	0.477	2.444	0.012	24 hours
16 Sep 2011	0.510	1.754	0.008	24 hours
20 Sep 2011	0.513	1.304	0.005	24 hours
02 Oct 2011	0.483	1.821	0.002	24 hours
17 Dec 2011	0.535	1.776	0.010	24 hours

Table 5.2: *Estimated 2-node natural frequency, ω_2, damping, ξ, and standard deviation of the damping, s_ξ, from operational modal analysis for the 9,400 TEU ship. Damping is % of critical damping.*

Date	ω_2 [Hz]	ξ [%]	s_ξ [%]	Time
17 Nov 2010	0.504	2.379	0.010	24 hours
30 Dec 2011	0.507	1.993	0.032	24 hours

Table 5.3: *Estimated 2-node natural frequency, ω_2, damping, ξ, and standard deviation of the damping, s_ξ, from operational modal analysis for the 8,600 TEU ship. Damping is % of critical damping.*

and, especially, the damping with the operational parameters could be subject for future studies.

Date	ω_2 [Hz]	ξ [%]	s_ξ [%]	Time
21 Jul 2011	0.444	2.451	0.086	1 hour
29 Sep 2011	0.501	1.380	0.014	2 hours

Table 5.4: *Estimated 2-node natural frequency, ω_2, damping, ξ, and standard deviation of the damping, s_ξ, from operational modal analysis for the 14,000 TEU ship. Damping is % of critical damping.*

Date	ω_2 [Hz]	ξ [%]	s_ξ [%]	Time
02 Nov 2007	0.663	1.843	0.005	24 hours
01 Jul 2008	0.604	1.766	0.006	6 hours

Table 5.5: *Estimated 2-node natural frequency, ω_2, damping, ξ, and standard deviation of the damping, s_ξ, from operational modal analysis for the 4,400 TEU ship. Damping is % of critical damping.*

5.2.2 *2-node mode shape*

The 2-node vertical bending mode shape of the 9,400 TEU ship is determined using the in-house non-linear strip-theory code SHIPSTAR (see Xia et al., 1998) with the ship hull modelled as an elastic non-uniform Timoshenko beam with the actual stiffness $EI(x)$ and mass $m(x)$ variation along the length of the hull including the added mass of water. The mode shape is illustrated in Figure 5.8 and compared to that determined by Bureau Veritas in Figure 5.9 by the use of a finite element beam model, and the two are found to be almost identical. For the mode shape determination in Figure 5.8 the mass distribution from 02 October 2011 is used (see also Figure 10.1), but the mode shape does not vary much with the loading condition. Using least square fit and a 6th order polynomial the 2-node mode shape in Figure 5.8 can be approximated by:

$$\begin{aligned}\nu_2(x) = &-1.27 \cdot 10^{-14} x^6 + 1.27 \cdot 10^{-11} x^5 - 5.56 \cdot 10^{-9} x^4 + \\ &1.4 \cdot 10^{-6} x^3 - 1.45 \cdot 10^{-4} x^2 - 5.67 \cdot 10^{-3} x + 1.01,\ 0 \leq x \leq 349\,\mathrm{m}\end{aligned} \tag{5.9}$$

where x is the distance from the stern. The first derivative $\nu_2'(x)$ is the angular displacement and the second derivative $\nu_2''(x)$ is the curvature of the mode shape. The latter must of course be zero at the ends of the ship, which is not the case for the approximation in Eq. (5.9). However, as shown in Chapter 8 it does not matter for the present investigation as the second derivative is only needed amidships.

If sufficient full scale measurements are available the mode shapes can also be estimated from OMA. This is however, omitted from this study but may be subject for future studies.

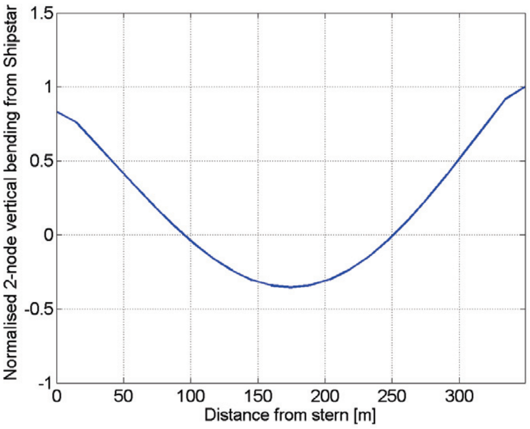

Figure 5.8: *The normalised 2-node vertical bending mode $\nu_2(x)$ for the 9,400 TEU container ship determined using a Timoshenko beam model.*

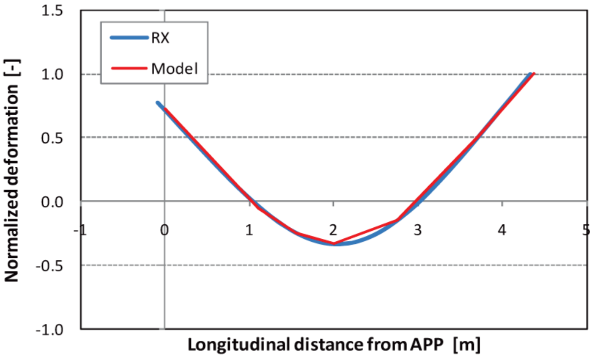

Figure 5.9: *The normalised 2-node vertical bending mode $\nu_2(x)$ for the 9,400 TEU container ship determined by BV. $x = 0$ is AP. From Kapsenberg et al., 2010. RX denotes data from the full scale ship.*

Chapter 6

Fatigue Damage Estimation from Full Scale Measurements

The parts of this chapter dealing with the 9,400 TEU ship is published by Andersen and Jensen, 2013.

6.1 Introduction

For ocean going ships, fatigue is an important failure mode. For some ships the hydro-elastic structural responses, such as springing and whipping, may contribute significantly to the accumulated fatigue damage in the hull girder during the life time of the ship, which should be carefully taken into consideration in their operation and design.

On-board monitoring and decision support systems must be able to run real-time and give fast, reliable estimation of fatigue damage rates based on measured strains taking into account both wave-induced and vibration-induced stresses. Time-domain analysis of long time series of measured stress is accurate and widely used and, with today's computers, possible to carry out real-time. However, for decision support applications where CPU capacity and storage may be limited, spectral analysis, which is computationally more efficient and only requires a few parameters derived from the power spectrum of the stress response, may be beneficial. Spectral methods can also be used to estimate fatigue damage for different route alternatives and for hypothetical changes in ship speed and course as e.g. described in Nielsen et al., 2011.

This chapter describes different methods for estimating the fatigue damage rates from full scale measurements of hull strains in two different, relatively large container ships (the 9,400 and 8,600 the TEU vessel, see Section 2.3 and 2.4). The primary focus is on assessing the influence of the high-frequency, wave-induced vibrations on the fatigue damage rates in ships. Damage accumulation over a ship's life time is not explicitly considered.

6.2 Fatigue Life

The 9,400 TEU ship is designed for a service life of 25 years while the 8,600 TEU ship has a design life of 40 years in world wide trade cf. Barhoumi and Storhaug, 2013. Based on this, the one-hour budget damage, defined as the average allowed expected fatigue damage during one hour, for the two ships is given in Table 6.1 for two different lifetime damage sums; $D = 1$ and $D = 0.5$. In the service life budget damage stress concentrations, residual stresses, corrosion, etc., are implicitly accounted for.

D/Service life	**25 years**	**30 years**	**35 years**	**40 years**
$D = 1.0$	$4.56 \cdot 10^{-6}$	$3.80 \cdot 10^{-6}$	$3.26 \cdot 10^{-6}$	$2.85 \cdot 10^{-6}$
$D = 0.5$	$2.28 \cdot 10^{-6}$	$1.90 \cdot 10^{-6}$	$1.63 \cdot 10^{-6}$	$1.43 \cdot 10^{-6}$

Table 6.1: *One hour budget damage for different service life and damage sum* $D = 1.0$ *and* $D = 0.5$.

For ship types such as bulk carriers and ore carriers global structural failure due to fatigue has been observed, but fatigue is currently generally not considered to be of great concern for large container ships. However, the fleet of ultra large container ships is young and fatigue related problems may take many years to develop. Furthermore, most large container carriers operate on the Europe - Asia trade which is relatively calm compared to the North Atlantic. Heggelund et al., 2011 consider the 8,600 TEU vessel on the Europe - Asia route and state that the estimated fatigue damage is significantly lower than what the vessel is designed for. Barhoumi and Storhaug, 2013 consider the same ship over a period covering June 2009 to March 2013 and conclude that the average estimated fatigue damage amidships in the deck corresponds to fatigue life of 222 and 158 years for the port and starboard side, respectively. For the 8,600 TEU ship, the 5 minute fatigue damage rates are below 0.01 (1% of the 5 minute budget damage) 83% of the time. 98% of the time the 5 minute fatigue damage is below the budget damage corresponding to 11% of the total damage. The periods where the 5 minute fatigue damage is above ten times the budget damage account for 56% of the total damage and constitute less than 0.5% of the total time (Barhoumi and Storhaug, 2013). Even though the the fatigue life is thus not of importance for this ship and trade, most of the fatigue damage is accumulated during very limited periods of time where the fatigue damage is dominated by hull girder vibrations.

The same conclusion is drawn for the 9,400 TEU ship. Long-term fatigue damage is estimated from full scale measurements by Renaud et al., 2013 during a measurement campaign lasting almost six years. It is concluded that the yearly accumulated fatigue damage was far lower than what the ship was designed for (25 year service life) and that, with respect to fatigue, the design is conservative.

However, for smaller container ships trading on the North Atlantic, fatigue damage has been observed to be an issue, cf. e.g. Storhaug and Heggelund, 2008 who found fatigue damage in a 2,800 TEU vessel to be in excess of what the ship was designed for. Consequently, the service life was decreased from 20 years to 12 years and cracks were identified on this vessel after only eight years of trade. Although the estimates, due to most of the observations taking place during the winter months, were probably conservative they still indicate high fatigue damage rates on this trade.

6.3 Data and Filtering

For the 9,400 TEU ship the fatigue damage analysis is carried out for the four days of operation listed in Table 6.2. The information about the encountered sea states (significant wave height, peak period and relative wave direction) is primarily obtained from the WaMoS wave radar system installed on the bridge of the vessel. The sea state data for the four days is illustrated in Appendix A.1.2. It is noted, as described in Section 2.3.8, that the considered WaMoS system is generally thought to over-estimate H_s for higher sea states.

Date	H_s	**Wind speed**	**Ship speed**	**Wave heading**
12 August 2011	1-5 m	15-20 m/s	20-23 knots	bow-quartering
16 September 2011	1.5-2.5 m	7-9 m/s	18 knots	bow-quartering
20 September 2011	1.3-1.7 m	2-5 m/s	12-14 knots	beam sea
02 October 2011	3-10 m	15-25 m/s	9-14 knots	bow-quartering

Table 6.2: *Selected days for fatigue damage estimation for the 9,400 TEU ship.*

The analysis of measurements and the associated fatigue damage estimation for the 8,600 TEU ship is carried out for the seven days of operation listed in Table 6.3. Unfortunately, for this vessel less navigational and sea state information is available, see Appendix A.2.2. The days with highest response levels, i.e. highest vibration contribution, are selected for the analysis. The 5 minute and 30 minute statistical files are used to obtain the navigational data while the raw data files containing the stress measurements (see Section 2.4) are used for the fatigue damage estimation.

For both ships the stress measurements are obtained amidships near the deck as described in Section 2.3.6 for the 9,400 TEU ship and 2.4.2 for the 8,600 TEU ship.

The average of the port and starboard side signals is used for the fatigue damage estimation. The mean of each signal fluctuates and is not naturally zero due to differences in the still water load level, temperature differences, forward speed, etc. However, the mean of each time series used is set to zero so that that strain gauge measurements only include the wave-induced contribution. This is done before the filtering is carried out. This implies that the still-water bending moment is not considered to contribute to fatigue here. For container ships, the still-water bending moment is normally a hogging bending moment, i.e. with tension in the deck.

Date	Wind speed	Ship speed
05 February 2010	5-7 m/s	12 knots
07 November 2010	Unknown	Unknown
08 November 2010	Unknown	Unknown
17 November 2010	Unknown	Unknown
18 November 2010	Unknown	Unknown
01 December 2010	Unknown	8-10 knots
30 December 2011	15-25 m/s	7-10 knots

Table 6.3: *Selected days for fatigue damage estimation for the 8,600 TEU ship.*

In order to distinguish the wave-frequency (WF) and the high-frequency (HF) contribution to the fatigue damage a dividing frequency must be determined. This is done most conveniently from examining the response power spectrum, i.e. the Fast Fourier Transform (FFT) of the stress time history as illustrated in Figure 5.5. The dividing frequency between the wave-frequency part and the high frequency part is accordingly set to 0.3 Hz as illustrated by the change of colour and as recommended by Det Norske Veritas, 2013b. The WF and HF response are well separated in time and thus, the exact position of the cut-off frequency between the two is not very important.

In the high-frequency tail the signal is cut off at 1.6 Hz (10 rad/s) to filter out noise and in the low-frequency end contributions below 0.01 Hz are filtered out to remove low-frequency contributions such as e.g. temperature effects and drift as recommended by Det Norske Veritas, 2013b. The filtering boundaries are also given in Table 6.4 for clarity. Both ships have a 2-node vertical bending natural frequency of about 0.5 Hz and the same filtering is applied.

	Lower cutoff [Hz]	Upper cutoff [Hz]
WF	0.01	0.3
HF	0.3	1.6
Total	0.01	1.6

Table 6.4: *Frequency limits for filtering of measured strains.*

The filtering of the wave and high-frequency components is carried out in the frequency domain using FFT and inverse FFT. The HF response is a mixture of continuous (springing) and transient (whipping) contribution. A whipping event is a continuous vibration following a discontinuous slamming load so the use of FFT is not believed to introduce any errors in this case. However, this can be an issue for abruptly changing signals. The filtering is carried out in the frequency domain and then the signal is transferred back into time domain by inverse FFT. Consistency has been checked by adding the HF and the WF part together in the time domain that the original, unfiltered signal is recovered.

6.4 Fatigue Damage Estimation Methods

Fatigue damage estimation is a theoretical procedure. Structural failure can occur long before the damage sum D reaches 1 due to e.g. material imperfections, stress concentrations not accounted for, improper welding and corrosion.

Fatigue life of structures is normally estimated using one of two different approaches. The most commonly used method is to estimate the fatigue damage in the time domain using a cycle count method, such as rainflow counting (RFC), where the stress cycles which contribute to fatigue are counted and a fatigue model such as the linear Palmgren-Miner rule subsequently applied. Rainflow counting can be carried out real-time with no significant computational cost on a modern computer.

Spectral methods for fatigue damage estimation are, however, computationally even faster and can therefore be preferred in some cases; particularly for application in on-board decision support systems where predictions of fatigue damage for e.g. different route profiles are needed and computers are less powerful. In the following, the time-domain fatigue damage estimation is briefly described together with four different spectral approaches considering the total stress process as consisting of:

- One narrow-banded Gaussian process
- A combination of two narrow-banded Gaussian processes using the envelope process (Jiao and Moan, 1990)
- A combination of two narrow-banded Gaussian processes using the envelope process and with correction for amplification effects (Low, 2010)
- A combination of a stationary Gaussian process and a non-Gaussian transient process (Jiao and Moan, 1990)

6.4.1 *Rainflow counting and the Palmgren-Miner rule*

For irregular loads the fatigue damage can be estimated from time series in the time domain using a cycle count method in combination with a damage accumulation method. Here, rainflow counting is briefly described and applied together with the linear Palmgren-Miner law.

Rainflow counting establishes equivalent load cycles. The procedure can be visualised as the origin of the name of the method indicates: Rain flowing down a pagoda roof. The stress time history is turned 90 degrees and the rainflow cycles can be counted as illustrated in Figure 6.1.

The method was mathematically defined by Rychlik, 1987 and assumes stochastic loads and no sequence effects, i.e. the order of the loads does not matter. The rainflow counting and damage assessment from the cycle count is here carried out using the WAFO package (Brodtkorb et al., 2011). A log-scale factor, one-slope SN-curve with the slope $m = 3$ and $\log(K) = 12.65$ is used in all cases, and no stress concentration factor is included as

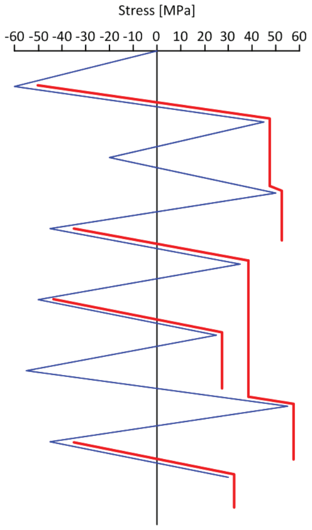

Figure 6.1: *Rainflow counting procedure for the tensile peaks.*

relative and not absolute fatigue damage estimates are discussed.

The fatigue damage estimation is carried out on the wave-frequency part of the stress signal and on the total signal. As suggested by e.g. Storhaug and Moe, 2007, the WF and HF contributions should not be considered as two independent signals, and thus the HF damage should not be assessed using a direct rainflow count of the high-frequency part of the signal since $D_{WF} + D_{HF} < D_{total}$ for rainflow counting. Considering the WF and HF components independently would yield very non-conservative results. Thus, the high-frequency contribution to the damage is taken as the difference between the total fatigue damage and the wave-frequency damage.

6.4.2 *Spectral methods*

Traditionally, for the spectral analysis the entire load history is assumed stationary, i.e. its statistical properties do not vary during the time period considered, and Gaussian. Furthermore, the process is assumed to be narrow-banded. In the following, the assumption of narrow-bandedness applies to the total process or to the different modes of the process depending on the method.

When hydro-elastic effects play a role, the stress response of the hull girder is usually more broad-banded. For broad-banded processes the narrow-band formulation yields conservative damage estimation as e.g. stated by Rychlik, 1993. In an attempt to reduce conservatism of the narrow-band approach it has been argued, that the individual frequency components of the response considered can be taken as narrow-banded cf. e.g. Jiao and Moan, 1990 and Low, 2010. In the following, by using $m = 3$, simplification and numerical evaluation of some of the expressions is possible.

Det Norske Veritas, 2013b recommends to consider the WF signal consisting of frequencies lower than 0.3 Hz while the HF part should be considered as contributions higher than 0.45 Hz. This plays no role when estimating the fatigue damage using RFC. However, for establishing the envelope process of the total process, the influence of the WF and HF components are treated independently. Therefore 0.3 Hz is chosen as dividing frequency between the WF and the HF signal as outlined in Table 6.4.

6.4.3 *One narrow-banded, Gaussian process*

Assuming that the total load history is a stationary, narrow-banded and Gaussian process, the expected damage D_{NB} over the time T is, cf. e.g. Jiao and Moan, 1990, given by the Rayleigh approximation to the stress cycles:

$$D_{NB} = \frac{\nu_0 T}{K} \left(2\sqrt{2}s\right)^m \Gamma\left(\frac{m}{2} + 1\right) \tag{6.1}$$

where ν_0 is the zero-upcrossing rate of the total stress signal, s is the standard deviation, and Γ is the gamma function.

Like for the RFC analysis, the narrow-band analysis is carried out for the total and the WF part of the signal and the HF part is taken as the difference between the two.

6.4.4 *Combination of two narrow-banded, Gaussian processes using the envelope process*

Using a bi-modal approach suggested by Jiao and Moan, 1990, the broad-banded process can be considered consisting of two individual narrow-banded, stationary Gaussian processes at low frequency (WF) and high frequency (HF), which is common in engineering problems such as ships encountering loads at the exciting wave frequency and vibrational loads excited at the lowest natural vibration frequency of the hull. In the bimodal approach, the total process can be assumed modelled by a wave frequency and a high frequency component:

$$X(t) = X_{WF}(t) + X_{HF}(t) \tag{6.2}$$

The spectra of the two components are assumed non-overlapping and thus the processes are statistically independent. The total expected damage is the sum of the contributions from the WF and HF components (large and small cycles, respectively, for this method):

$$D = D_L + D_S \tag{6.3}$$

For the large cycles the damage is estimated from the envelope of the total process (Jiao and Moan, 1990, Eq. (39)):

$$D_L = \frac{2^m \nu_{0,E} T}{K} \int_0^\infty r^m f_{R_L}(r) \mathrm{d}r \tag{6.4}$$

where $f_{R_L}(r)$ is the amplitude distribution of the large-cycle envelope stress amplitude R_L.

In order to avoid numerical integration of Eq. (6.4) it is suggested by Low, 2010 to divide R_L into the WF and HF parts:

$$R_L = R_{WF} + R_{HF} \tag{6.5}$$

As these two terms can be assumed statistically independent Eq. (6.4) can be re-written as:

$$D_L = \frac{2^m \nu_{0,E} T}{K} \int_0^\infty f_{R_{WF}}(r_{WF}) \int_0^\infty \left[r_{HF} + r_{WF}\right]^m \times f_{R_{HF}}(r_{HF}) \mathrm{d}r_{HF} \mathrm{d}r_{WF} \tag{6.6}$$

where $\nu_{0,E}$ is the zero-upcrossing rate of the envelope process:

$$\nu_{0,E} = \nu_{0,WF} \frac{\sqrt{1 + (\theta\beta\delta_{HF})^2}}{1 + \theta^2} \tag{6.7}$$

In Eq. (6.7), θ describes the relative dominance of the high-frequency contribution, β describes the frequency spacing between the WF and HF parts and, δ_{HF} is the bandwidth parameter of the high-frequency process:

$$\theta = \frac{s_{HF}}{s_{WF}} \tag{6.8}$$

$$\beta = \frac{\nu_{0,HF}}{\nu_{0,WF}} \tag{6.9}$$

$$\delta_{HF} = \sqrt{1 - \frac{\lambda_{1,HF}^2}{\lambda_{0,HF}\lambda_{2,HF}}} \tag{6.10}$$

In Eq. (6.10) $\lambda_{i_{HF}}$ denotes the i'th spectral moment of the HF process. By writing the integral in Eq. (6.4) as double integration as done in Eq. (6.6) the exact result of the damage related to the envelope process can be found in terms of a binomial series with $m + 1$ terms as suggested by Low, 2010:

$$D_L = \frac{\left(2\sqrt{2}\right)^m \nu_{0,E} T}{K} \sum_{k=0}^{m} \binom{m}{k} s_{HF}^k s_{WF}^{m-k} \Gamma\left(1 + \frac{m-k}{2}\right) \tag{6.11}$$

The damage from the small cycles, D_S, is for this method equal to the HF damage and is calculated from the high-frequency process in accordance with Eq. (6.1):

$$D_S = \frac{\nu_{0,HF} T}{K} \left(2\sqrt{2} s_{HF}\right)^m \Gamma\left(\frac{m}{2} + 1\right) \tag{6.12}$$

6.4.5 *Combination of two narrow-banded, Gaussian processes with correction for amplification effects*

In the method by Jiao and Moan, 1990 outlined above, the small cycle amplitudes are assumed equal to those of the HF process. However, the approach by Low, 2010 takes into account two effects which reduce the amplitudes of the small cycles and the large cycles respectively, and thereby attempts to reduce the conservatism of the fatigue damage estimation. It is argued that the presence of an underlying low-frequency process will decrease the amplitude of the small cycles. Furthermore, for the large cycles, the cycle amplitude is generally lower than what is obtained by simple addition of the peaks due to the fact that the peak of the HF process cannot always be assumed to coincide with the peak of the low-frequency process but will be affected by the phase difference, Θ, as described below. The aim by Low, 2010 was to develop a bi-modal method that matches the rainflow counting results more closely than the narrow-band approximations by taking the two mentioned reducing effects into account. According to Low, 2010 the small-cycle damage can then be expressed as:

$$\begin{aligned} D_S =& \frac{2^m \left[\nu_{0,HF} - \nu_{0,WF}\right] T}{K} \int_0^\infty \int_{\frac{\pi}{4\beta}}^{\frac{\pi}{2}} \int_{\epsilon(r_{WF},\kappa)}^\infty \left[r_{HF} - \epsilon(r_{WF},\kappa)\right]^m \\ & \times f_{R_{HF}}(r_{HF}) f_\Theta(\kappa) f_{R_{WF}}(r_{WF} \mathrm{d}r_{HF}) \mathrm{d}\kappa \mathrm{d}r_{WF} \end{aligned} \tag{6.13}$$

where

$$\epsilon(r_{WF},\kappa) = \frac{\pi}{2\beta} r_{WF} \sin\kappa \tag{6.14}$$

The functions $f_{R_{WF}}(r_{WF})$ and $f_{R_{HF}}(r_{HF})$ are the Rayleigh distributions of the WF and HF processes, respectively. The phase Θ between the peaks of the two processes is assumed uniformly distributed:

$$f_\Theta(\kappa) = \left(\frac{\pi}{2} - \frac{\pi}{4\beta}\right)^{-1}, \frac{\pi}{4\beta} \leq \kappa < \frac{\pi}{2} \tag{6.15}$$

The triple integration of Eq. (6.13) must be carried out numerically. However, the innermost integral can be evaluated by a series expansion reducing the problem to a double integral. The analytical solution to the innermost integral J_S in Eq. (6.13) reads, Low, 2010:

$$J_S = \int_\epsilon^\infty \left[r - \epsilon\right]^m \frac{r}{s_{HF}^2} \exp\left(-\frac{r^2}{2s_{HF}^2}\right) \mathrm{d}r \tag{6.16}$$

A binomial series expansion leads to:

$$J_S = \sum_{k=0}^{m} \binom{m}{k} (-\epsilon)^{m-k} I_k \tag{6.17}$$

where

$$I_k = \int_\epsilon^\infty r^k \frac{r}{2s_{HF}^2} \exp\left(-\frac{r^2}{2s_{HF}^2}\right) \mathrm{d}r \tag{6.18}$$

Setting $m = 3$ the series expansion has four terms and thus the solution for J_S reduces to:

$$J_S = \exp\left(-\frac{\epsilon^2}{2s_{HF}^2}\right)\left(-3\epsilon s_{HF}^2\right) + 3\left(\epsilon^2 + s_{HF}^2\right)\sqrt{2\pi} s_{HF} \Phi\left(-\frac{\epsilon}{s_{HF}}\right) \tag{6.19}$$

where $\Phi()$ is the standard normal cumulative distribution function.

The large cycle damage D_L can be expressed as, Low, 2010:

$$\begin{aligned} D_L =& \frac{2^m \nu_{0,WF} T}{\pi K} \int_0^\infty \int_0^\infty \int_0^\pi \left(r_{WF} \cos(c(r_{WF},r_{HF})\psi) + r_{HF} \cos\left[(\beta c(r_{WF},r_{HF}) - 1)\psi\right]\right)^m \\ & \times f_{R_{HF}}(r_{HF}) f_{R_{WF}}(r_{WF}) \mathrm{d}\psi \mathrm{d}r_{HF} \mathrm{d}r_{WF} \end{aligned} \tag{6.20}$$

where

$$c\left(r_{WF}, r_{HF}\right) = \frac{r_{HF}\beta}{r_{WF} + r_{HF}\beta^2} \tag{6.21}$$

As it was the case for the small cycle damage Eq. (6.20) is too complex to evaluate analytically. The innermost integral in Eq. (6.20) reads:

$$J_L = \int_0^{\pi} \left[r_{WF}\cos(c\psi) + r_{HF}\cos([\beta c - 1]\,\psi)\right]^m \mathrm{d}\psi \tag{6.22}$$

Again, setting $m = 3$, Eq. (6.22) can be evaluated analytically. The integral can be solved using standard integrations of cosine to power 3:

$$\int \cos^3 \alpha x \mathrm{d}x = \frac{1}{\alpha}\left(\sin \alpha x - \frac{1}{3}\sin^3 \alpha x\right)$$

and

$$\int \cos^2 \alpha x \cos \beta x \mathrm{d}x = \frac{1}{2\beta}\sin \beta x +$$
$$\frac{1}{4\left(2\alpha - \beta\right)}\sin\left[\left(2\alpha - \beta\right)x\right] + \frac{1}{4\left(2\alpha + \beta\right)}\sin\left[\left(2\alpha + \beta\right)x\right]$$

The upper limit of the outermost integral in Eq. (6.13) can be set to 5 standard deviations, s_{WF}, without any loss of accuracy. In Eq. (6.20), the upper limit of the outermost integral is also set to $5s_{WF}$ and for the middle integral the limit is set to $5s_{HF}$.

The method above thus involves evaluating two double integrals numerically. The method was sought simplified by Huang, 2013 and benchmarked with the results of RFC and against the results from the methods proposed by Low, 2010. However, the method is not found to be any simpler or computationally faster than the method proposed by Low, 2010.

6.4.6 *Combination of a stationary, Gaussian process and a non-Gaussian, transient process*

In another approach suggested by Jiao and Moan, 1990, the process can be assumed composed by a narrow-banded Gaussian process and a transient component, which is typically the case for slamming induced loads in ships. Results from Nielsen et al., 2011 indicate that it may be an accurate approximation to combine a stationary Gaussian process with a transient response assuming Rayleigh distributed transient peaks. In this analysis, the stationary part corresponds to the WF signal and the transient part to the HF signal.

The total damage can be estimated as the sum of the damage from the envelope process, D_E and the transient process D_2. The inter-arrival time between each transient event, T_0, is to be included in Eq. (6.1) in the estimation of the damage from the envelope process:

$$D_E = \frac{\nu_{0,WF}T}{K}\left(2\sqrt{2}s_{WF}\right)^m \Gamma\left(\frac{m}{2} + 1\right)\eta(T_0) \tag{6.23}$$

The estimated fatigue damage caused by the transient process during the time period T, can be expressed by:

$$D_2 = \frac{T}{T_0 K} \left(2\sqrt{2} s_{HF}\right)^m \Gamma\left(\frac{m}{2}+1\right) \frac{1}{1-\exp(-2\pi\xi m)} \tag{6.24}$$

where ξ is the total structural damping ratio; here taken as 0.01 in accordance with findings in Storhaug and Moe, 2007. The term $\eta(T_0)$ in Eq. (6.23) is expressed by Jiao and Moan, 1990 as:

$$\begin{aligned} \eta(T_0) = {} & \frac{1}{T_0}\int_0^{T_0} \frac{1-\theta\exp(-\xi\omega_{HF}t)}{\left[1+\theta^2\exp(-2\xi\omega_{HF}t)\right]^3}\mathrm{d}t + \frac{\sqrt{\pi}\theta m\Gamma\left(\frac{m}{2}+\frac{1}{2}\right)}{T_0\Gamma\left(\frac{m}{2}+1\right)} \\ & \times \int_0^{T_0} \exp(-\xi\omega_{HF}t)\left[1+\theta^2\exp(-2\xi\omega_{HF}t)\right]^{\frac{m}{2}-2}\mathrm{d}t \end{aligned} \tag{6.25}$$

where $\omega_{HF} = 2\pi\nu_{0,HF}$. Setting $m = 3$ the integrals in Eq. (6.25) can be evaluated analytically by substituting $u = \theta\exp(-\xi\omega_{HF}t)$ as shown by Nielsen et al., 2011.

This method has a disadvantage in being rather sensitive to the (manual) choice of inter-arrival time, T_0, and the uncertainty associated with the determination of the structural damping. Due to these two extra uncertainties the results from this method are not compared to the results of the other methods here. However, the influence of the variation of T_0 is discussed in Appendix C.3.

6.5 Results

For each day, 24 hours of data is analysed with respect to the estimated fatigue damage per one hour. One hour of data is considered enough to make the RFC results stable. The resulting estimated fatigue damage is illustrated in Appendix C.1 and C.2 for the 9,400 and the 8,600 TEU vessel respectively using the following four methods:

- Rainflow counting and the Palmgren-Miner rule. WF, HF and total damage given ($D_{HF} = D_{total} - D_{WF}$).
- One narrow-banded Gaussian process. WF, HF and total damage given ($D_{HF} = D_{total} - D_{WF}$).
- A combination of two narrow-banded Gaussian processes using the envelope process (Jiao and Moan, 1990). Total, large and small cycle damage given ($D_{total} = D_L + D_S$).
- A combination of two narrow-banded Gaussian processes with correction for amplification effects (Low, 2010). Total, large and small cycle damage given ($D_{total} = D_L + D_S$).

The total estimated fatigue damage for the 9,400 TEU vessel is illustrated in in Appendix C.1, Figures C.5, C.15, C.25 and C.35. For the 8,600 TEU vessel the total estimates are given in Appendix C.2, Figures C.45, C.55, C.65, C.75, C.85, C.95 and C.105. For the

9,400 TEU ship the outcome for 02 October 2011 is also shown in Figure 6.2 and for the 8,600 TEU ship the results for 17 November 2011 are shown in Figure 6.3.

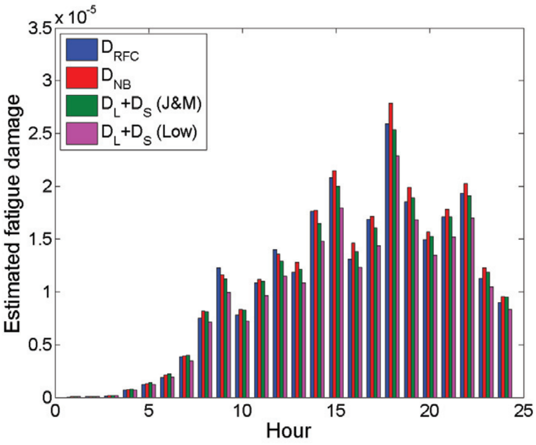

Figure 6.2: *Comparison of total estimated fatigue damage per hour during 24 hours on 02 October 2011 for the 9,400 TEU ship. Same figure as Figure C.35 in Appendix C.1.*

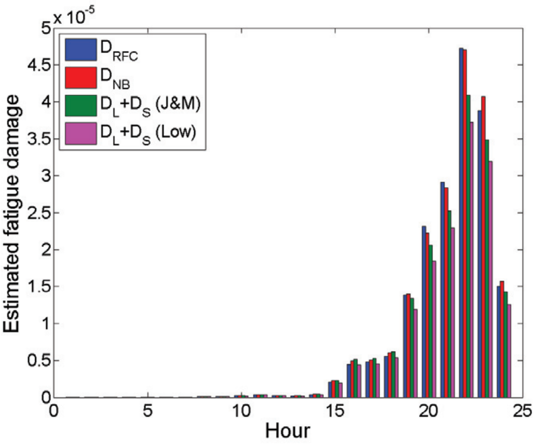

Figure 6.3: *Comparison of total estimated fatigue damage per hour during 24 hours on 17 November 2010 for the 8,600 TEU ship. Same figure as Figure C.75 in Appendix C.2.*

Generally, a clear correlation between the trend in significant wave height recorded by WaMoS (Appendix A.1.2, Figures A.13, A.30, A.47 and A.64) and the estimated fatigue damage can be observed for the 9,400 TEU ship. For the 8,600 TEU ship no sea state data is available for comparison.

For the 9,400 TEU ship the budget damage is exceeded for one of the four considered days: on 02 October 2011. On this day, the estimated 24 hour damage using RFC is 2.3 times the 24 hour budget damage based on 25 year service life and $D = 1$. For the worst hour (starting at 17:00) the estimated damage is 5.7 times the one-hour budget damage.

For the 8,600 TEU vessel having a design service life of 40 years, the hourly budget damage is lower than for the 9,400 TEU ship by a factor 25/40 (see Table 6.1). For the 8,600 TEU ship the budget damage is exceeded at several occasions as listed in Table 6.5. However, for the worst of the days the estimated fatigue damage using RFC is only about 2.6 times the 24-hour budget damage.

In the majority of the cases the narrow-band approach or the method by Jiao and Moan, 1990 yield the highest estimate of the fatigue damage. However, on some occasions RFC, quite unexpectedly, gives the highest estimate of the damage of all the methods. This will be further elaborated on in the discussion in Section 6.7.

In Appendix C.1 and C.2 the bandwidth parameter δ (Eq. (6.10)), the relative dominance of the HF process θ (Eq. (6.8)), the frequency spacing β (Eq. (6.9)) and the HF contribution to the fatigue are given for each day, and their influence will be discussed in Section 6.7.

Date	**24-hour exceedance**	**Max 1-hour exceedance**
08 November 2010	1.03	2.48
17 November 2010	2.71	16.6
18 November 2010	2.59	7.49
30 December 2011	2.04	13.7

Table 6.5: *Exceedance of one-hour budget damage for 8,600 TEU ship based on 40 year design service life and damage sum $D = 1$. The exceedance is given as the estimated damage using RFC and the Palmgren-Miner rule divided with the budget damage.*

6.6 Use of the Envelope Processes in Fatigue Damage Estimation

As suggested by e.g. Fricke and Paetzold, 2012 the majority of the fatigue damage is due to the stress cycles being enlarged by the superimposition of the HF part onto the large amplitude (WF) part. The small amplitude HF contribution alone have no significant effect on the fatigue damage. In the tests performed by Fricke and Paetzold, 2012 two different amplitude ratios between the WF and HF amplitudes were used. For the small amplitude ratio of 0.5 (high-frequency process amplitude half of the low-frequency process amplitude) the influence of the small cycles can be almost neglected and a simplified procedure using the envelope process of the low-frequency and high-frequency process can be used to estimate the fatigue life as long as the HF stress amplitudes are smaller than the WF stress amplitudes.

Japanese researchers, Kitamura et al., 2012, similarly suggest that the fatigue damage can be estimated sufficiently accurately using the envelope process by comparing a regular bi-modal process with its envelope process. The bi-modal process considered in their study has a small/large cycle amplitude ratio of 0.2 and the frequency of the HF component is five times that of the low frequency part. The fatigue damage estimation from the envelope process is found to be in good agreement with that from the bi-modal process using RFC.

In order to investigate whether the envelope approach works in practical fatigue damage estimation for ships, where the amplitude of the HF stresses can be of same magnitude as the WF stresses (see Chapter 8), the results of the RFC (total) fatigue damage estimate are compared to the two different (large cycle) envelope processes. The one by Jiao and Moan, 1990, Eq. (6.4) and the other one by Low, 2010, Eq. (6.20).

The Figures C.6, C.16, C.26, C.36, C.46, C.56, C.66, C.76, C.86, C.96 and C.106 in Appendix C.1 and C.2 illustrate the two different envelope processes compared to RFC. The additional small cycle damage is not considered. An example of the comparison is also given in Figure 6.4 and 6.5 for the two days with highest fatigue rates for the two ships.

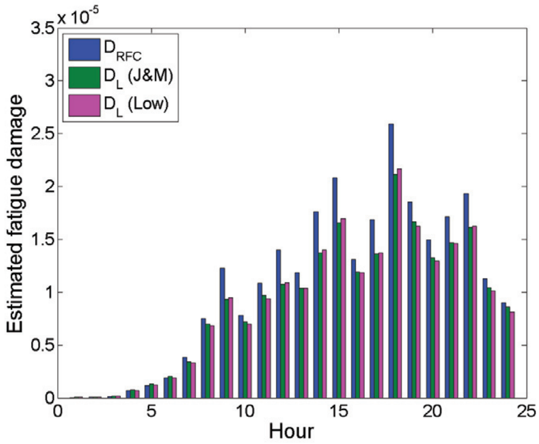

__Figure 6.4:__ RFC compared to the two envelope processes for 02 October 2011 for the 9,400 TEU ship. Same figure as Figure C.36 in Appendix C.1.

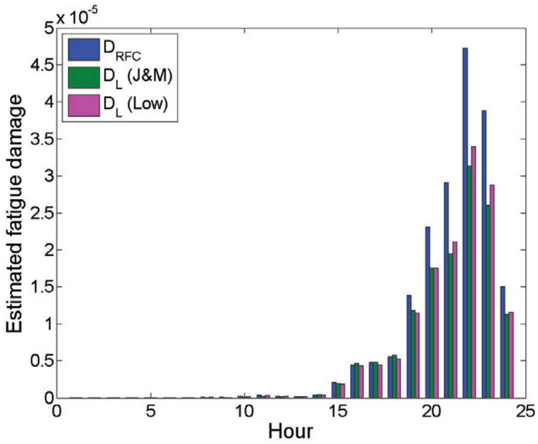

__Figure 6.5:__ RFC compared to the two envelope processes for 17 November 2010 for the 8,600 TEU ship. Same figure as Figure C.76 in Appendix C.2.

The envelope processes seem to be in good agreement with RFC when the fatigue damage rate is low, which it is believed to be in the majority of the time cf. e.g. Barhoumi and Storhaug, 2013. Particularly, considering the full scale data, the envelope process proposed by Low, 2010 mostly matches RFC very well even though the method is not designed for the spectral properties of full scale measurements from ships. The method by Low assigns very little or no influence on the fatigue damage to the small cycles when fatigue damage rates are low, so the envelope process here accounts for the majority of the damage.

It can be observed from full scale measurements (see Chapter 8) that the amplitude of the HF part can be equal to that of the WF part at high response levels. From the days with highest fatigue damage rates, the two envelope processes are here found to under-estimate the damage as seen in Figures 6.4 and 6.5. The same is the case on 01 December, where the total stress response levels are quite low, but where the amplitude of the HF stress exceeds that of the WF stess (see Figure 6.8) in a springing-like response.

The findings by Fricke and Paetzold, 2012 and Kitamura et al., 2012 regarding the use of the envelope process for the fatigue damage estimation are thus confirmed in the cases where the total fatigue damage rates and the HF stresses are low. However, the amplitude of the HF stress can easily exceed that of the WF stress, and in those cases the envelope process cannot be considered to give a good estimate of the fatigue damage as the damage is under-estimated by the envelope process using the two spectral methods.

6.7 Discussion

For the spectral analysis the one-hour time series are assumed to be stationary even though they may not necessarily be so. At sea, time series of 20-30 minutes can normally be considered stationary.

6.7.1 *Effect of vibrations*

It can be seen from the plots in Appendix C.1 and C.2, considering the RFC results that the HF vibrations contribute significantly to the fatigue damage in the cases considered here, keeping in mind that the roughest periods of operation have been selected for the analysis. In several cases the HF contribution constitutes more than half of the total fatigue damage, and in the worst cases the HF contribution is by far dominating the fatigue damage estimate. The narrow-band approximation (Eq. (6.1)) yields results very similar to those of RFC except that the narrow-band approximation, expectedly, in most cases yield a slightly higher estimate.

For the bi-modal approaches by Jiao and Moan, 1990 and Low, 2010 it is noted that the large and small cycle contributions cannot be compared directly with RFC and the narrow-band approximation. For the method by Jiao and Moan, 1990 the large cycle part is the envelope process of the WF and HF cycles, while the small cycle part is considered equal to the Rayleigh approximation to the HF process. For the method by Low, 2010 the large (envelope) and small cycle damages are both influenced by the WF and HF processes and the small cycles are not assumed equal to the HF part of the process and thus, the illustrated results from the method cannot be interpreted as the high-frequency part of the process having a negligible or small influence of the total fatigue damage.

It generally seems that the narrow-band formulation (Eq. (6.1)) in most cases yield results close to the bi-modal formulation by Jiao and Moan, 1990 (Eqs. (6.11) and (6.12)). Thus, one may simply choose to use the narrow-band formulation for the fatigue damage estimation. The method by Jiao and Moan, 1990 is not found to consistently increase the accuracy of the fatigue damage estimate here. The method by Low, 2010 is aimed at reducing the conservatism of the spectral approach and generally seems to yield results closer to the RFC-results than the two other spectral methods. Even though the method may be time-consuming to programme the computational time is small and comparable to the other spectral methods. The method is developed for cases with quite large frequency spacing (β between 4 and 10) and well-separated response spectra. For the 9,400 TEU ship the frequency spacing β is around 3-4 which is quite low. For the 8,600 TEU ship β varies considerably more and attains values up to 12. Since the natural frequency of the ship does not change noticeably β only depends on the encounter wave-frequency. However, no sensitivity to the frequency spacing in the results from the method by Low, 2010 can be observed from the analysis carried out here.

In some cases, RFC yields the highest estimate of the fatigue damage of the methods considered. This is the case for the 9,400 TEU ship on 02 October 2011 (Figure 6.2). For the 8,600 TEU ship it is the case for 17 November 2010 (Figure 6.3), 18 November 2010 and 30 December 2011 (Figures C.85 and C.105 in Appendix C.2). Narrow-banded methods are generally considered as the conservative estimate and upper bound of the fatigue damage estimation. According to many sources, e.g. Rychlik, 1993, the narrow-band approximation is proven to be conservative if the process is stationary and Gaussian. As seen from examples of the response spectra for two of the days where RFC give the highest fatigue damage estimate in Figure 6.6 and 6.7 the response spectra are broad-banded. On ocean going ships, the stress response can rarely be considered narrow-banded. The individual processes in e.g. Figure 6.6 and 6.7 may be well-separated but are not necessarily narrow-banded. The figures illustrate the most broad-banded and most narrow-banded WF and HF processes found during the one-hour time series for the 9,400 TEU ship. Note that the scale of the y-axes on the plots are not the same.

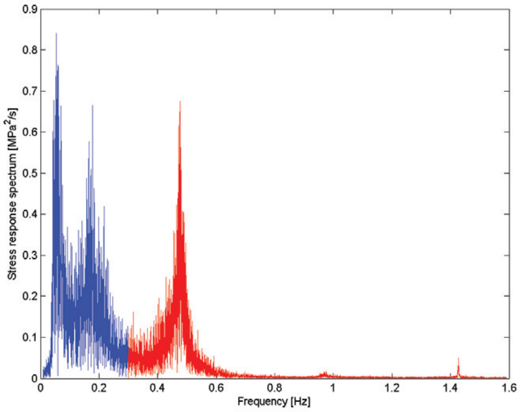

Figure 6.6: *FFT of filtered stress time series with wave-frequency (WF) response and high-frequency (HF) response outlined. FFT of one hour of data from 12 August 2011 at 11 hours.* $\delta_{total} = 0.62$, $\delta_{WF} = 0.48$ *and* $\delta_{HF} = 0.12$.

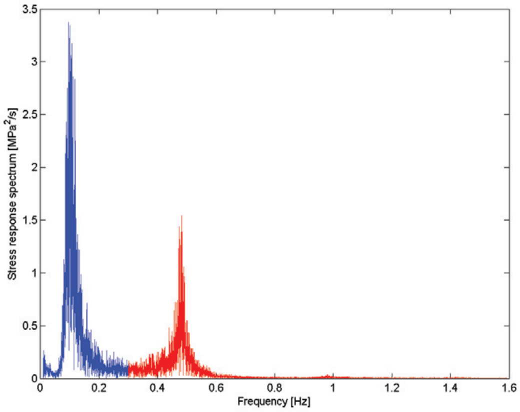

Figure 6.7: *FFT of filtered stress time series with wave-frequency response and high-frequency response outlined. FFT of one hour of data from 02 October 2011 at 18 hours.* $\delta_{total} = 0.63$, $\delta_{WF} = 0.21$ *and* $\delta_{HF} = 0.09$.

All spectral methods assume the process to be Gaussian and a possible explanation for the RFC giving the highest estimate in some cases may well be that the processes considered here are slightly non-Gaussian.

In all cases, the methods used for estimating fatigue damage are theoretical and the absolute truth is unknown. Using experimental investigation of a welded specimen exposed to cyclic loads and load histories measured in the deck of a Panamax container ship Fricke and Paetzold, 2013 conclude that RFC combined with the linear Palmgren-Miner rule is suitable for estimating fatigue damage in ships where the stresses are composed of WF and HF (whipping) components.

A springing-like response, where the HF stress amplitudes considerably exceed the WF stress amplitudes, is identified from the measurements from the 8,600 TEU ship during quite a long period of operation on 01-02 December 2010. Even though the total hull girder stress levels and the fatigue damage rates are low during December 01, the HF contribution is very high and is responsible for the majority (about 80%) of the fatigue damage accumulation (Appendix C.2, Figures C.91 to C.96). A cut-out of the filtered stress time series for 01 December 2010 can be seen in Figure 6.8.

Generally, springing does not seem to contribute critically to fatigue for these ships. Drummen et al., 2006 suggest that the damping in container vessels is larger than for similar sized ships due to friction in the container stacks and lashings, and this limits the

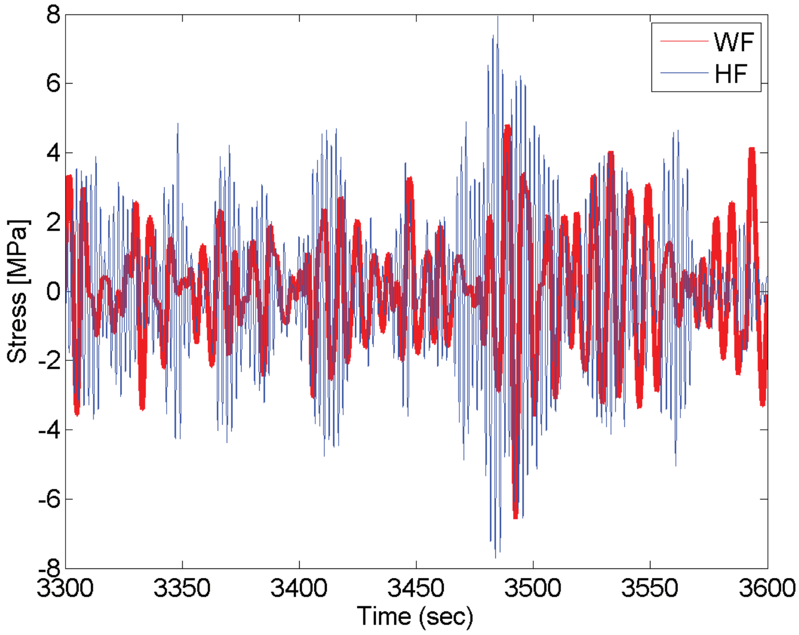

Figure 6.8: *WF and HF part of the stress signal (average of port and starboard side) illustrating springing excitations. 8,600 TEU ship on 01 December 2012 at 21 hours.*

influence of springing on the fatigue damage accumulated in container ships compared to other ship types.

Long-term effects of vibrations on fatigue cannot be assessed here due to the limited number of time series considered. Barhoumi and Storhaug, 2013 state that for the 8,600 TEU container ship the HF vibrations account for 57% of the total estimated fatigue damage for the port side strain gauge in the deck and 55% for the starboard sensor for the 4 year period analysed.

Fricke and Paetzold, 2012 carried out tests with two different amplitude ratios of 0.5 and 1 and concluded that for the smallest of the amplitude ratios a damage sum $D = 1$ seems appropriate, but a damage sum $D = 0.75$ fits the case with the large HF amplitudes better. In Fricke and Paetzold, 2013 $D = 0.5$ is found to be conservative and the real damage sum is to be found somewhere between $D = 0.1$ and $D = 0.5$.

6.7.2 *Size effects*

The two container ships analysed here are too similar in size to reveal any significant size effects. Compared to a 4,400 TEU Panamax container ship investigated in Nielsen et al., 2011 the effects of HF hull girder vibrations seem more pronounced for the two larger ships. In Nielsen et al., 2011 it was concluded that the HF vibrations give rise to a quite significant contribution to the fatigue damage and might increase the expected fatigue damage by 20-40%.

Storhaug and Heggelund, 2008 performed full scale measurements on board somewhat smaller container ships. On a 2,800 TEU container ship trading in the North Atlantic the HF vibration contribution to the fatigue damage was found to 27% of the total damage in the deck amidships. In the same study a 4,400 TEU was similarly investigated. Here, the fatigue damage caused by HF vibration likewise contributed with about 27% of the total fatigue damage during almost a year of effective measurements from operation on the North Atlantic. No effect of size between the two smaller vessels was thus found.

Kahl et al., 2014 compared measured stress range spectra from two different sized container ships (4,600 and 14,000 TEU) operating on two different routes and compared the ratio of the cumulated fatigue damage for the HF response to the total response. The small ship was in world-wide operation including the North Sea and the Pacific while the large ship was operated on the Europe - Asia route. For the smaller ship the HF damage accounted for 35% of the total damage while for the larger ship the HF contribution was 53% despite the larger ship being operated on a generally calmer trade.

6.8 Conclusions

In order to assess whether spectral methods for fatigue damage estimation are applicable in on-board systems to monitor rates of fatigue damage on board ships, four spectral methods have been applied on full scale measurements of the strains amidships in the hull of two container ships and compared with the outcome of RFC.

Despite both the total and the individual processes at times clearly not being narrow-banded the spectral methods generally have good agreement with the outcome of RFC. As expected, the narrow-band formulation (Eq. 6.1) generally estimates higher fatigue rates than RFC. In some cases where the response levels are high and dominated by hull girder vibrations, the fatigue damage estimation from RFC was found to exceed those of the spectral methods. The different methods generally yield quite similar results and it can generally be concluded that fatigue can be fairly accurately estimated using spectral methods.

The method by Jiao and Moan, 1990 where the process is assumed to be composed of a narrow-banded Gaussian process and a transient component is discussed separately in Appendix C.3. The method is quite sensitive to the choice or determination of inter-arrival time between the transient events. The effort to accurately determine the structural damping and the inter-arrival time is not believed to be justified, and the method is not believed to be capable of yielding more accurate results than the other methods considered here.

Considering the envelope process of a typical stress response composed by WF and HF parts using spectral analysis can give a fairly accurate estimate of the fatigue damage as long as the HF stresses are not dominating the response.

Only a limited number of days is considered in this analysis so no conclusions can be drawn about the fatigue life of the two ships from the analysis carried out here. From the analysis of the days with highest fatigue damage it can be concluded that the expected fatigue damage can be high; up to 2.5 times the 24-hour budget damage and 17 times the one-hour budget damage, but this only occurs for very limited time relative to the total operational life of the ship.

At times, the HF component can contribute significantly more to the fatigue damage than the WF components. However, in most cases for the ships on routes considered here, fatigue damage is not critical due to the long periods of operation with no or very little accumulated fatigue damage on the Europe - Asia trade. It may become an issue if ships on the Europe - Asia route are shifted to e.g. the North Pacific or North Atlantic.

To summarize, the HF wave-induced vibrations can have a significant effect on the fatigue damage for relatively short periods of time, but for larger ships in relatively calm trades fatigue is normally not an issue during the life time of the ship.

Chapter 7

Influence of the Hull Girder Flexibility on the Wave-Induced Vertical Bending Moment

Part of this chapter is published by Andersen and Jensen, 2012.

7.1 Introduction

To initiate the investigation of the influence of the hull girder flexibility on the wave-induced vertical bending moment numerical analysis is carried out for the 9,400 TEU ship. A non-linear strip theory analysis is applied comparing the rigid and flexible modelling of the ship using a pre-specified maximum vertical bending moment amidships in both sagging and hogging. The specified maximum bending moment is less than the rule bending moments stated by the classification societies (See Section 9.2) and is thus not necessarily related to the more severe sea states. No green water on deck is accounted for.

Transient, linear conditional waves representing the most probable wave scenario yielding the specified wave-induced response are generated using the First Order Reliability Method (FORM) and the corresponding statistics are cross-checked with Monte Carlo Simulations (MCS). The strip-theory calculations in the conditional waves are carried out for head sea with one forward speed. Furthermore, comparison with model tests with a flexible model of the 9,400 TEU ship.

The in-house non-linear time-domain strip-theory seakeeping code, SHIPSTAR, which is capable of predicting both linear and non-linear wave loads and ship responses is used in the following. The linear strip-theory is a classical strip-theory based on work by Salvesen et al., 1970, but modified with the Smith correction factor approach. In the non-linear mode the forces are estimated exactly over the instantaneous wetted surface and the non-linear memory effect due to the free surface and the momentum slamming are included as outlined below.

7.2 Linear Time-Domain Strip-Theory

Generally, the time-domain linear hydrodynamic force acting on a section at body coordinate x at time t on a floating body with forward speed can be expressed by

$$F(x,t) = \frac{\mathrm{D}I}{\mathrm{D}t} + \rho g \bar{z} B \tag{7.1}$$

where B is the waterline breadth, and I consists of the linear impulsive and memory terms

$$I(x,t) = -\bar{m}(x) \cdot \frac{\mathrm{D}\bar{z}(x,t)}{\mathrm{D}t} - \int_0^t K(x,t-\tau) \cdot \frac{\mathrm{D}\bar{z}(x,\tau)}{\mathrm{D}\tau} \mathrm{d}\tau \tag{7.2}$$

where $\bar{m}$ is the sectional added mass at infinite frequency and the total derivative

$$\frac{\mathrm{D}}{\mathrm{D}t} = \frac{\partial}{\partial t} - U\frac{\partial}{\partial x} \tag{7.3}$$

where U is the ship speed. Furthermore, $\bar{z}$ is the relative effective motion:

$$\bar{z} = h - x\theta - \kappa H$$

Here h is the heave motion, θ is the pitch motion, H is the incident wave elevation and κ is the Smith correction factor cf. Jensen, 2001. The restoring force $\rho g \bar{z}$ depends on the density of the water ρ and the acceleration of gravity g. Finally, K is the hydrodynamic impulsive response function which is related to the added mass and damping coefficients $m(x,\omega)$ and $N(x,\omega)$ through the Fourier transformation

$$K(x,t) = \frac{2}{\pi}\int_0^\infty \frac{N}{\omega}\sin\omega t \mathrm{d}\omega = \frac{2}{\pi}\int_0^\infty (m-\bar{m})\cos\omega t \mathrm{d}\omega \tag{7.4}$$

In the present procedure the sectional added mass m and the damping N are modelled cf. Tick, 1959:

$$\mathrm{i}\omega m - N = \frac{\sum_{j=0}^{J} A_j(-\mathrm{i}\omega)^{j+1}}{\sum_{j=0}^{J} B_j(-\mathrm{i}\omega)^{j}} \tag{7.5}$$

where $A_j(x)$ and $B_j(x)$ are functions of the sectional geometry only. The coefficients are frequency-independent and determined by a least square fit to the results from a singularity distribution mapping procedure by Yeung, 1973. Usually, only a few terms (J = 3 or 4) are needed in order to achieve accurate results. By integration, Eq. (7.2) can be replaced by the set of linear equations

$$I(x,t) = -\bar{m}(x,\bar{z})\frac{\mathrm{D}\bar{z}(x,t)}{\mathrm{D}t} - q_J(x,t) \tag{7.6}$$

with $q_J(x,t)$ representing the hydrodynamic memory effect and determined by:

$$\frac{\partial q_j(x,t)}{\partial t} = q_{j-1}(x,t) - B_{j-1}q_J(x,t) - (\bar{m}B_{j-1} + A_{j-1})\frac{\mathrm{D}\bar{z}(x,t)}{\mathrm{D}t},$$
$$j = 1,2,...,J; \quad q_0 = 0$$

Thus the total linear force acting on the section becomes:

$$F(x,t) = -\bar{m}\frac{\mathrm{D}^2\bar{z}}{\mathrm{D}t^2} + U\frac{\partial\bar{m}}{\partial x}\frac{\mathrm{D}\bar{z}}{\mathrm{D}t} - \frac{\mathrm{D}q_J}{\mathrm{D}t} + \rho g\bar{z}B \tag{7.7}$$

7.3 Non-Linear Time-Domain Strip-Theory

Eq. (7.7) can be extended to include the loading effect due to the time variation of the wetted surface of the ship hull by assuming that A_j and B_j vary with both the sectional longitudinal position and the submergence, i.e. $A_j(x,\bar{z})$ and $B_j(x,\bar{z})$ cf. Xia et al., 1998. Eq. (7.1) and Eq. (7.6) thus give the non-linear time-domain sectional hydrodynamic force as

$$F(x,t) = -\bar{m}\frac{\mathrm{D}^2\bar{z}}{\mathrm{D}t^2} + U\frac{\partial\bar{m}}{\partial x}\frac{\mathrm{D}\bar{z}}{\mathrm{D}t} - \frac{\mathrm{D}q_J}{\mathrm{D}t} - \frac{\partial\bar{m}}{\partial\bar{z}}\left(\frac{\mathrm{D}\bar{z}}{\mathrm{D}t}\right)^2 + \rho g S \tag{7.8}$$

The non-linear fourth term in Eq. (7.8) is the "momentum slamming" term. This term is of particular interest when a ship section enters the water, i.e. when a rapid change in the added mass occurs and thus only comes into play when the section enters the water. Furthermore, the instantaneous non-linear Froude-Krylov term, $\rho g S$, replaces the linear term $\rho g\bar{z}B$ in Eq. (7.8) to account for the non-linear hydrostatic action (buoyancy) and obtain the total non-linear external fluid force acting on the section. S is the instantaneous submerged area of the ship section, including account for the Smith coefficient, and Eq. (7.8) thus also includes the still water load.

Results from the non-linear strip-theory for the case-ship have been compared to similar results from a fully 3D RANSE/VOF procedure and good agreement was found for both the rigid-body motions and the vertical bending moment, cf. Seng and Jensen, 2012.

7.4 Hydro-Elastic Equations of Motion

The ship hull is modelled as a linear, elastic non-uniform Timoshenko beam with the assumption of small rigid-body motions and structural distortions. Necessary parameters such as weight distribution, sectional moments of inertia, shear areas and modulus of elasticity are known for the ship for the loading condition for 02 October 2011 and for the strip-theory calculations the ship is considered consisting of 80 segments.

7.5 The Conditional Wave

The prescribed wave-induced vertical bending moment used in the present numerical study is 5,000 MNm in both the sagging and hogging condition. This is slightly below the design rule for the vessel in the hogging condition (6,270 MNm) and well below the design value in the sagging condition (-7,480 MNm) and thus the selected bending moment is likely to appear in realistic, moderate to large sea states as described in Chapter 8.

The transient, linear input waves are conditioned on the maximum vertical bending moment occurring at $t = 50$ s and represents the most probable wave scenarios yielding the prescribed response of 5,000 MNm in sagging and hogging respectively. The wave spectrum is taken as a Pierson-Moskowitz spectrum with the wave parameters listed in Table 7.1.

T_z	10.45 s
H_s	10 m

Table 7.1: *Wave spectrum parameters.*

Conditioning the wave for a maximum bending moment occurring at $t = 50$ s from the start of the simulations ensures that the initial conditions at $t = 0$ have negligible influence on the results. The incoming wave is considered as long crested and linear and the ship is sailing in head sea with a speed of 5 m/s (9.7 knots). The conditional wave is determined using the Proban software by DNV GL[1] and the First Order Reliability Method (FORM), see Jensen and Capul, 2006. Basically, the FORM analysis determines the design point, i.e. the wave parameters corresponding to the most probable wave scenario yielding the specified response. The design point is obtained by finding the minimum distance to the so-called failure surface: Response (prescribed) = response (calculated at $t = 50$ s) in a space described by the standard normal distributed and statistically independent parameters in the stochastic wave description. The most probable conditional wave scenarios that will cause a vertical bending moment of 5,000 MNm in sagging and hogging condition for the flexible ship are illustrated in Figure 7.1 and Figure 7.2, respectively. The illustrated wave is the encountered wave as seen from amidships.

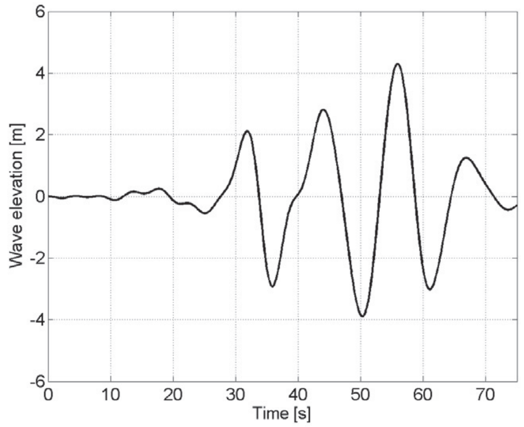

Figure 7.1: *The incoming wave amidships conditioned on a vertical bending moment of 5,000 MNm at t = 50 s in the sagging condition.*

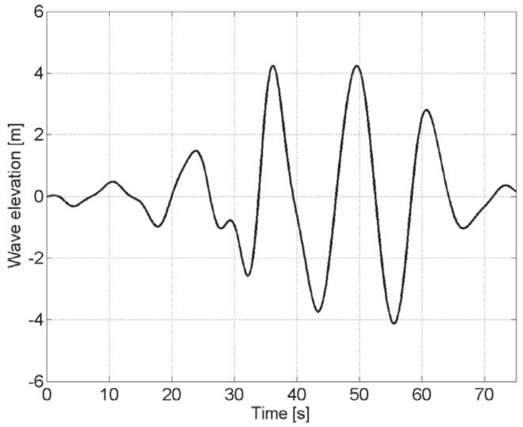

Figure 7.2: *The incoming wave amidships conditioned on a vertical bending moment of 5,000 MNm at t = 50 s in the hogging condition.*

---

[1] `http://www.dnv.com/services/software/products/sesam/sesam_probability/proban.asp`

7.6 Vertical Bending Moment in the Conditional Wave

Below the results from the non-linear strip-theory calculations are illustrated and discussed comparing the calculations for the flexible ship with the corresponding calculations for the rigid ship in the same wave.

7.6.1 *The sagging condition*

The wave elevation along the ship at $t = 50$ s for the sagging conditional wave is illustrated in Figure 7.3 and the vertical bending moment in the sagging condition for the flexible ship is illustrated in Figure 7.4. The effect of the hull flexibility is clearly seen and it can be observed that the hull becomes excited just after $t = 50$ s as a result of whipping. In the same figure the vertical bending moment in sagging condition is illustrated for the rigid ship using the same conditional wave as for the flexible ship in order to illustrate the effect of hull flexibility. It is observed that the hull flexibility increases the maximum amplitude of the subsequent hogging bending moment.

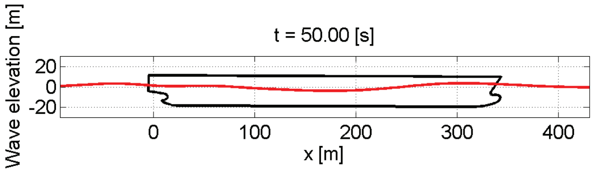

Figure 7.3: *Wave elevation along the flexible ship in sagging condition at* $t = 50$ *s.*

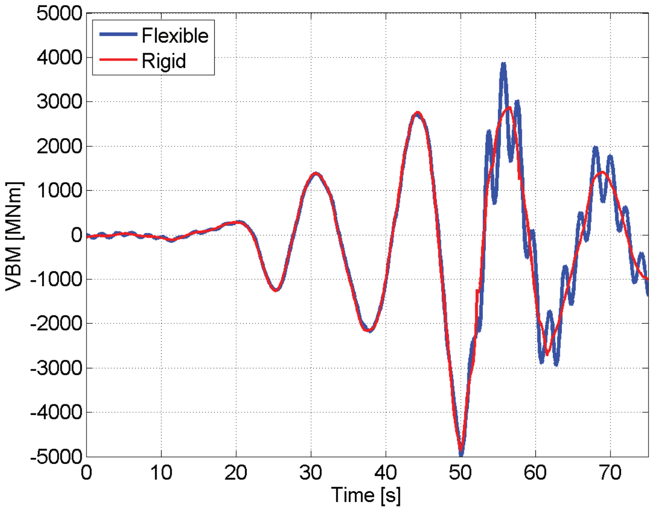

Figure 7.4: *Vertical bending moment amidships of the flexible ship and rigid ship in sagging condition. Conditional wave for the flexible ship. Hogging is positive*

7.6.2 *The hogging condition*

The wave elevation along the ship at $t = 50$ s for the hogging conditional wave is plotted in Figure 7.5 and the vertical bending moment for the flexible and the rigid ship in hogging condition is illustrated in Figure 7.6. The hull flexibility causes the whipping taking place at the sagging condition at around $t = 43$ s (illustrated in Figure 7.7) to influence (increase) the maximum vertical bending moment in the hogging condition quite significantly at $t = 50$ s.

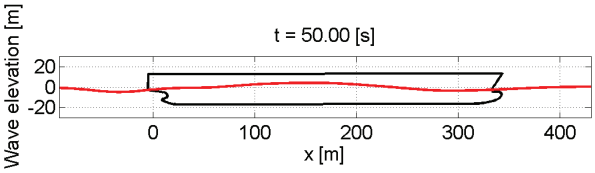

Figure 7.5: *Wave elevation along the flexible ship in hogging condition at* $t = 50$ *s.*

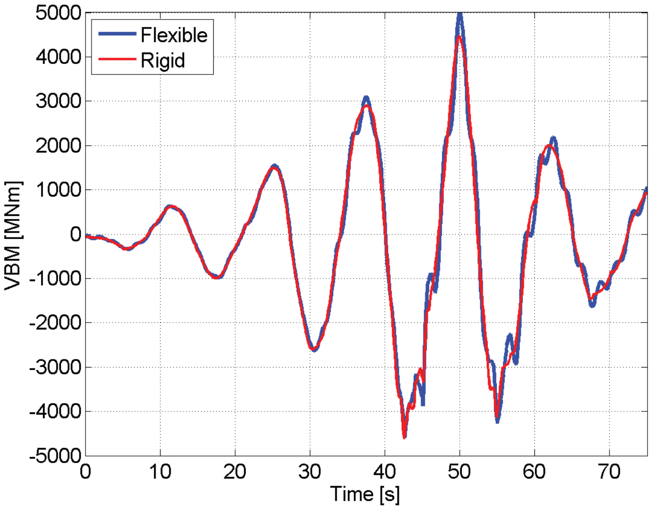

Figure 7.6: *Vertical bending moment amidships of the flexible ship and rigid ship in hogging condition. Conditional wave for the flexible ship. Hogging is positive.*

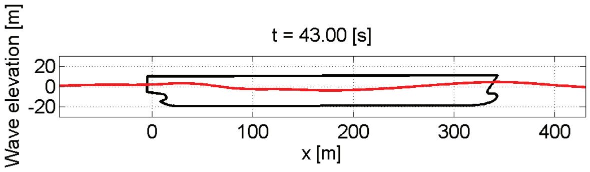

Figure 7.7: *Wave elevation along the flexible ship conditional on a hogging condition at* $t = 50$ *s. The plot shows the preceding sagging condition at* $t = 43$ *s.*

7.7 Statistical Properties

The main advantage of the FORM as compared to direct Monte Carlo Simulations (MCS) is that FORM usually provides a rather accurate estimate of the reliability index, β_{FORM}, related to exceedance of a response level, ϕ_0, at only a small fraction of the CPU time required for MCS. Furthermore, within the FORM approximation the reliability index β_{FORM} directly provides the mean upcrossing rate $\nu(\phi_0)$:

$$\nu(\phi_0) = \nu_0 e^{-0.5\beta^2_{FORM}(\phi_0)} \tag{7.9}$$

and thereby the extreme value distribution of the response. The coefficient ν_0 depends slightly on the response, ϕ_0, but is close to the zero-upcrossing rate, Jensen and Capul, 2006. The return period T of the response, ϕ_0, is simply obtained as $1/\nu(\phi_0)$. An additional advantage of the FORM is that it can identify the most probable input process (here the wave elevation), that leads to the required peak response ϕ_0 (here the wave bending moment amidships).

The main disadvantage of the FORM is that the linearisation around the most probably input process makes the reliability index less accurate than direct (exact) MCS, especially at high exceedance levels. This is a consequence of the FORM being only asymptotically correct in the limit of very small exceedance levels. The problem can be reduced by using a combination of MCS and FORM calculations in which a few MCS are performed with amplified load intensities (and thereby less CPU time) and with one FORM calculation used to subsequently scale the MCS results to the actual load intensity, see Garré and Der Kiureghian, 2010 and Jensen et al., 2011.

In the following, the FORM procedure has been used to identify four critical load scenarios related to a maximum wave bending moment amidships of 5,000 MNm in sagging and hogging conditions, taking the ship hull as either rigid or flexible. Physical explanations of the results in these scenarios have been given in the previous sections. The corresponding reliability indices are given in Table 7.2.

Scenario	FORM	MCS-low	MCS-mean	MCS-high
Sag, rigid	2.373	2.459	2.487	2.518
Sag, flexible	2.340	2.395	2.424	2.455
Hog, rigid	2.900	2.767	2.792	2.820
Hog, flexible	2.721	2.489	2.517	2.547

Table 7.2: *Reliability index β for the four scenarios.*

The results from the MCS are all based on a required Coefficient of Variation (COV) = 0.05 and the lower and higher values are the 90% confidence interval of the reliability index. The calculation time for the present MCS is two orders of magnitude larger than for the corresponding FORM calculations.

As expected, the reliability index is higher for the hogging conditions than for the corresponding sagging conditions implying higher sagging bending moments than hogging bending moments at the same probability level. This is in agreement with the measurements in Figures 9.2 and 9.1. Account for the hull flexibility also leads to higher probability of exceedance (lower reliability indices). This is especially true for the hogging condition due to the whipping excitation taking place at the preceding sagging condition as discussed previously.

For the present vessel and the considered response the FORM results are seen to be slightly higher than 90 percent bound on the corresponding MCS for hogging and the opposite for sagging. Hence, the linearisation in the FORM procedure here leads to non-conservative hogging results in the sense than the exceedance probabilities from the FORM become slightly less than from the MCS. For sagging the FORM yields conservative results. The main reason for the somewhat large difference between the FORM and MCS results is that the reliability indices considered here are rather small, corresponding to high exceedance probabilities (i.e. with a return period T of the order 10 minutes in this severe sea state) and, hence, implying less accurate FORM results in general. For long-term extremes these differences will usually be smaller as the FORM analysis becomes more accurate for small exceedance probabilities.

7.8 Comparison of Non-Linear Strip-Theory with Model Tests in Regular Waves

Non-linear strip-theory calculations using the flexible modelling of the ship have been carried out and compared to model tests with the segmented, flexible model of the 9,400 TEU ship described in Section 2.3.7. The comparison with the non-linear strip-theory results is done with the model tests performed in regular waves. The measurement results for the cut amidships (cut C) are utilised for the comparison. The comparisons are done for a wave height of 8.0 m for four different wave periods of 14.91, 14.32, 12.02 and 11.66 seconds with a ship forward speed of 15 knots in head sea. For the comparison, for the model tests the mean has been subtracted to correct for the static sagging moment induced by the forward speed which is not taken into account by SHIPSTAR.

The results of the comparison are shown below for decreasing wave lengths. For the longest of the waves ($\lambda/L_{pp} \simeq 1$), illustrated in Figure 7.8 the agreement is generally good and only a small effect of the hull girder flexibility can be observed in the sagging condition.

For the shorter waves the measurements show larger effects of the hull flexibility than the strip-theory results. The structural damping used in the strip-theory model is taken to be very low and can thus not be the cause of the lower response amplitudes.

In all cases, it can be seen that the 2-node natural frequency of the ship used in the strip-theory corresponds well to the natural frequency of the model for the 2-node vibration. This is particularly visible for the two shortest waves in Figure 7.10 and Figure 7.11.

The explanation of the lower response for the strip-theory calculations compared to the model tests is thus not to be found in the modelling of the mass, stiffness or the damping and must be found either in the hydrodynamic damping in the strip-theory modelling or in the way the exciting slamming force from the waves is modelled. The latter is particularly

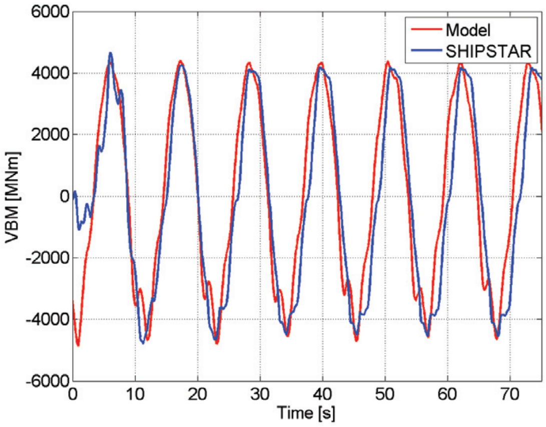

Figure 7.8: *Vertical bending moment amidships, wave period* $T = 14.91$ *s.*

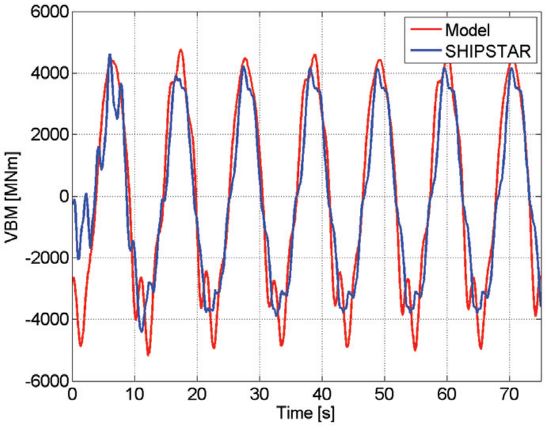

Figure 7.9: *Vertical bending moment amidships, wave period* $T = 14.32$ *s.*

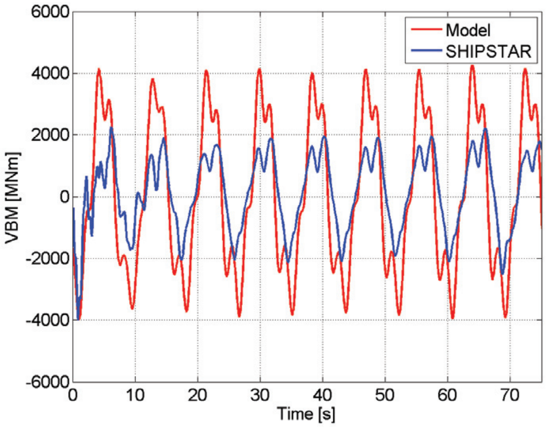

Figure 7.10: *Vertical bending moment amidships, wave period* $T = 12.02$ *s.*

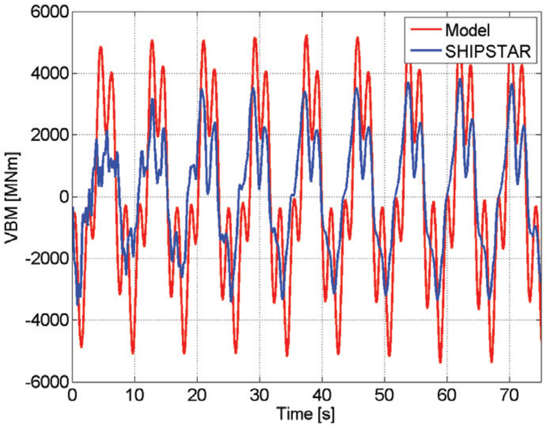

Figure 7.11: *Vertical bending moment amidships, wave period* $T = 11.66$ *s.*

important when slamming occurs, and it is believed that the difference between the model tests and the strip-theory calculation can be found in the non-linear momentum (fourth) term in Eq. (7.8). Both the timing and time duration of the term in the calculations and its size will influence the results.

7.9 Discussion and Conclusions

Both for the flexible and the rigid ship the vertical bending moment of 5,000 MNm is found to be more likely to occur in a sagging than in a hogging condition, cf. Table 7.2. The vertical bending moment in hogging is thus smaller than the sagging case for the same probability level. However, the hull flexibility increases the probability of the prescribed vertical bending moment in both sagging and hogging, but the vertical bending moment in the hogging condition is considerably more influenced by the hull flexibility than in the sagging condition.

The comparison with the model tests show good agreement for the longest of the waves where very little hydro-elastic response is found and poorer agreement for shorter waves, where the influence of the hull-girder flexibility is significantly underestimated. This was also found by Seng et al., 2012 who similarly compared the results from the model tests in regular waves to a free surface CFD method and the SHIPSTAR method. They found the CFD and the SHIPSTAR to be very similar in accuracy but the estimate of the influence of the hull girder flexibility was significantly lower (about 50%) for the smallest wave period of 11.66 s for the two numerical modelling methods than what the model tests showed. The flexible beam model used in strip-theory program seem to model the natural frequencies of the model well. The difference between the model tests and the SHIPSTAR results could be explained by the way momentum slamming is modelled in the non-linear strip-theory program. However, as the outcome from the non-linear strip-theory and the CFD calculations are very similar cf. Seng et al., 2012, the explanation cannot immediately be found in the hydrodynamic modelling.

In Chapter 10 the results from this chapter are compared to two relatively simple procedures for estimation of the non-linear and the hydro-elastic behaviour of the wave bending moment based on measured rigid-body responses relative motion in the bow together with the skewness of the wave bending moment amidships. From these comparisons with full scale measurements it can also be concluded that the hydro-elastic effects are underestimated in the non-linear strip-theory method used here.

The comparison with full scale measurements in Chapter 10, Figure 10.3 and the model test results in regular waves, Figures 7.8-7.11 indicate that a standard momentum slamming formulation as the one in Eq. (7.8) might yield non-conservative results and the semi-empirical formulation in Jensen et al., 2009 seems to provide better predictions when compared to full scale measurements.

Chapter 8

Measurements of Large Hull Girder Stresses in Container Ships

Part of this chapter is published by Andersen and Jensen, 2014. Supplementary plots of measured time series are given in Appendix D.

8.1 Introduction

In this chapter, full scale measurements of hull girder stresses will be analysed focusing on the largest measured events for four different container ships of 9,400 TEU, 8,600 TEU, 14,000 TEU and 4,400 TEU. For all four ships the measurements are taken amidships near the deck. Focus is on the influence of hull girder flexibility on the extreme load amidships. In all cases, tensile stress (i.e. the hogging condition) is positive. Beam theory will be used in the verification of the full scale measurements for the 9,400 TEU ship.

8.2 9,400 TEU Container Ship, 02 October 2011

On 02 October 2011 the ship went through a storm while approaching Hong Kong and was sailing about 10 knots in H_s of about 8 m in bow quartering seas from starboard side cf. Appendix A.1, Figures A.4, A.58, A.64 and A.70. The stress measurements amidships were obtained using two long-base strain gauges mounted in the passageways just below deck approximately amidships as described in Section 2.3.6. A 30 minute cut-out of the signal starting at 16 hours is illustrated in Figure 8.1.

The mean value of the time series is set to zero to remove the variation in still-water level, temperature effects, etc. However this may not be the true mean of the wave-induced vertical-bending moment due to non-linear effects. The signals are band-pass filtered to get the wave-frequency (WF) and high-frequency (HF) contribution as described in Section 6.3. The decomposed signal is illustrated in Figure 8.2 focusing on the time around $t = 350$ s where the largest stresses are measured. It is seen that the amplitudes of the WF and the HF part of the signal are comparable and both contribute with stress amplitudes of about 50 MPa. The maximum stress in hogging is 97 MPa while the maximum

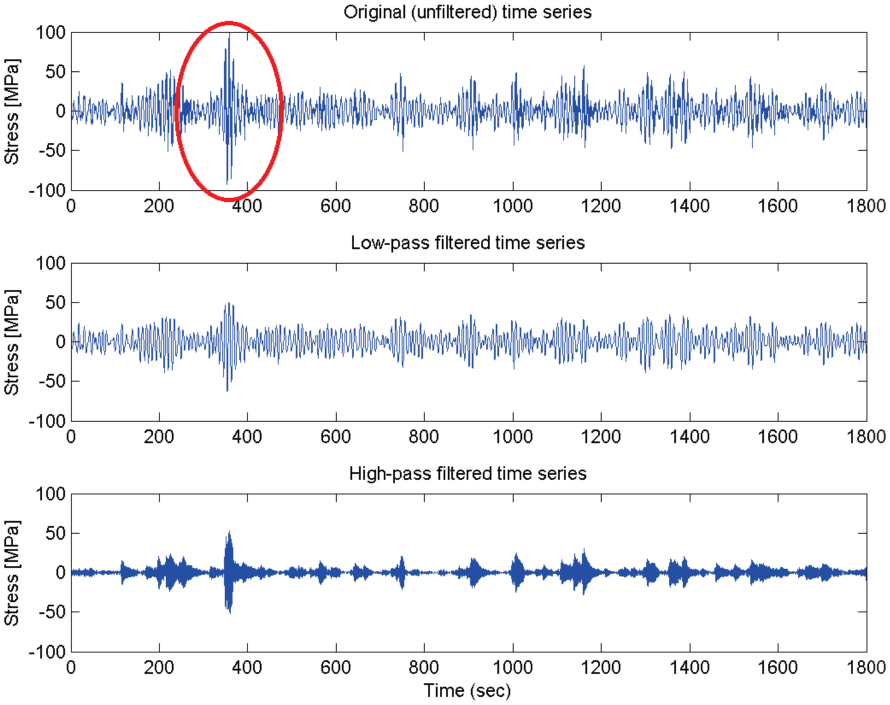

Figure 8.1: *Unfiltered, low-pass and high-pass filtered time series signal of stress (average of port and starboard side). Half an hour of data from 02 Oct 2011 starting at 16 hours showing the largest stresses at about 350 s as marked with red.*

in sagging is -96 MPa and the HF vibrations seem to be initiated in the hogging condition.

There is a small very low-frequency (below 0.01 Hz) contribution to the bending moment (seen as the lowermost sub-plot in Figure D.1 in Appendix D which contributes to about 3% of the maximum bending moment. This might be due to higher-order difference frequency terms from both the wave and the high-frequency response. The maximum measured stress amplitudes from the unfiltered signal are 100 and -93 MPa in hogging and sagging respectively. For consistency throughout the thesis the very low-frequency contribution below 0.01 Hz is filtered off.

In addition to strain gauges, the 9,400 TEU ship is equipped with accelerometers in the bow, local strain gauges in the bow flare area, a directional wave radar on the bridge extracting wave statistics and two down-looking wave radars in the bow measuring the relative wave elevation as described in Section 2.3. The data from this equipment will be used in the verification of the strain measurements in the following. The same filtering as for the strains is applied to the other ship responses.

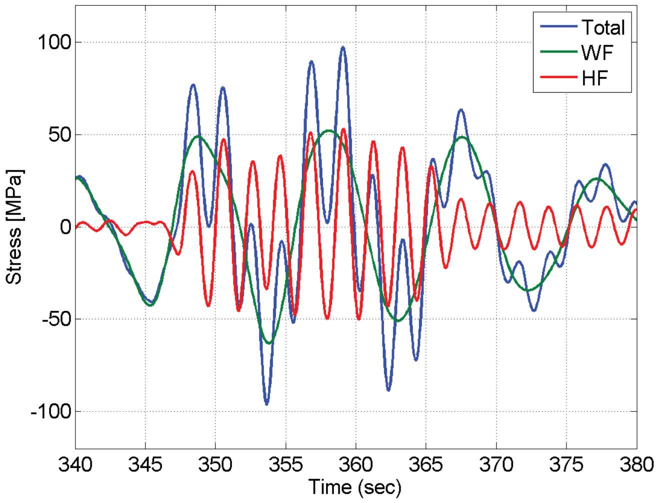

Figure 8.2: *Filtered time series signal of stress (average of port and starboard side) from 9,400 TEU ship on 02 October 2011. The total response is equal to the sum of the WF and HF contributions.*

8.2.1 *Verification of measurements using high-frequency response amplitudes*

The hull girder vibrations are initiated in the hogging condition for this event. Usually, hull girder vibrations in container ships are initiated by bow flare slamming in the sagging condition, but have also been observed to be initiated in hogging in model tests cf. e.g. Zhu et al., 2011 where the vibrations were initiated in the hogging condition due to a large downwards suction force acting on the bottom of the bow. However, the model used by Zhu et al., 2011 had a block coefficient of 0.9 and did not feature a typical flared container ship bow. There are only few examples of vertical hull girder vibrations being initiated in the hogging condition from full scale measurements, but one example from a 2,800 TEU container ship is described by Storhaug and Heggelund, 2008.

In order to validate that the measurements are initiated in the hogging condition the HF surge motion is compared to the HF hull girder strain in Figure 8.3. Positive surge motion corresponds to elongation of the deck (see Table B.1) and is seen to coincide with the positive HF stress peaks.

By considering the time series for the measurements of the stresses, ship motions, local bow flare loads and ship speed/relative wave elevations in Figure 8.2, 8.4, 8.5, 8.6, 8.7 and 8.8 respectively more information about this event can be obtained. From the surge and heave accelerations in Figures 8.4 and 8.5, it is clear that something happens abruptly around $t = 348$ s. Furthermore, from Figure 8.6 it can be seen from the relative wave elevation measured in the fore part that the ship encounters a large wave train entering from the port side of the ship. Particularly, the wave encountered by the ship between $t = 346 - 350$ s seems large and steep (indicated on the plot). Accordingly, the ship speed

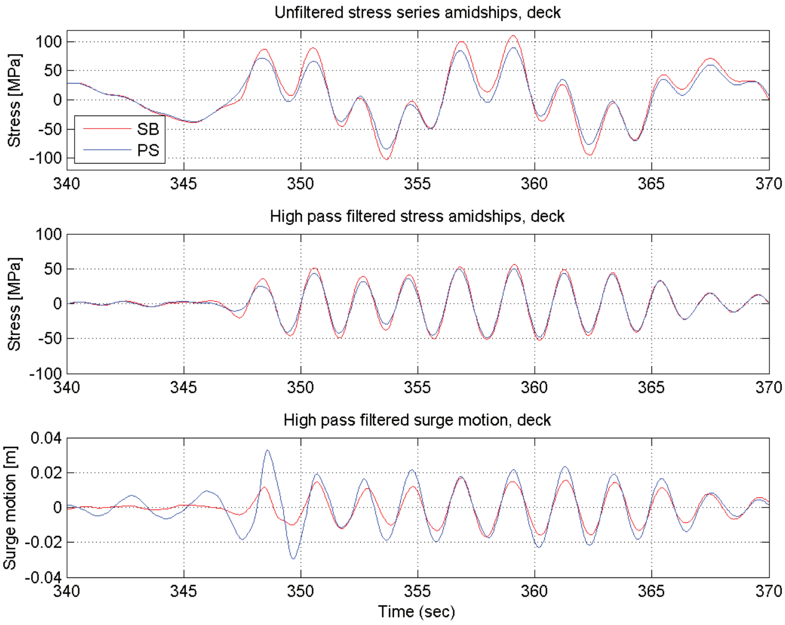

Figure 8.3: *Unfiltered and high pass filtered stress amidships compared to the surge motion measured in the deck at FP. Same event as Figure 8.2.*

is decreased about 0.5 knots as also seen from Figure 8.6.

From the measurements from the strain gauges mounted in the bow flare area to measure slamming pressures (Figure 8.7), two large and a small stress peak are seen on the port side. These peaks are seen to occur slightly earlier than the initiation of the vertical vibration as expected due to inertia effects. Thus, it seems very plausible that these peaks indicate the event that initiated the vertical vibrations.

There is no pronounced roll or pitch motion at the time of the event as indicated in Figure 8.8. However the ship is rolling towards port and the bow is going down at the time of the impulsive load on the port side seen in Figure 8.7. Both motions tend to increase the magnitude of the impulse loads entering from the port side.

The vibrations last for a relatively long time (about 15 seconds) and do not decay as expected for this type of response. The reason for the very low whipping decay shown in Figure 8.2 is thus not only due to low damping but also due to the excitation which consists of two to three wave impacts spaced about eight seconds in time. Hence, the whipping initiated from the first impact does not die out before the next takes place.

As the overall qualitative behaviour seems plausible, the next step is to investigate the consistency of the measured response amplitudes. This will be done using Bernoulli-Euler beam theory applicable for 2-node vertical vibrations and the associated relationships between the measured response amplitudes at different locations in the ship (accelerations in the bow and stresses amidships). The deflection, w, for the 2-node mode as function of time and location is given by Eq. (5.3) (repeated here):

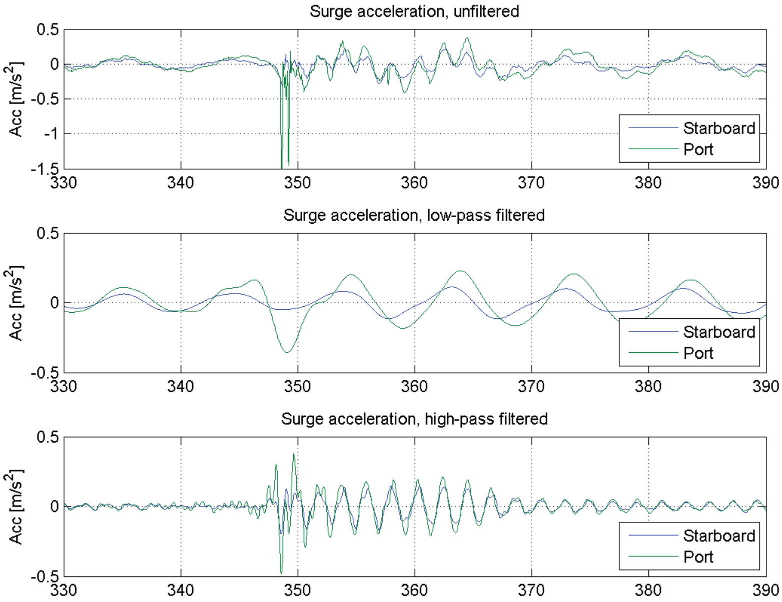

Figure 8.4: *Surge acceleration, unfiltered, high-pass and low-pass filtered. Note difference in the vertical-axes.*

$$w(x,t) = \nu_2(x)u(t)$$

where $\nu_2(x)$ is the 2-node mode shape approximated by Eq. (5.9) and $u(t) = u_0 \cos(\omega_2 t)$ considering free vibrations only, i.e. the response after the slamming impulse has ceased. Generally, the bending moment $M = EIw''$, implying that the bending stress due to the 2-node vertical vibration can be calculated as:

$$\sigma = Eu(t)\nu_2''(x_{sg})z_{sg} \tag{8.1}$$

where x_{sg} is the x-coordinate for the strain gauge location and z_{sg} is the vertical distance from the neutral axis to the strain gauge. The (horizontal) surge acceleration due to bending $\ddot{s}$ can be written as (see also Appendix G):

$$\ddot{s}(x,t) = \nu_2'(x_{acc})\ddot{u}(t)z_{acc} = -\omega_2^2\nu_2'(x_{acc})u(t)z_{acc} \tag{8.2}$$

where x_{acc} is the x-coordinate of the accelerometer measuring the surge acceleration in the bow and z_{acc} is the vertical distance from the neutral axis to the accelerometer. The (vertical) heave acceleration $\ddot{h}$ can correspondingly be written as:

$$\ddot{h}(x,t) = \ddot{w}(x,t) = \nu_2(x_{acc})\ddot{u}(t) = -\omega_2^2\nu_2(x_{acc})u(t) \tag{8.3}$$

The aim is to see if these different responses all correspond to the same vertical beam vibration. Therefore, the amplitude u_0 of $u(t)$ becomes irrelevant. However, later its magnitude will be estimated from the measured impulsive loads.

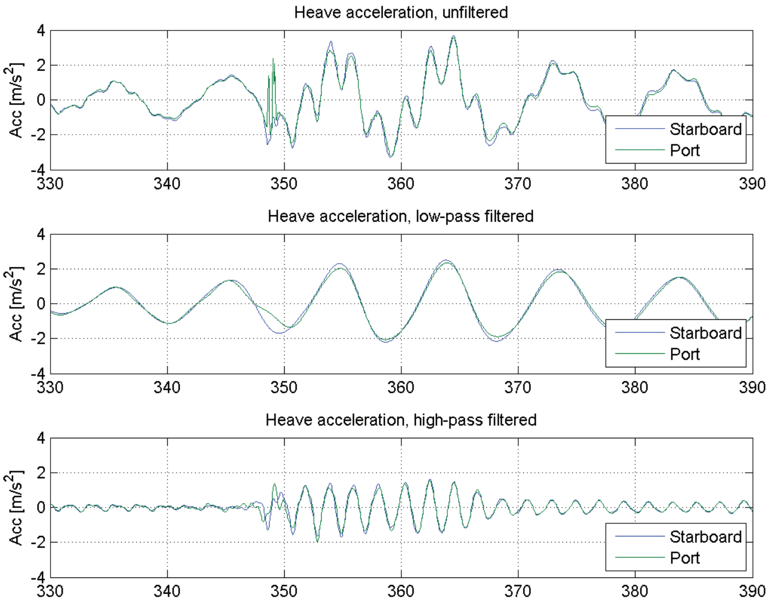

Figure 8.5: *Heave acceleration, unfiltered, high-pass and low-pass filtered.*

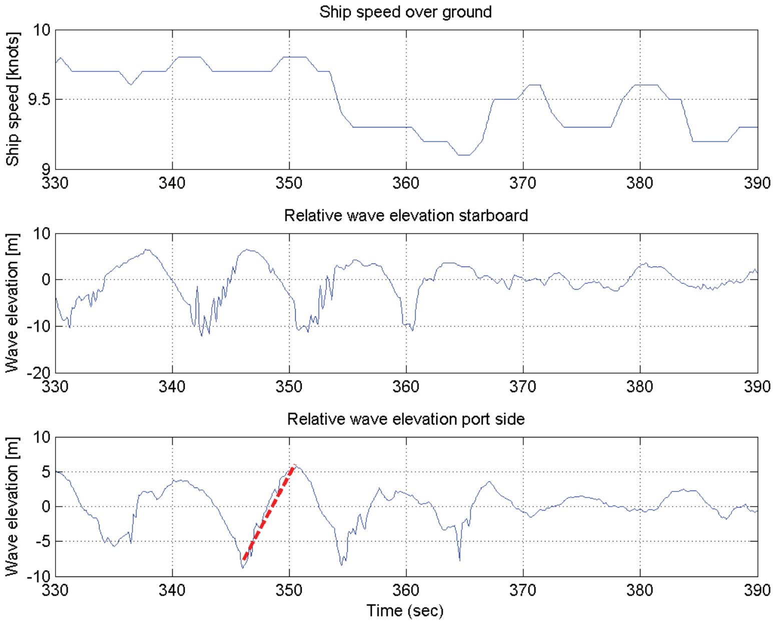

Figure 8.6: *Ship speed and relative wave elevation from wave radar measurements in the bow. Indication in red used for estimation of the maximum relative vertical velocity $\dot{h}$ at the instant of slamming on the lowermost plot.*

The surge measurement is low-pass and high-pass filtered in Figure 8.4. The frequency of the high-frequency contribution in the unfiltered part of the signal seen in Figure 8.4 around $t = 349$ s is much higher than the high-pass cut-off frequency of 1.6 Hz and is probably due to longitudinal vibrations in the hull girder where the natural vibration

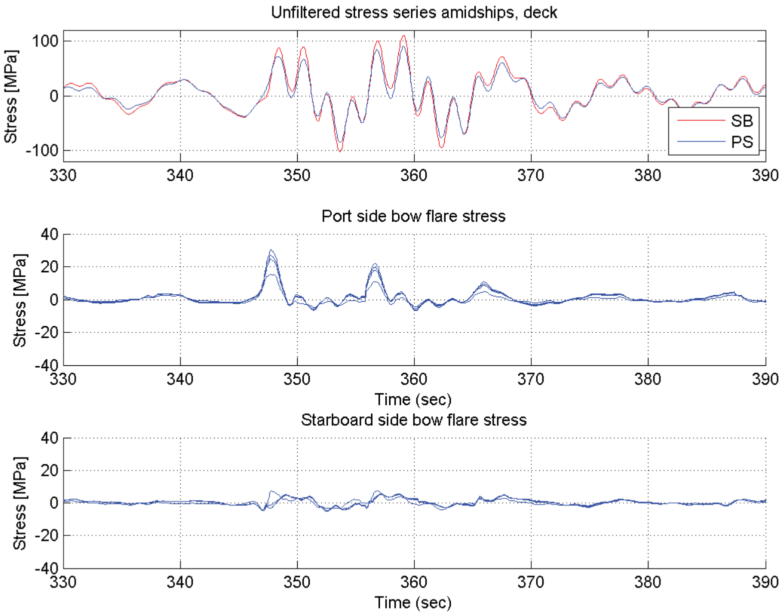

Figure 8.7: *Bow flare stresses measured close to FP. There are four strain gauges in each side of the bow. For comparison, the unfiltered stress amidships is illustrated in the top plot.*

frequency is much higher than the natural frequency for vertical bending.

From the measurements in Figures 8.2, 8.4 and 8.5 a HF stress amplitude of 50 MPa, a 2-node surge acceleration amplitude of 0.2 m/s^2 and a 2-node heave acceleration amplitude of 1.1 m/s^2 are estimated from the high-frequency part of the responses. Thus, comparing the ratios of the estimated high-frequency response amplitudes give:

$$\frac{\sigma}{\ddot{s}} = \frac{50\ \text{MPa}}{0.2\text{m/s}^2} = 250 \qquad \text{and} \qquad \frac{\sigma}{\ddot{h}} = \frac{50\ \text{MPa}}{1.1\text{m/s}^2} = 46$$

These estimates can be compared to the theoretical ratios obtained from Eqs. (8.1), (8.2) and (8.3) using Eq. (5.9) for the mode shape $\nu_2(x)$ and applying the same units:

$$\frac{\sigma}{\ddot{s}} = \frac{-E\nu_2''(x_{sg})z_{sg}}{\omega_2^2\nu_2'(x_{acc})z_{acc}} = 285 \qquad \text{and} \qquad \frac{\sigma}{\ddot{h}} = \frac{-E\nu_2''(x_{sg})z_{sg}}{\omega_2^2\nu_2(x_{acc})} = 41$$

Differentiation of Eq. (5.9) for the mode shape gives rise to uncertainties. Hence, instead of approximating the mode shape with the polynomial in Eq. (5.9), local derivatives of the mode shape might give a more accurate estimate in the desired locations. The following fits have been used, but as seen the difference in the outcome is small:

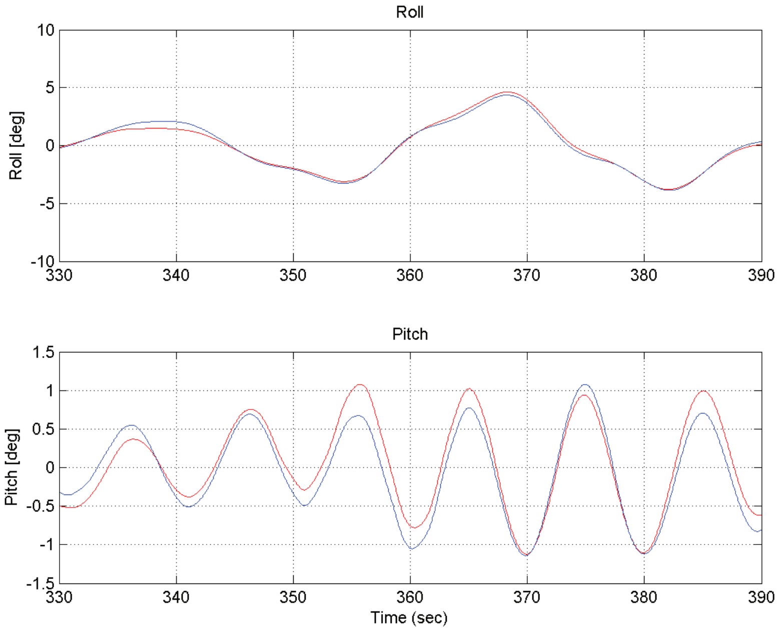

Figure 8.8: *Roll and pitch. Roll is positive when rolling to starboard and pitch is positive for the bow going down.*

$\nu_2'(x_{\mathrm{acc}}) = 0.0128$ using 6 order polynomial fit, Eq. (5.9).
$\nu_2'(x_{\mathrm{acc}}) = 0.0126$ using linear fit to 5 foremost mode shape data points.
$\nu_2''(x_{\mathrm{sg}}) = 0.000141$ using 6 order polynomial fit, Eq. (5.9).
$\nu_2''(x_{\mathrm{sg}}) = 0.000138$ using linear fit to the first derivative of Eq. (5.9) and 9 central mode shape data points.

The estimated ratios from the high-frequency responses are seen to fit quite well with the theoretical ones from Bernoulli-Euler beam theory confirming the consistency and accuracy of the full scale measurements and the assumption that the hydro-elastic response is dominated by the 2-node vertical vibration.

8.2.2 *Impulsive loads*

The extreme response of the ship is believed to be initiated by an impulsive load in the bow. The next step is to estimate the magnitude of the impulsive load on the ship. Only the 2-node mode is included in the calculations. The vertical vibratory response can be modelled by applying a triangular impulsive load $P(t)$ on the ship with the duration T_c. From $0 < t < T_c$ the vibration is forced and for $t > T_c$ the vibration is free, but damped. The vertical slamming impulse is:

$$I_{vertical} = \int_0^{T_c} P(t)\mathrm{d}t \tag{8.4}$$

where the slamming load P is acting during the time T_c which is short compared with the natural vibration period. After the slamming impact the vibration in the hull girder will continue as a free vibration. The maximum modal displacement u_{max} can, cf. Jensen et al., 2009, be estimated to be:

$$u_{max} = \frac{I_{vertical}}{\omega_2 M_2} \exp(-\xi \omega_2 T_c) \tag{8.5}$$

where ξ is the structural damping coefficient (% of critical damping) and M_2 is the modal mass from Eq. (5.7). No phase lag between modes is considered since only one mode is taken into account.

The maximum high-frequency surge acceleration $\ddot{s}$ was estimated from Figure 8.4 to 0.2 m/s^2. Then u_{max} can be found from Eq. (8.2). Neglecting the exponential term in Eq. (8.5) i.e. assuming a very short duration of the impulse T_c, the impulse in the vertical direction can be found as:

$$I_{vertical} \simeq u_{max} M_2 \omega_2 = 0.11 \text{ m/s} \cdot \Delta$$

where Δ is the displacement of the ship in tons. Eq. (8.5) overestimates the response as a direct solution of the governing equation, Eq. (5.8), shows. For an assumed value of $T_c = 0.5$ s and a damping coefficient $\xi = 0.01$, the value found by Eq. (8.5) should be reduced by 8% according to Figure 8.9, where the ratio between u_{max} and the maximum response is 1.085. Hence, the estimation becomes:

$$I_{vertical} \simeq 0.10 \text{ m/s} \cdot \Delta \tag{8.6}$$

The same is done for a damping coefficient $\xi = 0.03$ in Figure 8.10 and the difference is small. It is difficult to accurately determine the damping from full scale measurements as stated by e.g. Storhaug et al., 2003 but the uncertainty of using a damping coefficient $\xi = 0.01$ does not seem significant. As seen from Table 5.1 in Chapter 5 the damping estimated from 24 hours of data on 02 October is 0.018.

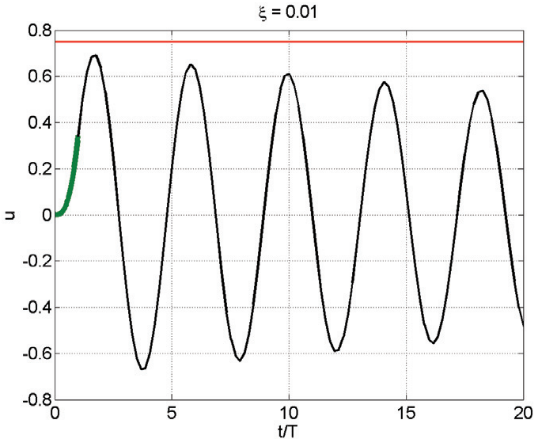

Figure 8.9: *Damped free vibration initiated by the impulse $I_{vertical}$ of duration $T_c = 0.5$ s and damping coefficient $\xi = 0.01$.*

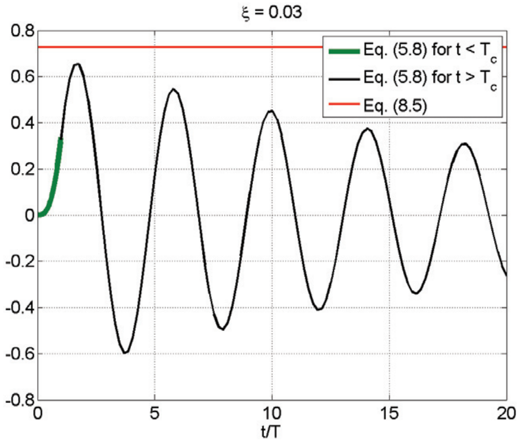

Figure 8.10: *Same as Figure 8.9, but with a damping coefficient $\xi = 0.03$.*

Alternatively, using the closed-form expression by Pedersen and Jensen, 2009, the vertical slamming impulse can be estimated by:

$$I_{vertical} = \frac{\pi^2}{24} \beta L \rho \nu_2(x_0) B_l^2 \dot{z}(x_0) \tag{8.7}$$

where B_l is the local waterline breadth, β is the longitudinal extent of the slamming pressure as fraction of the total ship length, and $\dot{z}$ is the relative vertical velocity between the ship and the wave. The relative vertical velocity $\dot{z}(x_0)$ at the instant of slamming can be estimated from Figure 8.6 (red dashed line) to be around 3 m/s. β is taken as 0.05 as in Jensen et al., 2009, L is taken as L_{oa}, B_l is taken as 28 m, and x_0 is taken as $x_0 = x_{acc}$. Then, Eq. (8.7) yields the following estimate:

$$I_{vertical} = 0.11 \, \mathrm{m/s} \cdot \Delta \tag{8.8}$$

Thus, the two independent estimates Eq. (8.7) and Eq. (8.6) give nearly the same value, supporting the validity of the result. However, quite a large uncertainty is associated with the estimation of $\dot{z}(x_0)$ and the longitudinal extent β used in Eq. (8.7).

As seen from Figure 8.6 the ship speed is decreased by about 0.5 knots during the time of the event. The impulse in the longitudinal direction needed to slow down the ship is the change in momentum:

$$I_{longitudinal} = 0.26 \, \mathrm{m/s} \cdot \Delta \tag{8.9}$$

A small amount (10%) could be added to Δ to account for the added mass of water in the surge motion. Generally, it seems reasonable that $I_{longitudinal}$ is considerably larger than $I_{vertical}$ since the majority of the impact load here contributes to slowing down the ship.

The first estimation (Eq. (8.6)) of the vertical impulse is based on the measured 2-node surge acceleration $\ddot{s}$. The only assumption made is Bernoulli-Euler beam theory, i.e. $w(x,t) = \nu_2(x)u(t)$ and that the impulse acts on the fore part of the ship. The surge acceleration $\ddot{s} = 0.2$ m/s thus leads to $I_{vertical} = 0.1 \, \mathrm{m/s} \cdot \Delta$. This result is obviously difficult to use in design or operational guidance because it requires measurements of the 2-node response. Contrarily, the alternative way of arriving at the vertical impulse using Eq. (8.7) can be used in the design phase since it requires only an estimate of the relative vertical rigid-body velocity $\dot{z}$ at the FP which can be obtained easily from e.g. strip-theory. Eq. (8.7) has not earlier been verified from full scale measurements, but the agreement here seems good.

In the remaining part of the chapter, other large measured responses are discussed for this vessel as well as for three other container ships. Additional figures are given as supplement in Appendix D.

8.3 9,400 TEU Container Ship, 12 August 2011

For the 9,400 TEU ship a large event took place on 12 August 2011 at 01 hours. The maximum total stress amplitude (blue) is 34 MPa in hogging and -31 MPa in sagging as seen in Figure 8.11 (average of port and starboard signal), which is not a very large response, but the hydro-elastic effects (red) are also considerable in this case and more than doubles the total response. Again, the somewhat uncertain definition of the zero value of the wave-induced response must be noticed.

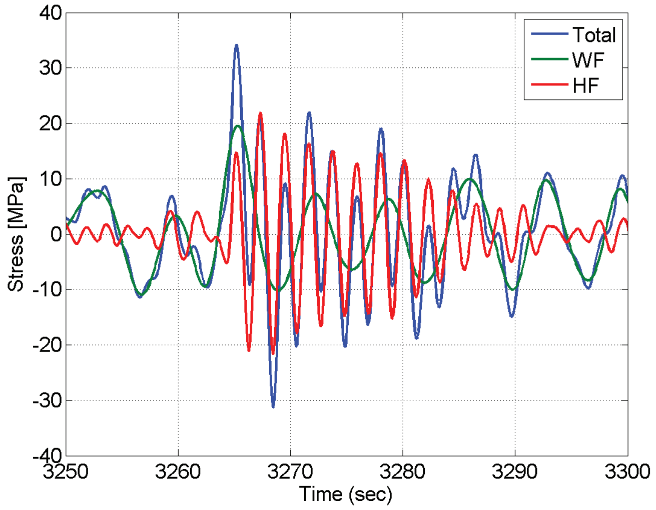

Figure 8.11: *Filtered time series signal of stress (average of port and starboard side) from 9,400 TEU ship on 12 August 2011. The total response is equal to the sum of the WF and HF contributions.*

The large, positive stress peak at 3,265 seconds indicate that the vibrations started in the hogging condition. From Appendix A.1.2 it can be seen that the ship was sailing about 21 knots (Figure A.7) in H_s of about 5 m (Figure A.13) in bow-quartering seas from port side (Figure A.19).

It is seen that the amplitude of the HF vibrations is at times higher than the WF contribution and, similarly to what was found for the response taking place on 02 October 2011 (Figure 8.2), the HF whipping contribution more than doubles the response amplitude of the stress amidships, even for this moderate response.

The 30 minute time history associated with the response is found i Appendix D, Figure D.2 and the filtered components are found in Figure D.3. The low-frequency contribution below 0.01 Hz is seen from Figure D.3 to be insignificant in this case.

8.4 9,400 TEU Container Ship, 17 December 2011

For the 9,400 TEU ship the second largest measured stress response is found on 17 December 2011 at 14 hours. The port side strain gauge was off-line that day so only the measurements from the starboard side sensor are used. The maximum stress amplitude is 51 MPa in hogging and -42 MPa in sagging cf. Figure 8.12.

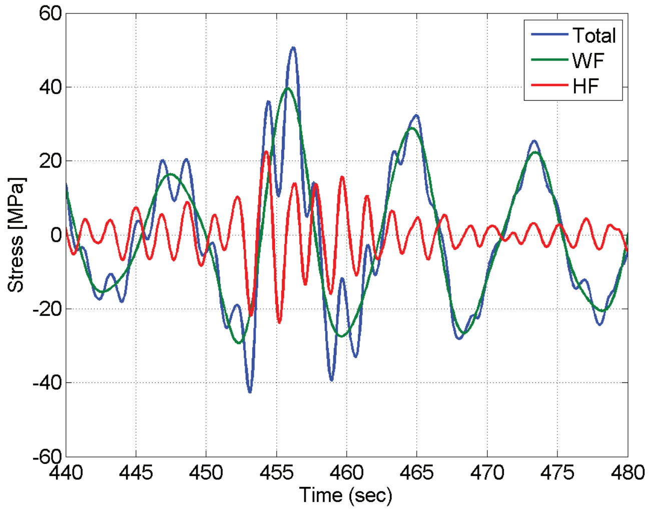

Figure 8.12: *Filtered time series signal of stress (starboard strain gauge) from 9,400 TEU ship on 17 December 2011. The total response is equal to the sum of the WF and HF contributions.*

Cf. the navigational data in Appendix A.1.2 the ship was sailing about 16 knots (Figure A.75) in head sea (Figure A.87) in H_s of 6-7 m (Figure A.82).

It is seen that the amplitude of the HF vibrations is not as large as for the previous two events. Furthermore, it is seen from Figure 8.12 that the hull girder vibrations are initiated in the sagging condition.

The 30 minute time history associated with the response is found i Appendix D, Figure D.4 and the filtered components are found in Figure D.5.

8.5 8,600 TEU Container Ship, 17 November 2010

For the 8,600 TEU container ship measurements of the strains amidships in the deck were obtained as described in Section 2.4.2. It is noted that this ship has a very large bow flare angle of 58 deg determined in accordance with Det Norske Veritas, 2013a which is expected to make the ship more susceptible to slamming loads compared to the 9,400 TEU ship described in the previous sections which has a smaller flare angle.

The measurements are filtered and presented in the same way as for the 9,400 TEU ship in the previous section. The largest response took place on 17 November 2010 at 22 hours. The GPS position and navigational information was unavailable from the measurement data during this period, but according to Mondher, 2012 the ship was bound for Asia sailing in the English Channel on a Westerly course and the ship's master reported a significant wave height, H_s, of about 5.5 meters and the relative heading being mainly head sea. The largest event is found at around 3,550 seconds and a zoom on the extreme event is seen in Figure 8.13.

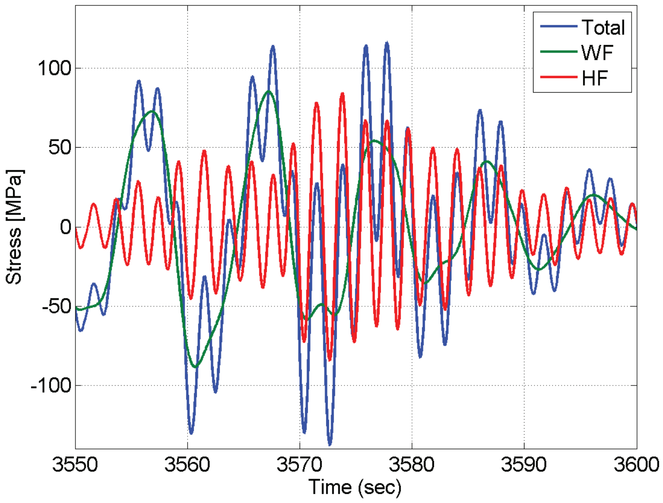

Figure 8.13: *Filtered time series signal of stress (average of port and starboard side) from 8,600 TEU ship on 17 November 2010. The total response is equal to the sum of the WF and HF contributions.*

The maximum hull girder stress in hogging is 117 MPa while it is -138 MPa in sagging. The maximum WF stress is 85 MPa in hogging and -88 MPa in sagging. Finally, the maximum HF stress is 84 MPa in hogging and -84 MPa in sagging. Clearly, the total response is greatly increased by the effect of HF whipping vibrations. The 30 minute time history associated with the response is found in Appendix D, Figure D.6 and the filtered components are found in Figure D.7. As also observed for the 9,400 TEU ship, a very low-frequency component is present in the measurements.

8.6 8,600 TEU Container Ship, 30 December 2011

Another large response for the 8,600 TEU ship took place on 30 December 2011 at 7 hours and is illustrated in Figure 8.14. Cf. Appendix A.2, Figures A.127 the ship was sailing west in the Mediterranean Sea with about 10 knots. No information about the sea state is available for this period.

The maximum total stress is 95 MPa in hogging and -94 MPa in sagging. The maximum WF stress is 46 MPa in hogging and -52 MPa in sagging. For the HF part the maximum is 53 MPa in hogging and -55 MPa in sagging. Here the HF contribution is slightly larger than the WF contribution. The duration of the large HF vibrations is quite long (about a minute) compared to the previously considered events. A plausible explanation is that the ship probably experiences more than one slamming event during that period which maintain the hull girder vibrations. It is noted that the vibrations are here clearly initiated in the sagging condition.

The 30 minute time history associated with the response is found i Appendix D, Figure D.8 and the filtered components are found in Figure D.9.

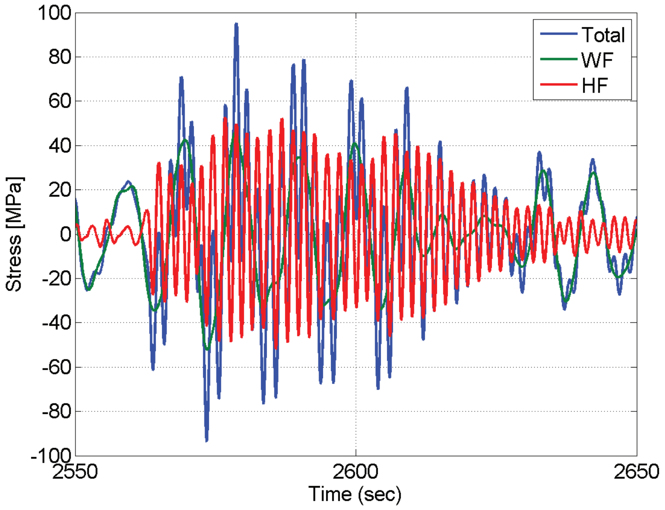

Figure 8.14: *Filtered time series signal of stress (average of port and starboard side) from 8,600 TEU ship on 30 December 2011. The total response is equal to the sum of the WF and HF contributions.*

8.7 14,000 TEU Container Ship, 29 September 2011

For the 14,000 TEU ship, the largest measured stress response took place on 29 September 2011. The GPS was off-line and no information of the ship's position, course or speed is available. The largest response is found in hogging at around 750 s and just in excess of 100 MPa. The contribution to the total response from the HF vibrations is smaller than the WF part.

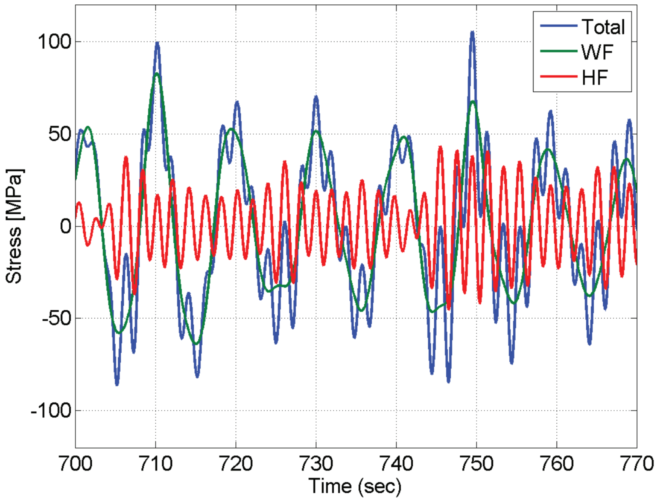

Figure 8.15: *Filtered time series signal of stress (average of port and starboard side) from 14,000 TEU ship on 29 September 2011. The total response is equal to the sum of the WF and HF contributions.*

It is difficult to determine whether the vibrations are initiated in hogging or sagging because there is a rather constant HF vibration present, but the vibrations seem to be initiated in the sagging condition. Furthermore, the ship seems to be experiencing two successive slamming events about 40 seconds apart. It is noted that the WF hogging peaks are generally larger than the corresponding sagging peaks.

The filtered components are found in Figure D.10 in Appendix D. As also found for the other ships, a low-frequency contribution below 0.01 Hz is found. Contributions below 0.01 Hz are filtered off for the extreme value analysis, but here constitute about 2% of the total stress. The port and starboard side signal in Figure D.11 are seen to be quite similar. Although no navigational data is available the ship is thought to encounter head sea in the situation considered here.

8.8 14,000 TEU Container Ship, 21 July 2011

For the 14,000 TEU ship the second largest event takes place on 21 July 2011. For this day the navigational data given in Appendix A.3.1 is available. The ship is heading west sailing around 18-20 knots. The response is seen in Figure 8.16. The highest stress is 80 MPa in hogging and -65 MPa in sagging. The contribution from the HF vibrations is of the same magnitude as the WF response.

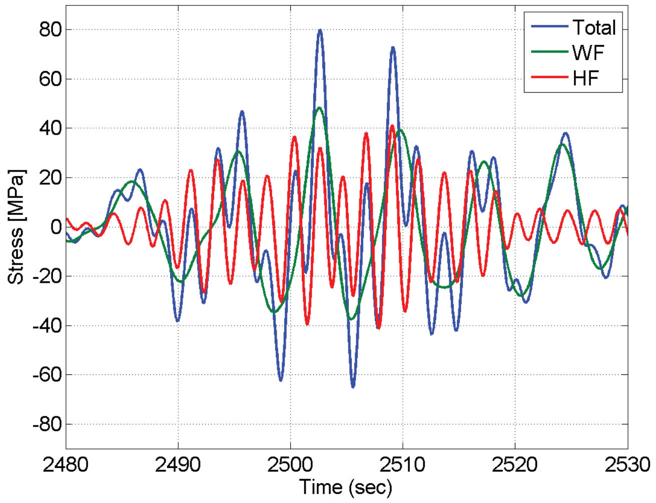

Figure 8.16: *Filtered time series signal of stress (average of port and starboard side) from 14,000 TEU ship on 21 July 2011. The total response is equal to the sum of the WF and HF contributions.*

Although difficult to determine, the vibrations seem to be initiated in the hogging condition. The filtered components are found in Figure D.12 in Appendix D. From Figure D.13, where the port and starboard signals are plotted, it is seen that there is rather large difference between the port and starboard side signal and the ship is thought to have encountered oblique seas in this case.

8.9 4,400 TEU Container Ship, 02 November 2007

In order to shed light on the size effects on the hydro-elastic response some events of large stresses for a smaller container vessel are selected. The vessel is a 4,400 TEU Panamax container ship described in section 2.6. The ship is operated on the North Atlantic and the full scale measurements obtained were also investigated by Mathisen et al., 2009. The ship has a higher 2-node natural frequency in vertical bending than the three larger container ships (around 0.6 Hz). Hence, in the filtering the dividing frequency between the WF and the HF part is set to 0.4 Hz. Apart from this, the filtering is the same as applied on the previous time series.

The largest stresses are measured on 02 November 2007. At this time the ship was sailing about 13 knots in waves with a significant wave height of about 6 m. Accurate sea state information from the wave radar on board is not available for this period cf. Mathisen et al., 2009. During the day, two large events are measured: one at 11 hours and one at 16 hours. The first event includes the largest measured sagging response and the latter is the largest measured hogging response. The time series from 11 hours is seen in Figure 8.17.

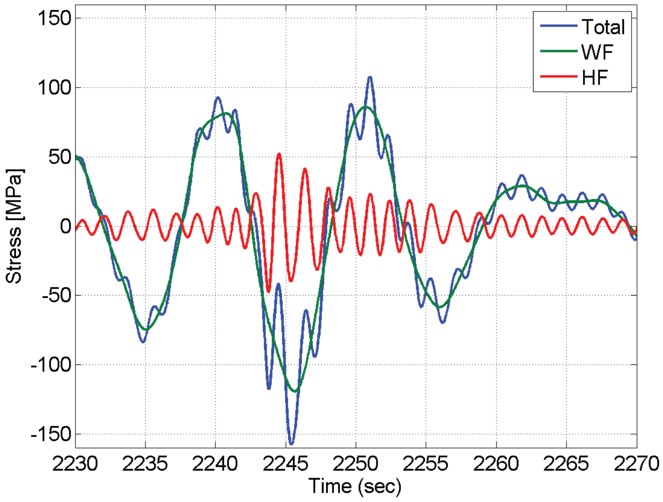

Figure 8.17: *Filtered time series signal of stress (average of port and starboard side) from 4,400 TEU ship on 02 November 2007 at 11 hours. The total response is equal to the sum of the WF and HF contributions.*

The largest response is found in sagging and is -158 MPa which makes it the largest response measured on board the four container ships considered here. The maximum WF response is -119 MPa and for the HF response the maximum stress amplitude is -49 MPa. The vibrations seem to be initiated in the sagging condition. It is noted that the maximum amplitudes found here differ from the ones found in Mathisen et al., 2009 due to differences in the cut-off limits applied for the band-pass filtering.

For the other large event taking place around 16 hours, where the largest hogging response is found, the response is illustrated in Figure 8.18. The largest response amplitude is also found in sagging and is -133 MPa. The maximum WF response in sagging is -72 MPa and the maximum HF stress is -61 MPa. For hogging the maximum stress is 131 MPa. The maximum WF response is 71 MPa and for the HF response the maximum stress amplitude is 63 MPa. The vibrations also seem to be initiated in the sagging condition here.

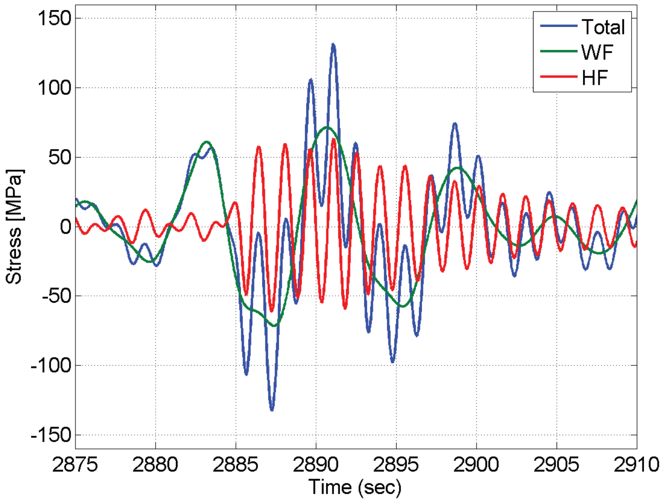

Figure 8.18: *Filtered time series signal of stress (average of port and starboard side) from 4,400 TEU ship on 02 November 2007 at 16 hours. The total response is equal to the sum of the WF and HF contributions.*

A 30 minute cut-out of the signal from around 11 hours, where the largest sagging response is found, is seen in Figure D.14 and the filtered components are found in Figure D.15. For the response at 16 hours a 30 minute cut-out of the signal is seen in Figure D.16 and the filtered components are found in Figure D.17.

8.10 4,400 TEU Container Ship, 01 July 2008

For 01 July at 19 hours there are two large events during 30 minutes, which are also the two largest event measured during that day. One at around 1,650 seconds and one at around 2,700 seconds as are illustrated in Figures 8.19 and 8.20.

For the first event the largest response of almost -100 MPa is found in sagging while for the second event the largest response of slightly more than 100 MPa is in hogging. The HF contribution here is generally much smaller than for the three larger container ships described in the previous sections and they are less than half of the WF contribution in the worst case.

A 30 minute cut-out of the signal is seen in Figure D.18 and the filtered components of the two events are seen in Figure D.19 and D.20 in Appendix D.

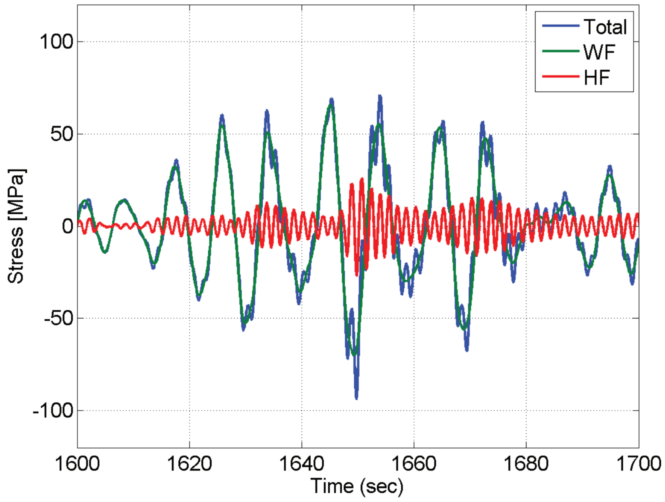

Figure 8.19: *Filtered time series signal of stress (average of port and starboard side) from 4,400 TEU ship on 01 July 2008 at 19 hours, first event. The total response is equal to the sum of the WF and HF contributions.*

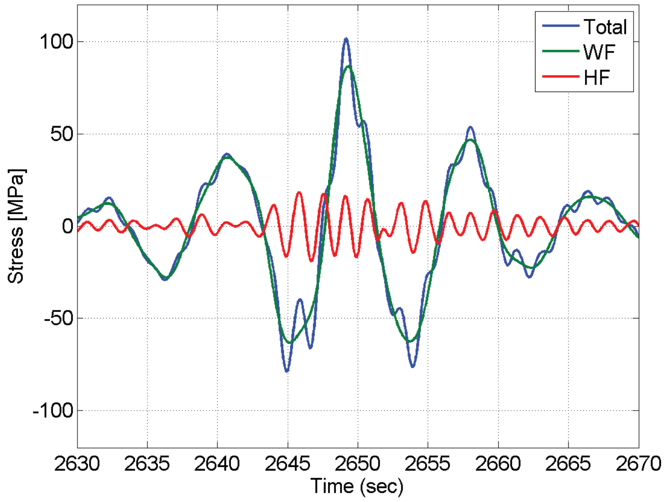

Figure 8.20: *Filtered time series signal of stress (average of port and starboard side) from 4,400 TEU ship on 01 July 2008 at 19 hours, second event. The total response is equal to the sum of the WF and HF contributions.*

8.11 Torsional Vibrations

Koning and Kapsenberg, 2012 also investigated the time series from 02 October 2011 for the 9,400 TEU container ship and similarly found large flexural deformations due to vertical bending, but found no resonant torsion, even though the ship was sailing in bow quartering seas. They suggest high damping between container stacks in the torsional mode to be an explanation for the unexpected lack of torsional vibratory response. From full scale measurements Storhaug and Moe, 2007 also found that vibrations only occurred in the vertical bending mode.

The shear center of the hull of container ships is located below the keel of the ship, so horizontal deformation modes are coupled to a torsional deformation. The lowest coupled mode (2-node horizontal bending and 2-node torsion) natural frequency for the 9,400 TEU ship is 0.51 Hz, i.e. very close to the natural 2-node vertical bending frequency of 0.48 Hz. The natural frequency for 1-node torsion is 0.35 Hz. For the other ships the torsional modes are unknown.

The high-frequency response of the port and starboard signals are discussed in the following. As illustrated in Figure 8.21 and 8.22 there is little difference between the starboard and port HF signals for the 9,400 TEU ship on 02 October 2011 and 12 August 2011, so torsion does not seem to be present in the HF part of the response. It might still be present in the WF part, but that is not considered here, as the focus is on the hydro-elastic response.

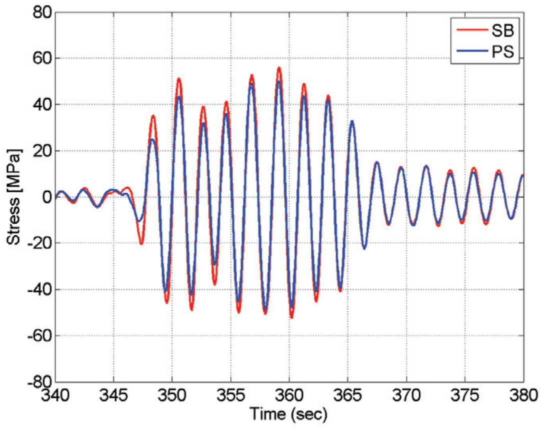

Figure 8.21: *High-frequency component (high-pass filtered) of stress measurements on starboard and port side. Data from 9,400 TEU container ship on 02 Oct 2011 at 16 hours (same time series as in Figure 8.2).*

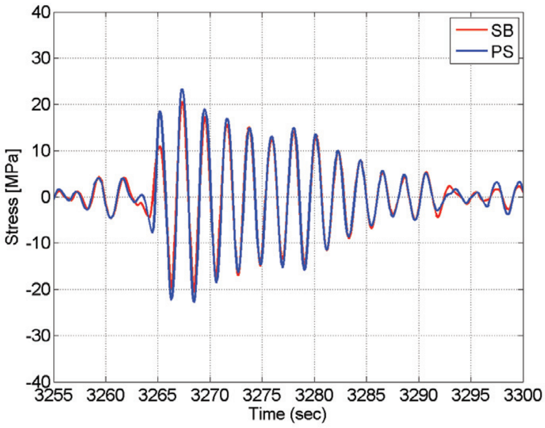

Figure 8.22: *High-frequency component (high-pass filtered) of stress measurements on starboard and port side. Data from 9,400 TEU container ship on 12 August 2011 at 01 hours (same time series as in Figure 8.11).*

Similar plots for the remaining three container ships are found in Appendix D, Figures D.21-D.26. Generally, for all the cases there is little difference between the port and starboard side signal indicating that the HF vibration is in all cases pure vertical bending. For the 14,000 TEU ship on 01 July 2011 in Figure D.24 there is a difference in amplitude between the port and starboard signal but not in the phase. It was also concluded by Kahl et al., 2014 that the influence of torsional vibrations was negligible compared to the influence of the 2-node vertical hull girder vibrations.

For the 4,400 TEU ship only two of the four large events are illustrated in Appendix D. The HF response for the largest event for 02 November 2007 is seen in Figure D.25 and for 01 July 2008 in Figure D.26.

It cannot from the present study be concluded that torsional vibrations do not occur in general, but they cannot be observed in the data analysed here and as shown in the previous section for the 9,400 TEU ship the high-frequency strain measurements fit exactly to a pure 2-node vertical bending vibration mode.

8.12 Discussion and Conclusions

In this chapter, full scale measurements from four different container ships have been analysed. Although the events considered here represent a very limited time window of the total operation of the ships they provide some insight into the behaviour of the ship response to large wave loads.

For the 9,400 TEU ship the analysis in Section 8.2 shows good consistency between the measured strains and accelerations. The conclusion is that the largest peaks should not be considered as outliers and that full scale strain measurements carried out as parts of the TULCS project can be considered reliable. The same was the conclusion by Koning and Kapsenberg, 2012 who estimated the vertical bending moment from the accelerometer measurements.

It is difficult to directly compare the three events analysed for the 9,400 TEU vessel. On 02 October the ship was sailing relatively slowly (around 10 knots) in rather large waves and on 12 August 2011 the ship was sailing twice as fast in smaller waves, but in both cases a very significant hydro-elastic effect is measured. On 17 December 2011 the HF contribution was smaller than for the two other cases. On 02 October 2011 and 12 August 2011 the ship is believed to have encountered oblique seas and on 17 December 2011 the ship is believed to have encountered head sea. For the other ships less navigational data is available and it is not possible to discuss the effect of speed and weather.

For the 9,400 TEU, 8,600 TEU and 14,000 TEU ships the HF vibrations are observed to double the total response in several cases. For the 4,400 TEU ship the HF contribution during the large responses is generally smaller, even though, on 02 November 2007 at 16 hours (Figure 8.18), the HF contribution also almost doubles the response. The largest HF contributions are found for the 8,600 TEU ship. For the time series considered here the largest HF contributions are not necessarily associated with the largest total responses; e.g. the largest total response for the 8,600 TEU ship is found on 17 November 2010 while the highest HF contribution is found on 30 December 2011.

Overall, it is found that the hydro-elastic effects greatly increase the extreme value of the wave-induced hull girder stresses compared to the pure wave-frequency response. Whipping can thus contribute very significantly to the total hull girder loads - even for low speed as it was seen for the 9,400 TEU vessel that only sailed at about 10 knots at the time of the largest impact. For the 8,600 TEU ship the HF vibrations also significantly increase the stress amplitude for the extreme event and it is concluded that for extreme event analysis for container ships of this size it is not unrealistic to assume a 100% amplification of the hull girder stress from whipping.

For all three considered events for the 9,400 TEU ship the measured stress in hogging is larger than the corresponding stress in sagging. For the 14,000 TEU ship the largest stresses are also found in the hogging condition. For the 8,600 and 4,400 TEU ships large responses are also found in sagging. The consideration of individual events does not reveal any general information about the influence of hydro-elasticity on the hogging and sagging conditions respectively, but will be discussed in Chapter 9.

It is found that even though the 9,400 TEU ship is sailing in bow quartering sea, the hydro-elastic vibrations is apparently takes place purely in the 2-node vertical vibration mode. No torsional vibration contributions are observed, but on the other hand it cannot be concluded that torsional vibrations do not take place under other operational conditions.

The mean value of the stress signal has been set to zero in all cases by subtracting the mean measured value during one hour. Thus, some uncertainty in the sagging and hogging peak values is evident as non-linear wave effects may lead to a dynamic change in the mean value. However, no consistent way to derive the true dynamic sagging and hogging peak values has been found and the non-linear effects are considered to be small. The filtering applied here removes frequency contributions below 0.01 Hz. These contributions are illustrated in the figures in Appendix D and thought to be caused by higher-order (non-linear) difference frequencies in the response. The filtering does not generally decrease or increase the maximum stress and only contribute to 2-3% of the total value in the cases considered here.

The critical conditions for large wave-induced hull girder loads and the influence of wave height, wave period, ship speed and relative heading cannot be properly assessed from the full scale measurements available for this study as the knowledge of the encountered sea state is limited in most cases.

Chapter 9

Extreme Value Prediction of the Vertical Bending Moment Based on Full Scale Measurements

Parts of this chapter published by Andersen and Jensen, 2014.

9.1 Introduction

In the previous chapter it was illustrated that whipping-induced vibrations play a significant role for the extreme load in container ships. The whipping response is typically caused by bow flare slamming but has also been observed to occur in oblique seas and initiated in the hogging condition. The whipping response is influenced by the ship speed, bow flare angle and the wave environment and is difficult to simulate numerically. Even if a given sea state can be reproduced numerically, it is difficult to determine accurately which wave condition is the most critical for whipping. Furthermore, numerical simulations of whipping using CFD are extremely computationally heavy and not useful for deriving statistics covering hours of operation and for extreme value prediction.

Longer time series of whipping events can be generated in a model basin, but there are uncertainties regarding the choice of relevant sea states and the most critical events are not necessarily reproduced. Therefore, statistics from full scale measurements of whipping events from container ships may provide the most realistic and valuable information of the influence of whipping. Furthermore, for on-board decision support prediction of future extreme events based on real-time measurements can be beneficial in order to avoid large hull girder loads.

This chapter deals with prediction of extreme values based on full scale measurements using statistical methods. The aim of the analysis is to investigate the longer-term effects of whipping and extreme value prediction in relation to on-board decision support systems. The measured strains are converted into vertical bending moments amidships. The analysis is carried out on longer time series containing the periods of highest measured hull girder stresses on board the four container ships (two or three cases per ship). The times series are the ones containing the largest events described in the previous chapter.

For the extreme value analysis, the average of the port and starboard stress signal is used in order to exclude possible contributions from horizontal and torsional stress components which, however, are found to be small in the HF part of the response (see Section 8.11). The time series considered for the extreme value prediction should be stationary and as long as possible. This is contradictory since conditions at sea are normally not stationary during long periods of time, so here time series of three hours or less have been selected.

In the following, extreme value prediction is carried out for the four considered container ships. For three of the ships, data is logged continuously and three-hour time series are used for the analysis. For the 14,000 TEU ship, only large events are stored, and here several time series from the same day form the basis for the analysis. The statistical analysis is carried out on the peaks and not on the time series signal itself. Only hogging is considered except for the probability of exceedance which is initially established for both hogging and sagging. Three methods for the extreme value prediction are used: First, the Weibull distribution is fitted to the full data set and used to derive the corresponding Gumbel distribution. Then the peak-over-threshold (POT) method is used and the peaks over the given thresholds are fitted with the exponential distribution such that the peaks become Gumbel distributed. The effect of correlated peaks is investigated in connection with the POT analysis. Finally, a method for extreme value prediction proposed by Naess and Gaidai, 2009 is applied to the data sets. The methods are described in connection with the analysis carried out for the first case and the analysis is then repeated for the other cases. The results are discussed and compared at the end of the chapter. The illustrations and tables related to the analysis for the 9,400 TEU ship on 02 October 2011 are included in the main thesis. The procedures are described in connection with the analysis carried out for 02 October and the same procedures repeated for the other days and ships. Some plots are included in the main thesis for illustration but, due to space constraints, most of the results are illustrated in Appendix E for the remaining time series. A comparison of the results and main findings are included by the end of this chapter.

9.2 Design Wave Loads

In the following, the minimum design wave-induced bending moments is determined in sagging and hogging for the four container ships considered. By definition, the sagging bending moment is negative while the hogging bending moment is positive.

The maximum wave-induced vertical bending moment M at the location of the strain gauge amidships can be found from Navier's formula:

$$M = \frac{\sigma I}{z_{sg}} \tag{9.1}$$

where z_{sg} is the vertical distance from the neutral axis to the strain gauge, σ is the stress associated with pure vertical bending and I is the sectional moment of inertia of the hull.

The design minimum wave-induced bending moments for ships longer than 100 m are (International Association of Classification Societies, 2010a):

$$\begin{aligned} M_W &= -0.11KCL^2B(C_b + 0.7) && \text{kNm, sagging} \\ M_W &= 0.19KCL^2BC_b && \text{kNm, hogging} \end{aligned}$$

where

- K is the distribution factor equal to 1 amidships.
- C is equal to 10.75 for ships with a rule length, L, between 300 and 350 meters.
- L is the rule length of the ship in m defined by International Association of Classification Societies, 2010b.
- B is the greatest moulded breadth in m, measured at the summer waterline.
- C_b is the block coefficient (not to be taken less than 0.6).

For the 9,400 TEU ship this yields a design wave-induced bending moment in hogging of 6,270 MNm and -7,480 MNm in sagging. For the 8,600 TEU ship, the rule wave VBM in hogging is 5,864 MNm and -7,222 MNm in sagging. For the 14,000 TEU ship the rule VBM in hogging and sagging are taken from the main dimensions of a standard 14,000 TEU container ship design to be 8,230 MNm in hogging and -9,740 MNm in sagging, and for the 4,400 TEU ship the rule VBM is estimated to 3,462 MNm in hogging and -4,038 MNm in sagging.

In the following, the wave-frequency (WF) part of the signal corresponds to what is normally considered the rigid-body response and the wave-frequency + high-frequency (WF+HF) part is considered as the dynamic or flexible-body response. The filtering of the data is carried out as described in Section 6.3. When considering the ultimate strength of the ship, the maximum wave-induced VBM must obviously be considered in relation to the corresponding still-water moment. Due to the design and typical weight distribution of container ships the still-water bending moment is nearly always a hogging bending moment for a container ship, and hence the subsequent analysis only deals with extreme value prediction of the wave-induced hogging bending moment.

9.3 9,400 TEU Container Ship, 02 October 2011

Extreme value prediction is carried out based on three hours of data from the 9,400 TEU container ship operating in severe weather conditions on 02 October 2011 at 16-18 hours. During the three hours the ship speed was around 9-10 knots, the significant wave height was about 7-8 m and the seas were bow quartering from starboard (See Appendix A.1.2 for the navigational and sea state data).

The three-hour time series of the vertical wave-induced bending moment (VBM) is shown in Figure E.1 in Appendix E compared to the rule wave VBM in hogging and sagging found above. The maximum wave-induced hogging VBM in the deck amidships is slightly above the design value of 6,413 MNm. It is noted that the filtering here reduces the maximum VBM in hogging slightly. The reason is that a very low-frequency contribution (below 0.01 Hz) is present in the measurement and is responsible for about 2.5% of the total VBM cf. Figure D.1. However, for consistency all time series are filtered in the same way. Using the unfiltered signal, the maximum VBM amidships is 6,601 MNm. The statistics for 02 October 2011 are presented in Table 9.1. It is seen that the maximum hogging VBM is slightly larger than the maximum sagging VBM, but the WF (rigid-body) sagging VBM is larger than the WF hogging VBM. The total mean of the signal is set to zero and after the filtering the mean of the WF and HF parts of the signal are also zero. The number of positive and negative peaks are approximately the same and due to the lack of more advanced procedures to establish the true mean of the wave-induced response, this practise is applied throughout the thesis.

	Max VBM [MNm]	Max VBM, WF [MNm]
Sagging	-6,376	-4,171
Hogging	6,434	4,035
	No. of peaks	No. of peaks, WF
Sagging	3,083	1,231
Hogging	3,048	1,214
Duration	s_M [MNm]	$s_{M,WF}$ [MNm]
3:00 hours	1,068	983

Table 9.1: *Maximum measured VBM and number of peaks for sagging and hogging for the flexible and rigid-body response and duration and standard deviation of the flexible (s_M) and rigid-body ($s_{M,WF}$) response. 9,400 TEU ship on 02 October 2011.*

The probability of exceedance for the VBM for the three-hour time period is plotted in Figure 9.1 for sagging and Figure 9.2 for hogging. As expected the WF (rigid-body) sagging and hogging bending moments (blue) are very similar. The amplification of the VBM due to the hull girder flexibility is slightly larger in hogging than in sagging in this case.

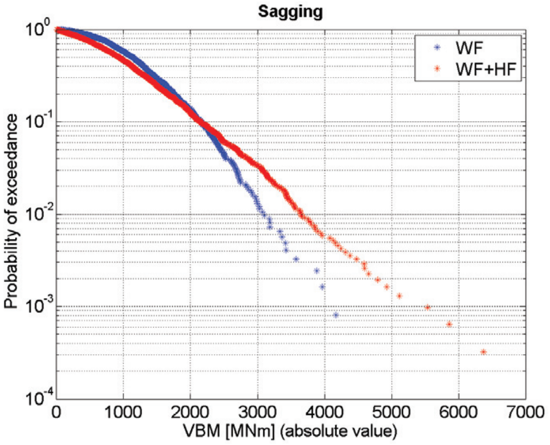

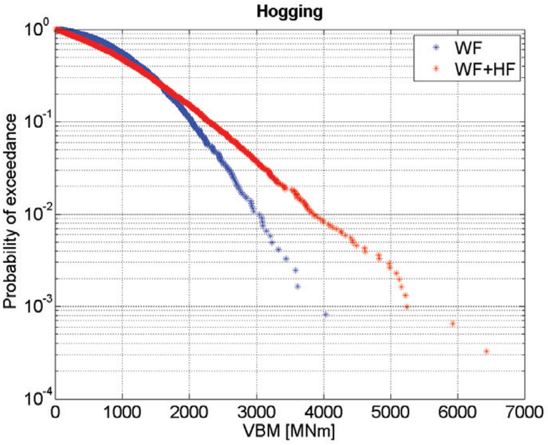

Figure 9.1: *Individual peak value probability of exceedance for sagging - WF and WF+HF response. Note, that even though the sagging moment is defined as negative, the absolute value is shown here. 9,400 TEU ship on 02 October 2011.*

Figure 9.2: *Individual peak value probability of exceedance for hogging - WF and WF+HF response. 9,400 TEU ship on 02 October 2011.*

9.3.1 *Gumbel fit from Weibull parameters*

The peak value distribution for the wave-frequency and the total VBM including the high-frequency vibrations is fitted with the Weibull distribution using all the hogging peaks as shown in Figures 9.3 and 9.4 using the Matlab WAFO package (Brodtkorb et al., 2011). The standard Weibull probability distribution function is given by:

$$F(x, a, c) = 1 - \exp(-(x/a)^c) \tag{9.2}$$

The Weibull parameters a and c are derived from the Weibull fits to the data (red dotted curve) in Figures 9.4 and 9.3 using the least squares method (Brodtkorb et al., 2011):

$$\ln(-\ln[1 - F(x, a, c)]) = c\ln(x) - c\ln(a) \tag{9.3}$$

Cf. Figure 9.2 the tail of the distribution is not smooth and it is questionable to fit a continuous function like the Weibull distribution to the data for extreme value prediction.

For the hogging condition the Weibull parameters estimated for the rigid-body and the flexible response are given in Table 9.2. The Rayleigh distribution is a special case of the Weibull distribution with $c = 2$. The other special case of the Weibull distribution is the exponential distribution, where $c = 1$. It is seen, that for the flexible response the peaks are closer to being exponentially distributed, which was also found by Gaidai et al., 2010 for a smaller container ship, while the rigid-body response is closer to the Rayleigh distribution (see Appendix G for the different probability distribution functions).

When the individual peak distribution follows a Weibull distribution, the extreme peaks asymptomatically follow a Gumbel distribution and the Gumbel distribution will be used in the following as the main result. This is also convenient when comparing the results

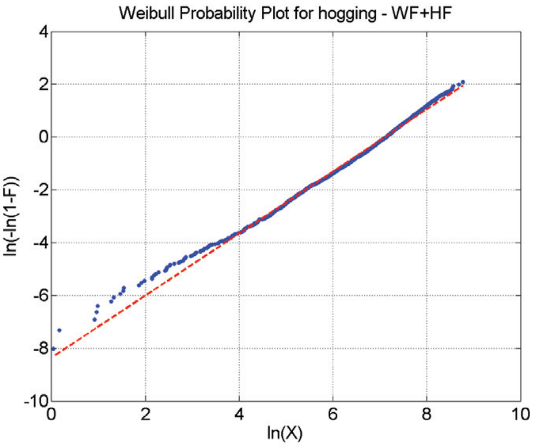

__Figure 9.3:__ Weibull probability plot for the hogging bending moment - WF+HF response. 9,400 TEU ship on 02 October 2011.

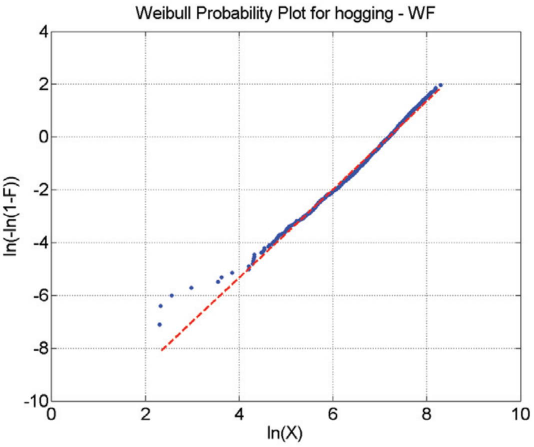

__Figure 9.4:__ Weibull probability plot for the hogging bending moment - WF response. 9,400 TEU ship on 02 October 2011.

	a	c
Flexible response	1,229	1.18
Rigid-body response	1,324	1.67

__Table 9.2:__ Weibull parameters for hogging for the WF and WF+HF response. Estimated from Figures 9.3 and 9.4. 9,400 TEU ship on 02 October 2011.

based on other fitting procedures in the discussion. The limitation of using the Gumbel distribution is that the time duration should be sufficiently large so that the number of peaks, N, is large. Here, three hours is assumed to be adequate. Using the Weibull parameters for the flexible response a Gumbel fit can be derived for the prediction of the extreme values in the tail, i.e. the distribution of the largest peak among N peaks. The Gumbel distribution function is given by:

$$F(x, b, d) = \exp(-\exp(-(x-b)/d)) \tag{9.4}$$

The most probable largest value, the Gumbel parameter b, is found from the Weibull parameters for the individual peak distribution (Eq. (9.2)) (Soares and Teixeira, 2000):

$$b = a\sqrt[c]{\ln(N)} \tag{9.5}$$

where N is the number of peaks in three hours. The Gumbel parameter d is correspondingly found as (Soares and Teixeira, 2000):

$$d = \frac{a}{c}\left[\ln(N)\right]^{1/c-1} \tag{9.6}$$

The resulting Gumbel density function is shown in Figure 9.5. Here, the most probable largest value is found from Eq. (9.5) to 7,222 MNm, which can also be seen from Figure 9.5 as the value with the largest probability. The most probable largest value from the

Gumbel fit is considerably larger than the maximum measured value, which makes the estimate rather conservative.

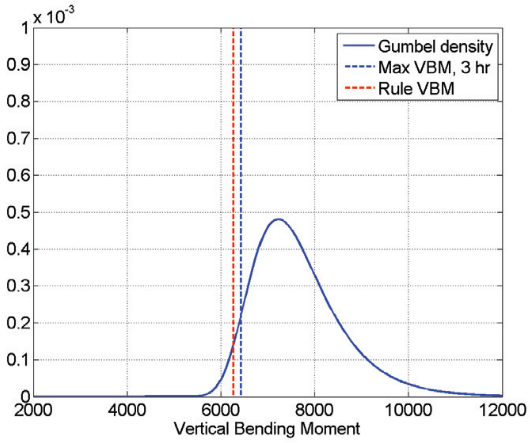

Figure 9.5: *Gumbel density function for the hogging VBM based on Weibull parameters for the individual peak for the flexible-body response in Table 9.2. The maximum measured hogging VBM during the three hours and the rule wave VBM are included for comparison. 9,400 TEU ship on 02 October 2011.*

9.3.2 *Peak-over-threshold method*

A widely used procedure for estimation of the distribution of extreme values is the peak-over-threshold (POT) method. The method assumes that the peaks in the tail of the distribution occur approximately randomly and independently of each other even though, for whipping events, this may not truly be the case. Different probability distributions can then be fitted to the peaks over the threshold. Provided the excess over the given threshold is exponentially distributed, the extreme distribution becomes the Gumbel distribution with parameters defined by the exponential distribution. In order to explore this procedure consistently for different time series, the threshold values, u, are chosen as different percentages of the average of the three largest peaks measured during considered period. Six different threshold levels are chosen: 30%, 40%, 50%, 60%, 70% and 80%. In the following, only the flexible-body response in hogging is considered.

The Weibull probability plots for the excess over the given thresholds for the flexible ship can be seen in Figures 9.6-9.11. The corresponding Weibull parameters are given in Table 9.3 together with the threshold levels. As expected, the peaks are nearly exponentially distributed as the Weibull parameter c is close to 1 in most cases.

The Gumbel parameter d is determined from an exponential fit to the excess of the different threshold levels. In this case WAFO is used to establish the exponential fit to the peaks. d is the mean of the peaks over the threshold value u (excess), and if c is exactly 1 then $d = a$ from the Weibull distribution. The most probable largest value b can be found as $b = u + d \ln N_u$, where N_u is the number of peaks above the threshold u during the three hours. The Gumbel parameters determined at the different threshold levels are

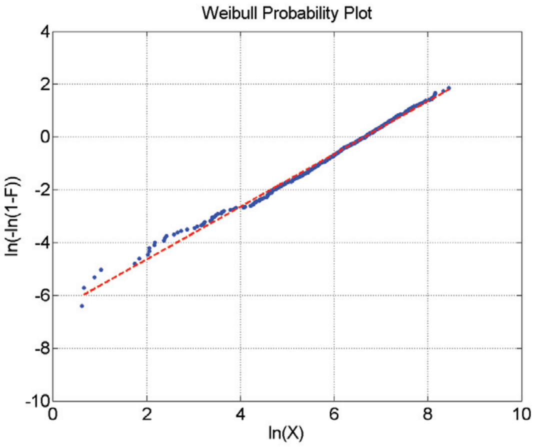

Figure 9.6: *Weibull probability plot for the excess of the hogging bending moment. Threshold 1,761 MNm. 9,400 TEU ship on 02 October 2011.*

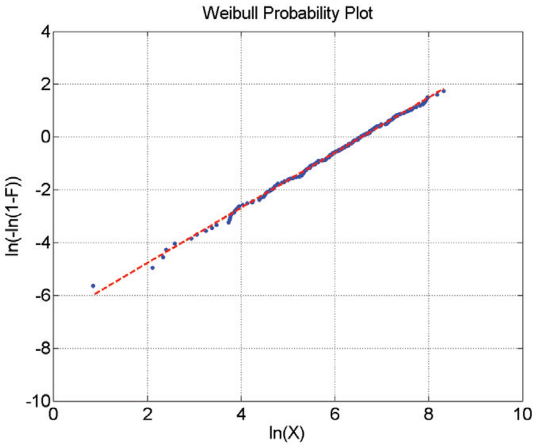

Figure 9.7: *Weibull probability plot for the excess of the hogging bending moment. Threshold 2,348 MNm. 9,400 TEU ship on 02 October 2011.*

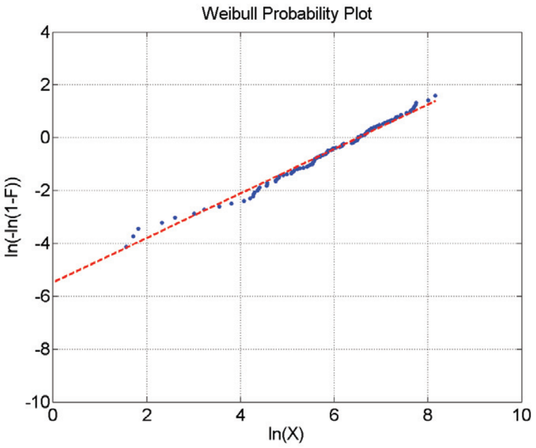

Figure 9.8: *Weibull probability plot for the excess of the hogging bending moment. Threshold 2,945 MNm. 9,400 TEU ship on 02 October 2011.*

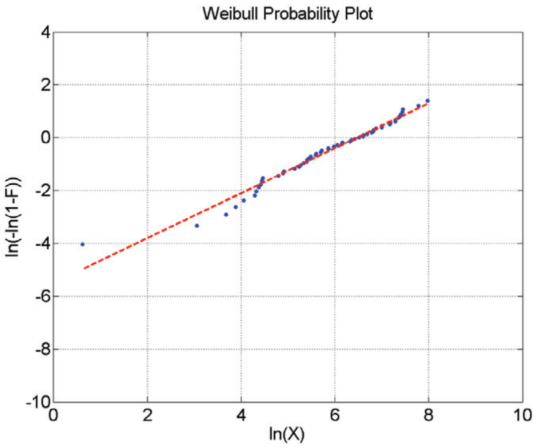

Figure 9.9: *Weibull probability plot for the excess of the hogging bending moment. Threshold 3,521 MNm. 9,400 TEU ship on 02 October 2011.*

given in Table 9.4.

Figure 9.12 shows the Gumbel density functions for the different threshold levels. Obviously, for high thresholds the number of peaks used for the fit decreases and thus increases the uncertainty of the estimate, which is the trade-off of this method. When deciding on an appropriate threshold plotting the mean excess over the threshold level u can be helpful. For a Gumbel distribution the mean excess over the threshold level u should be independent of u and equal to d. In Figure 9.13 the mean excess is plotted as function of the threshold level, and the plot suggests that threshold levels between 2,000 MNm and 3,000 MNm satisfy this condition. This is in agreement with Figure 9.12 as the plots show that the associated Gumbel distribution for the extreme response is rather insensitive to the choice of threshold level as long as the threshold level is in the range 40-60% of the

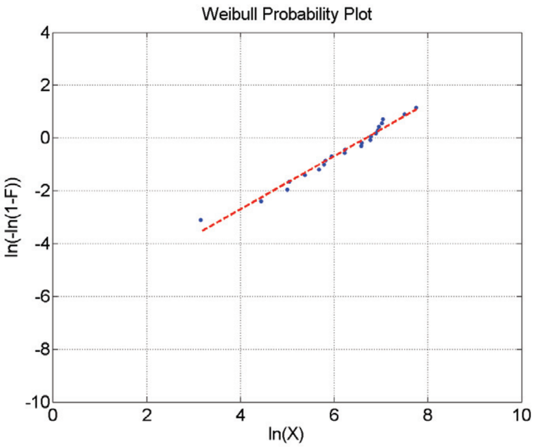

Figure 9.10: *Weibull probability plot for the excess of the hogging bending moment. Threshold 4,108 MNm. 9,400 TEU ship on 02 October 2011.*

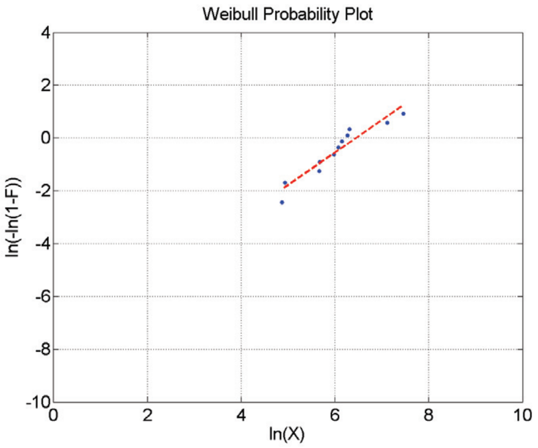

Figure 9.11: *Weibull probability plot for the excess of the hogging bending moment. Threshold 4,695 MNm. 9,400 TEU ship on 02 October 2011.*

mean of the three largest peaks. It is seen that the probability of exceeding the rule VBM is quite significant regardless of the threshold level for this method.

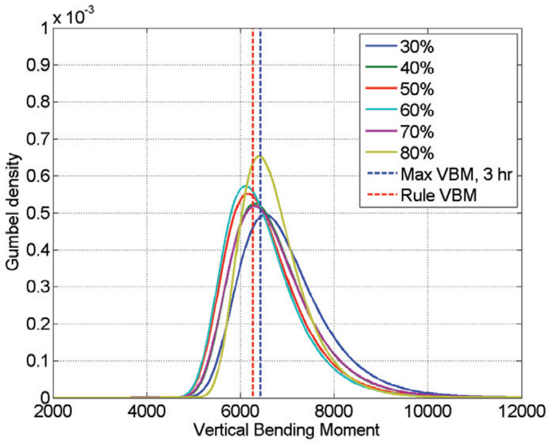

Figure 9.12: *Gumbel density function for the hogging VBM for the different threshold levels given in Table 9.4. The maximum measured hogging VBM during the three hours and the rule wave VBM are included for comparison. 9,400 TEU ship on 02 October 2011.*

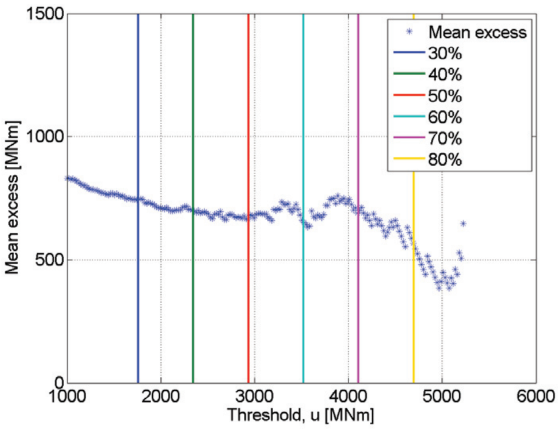

Figure 9.13: *Mean excess of the threshold level u as function of u. 9,400 TEU ship on 02 October 2011 with the thresholds indicated.*

Threshold, u	a	c
1,761 MNm	772	1.00
2,348 MNm	715	1.04
2,935 MNm	676	0.84
3,521 MNm	646	0.85
4,184 MNm	798	1.01
4,695 MNm	634	1.23

Table 9.3: *Weibull parameters a and c for for the excess of the hogging VBM for different threshold values. A value of* $c = 1$ *corresponds to exponentially distributed peaks. 9,400 TEU ship on 02 October 2011.*

Threshold, u	d	b
1,761 MNm	774	6,532
2,348 MNm	701	6,310
2,935 MNm	667	6,160
3,521 MNm	643	6,109
4,184 MNm	710	6,304
4,695 MNm	563	6,340

Table 9.4: *Gumbel parameters b and d from an exponential fit to the excess. 9,400 TEU ship on 02 October 2011.*

9.3.3 *Clustering effects*

As described earlier, the peak-over-threshold method assumes that the peaks occur randomly and independently of each other. In real life, this is not the case and the peaks will be somehow clustered for each whipping event, which is also observed for the time series considered here. A small illustrative study of the clustering of peaks in hogging for the considered time series is made in the following. For the 9,400 TEU ship on 02 October 2011 six larger responses above 4,000 MNm (red line) are immediately identified from visual inspection of Figure 9.14. The large responses are considered uncorrelated, but the number of hogging peaks above 4,000 MNm associated with each of the six large responses is 5, 3, 1, 5, 2 and 4 respectively.

Naess and Gaidai, 2009 have developed a method for extreme value estimation based on sampled time series. The method accounts for the statistical dependence between the peaks in a time series of measured data points and applies to cases where the asymptotic extreme value distribution is the Gumbel distribution. The procedure is described below.

Consider the extreme value distribution for N peaks: X_i; $i = 1, 2, ..., N$:

$$P(\max X_i \leq x | i = 1, 2, ..., N) = P(X_1 \leq x, X_2 \leq x, ..., X_N \leq x) \tag{9.7}$$

The peaks are numbered according to their appearance in time. If the peaks are statistically independent then the usual order statistics result is found:

$$P(\max X_i \leq x | i = 1, 2, ..., N) = \Pi_{i=1}^{N} P(X_i < x) = \Pi_{i=1}^{N} (1 - \alpha_{1i}(x))$$

where

$$\alpha_{1i}(x) \equiv P(X_i > x) \tag{9.8}$$

Considering only high exceedance levels x: $\alpha_{1i}(x) << 1$, then

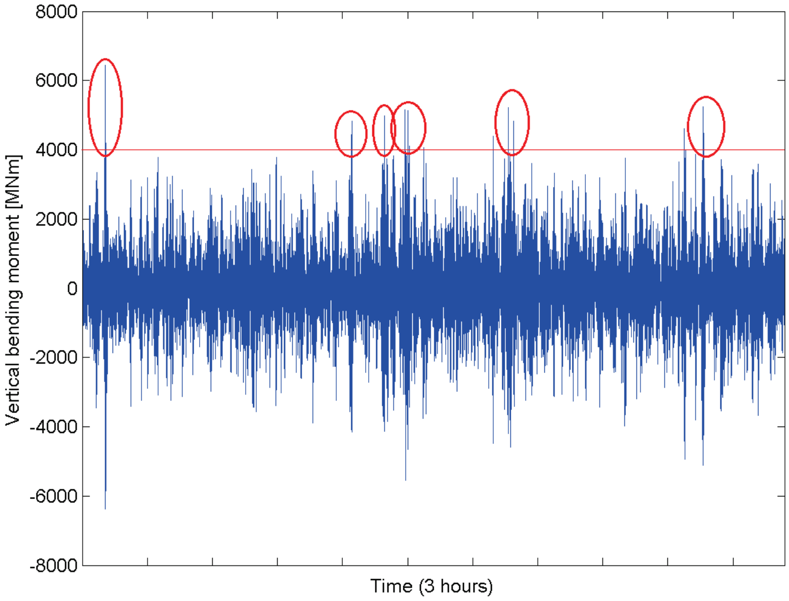

Figure 9.14: *Wave-induced vertical bending moment amidships compared to the minimum design wave-induced vertical bending moments (VBM) in hogging and sagging from International Association of Classification Societies, 2010a for the 9,400 TEU ship on 02 October 2011 at 16-18 hours. Indication of the groups of peaks including the six largest peaks.*

$$1 - \alpha_{1i}(x) \simeq \exp(-\alpha_{1i}(x))$$

and

$$P(\max X_i \leq x | i = 1, 2, ..., N) \simeq \exp(-\sum_{i=1}^{N} \alpha_{1i}(x))$$

For stationary (ergodic) processes the peaks are identically distributed:

$$\alpha_{1i}(x) \equiv \epsilon_1(x)$$

such that

$$P(\max X_i \leq x | i = 1, 2, ..., N) \simeq \exp(-N\epsilon_1(x))$$

Compared to the standard Poisson model, the following relation is found:

$$N\epsilon_1(x) = \nu(x)T$$

or

$$\epsilon_1(x) = \frac{\nu(x)}{\nu(0)}$$

where $\nu(x)$ is the mean upcrossing rate of x and $\nu(0) = N/T$ is the mean zero-upcrossing rate. Thus, $\epsilon_1(x)$ can also be estimated from the spectral moments of the response. See e.g. Appendix G for general relations between order statistics, the Poisson model and the Weibull and Gumbel distributions.

However, if the peaks are fully correlated then peaks exceeding x should be counted only when the preceding peak(s) does not exceed x. In the following, $k-1$ denotes the number of correlated preceding peaks. The de-clustering procedure in Naess and Gaidai, 2009 covers correlation between any number of preceding peaks, but here for simplicity only one preceding peak is accounted for. Thus, Eq. (9.7) can be written:

$$\begin{aligned} &P(\max X_i \leq x | i = 1, 2, ..., N) = \Pi_{i=2}^{N} P(X_i \leq x | X_{i-1} \leq x) \cdot P(X_1 \leq x) \\ &= \Pi_{i=2}^{N}(1 - \alpha_{2i}(x))P(X_1 \leq x) \end{aligned} \tag{9.9}$$

where

$$\alpha_{2i}(x) = P(X_i > x | X_{i-1} \leq x) \tag{9.10}$$

Again, assuming a high exceedance level, $\alpha_{2i}(x) << 1$ and $P(X_1 \leq x) \simeq 1$ implying

$$P(\max X_i \leq x | i = 1, 2, ..., N) \simeq \exp(-\sum_{i=2}^{N} \alpha_{2i}(x)) \tag{9.11}$$

For stationary ergodic processes $\alpha_{2i}(x)$ is the same for all peaks $\alpha_{2i}(x) \equiv \epsilon_2(x)$, thus:

$$P(\max X_i \leq x | i = 1, 2, ..., N) \simeq \exp(-N\epsilon_2(x))$$

for large N. Thus, the similarity with the Poisson upcrossing model is again seen:

$$\epsilon_2(x) = \frac{\tilde{\nu}(x)}{\nu(0)}$$

where

$$\tilde{\nu}(x) \simeq \epsilon_2(x)N/T$$

can be considered as an effective upcrossing rate of the level x excluding upcrossings if the preceding peak is larger than x. The value of $\epsilon_2(x)$ is easily estimated from the actual time series:

$$\epsilon_2(x) \simeq \frac{1}{N-1} \sum_{i=2}^{N} \alpha_{2i}(x) \tag{9.12}$$

using Eq. (9.10) through an indicator function

$$\alpha_{2i} = \begin{cases} 1 & \text{if } X_i > x \text{ and } X_{i-1} \leq x \\ 0 & \text{otherwise} \end{cases} \tag{9.13}$$

From the figure it is seen that the normalised autocorrelation is 0.6 for a period of about 10 s, which corresponds very well to the period of the WF part of the signal as seen in e.g. Figure 8.2.

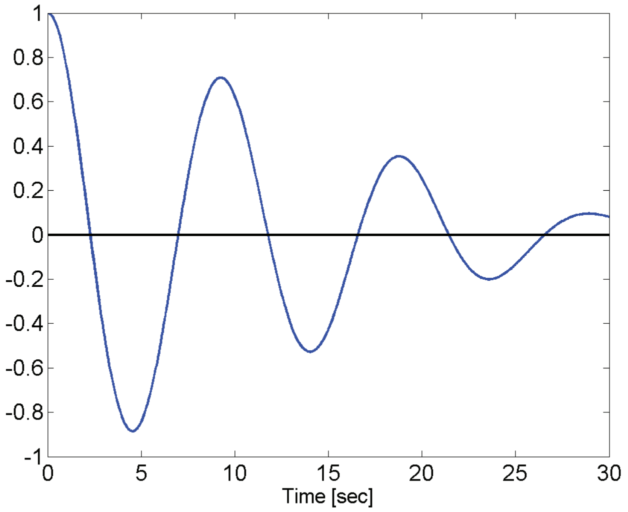

Figure 9.15: *Normalised autocorrelation function for the WF stress signal based on one hour of data. 9,400 TEU ship on 02 October 2011.*

The exceedance rates $\epsilon_1(x)$ and $\epsilon_2(x)$ are illustrated in Figure 9.16. It is noted, that for small values of x ϵ_2 does not make physical sense due to the assumption in Eq. (9.11). Clearly, clustering effects are important for this case and the two largest peaks are seen from Figure 9.16 to be considered correlated in this case.

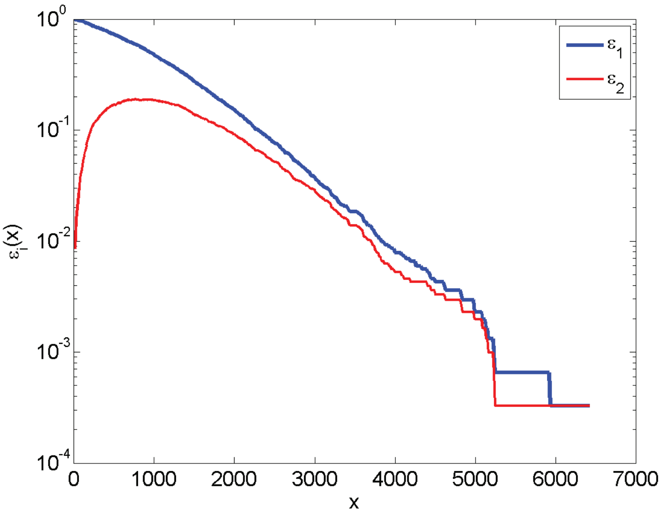

Figure 9.16: *The exceedance rates $\epsilon_1(x)$ (Eq. (9.8)) and $\epsilon_2(x)$ (Eq. (9.10)) for the hogging VBM. 9,400 TEU ship on 02 October 2011.*

The POT analysis can be applied on only the effective upcrossings, i.e. excluding upcrossings if the preceding peak is larger than x, and thereby the clustering effect is taken into account. The same threshold levels as in the previous section is used, i.e. 30%, 40%, 50%, 60%, 70% and 80% of the average of the three largest measured values during the three hour time period. The Weibull parameter c and the Gumbel parameters

Threshold, u	c	d	b
1,761 MNm	0.96	559	5,021
2,348 MNm	1.02	532	5,137
2,935 MNm	0.86	566	5,496
3,521 MNm	0.83	523	5,475
4,184 MNm	0.86	678	5,899
4,695 MNm	1.35	463	5,713

Table 9.5: *Weibull parameter c and Gumbel parameters d and b for different threshold values. A value of $c = 1$ corresponds to exponentially distributed peaks. 9,400 TEU ship on 02 October 2011.*

d and b are found using WAFO as described in the previous section and listed in Table 9.5.

A fairly large and threshold dependant deviation from the exponential distribution ($c = 1$) is noted. Thereby, a Gumbel fit for the extreme value will depend very much on the threshold level chosen as illustrated in Figure 9.17 showing the Gumbel density functions for the different threshold levels. Figure 9.18 is shown for comparison where no de-clustering is applied. As expected the removal of some peaks results in a Gumbel distribution that is moved to the left.

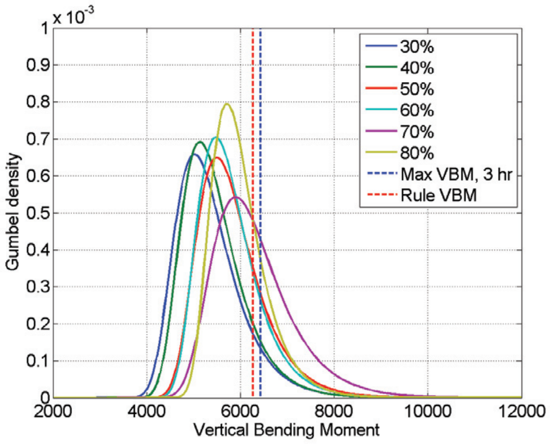

Figure 9.17: *Gumbel density function for the hogging VBM for the different threshold levels given in Table 9.5 for the declustered signal. The maximum measured hogging VBM during the three hours and the rule wave VBM are included for comparison. 9,400 TEU ship on 02 October 2011.*

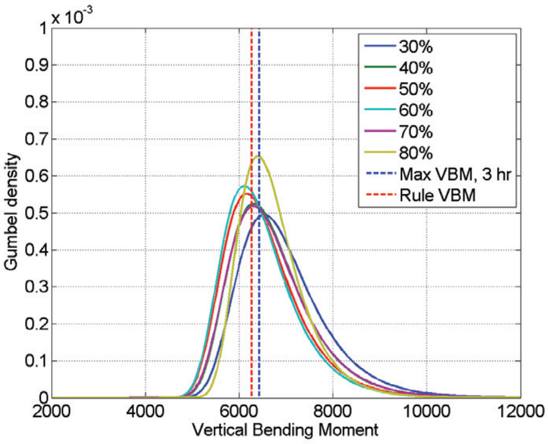

Figure 9.18: *Gumbel density function for the hogging VBM for the different threshold levels given in Table 9.4. The maximum measured hogging VBM during the three hours and the rule wave VBM are included for comparison. 9,400 TEU ship on 02 October 2011. Same figure as Figure 9.12 shown here for comparison.*

The procedure above have has been generalised to take into account up to five preceding peaks cf. e.g. Naess and Gaidai, 2009. The function $\epsilon_k(x)$

$$\epsilon_k(x) = \frac{1}{N-k+1}\sum_{i=k}^{N}\alpha_{ki}x, \quad k = 1, 2, ... \tag{9.14}$$

with, for $k \geq 2$ (i.e. for one or more than one preceding peaks)

$$\alpha_{ki}(x) = P(X_i > x|X_{i-k-1} \leq x, ..., x_{i-1\leq x})$$

is denoted the Average Conditional Exceedance Rate (ACER) and directly yields the extreme value distribution

$$P(\max X_i \leq x|i = 1, 2, ..., N) = \exp(-\epsilon_k(x)N) \tag{9.15}$$

The ACER procedure will be applied in the following using the ACER program downloaded from NTNU[1].

For the 9,400 TEU container ship considering the same three-hour time series as in the sections above the ACER functions $\epsilon_k(x)$ for six different values of k are given in Figure 9.19. From Figure 9.19 it can be difficult to distinguish the curves for different k, so they are also plotted individually in Appendix E, Figures E.2-E.7. Again, due to the assumptions taken similar to in Eq. (9.11) the results are only meaningful for high values of η (η in Figure 9.19 corresponds to x).

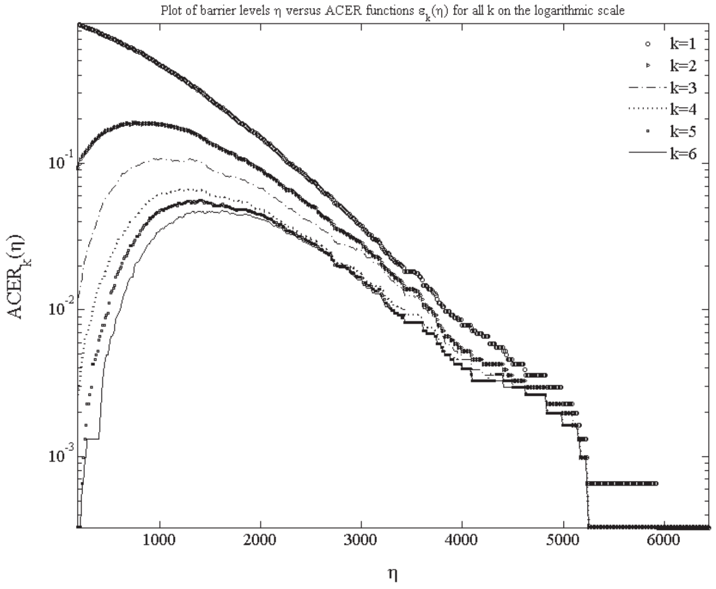

Figure 9.19: *ACER function $\epsilon_k(\eta)$ for six different values of k for the hogging VBM. 9,400 TEU ship on 02 October 2011. Note, that η in the legends corresponds to the level x in the equations in this chapter.*

Figure 9.19 for $k = 2$ (see also Figure E.3 in Appendix E) can be compared to Figure 9.16, and exact agreement is found. In addition to the de-clustering procedure outlined above Naess and Gaidai, 2009 also suggest to fit the numerical distribution for $\epsilon_k(x)$ with an analytical distribution of the form

---

[1] Download available from `http://folk.ntnu.no/karpa/ACER/`

$$\epsilon_k(x) = q_k \mathrm{exp}\left(-r_k \left(x - s_k\right)^{t_k}\right), \quad x \geq s_k \tag{9.16}$$

guided by the expected Gumbel type of asymptotic extreme value distribution of the response. In the following, the index k is omitted in the expressions for simplicity. Naess and Gaidai, 2009 also use a fitting procedure for determination of the parameters q, r, s and t. This fitting procedure removes the largest peaks where the uncertainty is highest and also introduces a tail marker to identify where the tail of the distribution starts which essentially also makes ACER a kind of peak-over-threshold method.

From Eq. (9.16) it follows:

$$-\log\left[\log(\epsilon)(x)/q\right] \approx -t\mathrm{log}(x - s) - \log(r) \tag{9.17}$$

When plotted, Eq. (9.17) will exhibit linear a behaviour in the tail and thus, the optimised curve from ACER has the form given in Eq. (9.16) where q, r, s and t are the ACER parameters to be determined for each value of k.

The resulting optimised ACER functions, Eq. (9.16) with optimised values of q, r, s and t, are shown for $k = 1-6$ in Appendix E, Figures E.8-E.13 with a 95% confidence interval. The parameters from the optimisation for the six different k are given in Table E.1 in Appendix E. The plots in Figures E.8-E.13 in Appendix E show that the clustering may not play a role for the time series considered here as the predicted return value at 10^{-6} level does not vary a lot with the different k.

The ACER method is limited to the cases where the extreme values follow the Gumbel distribution like it was also assumed in Section 9.3.2. The ACER procedure is aimed at providing an accurate estimation of the return period rather than a global extreme value distribution. However, in order to facilitate the comparison with the previous extreme value predictions using the Weibull and POT procedures the results from the optimised ACER functions are transformed into the Gumbel distribution (Eq. (9.4)). The Gumbel parameters are denoted b and d and the linearisation is carried out around the most probable largest value $x = b$ derived from the ACER parameters using

$$\tilde{\nu}(x)T = \epsilon(x)N = 1$$

where N is the total number of peaks during the time T, corresponding to one upcrossing (the largest peak) during the time T. Thus

$$q \cdot \exp\left(-r\left(b - s\right)^t\right) = \frac{1}{N} \tag{9.18}$$

and the most probable largest value b for the Gumbel distribution:

$$b = s + \sqrt[t]{\frac{1}{r}\ln(Nq)} \tag{9.19}$$

Similarly, d can be found from:

$$\frac{1}{d} = \frac{\mathrm{d}}{\mathrm{d}x}\left[\ln q - r(x-s)^t\right]_{x=b} = tr(b-s)^{t-1} \tag{9.20}$$

which leads to

$$d = t^{-1}r^{-1/t}\left(\ln(Nq)\right)^{1/t-1} \tag{9.21}$$

The corresponding Gumbel parameters for the six different values of k are given in Table 9.6.

	$k=1$	$k=2$	$k=3$	$k=4$	$k=5$	$k=6$
b	5,897	5,891	5,867	5,864	5,860	5,951
d	550	584	582	618	624	669

Table 9.6: *Gumbel parameters b and d from the optimised ACER functions for hogging for six different k. 9,400 TEU ship on 02 October 2011.*

The corresponding Gumbel density functions for the parameters in Table 9.6 are plotted in Figure 9.20. It is again seen that there is very little difference between the estimated functions implying that clustering of the peaks may not play a very important role for this case. However, there is still a remarkable difference between the outcome of POT with the removal of one preceding peak in Figure 9.17 and the outcome of ACER in Figure 9.20. Since the removal of peaks is the same for the two methods (see Figure 9.16 and 9.19 for $k = 2$) the most plausible explanation of the difference between the two results is found in the fit of Eq. (9.16) to the peaks and associated removal of outliers outside the given confidence interval.

The tail marker must be determined from visual inspection of Figure 9.19 and must correspond to the beginning of the regular tail cf. Naess and Gaidai, 2009 and Karpa, 2012. A tail marker of 10 has been used here for $k = 1$. In a few cases it is not possible to get the ACER program to yield a positive optimised s for $k = 1$. The outcome of the ACER method is sensitive to the choice of the tail marker. For $k > 1$ ACER suggests a tail marker corresponding to the highest value s of the ACER function for the plots in Figure 9.19 and the tail marker suggested by ACER is generally used. The tail marker essentially corresponds to the threshold level in the POT analysis. In Figure 9.21 the sensitivity on the result of the tail marker is analysed by illustrating the outcome for the ACER method for $k = 2$ for different tail markers. The tail markers are chosen as the same thresholds as for the POT analysis above, see e.g. Table 9.5. For the tail markers of 2,935 and 3,521 MNm the outcome of the ACER optimisation does not yield a useful result.

It is seen that the most probable largest value is not so sensitive to the choice of tail marker but it influences the long-term return values quite significantly.

In the following, more time series from the 9,400 TEU ship and three other container ships are analysed using the same procedures as outlined above. The outcome of the Weibull

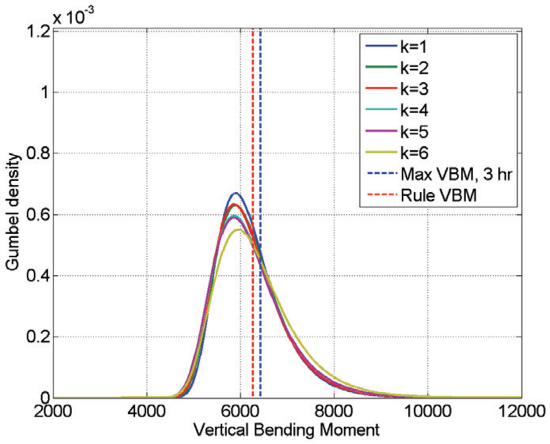

Figure 9.20: *Gumbel density function from the parameters derived from the optimised ACER functions for six different values of k (Table 9.6). The maximum measured hogging VBM during the three hours and the rule wave VBM are included for comparison. 9,400 TEU ship on 02 October 2011.*

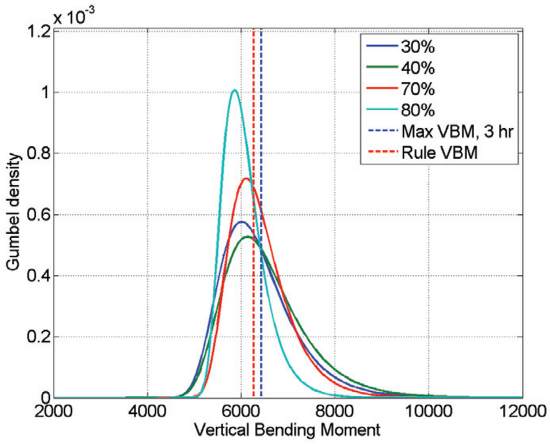

Figure 9.21: *Gumbel density function from the optimised ACER parameters for $k = 2$ and tail marker values corresponding to the thresholds in Table 9.5 (1,761, 2,348, 4,184 and 4,695 MNm). ACER does not yield useful results for the tail marker values corresponding to 50% and 60% of the mean of the three largest peaks. 9,400 TEU ship on 02 October 2011.*

fits, the Gumbel parameters from the POT analysis and the results of the ACER method are given in Appendix E.

9.4 9,400 TEU Container Ship, 12 August 2011

On 12 August 2011 the 9,400 TEU ship ship was sailing about 21 knots (Figure A.7) in H_s of about 5 m (Figure A.13) in bow-quartering seas entering from port side (Figure A.19). The time series of the VBM for the three hours (00-02 hours) are plotted in Figure E.14 in Appendix E. The statistics of the time series are presented in Table 9.7. As seen, the largest sagging VBM is slightly larger than the largest hogging VBM in this case.

	Max VBM [MNm]	Max VBM, WF [MNm]
Sagging	-2,271	-1,438
Hogging	2,264	1,440
	No. of peaks	No. of peaks, WF
Sagging	3,723	1,718
Hogging	3,772	1,710
Duration	s_M [MNm]	$s_{M,WF}$ [MNm]
3:00 hours	445	377

Table 9.7: *Maximum measured VBM and number of peaks for sagging and hogging for the flexible and rigid-body response and duration and standard deviation of the flexible (s_M) and rigid-body ($s_{M,WF}$) response. 9,400 TEU ship on 12 August 2011.*

The probability of exceedance for the three-hour time period is plotted in Figure 9.22 for sagging and Figure 9.23 for hogging. Hogging and sagging is very similar both for the flexible and rigid-body responses. The amplification of the response due to the hull girder flexibility is slightly larger in sagging than in hogging in this case.

From the Weibull fit to the full data set in Figure E.15 and E.16 in Appendix E it is also seen in this case that the Weibull distribution does not fit the tail of the peak distribution well. The estimated most probable largest value from the Weibull fit of 2,649 MNm is found to be quite conservative compared to the largest measured value of 2,264 MNm (Figure E.17).

Figure 9.24 shows the Gumbel density function for the different threshold levels and the mean excess is shown in Figure 9.25. As seen from Figure 9.25 a threshold between 1,200-1,400 would seem appropriate. From Figure 9.24 the prediction is quite insensitive to the threshold value between 50-70% (about 1,000 - 1,400 MNm) which is the range where the mean excess can roughly be approximated with a horizontal line.

The exceedance rates $\epsilon_1(x)$ and $\epsilon_2(x)$ are illustrated in Figure 9.26. In this case, the clustering effect, i.e. removal of one preceding peak in accordance with Eq. (9.10) is seen to be of minor importance. From the outcome of the ACER method illustrated Appendix E in Table E.6 and Figure E.19 the same can be concluded as the result is very similar

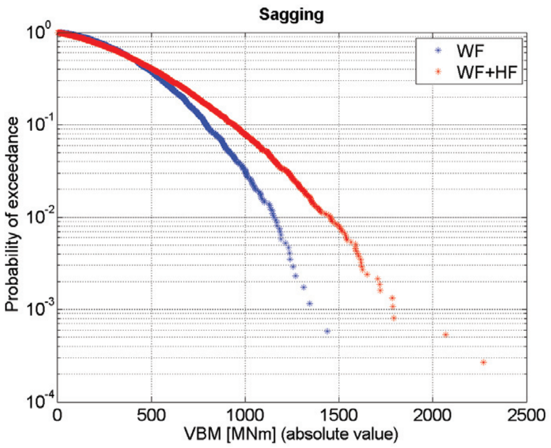

Figure 9.22: *Individual peak value probability of exceedance for sagging - WF and WF+HF response. Note, that even though the sagging moment is defined as negative, the absolute value is shown here. 9,400 TEU ship on 12 August 2011.*

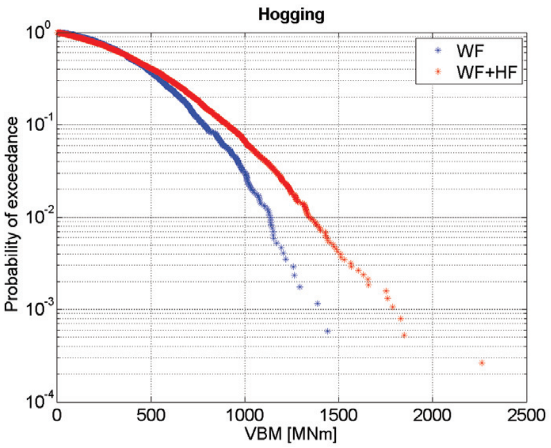

Figure 9.23: *Individual peak value probability of exceedance for hogging - WF and WF+HF response. 9,400 TEU ship on 12 August 2011.*

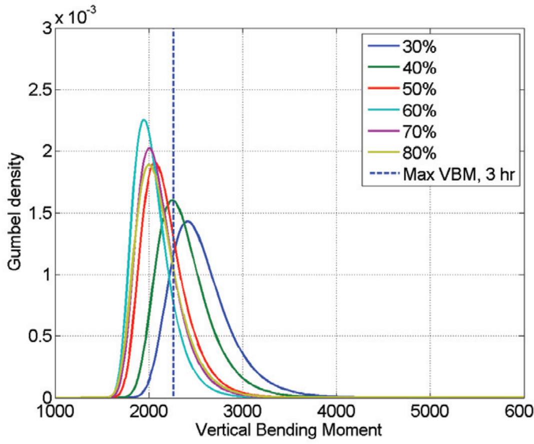

Figure 9.24: *Gumbel density function for the hogging VBM for the different threshold levels given in Table E.4. The maximum measured hogging VBM during the three hours is included for comparison. 9,400 TEU ship on 12 August 2011.*

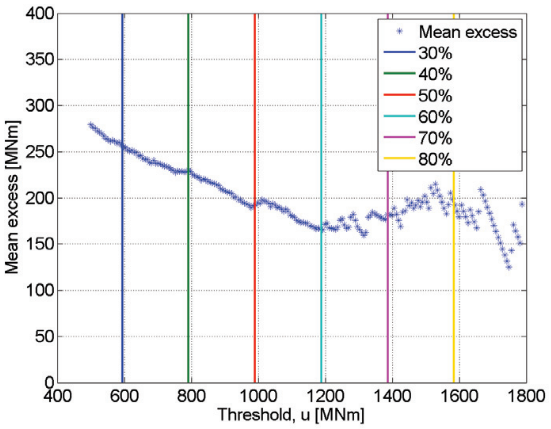

Figure 9.25: *Mean excess of the threshold level u as function of u. 9,400 TEU ship on 12 August 2011.*

for all values of k.

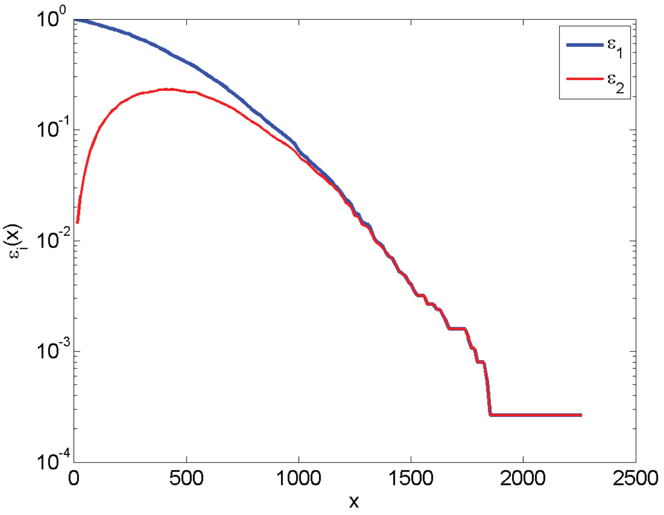

Figure 9.26: *The exceedance rates $\epsilon_1(x)$ (Eq. (9.8)) and $\epsilon_2(x)$ (Eq. (9.10)) for the hogging VBM. 9,400 TEU ship on 12 August 2011.*

9.5 9,400 TEU Container Ship, 17 December 2011

For the 9,400 TEU ship on 17 December 2011 only the starboard side strain gauge was functioning at the time, but this does not play any role for the extreme value prediction carried out here. The time series of the VBM for the three hours (12-14 hours) is plotted in Figure E.20 in Appendix E. According to the navigational data provided in Appendix A.1.2 the ship was sailing about 16 knots (Figure A.75) in H_s of 6-7 m (Figure A.81) in head sea (Figure A.87). The statistics of the time series are presented in Table 9.8. As seen the maximum hogging VBM is larger than the maximum sagging VBM for both the rigid-body and the flexible response.

	Max VBM [MNm]	Max VBM, WF [MNm]
Sagging	-2,828	-1,938
Hogging	3,349	2,617
	No. of peaks	No. of peaks, WF
Sagging	3,559	1,507
Hogging	3,511	1,456
Duration	s_M [MNm]	$s_{M,WF}$ [MNm]
3:00 hours	552	524

Table 9.8: *Maximum measured VBM and number of peaks for sagging and hogging for the flexible and rigid-body response and duration and standard deviation of the flexible (s_M) and rigid-body ($s_{M,WF}$) response. 9,400 TEU ship on 17 December 2011.*

The probability of exceedance for the three-hour time period is plotted in Figure 9.27 for sagging and Figure 9.28 for hogging. In this case, the VBM is only amplified by the HF vibrations for high response levels. The rigid-body WF response is larger for hogging than for sagging at all probability levels which is unexpected as the linear, rigid body response in hogging and sagging are expected to be similar. No explanation is found, but could be due to the operational conditions.

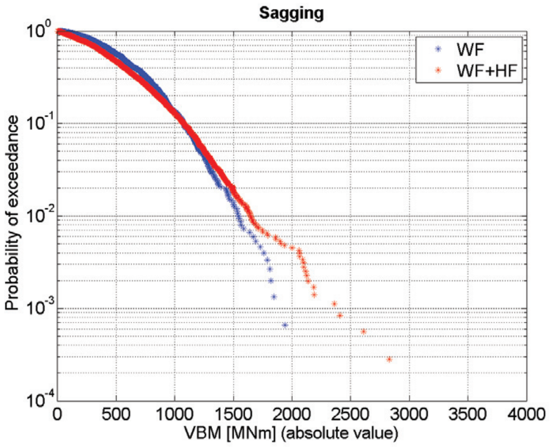

Figure 9.27: *Individual peak value probability of exceedance for sagging - WF and WF+HF response. Note, that even though the sagging moment is defined as negative, the absolute value is shown here. 9,400 TEU ship on 17 December 2011.*

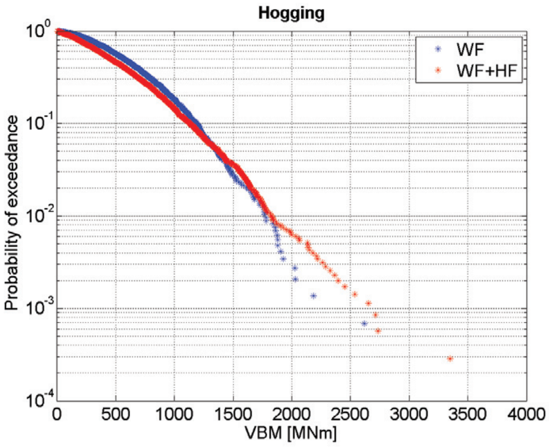

Figure 9.28: *Individual peak value probability of exceedance for hogging - WF and WF+HF response. 9,400 TEU ship on 17 December 2011.*

From Figure E.21 in Appendix E it is seen that the Weibull fit to the flexible response is fairly good at high response levels. The most probable largest value from the Gumbel fit to the full data set using the Weibull parameters in Table E.7 is 3,422 MNm, which is quite close to the maximum measured value of 3,349 MNm (Figure E.23).

Figure 9.29 shows the Gumbel density function for the different threshold levels and the mean excess is shown in Figure 9.30. In this case it is seen that the outcome of the POT analysis is quite insensitive to the threshold level even though the mean excess plots is quite irregular.

The exceedance rates $\epsilon_1(x)$ and $\epsilon_2(x)$ are illustrated in Figure 9.31. Here, the removal of one preceding peak in accordance with Eq. (9.10) shows that clustering is not important. The same is clearly seen from the outcome of the ACER method illustrated Appendix E in Table E.11 and Figure E.25 as the ACER method yields almost the same result for all k.

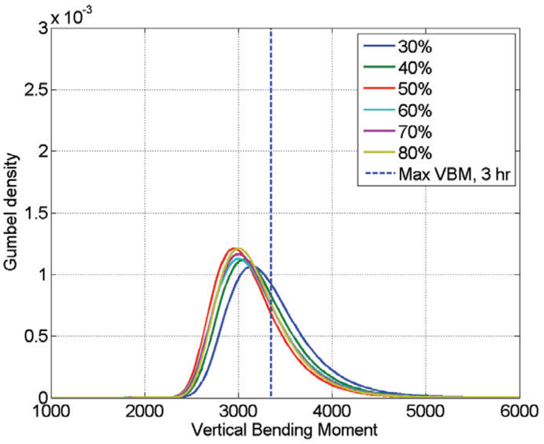

Figure 9.29: Gumbel density function for the hogging VBM for the different threshold levels given in Table 9.4. The maximum measured hogging VBM during the three hours is included for comparison. 9,400 TEU ship on 17 December 2011.

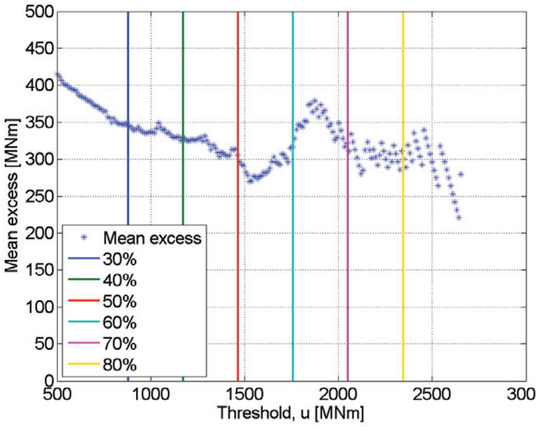

Figure 9.30: Mean excess of the threshold level u as function of u. 9,400 TEU ship on 17 December 2011.

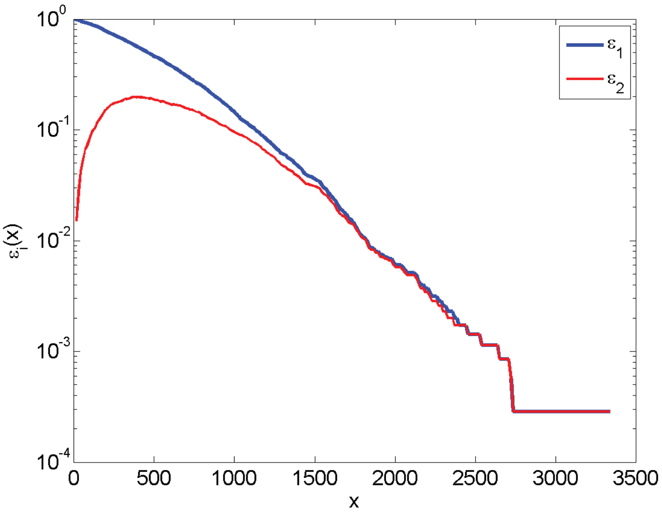

Figure 9.31: The exceedance rates $\epsilon_1(x)$ (Eq. (9.8)) and $\epsilon_2(x)$ (Eq. (9.10)) for the hogging VBM. 9,400 TEU ship on 17 December 2011.

9.6 8,600 TEU Container Ship, 17 November 2010

In the following, extreme value prediction is carried out based on three hours of data from the 8,600 TEU container ship from 17 November 2010 at 20-22 hours. The time series of the VBM is shown in Figure E.26 in Appendix E. The analysis carried out here is the same as in Section 9.3. The statistics of the time series are presented in Table 9.9. The maximum sagging VBM is larger than the maximum hogging VBM for both the flexible and the rigid-body response. It is noted, that the IACS rule VBMs are exceeded in both hogging and sagging.

	Max VBM [MNm]	Max VBM, WF [MNm]
Sagging	-7,760	-5,020
Hogging	6,299	4,683
	No. of peaks	No. of peaks, WF
Sagging	3,460	1,236
Hogging	3,592	1,259
Duration	s_M [MNm]	$s_{M,WF}$ [MNm]
3:00 hours	1,045	920

Table 9.9: *Maximum measured VBM and number of peaks for sagging and hogging for the flexible and rigid-body response and duration and standard deviation of the flexible (s_M) and rigid-body ($s_{M,WF}$) response. 8,600 TEU ship on 17 November 2010.*

The probability of exceedance is plotted in Figure 9.32 for sagging and Figure 9.33 for hogging. Like it was the case for the 9,400 TEU ship the hull girder flexibility significantly increases the probability of exceedance of a given bending moment in both sagging and hogging. The rigid-body responses are very alike to a level of exceedance of 10^{-2}, but at lower probability levels the rigid-body hogging VBM is larger than the rigid-body sagging VBM. The VBM seems slightly more amplified by the hull girder flexibility in the sagging than in the hogging condition.

From Figure E.27 in Appendix E it is seen that the Weibull fit to the flexible response is fairly good at high response levels. The most probable largest value from the Gumbel fit to the full data set using the Weibull parameters in Table E.12 is 6,533 MNm, which is quite close to the largest measured value of 6,299 MNm (Figure E.29).

Figure 9.34 shows the Gumbel density functions for the different threshold levels. The mean excess is plotted in Figure 9.35. From the figure an appropriate threshold level could be taken as between 2,500-4,000 MNm.

The exceedance rates $\epsilon_1(x)$ and $\epsilon_2(x)$ are illustrated in Figure 9.36. Here, the removal of one preceding peak shows that clustering could be of some importance. From the outcome of the ACER method illustrated Appendix E in Table E.16 and Figure E.31 the results are, however, quite similar for all values of k indicating that clustering is not important in this case.

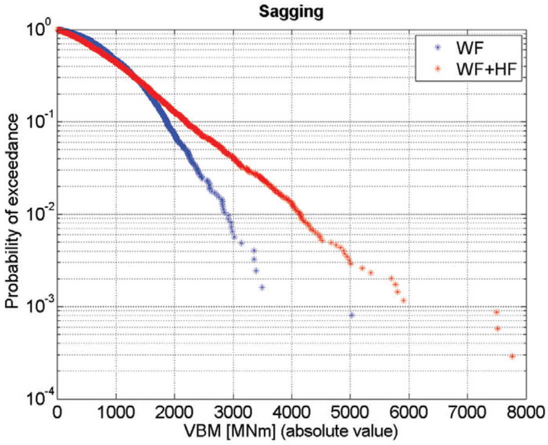

Figure 9.32: *Individual peak value probability of exceedance for sagging - WF and WF+HF response. Note, that even though the sagging moment is defined as negative, the absolute value is shown here. 8,600 TEU ship on 17 November 2010.*

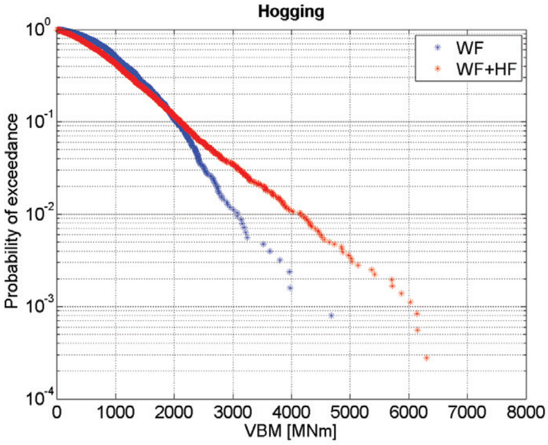

Figure 9.33: *Individual peak value probability of exceedance for hogging - WF and WF+HF response. 8,600 TEU ship on 17 November 2010.*

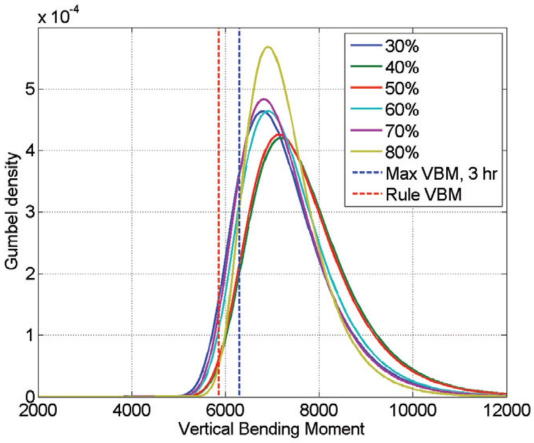

Figure 9.34: *Gumbel density function for the hogging VBM for the different threshold levels given in Table E.14. The maximum measured hogging VBM during the three hours and the rule wave VBM are included for comparison. 8,600 TEU ship on 17 November 2010.*

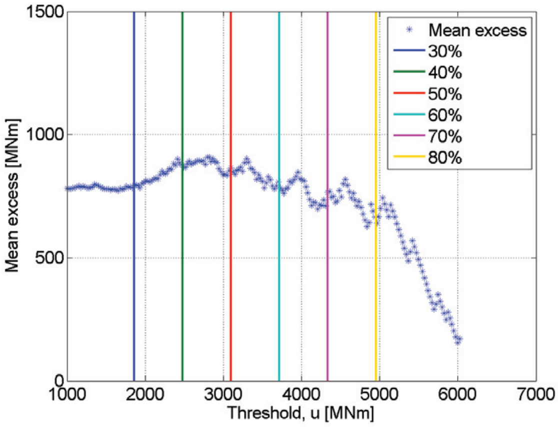

Figure 9.35: *Mean excess of the threshold level u as function of u. 8,600 TEU ship on 17 November 2010.*

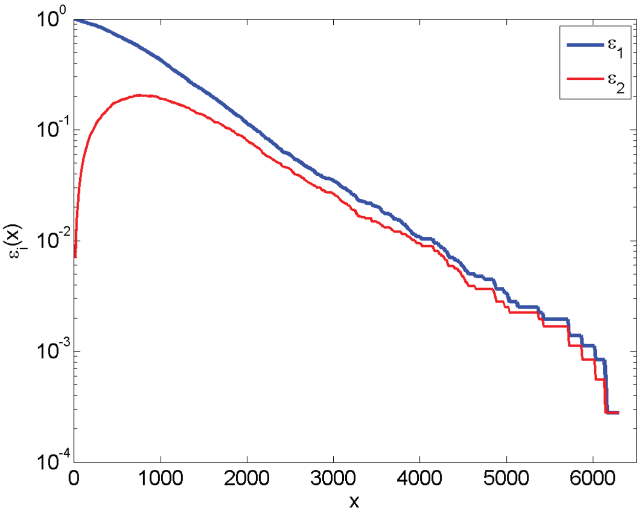

Figure 9.36: *The exceedance rates $\epsilon_1(x)$ (Eq. (9.8)) and $\epsilon_2(x)$ (Eq. (9.10)) for the hogging VBM. 8,600 TEU ship on 17 November 2010.*

9.7 8,600 TEU Container Ship, 30 December 2011

The three hour time series for the 8,600 TEU container ship for 30 December 2011 at 7-9 hours is shown in Figure E.32 in Appendix E. The statistics of the time series are presented in Table 9.10. Here, the maximum hogging VBM is the largest for both the flexible and the rigid-body response.

	Max VBM [MNm]	Max VBM, WF [MNm]
Sagging	-5,320	-2,964
Hogging	5,450	3,258
	No. of peaks	No. of peaks, WF
Sagging	4,920	1,845
Hogging	4,916	1,807
Duration	s_M [MNm]	$s_{M,WF}$ [MNm]
3:00 hours	809	686

Table 9.10: *Maximum measured VBM and number of peaks for sagging and hogging for the flexible and rigid-body response and duration and standard deviation of the flexible (s_M) and rigid-body ($s_{M,WF}$) response. 8,600 TEU ship on 30 December 2011.*

The probability of exceedance is plotted in Figure 9.37 for sagging and Figure 9.38 for hogging. As it was the case for the same ship on 17 November 2010 the rigid-body hogging VBM is slightly larger than the rigid-body sagging VBM as it was also found for the 9,400 TEU ship on 17 December 2011.

From Figure E.33 in Appendix E it is seen that the Weibull fit to the flexible response is also fairly good at high response levels in this case. The most probable largest value from the Gumbel fit to the full flexible data set using the Weibull parameters in E.17 is 5,335 MNm, which is quite close to the largest measured value of 5,450 MNm (Figure E.35).

The Gumbel density functions for the different thresholds are illustrated in Figure 9.39 and the mean excess is plotted in Figure 9.40. As it is difficult to approximate any part of the plot of the mean excess with a horizontal line Figure 9.40 may suggest that the Gumbel type asymptotic extreme distribution is not necessarily the correct one. However, the variation with threshold levels shown in the Gumbel distributions, Figure 9.39 is modest for threshold levels between 40-60%.

The exceedance rates $\epsilon_1(x)$ and $\epsilon_2(x)$ are illustrated in Figure 9.41. Here, the figure suggest that clustering is not important.

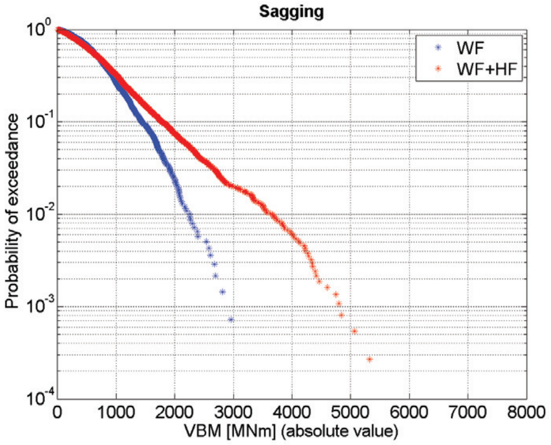

Figure 9.37: *Individual peak value probability of exceedance for sagging - WF and WF+HF response. Note, that even though the sagging moment is defined as negative, the absolute value is shown here. 8,600 TEU ship on 30 December 2011.*

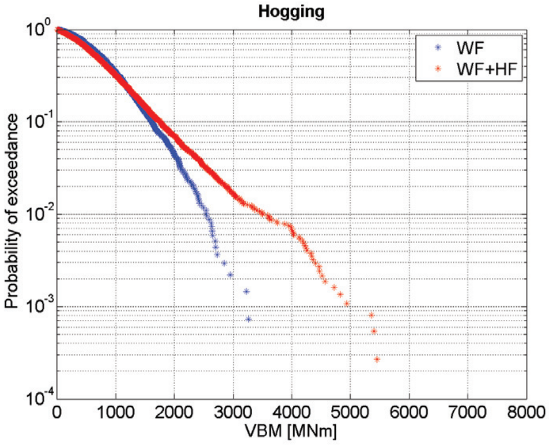

Figure 9.38: *Individual peak value probability of exceedance for hogging - WF and WF+HF response. 8,600 TEU ship on 30 December 2011.*

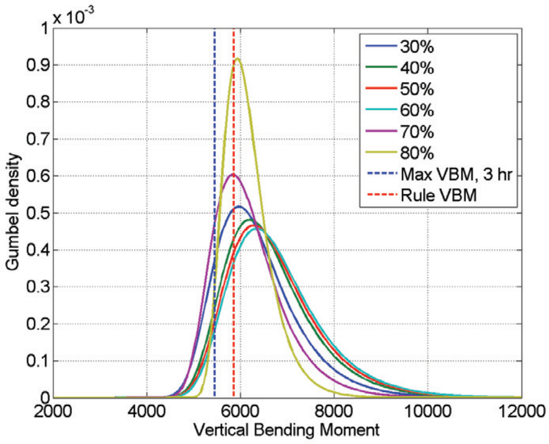

Figure 9.39: *Gumbel density function for the hogging VBM for the different threshold levels given in Table E.14. The maximum measured hogging VBM during the three hours and the rule wave VBM are included for comparison. 8,600 TEU ship on 30 December 2011.*

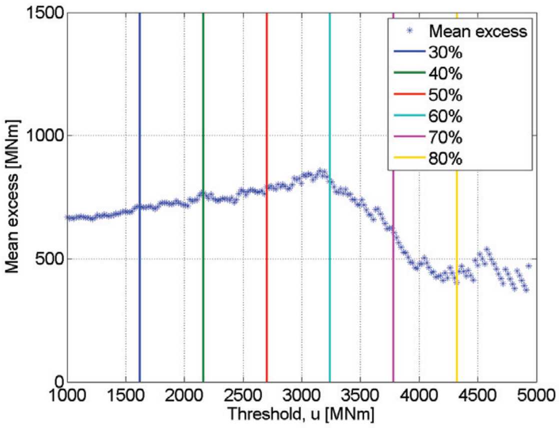

Figure 9.40: *Mean excess of the threshold level u as function of u. 8,600 TEU ship on 30 December 2011.*

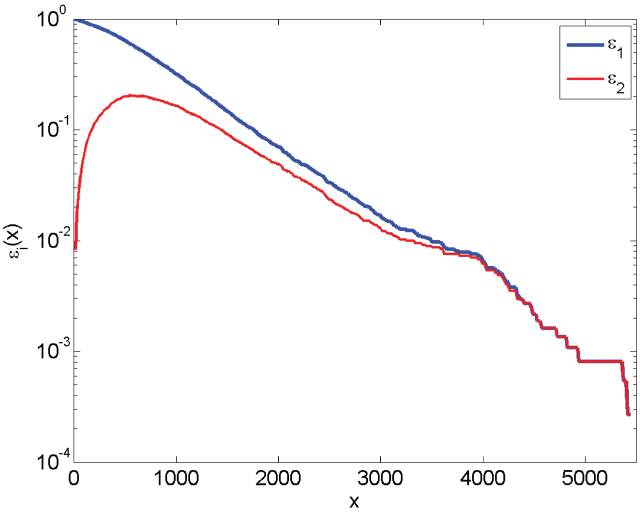

Figure 9.41: *The exceedance rates* $\epsilon_1(x)$ *(Eq. (9.8)) and* $\epsilon_2(x)$ *(Eq. (9.10)) for the hogging VBM. 8,600 TEU ship on 30 December 2011.*

9.8 14,000 TEU Container Ship, 29 September 2011

For the 14,000 TEU ship the stress time series are not logged continuously. Large events trigger the storage of data as described in Section 2.5. In the previous sections three hours of data were used. Here, three non-continuous time series from the same day is used. The time series are plotted in Appendix E, Figure E.38. The total length of the three time series combined is 2 hours and 47 minutes hours as seen from Table E.22 in Appendix E. Since the standard deviation of the time series varies little during the period considered (see Table E.22) the conditions are considered stationary. The statistics of the time series are presented in Table 9.11. Here, the maximum hogging VBM is significantly larger than the maximum sagging VBM for both the rigid-body and the flexible response. The reason may be found in the sea state encountered, but the sea state the ship was operated in is not known in this case.

	Max VBM [MNm]	Max VBM, WF [MNm]
Sagging	-6,517	-4,819
Hogging	7,958	6,235
	No. of peaks	No. of peaks, WF
Sagging	3,097	1,273
Hogging	2,893	1,261
Duration	s_M [MNm]	$s_{M,WF}$ [MNm]
2:47 hours	1,500	1,410

Table 9.11: *Maximum measured VBM and number of peaks for sagging and hogging for the flexible and rigid-body response and duration and standard deviation of the flexible (s_M) and rigid-body ($s_{M,WF}$) response. 14,000 TEU ship on 29 September 2011.*

The probability of exceedance for the VBM for three time series together are given in Figure 9.42 and 9.43 for sagging and hogging respectively. Quite unexpectedly, the rigid-body hogging VBM is significantly larger than the corresponding sagging VBM at all probability levels.

From the Weibull fit to the full data set in Figure E.39 it is also seen here that the Weibull distribution does not fit the tail of the peak distribution well and that the measured largest peaks fall above the Weibull fit. The most probable largest value from the Gumbel fit to the full data set using the Weibull parameters in Table E.23 is 9,760 MNm, which is very conservative compared to the largest measured value of 7,958 MNm (Figure E.41).

The Gumbel density functions for the different thresholds are illustrated in Figure 9.44 and the mean excess is plotted in Figure 9.45. Here, a significant, almost linear variation of the mean excess with the threshold is seen, which is also reflected in the large variation

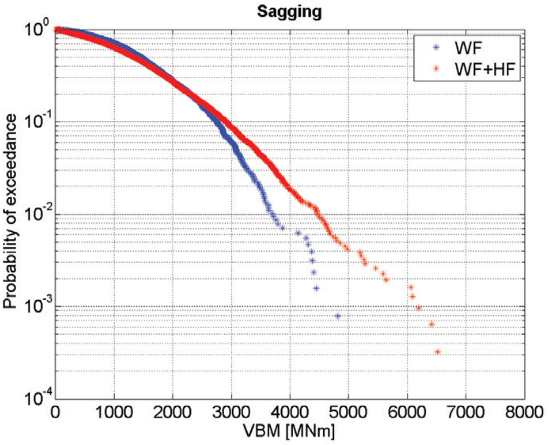

__Figure 9.42:__ Individual peak value probability of exceedance for sagging - WF and WF+HF response. Note, that even though the sagging moment is defined as negative, the absolute value is shown here. 14,000 TEU ship on 29 September 2011.

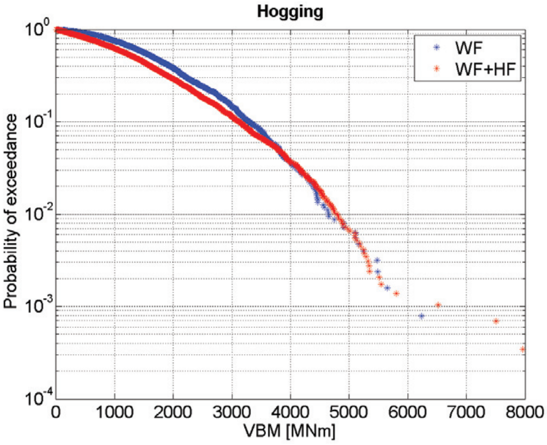

__Figure 9.43:__ Individual peak value probability of exceedance for hogging - WF and WF+HF response. 14,000 TEU ship on 29 September 2011.

in the Gumbel distributions with the threshold levels used.

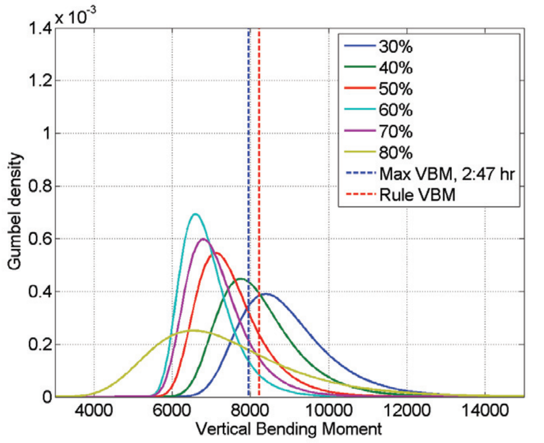

__Figure 9.44:__ Gumbel density function for the hogging VBM for the different threshold levels given in Table E.25. The maximum measured hogging VBM during the three hours and the rule wave VBM are included for comparison. 14,000 TEU ship on 29 September 2011.

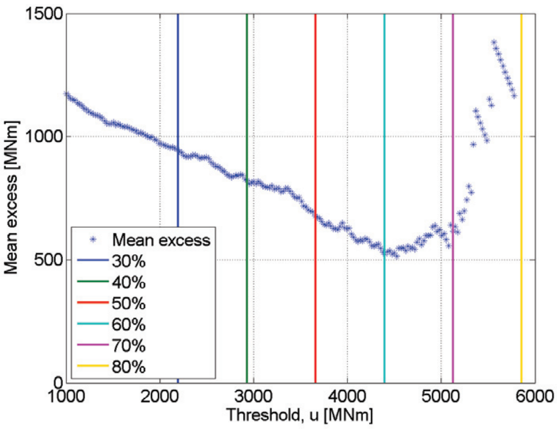

__Figure 9.45:__ Mean excess of the threshold level u as function of u. 14,000 TEU ship on 29 September 2011.

The exceedance rates $\epsilon_1(x)$ and $\epsilon_2(x)$ illustrated in Figure 9.46 suggest that clustering is not important.

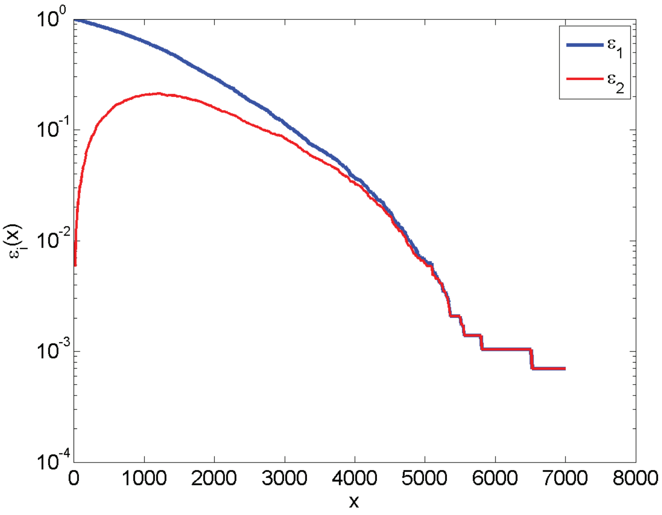

Figure 9.46: *The exceedance rates $\epsilon_1(x)$ (Eq. (9.8)) and $\epsilon_2(x)$ (Eq. (9.10)) for the hogging VBM. 14,000 TEU ship on 29 September 2011.*

9.9 14,000 TEU Container Ship, 21 July 2011

For the 14,000 TEU ship on 21 July 2011 the extreme value prediction is carried out based on two time series. The total time series is plotted in Appendix E, Figure E.44. The length of the two time series combined is 1 hour and 45 minutes as seen from Table E.28. Since the standard deviation of the time series varies little during the period considered the conditions are considered stationary. The statistics of the time series are presented in Table 9.12. Here, the maximum hogging VBM is also larger than the maximum sagging VBM for both the flexible and the rigid-body response.

	Max VBM [MNm]	Max VBM, WF [MNm]
Sagging	-5,528	-3,347
Hogging	6,048	3,661
	No. of peaks	No. of peaks, WF
Sagging	2,105	924
Hogging	2,102	915
Duration	s_M [MNm]	$s_{M,WF}$ [MNm]
1:45 hours	1,122	930

Table 9.12: *Maximum measured VBM and number of peaks for sagging and hogging for the flexible and rigid-body response and duration and standard deviation of the flexible (s_M) and rigid-body ($s_{M,WF}$) response. 14,000 TEU ship on 21 July 2011.*

The probability of exceedance for the VBM for three time series together are given in Figure 9.47 and 9.48 for sagging and hogging respectively. Here, the rigid-body sagging and hogging VBM are quite similar for high probabilities of exceedance while the rigid-body hogging VBM is slightly larger than the corresponding sagging VBM at smaller probability levels.

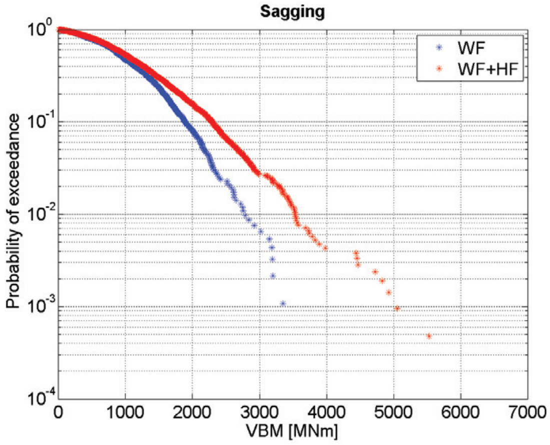

Figure 9.47: *Individual peak value probability of exceedance for sagging - WF and WF+HF response. Note, that even though the sagging moment is defined as negative, the absolute value is shown here. 14,000 TEU ship on 21 July 2011.*

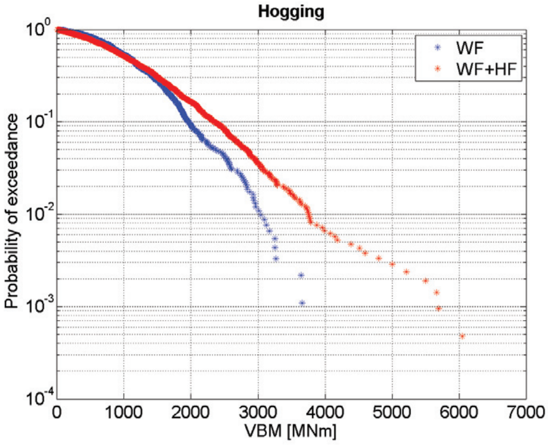

Figure 9.48: *Individual peak value probability of exceedance for hogging - WF and WF+HF response. 14,000 TEU ship on 21 July 2011.*

From the Weibull fit to the full data set in Figure E.45 the Weibull fit is seen to fit the largest measured values quite well. The most probable largest value from the Gumbel fit to the full data set using the Weibull parameters in Table E.29 is 6,597 MNm and the maximum measured response is 6,048 MNm (Figure E.47).

The Gumbel density functions for the different thresholds are illustrated in Figure 9.49 and the mean excess is plotted in Figure 9.50. The variation of the mean excess with threshold is modest up to about 3,500 MNm reflecting in only minor differences in the resulting Gumbel distributions.

The exceedance rates $\epsilon_1(x)$ and $\epsilon_2(x)$ illustrated in Figure 9.51 suggest that clustering is not important in this case either and this is also reflected in the outcome from the ACER method illustrated Appendix E in Table E.33 and Figure E.49.

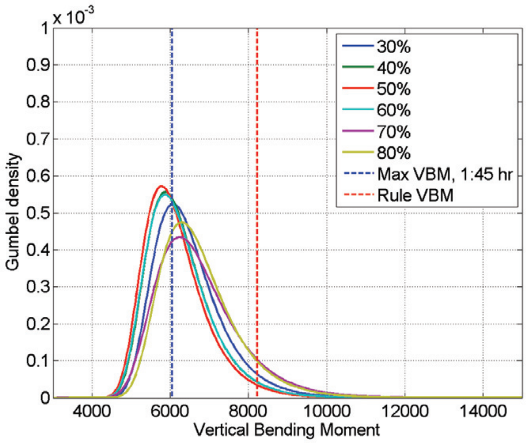

Figure 9.49: *Gumbel density function for the hogging VBM for the different threshold levels given in Table E.31. The maximum measured hogging VBM during the three hours and the rule wave VBM are included for comparison. 14,000 TEU ship on 21 July 2011.*

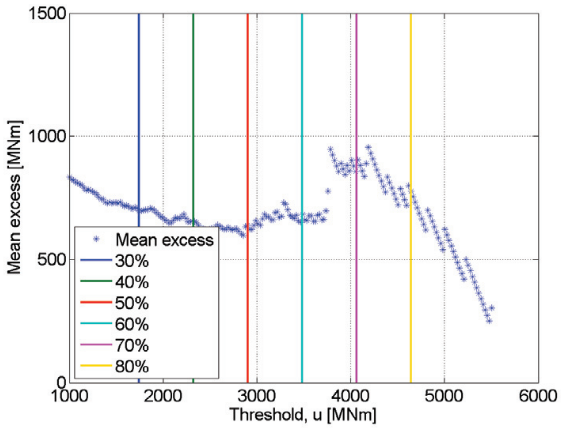

Figure 9.50: *Mean excess of the threshold level u as function of u. 14,000 TEU ship on 21 July 2011.*

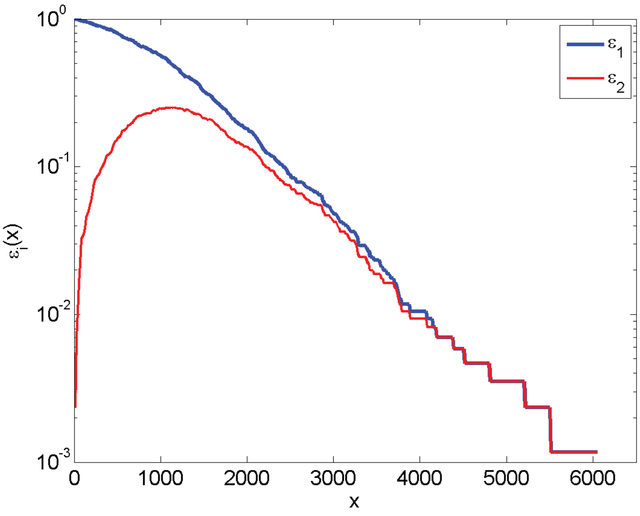

Figure 9.51: *The exceedance rates $\epsilon_1(x)$ (Eq. (9.8)) and $\epsilon_2(x)$ (Eq. (9.10)) for the hogging VBM. 14,000 TEU ship on 21 July 2011.*

9.10 4,400 TEU Container Ship, 02 November 2007, 11-13 hours

For the 4,400 TEU ship the largest response took place on 02 November 2007 at 11 hours. The length of the considered time series is 3 hours. The time series is plotted in Appendix E, Figure E.50. The statistics of the time series are given in Table 9.13. For this time series, the maximum sagging VBM is larger than the maximum hogging VBM for both the flexible and the rigid-body response.

	Max VBM [MNm]	Max VBM, WF [MNm]
Sagging	-5,081	-3,844
Hogging	3,672	2,767
	No. of peaks	No. of peaks, WF
Sagging	3,340	1,262
Hogging	3,276	1,249
Duration	s_M [MNm]	$s_{M,WF}$ [MNm]
3 hours	780	763

Table 9.13: *Maximum measured VBM and number of peaks for sagging and hogging for the flexible and rigid-body response and duration and standard deviation of the flexible (s_M) and rigid-body ($s_{M,WF}$) response. 4,400 TEU ship on 02 November 2007, 11-13 hours.*

The probability of exceedance for the VBM for three time series together are given in Figure 9.62 and 9.63 for sagging and hogging respectively. Both the flexible and rigid-body VBM is similar in hogging and sagging in this case although the sagging VBM is slightly larger than the hogging VBM at low levels of probability.

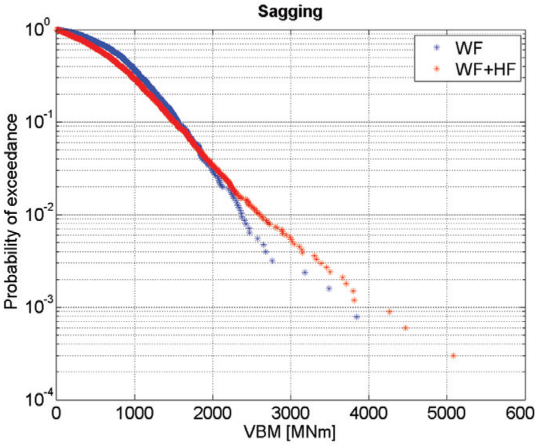

Figure 9.52: *Individual peak value probability of exceedance for sagging - WF and WF+HF response. Note, that even though the sagging moment is defined as negative, the absolute value is shown here. 4,400 TEU ship on 02 November 2007, 11-13 hours.*

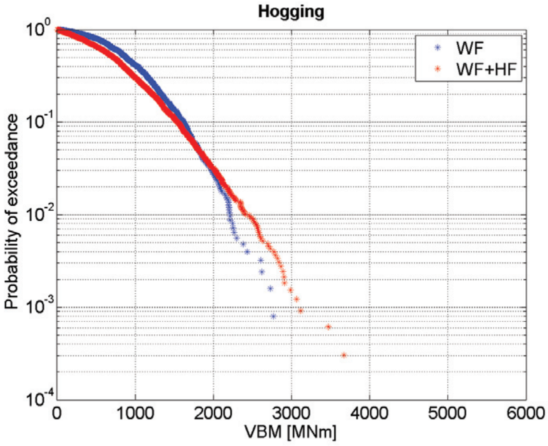

Figure 9.53: *Individual peak value probability of exceedance for hogging - WF and WF+HF response. 4,400 TEU ship on 02 November 2007, 11-13 hours.*

From the Weibull fit to the full data set in Figure E.51 it is seen that the Weibull fit does not match the largest peaks very well and that the measurements fall above the Weibull

Fit. This results in a conservative estimate of the most probable largest value from the Gumbel fit using the Weibull parameters in Table E.34 of 4,652 MNm. The maximum measured value is 3,672 MNm (Figure E.53).

The Gumbel density functions for the different thresholds are illustrated in Figure 9.54 and the mean excess is plotted in Figure 9.55. From the mean excess it is difficult to decide on an appropriate threshold level and the Gumbel density functions for different thresholds also show quite large variation with the threshold level.

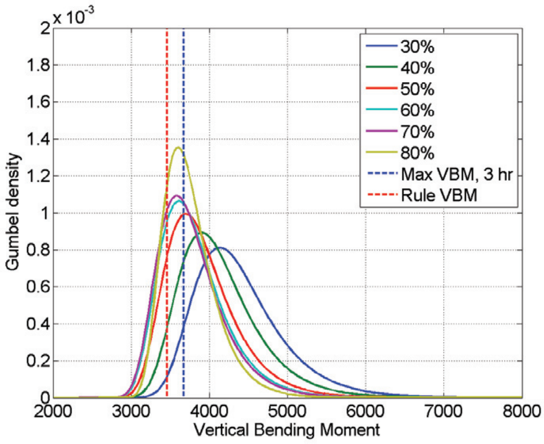

Figure 9.54: *Gumbel density function for the hogging VBM for the different threshold levels given in Table E.46. The maximum measured hogging VBM during the three hours and the rule wave VBM are included for comparison. 4,400 TEU ship on 02 November 2007, 11-13 hours.*

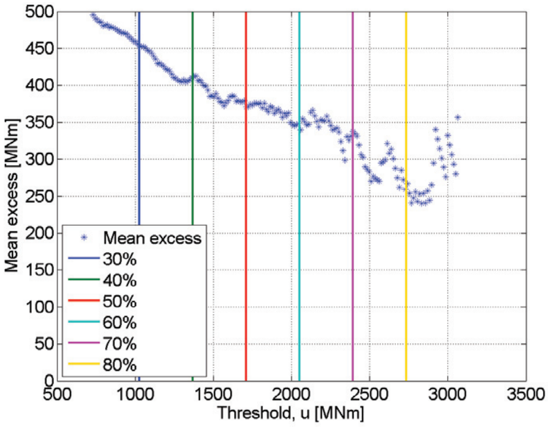

Figure 9.55: *Mean excess of the threshold level u as function of u. 4,400 TEU ship on 02 November 2007, 11-13 hours.*

The exceedance rates $\epsilon_1(x)$ and $\epsilon_2(x)$ illustrated in Figure 9.56 suggest that clustering is not important in this case either and this is also reflected in the outcome from the ACER method illustrated Appendix E in Table E.38 and Figure E.55 where the outcome for all k are similar.

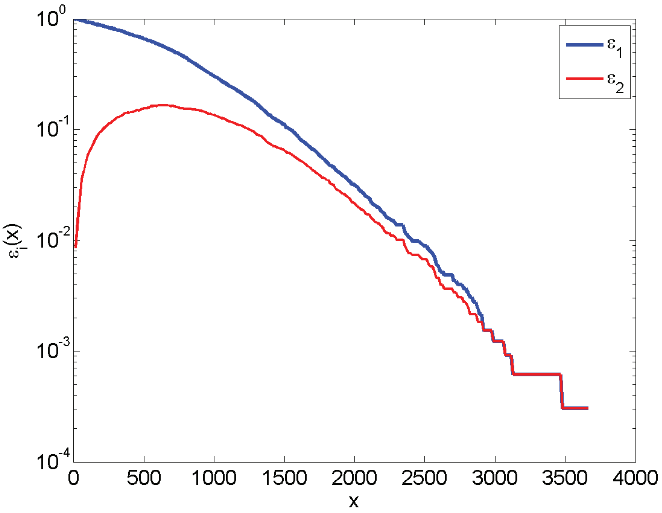

Figure 9.56: *$\epsilon_1(x)$ (Eq. (9.8)) and $\epsilon_2(x)$ (Eq. (9.10)) for the hogging VBM. 4,400 TEU ship on 02 November 2007, 11-13 hours.*

9.11 4,400 TEU Container Ship, 02 November 2007, 16-18 hours

For the 4,400 TEU ship another large response on 02 November 2007 took place at 16 hours. The length of the considered time series is 3 hours. The time series is plotted in Appendix E, Figure E.56. The statistics of the time series are given in Table 9.14. The maximum sagging VBM is slightly larger than the maximum hogging VBM for both the flexible and the rigid-body response.

	Max VBM [MNm]	Max VBM, WF [MNm]
Sagging	-4,269	-2,548
Hogging	4,233	2,295
	No. of peaks	No. of peaks, WF
Sagging	3,459	1,396
Hogging	3,321	1,392
Duration	s_M [MNm]	$s_{M,WF}$ [MNm]
3 hours	634	619

Table 9.14: *Maximum measured VBM and number of peaks for sagging and hogging for the flexible and rigid-body response and duration and standard deviation of the flexible (s_M) and rigid-body ($s_{M,WF}$) response. 4,400 TEU ship on 02 November 2007, 16-18 hours.*

The probability of exceedance for the VBM for three time series together are given in Figure 9.57 and 9.58 for sagging and hogging respectively. Again, the hogging and the sagging response are found to be quite similar.

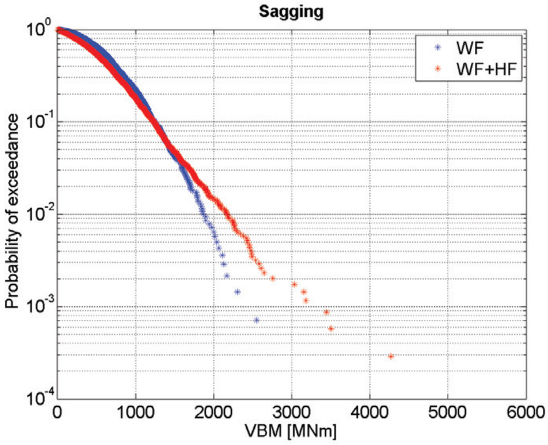

Figure 9.57: *Individual peak value probability of exceedance for sagging - WF and WF+HF response. Note, that even though the sagging moment is defined as negative, the absolute value is shown here. 4,400 TEU ship on 02 November 2007, 16-18 hours.*

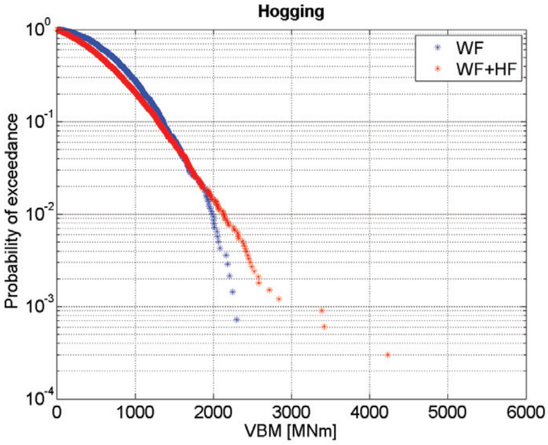

Figure 9.58: *Individual peak value probability of exceedance for hogging - WF and WF+HF response. 4,400 TEU ship on 02 November 2007, 16-18 hours.*

The Weibull fit to the full data set is seen in Figure E.57. The most probable largest value from the Gumbel fit to the full data set using the Weibull parameters in Table E.39 is 4,050 MNm which is non-conservative compared to the maximum measured value of 4,233 MNm (Figure E.59).

The Gumbel density functions for the different thresholds are illustrated in Figure 9.59 and the mean excess is plotted in Figure 9.60. From the plots of the mean excess it is clearly seen that the threshold level must be chosen below about 2,200 MNm. This is also reflected in the Gumbel density functions which deviate significantly for high threshold levels.

The exceedance rates $\epsilon_1(x)$ and $\epsilon_2(x)$ illustrated in Figure 9.61 suggest that clustering may be of some importance in this case. From the outcome of the ACER method illustrated Appendix E in Table E.43 and Figure E.61, however, there is not much difference for different k.

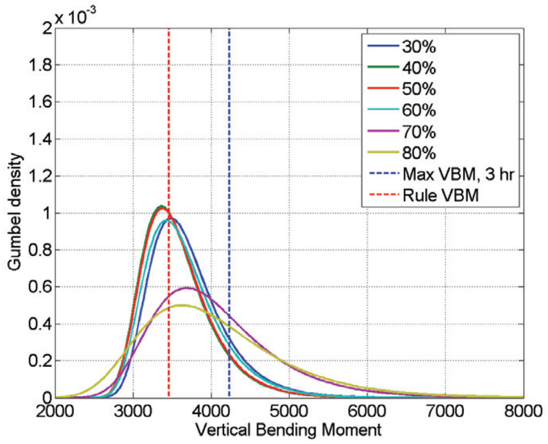

Figure 9.59: *Gumbel density function for the hogging VBM for the different threshold levels given in Table E.46. The maximum measured hogging VBM during the three hours and the rule wave VBM are included for comparison. 4,400 TEU ship on 02 November 2007, 16-18 hours.*

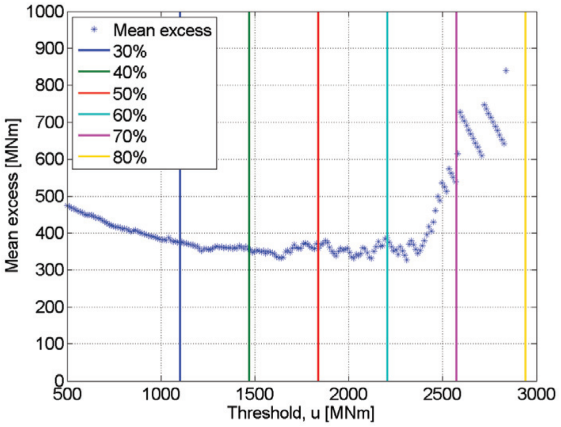

Figure 9.60: *Mean excess of the threshold level u as function of u. 4,400 TEU ship on 02 November 2007, 16-18 hours.*

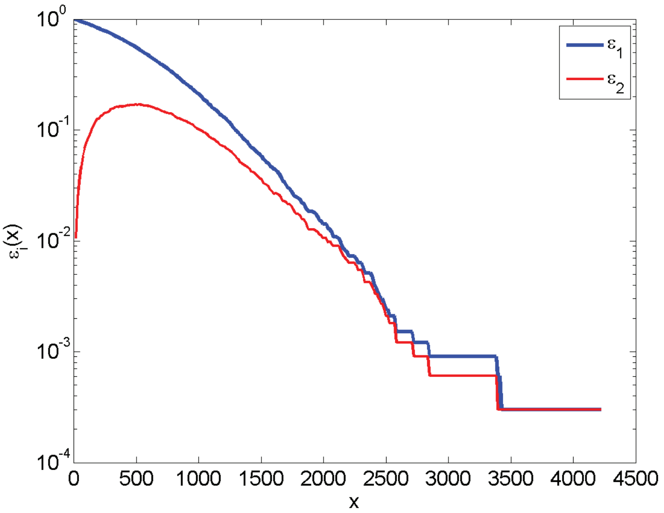

Figure 9.61: *The exceedance rates $\epsilon_1(x)$ (Eq. (9.8)) and $\epsilon_2(x)$ (Eq. (9.10)) for the hogging VBM. 4,400 TEU ship on 02 November 2007, 16-18 hours.*

9.12 4,400 TEU Container Ship, 01 July 2008

For the 4,400 TEU ship another large response took place on 01 July 2008. The length of the considered time series is 3 hours. The time series is plotted in Appendix E, Figure E.62. The statistics of the time series are given in Table 9.15. For this time series, the maximum hogging VBM is larger than the maximum sagging VBM for both the flexible and the rigid-body response.

	Max VBM [MNm]	Max VBM, WF [MNm]
Sagging	-3,022	-2,252
Hogging	3,271	2,783
	No. of peaks	No. of peaks, WF
Sagging	3,407	1,428
Hogging	3,266	1,454
Duration	s_M [MNm]	$s_{M,WF}$ [MNm]
3 hours	594	578

Table 9.15: *Maximum measured VBM and number of peaks for sagging and hogging for the flexible and rigid-body response and duration and standard deviation of the flexible (s_M) and rigid-body ($s_{M,WF}$) response. 4,400 TEU ship on 01 July 2008.*

The probability of exceedance for the VBM for three time series together are given in Figure 9.62 and 9.63 for sagging and hogging respectively. Again, the hogging and the sagging response are found to be quite similar.

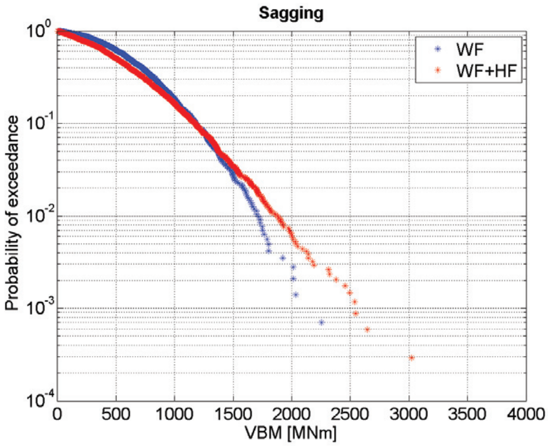

Figure 9.62: *Individual peak value probability of exceedance for sagging - WF and WF+HF response. Note, that even though the sagging moment is defined as negative, the absolute value is shown here. 4,400 TEU ship on 01 July 2008.*

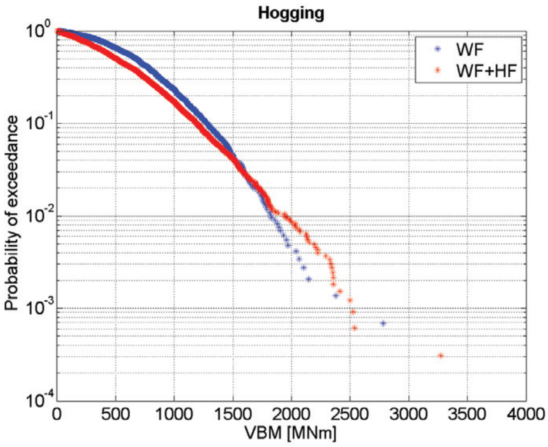

Figure 9.63: *Individual peak value probability of exceedance for hogging - WF and WF+HF response. 4,400 TEU ship on 01 July 2008.*

The Weibull fit to the full data set is seen in Figure E.63. The most probable largest value from the Gumbel fit to the full data set using the Weibull parameters in Table E.44 is 3,737 MNm which is conservative compared to the maximum measured value of 3,271 MNm (Figure E.65).

The Gumbel density functions for the different thresholds are illustrated in Figure 9.64 and the mean excess is plotted in Figure 9.65. The mean excess cannot in any interval be approximated with a horizontal line, and the Gumbel density functions for the different thresholds are all slightly different.

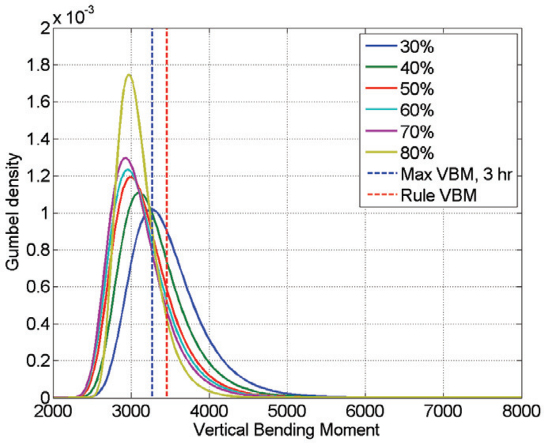

Figure 9.64: *Gumbel density function for the hogging VBM for the different threshold levels given in Table E.46. The maximum measured hogging VBM during the three hours and the rule wave VBM are included for comparison. 4,400 TEU ship on 01 July 2008.*

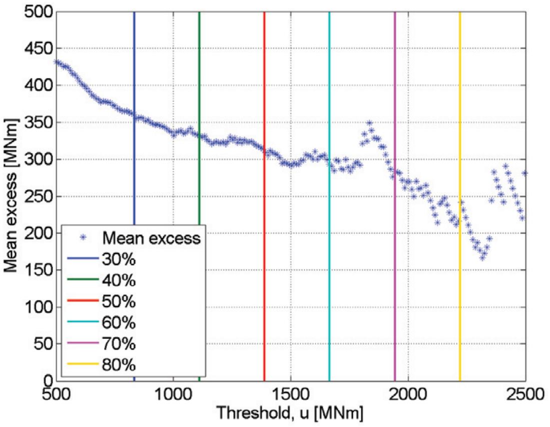

Figure 9.65: *Mean excess of the threshold level u as function of u. 4,400 TEU ship on 01 July 2008.*

The exceedance rates $\epsilon_1(x)$ and $\epsilon_2(x)$ illustrated in Figure 9.66 suggest that clustering is not important in this case. From the outcome of the ACER method illustrated Appendix E in Table E.48 and Figure E.67 there is very little difference for different k.

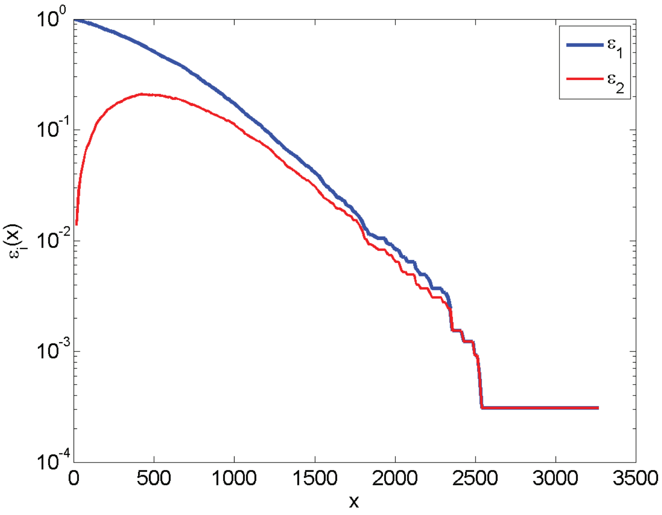

Figure 9.66: *The exceedance rates $\epsilon_1(x)$ (Eq. (9.8)) and $\epsilon_2(x)$ (Eq. (9.10)) for the hogging VBM. 4,400 TEU ship on 01 July 2008.*

9.13 Clustering and De-Clustering of Peaks

In the previous sections clustering of the largest peaks is found to play a role for some of the considered time series as illustrated in e.g. Figure 9.14 for the 9,400 TEU ship. From a similar visual analysis for the same ship on 12 August 2011 (Figure E.14) all the largest response are found to be associated with only one or maximum two peaks.

For the 8,600 TEU ship on 17 November 2010 (Figure 9.67) it is hard to distinguish the separate large events because the response level is generally high. However, the largest groups of peaks indicated above 4,000 MNm consist of 2, 2, 5, 7 and 1 peak. On 30 December 2011 the largest response (Figure E.32) is associated with 4 peaks and the rest of the large events are associated with only 1 or 2 peaks.

For the 14,000 TEU ship on 29 September 2011 the response level is also generally high and it is difficult to identify distinct slamming events. For the 4,400 TEU ship in 02 November 2007 the four largest responses are found to be associated with 3, 2, 5 and 4 peaks above 2,000 MNm, see Figure 9.68.

It is noted, that none of the considered peaks seems to be distinct outliers or faulty measurements. Obviously, visual investigation of the time series is not a very scientific way of identifying clustered peaks but might be helpful in the discussion of the methods in the following.

The high-frequency part of the response generally increases clustering. As described previously there are different ways to account for correlation between large peaks when carrying out extreme value prediction. The described method by Naess and Gaidai, 2009 removes one or more (up to 5) preceding peaks if they are above a certain threshold level. Another method could be to only count one peak per zero-upcrossing of the signal.

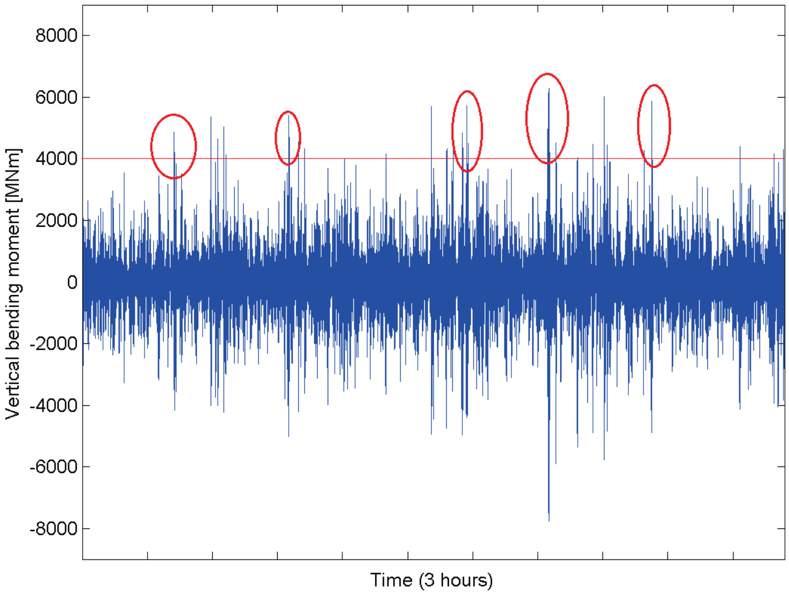

Figure 9.67: *Wave-induced vertical bending moment amidships compared to the minimum design wave-induced vertical bending moments (VBM) in hogging and sagging from International Association of Classification Societies, 2010a for the 8,600 TEU ship on 17 November 2010. Indication of the groups of peaks including five of the largest peaks.*

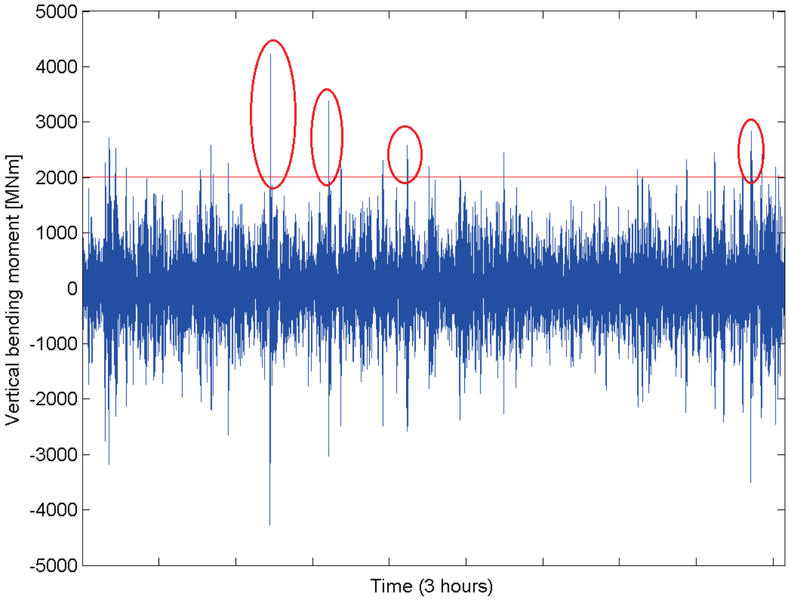

Figure 9.68: *Wave-induced vertical bending moment amidships compared to the minimum design wave-induced vertical bending moments (VBM) in hogging and sagging from International Association of Classification Societies, 2010a for the 4,400 TEU ship on 02 November 2007. Indication of the groups of peaks including four of the largest peaks.*

The WAFO package (Brodtkorb et al., 2011) also contains a de-clustering routine to be applied to peaks over a given threshold and identifies the largest peak in each cluster of peaks. The WAFO algorithm requires a minimum time between peaks to ensure statistical independence, which must be estimated from the time series.

9.14 Discussion and Conclusions

In the following, the outcome of the extreme value prediction based on the measurements from the the four container ships is discussed and the methods are compared. The influence of the hull girder flexibility on the structural response and the rigid-body VBM response will be addressed in Chapter 12.

The correlation between peaks is found to be an issue of concern for some of the considered time series. The correlation is only partial and therefore it is difficult to suggest a statistical method to properly account for clustering effect and other methods to ensure statistical independence of peaks for the extreme value estimation could be subject for future studies.

The clustering effect is found to be more pronounced for the 8,600 TEU ship than for the 9,400 TEU ship. When investigating the time series from the 9,400 TEU ship in Figure 9.14 the two largest peaks in hogging, which are also seen in Figure 9.2, are found to be clustered with at least three peaks over 5,000 MNm and the two largest peaks during three hours are spaced only about 2.3 seconds in time. Clusters of more than 3 large peaks are not immediately observed from the other time series for the 9,400 TEU ship. In agreement with Gaidai et al., 2010 $k = 2$ generally seems sufficient to account for the clustering effect. Gaidai et al., 2010 state that by increasing k more peaks are excluded, resulting in decreased accuracy of the estimate, so k should be as small as possible for practical use. From the analyses here $k = 2$ or 3 would be sufficient in most cases and $k = 2$ is used for comparison with the Weibull procedure and POT procedures in the following.

For all four ships, the results from the Gumbel fits derived from the Weibull parameters, from the POT method using a threshold of 50% of the average of the three largest measured values, from the POT applied on the de-clustered signal where one preceding peak is removed and from the ACER program using $k = 2$ are illustrated for comparison in Figures 9.69-9.79. The maximum measured hogging VBM and the rule VBM are included in the plots.

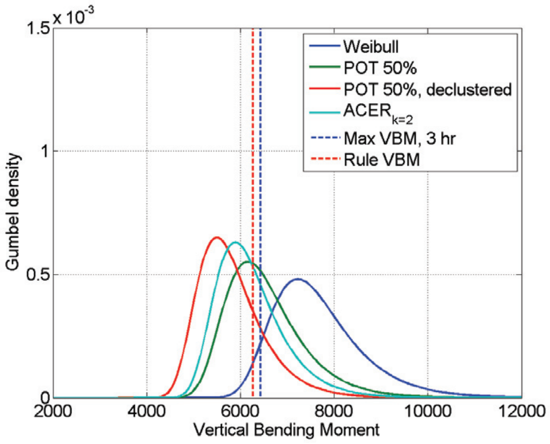

Figure 9.69: *Gumbel fit from Weibull parameters, POT with threshold 50% of the mean of the three measured largest values, compared with ACER for k = 2 for 9,400 TEU ship, 02 October 2011.*

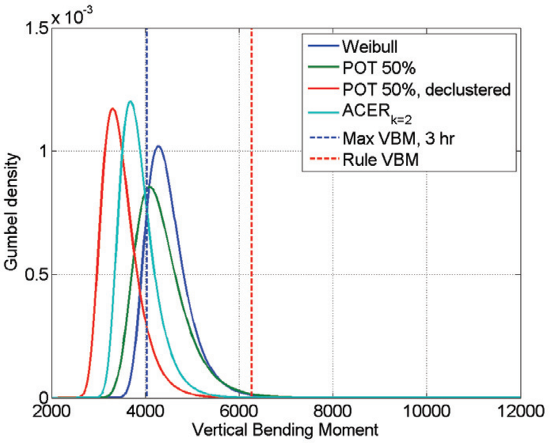

Figure 9.70: *Gumbel fit from Weibull parameters, POT with threshold 50% of the mean of the three measured largest values, compared with ACER for k = 2 for the rigid-body response only. 9,400 TEU ship, 02 October 2011.*

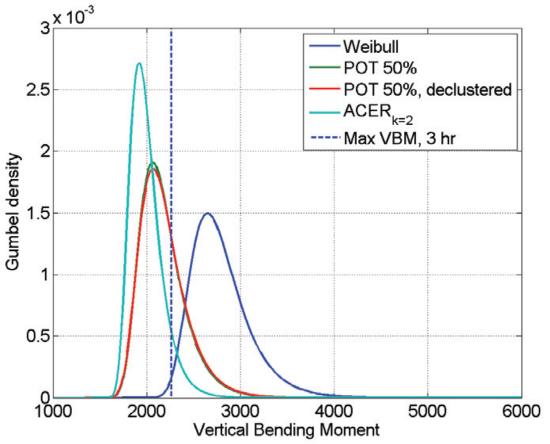

Figure 9.71: *Gumbel fit from Weibull parameters, POT with threshold 50% of the mean of the three measured largest values, compared with ACER for k = 2 for 9,400 TEU ship, 12 August 2011.*

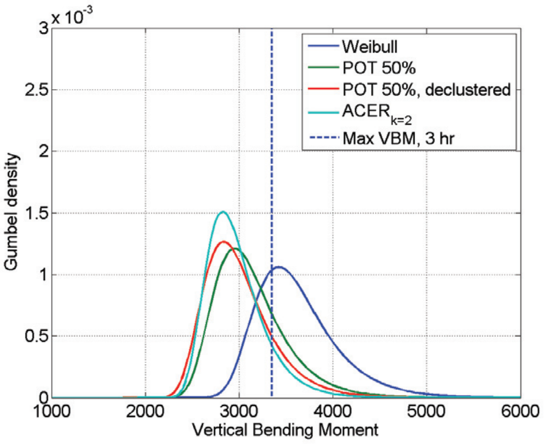

Figure 9.72: *Gumbel fit from Weibull parameters, POT with threshold 50% of the mean of the three measured largest values, compared with ACER for k = 2 for 9,400 TEU ship, 17 December 2011.*

For the 9,400 TEU ship on 02 October 2011, Figure 9.70 is furthermore included illustrating the difference in the outcome of the extreme value prediction if only the rigid-body response is considered. Clearly, the influence of the hull girder flexibility on the extreme value predition is significant. The most probable largest value for the POT prediction is 6,160 MNm when the hull girder flexibility is included (Figure 9.69) and 4,092 MNm when only the rigid-body response is considered (Figure 9.70).

In most of the cases it is seen that the Gumbel distribution derived from the Weibull parameters (dark blue line) yields the most conservative estimate. The reason for this can be observed from the Weibull probability plots for the flexible response (Figures 9.3, E.15, E.27, E.33, E.39, E.45, E.51, E.57 and E.63). For the 9,400 TEU, the 14,000 TEU and in two cases for the 4,400 TEU ship the largest peaks fall slightly above the line for Weibull fit, which gives a conservative estimate. For the 8,600 TEU ship the opposite is the case. The ACER program was used by Gaidai et al., 2010 to analyse the extreme value statistics of the whipping response of a 2,800 TEU container ship and compared to the Weibull fit. For a 20 year return period the Weibull result also yielded more conservative return values than ACER. Generally, it is concluded that the Weibull distribution does not fit the tail of the extreme value distribution very well and that it is not useful in extreme value prediction of hull girder loads in ships.

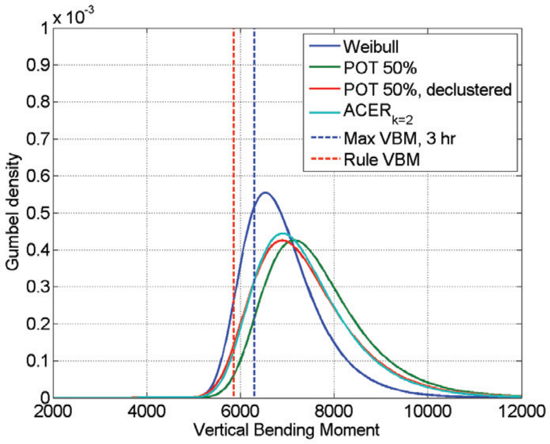

Figure 9.73: *Gumbel fit from Weibull parameters, POT with threshold 50% of the mean of the three measured largest values, compared with ACER for k = 2 for 8,600 TEU ship, 17 November 2010.*

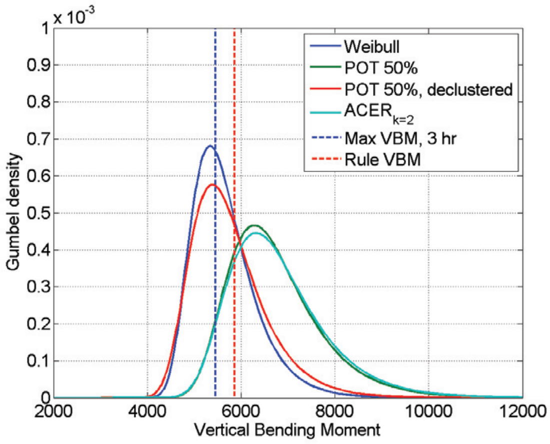

Figure 9.74: *Gumbel fit from Weibull parameters, POT with threshold 50% of the mean of the three measured largest values, compared with ACER for k = 2 for 8,600 TEU ship, 30 December 2011.*

The POT method without any removal of peaks yields the most probable largest values closest to the measured maximum values in most cases. In some cases, when the clustering effect plays a role, the de-clustering applied before the POT analysis is seen the decrease the most probable largest value and in other cases there is no effect of the de-clustering on the result, indicating that the clustering effect is not important.

ACER is generally expected to yield lower estimates than POT for the same threshold level because the ACER methods removes some peaks due to clustering and also some peaks that fall outside a 95% confidence interval. In the ACER program the upcrossing rate function $\epsilon_k(x)$ is used together with an optimisation routine and it is not immediately possible to distinguish the effect of removing some peaks due to clustering and peaks that are outside the considered confidence interval. When comparing the outcome of POT and ACER for the same removal of peaks, the results are seen to be quite different indicating that the optimisation routine in ACER, which removes some peaks which are considered outliers can also be of significant importance for the outcome. It was shown in Chapter 8 that the largest peaks for the 9,400 TEU ship were not outliers understood as a faulty signal. Hence, by removing the largest peaks, valuable information is lost when estimating

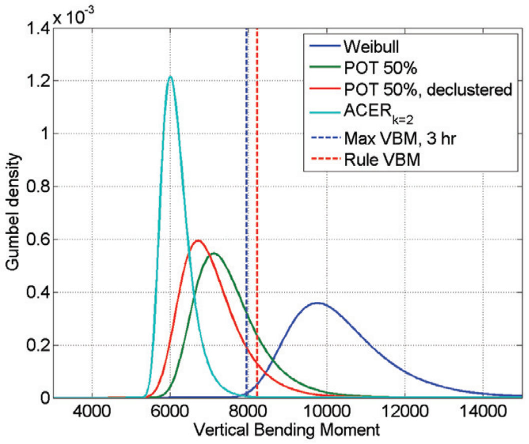

Figure 9.75: *Gumbel fit from Weibull parameters, POT with threshold 50% of the mean of the three measured largest values, compared with ACER for k = 2 for 14,000 TEU ship, 29 September 2011.*

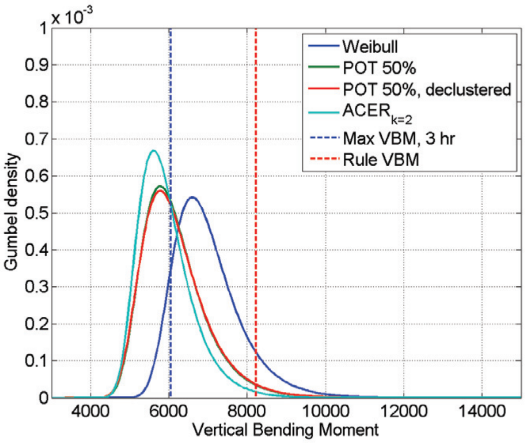

Figure 9.76: *Gumbel fit from Weibull parameters, POT with threshold 50% of the mean of the three measured largest values, compared with ACER for k = 2 for 14,000 TEU ship, 21 July 2011.*

the extreme peak distribution, which is considered a draw-back of the ACER method as applied here. In cases where the data can be considered reliable it would be desirable to use the ACER method with only the removal of preceding peaks and no additional removal of peaks during the optimisation procedure. For $k > 1$ ACER in most cases automatically determines the tail marker as the value corresponding to the highest value s of the ACER function for the plots in e.g Figure 9.19. The optimisation algorithm estimates the pair of parameters (q, s) in order to linearise the tail. As explained in Naess and Gaidai, 2009 in some cases during the optimisation for $k > 1$ the optimal value of s ends up being a very large negative value, which is also observed here in several cases for $k = 2$. It is stated by Gaidai et al., 2010 that the tail marker should be as low as possible, so in cases where the optimisation procedure determines a negative s for $k > 1$ a smaller tail marker is chosen manually as a sufficiently low value that yields a positive s.

The tail of the flexible hogging VBM shown in the probability of exceedance plots exhibit very different behaviours for the four different ships. If considering only the flexible hogging response the tail in several cases shows a tendency towards a saturation (maximum) level or an upper bound and can almost be approximated by a vertical line. This is e.g. the case for the 8,600 TEU ship (Figure 9.33 and 9.38). For the 9,400 TEU ship the same tendency is seen (Figure 9.2, 9.23 and 9.28), but here, in the tail, some larger values are also present and the tail behaviour is not continuous. The discontinuities may be due to "one-of" events such as green water on the deck.

The plots of the mean excess over the thresholds (Figures 9.13, 9.25, 9.35 and 9.40) can give some guidance on the choice of proper thresholds, and the plots of the mean excess also illustrate the large differences in the tail behaviour for the different cases. Linear, but not horizontal, variation of the mean excess with threshold u indicate that the limiting generalised asymptotic extreme value distribution might not be of the Gumbel type. This implies that care must be taken when extrapolating the results to a very low level

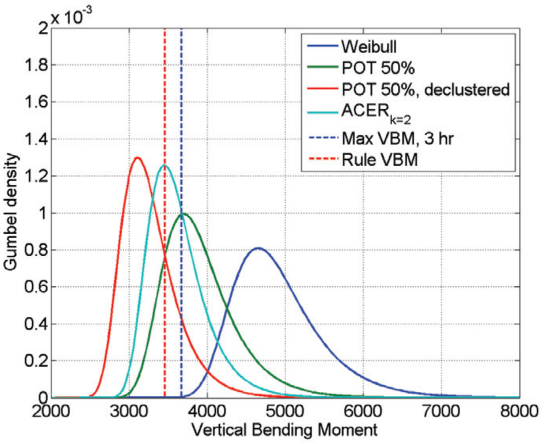

Figure 9.77: *Gumbel fit from Weibull parameters, POT with threshold 50% of the mean of the three measured largest values, compared with ACER for $k = 2$ for 4,400 TEU ship, 02 November 2007 at 11-13 hours.*

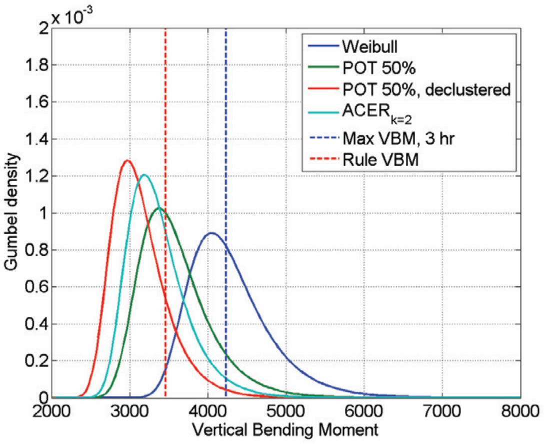

Figure 9.78: *Gumbel fit from Weibull parameters, POT with threshold 50% of the mean of the three measured largest values, compared with ACER for $k = 2$ for 4,400 TEU ship, 02 November 2007 at 16-18 hours.*

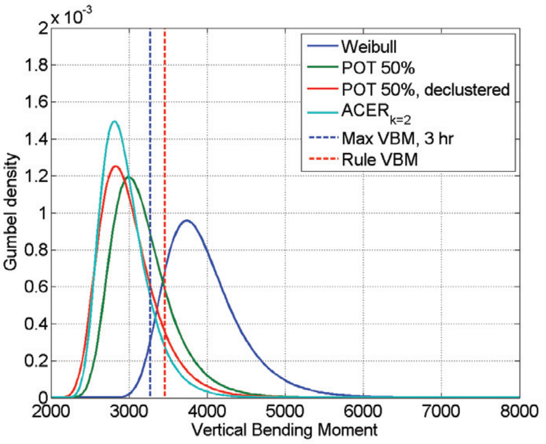

Figure 9.79: *Gumbel fit from Weibull parameters, POT with threshold 50% of the mean of the three measured largest values, compared with ACER for $k = 2$ for 4,400 TEU ship, 01 July 2008.*

of probability. In any case, the bending moment is upward bounded by nature and thus extrapolation to very large values is not meaningful.

Other distributions than the exponential distribution could be fitted to the excess, e.g. the Generalised Pareto Distribution (GPD) given by

$$F(x) = \begin{cases} 1-(1-mx/\sigma)^{1/m} & \text{if} \quad m \neq 0 \\ 1-\exp(-x/\sigma) & \text{if} \quad m = 0 \end{cases} \tag{9.22}$$

with the corresponding Generalised Extreme Value (GEV) distribution:

$$F(x) = \begin{cases} \exp(-(1 - m(x-\mu)/\sigma)^{1/m} & \text{if} \quad m \neq 0 \\ \exp(-\exp(-(x-\mu)/\sigma)) & \text{if} \quad m = 0 \end{cases} \tag{9.23}$$

The Generalised Pareto distribution could be applied for higher threshold levels leading to a asymptotic extreme value distribution different from the Gumbel distribution. For the GPD if $m > -1$ the mean excess over the threshold level u should be a linear function of u. However, from the mean excess plots it can be seen that is it difficult the determine one linear function of u for a range of thresholds, and in most cases the mean excess has different slopes for different threshold ranges. Hence, the present study only consider the case with the Gumbel distribution as the GEV distribution ($m = 0$). Fitting the tail with other extreme value distributions could be subject of future studies.

A general problem with the peak-over-threshold method is the proper choice of threshold level. The choice of threshold level is important and a trade-off between only considering the actual tail of the distribution by setting a high threshold and at the same time the desire to have as many data points available for the analysis as possible. For use in on-board decision support systems a robust method to select thresholds automatically must be developed as the results are found in some cases to be sensitive to the choice of threshold level as illustrated in the mean excess plots. The mean excess could be used in the selection of proper threshold levels and could be the subject of future studies.

Finally, it should be noted that the estimated probabilities are based on data from the ships sailing in different operational conditions and the outcome of the analysis would be different for other operational parameters (speed, relative heading and encounter wave period). The dependency cannot be assessed here, but the model tests of the 9,400 TEU ship analysed in Chapter 11 give some indications.

Chapter 10

Estimation of the Hull Girder Hydro-Elastic Behaviour

This chapter is published by Andersen and Jensen, 2014.

10.1 Introduction

In the following, two simple procedures are described for estimation of the non-linear hydro-elastic behaviour of the wave-induced vertical bending moment. The aim is to investigate whether the measured hydro-elastic response can be estimated by rather simple means for use at the design stage of container ships or in on-board decision support systems. The procedures are based on the work in Jensen et al., 2009 and Pedersen and Jensen, 2009. The focus here is on the hogging bending moment, but the sagging bending moment can be treated likewise. The data from the 9,400 TEU ship on 02 October 2011 is used.

The first procedure to be outlined makes use of the measured rigid-body responses in terms of the standard deviations of the vertical bending moment amidships and the relative motion in the bow together with the skewness of the measured bending moment. The second method estimates these parameters from closed-form expressions, Jensen et al., 2004, for the relevant rigid-body response amplitude operators together with input of the sea state. The resulting individual peak value distributions for the bending moment will be compared to the full scale measurements in order to judge the accuracy of these two, very simple, procedures.

10.2 Hermite Transform based on Skewness and Standard Deviation

First, the effect of non-linearities on the wave-frequency (rigid-body) response is considered. The low-pass filtered signal of the wave bending moment is used when calculating the associated statistical properties, namely the standard deviation (s_M), skewness (κ_3) and kurtosis (κ_4). The results are shown in Table 10.1 as measured during the period of three hours. As seen, the hourly variation over the three hours is rather small indicating fairly stationary conditions. Furthermore, the skewness is small and the kurtosis close to 3, signifying a nearly normal distributed wave bending moment with equal sagging and hogging bending moments as also observed when comparing the rigid-body response distributions in Figures 9.1 and 9.2. However, the negative skewness in this case means that large hogging bending moments occur with slightly smaller probabilities than sagging bending moments of similar magnitude and thus this effect can be important to include in order to avoid conservative hogging results. The effect is, however, very small for the present measurements, but could be larger in other cases as observed in Chapter 9 where larger deviation between the rigid-body sagging and hogging VBM was found for some of the other ships.

Time	s_M	κ_3	κ_4
16 hours	899	-0.0125	3.088
17 hours	1,051	-0.0240	3.0237
18 hours	993	-0.0117	3.1772
Total 3 hours	993	-0.017	3.14

Table 10.1: *Standard deviation, s_M; skewness, κ_3 and kurtosis, κ_4 of one-hour time series and for the 3 hours as one time series for the rigid-body part for the 9,400 TEU ship on 02 October 2011.*

The measured skewness and standard deviation of the rigid-body response can be used to derive a probability distribution for the peaks of the rigid-body hogging bending moment by using second order Hermite series, cf. Pedersen and Jensen, 2009. The probability P that the individual peak M exceeds a level m is then given by:

$$P(M > m) = \exp(-\frac{1}{2}y^2(m)) \tag{10.1}$$

where, for hogging, the transformation $y = y(m)$ from m to a standard normal distributed variable y is given by

$$y = \frac{-1 + [1 + 3\chi(\chi + \bar{m}]^{1/3}}{\chi} \tag{10.2}$$

with

$$\chi = \frac{\kappa_3}{6}, \quad \bar{m} = \frac{m}{s_M} \tag{10.3}$$

This transformation ensures that the standard deviation and skewness of the response M are kept through the transformation.

10.3 Whipping Response Estimation

The probability that the combined rigid-body and slamming-induced hydro-elastic response exceeds m can be estimated as:

$$P(M_{w+whipping} > m) = (1-\eta)P(M_w > m) + \eta P(M_{wh,2} > m) \tag{10.4}$$

Here M_w and $M_{wh,2}$ denote the wave-induced rigid-body bending moment and the vertical bending moment including the 2-node hydro-elastic response, respectively.

The procedure, described in Jensen et al., 2009, will be applied in the following. In this procedure the whipping bending moment depends linearly on the relative vertical velocity and thus becomes normal distributed with a standard deviation given by the following expression:

$$s_{whipping} = \frac{\pi^2}{24}\beta L^2 B_l^2 \rho s_{\dot{z}}(x_0)\nu_2(x_0)\omega_2 \frac{S_2(x)}{LM_2} \tag{10.5}$$

where, in accordance with the values used in Section 8.2.2:

- The longitudinal extent β of the slamming pressure as a fraction of the ship length is taken as 0.05.
- The local water line breadth B_l is taken as 28 m.
- The location of the slamming force x_0 is taken as the location x_{acc} of the accelerometer at FP.
- The relative frequency of slamming η is taken to 0.1, implying on average one slamming load for every ten wave cycles, i.e. every two minutes. This value is chosen by analysing the actual time series for the wave bending moment.
- L is here taken as the length overall L_{oa}.
- The standard deviation $s_{\dot{z}}$ of the relative vertical velocity is taken at the location x_{acc} of the accelerometer at FP and takes the value of 1.95 m/s for the present measurements.

The normalised whipping bending moment variation for the ship $\frac{S_2(x)}{LM_2}$ is calculated, assuming inertia loads only, as described by Jensen et al., 2009:

$$S_2(x) = \int_x^L m(u)\nu_2(u)(u-x)\mathrm{d}u \tag{10.6}$$

and $\frac{S_2(x)}{LM_2}$ takes the value of 0.185 at the longitudinal location $x = x_{sg}$ of the strain gauge close to amidships using the mass distribution shown in Figure 10.1. The variation of the whipping bending moment $S_2(x)$ along the ship length is shown in Figure 10.2.

Compared to the analysis in Jensen et al., 2009, the phase lag term in the standard deviation, Eq. (10.5), is omitted as the phase lag is difficult to estimate. Instead, it is assumed that the rigid-body and the slamming-induced hydro-elastic response are statistically independent so that the standard deviation of $M_{wh,2}$ can be calculated as

$$s_{wh,2} = \sqrt{s_M^2 + s_{whipping}^2} \tag{10.7}$$

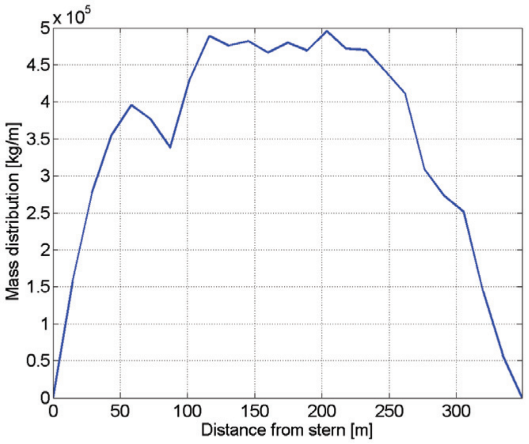

Figure 10.1: *Mass distribution of the considered container ship for determination of* M_2 *and* S_2.

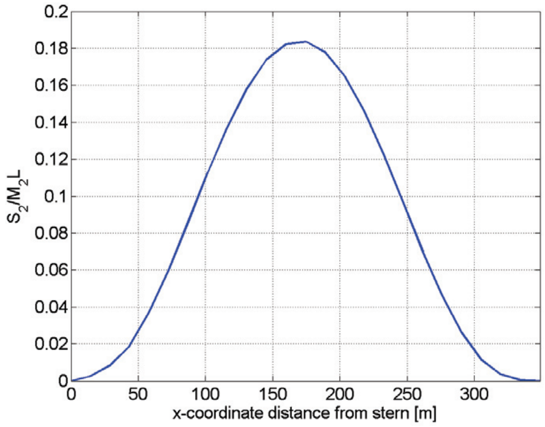

Figure 10.2: *Normalised bending moment variation* S_2/M_2L *for the considered container ship in 2-node vertical vibration mode.*

Furthermore, in Eq. (10.4), only the 2-node term is included as higher-order vibration modes have previously been found negligible.

The outcome using Eqs. (10.1) and (10.4) is plotted in Figure 10.3. A number of observations can be derived from this figure. For the rigid-body response a good agreement is found between the calculated response using Eq. (10.1) and the measurements. This is to be expected as measured values of the standard deviation and skewness are used in the calculation. It is also seen that the simple and fully analytical results from Jensen et al., 2004 using solely the main dimensions of the vessel together with a Pierson-Moskowitch wave spectrum with a significant wave height of 8 m and a zero-upcrossing period of 10 s give surprisingly accurate results.

When the hull girder flexibility is included, fairly good agreement is found between the measured results and both the predictions based on measured standard deviations and standard deviations obtained from the closed-form expression given in Jensen et al., 2004 together with the relevant sea state information. This implies that reliable results for the hydro-elastic effects can be obtained by just measuring the rigid-body responses or even by using purely analytical results. The main drawback with the analytical results is that they require a good estimate of the sea state which is not needed if measured standard deviations of the relative vertical velocity is available.

Finally, in Figure 10.3, the measured results are compared with the First Order Reliability Results presented in Chapter 7, Table 7.2. These purely numerical results are obtained using the non-linear strip-theory code SHIPSTAR (Xia et al., 1998) in connection with the conditional wave scenario leading to exceedance of a prescribed response level, here 5,000 MNm, and the associated probability. The sea state on 02 October 2011 was slightly higher than what was used in Chapter 7. However, the FORM procedure allows for exact scaling with respect to the significant wave height and the FORM results shown in Figure 10.3 are thus valid for a significant wave height of 8 m, which was the approximate wave

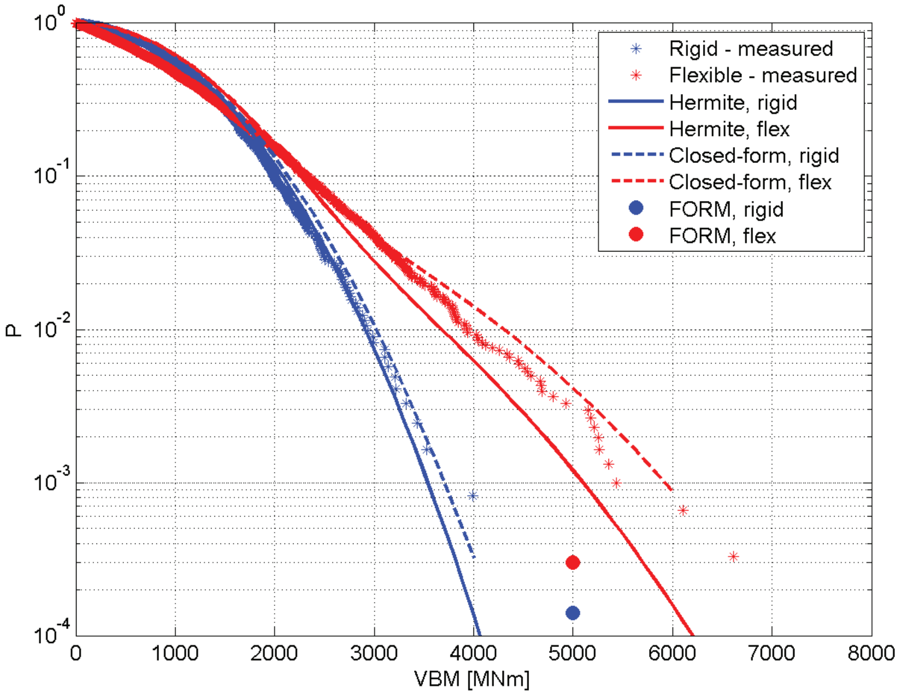

Figure 10.3: *Probability of exceedance for the individual peak values of the wave-induced hogging bending moment amidships using measurements, Hermite transformation with measured skewness and standard deviation and closed-form expressions for three hours for the 9,400 TEU ship on 02 October 2011.*

height encountered on 02 October 2011.

It is clearly seen that whereas the FORM analysis reasonably well fits with an extrapolation of the measured rigid-body behaviour this is not so for the flexible model as it significantly underestimates the whipping-induced vertical bending moment. Whether this is due to the non-linear strip theory formulation or the optimisation routine searching for the most probable wave scenario used in the non-linear strip-theory calculation is not clear, but, as also discussed in Chapter 7, use of CFD instead of the non-linear strip-theory does not resolve this problem, cf. Seng and Jensen, 2013.

10.4 Conclusions

A simple, but seemingly quite accurate estimate of the hydro-elastic contribution to the vertical bending moment amidships can be derived derived based either on measured rigid-body ship motion responses or the measured sea state in combination with analytical expressions for the response amplitude operator of the ship motions derived from closed-form expressions. The possibility to use such procedures in decision support systems to give the captain guidance for avoiding excessive hull girder vibrations could be further investigated.

Chapter 11

Model Tests with 9,400 TEU Container Ship

11.1 Introduction

In order to verify the whipping influence on the vertical wave-induced bending moment amidships, model tests were carried out in long-crested, irregular seas with a flexible model of the 9,400 TEU container ship in the TULCS project work package 6. The objective of the model tests was to produce data suitable for the validation of linear seakeeping programs and a non-linear post-processor developed by other TULCS partners. See Section 2.3.7 for general information about the model and the test basin used. A limited number of runs were carried out focusing on whipping. The tests were done in irregular waves using a Jonswap spectrum and carried out in steep head and bow-quartering waves. Because of the wave steepness in the tank, the ship model also encountered breaking waves (Kapsenberg et al., 2010).

Due to the limited width of the towing tank, runs in bow-quartering waves could not be very long and were thus repeated to get a sufficient run length making the total number of waves encountered around 150 and the total run duration 15-20 minutes in full scale. See Figures F.1, F.4, F.7, F.10, F.13 and F.16 in Appendix F for the run length for the individual runs. The measurements are scaled to full scale by the test facility. The data has been filtered using the same procedures as described in Section 6.3 and the cut-off limits given in Table 6.4. The mean has initially been subtracted to remove the static sagging moment induced by the water elevation along the model at forward speed as it was also done in Chapter 7.

In this chapter, the focus is on the amplification effect of the whipping-induced high-frequency vibrations on the vertical bending moment amidships in both hogging and sagging and the effects of speed, heading, wave height and wave length. Furthermore, the effect of the hull girder flexibility on the rigid-body response in hogging and sagging is compared. The study carried out here is by no means exhaustive, but serve as comparison to the observations done in Chapter 9.

Two different significant wave heights of 6.5 and 9.5 m are considered in the following. For $H_s = 6.5$ m the tests were performed for one peak period and for $H_s = 9.5$ m the tests were done for two different peak periods. The test matrix from the TULCS model test campaign does not allow for comparison of the model sailing in the same wave height with different speeds nor the same speed in different wave heights. However, it is possible to compare runs in identical sea states for the heading angles 180 deg and 150 deg (head sea and bow-quartering sea, respectively) which will be done in the following. It is noted that, as found in Section 9.2 the minimum design vertical wave induced bending moment is 6,270 MNm in hogging and -7,480 MNm in sagging for the considered 9,400 TEU container ship.

Some of the results are discussed at the end of this chapter, but the main discussion of the results is given in Chapter 12 where results from model tests with other container ships are also discussed together with relevant full scale measurements.

11.2 Significant Wave Height of 6.5 m

For the smallest wave height the model tests were carried out for a forward speed of 22 knots. The tests were done for two different headings: 180 deg (head sea) and 150 deg (bow-quartering sea) in a sea state with the wave parameters given in Table 11.1. The high and low-pass filtered time series are found in Appendix F, Figure F.1 and F.4 together with the response power spectra of the considered time series in Figure F.2 and F.5.

H_s [m]	T_p [s]	γ
6.5	13.37	1

Table 11.1: *Sea state parameters. γ is the peak enhancement factor for the Jonswap spectrum.*

The maximum observed hogging and sagging bending moments amidships are listed in Table 11.2. The maximum total VBM in hogging and sagging is given. At the same point in time the WF and the HF contribution are determined, and the amplification factor (Amp.) is determined as the ratio between the total VBM and the WF contribution. The WF and HF values are not necessarily the maximum values found during the measurements but the values associated with the maximum total VBM in hogging and sagging.

It can be seen from Table 11.2 that the maximum hogging and sagging bending moment are not necessarily associated with the same whipping event. It can also be seen that the amplification of the total bending moment from the HF contribution is significant - particularly in sagging.

The probability of exceedance is illustrated for sagging and hogging for the rigid-body and flexible response for the two different headings in Figures 11.1-11.2 and Figures 11.3-11.4

	Time [s]	Total [MNm]	WF [MNm]	HF [MNm]	Amp.
Hogging, head sea	398	5,337	3,327	2,010	1.60
Sagging, head sea	42.7	-5,892	-2,500	-3,393	2.36
Hogging, bow-quartering	1,034	6,173	3,536	2,638	1.75
Sagging, bow-quartering	1,031	-6,427	-2,188	-4,239	2.94

Table 11.2: *Extreme values of the vertical bending moment and amplification due to HF vibrations. Time series correspond to Figure F.1 for the head sea case and Figure F.4 for the bow-quartering sea case.*

for head sea and bow-quartering sea respectively.

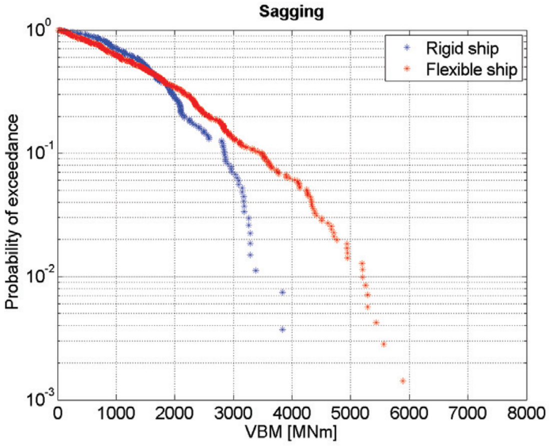

Figure 11.1: *Individual peak value probability of exceedance for sagging - rigid-body and flexible model response (absolute value).* $H_s = 6.5$ *m, heading 180 deg (head sea).*

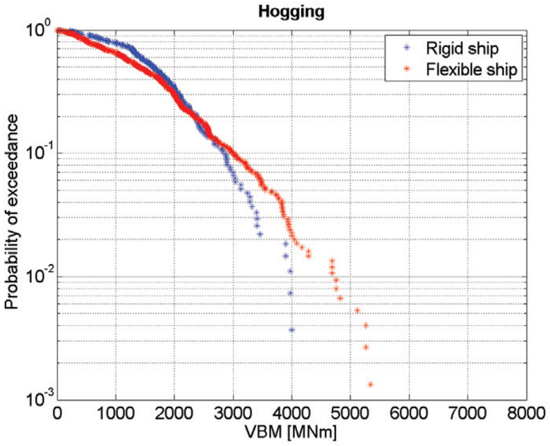

Figure 11.2: *Individual peak value probability of exceedance for hogging - rigid-body and flexible model response.* $H_s = 6.5$ *m, heading 180 deg (head sea).*

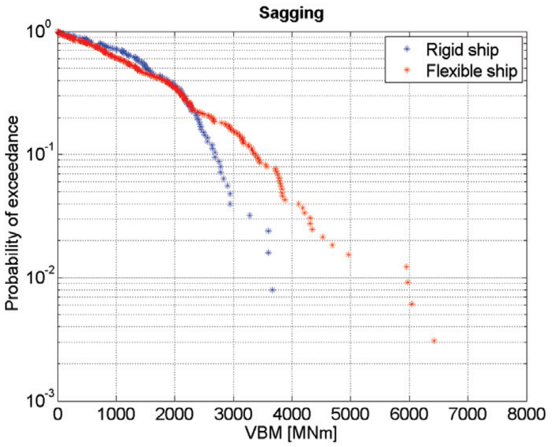

Figure 11.3: *Individual peak value probability of exceedance for sagging - rigid-body and flexible model response (absolute value). $H_s = 6.5$ m, heading 150 deg (bow-quartering sea).*

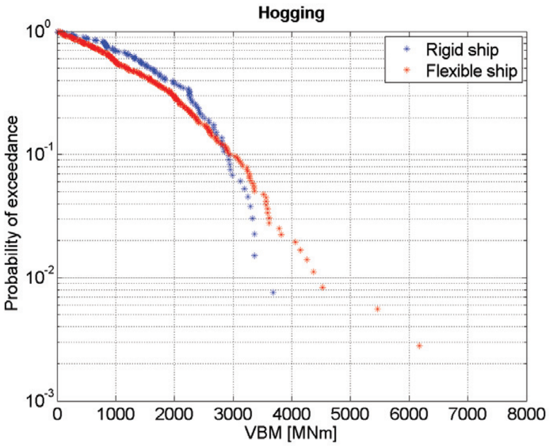

Figure 11.4: *Individual peak value probability of exceedance for hogging - rigid-body and flexible model response. $H_s = 6.5$ m, heading 150 deg (bow-quartering sea).*

11.3 Significant Wave Height of 9.5 m

Tests were also carried out for $H_s = 9.5$ m and ship speed of 15 knots for two different wave lengths. These tests are also done for the two different headings of 180 deg and 150 deg in a sea state with the parameters stated in Table 11.3 for two different peak periods.

	H_s [m]	T_p [s]	γ
Run 1	9.5	12.22	3.3
Run 2	9.5	9.93	5

Table 11.3: *Sea state parameters. γ is the peak enhancement factor for the Jonswap spectrum.*

11.3.1 *Long waves* ($T_p = 12.22$ *s*)

For a peak period of 12.22 s the maximum observed hogging and sagging bending moments amidships are given in Table 11.4.

It is seen from Table 11.4 that the rule bending moment is exceeded significantly in both hogging and sagging for both headings.

The probability of exceedance is illustrated for sagging and hogging for the rigid-body and flexible model response for the two headings in Figures 11.5-11.6 and 11.7-11.8 for head sea and bow-quartering sea respectively.

	Time [s]	Max total [MNm]	WF [MNm]	HF [MNm]	Amp.
Hogging, head sea	668	9,504	6,653	2,851	1.43
Sagging, head sea	9.2	-10,776	-5,888	-4.888	1.83
Hogging, bow-quartering	178	9,690	5,963	3.727	1.63
Sagging, bow-quartering	173	-13,221	-6,975	-6,246	1.90

Table 11.4: *Extreme values of the vertical bending moment and amplification due to HF vibrations. Head sea. Time series correspond to Figure F.7 for the head sea case and Figure F.10 for the bow-quartering sea case.*

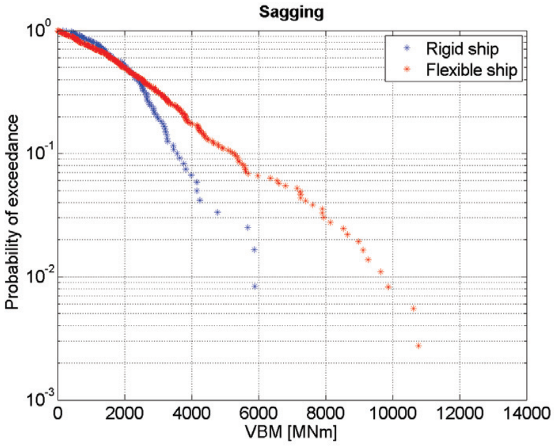

Figure 11.5: *Individual peak value probability of exceedance for sagging - rigid-body and flexible model response (absolute value). $H_s = 6.5$ m, $T_p = 12.22$ s, heading 180 deg (head sea).*

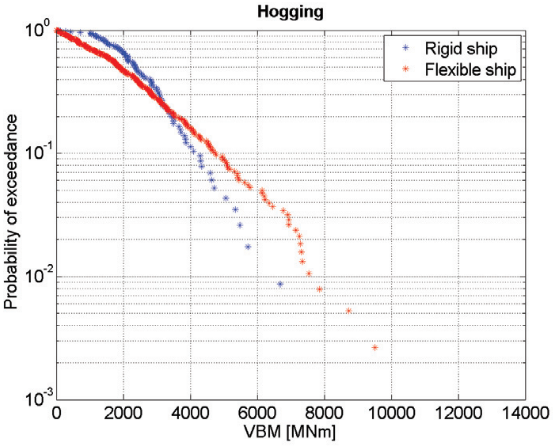

Figure 11.6: *Individual peak value probability of exceedance for hogging - rigid-body and flexible model response. $H_s = 6.5$ m, $T_p = 12.22$ s, heading 180 deg (head sea).*

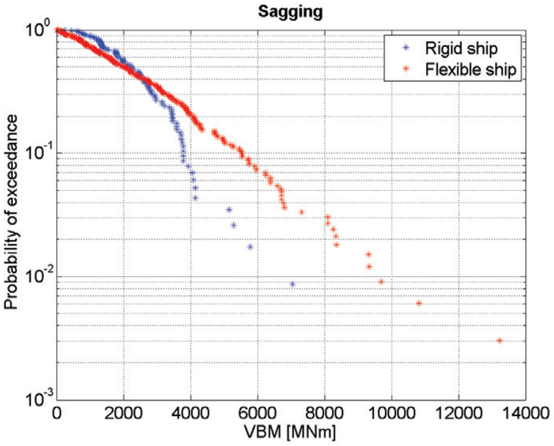

Figure 11.7: *Individual peak value probability of exceedance for sagging - rigid-body and flexible model response (absolute value).* $H_s = 6.5$ *m,* $T_p = 12.22$ *s, heading 150 deg (bow-quartering sea).*

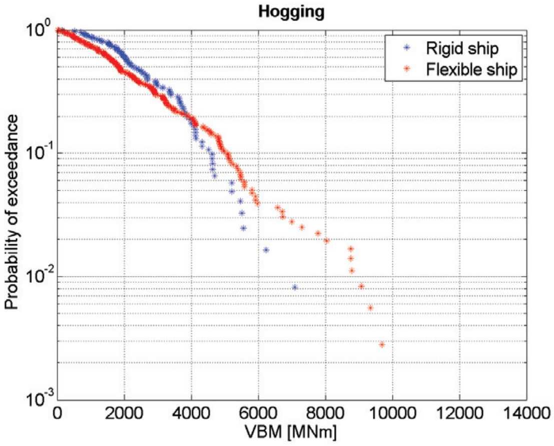

Figure 11.8: *Individual peak value probability of exceedance for hogging - rigid-body and flexible model response.* $H_s = 6.5$ *m,* $T_p = 12.22$ *s, heading 150 deg (bow-quartering sea).*

11.3.2 Short waves ($T_p = 9.93$ s)

For a peak period of 9.93 s the maximum observed hogging and sagging bending moments amidships are given in Table 11.5.

	Time [s]	Total [MNm]	WF [MNm]	HF [MNm]	Amp.
Hogging, head sea	792	6,244	3,915	2,328	1.59
Sagging, head sea	789	-7,087	-3,714	-3,373	1.91
Hogging, bow-quartering	153	7,875	4,063	3,813	1.94
Sagging, bow-quartering	150	-7,895	-2,835	-5,061	2.80

Table 11.5: *Extreme values of the vertical bending moment and amplification due to HF vibrations. Head sea. Time series correspond to Figure F.13 for the head sea case and Figure F.16 for the bow-quartering sea case.*

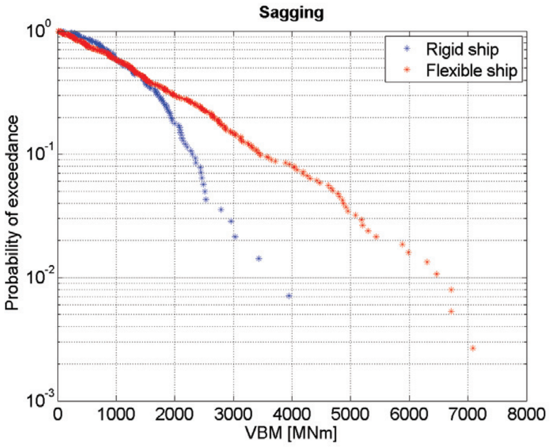

Figure 11.9: *Individual peak value probability of exceedance for sagging - rigid-body and flexible model response (absolute value). $H_s = 6.5$ m, $T_p = 9.93$ s, heading 180 deg (head sea).*

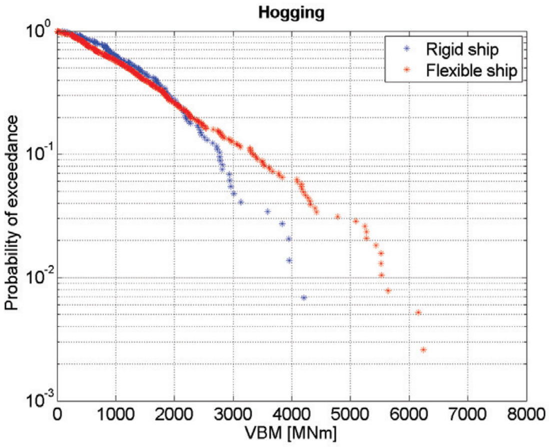

Figure 11.10: *Individual peak value probability of exceedance for hogging - rigid-body and flexible model response. $H_s = 6.5$ m, $T_p = 9.93$ s, heading 180 deg (head sea).*

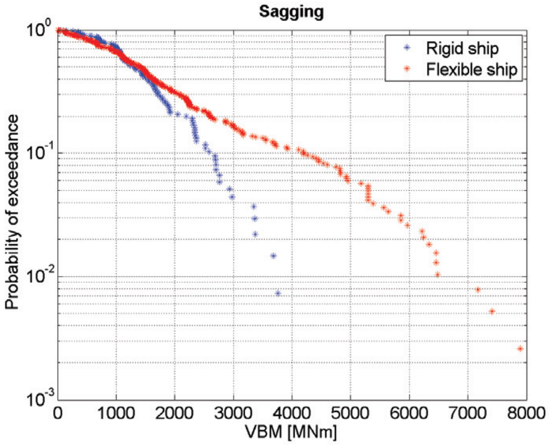

Figure 11.11: *Individual peak value probability of exceedance for sagging - rigid-body and flexible model response (absolute value).* $H_s = 6.5$ *m,* $T_p = 9.93$ *s, heading 150 deg (bow-quartering sea).*

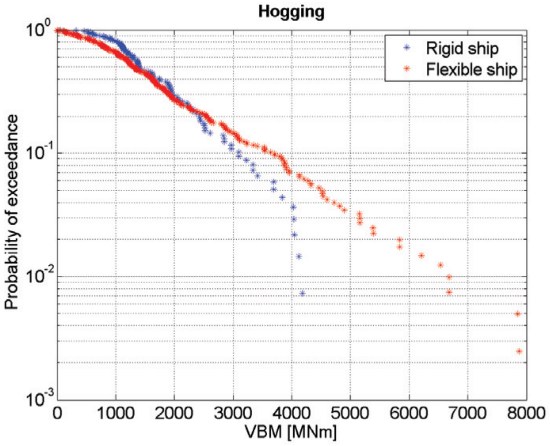

Figure 11.12: *Individual peak value probability of exceedance for hogging - rigid-body and flexible model response.* $H_s = 6.5$ *m,* $T_p = 9.93$ *s, heading 150 deg (bow-quartering sea).*

11.4 Discussion and Conclusions

In the following, the results from the model tests with the 9,400 TEU ship will be discussed. The comparison of the results to other references dealing with model tests with flexible models of large container ships is left to Chapter 12.

The test runs are relatively short and do not necessarily contain the extreme events. On the other hand, very large bending moments exceeding the rule wave VBM significantly are found during the tests considered here. Generally, model test runs should be longer than what is the case for the TULCS model tests and in the order of 30-45 minutes in full scale to yield reliable results for statistics. The natural 2-node vertical bending frequency seen in the plots of the power frequency spectra in Appendix F, Figures F.2, F.5, F.8, F.11, F.14 and F.17 seems to match the full scale natural frequency of about 0.47 Hz well.

There are no tests comparing different forward speeds in the same sea state so it is difficult to conclude on the influence of speed, but higher speeds are expected to increase the VBM due to increased whipping. For the significant wave height of 9.5 m where test with two different peak periods were carried out, the largest responses are found for the largest peak wave period of 12.22 s corresponding to an effective wave length of about 53% of the ship's total length.

Despite the total sagging moment being larger than the total hogging bending moment in all cases, the WF (rigid-body) hogging bending moment is larger than the WF sagging bending moment in all cases except one. The probability of exceedance for the WF (rigid-body) response is illustrated in Appendix F, Figures F.3, F.6, F.9, F.12, F.15 and F.18. For $H_s = 6.5$ m the WF (rigid-body) hogging and sagging vertical bending moment have very similar probability of exceedance, cf. Figures F.3 and F.6. However, for the larger wave height of 9.5 m the WF hogging VBMs are generally larger at the same level of exceedance than the sagging VBMs.

Chapter 12

Extreme Hydro-Elastic Response of Container Ships

12.1 Introduction

The four container ships considered in the present thesis are quite different. The 9,400 TEU and the 14,000 TEU ships have larger block coefficients and smaller bow flare angles than the 8,600 TEU ship which is designed for a larger service speed. The small container ship of 4,400 TEU has a high block coefficient and is mainly included in the thesis to illustrate size effects in the hydro-elastic response. Based on model tests, full scale measurements and numerical simulations there is no doubt that the hull girder flexibility of large container ships can considerably increase the extreme structural response.

In the IACS rules for the wave-induced VBM (International Association of Classification Societies, 2010a) the amplitude of the minimum design wave VBM is considerably larger in sagging than in hogging. Generally, the design wave VBM in hogging is only 83-85% of the value in sagging implying that the non-linear effects in the response increase the sagging bending moment more than the hogging bending moment. However, this considerable difference between the class rules for the design wave-induced hogging and sagging VBM is not found in the full scale measurements considered in the present work and one concern is whether the wave-induced hogging VBM is underestimated in the current design rules.

This chapter joins the ends of the chapters concerning the extreme hydro-elastic hull girder response of container ships (7, 8, 9, 10 and 11) and includes some relevant references. A short discussion relating some of the findings from those chapters to the MOL COMFORT incident in 2013 (Committee on Large Container Ship Safety, 2013) is included at the end of the chapter.

12.2 Response of Large Container Ships

In the linear case the wave-induced hogging and sagging VBMs are symmetric. However, in reality ocean waves and ship responses are non-linear. The importance of the non-linearity of the ship response is generally larger than the importance of the non-linearity of the ocean waves; except perhaps in rare wave scenarios, e.g. "freak" waves, see Faulkner, 2003. As reflected in the design rules, the non-linear effects in the response are expected to increase the wave-induced sagging bending moment more than the hogging bending moment.

From the considered full scale measurements in Chapter 9, the total hogging VBM is larger than the total sagging VBM in six of ten cases which is somewhat surprising. The time series have been selected from the criteria of containing large stress amplitudes in general and not large hogging responses in particular.

For the 9,400 TEU ship the maximum total hogging VBM is largest for two of the three cases considered (02 October and 17 December; the days where the largest stresses were measured). The maximum rigid-body bending moment is largest in sagging in the first case (02 October), similar for hogging and sagging in the second case (12 Aug) and largest for hogging in the last case (17 December). For the 8,600 TEU ship the total maximum sagging VBM is considerably larger than the corresponding maximum hogging VBM in one case (17 November) and for the other case (30 December) hogging is slightly larger than sagging. The maximum rigid-body VBM is largest in sagging for the first case and in hogging for the second case. For the 14,000 TEU ship the maximum hogging VBM is considerably larger the the maximum sagging VBM in both cases and for both the flexible and the rigid-body response. For the 4,400 TEU ship the maximum sagging VBM is larger than the hogging VBM in two of the three cases. Additionally, six different time series of full scale measurements from the same 4,400 TEU ship were analysed in Mathisen et al., 2009 and in two of these the total sagging VBM was found to be clearly larger than the total hogging VBM, in one case the maximum hogging was largest and in the rest of the cases the maximum response amplitudes were very similar in hogging and sagging. It is difficult to conclude whether the maximum VBM is more likely to be a hogging bending moment than a sagging bending moment and no clear trend is found from the full scale measurements considered here.

In the model tests with a model of the 9,400 TEU ship described in Chapter 11, the maximum total amplitude of the sagging bending moment is larger than the maximum hogging bending moment in all cases. In the model tests for the 9,400 TEU ship the largest VBM are found in bow-quartering seas. Compared to model tests in head sea with the 8,600 TEU ship and a 13,000 TEU ship (Storhaug et al., 2010b and Storhaug et al., 2010a respectively) and for a 13,000 TEU ship in bow-quartering sea (Storhaug et al., 2011) the sagging response was not always found to be largest. For the 13,000 TEU ship model in head sea, the maximum sagging bending moment amidships is higher than the maximum hogging bending moment for the highest sea states ($H_s = 7.5 - 11.5$ m) and the largest VBM were also found in bow-quartering seas. For the 8,600 TEU ship model (only tested in head sea) the maximum sagging bending moment was generally higher than the hogging bending moment.

By far, the largest amplification of the total structural response due to hull girder vibrations are found from the full scale measurements with the 8,600 TEU ship where the amplitude of the HF vibrations in both cases exceed those of the WF response (Figures 8.13 and 8.14). Full scale measurements from the 4,400 TEU ship have also been analysed by Mathisen et al., 2009. Here, the measurements were also amplified by the hull girder vibrations, and the amplification was similar in hogging and sagging.

For the 9,400 TEU ship on 02 October the hogging is slightly more amplified by the HF vibrations than the sagging VBM (Figures 9.1 and 9.2). The amplification is largest for the two cases where the ship is sailing in oblique seas (02 October and 12 August) and smaller for the third case, where the ship encountered head sea (17 December), which could indicate that the amplification due to the hull girder flexibility is largest in oblique seas than in head sea. The findings from the full scale measurements with the 9,400 TEU ship can be compared to the findings in Chapter 7 where the influence of the hull girder flexibility was assessed using strip-theory and a conditional wave, the amplification effect was found to be more pronounced in the hogging than in the sagging condition.

The influence of the hull girder flexibility on the total response is more advantageously assessed by considering the probability of exceedance for longer time series of measurements or model tests. From the full scale measurements the flexibility of the hull increases the probability of exceedance of a prescribed bending moment for both sagging and hogging for all the considered ships in all cases, and generally, the amplification of the sagging and hogging bending moments due to the hull girder flexibility is similar from the full scale measurements.

From model tests with the 9,400 TEU ship the total sagging VBM, as mentioned, is larger than the total hogging VBM in all cases. However, in all cases except one the WF hogging VBM is larger than the WF sagging bending moment, meaning that sagging is more amplified by whipping than hogging. In all cases the amplification factor is highest in sagging with the largest amplification being 2.94. The largest amplification factor in hogging is 1.94. For the model tests with the 9,400 TEU ship the largest amplification factors are found in bow-quartering seas which was also the case in Storhaug et al., 2011.

From model tests with the 8,600 TEU and a 13,000 TEU ship considered by Storhaug et al., 2010b and Storhaug et al., 2010a there is no clear trend in the amplification factors, but the largest values are found in sagging for both ships. The maximum factors are larger for the 8,600 TEU ship model (2.67 in hogging and 2.89 in sagging) than for the 13,000 TEU ship model (1.68 in hogging and 2.10 in sagging). The larger values for the 8,600 TEU ship may be due to the larger bow flare angle of this ship. In Storhaug et al., 2011, tests were carried out in bow-quartering sea and the the amplification effect for hogging was also found to be larger than for sagging in several of the model tests performed with a model of a 13,000 TEU container ship. However, the opposite conclusion was drawn in Zhu and Moan, 2012 where the amplification effect was generally largest for sagging.

Takaoda et al., 2012 carried out model tests with flexible models of a 5,000 TEU and a 13,000 TEU ship in head sea in regular waves. They concluded that the amplification of the vertical bending moment due to whipping was larger for the 5,000 TEU ship than for the 13,000 TEU ship. The difference in amplification ratios was attributed to the geometrical difference of the ships, with the 5,000 TEU ship having larger bow flare angle than the 13,000 TEU ship. Also Storhaug, 2014 and Takaoda et al., 2012, suggest that the bow flare angle is more important for the extreme loads than vessel size and the concern regarding large hydro-elastic hull girder loads in container ships may not be related to the largest container vessels.

Zhu and Moan, 2012 conclude, based on analysis of model tests the 8,600 TEU ship and a 13,000 TEU ship in regular and irregular waves, that the contribution from high-frequency vibrations cause the vertical bending moment amidships to be slightly more affected in sagging than in hogging. However, in short waves the hogging peaks are increased more than the sagging peaks by the high-frequency vibrations. Generally, Zhu and Moan, 2012 emphasize that the hogging bending moment should be carefully assessed for ultra large container ships.

Considering the rigid-body response there is generally little difference between the rigid-body sagging and hogging bending moments in the full scale measurements. For the 9,400 TEU ship on 17 December (Figures 9.27 and 9.28) the rigid-body hogging VBM is slightly larger at small probabilities of exceedance than the sagging VBM. The same is the case for the 8,600 TEU ship on 30 December (Figures 9.37 and 9.38). For the 4,400 TEU ship considered by Mathisen et al., 2009 WF hogging and sagging ware found to be identical and they are also found to be almost identical in the time series considered in the present study.

The rigid-body response of the 14,000 TEU ship is larger in hogging than in sagging for both days considered (Figures 9.42, 9.43, 9.47 and 9.48). Particularly on 29 September the rigid-body hogging VBM is considerably larger at all probability levels than the corresponding sagging VBM. From full scale measurements the total hogging VBM has been observed to exceed the sagging VBM, but it is unexpected to find this to also generally be the case for the rigid-body response.

No other full scale measurements with large container ships are available for comparison, but the findings above regarding the rigid-body response can be compared to model tests. For the TULCS model tests analysed here for the 9,400 TEU ship the maximum rigid-body hogging VBM was larger than the corresponding sagging VBM in all cases. Considering the probability of exceedance plots in in Appendix F, Figures F.3, F.6, F.9, F.12, F.15 and F.18, the hogging and sagging is seen to be similar at the same probability of exceedance for the smallest wave height of 6.5 m, while, for the tests carried out in the larger waves with H_s of 9.5 m, the rigid-body hogging response is clearly larger than the sagging response at the same level of probability.

Zhu and Moan, 2012 studied model test results for the 8,600 TEU container ship in head sea with a ship speed of 15 knots and H_s of 9.5 m for T_z of 7.5, 9.5, 11.5 and 13.5 s. For the largest T_z the rigid-body hogging VBM was slightly larger than the sagging VBM, but for $T_z = 7.5$ s the WF hogging and sagging VBM were very similar. For the 13,000 TEU ship in the same study the WF hogging was also generally larger than WF sagging with the largest difference between hogging and sagging also being for the largest peak periods.

According to Zhu and Moan, 2012 the non-linear pressure under the bow of large container ships can be one of the contributing factors to the increase in the hogging VBM because the change in added mass at water exit can cause a negative suction pressure. Apart from this possible explanation it has not been possible to explain this phenomenon, although Zhu and Moan, 2012 mention several non-linear effects that can increase the rigid-body hogging VBM for ultra large container ship. When comparing model tests from the 8,600 TEU and a 13,000 TEU ship they found that the rigid-body hogging VBM was increased more for the largest of the ships and they conclude that when the ship speed is reduced the rigid-body sagging VBM is reduced more than the rigid-body hogging VBM. Zhu and Moan, 2012 also raise the question that for very large container ships the sagging/hogging asymmetry reflected by the design rule may be non-existent and that this should be investigated further for ultra large container ships.

In the present thesis, only the wave-induced loads are dealt with, but when considering the extreme structural response the still-water level is obviously also of importance. In addition to the dynamic wave-induced VBM and the static still-water VBM there may be some quasi-static effects present in the measurements such as temperature differences, transfer of ballast water or fuel between tanks, the effect of forward speed and water depth and non-linearities in the structural response to waves.

One issue of concern when analysing full scale measurements is the difficulty associated with determining the true zero value of the wave-induced VBM. In addition to the subtraction of the mean the low frequency variation with a period of more than 100 s (0.01 Hz) is removed by filtering (see Chapter 6) throughout this thesis. This filtering results in a very similar number of positive and negative peaks in the signal but does not necessarily give the "true" zero of the wave-induced bending moment. Examples of this very low-frequency variation in the stress signal from full scale measurements are given in Figure 12.1 and 12.2. Simply subtracting the mean of the signal may not be the correct procedure to account for the quasi-static shift of the signal.

The non-linear effects are generally thought to give a negative shift of the signal which it is not possible to determine from the full scale measurements. Part of the low-frequency contribution in the signal may also be due to higher order, non-linear difference frequency effects in the response, but generally, the non-linear effects on the mean value of the signal are considered to be small.

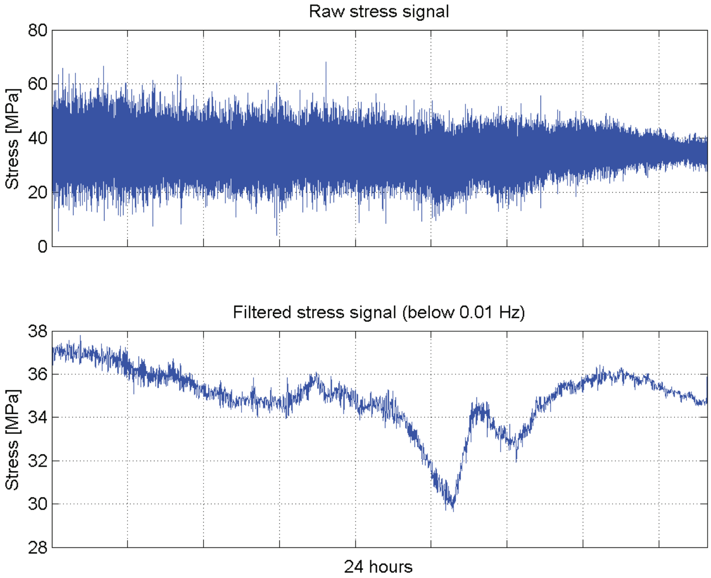

Figure 12.1: *Measured 24 hour raw stress signal and the underlying low-frequency process with frequency below 0.01 Hz for 9,400 TEU container ship on 12 August 2011*

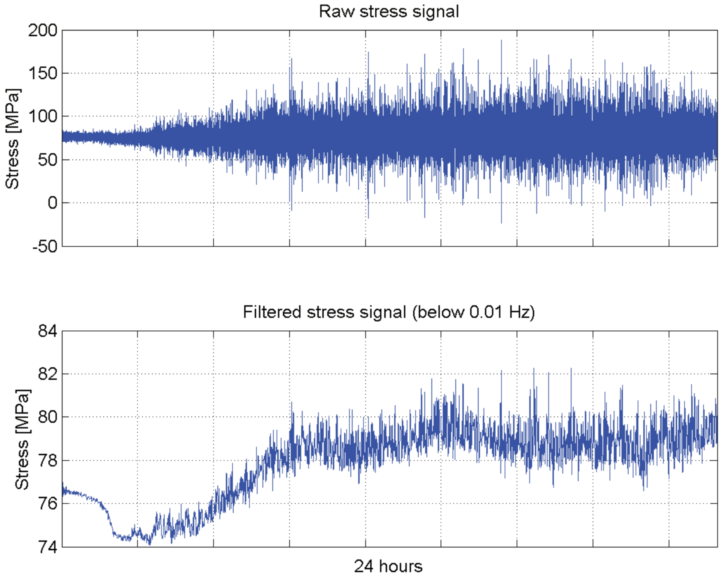

Figure 12.2: *Measured 24 hour raw stress signal and the underlying low-frequency process with frequency below 0.01 Hz for 9,400 TEU container ship on 02 October 2011*

The effect of routing and seamanship on the extreme loads are important factors but troublesome to assess. From the full scale measurements it is difficult to conclude on the effect of the operational parameters and the encountered sea state since detailed information on these parameters is not always available.

Ogawa and Takagi, 2012 used a finite element model and a non-linear seakeeping program to quantify the effect of operation (ship speed and heading) on the hydro-elastic response of two container ships and found that speed reduction significantly reduces whipping and that course change from head sea to bow-quartering sea (170 deg) also reduced whipping. The model tests (Chapter 11) contrarily indicate that the largest bending moments can be found in bow-quartering seas and that the largest bending moments do not necessarily occur in the largest waves. According to e.g. Storhaug et al., 2011, based on model tests with a model of a 13,000 TEU ship, changing the course from head sea to bow-quartering sea is not found to be an effective way to reduce the extreme loading, but could actually increase the extreme loads on large container ships.

In the real-life, captains may slow down the ship in adverse weather. However, in less severe conditions relatively large speed is maintained which can lead to relatively large responses. It has been concluded by e.g. Storhaug, 2014 that the largest responses are not found in the largest waves, but that moderate sea states of H_s 7-9 m yield the maximum responses.

12.3 Hull Girder Ultimate Strength

Although rare, severe incidents involving large container ships have happened and include the MSC NAPOLI incident from 2007 (Figure 12.3) and MOL COMFORT from 2013 (Figure 12.4). Both incidents are thought to be due to the wave-induced load exceeding the capability of the hull and not fatigue related. In both cases, the ship structure failed in a hogging condition due to collapse of the hull girder. Information of the two vessels can be found in Table 12.1.

	IMO number	L_{oa}	Beam	TEU	Age by incident
MSC NAPOLI	9000601	275.6 m	42.8 m	4,420	16 years
MOL COMFORT	9358761	316.0 m	45.6 m	8,110	5 years

Table 12.1: *Principal data for MSC NAPOLI and MOL COMFORT.*

In January, 2007 the 4,420 TEU container ship MSC NAPOLI experienced structural failure of the hull just forward of the engine room which resulted in a total loss. The investigation of the incident (Marine Accident Investigation Branch, 2009) identified the following factors contributing to the failure:

- The hull did not have sufficient buckling strength forward of the engine room
- The classification rules applicable at the time of the vessel's construction did not require buckling strength calculations to be undertaken beyond the vessel's amidships area
- There was no, or insufficient, safety margin between the hull's design loading and its ultimate strength

- The load on the hull was likely to have been increased by whipping effect
- The ship's speed was not reduced sufficiently in the heavy seas encountered

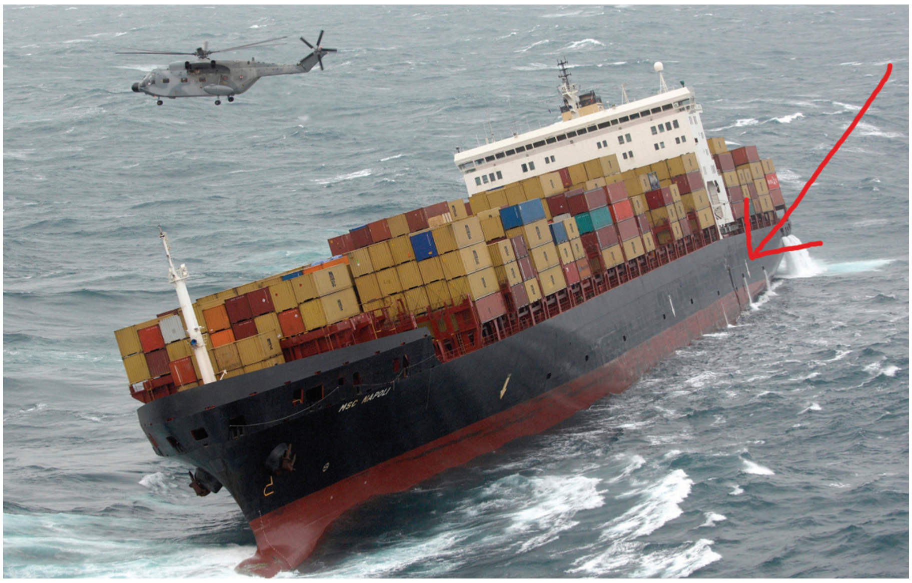

Figure 12.3: *4,420 TEU container ship MSC NAPOLI which broke on 18 January 2007 off the UK coast. Photo courtesy of the French Ministry of Defence.*

Another severe and more recent incident involved the 8,110 TEU container ship MOL COMFORT. The ship broke in two in relatively rough weather in the Indian Ocean on 17 June 2013 and both parts subsequently sank. According to the official investigation report from the Committee on Large Container Ship Safety, 2013 the ship broke in two in a hogging condition. The failure was initiated in the double bottom amidships, progressed upwards along the sides of the ship and ultimately resulted in the ship breaking in two (See Figure 12.4).

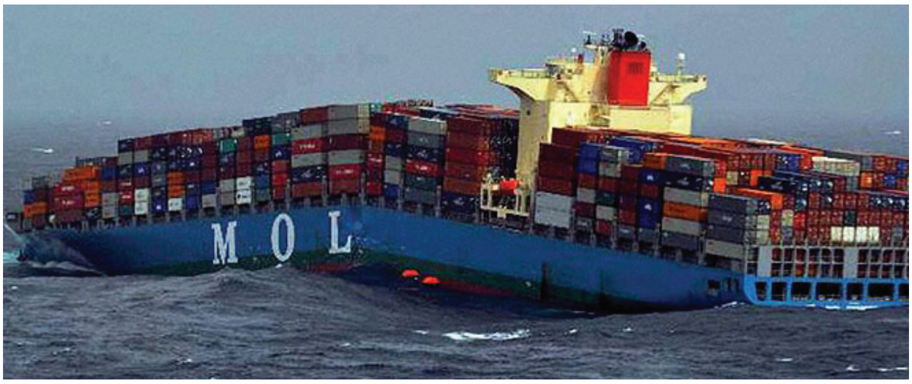

Figure 12.4: *8,540 TEU container ship MOL COMFORT before the vessel broke in two and sank on 17 June 2013. Photo courtsey of PTI Photo.*

The still-water bending moment at departure was positive, i.e. the ship was in a hogging condition. It is difficult to accurately assess the still-water bending moment for container ships due to the uncertainty associated with the weight declaration of the individual containers. The declared weights were used in the assessment by the Committee on Large Container Ship Safety, 2013 and the still-water VBM amidships was determined to 6,000 MNm, which is 103% of the design value. However, the deflection of the hull amidships based on the measured draught values was 0.63 m at the departure which corresponds to a VBM amidships of 126% of the still-water design value determined using a full-ship FEM model for the hull deflection.

The sea state at the time of the incident was reported with H_s of 5.5 m and a mean wave period of 10.3 s estimated from hindcast data. The mean wave direction was estimated to 66 deg from the port side (0 deg being head sea). The ship was sailing around 17 knots. Using this sea state and assuming long crested irregular seas, the maximum wave load acting on the ship was estimated by the Committee on Large Container Ship Safety, 2013 using a non-linear strip-theory program to 2,000 MNm plus a whipping contribution of 1,400 MNm to give a total wave VBM of 3,400 MNm. The design wave bending moment in hogging is (International Association of Classification Societies, 2010a) around 5,300 MNm.

The total load acting on the hull at the time of the incident was thus estimated to 9,400 MNm. Using an elasto-plastic finite element model (FEM) simulation for three holds the ultimate hull strength was determined to 14,000 MNm, so the calculated loads are considerably below the capacity of the hull. The conclusions of the interim report from the (Committee on Large Container Ship Safety, 2013) are:

- The real loads (wave and still-water) acting on the ship at the time of the incident were larger than what could be estimated.
- The hull strength was reduced due to possible presence of residual buckling deformations in the bottom shell plates or for some other reason.
- Both of the above elements combined.

As described in Chapter 3 there is a large uncertainty associated with the estimation of the sea state and thus there is also a large uncertainty associated with the estimated maximum wave load. From the findings in Chapter 8 it seems plausible that the total wave-induced load on MOL COMFORT could possibly have been higher than what is estimated by the Committee on Large Container Ship Safety, 2013. For both the 9,400 and 8,600 TEU ships, which are comparable in size to MOL COMFORT, VBMs exceeding 6,000 MNm are observed from full scale measurements and for both ships the HF vibrations are found capable of doubling the total response. The bow flare of MOL COMFORT is rather large as illustrated from a sister ship in Figure 12.5. The high strength steel used for the construction of the ship will result in a slightly lower natural frequency and possibly, together with the pronounced bow flare, making the vessel more susceptible to whipping vibrations. Furthermore, from the extreme value prediction in Chapter 9 the probability of exceedance of high response levels is relatively high due to the fatness of the tail of the Gumbel probability distribution, see e.g. Figure 9.73.

MOL CREATION

Figure 12.5: *Bow of the sister ship of MOL COMFORT; MOL CREATION. Photo by Yoshihiro Matsuo,* `http://shipbuild2.exblog.jp`.

As also concluded by the Committee on Large Container Ship Safety, 2013 the mechanism on dynamic collapse caused by whipping in ship hulls is not thoroughly studied. Xu et al., 2012 have studied the topic on a bulk carrier to quantify the post-ultimate strength of a bulk carrier under extreme wave loads using two rigid hull segments coupled with a elasto-plastic hinge amidships to evaluate the extent of the collapse. The risk of buckling and collapse may be increased greatly by the additional hull girder vibrations and as seen from the records of the largest responses investigated in this thesis a ship may experience several large loading peaks during a slamming event. See e.g. Figure 8.13 for the 8,600 TEU ship where six peaks with a magnitude of around 100 MPa are observed over a period of 20 seconds. The duration of each peak load is short and might not be able to trigger collapse, but if the hull girder is exposed to many successive loading peaks due to whipping it may become critical and the subject should be studied further.

Chapter 13

Data-Based Decision Support for Ship Operations

This chapter wraps up the thesis regarding decision support for operation of ships based on on-board measurements in general and broadens the scope to also include an outline of the use of data-based decision support in the shore-based part of the organisation.

13.1 Data

Any decision support system relies on input of good quality data in order to produce a useful output. This well known principle is commonly referred to as the ”garbage in - garbage out” principle. Sensors for logging data on board ships are becoming cheaper and more readily available and sensor technology is increasingly sophisticated offering a potential for automatic logging of data from ships. Recording data from ships can, however, still be cumbersome and an expensive task to carry out due to the ship being a complex structure composed by many sub-systems such as systems for propulsion, cargo handling, manoeuvring and navigation. Automation systems on ships are different and no standards or standard systems for collecting data on board ships exist. Furthermore, ships often move far from the shore in the ever changing and often harsh ocean environment. Consequently, despite modern sensor technology and means of data transfer, many shipowners still rely on noon-reports and manual reporting as their main source of data for decision support on board the ships and on land.

When automatically logging sensor data from ships large amounts of information can quickly be generated and thanks to better and cheaper satellite connectivity between ship and shore, large amounts of data can be transferred real-time. As greater volumes of data are generated, proper routines for the handling and analysis of the data become crucial. Faults, errors and inaccuracies are frequently found in both manually and automatically logged data from ships and must be handled properly before the data is used in any decision support system.

Still, on-board measurements and logging of data from ships involve costs and the data itself does not represent any value until it is utilised for decision support. During this process data and information can get lost at different links in the data handling chain, mainly:

- Data logging and recording: The data can be logged wrongly or the quality is too low due to e.g. low quality sensors, wrong installation of sensors, low sample rate, cross-talk between sensors. This can be caused by bad planning and lack of skill during the installation phase. If data is recorded manually, reading errors or reporting errors can be present due to human error. The on-board crew changes and different people may have had different training, and may simply report the same observation differently.
- Data storage and transfer: The data storage fails or data is not transferred from the ship to shore. The reasons can be limited storage space on board ships where data is overwritten automatically when the disc capacity is exceeded. Problems with the satellite connection and limited band-width for data transfer can also cause trouble during this phase.
- Data management and analysis: The data is logged and stored but not accessible to the people capable of working with it. Perhaps one part of the organisation is responsible for collecting the data and another is responsible for the analysis and one group fails to make the data available for the analysts or, probably more commonly, data is available but not analysed due to lack of time, skills and/or resources.
- Visualisation and communication: The data is analysed but the results are not communicated to the decision makers. This can be due to lack of methods for visualisation of data or non-optimal communication between the people analysing the data and the people making the decisions.
- Data is presented to the decision makers but not used in the decision making. The reason can be that they do not understand the way the results are presented, or that decision makers traditionally base their decisions on experience and gut feeling rather than on technical data.

If the hurdles listed above can be overcome, proper data harvesting, analysis, communication and utilisation of the data can provide an organisation with many advantages in the operation of ships, at sea or on land, as outlined in the following.

13.2 On-Board Decision Support

The aim of on-board decision support systems is to provide decision support to the master of the ship from an economical (fuel efficiency) or safety perspective. The decision support system can be dependant only on data recorded on board the ship or it can additionally receive data from elsewhere, e.g. the shore-based part of the organisation or an external provider of meteorological data.

Obviously, on-board systems must be robust and preferably fault-tolerant, i.e. able to handle errors in measurements and function in all conditions. Typically, decision support systems receive data from many different sensors and the quality must continuously be secured. Faults can be automatically detected and warnings can be issued when faults are present cf. e.g. Lajic and Nielsen, 2009 during operation. Ideally, as described by Nielsen et al., 2012 and Lajic et al., 2010, detected faults can be isolated and the decision support system made fault-tolerant, i.e. able to react to the presence of a fault and continue to function fully or partially, using redundant sensor signals if available.

Ship responses can be monitored real-time using sensors. The critical responses depend on the ship type, but for container ships they are typically the roll angle and transverse acceleration, slamming events and excessive hull girder loads. Critical response levels can be defined for each ship or loading condition and warnings can be issued when there is a certain risk of exceeding the prescribed limit, e.g. when a value exceeds 80% of a threshold value, cf. Det Norske Veritas, 2013b. From real-time measurements the decision support system can also predict trends in future responses. There are only few standards for decision support systems related to hull and ship response monitoring, but it is suggested in Det Norske Veritas, 2013b that a four hour sequence of measurements c form the basis for a forecast or trend prediction of the expected response for at least the next hour. The rules do, however, not prescribe any method for the trend prediction of future responses. Parametric roll is a critical response which can be detected early based on real-time measurements of the roll and pitch responses cf. Galeazzi et al., 2012 to avoid dangerous situations to the crew and loss of containers over board as illustrated in Figure 13.1.

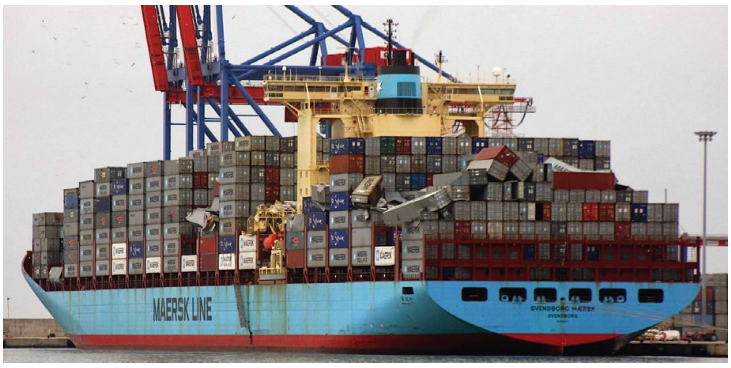

Figure 13.1: *8,600 TEU container ship SVENDBORG MÆRSK after losing over 500 containers over board in February 2014. Photo by Santiago Sáez.*

Decision support systems can be passive, i.e. simply display information and measurements and issue alarms when response levels become critical and leave the decision of the appropriate action to be taken in a given situation to the master of the ship. The decision support systems can also actively advise on the action to be taken in a given situation as e.g. change of speed and heading. One such system, the SeaSense system (Nielsen et al., 2006), is illustrated in Figure 13.2. The level of advise given is one consideration to take into account when designing decision support systems. An experienced and well trained master who is thoroughly familiarised with the behaviour of his ship will most likely know what action to take to avoid critical response levels. This is a question of awareness, training and level of education of the crew. However, sometimes good seamanship is not enough, and a captain may not necessarily know the most appropriate action to take when the ship experiences critical conditions and in some cases, decisions may be so difficult that good seamanship is simply not enough and decision support is required.

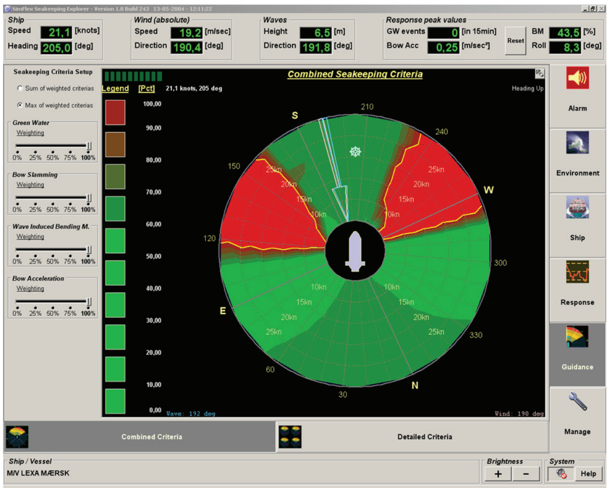

SimFlex Seakeeping Explorer - Version 1.0 Build 243 13-05-2004 - 12:11:22

Ship
Speed 21,1 [knots]
Heading 205,0 [deg]

Wind (absolute)
Speed 19,2 [m/sec]
Direction 190,4 [deg]

Waves
Height 6,5 [m]
Direction 191,8 [deg]

Response peak values
GW events 0 [in 15min]
Bow Acc 0,25 [m/sec²]
BM 43,5 [%]
Roll 8,3 [deg]

Seakeeping Criteria Setup
○ Sum of weighted criterias
● Max of weighted criterias

Ship / Vessel
M/V LEXA MÆRSK

Reset
Green Water
Weighting
Bow Slamming
Weighting
Wave Induced Bending M.
Weighting
Bow Acceleration
Weighting
0% 25% 50% 75% 100%
Combined Seakeeping Criteria
Legend
[Pct]
21,1 knots, 205 deg
Heading Up
100,00
90,00
80,00
70,00
60,00
50,00
40,00
30,00
20,00
10,00
0,00
S
W
E
N
210
240
300
330
30
60
120
150
10kn
15kn
20kn
25kn
Wave: 192 deg
Wind: 190 deg
Alarm
Environment
Ship
Response
Guidance
Manage
Combined Criteria
Detailed Criteria
Brightness
+
−
System
Help

Figure 13.2: *Screendump from the decision support system SeaSense illustrating combined sea keeping criteria in a polar diagram to enable assessment of the navigable combinations of speed and heading.*

Providing the on-board crew navigating the ship with decision support is a delicate balance. If the information given to the crew is faulty or misleading, the system is not trusted by the crew and in worst case switched off. In these cases crew experience or alternative decision support systems such as the one illustrated in Figure 13.3 may take over. The decision support system illustrated in Figure 13.3 may not be technically sophisticated, but has the advantage of being simple, cheap and easy to interpret. If the pot plants start falling on the floor action should taken to reduce the wave-induced response of the ship.

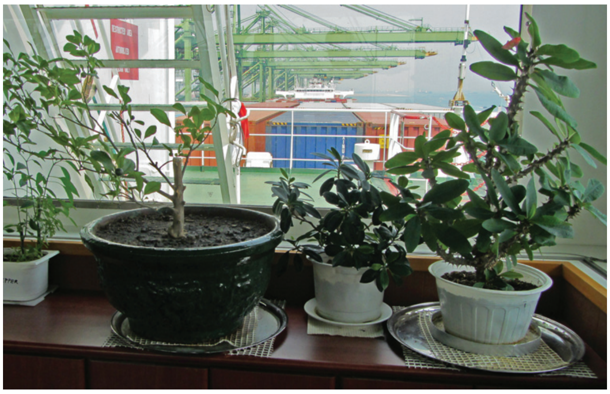

Figure 13.3: *Decision support system on the bridge of a large container ship.*

The factors mentioned above put demand on the decision support system to be robust and user friendly and only provide the necessary information. The information given must be easy to interpret and of good quality, cf. e.g. Petersen, 2012. A conclusion is that a bad decision support system is worse than no system and effective communication of information to the decision makers on the bridge is essential.

When ships become larger masters may lose feel with what is happening at the ends of the ship. As illustrated in Figure 13.4 the stern of the ship is 231 m away from the bridge and acceleration and local loads may not be felt as severely on the bridge as in the bow. Some responses, as e.g. roll is much easier for the master to perceive than the structural loads on the ship. The hull girder vibrations may be felt, but it is very difficult for a captain to assess whether e.g. the vertical bending moment approaches a critical level.

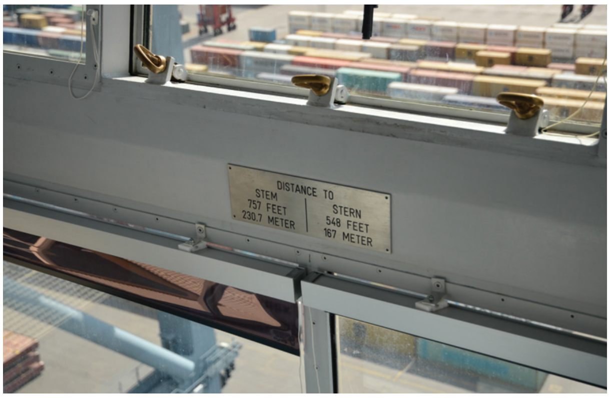

Figure 13.4: *Distance from bridge to stem and stern on 15,000 TEU container ship. Photo by Frederik Holten-Tingleff*

As part of the TULCS project some captains of large and ultra large container ships were interviewed about their behaviour in harsh sea conditions, and the outcomes of the interviews are available in a confidential report by Renaud, 2011. The main conclusion drawn in the available executive summary of the report is that the ship responses specific to large container ships, i.e. the global hydro-elastic responses are poorly addressed by the masters. The conventional responses of interest, particularly roll, was stated as being the main concern, as the roll motion associated with large transverse accelerations can cause cargo damage or loss of containers over board. The main concern of the masters is the safety of crew, cargo and ship and heavy weather is effectively avoided though proper route-planning. In case heavy weather is encountered, bow-quartering waves in low speed is the best operational solution according to the interviewed masters. However, as shown previously, bow-quartering seas may, in some cases, induce larger structural loads on container ships than direct head sea. These findings illustrate the need for either training the crew in navigation of large container ships in adverse weather conditions or use of on-board decision support systems which can aid in the avoidance of large hydro-elastic loads in container ships.

Human factors, training and the human-technology interface on board ships are very important aspects to consider in connection with decision support systems and have been studied by e.g. Karwowski, 2005 and Sampson and Tang, 2011. Little research within human factors in ship handling is available, but the topic has been studied by e.g. Prison et al., 2013. The behaviour of the master on board large container ships in adverse sea conditions plays an important role in relation to the structural loads on the ship. To the knowledge of the author, this particular field of ship manoeuvring in bad weather has not been thoroughly investigated, but could be an interesting subject to future studies.

13.3 On-Shore Decision Support

All good decision support systems rely on proper recording, handling and analysis of data and, as discussed above, decision support systems can be very useful on board ships when decisions become complex. In addition to the usefulness on board ships the recorded data can be stored, transferred to land and used to provide valuable information to the land-based part of the organisation. Used intelligently and communicated correctly, technical data from ships can be used on various levels in the organisation in business intelligence to minimise costs, optimise the operation and maximise competitiveness. Some of the challenges related to decision making in the shore-based part of the organisation are:

- Increased complexity of ship operation
- Increased amount of data potentially available
- Conservative mindset in the industry
- Lack of technical skills and resources in the organisation
- Communication between people with technical knowledge and people making the decisions

Some of the items above are further complicated by the organisation of shipping companies. Some operate a fleet of owned ships and employ their own on-board crew, but most shipowners charter ships in and out of the fleet, and in some trades charter contracts are very short-term. The picture is made even more blurred by sub-charter contracts and the fact that the crew on board the vessels can be employed by a third party ship management company. Some shipping companies keep their technical management and performance monitoring in-house, but many outsource it to a greater or lesser extent, and the different parties involved in the operation of the ships can have different (or no) interests or incentives for driving changes. This, in all, makes the decision making process quite complex . The complexity of decision making generally increases with increasing company size and so does the need for performance management and decision support in order to reduce the level of uncertainty in the decisions to be made.

With today's high bunker prices and low freight rates focus on ship energy efficiency improvements is strong. Data from ships is today being used more and more extensively in performance monitoring to evaluate ship performance and facilitate improvement of the energy efficiency.

When carrying out full scale measurement campaigns on board ships very large amounts of data are quickly generated. In many cases the data remains unanalysed and unused even though it, when utilised properly could provide valuable information to e.g. shipowners, operators and classification societies. Analysis and handling of large amounts of data are challenging tasks and typically not the core competence of the technical organisations in shipping companies. The availability of competences and skills required to perform the data analysis depend on the organisation size and structure and vary greatly within different shipowners and operators. Traditionally, and particularly in a conservative business like the shipping industry, decisions are often based on experience, tradition and gut feeling rather than knowledge obtained from skilful analysis of good quality technical data. When it comes to utilisation of fleet data, the shipping industry could potentially learn from other industries, as the aviation or the rail industries which use data more extensively in e.g. routing, maintenance and optimisation of the operation, cf. e.g. Larsen, 2013.

Performance monitoring systems is a kind of decision support system which can be used to establish base lines and key performance indicators for energy efficiency for individual ships or to provide key performance indicators enabling comparison between sister ships and thereby facilitate knowledge sharing, identification of best practise and efficiency improvements if the information is fed back to the ships. The systems can also be used to evaluate hull, propeller and engine performance for better maintenance planning and for reduced maintenance costs. Performance monitoring is a complex task due to many variables, where several are difficult to measure accurately. A critical uncertainty is the effect of waves, wind and current on the ship performance, cf. e.g. Hansen, 2011. The environmental parameters have a great effect but are difficult to measure. Often, the sea state parameters are estimated visually or obtained from meteorological models and are associated with significant uncertainty as described in Chapter 3.

The shipping industry is technology heavy and asset heavy and investment costs in e.g. new ships or retrofitting of old ships are high. When evaluating possible future investments it must be made sure that the right decisions are made and that the business case is good. The availability of information based on technical data can aid the construction of the business model for e.g. a retrofit installation. After installation or retrofitting of new technology such as the retrofitting of new bulbous bows on container ships illustrated in Figure 13.5 the performance of the ship must be assessed in order to evaluate the investment made, cf. e.g. Cerup-Simonsen et al., 2010.

Operational data from ships can feed back to design of new-buildings regarding determination of design speed, draught, etc. With today's container ships becoming larger simply scaling up the classification societies' design rules may not be sufficient in order to account for e.g. hydro-elastic effects. When calculations, simulations and mathematical models are insufficient full scale measurements from ships can be analysed and used by classification societies to assess whether container ships today are sufficiently designed to withstand wave loads.

Lastly, the shipping industry is exposed to increased demands for reporting of environmental performance, international and national regulations require increased reporting of energy efficiency and transport work. The Energy Efficiency Operational Indicator (EEOI) is part of the mandatory Ship Energy Efficiency Management Plan (SEEMP, see International Maritime Organization, 2009) and meant as a decision support tool to

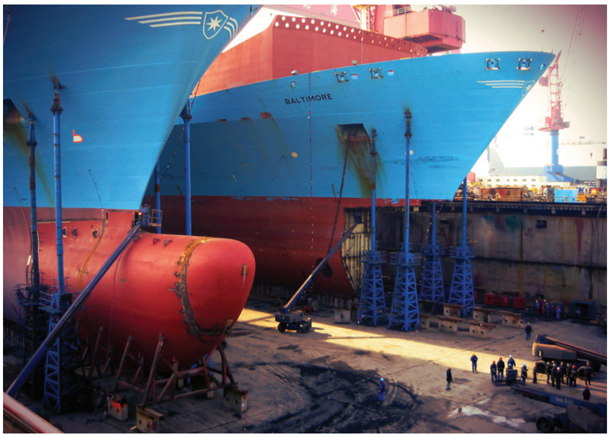

Figure 13.5: *Retrofit of new bulbous bows on the Maersk Boston class in 2012. Photo by Maersk Line.*

drive energy efficiency. A shipowner must ensure that the correct data can be collected in order to fulfil the requirements for the SEEMP. Future international legislation related to the energy efficiency of ships is likely to be based on actual recorded data from the international merchant fleet, e.g. International Maritime Organization, 2014, which also emphasises the importance of the availability of reliable data from ship operations.

Chapter 14

Conclusions and Recommendations for Future Work

Throughout the thesis the conclusions are summarised by the end of each chapter. The main conclusions and findings are outlined in the following together with some recommendations for future work.

14.1 Sea State Estimation and Response Prediction

Knowledge of the sea state encountered by the ship is a fundamental input for decision support systems and can be used for e.g. short-term navigational advice and guidance regarding course and speed changes, short-term prediction of future responses, determination of operational windows for offshore service vessels, voyage evaluation, performance monitoring and analysis of full scale response measurements.

Due to the randomness of ocean waves they are difficult to describe and estimate. However, it is clear that the need for accurate estimation of the sea state will increase due to increasing focus on cost-effective, safe and environmentally friendly transport. Various means exist for estimating the sea state. The accuracy greatly varies and the cost of such systems is often relatively high, which partially prohibits their use in many decision support systems. Work remains to develop cheap, reliable methods for estimating the on-site sea state encountered by the ship.

The wave-buoy analogy outlined in Chapter 3 potentially has some advantages for utilisation in on-board decision support systems, as it is capable of estimating the on-site wave spectrum using relatively simple and low-cost motion sensor technology. One disadvantage of the method is that the ship acts as a filter and only responds to some waves, and thus, only waves that produces a measurable ship response can be estimated. Further work remains in order to make the method robust and capable of automatically and continuously selecting the most suitable ship response measurements for the sea state estimation. The uncertainty of the sea state estimate is mainly related to the uncertainty in the calculation of the linear transfer functions and in the response measurements. These uncertainties should be quantified in order to assess the overall uncertainty related to the sea state estimation.

In Chapter 4, three different procedures for very short-term response prediction based on measured time series are discussed: Conditional processes with analytical estimates of the mean values and standard deviations, the autoregressive predictor method and a method based on superposition of sinusoidal components. The conditional processes has been applied to measured time series in order to evaluate the accuracy of response predictions within 5-15 seconds. A procedure based on 11 measured points spaced 1 second, covering the last 10 seconds of the instantaneous measured signal seems to give fair predictions of the response up to 5-15 seconds ahead of the current time, but in future work, the performance of the procedure should be investigated for the ships and responses of relevance.

14.2 Fatigue Damage Estimation

As found in Chapter 6, the effect of hull girder vibrations can influence the fatigue damage rate significantly. In some cases the high-frequency contribution to the estimated fatigue damage is larger than the wave-frequency contribution. This could make fatigue damage a critical issue for container ships. Accumulated fatigue damage can be estimated from strain measurements by applying an appropriate stress concentration factor, but actual damage assessment must be carried out by inspection and measurement of visible fatigue cracks.

For monitoring of the fatigue damage rates for decision support systems the estimation can be carried out in the time-domain or in the frequency-domain. Using today's computers, computational time is not considered an issue and the time-domain approach (here rainflow counting in combination the Palmgren-Miner rule) is thought to be capable of effectively estimating the fatigue damage rates accurately including the effect of hull girder vibrations.

The hull girder response to wave-induced loads is clearly not a narrow-banded process. When hull girder vibrations are present, the response can in most cases be considered bi-modal, but the individual processes are not necessarily narrow-banded. Nevertheless, the spectral formulations are generally in good agreement with the estimate from rainflow counting; even though they, as expected, generally estimate slightly higher fatigue rates. However, in some cases, when the response levels are high and dominated by hull girder vibrations, the fatigue damage estimates from rainflow counting are found to exceed those of the spectral methods. The spectral methods aimed at reducing the conservatism of the fatigue damage estimation seem to perform well in most cases and generally yield results quite similar to rainflow counting.

For the two container ships considered (9,400 TEU and 8,600 TEU), the high-frequency vibrations are found to contribute significantly to the estimated fatigue damage in cases where the high-frequency vibrations are dominating the hull girder stress response, i.e. in cases of whipping and springing. High fatigue damage rates are found in some cases, but during relatively small time periods and overall, the fatigue damage rates are small most of the time. The two considered ships are trading on the rather calm Europe - Asia route which might explain that only few, short periods of high fatigue damages rates are found. On other, rougher trades, fatigue may a greater issue for large container ships. The fatigue damage estimated here is based on uni-directional strain measurements in the deck longitudinals where pure vertical bending dominate the response. Fatigue may be of bigger concern in e.g. hatch corners where stresses are larger due to stress concentrations and multi-directional stresses.

14.3 Extreme Hydro-Elastic Response of Container Ships

The hydro-elastic response of container ships has been assessed through full scale measurements, model tests and numerical simulations focusing on the influence of the hull girder flexibility on the extreme structural response. Obviously, even though large amounts of full scale data has been analysed in the present work, the data only represents a very limited part of the total service life of the four container ships considered.

From analysis of full scale data from the 9,400 TEU ship, the largest structural response was concluded not to be an outlier or faulty measurement. The high-frequency parts of the ship responses (vertical and horizontal acceleration and stress) were compared using simple beam theory and found to correspond well to the vertical 2-node vibration mode of the ship. No torsional vibrations were identified from the full scale measurements for any of the ships considered here, but it cannot in general be concluded that torsional vibrations are not present. From the consideration of full scale measurements the hydro-elastic response of container ships is believed to be dominated by the 2-node vertical vibration mode.

It is clear, that the hull girder flexibility in large container ships considerably influences the structural response of the ship. For several of the considered individual large events the effect of the hull girder flexibility more than doubles the total structural response amidships. The amplification effect is largest for the 9,400 TEU and the 8,600 TEU ships. However, from the full scale measurements it cannot generally be concluded that the influence of the hull girder flexibility is largest for ships in this size range. The number of analysed events is limited, and the influence of bow flare and ship speed may be important in addition to the influence of ship size. From the measurements analysed it is considered safe to assume a 100% amplification of the rigid-body response due to the hull girder flexibility in larger container ships.

The damping of the 2-node vertical bending mode is estimated for the four ships using operational modal analysis. The estimate includes the structural and the hydrodynamic damping and varies between 1.3% and 2.5% of the critical damping for the considered time series. Large container ships are believed to have higher structural damping than smaller container ships. From the damping estimates carried out here it is not possible to identify any size dependency, but in any case, the damping is low. The low damping of the 2-node vertical bending mode for container ships is one of the reasons for the importance of the hydro-elastic effects. Due to the low damping, the hull girder vibrations, most commonly initiated by a slamming event in the sagging condition, will continue long enough to also amplify the succeeding hogging bending moment.

The largest measured structural responses are found in the hogging condition in six out of ten cases when considering 2-3 hour time series. In some cases, unexpectedly and particularly for the three largest ships, the hogging bending moment is amplified more by the hull girder vibrations than the sagging bending moment. It is difficult to determine in what conditions the hogging bending moment is amplified more than the sagging bending moment, and the amplification most likely depends on speed and heading of the ship relative to the waves. Full scale measurements and model tests indicate that the amplification is largest in bow-quartering seas, and this should be investigated further for large and ultra large container ships.

Generally, the significant difference between the sagging and hogging amidships in the design rules for the wave-induced vertical bending moment is not reflected in the full scale measurements, and no trend indicating that the wave-induced bending moment in sagging is larger than in hogging is found. The findings related hereto should be studied further and taken into account by the classification societies in the design rules for large container ships.

Somewhat unexpected, in some cases, the rigid-body hogging bending moment is found to be considerably larger than the corresponding sagging bending moment for both the full scale measurements and the model tests. Particularly for the largest of the ships, this effect is pronounced and should be investigated further for large and ultra large container ships.

From the full scale measurements, it is difficult to determine the true zero of the wave-induced bending moment as the still-water bending moment in most cases cannot continuously be accurately determined. Non-linearities in the response induce quasi-static effects, but, however, the non-linear effects are considered only to be of minor importance for the total response. Simply subtracting the mean of the signal results in nearly an equal number of positive and negative peaks and is believed to be the only feasible way to assess the wave-induced loads from full scale measurements.

In connection with the prediction of the extreme value of the vertical bending moment amidships, the tails of the peak distributions for the four different ships are found to be very different from ship to ship, for the different time series and in the hogging and the sagging condition without any general trend. In several cases, the tail of the peak distribution of the VBM shows a tendency towards an upper bound, but in some cases there are larger peaks present which make the tail behaviour very irregular. The irregular tail behaviour implies that it is generally difficult to decide on an appropriate extreme value distribution. The Gumbel distribution is fundamentally believed to be the best choice of distribution for this application. It may, however, be necessary to fit other types of extreme value distributions to the largest peaks and more work should be carried out in order to determine a reliable method for extreme value prediction based on full scale measurements. Use of the peak-over-threshold method in combination with the Generalised Pareto Distribution for the tail could be a subject of future studies.

The statistical dependence between large peaks is found to play a role in some, but not all, cases and clustering of peaks is thus only necessary to take into account in those cases. For the extreme value prediction it is not beneficial to remove too many peaks, and, as shown, statistical outliers may not be physical outliers. Development of a robust method to remove only true outliers and statistically correlated peaks should be explored in future work. The choice of a proper threshold level for the peak-over threshold is also not straight forward as illustrated by the plots of the mean excess. For on-board decision support systems, the threshold level should be determined automatically, and a development of a robust method for this, perhaps based on the mean excess, could also be subject for future studies.

From full scale measurements it is difficult to assess the influence of operational parameters (particularly ship speed, relative heading and wave height) on the extreme response, because reliable data for these parameters is often not available and the influence of operational parameters is more easily investigated in model tests. Model tests indicate that bow-quartering sea may induce larger structural loads on the ship than direct head sea. However, this is not necessarily reflected in the behaviour of the ship masters who seemingly tend to prefer bow-quartering sea to head sea when encountering bad weather.

Model tests indicate that the largest container ships are not necessarily the most critical ships to consider regarding extreme hydro-elastic hull girder responses. The largest container ships often have lower design speed, larger block coefficient and smaller bow flare than the ships in the 8,000-9,000 TEU capacity range, which may make the ultra large container ships with a capacity of 14,000-18,000 TEU less susceptible to whipping-induced vibrations.

Numerical tools may not be able to fully capture the effect of the hull girder flexibility and uncertainties are associated with both the modelling of the wave scenario, the hydrodynamics and the structural response. Even highly sophisticated CFD models may not be able to fully capture important effects. Hence, full scale measurements from ships are very valuable in the evaluation of existing designs and may reveal effects that cannot currently be assessed numerically. It is, however, difficult, to make good use of full scale measurements for this purpose without rather accurate knowledge of the encountered sea state, which must be taken into consideration when carrying out full scale measurements.

Lastly, a subject for further studies could be regarding the dynamic collapse mechanism of large container ships taking the hydro-elastic effects into account.

Bibliography

Andersen, I. M. V. and J. J. Jensen (2012). On the Effect of Hull Girder Flexibility on the Vertical Wave Bending Moment for Ultra Large Container Vessels. *Proceedings of the International Conference on Offshore Mechanics and Arctic Engineering (OMAE, paper no. 83043).*

Andersen, I. M. V. and J. J. Jensen (2013). Fatigue Damage Estimations in the Hull Girder of a Large Container Vessel by Spectral Analysis. *Proceedings of the PRADS Conference, Changwon City, Korea.*

Andersen, I. M. V. and J. J. Jensen (2014). Measurements in a Container Ship of Wave-Induced Hull Girder Stresses in Excess of Design Values. *Marine Structures 37*, 54–85.

Andersen, I. M. V., J. J. Jensen, and U. D. Nielsen (2013). Evaluation of Response Prediction Procedures using Full Scale Measurements for a Container Ship. *Proceedings of the PRADS Conference, Changwon City, Korea.*

Andersen, I. M. V. and G. Storhaug (2012). Dynamic Selection of Ship Responses for Estimation of On-Site Directional Wave Spectra. *Proceedings of the International Conference on Offshore Mechanics and Arctic Engineering (OMAE, paper no. 83206).*

Barhoumi, M. and G. Storhaug (2013). Assessment of Whipping and Springing on a Large Container Vessel. *Proceedings of the PRADS Conference, Changwon City, Korea.*

Bhattacharyya, R. (1978). *Dynamics of Marine Vehicles* (2 ed.). John Wiley & Sons.

Brodtkorb, A., P. Johannesson, G. Lindgren, and I. Rychlik (2011). *WAFO - a Matlab Toolbox for Analysis of Random Waves and Loads.* Mathematical Statitics, Center for Mathematical Sciences, Lund University. http://www.maths.lth.se/matstat/wafo/.

Cerup-Simonsen, B., J. O. de Kat, and O. G. Jakobsen (2010). An Integrated Approach towards Cost-Effective Operation of Ships with Reduced GHG Emissions. *Transactions of the Society of Naval Architects and Marine Engineers (SNAME) 118*, 381–396.

Chung, J. C., Z. Bien, and Y. S. Kim (1990). A Note on Ship-Motion Predictions based on Wave-Excitation Input Estimation. *IEEE Journal of Oceanic Engineering 15(3)*, 244–250.

Committee on Large Container Ship Safety (2013). Interim Report of Committee on Large Container Ship Safety (English version). Downloaded from http://www.mlit.go.jp/common/001029660.pdf.

Det Norske Veritas (2013a, July). *Classification Note 30.12. Fatigue Strength and Ultimate Capacity Check of Container Vessels Including the Effect of Springing and Whipping.*

Det Norske Veritas (2013b, January). *Rules for Classification of Ships/High Speed, Light Craft and Naval Surface Craft, Part 6, Chapter 11. Hull Monitoring Systems.*

Döhler, M., P. Andersen, and L. Mevel (2012). Operational Modal Analysis using a Fast Stochastic Subspace Identification Method. *Proceedings of the 30th International Modal Analysis Conference (IMAC) Jacksonville, Florida USA.*

Drummen, I., T. Moan, G. Storhaug, and E. Moe (2006). Experimental and Full Scale Investigation of the Importance of Fatigue Damage due to Wave-Induced Vibration Stresses in a Container Vessel. *Transactions of Design & Operation of Container Ships, Royal Institution of Naval Architects, London, UK*, 61–74.

Faulkner, D. (2003). Freak Waves - A Suggested Way Ahead for Survival Design. *The Honourable Company of Master Mariners Strategic Seminar*.

Fresser, C. (2011). *TULCS Project Installation report. Experimental Device Integration o/b Container Ship CMA-CGM RIGOLETTO for Sea State Measurement.* SIREHNA.

Fricke, W. and H. Paetzold (2012). Experimental Investigation of the Effect of Whipping Stresses on the Fatigue Life of Ships. *Proceedings of the International Marine Design Conference (IMDC), Glasgow, Scotland*, 3–10.

Fricke, W. and H. Paetzold (2013). Experimental Investigation on Fatigue Damage of Ship Structures Caused by Whipping Stresses. *Proceedings of the PRADS Conference, Changwon City, Korea*, 465–470.

From, P. J., J. T. Gravdahl, T. Lillehagen, and P. Abbeel (2011). Motion Planning and Control of Robotic Manipulators on Seaborne Platforms. *Control Engineering Practice 19*, 809–819.

Gaidai, O., A. Naess, and G. Storhaug (2010). Extreme Value Statistics of Whipping Response for Large Ships. *Proceedings of the PRADS Conference, Rio de Janeiro, Brazil 2*, 1210–1221.

Galeazzi, R., M. Blanke, and N. K. Poulsen (2012). Early Detection of Parametric Roll Resonance on Container Ships. *IEEE Transactions on Control Systems Technology 21*, 489–503.

Garré, L. and A. Der Kiureghian (2010). Tail-Equivalent Linearization Method in Frequency Domain and Application to Marine Structures. *Marine Structures 23(3)*, 322–338.

Hansen, S. V. (2011). *Performance Monitoring of Ships.* Ph. D. thesis, Technical University of Denmark, Department of Mechanical Engineering.

Heggelund, S. E., G. Storhaug, and B. K. Choi (2011). Full Scale Measurements of Fatigue and Extreme Loading Including Whipping on an 8600 TEU Post Panamax Container Vessel in the Asia to Europe Trade. *Proceedings of the International Conference on Offshore Mechanics and Arctic Engineering (OMAE, paper no. 49378).*

Huang, W. (2013). The Rain-Flow Estimate of Fatigue Damage of Combined High and Low Frequency Load Effects. *Proceedings of the International Conference on Offshore Mechanics and Arctic Engineering (OMAE, paper no. 10794)*.

International Association of Classification Societies (2010a, May). *Unified Requirements Concerning Strength of Ships, Longitudinal Strength Standard, UR-S11*.

International Association of Classification Societies (2010b, May). *Unified Requirements Concerning Strength of Ships, UR-S2*.

International Maritime Organization (2009). *MEPC1. Circ. 683 Guidance for the Development of a Ship Energy Efficiency Management Plan (SEEMP)*.

International Maritime Organization (2014). *MEPC 66/4/9 Further Technical and Operational Measures for Enhancing Energy Efficiency of International Shipping - Framework for a Global Data Collection System for maritime transport covering fuel consumption, CO2 emissions and energy efficiency*.

Iseki, T. (2012). An Improved Stochastic Modeling for Bayesian Wave Estimation. *Proceedings of the International Conference on Offshore Mechanics and Arctic Engineering (OMAE, paper no. 83740)*.

Iseki, T. and D. Terada (2002). Bayesian Estimation of Directional Wave Spectra for Ship Guidance Systems. *International Journal of Offshore and Polar Engineering*, 25–30.

Jensen, J. J. (2001). *Load and Global Response of Ships* (4 ed.). Department of Naval Architecture and Offshore Engineering, Technical University of Denmark.

Jensen, J. J. (2009). Stochastic Procedures for Extreme Wave Load Predictions - Wave bending Moments in Ships. *Marine Structures 22*, 194–208.

Jensen, J. J. and J. Capul (2006). Extreme Response Predictions for Jack-up Units in Second Order Stochastic Waves by FORM. *Probabilistic Engineering Mechanics 21*, 330–337.

Jensen, J. J., A. E. Mansour, and A. S. Olsen (2004). Estimation of Ship Motions using Closed-Form Expressions. *Ocean Engineering 31*, 61–85.

Jensen, J. J., A. S. Olsen, and A. E. Mansour (2011). Extreme Wave and Wind Response Predictions. *Ocean Engineering 38*, 2244–2253.

Jensen, J. J., P. T. Pedersen, B. Shi, S. Wang, M. Petricic, and A. E. Mansour (2009). Wave Induced Extreme Hull Girder Loads on Containerships. *Transactions of the Society of Naval Architects and Marine Engineers (SNAME) 116*, 128–151.

Jiao, G. and T. Moan (1990). Probabilistic Analysis of Fatigue due to Gaussian Load Processes. *Probabilistic Engineering Mechanics 5*, 76–83.

Kahl, A., W. Fricke, H. Paetzold, and H. von Selle (2014). Whipping Investigations Based on Large-Scale Measurements and Experimental Fatigue Testing. *Proceedings of ISOPE-2014, Busan, Korea (to be published)*.

Kapsenberg, G. K., M. Schiere, and I. Drummen (2010). *TULCS Work Package 6: Model test. Specifications for experiments (confidential).* Maritime Research Institute Netherlands.

Karpa, O. (2012). *ACER User Guide.* Centre for Ships and Ocean Structures, NTNU, Trondheim, Norway. http://folk.ntnu.no/karpa/ACER/ACER_User_guide.pdf.

Karwowski, W. (2005). Ergonomics and Human Factors: The Paradigms for Science, Engineering, Design, Technology and Management of Human-Compatible Systems. *Ergonomics 48*, 436–463.

Kitamura, O., T. Sugimura, S. Nakayama, and K. Hirota (2012). A Consideration to the Effect of Whipping on the Fatigue Life based on the In-Service Monitoring and Fatigue Tests. *Proceedings of JASNAOE, Kobe, Japan.*

Koning, J. (2007, August). *Installation Report CMA-CGM Rigoletto, Lashing@Sea project* (3 ed.). Maritime Research Institute Netherlands.

Koning, J. (2010). *TULCS Project deliverable 7.1: Full scale plan & installation report, part A: Additional strain sensors (confidential).* Maritime Research Institute Netherlands.

Koning, J. and G. Kapsenberg (2012). Full Scale Container Ship Cross Section Loads - First Results. *Proceedings of Hydroelasticity in Marine Technology*, 311–320.

Kosleck, S. (2013). *Prediction of Wave-Structure Interaction by Advanced Wave-Field Forecast.* Ph. D. thesis, Technical University of Berlin, Department of Ocean Engineering.

Lajic, Z., M. Blanke, and U. D. Nielsen (2010). Fault Isolation for Shipboard Decision Support. *Proceedings 7th IFAC Symposium on Intelligent Autonomous Vehicles, Lecce, Italy*.

Lajic, Z. and U. D. Nielsen (2009). Fault Detection for Shipboard Monitoring and Decision Support Systems. *Proceedings of the International Conference on Offshore Mechanics and Arctic Engineering (OMAE, paper no. 49370).*

Larsen, T. (2013). Cross-Platform Aviaiton Analytics using Big Data methods. *Proceedings of the Integrated Communications, Navigation and Surveillance Conference*, 1–9.

Lindgren, G. (1970). Some Properties of a Normal Process near a Local Maximum. *The Annals of Mathematical Statistics 415*, 1870–1883.

Low, Y. M. (2010). A Method for Accurate Estimation of the Fatigue Damage Induced by Bimodal Processes. *Probabilistic Engineering Mechanics 25*, 75–85.

Malenica, S. and Q. Derbanne (2012). Hydro-Elastic Issues in the Design of Ultra Large Container Ships - TULCS Project. *Proceedings of Hydroelasticity in Marine Technology, Tokyo, Japan*, 233–246.

Marine Accident Investigation Branch (2009, April). *Report on the Investigation of the Structural Failure of MSC Napoli.*

Mathisen, J., G. Storhaug, and S. E. Heggelund (2009). Whipping Vibrations in Bending Stresses Measured under Harsh Stationary Conditions. *Proceedings of Hydroelasticity in Marine Technology, Southampton, UK*.

Mondher, B. (2012). *Measurements and Calculations of Fatigue Damage in Ship Structure (Master thesis).* Vestfold University College, Norway.

Montazeri, N. and U. D. Nielsen (2014). Parametric Estimation in the Wave Buoy Analogy - an Elaborated Approach based on Energy Considerations (to be published). *Proceedings of the International Conference on Offshore Mechanics and Arctic Engineering (OMAE).*

Naess, A. and O. Gaidai (2009). Estimation of Extreme Values from Sampled Time Series. *Structural Safety 31*, 325–334.

Nielsen, J. K., N. H. Pedersen, J. Michelsen, U. D. Nielsen, J. Baatrup, J. J. Jensen, and E. S. Petersen (2006). SeaSense - Real-Time Onboard Decision Support. *Proceedings of the Wold Maritime Technology Conference, London, UK*.

Nielsen, U. D. (2005). *Estimation of Directional Wave Spectra from Measured Ship Responses*. Ph. D. thesis, Technical University of Denmark, Department of Mechanical Engineering.

Nielsen, U. D. (2006). Estimations of On-Site Directional Wave Spectra From Measured Ship Responses. *Marine Structures 19*, 33–69.

Nielsen, U. D. (2008). The Wave Buoy Analogy - Estimating High-Frequnecy Wave Exitations. *Applied Ocean Research 30*, 100–106.

Nielsen, U. D., I. M. V. Andersen, and J. Koning (2013). Comparisons of Means for Estimating Sea States from an Advancing Large Container Ship. *Proceedings of the PRADS Conference, Changwon City, Korea*, 250–258.

Nielsen, U. D. and T. Iseki (2012). Blind Estimation of a Ship's Realtive Heading. *Proceedings of the International Conference on Offshore Mechanics and Arctic Engineering (OMAE, paper no. 83305).*

Nielsen, U. D., J. J. Jensen, P. T. Pedersen, and Y. Ito (2011). Onboard Monitoring of Fatigue Damage Rates in the Hull Girder. *Marine Structures 24*, 182–206.

Nielsen, U. D., Z. Lajic, and J. J. Jensen (2012). Towards Fault-Tolerant Decision Support Systems for Ship Operator Guidance. *Reliability Engineering and System Safety 104*, 1–14.

Nielsen, U. D. and D. C. Stredulinsky (2012). Sea State Estimation from an Advancing Ship - A Comparative Study using Sea Trial Data. *Applied Ocean Research 34*, 33–44.

Oberhagemann, J., M. Krömer, C. Cabos, and O. el Moctar (2012). A Fluid-Structure Coupling Method based on Field Methods and a Structural Mode Decomposition. *Proceedings of Hydroelasticity in Marine Technology, Tokyo, Japan*, 267–276.

Ogawa, Y. and K. Takagi (2012). A Study for the Effect of Operation on Hydroelasticity of Hull. *Proceedings of Hydroelasticity in Marine Technology*, 257–266.

Okada, T., Y. Takeda, and T. Maeda (2006). On Board Measurement of Stresses and Deflections of a Post-Panamax Containership and its Feedback to Rational Design. *Marine Structures 19*, 141–172.

Pascoal, R., C. G. Soares, and A. J. Sørensen (2007). Ocean Wave Spectral Estimation using Vessel Wave Frequency Motions. *Journal of Offshore Mechanics and Arctic Engineering 129*, 90–96.

Pedersen, P. T. and J. J. Jensen (2009). Estimation of Hull Girder Vertical Bending Moments Including Non-Linear and Flexbility Effects Using Closed-Form Expressions. *Journal of Engineering for the Maritime Environment 223*, 377–390.

Petersen, E. S. (2012). *Engineering Usability.* Ph. D. thesis, Chalmers University of Technology, Department of Shipping and Marine Technology.

Prison, J., J. Dahlman, and M. Lundh (2013). Ship Sense - Striving for Harmony in Ship Manouvring. *World Maritime University Journal of Maritime Affairs 12*, 115–127.

Renaud, M. (2011). *TULCS Project Work package 2: End User Requirements. Review of Physical Phenomena (confidential).* CMA CGM.

Renaud, M., E. D. Lorgeril, J. B. Boutillier, and L. Gerad (2013). Fatigue and Weather on Ultra Large Containerships. *Proceedings of the PRADS Conference, Changwon, Korea*, 384–394.

Rüdinger, F. (2002). *Modelling and Estimation of Damping in Non-linear Random Vibration.* Ph. D. thesis, Technical University of Denmark, Department of Mechanical Engineering.

Rychlik, I. (1987). A new Definition of the Rainflow Cycle Counting Method. *International Journal of Fatigue 9*, 119–121.

Rychlik, I. (1993). On the Narrow-band approximation for Expected Fatigue Damage. *Probabilistic Engineering Mechanics 8*, 1–4.

Salvesen, N., E. O. Tuck, and O. Faltinsen (1970). Ship Motions and Sea Loads. *Transactions of the Society of Naval Architects and Marine Engineers (SNAME) 78*, 250–287.

Sampson, H. and L. Tang (2011). New Shipboard Technology and Training Provision for Seafarers. *Seafarers International Research Centre (SIRC).*

Seng, S., I. M. V. Andersen, and J. J. Jensen (2012). On the Influence of Hull Gider Flexibility on the Wave Induced Bending Moments. *Proceedings of Hydroelasticity in Marine Technology, Tokyo, Japan*, 341–353.

Seng, S. and J. J. Jensen (2012). Slamming Simulations in a Conditional Wave. *Proceedings of the International Conference on Offshore Mechanics and Arctic Engineering (OMAE, paper no. 83310).*

Seng, S. and J. J. Jensen (2013). An Application of a Free Surface CFD method in the Short-Term Extreme Response Analysis of Ships. *Proceedings of the PRADS Conference, Changwon City, Korea.*

Senjanović, I., S. Malenica, and S. Tomašević (2008). Hydroelasticity of Large Container Ships. *Marine Structures 22*, 1–28.

Soares, C. G. and A. P. Teixeira (2000). Structural Reliability of two Bulk Carrier Designs. *Marine Structures 13*, 107–128.

Storhaug, G. (2007). *Experimental Investigation of Wave Induced Vibrations and their Effect on the Fatigue Loading of Ships.* Ph. D. thesis, Norwegian University of Science and Technology, Department of Marine Technology.

Storhaug, G. (2014). Are Container Vessels Sufficiently Designed to Withstand Extreme Loads? (to be published). *Proceedings of the International Conference on Offshore Mechanics and Arctic Engineering (OMAE).*

Storhaug, G., Q. Derbanne, B. K. Choi, T. Moan, and O. A. Hermundstad (2011). Effect of Whipping on Fatigue and Extreme Loading of a 13000 TEU Container Vessel in Bow Quartering Seas Based on Model Tests. *Proceedings of the International Conference on Offshore Mechanics and Arctic Engineering (OMAE, paper no. 49370).*

Storhaug, G. and S. E. Heggelund (2008). Measurements of Wave Induced Vibrations and Fatigue Loading onboard two Container Vessels Operating in Harch Wave Environment. *Transactions of Design & Operation of Container Ships, Royal Institution of Naval Architects, London, UK*, 81–100.

Storhaug, G., S. Malenica, B. K. Choi, S. Zhu, and O. A. Hermundstad (2010a). Consequence of Whipping and Springing on Fatigue and Extreme Loading for a 13000TEU Container Vessel Based on Model Tests. *Proceedings of the PRADS Conference, Rio de Janeiro, Brazil.*

Storhaug, G., S. Malenica, B. K. Choi, S. Zhu, and O. A. Hermundstad (2010b). Consequence of Whipping and Springing on Fatigue for a 8600TEU Container Vessel in Different Trades Based on Model Tests. *Proceedings of the PRADS Conference, Rio de Janeiro, Brazil.*

Storhaug, G., E. Moe, and G. Holtsmark (2007). Measurements of Wave Induced Hull Girder Vibrations of an Ore Carrier in Different Trades. *Journal of Offshore Mechanics and Arctic Engineering 129*, 279–289.

Storhaug, G. and G. Moe (2007). Measurements of Wave Induced Vibrations Onboard a large Container Vessel Operating in Harsh Environment. *Proceedings of the PRADS Conference, Houston, Texas 25*, 64–72.

Storhaug, G., J. Vidic-Perunovic, F. Rüdinger, G. Holtsmark, J. B. Helmers, and X. Gu (2003). Springing/Whipping Response of a Large Ocean Going Vessel- A Comparison Between Numerical Simulations and Full Scale Measurements. *Proceedings of Hydroelasticity in Marine Technology, Oxford, UK*, 117–131.

Stredulinsky, D. C. and E. M. Thornhill (2011). Ship Motion and Wave Radar Data Fusion for Shipboard Wave Measurement. *Journal of Ship Research 55(2)*, 73–85.

Takaoda, Y., A. Murakami, T. Yoshida, R. Miyake, N. Yamamoto, K. Terai, and K. Toyoda (2012). An Experimental Study on the Whipping Response of Large Container Carriers. *Proceedings of Hydroelasticity in Marine Technology, Tokyo, Japan*, 145–150.

Tannuri, J. V., A. N. Sparano, and J. J. D. Cruz (2003). Estimating Directional Wave Spectrum Based on Stationary Ship Motions. *Applied Ocean Research 25*, 243–261.

Tick, L. J. (1959). Differential Equations With Frequency-Dependent Coefficients. *Journal of Ship Research 3*, 45–46.

Xia, J., Z. Wang, and J. J. Jensen (1998). Non-Linear Wave Loads and Ship Responses by a Time-Domain Strip-Theory. *Marine Structures 11*, 101–123.

Xu, W., K. Iijima, and M. Fujikubo (2012). Investigation into Dynamic Collapse Behaviour of a Bulk Carrier Under Extreme Wave Loads. *Proceedings of Hydroelasticity in Marine Technology, Tokyo, Japan.*

Yeung, R. W. (1973). A Singularity Distribution Method for Free-Surface Flow Problems with an Oscillating Body. *University of California, College of Engineering, Rep. No. NA 73-6*, 45–46.

Zhao, X., R. Xu, and C. Kwan (2004). Ship-Motion Prediction: Algorithms and Simulation Results. *Proceedings of IEEE International Conference on Acoustics, Speech, and Signal Processing 5*, 125–128.

Zhu, S. and T. Moan (2012). New Insight into the Wave-Induced Nonlinear Vertical Load Effects of Ultra-Large Container Ships Based on Experiments. *Journal of Marine Science and Technology 18*, 87–114.

Zhu, S., M. Wu, and T. Moan (2011). Experimental Investigation of Hull Girder Vibrations of a Flexible Backbone Model in Bending and Torsion. *Applied Ocean Research 33*, 252–274.

List of Figures

1.1 18,000 TEU container ship MAJESTIC MÆRSK. 13

2.1 Definition of the coordinate system. 20
2.2 Sister ship of the TULCS case ship. Photo by CMA CGM. 20
2.3 Example of the display on the WaMoS PC screen on board the 9,400 TEU container ship. Illustration from Fresser, 2011. 22
2.4 Acceleration sensor set-up on board the 9,400 TEU container ship. Illustration from Koning, 2007. 23
2.5 Position of the strain gauges on board the 9,400 TEU container ship. Illustration from Koning, 2007. 24
2.6 Flexible ship model at CEHIPAR. Photo by Camille Fresser. 25

3.1 A TRIAXYS$^{\mathrm{TM}}$solar powered directional wave buoy. 34
3.2 Directional wave spectrum estimated using the parametric modelling on 12 August 2011 at 16 hours. Absolute ship heading is 0 deg. 37
3.3 Directional wave spectrum estimated using the parametric modelling on 02 October 2011 at 11 hours. Absolute ship heading is 0 deg. 37
3.4 Directional wave spectrum estimated using the Bayesian modelling on 12 August 2011 at 16 hours. Absolute ship heading is 0 deg. 38
3.5 Directional wave spectrum estimated using the Bayesian modelling on 02 October 2011 at 11 hours. Absolute ship heading is 0 deg. 38
3.6 Lack of measurable ship response in very low and very high frequency waves. Figure courtesy of Nielsen, 2005. 42

4.1 Normalised autocorrelation function *r(t)* and its time derivative *s(t)* and *u(t)* for the measured stress. 49
4.2 Normalised variances $s_0^2(t), s_{00}^2(t), s_{000}^2(t)$ of the conditional processes for the measured stress, Eq. (4.4). 49
4.3 Normalized variances $s_1^2(t)$; t_1= 1, 3, 5, 7, 10 and 20 seconds determined for the conditional process for the measured stresses, Eq. (4.11). 50
4.4 Normalised variances $s_n^2(t)$ for $n = 1$ and $n = 10$ with constant time step $t_i - t_{i+1} = 1$ s, determined for the conditional process for the measured stresses, Eqs. (4.12)-(4.13). 50
4.5 Measurements and conditional mean responses. 51
4.6 Measurements and conditional mean responses. 51
4.7 Measurements and conditional mean responses. 51
4.8 Measurements and conditional mean responses. 51
4.9 Measurements and conditional mean responses. 52

4.10 Measurements and conditional mean responses. 52
4.11 Measurements and conditional mean responses. 52
4.12 Measurements and conditional mean responses. 52
4.13 Subsea support vessel with heave compensated crane. Photo by Maersk Supply Service. 53

5.1 Total, wave-frequency and high-frequency ship hull stress response in the deck amidships. Example from the 9,400 TEU container ship. 55
5.2 Body plan of the 9,400 TEU container ship. Illustration courtesy of the TULCS project. 55
5.3 High-pass filtered stress signal amidships for a container ship sailing in bow-quartering sea illustrating a series of transient slamming/whipping events. Full scale measurements from the 9,400 TEU container ship. . . 56
5.4 The 2-node vertical bending mode of the 9,400 TEU container ship. Illustration courtesy of the TULCS project, WP.4. 57
5.5 FFT of stress time history (one hour) from 9,400 TEU container ship in rough sea on 02 October 2011. The vibration at the 2-node vertical mode is seen at about 0.48 Hz. 59
5.6 FFT of stress time history (one hour) in semi-logarithmic plot from 9400 TEU container ship in rough sea on 02 October 2011. The vibration at the 2-node vertical mode is seen at about 0.48 Hz and the 3-node vertical vibration frequency can be identified at about 0.99 Hz. FFT of the same time series as in Figure 5.5. 59
5.7 Screendump from ARTeMIS for estimating of modal parameters with indication of two stable modes (2 and 3-node vertical bending). 61
5.8 The normalised 2-node vertical bending mode $\nu_2(x)$ for the 9,400 TEU container ship determined using a Timoshenko beam model. 63
5.9 The normalised 2-node vertical bending mode $\nu_2(x)$ for the 9,400 TEU container ship determined by BV. $x = 0$ is AP. From Kapsenberg et al., 2010. RX denotes data from the full scale ship. 63

6.1 Rainflow counting procedure for the tensile peaks. 69
6.2 Comparison of total estimated fatigue damage per hour during 24 hours on 02 October 2011 for the 9,400 TEU ship. Same figure as Figure C.35 in Appendix C.1. 75
6.3 Comparison of total estimated fatigue damage per hour during 24 hours on 17 November 2010 for the 8,600 TEU ship. Same figure as Figure C.75 in Appendix C.2. 75
6.4 RFC compared to the two envelope processes for 02 October 2011 for the 9,400 TEU ship. Same figure as Figure C.36 in Appendix C.1. 77
6.5 RFC compared to the two envelope processes for 17 November 2010 for the 8,600 TEU ship. Same figure as Figure C.76 in Appendix C.2. 77
6.6 FFT of filtered stress time series with wave-frequency (WF) response and high-frequency (HF) response outlined. FFT of one hour of data from 12 August 2011 at 11 hours. $\delta_{total} = 0.62$, $\delta_{WF} = 0.48$ and $\delta_{HF} = 0.12$. . 79

6.7 FFT of filtered stress time series with wave-frequency response and high-frequency response outlined. FFT of one hour of data from 02 October 2011 at 18 hours. $\delta_{total} = 0.63$, $\delta_{WF} = 0.21$ and $\delta_{HF} = 0.09$. 79
6.8 WF and HF part of the stress signal (average of port and starboard side) illustrating springing excitations. 8,600 TEU ship on 01 December 2012 at 21 hours. 80

7.1 The incoming wave amidships conditioned on a vertical bending moment of 5,000 MNm at $t = 50$ s in the sagging condition. 86
7.2 The incoming wave amidships conditioned on a vertical bending moment of 5,000 MNm at $t = 50$ s in the hogging condition. 86
7.3 Wave elevation along the flexible ship in sagging condition at $t = 50$ s. . 87
7.4 Vertical bending moment amidships of the flexible ship and rigid ship in sagging condition. Conditional wave for the flexible ship. Hogging is positive 87
7.5 Wave elevation along the flexible ship in hogging condition at $t = 50$ s. . 88
7.6 Vertical bending moment amidships of the flexible ship and rigid ship in hogging condition. Conditional wave for the flexible ship. Hogging is positive. 88
7.7 Wave elevation along the flexible ship conditional on a hogging condition at $t = 50$ s. The plot shows the preceding sagging condition at $t = 43$ s. 88
7.8 Vertical bending moment amidships, wave period $T = 14.91$ s. 91
7.9 Vertical bending moment amidships, wave period $T = 14.32$ s. 91
7.10 Vertical bending moment amidships, wave period $T = 12.02$ s. 91
7.11 Vertical bending moment amidships, wave period $T = 11.66$ s. 91

8.1 Unfiltered, low-pass and high-pass filtered time series signal of stress (average of port and starboard side). Half an hour of data from 02 Oct 2011 starting at 16 hours showing the largest stresses at about 350 s as marked with red. 94
8.2 Filtered time series signal of stress (average of port and starboard side) from 9,400 TEU ship on 02 October 2011. The total response is equal to the sum of the WF and HF contributions. 95
8.3 Unfiltered and high pass filtered stress amidships compared to the surge motion measured in the deck at FP. Same event as Figure 8.2. 96
8.4 Surge acceleration, unfiltered, high-pass and low-pass filtered. Note difference in the vertical-axes. 97
8.5 Heave acceleration, unfiltered, high-pass and low-pass filtered. 98
8.6 Ship speed and relative wave elevation from wave radar measurements in the bow. Indication in red used for estimation of the maximum relative vertical velocity $\dot{h}$ at the instant of slamming on the lowermost plot. . . 98
8.7 Bow flare stresses measured close to FP. There are four strain gauges in each side of the bow. For comparison, the unfiltered stress amidships is illustrated in the top plot. 99
8.8 Roll and pitch. Roll is positive when rolling to starboard and pitch is positive for the bow going down. 100

8.9 Damped free vibration initiated by the impulse $I_{vertical}$ of duration $T_c = 0.5$ s and damping coefficient $\xi = 0.01$. 101
8.10 Same as Figure 8.9, but with a damping coefficient $\xi = 0.03$. 101
8.11 Filtered time series signal of stress (average of port and starboard side) from 9,400 TEU ship on 12 August 2011. The total response is equal to the sum of the WF and HF contributions. 103
8.12 Filtered time series signal of stress (starboard strain gauge) from 9,400 TEU ship on 17 December 2011. The total response is equal to the sum of the WF and HF contributions. 104
8.13 Filtered time series signal of stress (average of port and starboard side) from 8,600 TEU ship on 17 November 2010. The total response is equal to the sum of the WF and HF contributions. 105
8.14 Filtered time series signal of stress (average of port and starboard side) from 8,600 TEU ship on 30 December 2011. The total response is equal to the sum of the WF and HF contributions. 106
8.15 Filtered time series signal of stress (average of port and starboard side) from 14,000 TEU ship on 29 September 2011. The total response is equal to the sum of the WF and HF contributions. 106
8.16 Filtered time series signal of stress (average of port and starboard side) from 14,000 TEU ship on 21 July 2011. The total response is equal to the sum of the WF and HF contributions. 107
8.17 Filtered time series signal of stress (average of port and starboard side) from 4,400 TEU ship on 02 November 2007 at 11 hours. The total response is equal to the sum of the WF and HF contributions. 108
8.18 Filtered time series signal of stress (average of port and starboard side) from 4,400 TEU ship on 02 November 2007 at 16 hours. The total response is equal to the sum of the WF and HF contributions. 109
8.19 Filtered time series signal of stress (average of port and starboard side) from 4,400 TEU ship on 01 July 2008 at 19 hours, first event. The total response is equal to the sum of the WF and HF contributions. 110
8.20 Filtered time series signal of stress (average of port and starboard side) from 4,400 TEU ship on 01 July 2008 at 19 hours, second event. The total response is equal to the sum of the WF and HF contributions. . . . 110
8.21 High-frequency component (high-pass filtered) of stress measurements on starboard and port side. Data from 9,400 TEU container ship on 02 Oct 2011 at 16 hours (same time series as in Figure 8.2). 111
8.22 High-frequency component (high-pass filtered) of stress measurements on starboard and port side. Data from 9,400 TEU container ship on 12 August 2011 at 01 hours (same time series as in Figure 8.11). 111

9.1 Individual peak value probability of exceedance for sagging - WF and WF+HF response. Note, that even though the sagging moment is defined as negative, the absolute value is shown here. 9,400 TEU ship on 02 October 2011. 118
9.2 Individual peak value probability of exceedance for hogging - WF and WF+HF response. 9,400 TEU ship on 02 October 2011. 118

9.3 Weibull probability plot for the hogging bending moment - WF+HF response. 9,400 TEU ship on 02 October 2011. 119

9.4 Weibull probability plot for the hogging bending moment - WF response. 9,400 TEU ship on 02 October 2011. 119

9.5 Gumbel density function for the hogging VBM based on Weibull parameters for the individual peak for the flexible-body response in Table 9.2. The maximum measured hogging VBM during the three hours and the rule wave VBM are included for comparison. 9,400 TEU ship on 02 October 2011. 120

9.6 Weibull probability plot for the excess of the hogging bending moment. Threshold 1,761 MNm. 9,400 TEU ship on 02 October 2011. 121

9.7 Weibull probability plot for the excess of the hogging bending moment. Threshold 2,348 MNm. 9,400 TEU ship on 02 October 2011. 121

9.8 Weibull probability plot for the excess of the hogging bending moment. Threshold 2,945 MNm. 9,400 TEU ship on 02 October 2011. 121

9.9 Weibull probability plot for the excess of the hogging bending moment. Threshold 3,521 MNm. 9,400 TEU ship on 02 October 2011. 121

9.10 Weibull probability plot for the excess of the hogging bending moment. Threshold 4,108 MNm. 9,400 TEU ship on 02 October 2011. 122

9.11 Weibull probability plot for the excess of the hogging bending moment. Threshold 4,695 MNm. 9,400 TEU ship on 02 October 2011. 122

9.12 Gumbel density function for the hogging VBM for the different threshold levels given in Table 9.4. The maximum measured hogging VBM during the three hours and the rule wave VBM are included for comparison. 9,400 TEU ship on 02 October 2011. 122

9.13 Mean excess of the threshold level u as function of u. 9,400 TEU ship on 02 October 2011 with the thresholds indicated. 122

9.14 Wave-induced vertical bending moment amidships compared to the minimum design wave-induced vertical bending moments (VBM) in hogging and sagging from International Association of Classification Societies, 2010a for the 9,400 TEU ship on 02 October 2011 at 16-18 hours. Indication of the groups of peaks including the six largest peaks. 124

9.15 Normalised autocorrelation function for the WF stress signal based on one hour of data. 9,400 TEU ship on 02 October 2011. 126

9.16 The exceedance rates $\epsilon_1(x)$ (Eq. (9.8)) and $\epsilon_2(x)$ (Eq. (9.10)) for the hogging VBM. 9,400 TEU ship on 02 October 2011. 126

9.17 Gumbel density function for the hogging VBM for the different threshold levels given in Table 9.5 for the de-clustered signal. The maximum measured hogging VBM during the three hours and the rule wave VBM are included for comparison. 9,400 TEU ship on 02 October 2011. 127

9.18 Gumbel density function for the hogging VBM for the different threshold levels given in Table 9.4. The maximum measured hogging VBM during the three hours and the rule wave VBM are included for comparison. 9,400 TEU ship on 02 October 2011. Same figure as Figure 9.12 shown here for comparison. 127

9.19 ACER function $\epsilon_k(\eta)$ for six different values of k for the hogging VBM. 9,400 TEU ship on 02 October 2011. Note, that η in the legends corresponds to the level x in the equations in this chapter. 128
9.20 Gumbel density function from the parameters derived from the optimised ACER functions for six different values of k (Table 9.6). The maximum measured hogging VBM during the three hours and the rule wave VBM are included for comparison. 9,400 TEU ship on 02 October 2011. 131
9.21 Gumbel density function from the optimised ACER parameters for $k = 2$ and tail marker values corresponding to the thresholds in Table 9.5 (1,761, 2,348, 4,184 and 4,695 MNm). ACER does not yield useful results for the tail marker values corresponding to 50% and 60% of the mean of the three largest peaks. 9,400 TEU ship on 02 October 2011. 131
9.22 Individual peak value probability of exceedance for sagging - WF and WF+HF response. Note, that even though the sagging moment is defined as negative, the absolute value is shown here. 9,400 TEU ship on 12 August 2011. 133
9.23 Individual peak value probability of exceedance for hogging - WF and WF+HF response. 9,400 TEU ship on 12 August 2011. 133
9.24 Gumbel density function for the hogging VBM for the different threshold levels given in Table E.4. The maximum measured hogging VBM during the three hours is included for comparison. 9,400 TEU ship on 12 August 2011. 133
9.25 Mean excess of the threshold level u as function of u. 9,400 TEU ship on 12 August 2011. 133
9.26 The exceedance rates $\epsilon_1(x)$ (Eq. (9.8)) and $\epsilon_2(x)$ (Eq. (9.10)) for the hogging VBM. 9,400 TEU ship on 12 August 2011. 134
9.27 Individual peak value probability of exceedance for sagging - WF and WF+HF response. Note, that even though the sagging moment is defined as negative, the absolute value is shown here. 9,400 TEU ship on 17 December 2011. 135
9.28 Individual peak value probability of exceedance for hogging - WF and WF+HF response. 9,400 TEU ship on 17 December 2011. 135
9.29 Gumbel density function for the hogging VBM for the different threshold levels given in Table 9.4. The maximum measured hogging VBM during the three hours is included for comparison. 9,400 TEU ship on 17 December 2011. 136
9.30 Mean excess of the threshold level u as function of u. 9,400 TEU ship on 17 December 2011. 136
9.31 The exceedance rates $\epsilon_1(x)$ (Eq. (9.8)) and $\epsilon_2(x)$ (Eq. (9.10)) for the hogging VBM. 9,400 TEU ship on 17 December 2011. 136
9.32 Individual peak value probability of exceedance for sagging - WF and WF+HF response. Note, that even though the sagging moment is defined as negative, the absolute value is shown here. 8,600 TEU ship on 17 November 2010. 138
9.33 Individual peak value probability of exceedance for hogging - WF and WF+HF response. 8,600 TEU ship on 17 November 2010. 138

9.34 Gumbel density function for the hogging VBM for the different threshold levels given in Table E.14. The maximum measured hogging VBM during the three hours and the rule wave VBM are included for comparison. 8,600 TEU ship on 17 November 2010. 138
9.35 Mean excess of the threshold level u as function of u. 8,600 TEU ship on 17 November 2010. 138
9.36 The exceedance rates $\epsilon_1(x)$ (Eq. (9.8)) and $\epsilon_2(x)$ (Eq. (9.10)) for the hogging VBM. 8,600 TEU ship on 17 November 2010. 139
9.37 Individual peak value probability of exceedance for sagging - WF and WF+HF response. Note, that even though the sagging moment is defined as negative, the absolute value is shown here. 8,600 TEU ship on 30 December 2011. 141
9.38 Individual peak value probability of exceedance for hogging - WF and WF+HF response. 8,600 TEU ship on 30 December 2011. 141
9.39 Gumbel density function for the hogging VBM for the different threshold levels given in Table E.14. The maximum measured hogging VBM during the three hours and the rule wave VBM are included for comparison. 8,600 TEU ship on 30 December 2011. 141
9.40 Mean excess of the threshold level u as function of u. 8,600 TEU ship on 30 December 2011. 141
9.41 The exceedance rates $\epsilon_1(x)$ (Eq. (9.8)) and $\epsilon_2(x)$ (Eq. (9.10)) for the hogging VBM. 8,600 TEU ship on 30 December 2011. 142
9.42 Individual peak value probability of exceedance for sagging - WF and WF+HF response. Note, that even though the sagging moment is defined as negative, the absolute value is shown here. 14,000 TEU ship on 29 September 2011. 144
9.43 Individual peak value probability of exceedance for hogging - WF and WF+HF response. 14,000 TEU ship on 29 September 2011. 144
9.44 Gumbel density function for the hogging VBM for the different threshold levels given in Table E.25. The maximum measured hogging VBM during the three hours and the rule wave VBM are included for comparison. 14,000 TEU ship on 29 September 2011. 144
9.45 Mean excess of the threshold level u as function of u. 14,000 TEU ship on 29 September 2011. 144
9.46 The exceedance rates $\epsilon_1(x)$ (Eq. (9.8)) and $\epsilon_2(x)$ (Eq. (9.10)) for the hogging VBM. 14,000 TEU ship on 29 September 2011. 145
9.47 Individual peak value probability of exceedance for sagging - WF and WF+HF response. Note, that even though the sagging moment is defined as negative, the absolute value is shown here. 14,000 TEU ship on 21 July 2011. 146
9.48 Individual peak value probability of exceedance for hogging - WF and WF+HF response. 14,000 TEU ship on 21 July 2011. 146
9.49 Gumbel density function for the hogging VBM for the different threshold levels given in Table E.31. The maximum measured hogging VBM during the three hours and the rule wave VBM are included for comparison. 14,000 TEU ship on 21 July 2011. 147

9.50 Mean excess of the threshold level u as function of u. 14,000 TEU ship on 21 July 2011. . . . 147
9.51 The exceedance rates $\epsilon_1(x)$ (Eq. (9.8)) and $\epsilon_2(x)$ (Eq. (9.10)) for the hogging VBM. 14,000 TEU ship on 21 July 2011. . . . 147
9.52 Individual peak value probability of exceedance for sagging - WF and WF+HF response. Note, that even though the sagging moment is defined as negative, the absolute value is shown here. 4,400 TEU ship on 02 November 2007, 11-13 hours. . . . 148
9.53 Individual peak value probability of exceedance for hogging - WF and WF+HF response. 4,400 TEU ship on 02 November 2007, 11-13 hours. . . 148
9.54 Gumbel density function for the hogging VBM for the different threshold levels given in Table E.46. The maximum measured hogging VBM during the three hours and the rule wave VBM are included for comparison. 4,400 TEU ship on 02 November 2007, 11-13 hours. . . . 149
9.55 Mean excess of the threshold level u as function of u. 4,400 TEU ship on 02 November 2007, 11-13 hours. . . . 149
9.56 $\epsilon_1(x)$ (Eq. (9.8)) and $\epsilon_2(x)$ (Eq. (9.10)) for the hogging VBM. 4,400 TEU ship on 02 November 2007, 11-13 hours. . . . 150
9.57 Individual peak value probability of exceedance for sagging - WF and WF+HF response. Note, that even though the sagging moment is defined as negative, the absolute value is shown here. 4,400 TEU ship on 02 November 2007, 16-18 hours. . . . 151
9.58 Individual peak value probability of exceedance for hogging - WF and WF+HF response. 4,400 TEU ship on 02 November 2007, 16-18 hours. . . 151
9.59 Gumbel density function for the hogging VBM for the different threshold levels given in Table E.46. The maximum measured hogging VBM during the three hours and the rule wave VBM are included for comparison. 4,400 TEU ship on 02 November 2007, 16-18 hours. . . . 152
9.60 Mean excess of the threshold level u as function of u. 4,400 TEU ship on 02 November 2007, 16-18 hours. . . . 152
9.61 The exceedance rates $\epsilon_1(x)$ (Eq. (9.8)) and $\epsilon_2(x)$ (Eq. (9.10)) for the hogging VBM. 4,400 TEU ship on 02 November 2007, 16-18 hours. . . . 152
9.62 Individual peak value probability of exceedance for sagging - WF and WF+HF response. Note, that even though the sagging moment is defined as negative, the absolute value is shown here. 4,400 TEU ship on 01 July 2008. . . . 153
9.63 Individual peak value probability of exceedance for hogging - WF and WF+HF response. 4,400 TEU ship on 01 July 2008. . . . 153
9.64 Gumbel density function for the hogging VBM for the different threshold levels given in Table E.46. The maximum measured hogging VBM during the three hours and the rule wave VBM are included for comparison. 4,400 TEU ship on 01 July 2008. . . . 154
9.65 Mean excess of the threshold level u as function of u. 4,400 TEU ship on 01 July 2008. . . . 154
9.66 The exceedance rates $\epsilon_1(x)$ (Eq. (9.8)) and $\epsilon_2(x)$ (Eq. (9.10)) for the hogging VBM. 4,400 TEU ship on 01 July 2008. . . . 155

9.67 Wave-induced vertical bending moment amidships compared to the minimum design wave-induced vertical bending moments (VBM) in hogging and sagging from International Association of Classification Societies, 2010a for the 8,600 TEU ship on 17 November 2010. Indication of the groups of peaks including five of the largest peaks. 156
9.68 Wave-induced vertical bending moment amidships compared to the minimum design wave-induced vertical bending moments (VBM) in hogging and sagging from International Association of Classification Societies, 2010a for the 4,400 TEU ship on 02 November 2007. Indication of the groups of peaks including four of the largest peaks. 156
9.69 Gumbel fit from Weibull parameters, POT with threshold 50% of the mean of the three measured largest values, compared with ACER for $k = 2$ for 9,400 TEU ship, 02 October 2011. 158
9.70 Gumbel fit from Weibull parameters, POT with threshold 50% of the mean of the three measured largest values, compared with ACER for $k = 2$ for the rigid-body response only. 9,400 TEU ship, 02 October 2011. 158
9.71 Gumbel fit from Weibull parameters, POT with threshold 50% of the mean of the three measured largest values, compared with ACER for $k = 2$ for 9,400 TEU ship, 12 August 2011. 158
9.72 Gumbel fit from Weibull parameters, POT with threshold 50% of the mean of the three measured largest values, compared with ACER for $k = 2$ for 9,400 TEU ship, 17 December 2011. 158
9.73 Gumbel fit from Weibull parameters, POT with threshold 50% of the mean of the three measured largest values, compared with ACER for $k = 2$ for 8,600 TEU ship, 17 November 2010. 159
9.74 Gumbel fit from Weibull parameters, POT with threshold 50% of the mean of the three measured largest values, compared with ACER for $k = 2$ for 8,600 TEU ship, 30 December 2011. 159
9.75 Gumbel fit from Weibull parameters, POT with threshold 50% of the mean of the three measured largest values, compared with ACER for $k = 2$ for 14,000 TEU ship, 29 September 2011. 160
9.76 Gumbel fit from Weibull parameters, POT with threshold 50% of the mean of the three measured largest values, compared with ACER for $k = 2$ for 14,000 TEU ship, 21 July 2011. 160
9.77 Gumbel fit from Weibull parameters, POT with threshold 50% of the mean of the three measured largest values, compared with ACER for $k = 2$ for 4,400 TEU ship, 02 November 2007 at 11-13 hours. 161
9.78 Gumbel fit from Weibull parameters, POT with threshold 50% of the mean of the three measured largest values, compared with ACER for $k = 2$ for 4,400 TEU ship, 02 November 2007 at 16-18 hours. 161
9.79 Gumbel fit from Weibull parameters, POT with threshold 50% of the mean of the three measured largest values, compared with ACER for $k = 2$ for 4,400 TEU ship, 01 July 2008. 161

10.1 Mass distribution of the considered container ship for determination of M_2 and S_2. 166

10.2 Normalised bending moment variation S_2/M_2L for the considered container ship in 2-node vertical vibration mode. 166

10.3 Probability of exceedance for the individual peak values of the wave-induced hogging bending moment amidships using measurements, Hermite transformation with measured skewness and standard deviation and closed-form expressions for three hours for the 9,400 TEU ship on 02 October 2011. 167

11.1 Individual peak value probability of exceedance for sagging - rigid-body and flexible model response (absolute value). $H_s = 6.5$ m, heading 180 deg (head sea). 170

11.2 Individual peak value probability of exceedance for hogging - rigid-body and flexible model response. $H_s = 6.5$ m, heading 180 deg (head sea). . . 170

11.3 Individual peak value probability of exceedance for sagging - rigid-body and flexible model response (absolute value). $H_s = 6.5$ m, heading 150 deg (bow-quartering sea). 171

11.4 Individual peak value probability of exceedance for hogging - rigid-body and flexible model response. $H_s = 6.5$ m, heading 150 deg (bow-quartering sea). 171

11.5 Individual peak value probability of exceedance for sagging - rigid-body and flexible model response (absolute value). $H_s = 6.5$ m, $T_p = 12.22$ s, heading 180 deg (head sea). 172

11.6 Individual peak value probability of exceedance for hogging - rigid-body and flexible model response. $H_s = 6.5$ m, $T_p = 12.22$ s, heading 180 deg (head sea). 172

11.7 Individual peak value probability of exceedance for sagging - rigid-body and flexible model response (absolute value). $H_s = 6.5$ m, $T_p = 12.22$ s, heading 150 deg (bow-quartering sea). 173

11.8 Individual peak value probability of exceedance for hogging - rigid-body and flexible model response. $H_s = 6.5$ m, $T_p = 12.22$ s, heading 150 deg (bow-quartering sea). 173

11.9 Individual peak value probability of exceedance for sagging - rigid-body and flexible model response (absolute value). $H_s = 6.5$ m, $T_p = 9.93$ s, heading 180 deg (head sea). 174

11.10 Individual peak value probability of exceedance for hogging - rigid-body and flexible model response. $H_s = 6.5$ m, $T_p = 9.93$ s, heading 180 deg (head sea). 174

11.11 Individual peak value probability of exceedance for sagging - rigid-body and flexible model response (absolute value). $H_s = 6.5$ m, $T_p = 9.93$ s, heading 150 deg (bow-quartering sea). 175

11.12 Individual peak value probability of exceedance for hogging - rigid-body and flexible model response. $H_s = 6.5$ m, $T_p = 9.93$ s, heading 150 deg (bow-quartering sea). 175

12.1 Measured 24 hour raw stress signal and the underlying low-frequency process with frequency below 0.01 Hz for 9,400 TEU container ship on 12 August 2011 182

12.2 Measured 24 hour raw stress signal and the underlying low-frequency process with frequency below 0.01 Hz for 9,400 TEU container ship on 02 October 2011 182
12.3 4,420 TEU container ship MSC NAPOLI which broke on 18 January 2007 off the UK coast. Photo courtesy of the French Ministry of Defence. 184
12.4 8,540 TEU container ship MOL COMFORT before the vessel broke in two and sank on 17 June 2013. Photo courtsey of PTI Photo. 184
12.5 Bow of the sister ship of MOL COMFORT; MOL CREATION. Photo by Yoshihiro Matsuo, `http://shipbuild2.exblog.jp`. 186

13.1 8,600 TEU container ship SVENDBORG MÆRSK after losing over 500 containers over board in February 2014. Photo by Santiago Sáez. 189
13.2 Screendump from the decision support system SeaSense illustrating combined sea keeping criteria in a polar diagram to enable assessment of the navigable combinations of speed and heading. 190
13.3 Decision support system on the bridge of a large container ship. 190
13.4 Distance from bridge to stem and stern on 15,000 TEU container ship. Photo by Frederik Holten-Tingleff 191
13.5 Retrofit of new bulbous bows on the Maersk Boston class in 2012. Photo by Maersk Line. 194

A.1 Vessel track on 12 August 2011 in the Gulf of Aden (Going west, 24 hours).243
A.2 Vessel track on 16 September 2011 in the Gulf of Aden (Going east, 24 hours). 243
A.3 Vessel track on 20 September 2011 south of India (Going east, 24 hours). 244
A.4 Vessel track on 02 October 2011 in the South China Sea (Going north, 24 hours). 244
A.5 Vessel track on 17 December 2011 in the South China Sea (Going north, 24 hours). 244
A.6 Ship true heading from gyro compass and course over ground from GPS on 12 August 2011. 246
A.7 Ship speed through water (STW) and over ground (SOG) on 12 August 2011. 246
A.8 Wind speed on 12 August 2011. 246
A.9 Wind direction on 12 August 2011. 246
A.10 Current speed for 12 August 2011. 247
A.11 Current direction for 12 August 2011. 247
A.12 Logged water depth on 12 August 2011. Depths above 100 m cannot be measured. 247
A.13 Significant and maximum wave height from WaMoS on 12 August 2011, 24 hours. 247
A.14 Significant wave height for swell and wind driven component from WaMoS on 12 August 2011, 24 hours. 247
A.15 Peak periods from WaMoS on 12 August 2011, 24 hours. 248
A.16 Wave length with respect to T_p from WaMoS on 12 August 2011, 24 hours.248
A.17 Mean and peak wave direction from WaMoS on 12 August 2011, 24 hours. Given as coming from compass rose direction. 248

A.18 Peak wave direction for swell and wind driven component from WaMoS on 12 August 2011, 24 hours. Given as coming from compass rose direction. 248

A.19 Relative mean and peak wave direction from WaMoS on 12 August 2011, 24 hours. 180 deg is head sea. 249

A.20 Relative peak wave directions for swell and wind components from WaMoS on 12 August 2011, 24 hours. 180 deg is head sea. 249

A.21 Spreading parameter for Jonswap spectrum from WaMoS for 12 August 2011, 24 hours. 249

A.22 Wave height from Radac for 12 August 2011, 24 hours. 249

A.23 Ship true heading from gyro compass and course over ground from GPS on 16 September 2011. 250

A.24 Ship speed through water (STW) and over ground (SOG) on 16 September 2011. 250

A.25 Wind speed on 16 September 2011. 250

A.26 Wind direction on 16 September 2011. 250

A.27 Current speed for 16 September 2011. 251

A.28 Current direction for 16 September 2011. 251

A.29 Logged water depth on 16 September 2011. Depths above 100 m cannot be measured. 251

A.30 Significant and maximum wave height from WaMoS on 16 September 2011, 24 hours. 251

A.31 Significant wave height for swell and wind driven component from WaMoS on 16 September 2011, 24 hours. 251

A.32 Peak periods from WaMoS on 16 September 2011, 24 hours. 252

A.33 Wave length with respect to T_p from WaMoS on 16 September 2011, 24 hours. 252

A.34 Mean and peak wave direction from WaMoS on 16 September 2011, 24 hours. Given as coming from compass rose direction. 252

A.35 Peak wave direction for swell and wind driven component from WaMoS on 16 September 2011, 24 hours. Given as coming from compass rose direction. 252

A.36 Relative mean and peak wave direction from WaMoS on 16 September 2011, 24 hours. 180 deg is head sea. 253

A.37 Relative peak wave directions for swell and wind components from WaMoS on 16 September 2011, 24 hours. 180 deg is head sea. 253

A.38 Spreading parameter for Jonswap spectrum from WaMoS for 16 September 2011, 24 hours. 253

A.39 Wave height from Radac for 16 September 2011, 24 hours. 253

A.40 Ship true heading from gyro compass and course over ground from GPS on 20 September 2011. 254

A.41 Ship speed through water (STW) and over ground (SOG) on 20 September 2011. 254

A.42 Wind speed on 20 September 2011. 254

A.43 Wind direction on 20 September 2011. 254

A.44 Current speed for 20 September 2011. 255

A.45 Current direction for 20 September 2011. 255

A.46 Logged water depth on 20 September 2011. Depths above 100 m cannot be measured. 255
A.47 Significant and maximum wave height from WaMoS on 20 September 2011, 24 hours. 255
A.48 Significant wave height for swell and wind driven component from WaMoS on 20 September 2011, 24 hours. 255
A.49 Peak periods from WaMoS on 20 September 2011, 24 hours. 256
A.50 Wave length with respect to T_p from WaMoS on 20 September 2011, 24 hours. 256
A.51 Mean and peak wave direction from WaMoS on 20 September 2011, 24 hours. Given as coming from compass rose direction. 256
A.52 Peak wave direction for swell and wind driven component from WaMoS on 20 September 2011, 24 hours. Given as coming from compass rose direction. 256
A.53 Relative mean and peak wave direction from WaMoS on 20 September 2011, 24 hours. 180 deg is head sea. 257
A.54 Relative peak wave directions for swell and wind components from WaMoS on 20 September 2011, 24 hours. 180 deg is head sea. 257
A.55 Spreading parameter for Jonswap spectrum from WaMoS for 20 September 2011, 24 hours. 257
A.56 Wave height from Radac for 20 September 2011, 24 hours. 257
A.57 Ship true heading from gyro compass and course over ground from GPS on 02 October 2011. 258
A.58 Ship speed through water (STW) and over ground (SOG) on 02 October 2011. 258
A.59 Wind speed on 02 October 2011. 258
A.60 Wind direction on 02 October 2011. 258
A.61 Current speed for 02 October 2011. 259
A.62 Current direction for 02 October 2011. 259
A.63 Logged water depth on 02 October 2011. Depths above 100 m cannot be measured. 259
A.64 Significant and maximum wave height from WaMoS on 02 October 2011, 24 hours. 259
A.65 Significant wave height for swell and wind driven component from WaMoS on 02 October 2011, 24 hours. 259
A.66 Peak periods from WaMoS on 02 October 2011, 24 hours. 260
A.67 Wave length with respect to T_p from WaMoS on 02 October 2011, 24 hours. 260
A.68 Mean and peak wave direction from WaMoS on 02 October 2011, 24 hours. Given as coming from compass rose direction. 260
A.69 Peak wave direction for swell and wind driven component from WaMoS on 02 October 2011, 24 hours. Given as coming from compass rose direction. 260
A.70 Relative mean and peak wave direction from WaMoS on 02 October 2011, 24 hours. 180 deg is head sea. 261

A.71 Relative peak wave directions for swell and wind components from WaMoS on 02 October 2011, 24 hours. 180 deg is head sea. 261
A.72 Spreading parameter for Jonswap spectrum from WaMoS for 02 October 2011, 24 hours. 261
A.73 Wave height from Radac for 02 October 2011, 24 hours. 261
A.74 Ship true heading from gyro compass and course over ground from GPS on 17 December 2011. 262
A.75 Ship speed through water (STW) and over ground (SOG) on 17 December 2011. 262
A.76 Wind speed on 17 December 2011. 262
A.77 Wind direction on 17 December 2011. 262
A.78 Current speed for 17 December 2011. 263
A.79 Current direction for 17 December 2011. 263
A.80 Logged water depth on 17 December 2011. Depths above 100 m cannot be measured. 263
A.81 Significant and maximum wave height from WaMoS on 17 December 2011, 24 hours. 263
A.82 Significant wave height for swell and wind driven component from WaMoS on 17 December 2011, 24 hours. 263
A.83 Peak periods from WaMoS on 17 December 2011, 24 hours. 264
A.84 Wave length with respect to T_p from WaMoS on 17 December 2011, 24 hours. 264
A.85 Mean and peak wave direction from WaMoS on 17 December 2011, 24 hours. Given as coming from compass rose direction. 264
A.86 Peak wave direction for swell and wind driven component from WaMoS on 17 December 2011, 24 hours. Given as coming from compass rose direction. 264
A.87 Relative mean and peak wave direction from WaMoS on 17 December 2011, 24 hours. 180 deg is head sea. 265
A.88 Relative peak wave directions for swell and wind components from WaMoS on 17 December 2011, 24 hours. 180 deg is head sea. 265
A.89 Spreading parameter for Jonswap spectrum from WaMoS for 17 December 2011, 24 hours. 265
A.90 Wave height from Radac for 17 December 2011, 24 hours. 265
A.91 FFT of the heave response (measured in m). Smoothing using a Parzen window function is applied. 269
A.92 RAO for heave. 180 deg is head sea. 269
A.93 FFT of the sway response (measured in m). Smoothing using a Parzen window function is applied. 270
A.94 RAO for sway. 180 deg is head sea. 270
A.95 FFT of the pitch response (measured in deg). Smoothing using a Parzen window function is applied. 270
A.96 RAO for pitch. 180 deg is head sea. 270
A.97 FFT of the roll response (measured in deg). Smoothing using a Parzen window function is applied. 271
A.98 RAO for roll. 180 deg is head sea. 271

A.99 FFT of the vertical bending moment amidships (measured in MNm). Smoothing using a Parzen window function is applied. 271
A.100 RAO of the vertical bending moment amidships. 180 is head sea. 271
A.101 FFT of the vertical velocity. Smoothing using a Parzen window function is applied. One hour of data from 02 October 2011 at 11 hours. 272
A.102 FFT of the vertical acceleration. Smoothing using a Parzen window function is applied. One hour of data from 02 October 2011 at 11 hours. 272
A.103 FFT of the transverse velocity. Smoothing using a Parzen window function is applied. One hour of data from 02 October 2011 at 11 hours. . . 272
A.104 FFT of the transverse acceleration. Smoothing using a Parzen window function is applied. One hour of data from 02 October 2011 at 11 hours. 272
A.105 FFT of the pitch rate. Smoothing using a Parzen window function is applied. One hour of data from 02 October 2011 at 11 hours. 272
A.106 FFT of the pitch acceleration. Smoothing using a Parzen window function is applied. One hour of data from 02 October 2011 at 11 hours. 272
A.107 FFT of the roll rate. Smoothing using a Parzen window function is applied. One hour of data from 02 October 2011 at 11 hours. 273
A.108 FFT of the roll acceleration response. Smoothing using a Parzen window function is applied. One hour of data from 02 October 2011 at 11 hours. 273
A.109 Significant wave height from Bayesian and parametric modelling, from directional wave radar (WaMoS) and the down-looking wave radar in the bow (Radac). Figure from Nielsen et al. (2013). 12 August 2011. 274
A.110 Zero-upcrossing wave period T_z from Bayesian and parametric modelling, from directional wave radar (WaMoS) and the down-looking wave radar in the bow (Radac). Figure from Nielsen et al. (2013). 12 August 2011. . 274
A.111 Peak wave period T_p from Bayesian and parametric modelling, from directional wave radar (WaMoS) and the down-looking wave radar in the bow (Radac). Figure from Nielsen et al. (2013). 12 August 2011. 274
A.112 Relative wave direction χ from Bayesian and parametric modelling and from directional wave radar (WaMoS). The down-looking wave radar system (Radac) cannot estimate the relative wave direction). Figure from Nielsen et al. (2013). 12 August 2011. 274
A.113 Significant wave height from Bayesian and parametric modelling, from directional wave radar (WaMoS) and the down-looking wave radar in the bow (Radac). Figure from Nielsen et al. (2013). 16 September 2011. . . 275
A.114 Zero-upcrossing wave period T_z from Bayesian and parametric modelling, from directional wave radar (WaMoS) and the down-looking wave radar in the bow (Radac). Figure from Nielsen et al. (2013). 16 September 2011.275
A.115 Peak wave period T_p from Bayesian and parametric modelling, from directional wave radar (WaMoS) and the down-looking wave radar in the bow (Radac). Figure from Nielsen et al. (2013). 16 September 2011. . . 275
A.116 Relative wave direction χ from Bayesian and parametric modelling and from directional wave radar (WaMoS). The down-looking wave radar system (Radac) cannot estimate the relative wave direction). Figure from Nielsen et al. (2013). 16 September 2011. 275

A.117 Significant wave height from Bayesian and parametric modelling, from directional wave radar (WaMoS) and the down-looking wave radar in the bow (Radac). Figure from Nielsen et al. (2013). 20 September 2011. . . 276
A.118 Zero-upcrossing wave period T_z from Bayesian and parametric modelling, from directional wave radar (WaMoS) and the down-looking wave radar in the bow (Radac). Figure from Nielsen et al. (2013). 20 September 2011.276
A.119 Peak wave period T_p from Bayesian and parametric modelling, from directional wave radar (WaMoS) and the down-looking wave radar in the bow (Radac). Figure from Nielsen et al. (2013). 20 September 2011. . . 276
A.120 Relative wave direction χ from Bayesian and parametric modelling and from directional wave radar (WaMoS). The down-looking wave radar system (Radac) cannot estimate the relative wave direction). Figure from Nielsen et al. (2013). 20 September 2011. 276
A.121 Significant wave height from Bayesian and parametric modelling, from directional wave radar (WaMoS) and the down-looking wave radar in the bow (Radac). Figure from Nielsen et al. (2013). 02 October 2011. 277
A.122 Zero-upcrossing wave period T_z from Bayesian and parametric modelling, from directional wave radar (WaMoS) and the down-looking wave radar in the bow (Radac). Figure from Nielsen et al. (2013). 02 October 2011. 277
A.123 Peak wave period T_p from Bayesian and parametric modelling, from directional wave radar (WaMoS) and the down-looking wave radar in the bow (Radac). Figure from Nielsen et al. (2013). 02 October 2011. 277
A.124 Relative wave direction χ from Bayesian and parametric modelling and from directional wave radar (WaMoS). The down-looking wave radar system (Radac) cannot estimate the relative wave direction). Figure from Nielsen et al. (2013). 02 October 2011. 277
A.125 Vessel track on 05 February 2010 (Going north, 24 hours). 278
A.126 Vessel track on 01 December 2010 (Going east, 24 hours). 278
A.127 Vessel track on 30 December 2011 (Going west, 24 hours). 278
A.128 Ship course over ground (COG) compass heading on 05 February 2010. . 279
A.129 Ship speed over ground (SOG) and speed through water (STW) on 05 February 2010. 279
A.130 Wind speed on 05 February 2010. Not corrected for ship speed. 279
A.131 Wind direction relative to ship on 05 February 2010. 0 deg is head wind. 279
A.132 Ship course over ground (COG) compass heading on 07 November 2010. 280
A.133 Wind direction relative to ship on 07 November 2010. 0 deg is head wind.280
A.134 Ship course over ground (COG) compass heading on 08 November 2010. 280
A.135 Wind direction relative to ship on 08 November 2010. 0 deg is head wind.280
A.136 Ship course over ground (COG) compass heading on 17 November 2010. 281
A.137 Wind direction relative to ship on 17 November 2010. 0 deg is head wind.281
A.138 Ship course over ground (COG) compass heading on 18 November 2010. 281
A.139 Wind direction relative to ship on 18 November 2010. 0 deg is head wind.281
A.140 Ship course over ground (COG) compass heading on 01 December 2010. 282
A.141 Ship speed over ground (SOG) and speed through water (STW) on 01 December 2010. 282
A.142 Wind direction relative to ship on 01 December 2010. 0 deg is head wind. 282

A.143 Ship course over ground (COG) compass heading on 30 December 2011. 283
A.144 Ship speed over ground (SOG) and speed through water (STW) on 30 December 2011. 283
A.145 Wind speed on 30 December 2011. Not corrected for ship speed. 283
A.146 Wind direction relative to ship on 30 December 2011. 0 deg is head wind. 283
A.147 One year stress measurement (2010), port and starboard side, from 30 minute statistical file from 8,600 TEU container ship. Data from 50-150 days is regarded unreliable. 284
A.148 One year stress measurement (2011), port and starboard side, from 30 minute statistical file from 8,600 TEU container ship. 285
A.149 Ship course over ground (COG) and compass heading on 21 July 2011. . 285
A.150 Ship speed over ground on 21 July 2011. 285
A.151 Wind speed on 21 July 2011. Not corrected for ship speed and heading. 286
A.152 Wind direction relative to ship on 21 July 2011. 0 deg is head wind. Not corrected for ship speed and heading. 286

B.1 WaMoS II wave radar installed on board the 9,400 TEU container ship. Photo by the author. 287
B.2 Location of the WaMoS radar with possible sources of interference. Illustration from Fresser (2011) 288
B.3 Wiring Diagram for the WaMoS II wave radar. Illustration from Fresser (2011) 288
B.4 WaMoS II data processing flow chart. From Fresser (2011) 289
B.5 Location of the two Radac sensors on board the 9,400 TEU ship. Illustration from Fresser (2011) 290
B.6 Port side Radac sensor on board the 9,400 TEU ship. Photo by the author. 290
B.7 Acceleration sensor at frame 124 on board the 9,400 TEU ship. Illustration courtesy of MARIN. 291
B.8 Specifications of acceleration sensors on board the 9,400 TEU ship. Courtesy of MARIN. 291
B.9 Principle of the long base strain gauges used on board the 9,400 TEU ship. Illustration from Koning (2007). 293
B.10 Specifications of the long base strain gauges used on board the 9,400 TEU ship. Courtesy of MARIN. 294
B.11 Location of strain gauges at frame 102 on board the 9,400 TEU ship. Illustration from Koning (2010). 295
B.12 Strain gauge amidships at the location illustrated in Figure B.11. Photo by Gregoire Wencesla Guitard. 296
B.13 Principle of the Wheatstone bridge-type strain gauge mounted in the bow of the 9,400 TEU ship. 296
B.14 Location of strain gauges at frame 154/155 in the bow of the 9,400 TEU ship. Illustration from Koning (2010). 297
B.15 Location of strain sensors at frame 101/102 (amidships) the 8,600 TEU container ship. Illustration from Heggelund et al. (2011). 298
B.16 Location of strain sensors at frame 101/102 (amidships) in the deck of the 8,600 TEU container ship. Illustration from Heggelund et al. (2011). 299

C.1 Fatigue damage per hour during 24 hours on 12 August 2011 estimated using rainflow counting and the Palmgren-Miner rule. 300

C.2 Fatigue damage during 24 hours on 12 August 2011 estimated using narrow-banded spectral analysis (one narrow-banded process). 300

C.3 Fatigue damage during 24 hours on 12 August 2011 estimated using narrow-banded spectral analysis assuming two Gaussian narrow-banded processes (Jiao and Moan (1990)). 301

C.4 Fatigue damage during 24 hours on 12 August 2011 estimated using narrow-banded spectral analysis assuming two Gaussian, narrow-banded processes (Low (2010)). 301

C.5 Comparison of total estimated fatigue damage per hour during 24 hours on 12 August 2011. 301

C.6 Comparison of estimated fatigue damage for the two envelope processes (Eq. (6.4) and Eq. (6.20)) with the total estimate from RFC for 12 August 2011. 301

C.7 Bandwidth parameters, δ (Eq. (6.10)), for the total, WF and HF part of the process for 12 August 2011. 302

C.8 Relative dominance of the HF process, θ (Eq. (6.8)), for 12 August 2011. 302

C.9 Spacing between low and high frequency parts, β (Eq. (6.9)), for 12 August 2011. 302

C.10 High frequency (HF) contribution to the total estimated fatigue damage per hour for 12 August 2011 using RFC. 302

C.11 Fatigue damage per hour during 24 hours on 16 September 2011 estimated using rainflow counting and the Palmgren-Miner rule. 303

C.12 Fatigue damage during 24 hours on 16 September 2011 estimated using narrow-banded spectral analysis (one narrow-banded process). 303

C.13 Fatigue damage during 24 hours on 16 September 2011 estimated using narrow-banded spectral analysis assuming two Gaussian narrow-banded processes (Jiao and Moan (1990)). 303

C.14 Fatigue damage during 24 hours on 16 September 2011 estimated using narrow-banded spectral analysis assuming two Gaussian, narrow-banded processes (Low (2010)). 303

C.15 Comparison of total estimated fatigue damage per hour during 24 hours on 16 September 2011. 304

C.16 Comparison of estimated fatigue damage for the two envelope processes (Eq. (6.4) and Eq. (6.20)) with the total estimate from RFC for 16 September 2011. 304

C.17 Bandwidth parameters, δ (Eq. (6.10)), for the total, WF and HF part of the process for 16 September 2011. 304

C.18 Relative dominance of the HF process, θ (Eq. (6.8)), for 16 September 2011. 304

C.19 Spacing between low and high frequency parts, β (Eq. (6.9)), for 16 September 2011. 305

C.20 High frequency (HF) contribution to the total estimated fatigue damage per hour for 16 September 2011 using RFC. 305

C.21 Fatigue damage per hour during 24 hours on 20 September 2011 estimated using rainflow counting and the Palmgren-Miner rule. 306
C.22 Fatigue damage during 24 hours on 20 September 2011 estimated using narrow-banded spectral analysis (one narrow-banded process). 306
C.23 Fatigue damage during 24 hours on 20 September 2011 estimated using narrow-banded spectral analysis assuming two Gaussian narrow-banded processes (Jiao and Moan (1990)). 306
C.24 Fatigue damage during 24 hours on 20 September 2011 estimated using narrow-banded spectral analysis assuming two Gaussian, narrow-banded processes (Low (2010)). 306
C.25 Comparison of total estimated fatigue damage per hour during 24 hours on 20 September 2011. 307
C.26 Comparison of estimated fatigue damage for the two envelope processes (Eq. (6.4) and Eq. (6.20)) with the total estimate from RFC for 20 September 2011. 307
C.27 Bandwidth parameters, δ (Eq. (6.10)), for the total, WF and HF part of the process for 20 September 2011. 307
C.28 Relative dominance of the HF process, θ (Eq. (6.8)), for 20 September 2011. 307
C.29 Spacing between low and high frequency parts, β (Eq. (6.9)), for 20 September 2011. 308
C.30 High frequency (HF) contribution to the total estimated fatigue damage per hour for 20 September 2011 using RFC. 308
C.31 Fatigue damage per hour during 24 hours on 02 October 2011 estimated using rainflow counting and the Palmgren-Miner rule. 309
C.32 Fatigue damage during 24 hours on 02 October 2011 estimated using narrow-banded spectral analysis (one narrow-banded process). 309
C.33 Fatigue damage during 24 hours on 02 October 2011 estimated using narrow-banded spectral analysis assuming two Gaussian narrow-banded processes (Jiao and Moan (1990)). 309
C.34 Fatigue damage during 24 hours on 02 October 2011 estimated using narrow-banded spectral analysis assuming two Gaussian, narrow-banded processes (Low (2010)). 309
C.35 Comparison of total estimated fatigue damage per hour during 24 hours on 02 October 2011. 310
C.36 Comparison of estimated fatigue damage for the two envelope processes (Eq. (6.4) and Eq. (6.20)) with the total estimate from RFC for 02 October 2011. 310
C.37 Bandwidth parameters, δ (Eq. (6.10)), for the total, WF and HF part of the process for 02 October 2011. 310
C.38 Relative dominance of the HF process, θ (Eq. (6.8)), for 02 October 2011. 310
C.39 Spacing between low and high frequency parts, β (Eq. (6.9)), for 02 October 2011. 311
C.40 High frequency (HF) contribution to the total estimated fatigue damage per hour for 02 October 2011 using RFC. 311

C.41 Fatigue damage per hour during 24 hours on 05 February 2010 estimated using rainflow counting and the Palmgren-Miner rule. 312
C.42 Fatigue damage during 24 hours on 05 February 2010 estimated using narrow-banded, spectral analysis (one narrow-banded process). 312
C.43 Fatigue damage during 24 hours on 05 February 2010 estimated using narrow-banded spectral analysis assuming two Gaussian narrow-banded processes (Jiao and Moan (1990)). 312
C.44 Fatigue damage during 24 hours on 05 February 2010 estimated using narrow-banded spectral analysis assuming two Gaussian, narrow-banded processes (Low (2010)). 312
C.45 Comparison of total estimated fatigue damage per hour during 24 hours on 05 February 2010. 313
C.46 Comparison of estimated fatigue damage for the two envelope processes (Eq. (6.4) and Eq. (6.20)) with the total estimate from RFC for 05 February 2010. 313
C.47 Bandwidth parameters, δ (Eq. (6.10)), for the total, WF and HF part of the process for 05 February 2010. 313
C.48 Relative dominance of the HF process, θ (Eq. (6.8)), for 05 February 2010. 313
C.49 Spacing between low and high frequency parts, β (Eq. (6.9)), for 05 February 2010. 314
C.50 High frequency (HF) contribution to the total estimated fatigue damage per hour for 05 February 2010 using RFC. 314
C.51 Fatigue damage per hour during 24 hours on 07 November 2010 estimated using rainflow counting and the Palmgren-Miner rule. 315
C.52 Fatigue damage during 24 hours on 07 November 2010 estimated using narrow-banded, spectral analysis (one narrow-banded process). 315
C.53 Fatigue damage during 24 hours on 07 November 2010 estimated using narrow-banded spectral analysis assuming two Gaussian narrow-banded processes (Jiao and Moan (1990)). 315
C.54 Fatigue damage during 24 hours on 07 November 2010 estimated using narrow-banded spectral analysis assuming two Gaussian, narrow-banded processes (Low (2010)). 315
C.55 Comparison of total estimated fatigue damage per hour during 24 hours on 07 November 2010. 316
C.56 Comparison of estimated fatigue damage for the two envelope processes (Eq. (6.4) and Eq. (6.20)) with the total estimate from RFC for 07 November 2010. 316
C.57 Bandwidth parameters, δ (Eq. (6.10)), for the total, WF and HF part of the process for 07 November 2010. 316
C.58 Relative dominance of the HF process, θ (Eq. (6.8)), for 07 November 2010. 316
C.59 Spacing between low and high frequency parts, β (Eq. (6.9)), for 07 November 2010. 317
C.60 High frequency (HF) contribution to the total estimated fatigue damage per hour for 07 November 2010 using RFC. 317

C.61 Fatigue damage per hour during 24 hours on 08 November 2010 estimated using rainflow counting and the Palmgren-Miner rule. 318
C.62 Fatigue damage during 24 hours on 08 November 2010 estimated using narrow-banded, spectral analysis (one narrow-banded process). 318
C.63 Fatigue damage during 24 hours on 08 November 2010 estimated using narrow-banded spectral analysis assuming two Gaussian narrow-banded processes (Jiao and Moan (1990)). 318
C.64 Fatigue damage during 24 hours on 08 November 2010 estimated using narrow-banded spectral analysis assuming two Gaussian, narrow-banded processes (Low (2010)). 318
C.65 Comparison of total estimated fatigue damage per hour during 24 hours on 08 November 2010. 319
C.66 Comparison of estimated fatigue damage for the two envelope processes (Eq. (6.4) and Eq. (6.20)) with the total estimate from RFC for 08 November 2010. 319
C.67 Bandwidth parameters, δ (Eq. (6.10)), for the total, WF and HF part of the process for 08 November 2010. 319
C.68 Relative dominance of the HF process, θ (Eq. (6.8)), for 08 November 2010. 319
C.69 Spacing between low and high frequency parts, β (Eq. (6.9)), for 08 November 2010. 320
C.70 High frequency (HF) contribution to the total estimated fatigue damage per hour for 08 November 2010 using RFC. 320
C.71 Fatigue damage per hour during 24 hours on 17 November 2010 estimated using rainflow counting and the Palmgren-Miner rule. 321
C.72 Fatigue damage during 24 hours on 17 November 2010 estimated using narrow-banded, spectral analysis (one narrow-banded process). 321
C.73 Fatigue damage during 24 hours on 17 November 2010 estimated using narrow-banded spectral analysis assuming two Gaussian narrow-banded processes (Jiao and Moan (1990)). 321
C.74 Fatigue damage during 24 hours on 17 November 2010 estimated using narrow-banded spectral analysis assuming two Gaussian, narrow-banded processes (Low (2010)). 321
C.75 Comparison of total estimated fatigue damage per hour during 24 hours on 17 November 2010. 322
C.76 Comparison of estimated fatigue damage for the two envelope processes (Eq. (6.4) and Eq. (6.20)) with the total estimate from RFC for 17 November 2010. 322
C.77 Bandwidth parameters, δ (Eq. (6.10)), for the total, WF and HF part of the process for 17 November 2010. 322
C.78 Relative dominance of the HF process, θ (Eq. (6.8)), for 17 November 2010. 322
C.79 Spacing between low and high frequency parts, β (Eq. (6.9)), for 17 November 2010. 323
C.80 High frequency (HF) contribution to the total estimated fatigue damage per hour for 17 November 2010 using RFC. 323

C.81 Fatigue damage per hour during 24 hours on 18 November 2010 estimated using rainflow counting and the Palmgren-Miner rule. 324

C.82 Fatigue damage during 24 hours on 18 November 2010 estimated using narrow-banded, spectral analysis (one narrow-banded process). 324

C.83 Fatigue damage during 24 hours on 18 November 2010 estimated using narrow-banded spectral analysis assuming two Gaussian narrow-banded processes (Jiao and Moan (1990)). 324

C.84 Fatigue damage during 24 hours on 18 November 2010 estimated using narrow-banded spectral analysis assuming two Gaussian, narrow-banded processes (Low (2010)). 324

C.85 Comparison of total estimated fatigue damage per hour during 24 hours on 18 November 2010. 325

C.86 Comparison of estimated fatigue damage for the two envelope processes (Eq. (6.4) and Eq. (6.20)) with the total estimate from RFC for 18 November 2010. 325

C.87 Bandwidth parameters, δ (Eq. (6.10)), for the total, WF and HF part of the process for 18 November 2010. 325

C.88 Relative dominance of the HF process, θ (Eq. (6.8)), for 18 November 2010. 325

C.89 Spacing between low and high frequency parts, β (Eq. (6.9)), for 18 November 2010. 326

C.90 High frequency (HF) contribution to the total estimated fatigue damage per hour for 18 November 2010 using RFC. 326

C.91 Fatigue damage per hour during 24 hours on 01 December 2010 estimated using rainflow counting and the Palmgren-Miner rule. 327

C.92 Fatigue damage during 24 hours on 01 December 2010 estimated using narrow-banded, spectral analysis (one narrow-banded process). 327

C.93 Fatigue damage during 24 hours on 01 December 2010 estimated using narrow-banded spectral analysis assuming two Gaussian narrow-banded processes (Jiao and Moan (1990)). 327

C.94 Fatigue damage during 24 hours on 01 December 2010 estimated using narrow-banded spectral analysis assuming two Gaussian, narrow-banded processes (Low (2010)). 327

C.95 Comparison of total estimated fatigue damage per hour during 24 hours on 01 December 2010. 328

C.96 Comparison of estimated fatigue damage for the two envelope processes (Eq. (6.4) and Eq. (6.20)) with the total estimate from RFC for 01 December 2010. 328

C.97 Bandwidth parameters, δ (Eq. (6.10)), for the total, WF and HF part of the process for 01 December 2010. 328

C.98 Relative dominance of the HF process, θ (Eq. (6.8)), for 01 December 2010. 328

C.99 Spacing between low and high frequency parts, β (Eq. (6.9)), for 01 December 2010. 329

C.100 High frequency (HF) contribution to the total estimated fatigue damage per hour for 01 December 2010 using RFC. 329

C.101 Fatigue damage per hour during 24 hours on 30 December 2011 estimated using rainflow counting and the Palmgren-Miner rule. 330
C.102 Fatigue damage during 24 hours on 30 December 2011 estimated using narrow-banded, spectral analysis (one narrow-banded process). 330
C.103 Fatigue damage during 24 hours on 30 December 2011 estimated using narrow-banded spectral analysis assuming two Gaussian narrow-banded processes (Jiao and Moan (1990)). 330
C.104 Fatigue damage during 24 hours on 30 December 2011 estimated using narrow-banded spectral analysis assuming two Gaussian, narrow-banded processes (Low (2010)). 330
C.105 Comparison of total estimated fatigue damage per hour during 24 hours on 30 December 2011. 331
C.106 Comparison of estimated fatigue damage for the two envelope processes (Eq. (6.4) and Eq. (6.20)) with the total estimate from RFC for 30 December 2011. 331
C.107 Bandwidth parameters, δ (Eq. (6.10)), for the total, WF and HF part of the process for 30 December 2011. 331
C.108 Relative dominance of the HF process, θ (Eq. (6.8)), for 30 December 2011. 331
C.109 Spacing between low and high frequency parts, β (Eq. (6.9)), for 30 December 2011. 332
C.110 High frequency (HF) contribution to the total estimated fatigue damage per hour for 30 December 2011 using RFC. 332
C.111 Fatigue damage during 24 hours on 12 August 2011. $T_0 = 2$ s. 334
C.112 Fatigue damage during 24 hours on 12 August 2011. $T_0 = 5$ s. 334
C.113 Fatigue damage during 24 hours on 12 August 2011. $T_0 = 10$ s. 334
C.114 Fatigue damage during 24 hours on 12 August 2011. $T_0 = 20$ s. 334
C.115 Fatigue damage during 24 hours on 12 August 2011. $T_0 = 60$ s. 335
C.116 Fatigue damage during 24 hours on 12 August 2011. $T_0 = 120$ s. 335
C.117 Fatigue damage during 24 hours on 02 October 2011. $T_0 = 2$ s. 336
C.118 Fatigue damage during 24 hours on 02 October 2011. $T_0 = 5$ s. 336
C.119 Fatigue damage during 24 hours on 02 October 2011. $T_0 = 10$ s. 336
C.120 Fatigue damage during 24 hours on 02 October 2011. $T_0 = 20$ s. 336
C.121 Fatigue damage during 24 hours on 02 October 2011. $T_0 = 60$ s. 337
C.122 Fatigue damage during 24 hours on 02 October 2011. $T_0 = 120$ s. 337

D.1 Filtered time series signal of stress (average of port and starboard side) from 9,400 TEU ship. Extract of data from 02 Oct 2011 at 16 hours. . . 338
D.2 Filtered time series signal of stress (average of port and starboard side) from 9,400 TEU ship. Half an hour of data from 12 August 2011 starting at 01 hours. The largest stresses are found at about 3,300 s. 339
D.3 Filtered time series signal of stress (average of starboard and port side) from 9,400 TEU ship. 150 s of data from 12 August 2011 at 01 hours. . . 340
D.4 Filtered time series signal of stress from 9,400 TEU ship. Half an hour of data from 17 December 2011 starting at 14 hours. The largest stresses are found at about 455 s. 341

D.5 Filtered time series signal of stress from 9,400 TEU ship. 300 s of data from 17 December 2011 at 14 hours. 342
D.6 Unfiltered, low-pass and high-pass filtered time series signal of stress (average of port and starboard side) for 8,600 TEU ship. Half an hour of data from 17 November 2010 between 21 and 22 hours. 343
D.7 Filtered time series signal of stress (average of port and starboard side) from the 8,600 TEU vessel. Extract of data from 17 November 2010 at 21-22 hours. 344
D.8 Unfiltered, low-pass and high-pass filtered time series signal of stress (average of port and starboard side) for 8,600 TEU ship. Half an hour of data from 30 December 2011 at 7 hours. 345
D.9 Filtered time series signal of stress (average of port and starboard side) from the 8,600 TEU vessel. Extract of data from 30 December 2011 at 7 hours. 346
D.10 Filtered time series signal of stress (average of port and starboard side) from the 14,000 TEU vessel. Extract of data from 29 September 2011 around 10 hours. 347
D.11 Unfiltered time series signal of stress from port and starboard side from 14,000 TEU vessel. Extract of data from 29 September 2011. 347
D.12 Filtered time series signal of stress (average of port and starboard side) from the 14,000 TEU vessel. Extract of data from 21 July 2011. 348
D.13 Unfiltered time series signal of stress from port and starboard side from 14,000 TEU vessel. Extract of data from 21 July 2011. 348
D.14 Filtered time series signal of stress (average of port and starboard side) from 4,400 TEU ship. Half an hour of data from 02 November 2007 at 11 hours. 349
D.15 Filtered time series signal of stress (average of port and starboard side) from 4,400 TEU ship on 02 November 2007 at 11 hours. 350
D.16 Filtered time series signal of stress (average of port and starboard side) from 4,400 TEU ship. Half an hour of data from 02 November 2007 at 16 hours. 351
D.17 Filtered time series signal of stress (average of port and starboard side) from 4,400 TEU ship on 02 November 2007 at 16 hours. 351
D.18 Filtered time series signal of stress (average of port and starboard side) from 4,400 TEU ship. Half an hour of data from 01 July 2008 at 19 hours. 352
D.19 Filtered time series signal of stress (average of port and starboard side) from 4,400 TEU ship. 353
D.20 Filtered time series signal of stress (average of port and starboard side) from 4,400 TEU ship. 353
D.21 High-frequency component (high-pass filtered) of stress measurements on starboard and port side. Data from 8,600 TEU container ship on 17 November 2010 (same time series as in Figure 8.13). 354
D.22 High-frequency component (high-pass filtered) of stress measurements on starboard and port side. Data from 8,600 TEU container ship on 30 December 2011 (same time series as in Figure 8.14). 354

D.23 High-frequency component (high-pass filtered) of stress measurements on starboard and port side. Data from 29 September 2011 for 14,000 TEU ship. (same time series as in Figure 8.15). 354
D.24 High-frequency component (high-pass filtered) of stress measurements on starboard and port side. Data from 21 July 2011 for 14,000 TEU ship. (same time series as in Figure 8.16). 354
D.25 High-frequency component (high-pass filtered) of stress measurements on starboard and port side. Data from 02 November 2007 for 4,400 TEU ship. (same time series as in Figure 8.17). 355
D.26 High-frequency component (high-pass filtered) of stress measurements on starboard and port side. Data from 01 July 2008 for 4,400 TEU ship. (same time series as in Figure 8.19). 355

E.1 Wave-induced vertical bending moment amidships compared to the minimum design wave-induced vertical bending moment in hogging and sagging from International Association of Classification Societies (2010a) for the 9,400 TEU ship on 02 October 2011 at 16-18 hours. 356
E.2 ACER function $\epsilon_k(\eta)$ for $k = 1$. Hogging, flexible 9,400 TEU ship on 02 October 2011. 357
E.3 ACER function $\epsilon_k(\eta)$ for $k = 2$. Hogging, flexible 9,400 TEU ship on 02 October 2011. 357
E.4 ACER function $\epsilon_k(\eta)$ for $k = 3$. Hogging, flexible 9,400 TEU ship on 02 October 2011. 357
E.5 ACER function $\epsilon_k(\eta)$ for $k = 4$. Hogging, flexible 9,400 TEU ship on 02 October 2011. 357
E.6 ACER function $\epsilon_k(\eta)$ for $k = 5$. Hogging, flexible 9,400 TEU ship on 02 October 2011. 358
E.7 ACER function $\epsilon_k(\eta)$ for $k = 6$. Hogging, flexible 9,400 TEU ship on 02 October 2011. 358
E.8 Optimised curve from ACER, $k = 1$. 9,400 TEU ship on 02 October 2011 at 16-18 hours. 359
E.9 Optimised curve from ACER, $k = 2$. 9,400 TEU ship on 02 October 2011 at 16-18 hours. 359
E.10 Optimised curve from ACER, $k = 3$. 9,400 TEU ship on 02 October 2011 at 16-18 hours. 359
E.11 Optimised curve from ACER, $k = 4$. 9,400 TEU ship on 02 October 2011 at 16-18 hours. 359
E.12 Optimised curve from ACER, $k = 5$. 9,400 TEU ship on 02 October 2011 at 16-18 hours. 360
E.13 Optimised curve from ACER, $k = 6$. 9,400 TEU ship on 02 October 2011 at 16-18 hours. 360
E.14 Wave-induced vertical bending moment amidships for the 9,400 TEU ship on 12 August 2011 at 00-02 hours. 361
E.15 Weibull probability plot for the hogging bending moment - WF+HF response. 9,400 TEU ship on 12 August 2011. 362

E.16 Weibull probability plot for the hogging bending moment - WF response. 9,400 TEU ship on 12 August 2011. 362

E.17 Gumbel density function for the hogging VBM based on Weibull parameters for the individual peak for the flexible-body response in Table E.2. The maximum measured hogging VBM during the three hours is included for comparison. 9,400 TEU ship on 12 August 2011. 362

E.18 ACER function $\epsilon_k(\eta)$ for six different values of k for the hogging VBM. 9,400 TEU ship on 12 August 2011. 363

E.19 Gumbel density function from the parameters derived from the optimised ACER functions for six different values of k (Table 9.6). The maximum measured hogging VBM during the three hours is included for comparison. 9,400 TEU ship on 12 August 2011. 364

E.20 Wave-induced vertical bending moment amidships for the 9,400 TEU ship on 17 December 2011 at 12-14 hours. 365

E.21 Weibull probability plot for the hogging bending moment - WF+HF response. 9,400 TEU ship on 17 December 2011. 366

E.22 Weibull probability plot for the hogging bending moment - WF response. 9,400 TEU ship on 17 December 2011. 366

E.23 Gumbel density function for the hogging VBM based on Weibull parameters for the individual peak for the flexible-body response in Table E.7. The maximum measured hogging VBM during the three hours is included for comparison. 9,400 TEU ship on 17 December 2011. 366

E.24 ACER function $\epsilon_k(\eta)$ for six different values of k for the hogging VBM. 9,400 TEU ship on 17 December 2011. 367

E.25 Gumbel density function from the parameters derived from the optimised ACER functions for six different values of k (Table 9.6). The maximum measured hogging VBM during the three hours is included for comparison. 9,400 TEU ship on 17 December 2011. 368

E.26 Wave-induced vertical bending moment amidships compared to the minimum design wave-induced vertical bending moment in hogging and sagging from International Association of Classification Societies (2010a) for the 8,600 TEU ship on 17 November 2010 at 20-22 hours. 369

E.27 Weibull probability plot for the hogging bending moment - WF+HF response. 8,600 TEU ship on 17 November 2010. 370

E.28 Weibull probability plot for the hogging bending moment - WF response. 8,600 TEU ship on 17 November 2010. 370

E.29 Gumbel density function for the hogging VBM based on Weibull parameters for the individual peak for the flexible-body response in Table E.12. The maximum measured hogging VBM during the three hours and the rule wave VBM are included for comparison. 8,600 TEU ship on 17 November 2010. 370

E.30 ACER function $\epsilon_k(\eta)$ for six different values of k for the hogging VBM. 8,600 TEU ship on 17 November 2010. 371

E.31 Gumbel density function from the parameters derived from the optimised ACER functions for six different values of k (Table E.16). The maximum measured hogging VBM during the three hours is included for comparison. 8,600 TEU ship on 17 November 2010. 372
E.32 Wave-induced vertical bending moment amidships compared to the minimum design wave-induced vertical bending moment in hogging and sagging from International Association of Classification Societies (2010a) for the 8,600 TEU ship on 30 December 2011 at 07-09 hours. 373
E.33 Weibull probability plot for the hogging bending moment - WF+HF response. 8,600 TEU ship on 30 December 2011. 374
E.34 Weibull probability plot for the hogging bending moment - WF response. 8,600 TEU ship on 30 December 2011. 374
E.35 Gumbel density function for the hogging VBM based on Weibull parameters for the individual peak for the flexible-body response in Table E.17. The maximum measured hogging VBM during the three hours and the rule wave VBM are included for comparison. 8,600 TEU ship on 30 December 2011. 374
E.36 ACER function $\epsilon_k(\eta)$ for six different values of k for the hogging VBM. 8,600 TEU ship on 30 December 2011. 375
E.37 Gumbel density function from the parameters derived from the optimised ACER functions for six different values of k (Table E.21). The maximum measured hogging VBM during the three hours is included for comparison. 8,600 TEU ship on 30 December 2011. 376
E.38 Wave-induced vertical bending moment amidships compared to the minimum design wave-induced vertical bending moment in hogging and sagging from International Association of Classification Societies (2010a) for the 14,000 TEU ship on 29 September 2011. 377
E.39 Weibull probability plot for the hogging bending moment - WF+HF response. 14,000 TEU ship on 29 September 2011. 378
E.40 Weibull probability plot for the hogging bending moment - WF response. 14,000 TEU ship on 29 September 2011. 378
E.41 Gumbel density function for the hogging VBM based on Weibull parameters for the individual peak for the flexible-body response in Table E.23. The maximum measured hogging VBM during the period and the rule wave VBM are included for comparison. 14,000 TEU ship on 29 September 2011. 379
E.42 ACER function $\epsilon_k(\eta)$ for six different values of k for the hogging VBM. 14,000 TEU ship on 29 September 2011. 380
E.43 Gumbel density function from the parameters derived from the optimised ACER functions for six different values of k (Table E.27). The maximum measured hogging VBM during the three hours is included for comparison. 14,000 TEU ship on 29 September 2011. 381
E.44 Wave-induced vertical bending moment amidships compared to the minimum design wave-induced vertical bending moment in hogging and sagging from International Association of Classification Societies (2010a) for the 14,000 TEU ship on 21 July 2011. 382

E.45 Weibull probability plot for the hogging bending moment - WF+HF response. 14,000 TEU ship on 21 July 2011. 383
E.46 Weibull probability plot for the hogging bending moment - WF response. 14,000 TEU ship on 21 July 2011. 383
E.47 Gumbel density function for the hogging VBM based on Weibull parameters for the individual peak for the flexible-body response in Table E.29. The maximum measured hogging VBM during the period and the rule wave VBM are included for comparison. 14,000 TEU ship on 21 July 2011.383
E.48 ACER function $\epsilon_k(\eta)$ for six different values of k for the hogging VBM. 14,000 TEU ship on 21 July 2011. 385
E.49 Gumbel density function from the parameters derived from the optimised ACER functions for six different values of k (Table E.33). The maximum measured hogging VBM during the three hours is included for comparison. 14,000 TEU ship on 21 July 2011. 385
E.50 Wave-induced vertical bending moment amidships compared to the minimum design wave-induced vertical bending moment in hogging and sagging from International Association of Classification Societies (2010a) for the 4,400 TEU ship on 02 November 2007 at 11-13 hours. 386
E.51 Weibull probability plot for the hogging bending moment - WF+HF response. 4,400 TEU ship on 02 November 2007, 11-13 hours. 387
E.52 Weibull probability plot for the hogging bending moment - WF response. 4,400 TEU ship on 02 November 2007, 11-13 hours. 387
E.53 Gumbel density function for the hogging VBM based on Weibull parameters for the individual peak for the flexible-body response in Table E.44. The maximum measured hogging VBM during the three hours and the rule wave VBM are included for comparison. 4,400 TEU ship on 02 November 2007, 11-13 hours. 387
E.54 ACER function $\epsilon_k(\eta)$ for six different values of k for the hogging VBM. 4,400 TEU ship on 02 November 2007, 11-13 hours. 388
E.55 Gumbel density function from the parameters derived from the optimised ACER functions for six different values of k (Table E.38). The maximum measured hogging VBM during the three hours is included for comparison. 4,400 TEU ship on 02 November 2007, 11-13 hours. 389
E.56 Wave-induced vertical bending moment amidships compared to the minimum design wave-induced vertical bending moment in hogging and sagging from International Association of Classification Societies (2010a) for the 4,400 TEU ship on 02 November 2007 at 16-18 hours. 390
E.57 Weibull probability plot for the hogging bending moment - WF+HF response. 4,400 TEU ship on 02 November 2007, 16-18 hours. 391
E.58 Weibull probability plot for the hogging bending moment - WF response. 4,400 TEU ship on 02 November 2007, 16-18 hours. 391
E.59 Gumbel density function for the hogging VBM based on Weibull parameters for the individual peak for the flexible-body response in Table E.44. The maximum measured hogging VBM during the three hours and the rule wave VBM are included for comparison. 4,400 TEU ship on 02 November 2007, 16-18 hours. 391

E.60 ACER function $\epsilon_k(\eta)$ for six different values of k for the hogging VBM. 4,400 TEU ship on 02 November 2007, 16-18 hours. 392
E.61 Gumbel density function from the parameters derived from the optimised ACER functions for six different values of k (Table E.43). The maximum measured hogging VBM during the three hours is included for comparison. 4,400 TEU ship on 02 November 2007, 16-18 hours. 393
E.62 Wave-induced vertical bending moment amidships compared to the minimum design wave-induced vertical bending moment in hogging and sagging from International Association of Classification Societies (2010a) for the 4,400 TEU ship on 01 July 2008 at 17-19 hours. 394
E.63 Weibull probability plot for the hogging bending moment - WF+HF response. 4,400 TEU ship on 01 July 2008. 395
E.64 Weibull probability plot for the hogging bending moment - WF response. 4,400 TEU ship on 01 July 2008. 395
E.65 Gumbel density function for the hogging VBM based on Weibull parameters for the individual peak for the flexible-body response in Table E.44. The maximum measured hogging VBM during the three hours and the rule wave VBM are included for comparison. 4,400 TEU ship on 01 July 2008. 395
E.66 ACER function $\epsilon_k(\eta)$ for six different values of k for the hogging VBM. 4,400 TEU ship on 01 July 2008. 396
E.67 Gumbel density function from the parameters derived from the optimised ACER functions for six different values of k (Table E.48). The maximum measured hogging VBM during the three hours is included for comparison. 4,400 TEU ship on 01 July 2008. 397

F.1 Unfiltered, low-pass and high-pass filtered time series signal of vertical bending moment for model tests in head sea and H_s of 6.5 m. Total time series is 1,420 s long and comprised of two runs. 400
F.2 FFT of unfiltered VBM amidhips in head sea and H_s of 6.5 m. Same time series as Figure F.1. 401
F.3 Individual peak value probability of exceedance for the rigid ship comparing hogging and sagging in head sea and H_s of 6.5 m. 401
F.4 Unfiltered, low-pass and high-pass filtered time series signal of vertical bending moment for model tests in bow-quartering sea and H_s of 6.5 m. Total time series is 1,035 s long and comprised of five runs. 401
F.5 FFT of unfiltered VBM amidhips in bow-quartering sea and H_s of 6.5 m. Same time series as Figure F.4. 402
F.6 Individual peak value probability of exceedance for the rigid ship comparing hogging and sagging in bow-quartering sea and H_s of 6.5 m. . . . 402
F.7 Unfiltered, low-pass and high-pass filtered time series signal of vertical bending moment for model tests in head sea, H_s of 9.5 m and T_p of 12.22 s. Total time series is 1,039 s long and comprised of one run. 403
F.8 FFT of unfiltered VBM amidhips in head sea, H_s of 9.5 m and T_p of 12.22 s. Same time series as Figure F.7. 404

F.9 Individual peak value probability of exceedance for the rigid ship comparing hogging and sagging in head sea, H_s of 9.5 m and T_p of 12.22 s. 404
F.10 Unfiltered, low-pass and high-pass filtered time series signal of vertical bending moment for model tests in bow-quartering sea, H_s of 9.5 m and T_p of 12.22 s. Total time series is 1,053 s long and comprised of three runs. 404
F.11 FFT of unfiltered VBM amidhips in bow-quartering sea, H_s of 9.5 m and T_p of 12.22 s. Same time series as Figure F.10. 405
F.12 Individual peak value probability of exceedance for the rigid ship comparing hogging and sagging in bow-quartering sea, H_s of 9.5 m and T_p of 12.22 s. 405
F.13 Unfiltered, low-pass and high-pass filtered time series signal of vertical bending moment for model tests in head sea, H_s of 9.5 m and T_p of 9.93 s. Total time series is 1,061 s long and comprised of one run. 406
F.14 FFT of unfiltered VBM amidhips in head sea, H_s of 9.5 m and T_p of 12.22 s. Same time series as Figure F.13. 407
F.15 Individual peak value probability of exceedance for the rigid ship comparing hogging and sagging in head sea, H_s of 9.5 m and T_p of 9.93 s. 407
F.16 Unfiltered, low-pass and high-pass filtered time series signal of vertical bending moment for model tests in bow-quartering sea, H_s of 9.5 m and T_p of 9.93 s. Total time series is 1,057 s long and comprised of three runs. 407
F.17 FFT of unfiltered VBM amidhips in bow-quartering sea, H_s of 9.5 m and T_p of 9.93 s. Same time series as Figure F.16. 408
F.18 Individual peak value probability of exceedance for the rigid ship comparing hogging and sagging in bow-quartering sea, H_s of 9.5 m and T_p of 9.93 s. 408

List of Tables

2.1 Principal dimensions for the 9,400 TEU container ship. 21
2.2 Location of the accelerometers mounted in the bow of the 9,400 TEU ship. 23
2.3 Location of long-base strain gauges at frame 102 (amidships) in ship local coordinate system. 24
2.4 Principal dimensions for the 8,600 TEU container ship. 26
2.5 Location of the strain gauges on 8,600 TEU container ship. 27
2.6 Principal dimensions for the 14,000 TEU container ship. 28
2.7 Principal dimensions for the 4,400 TEU container ship. 29

5.1 Calculated dry and wet natural frequencies of the 9,400 TEU container ship. From (Kapsenberg et al., 2010). 59
5.2 Estimated 2-node natural frequency, ω_2, damping, ξ, and standard deviation of the damping, s_ξ, from operational modal analysis for the 9,400 TEU ship. Damping is % of critical damping. 61
5.3 Estimated 2-node natural frequency, ω_2, damping, ξ, and standard deviation of the damping, s_ξ, from operational modal analysis for the 8,600 TEU ship. Damping is % of critical damping. 61
5.4 Estimated 2-node natural frequency, ω_2, damping, ξ, and standard deviation of the damping, s_ξ, from operational modal analysis for the 14,000 TEU ship. Damping is % of critical damping. 62
5.5 Estimated 2-node natural frequency, ω_2, damping, ξ, and standard deviation of the damping, s_ξ, from operational modal analysis for the 4,400 TEU ship. Damping is % of critical damping. 62

6.1 One hour budget damage for different service life and damage sum $D = 1.0$ and $D = 0.5$. 65
6.2 Selected days for fatigue damage estimation for the 9,400 TEU ship. . . 66
6.3 Selected days for fatigue damage estimation for the 8,600 TEU ship. . . 67
6.4 Frequency limits for filtering of measured strains. 67
6.5 Exceedance of one-hour budget damage for 8,600 TEU ship based on 40 year design service life and damage sum $D = 1$. The exceedance is given as the estimated damage using RFC and the Palmgren-Miner rule divided with the budget damage. 76

7.1 Wave spectrum parameters. 86
7.2 Reliability index β for the four scenarios. 89

9.1 Maximum measured VBM and number of peaks for sagging and hogging for the flexible and rigid-body response and duration and standard deviation of the flexible (s_M) and rigid-body ($s_{M,WF}$) response. 9,400 TEU ship on 02 October 2011. 117
9.2 Weibull parameters for hogging for the WF and WF+HF response. Estimated from Figures 9.3 and 9.4. 9,400 TEU ship on 02 October 2011. . 119
9.3 Weibull parameters a and c for for the excess of the hogging VBM for different threshold values. A value of $c = 1$ corresponds to exponentially distributed peaks. 9,400 TEU ship on 02 October 2011. 123
9.4 Gumbel parameters b and d from an exponential fit to the excess. 9,400 TEU ship on 02 October 2011. 123
9.5 Weibull parameter c and Gumbel parameters d and b for different threshold values. A value of $c = 1$ corresponds to exponentially distributed peaks. 9,400 TEU ship on 02 October 2011. 127
9.6 Gumbel parameters b and d from the optimised ACER functions for hogging for six different k. 9,400 TEU ship on 02 October 2011. 130
9.7 Maximum measured VBM and number of peaks for sagging and hogging for the flexible and rigid-body response and duration and standard deviation of the flexible (s_M) and rigid-body ($s_{M,WF}$) response. 9,400 TEU ship on 12 August 2011. 132
9.8 Maximum measured VBM and number of peaks for sagging and hogging for the flexible and rigid-body response and duration and standard deviation of the flexible (s_M) and rigid-body ($s_{M,WF}$) response. 9,400 TEU ship on 17 December 2011. 134
9.9 Maximum measured VBM and number of peaks for sagging and hogging for the flexible and rigid-body response and duration and standard deviation of the flexible (s_M) and rigid-body ($s_{M,WF}$) response. 8,600 TEU ship on 17 November 2010. 137
9.10 Maximum measured VBM and number of peaks for sagging and hogging for the flexible and rigid-body response and duration and standard deviation of the flexible (s_M) and rigid-body ($s_{M,WF}$) response. 8,600 TEU ship on 30 December 2011. 140
9.11 Maximum measured VBM and number of peaks for sagging and hogging for the flexible and rigid-body response and duration and standard deviation of the flexible (s_M) and rigid-body ($s_{M,WF}$) response. 14,000 TEU ship on 29 September 2011. 143
9.12 Maximum measured VBM and number of peaks for sagging and hogging for the flexible and rigid-body response and duration and standard deviation of the flexible (s_M) and rigid-body ($s_{M,WF}$) response. 14,000 TEU ship on 21 July 2011. 145
9.13 Maximum measured VBM and number of peaks for sagging and hogging for the flexible and rigid-body response and duration and standard deviation of the flexible (s_M) and rigid-body ($s_{M,WF}$) response. 4,400 TEU ship on 02 November 2007, 11-13 hours. 148

9.14 Maximum measured VBM and number of peaks for sagging and hogging for the flexible and rigid-body response and duration and standard deviation of the flexible (s_M) and rigid-body ($s_{M,WF}$) response. 4,400 TEU ship on 02 November 2007, 16-18 hours. 150
9.15 Maximum measured VBM and number of peaks for sagging and hogging for the flexible and rigid-body response and duration and standard deviation of the flexible (s_M) and rigid-body ($s_{M,WF}$) response. 4,400 TEU ship on 01 July 2008. 153

10.1 Standard deviation, s_M; skewness, κ_3 and kurtosis, κ_4 of one-hour time series and for the 3 hours as one time series for the rigid-body part for the 9,400 TEU ship on 02 October 2011. 164

11.1 Sea state parameters. γ is the peak enhancement factor for the Jonswap spectrum. 169
11.2 Extreme values of the vertical bending moment and amplification due to HF vibrations. Time series correspond to Figure F.1 for the head sea case and Figure F.4 for the bow-quartering sea case. 170
11.3 Sea state parameters. γ is the peak enhancement factor for the Jonswap spectrum. 171
11.4 Extreme values of the vertical bending moment and amplification due to HF vibrations. Head sea. Time series correspond to Figure F.7 for the head sea case and Figure F.10 for the bow-quartering sea case. 172
11.5 Extreme values of the vertical bending moment and amplification due to HF vibrations. Head sea. Time series correspond to Figure F.13 for the head sea case and Figure F.16 for the bow-quartering sea case. 174

12.1 Principal data for MSC NAPOLI and MOL COMFORT. 183

A.1 ECDIS data for the 9,4000 TEU ship. Wind speed and direction is not corrected for the speed and heading of the ship. 245
A.2 Logged WaMoS data recorded on board the 9,400 TEU ship. 245

B.1 Definitions and sign conventions for the motion measurements on board the 9,400 TEU ship. Table reproduced from Koning (2007). 292

E.1 ACER parameters, hogging, for 02 October 2011, 16-18 hours. 358
E.2 Weibull parameters for hogging for the WF and WF+HF response. Estimated from Figures E.15 and E.16. 9,400 TEU ship on 12 August 2011. 361
E.3 Weibull parameters a and c for for the excess of the hogging VBM for different threshold values. 9,400 TEU ship on 12 August 2011. 363
E.4 Gumbel parameters b and d from an exponential fit to the excess. 9,400 TEU ship on 12 August 2011. 363
E.5 Optimised ACER parameters for 9,400 TEU ship on 12 August 2011. . . 364
E.6 Gumbel parameters b and d from the optimised ACER functions for hogging for six different k. 9,400 TEU ship on 12 August 2011. 364

E.7 Weibull parameters for hogging for the WF and WF+HF response. Estimated from Figures E.21 and E.22. 9,400 TEU ship on 17 December 2011. 365
E.8 Weibull parameters a and c for for the excess of the hogging VBM for different threshold values. 9,400 TEU ship on 17 December 2011. 367
E.9 Gumbel parameters b and d from an exponential fit to the excess. 9,400 TEU ship on 17 December 2011. 367
E.10 Optimised ACER parameters for 9,400 TEU ship on 17 December 2011. 368
E.11 Gumbel parameters b and d from the optimised ACER functions for hogging for six different k. 9,400 TEU ship on 17 December 2011. 368
E.12 Weibull parameters for hogging for the WF and WF+HF response. Estimated from Figures E.27 and E.28. 8,600 TEU ship on 17 November 2010. 369
E.13 Weibull parameters a and c for for the excess of the hogging VBM for different threshold values. 8,600 TEU ship on 17 November 2010. 371
E.14 Gumbel parameters b and d from an exponential fit to the excess. 8,600 TEU ship on 17 November 2010. 371
E.15 Optimised ACER parameters for 8,600 TEU ship on 17 November 2010. 372
E.16 Gumbel parameters b and d from the optimised ACER functions for hogging for six different k. 8,600 TEU ship on 17 November 2010. 372
E.17 Weibull parameters for hogging for the WF and WF+HF response. Estimated from Figures E.33 and E.34. 8,600 TEU ship on 30 December 2011. 373
E.18 Weibull parameters a and c for for the excess of the hogging VBM for different threshold values. 8,600 TEU ship on 30 December 2011. 375
E.19 Gumbel parameters b and d from an exponential fit to the excess. 8,600 TEU ship on 30 December 2011. 375
E.20 Optimised ACER parameters 8,600 TEU ship on 30 December 2011. . . 376
E.21 Gumbel parameters b and d from the optimised ACER functions for hogging for six different k. 8,600 TEU ship on 30 December 2011. 376
E.22 Time series information, 14,000 TEU ship, 29 November. 377
E.23 Weibull parameters for hogging for the WF and WF+HF response. Estimated from Figures E.39 and E.40. 14,000 TEU ship on 29 September 2011. 378
E.24 Weibull parameters a and c for for the excess of the hogging VBM for different threshold values. 14,000 TEU ship on 29 September 2011. . . . 380
E.25 Gumbel parameters b and d from an exponential fit to the excess. 14,000 TEU ship on 29 September 2011. 380
E.26 Optimised ACER parameters for 14,000 TEU ship on 29 September 2011.381
E.27 Gumbel parameters b and d from the optimised ACER functions for hogging for six different k. 14,000 TEU ship on 29 September 2011. . . . 381
E.28 Time series information, 14,000 TEU ship, 21 July 2011. 382
E.29 Weibull parameters for hogging for the WF and WF+HF response. Estimated from Figures E.45 and E.46. 14,000 TEU ship on 21 July 2011. 383
E.30 Weibull parameters a and c for for the excess of the hogging VBM for different threshold values. 14,000 TEU ship on 21 July 2011. 384

E.31 Gumbel parameters b and d from an exponential fit to the excess. 14,000 TEU ship on 21 July 2011. 384
E.32 Optimised ACER parameters for 14,000 TEU ship on 21 July 2011. . . . 384
E.33 Gumbel parameters b and d from the optimised ACER functions for hogging for six different k. 14,000 TEU ship on 21 July 2011. 385
E.34 Weibull parameters for hogging for the WF and WF+HF response. Estimated from Figures E.51 and E.52. 4,400 TEU ship on 02 November 2007, 11-13 hours. 387
E.35 Weibull parameters a and c for for the excess of the hogging VBM for different threshold values. 4,400 TEU ship on 02 November 2007, 11-13 hours. 388
E.36 Gumbel parameters b and d from an exponential fit to the excess. 4,400 TEU ship on 02 November 2007, 11-13 hours. 388
E.37 Optimised ACER parameters for the 4,400 TEU ship on 02 November 2007, 11-13 hours. 389
E.38 Gumbel parameters b and d from the optimised ACER functions for hogging for six different k. 4,400 TEU ship on 02 November 2007, 11-13 hours. 389
E.39 Weibull parameters for hogging for the WF and WF+HF response. Estimated from Figures E.57 and E.58. 4,400 TEU ship on 02 November 2007, 16-18 hours. 391
E.40 Weibull parameters a and c for for the excess of the hogging VBM for different threshold values. 4,400 TEU ship on 02 November 2007, 16-18 hours. 392
E.41 Gumbel parameters b and d from an exponential fit to the excess. 4,400 TEU ship on 02 November 2007, 16-18 hours. 392
E.42 Optimised ACER parameters for the 4,400 TEU ship on 02 November 2007, 16-18 hours. 393
E.43 Gumbel parameters b and d from the optimised ACER functions for hogging for six different k. 4,400 TEU ship on 02 November 2007, 16-18 hours. 393
E.44 Weibull parameters for hogging for the WF and WF+HF response. Estimated from Figures E.63 and E.64. 4,400 TEU ship on 01 July 2008. . 394
E.45 Weibull parameters a and c for for the excess of the hogging VBM for different threshold values. 4,400 TEU ship on 01 July 2008. 396
E.46 Gumbel parameters b and d from an exponential fit to the excess. 4,400 TEU ship on 01 July 2008. 396
E.47 Optimised ACER parameters for the 4,400 TEU ship on 01 July 2008. . 397
E.48 Gumbel parameters b and d from the optimised ACER functions for hogging for six different k. 4,400 TEU ship on 01 July 2008. 397

Appendix A

Measurements from Ships

A.1 9,400 TEU Container Ship

A.1.1 Plots of 9,400 TEU ship tracks

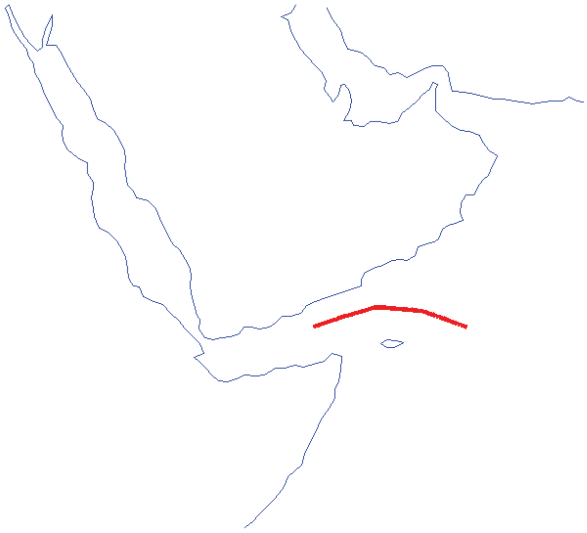

Figure A.1: *Vessel track on 12 August 2011 in the Gulf of Aden (Going west, 24 hours).*

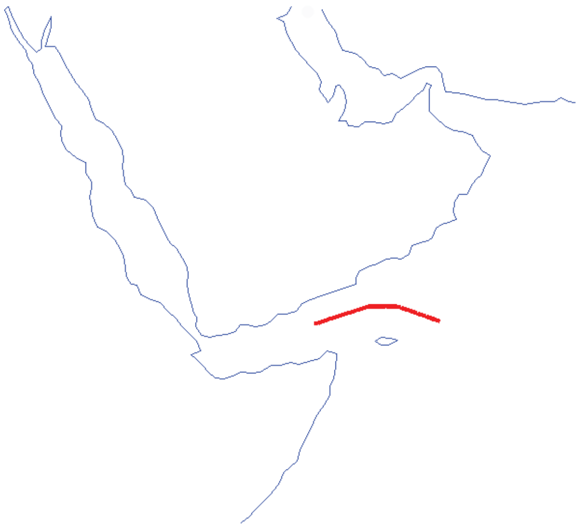

Figure A.2: *Vessel track on 16 September 2011 in the Gulf of Aden (Going east, 24 hours).*

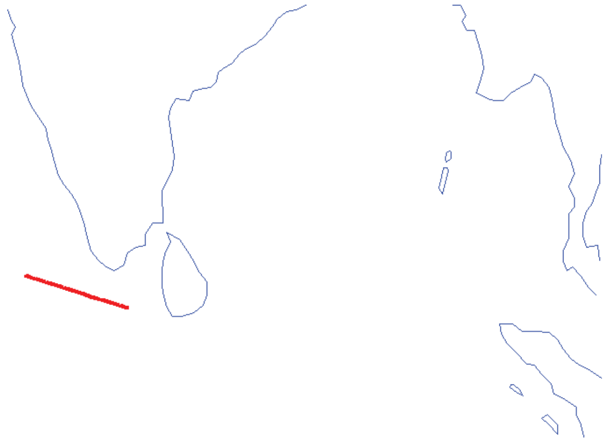

Figure A.3: Vessel track on 20 September 2011 south of India (Going east, 24 hours).

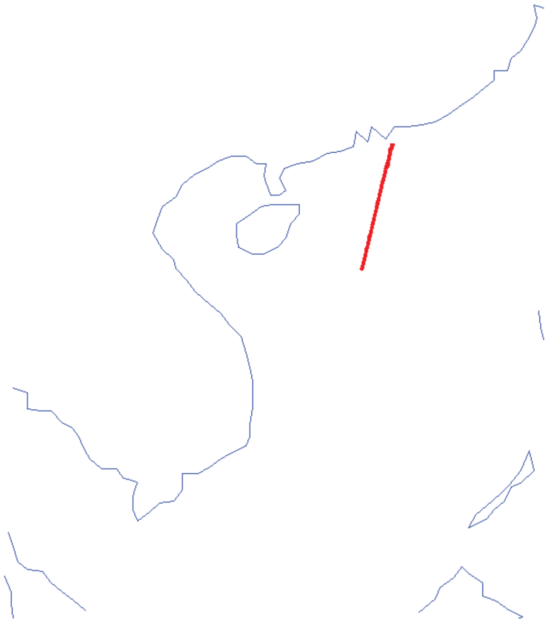

Figure A.4: Vessel track on 02 October 2011 in the South China Sea (Going north, 24 hours).

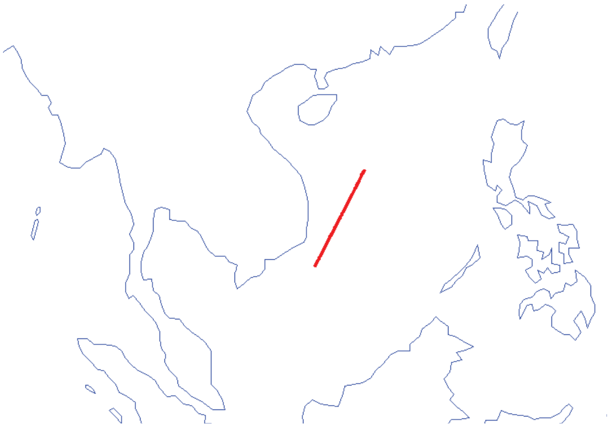

Figure A.5: Vessel track on 17 December 2011 in the South China Sea (Going north, 24 hours).

A.1.2 Navigational information and sea state measurements

Data	**Unit**
Latitude	deg
Longitude	deg
Compass heading (true)	deg (going to)
Course over ground	deg (going to)
Speed through water	knots
Speed over ground	knots
Wind speed	m/s
Wind direction relative to ship	deg (coming from)
Current direction relative to ship	deg
Current speed	knots
Water depth	m

Table A.1: *ECDIS data for the 9,4000 TEU ship. Wind speed and direction is not corrected for the speed and heading of the ship.*

Data	**Unit**
Significant wave height (total, swell and wind)	m
Maximum wave height	m
Peak wave period (total, swell and wind)	s
Mean wave direction (coming from)	deg
Peak wave direction (total, swell and wind) (coming from)	deg
Wave length with respect to T_p	m
Spectrum spreading parameter	-

Table A.2: *Logged WaMoS data recorded on board the 9,400 TEU ship.*

12 August 2011

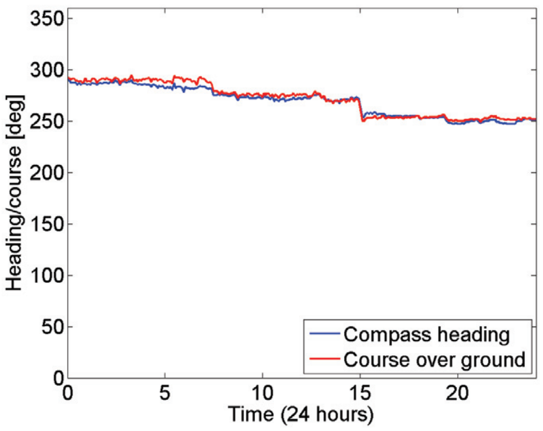

Figure A.6: *Ship true heading from gyro compass and course over ground from GPS on 12 August 2011.*

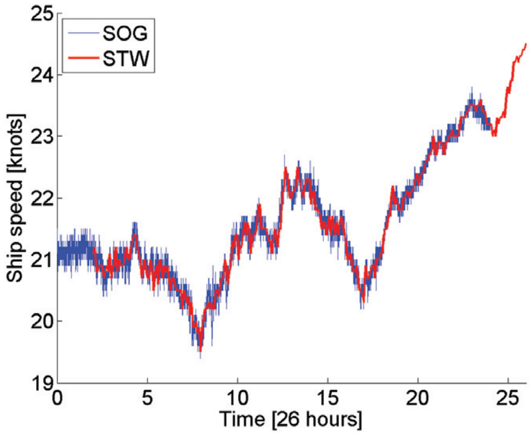

Figure A.7: *Ship speed through water (STW) and over ground (SOG) on 12 August 2011.*

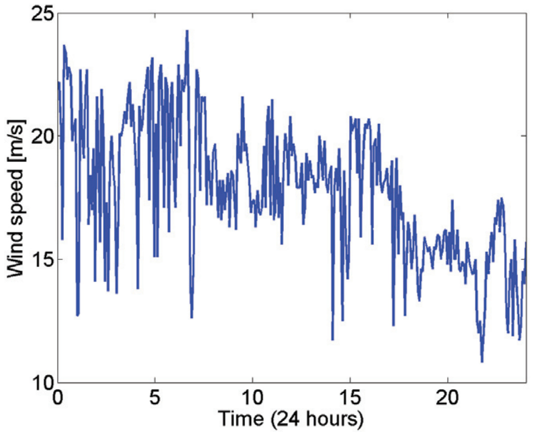

Figure A.8: *Wind speed on 12 August 2011.*

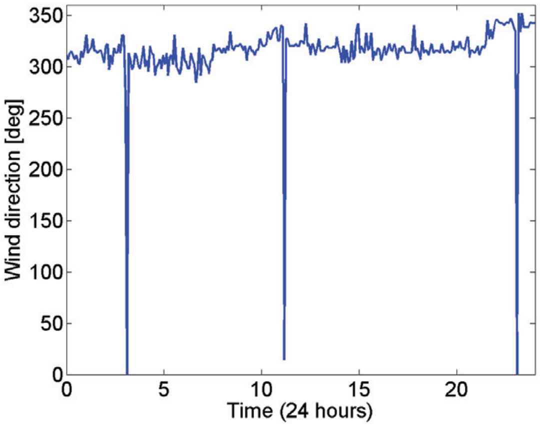

Figure A.9: *Wind direction on 12 August 2011.*

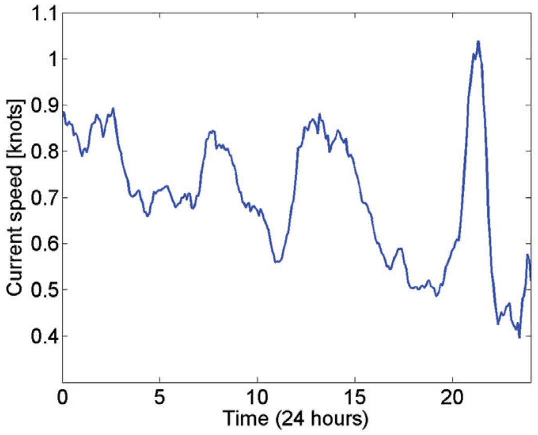

Figure A.10: *Current speed for 12 August 2011.*

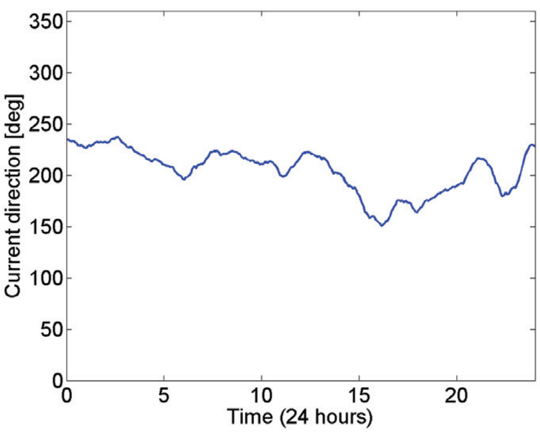

Figure A.11: *Current direction for 12 August 2011.*

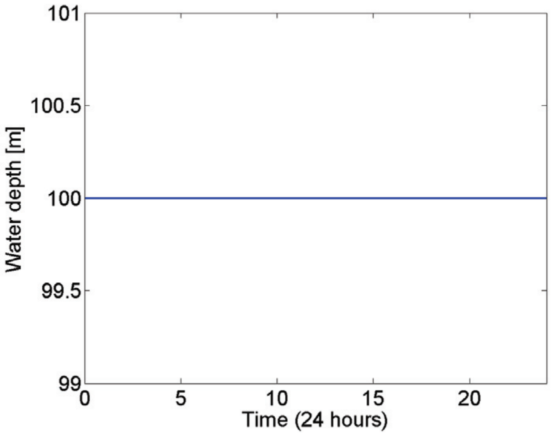

Figure A.12: *Logged water depth on 12 August 2011. Depths above 100 m cannot be measured.*

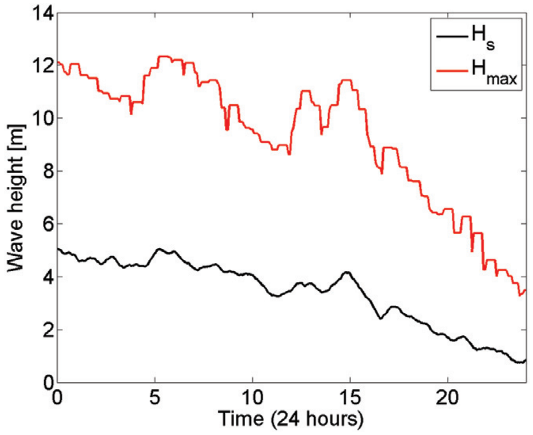

Figure A.13: *Significant and maximum wave height from WaMoS on 12 August 2011, 24 hours.*

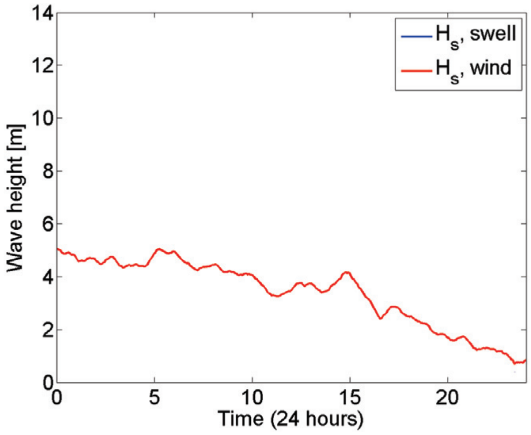

Figure A.14: *Significant wave height for swell and wind driven component from WaMoS on 12 August 2011, 24 hours.*

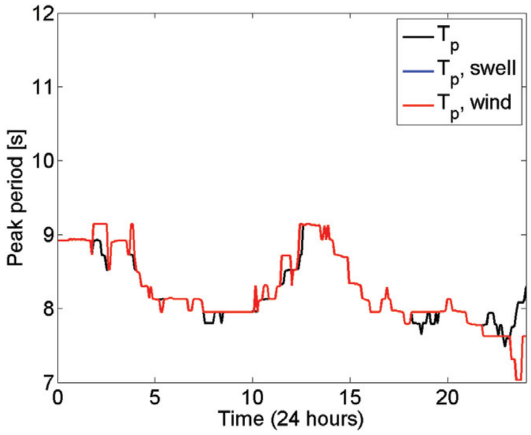

Figure A.15: *Peak periods from WaMoS on 12 August 2011, 24 hours.*

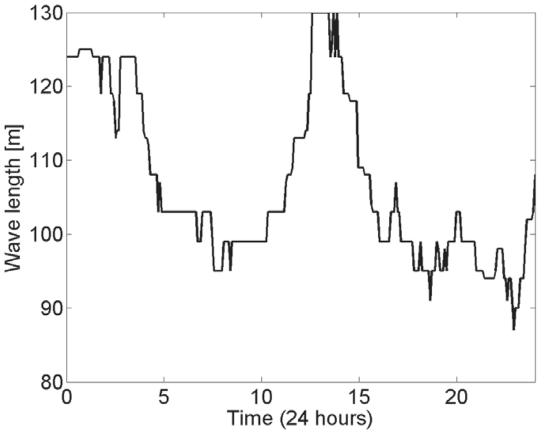

Figure A.16: *Wave length with respect to T_p from WaMoS on 12 August 2011, 24 hours.*

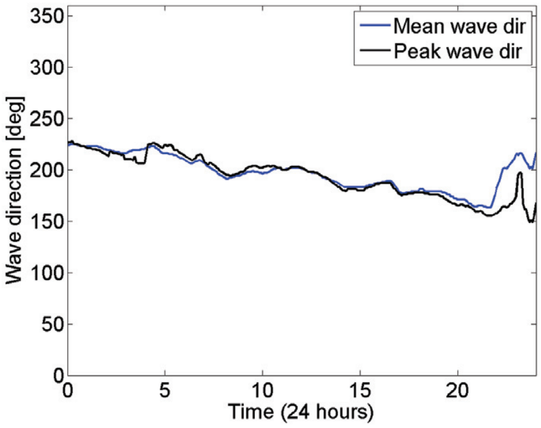

Figure A.17: *Mean and peak wave direction from WaMoS on 12 August 2011, 24 hours. Given as coming from compass rose direction.*

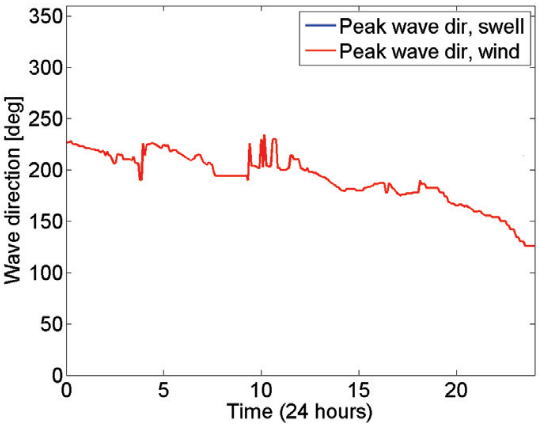

Figure A.18: *Peak wave direction for swell and wind driven component from WaMoS on 12 August 2011, 24 hours. Given as coming from compass rose direction.*

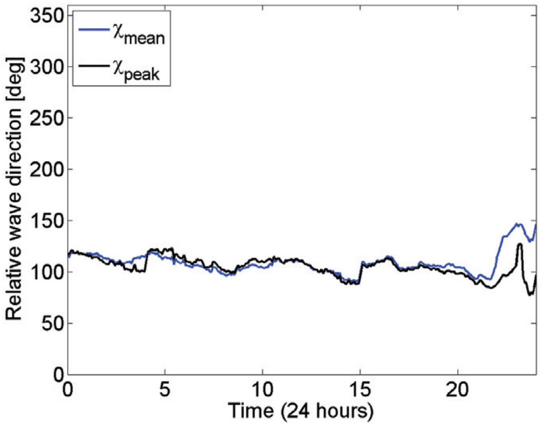

Figure A.19: *Relative mean and peak wave direction from WaMoS on 12 August 2011, 24 hours. 180 deg is head sea.*

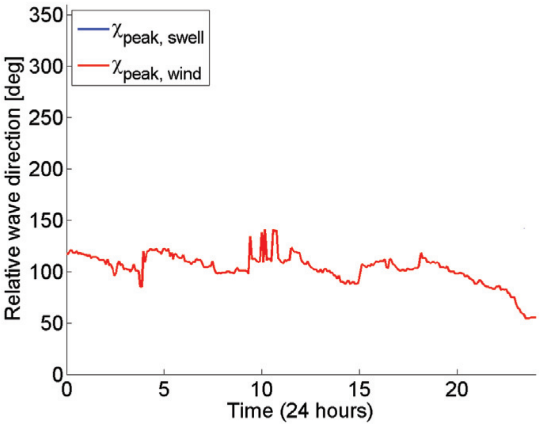

Figure A.20: *Relative peak wave directions for swell and wind components from WaMoS on 12 August 2011, 24 hours. 180 deg is head sea.*

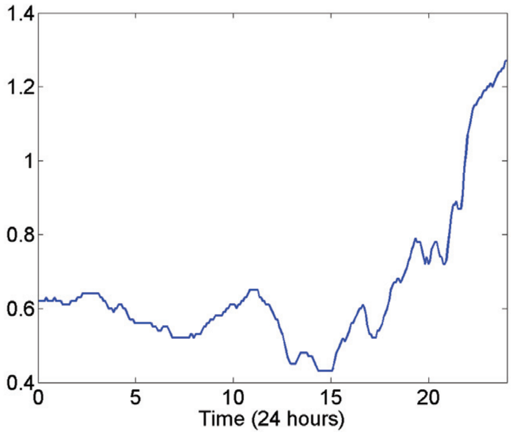

Figure A.21: *Spreading parameter for Jonswap spectrum from WaMoS for 12 August 2011, 24 hours.*

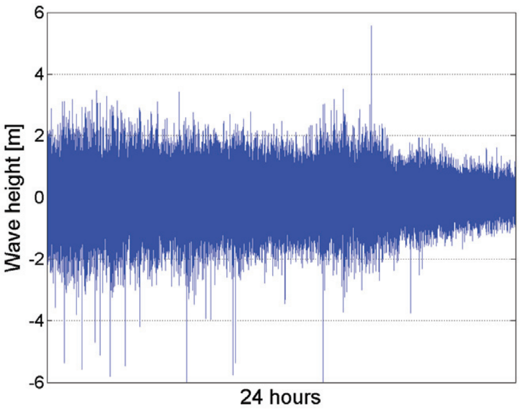

Figure A.22: *Wave height from Radac for 12 August 2011, 24 hours.*

16 September 2011

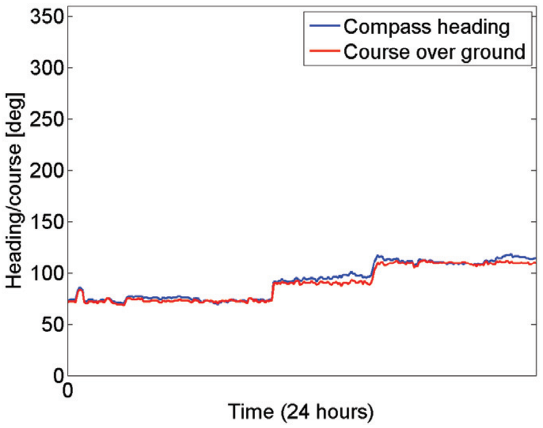

Figure A.23: *Ship true heading from gyro compass and course over ground from GPS on 16 September 2011.*

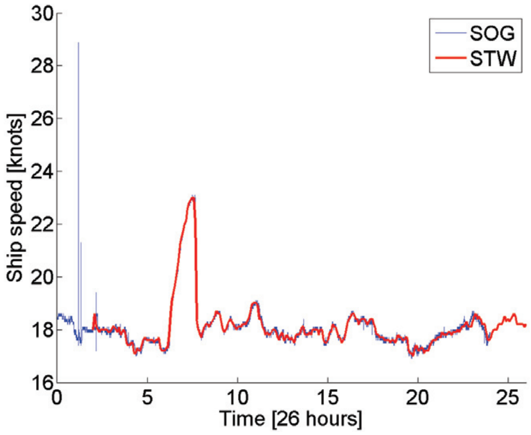

Figure A.24: *Ship speed through water (STW) and over ground (SOG) on 16 September 2011.*

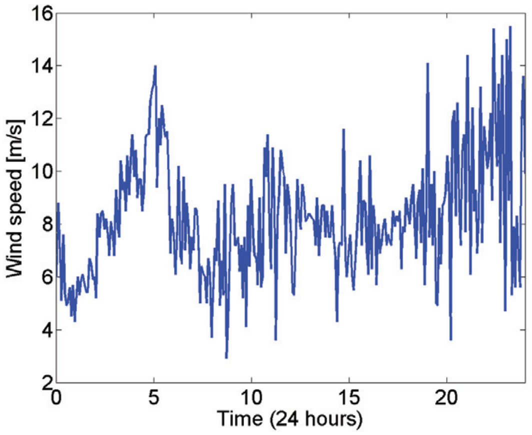

Figure A.25: *Wind speed on 16 September 2011.*

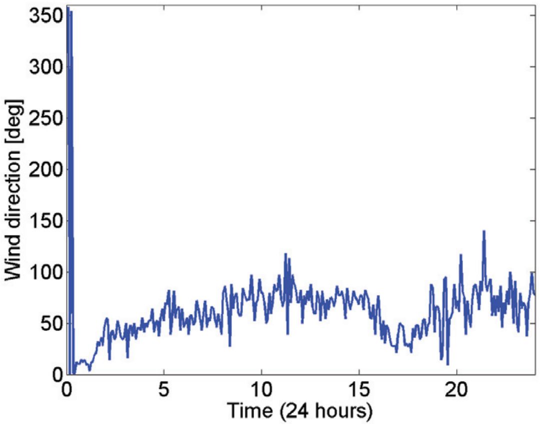

Figure A.26: *Wind direction on 16 September 2011.*

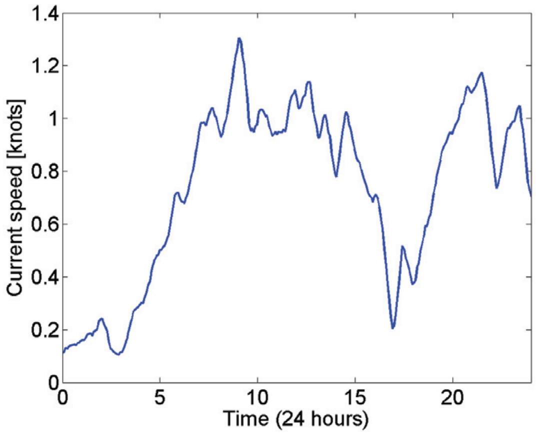

Figure A.27: Current speed for 16 September 2011.

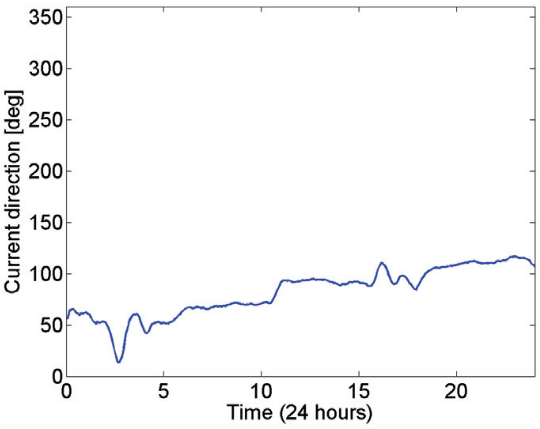

Figure A.28: Current direction for 16 September 2011.

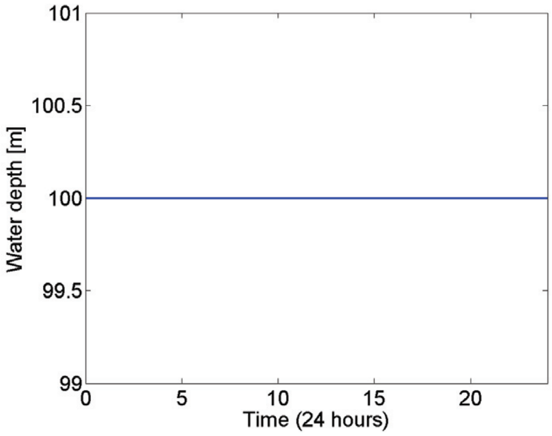

Figure A.29: Logged water depth on 16 September 2011. Depths above 100 m cannot be measured.

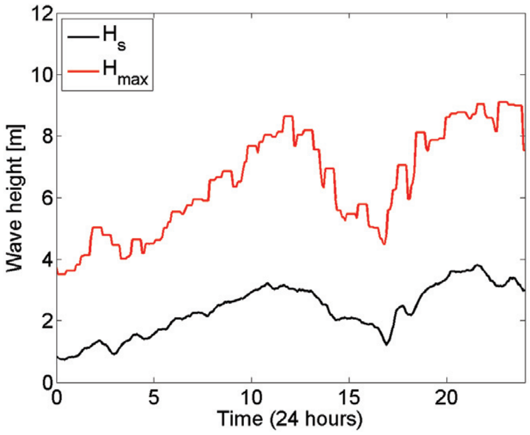

Figure A.30: Significant and maximum wave height from WaMoS on 16 September 2011, 24 hours.

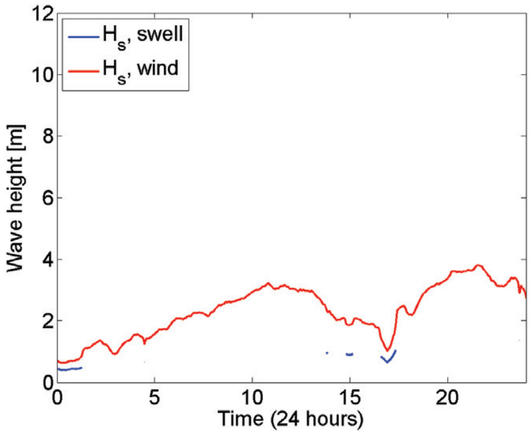

Figure A.31: Significant wave height for swell and wind driven component from WaMoS on 16 September 2011, 24 hours.

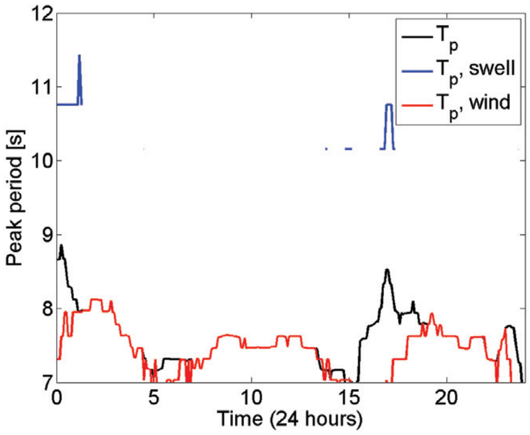

Figure A.32: *Peak periods from WaMoS on 16 September 2011, 24 hours.*

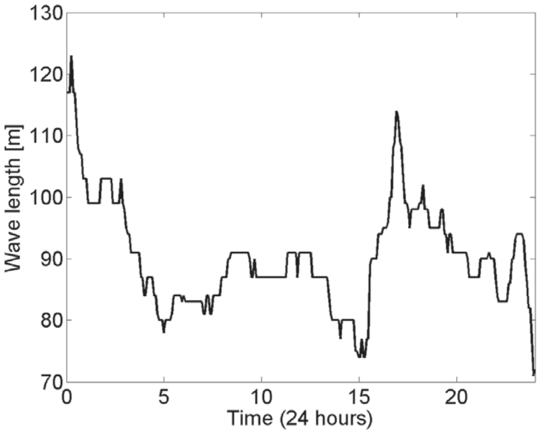

Figure A.33: *Wave length with respect to T_p from WaMoS on 16 September 2011, 24 hours.*

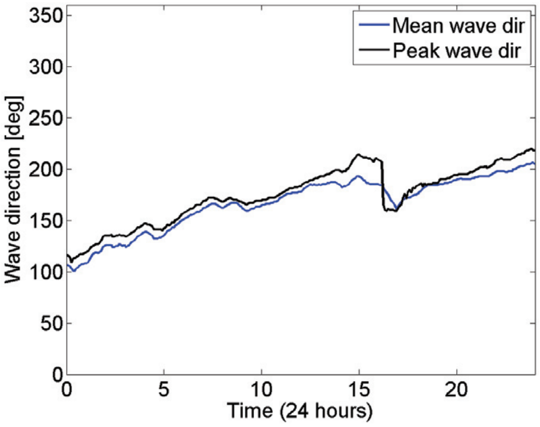

Figure A.34: *Mean and peak wave direction from WaMoS on 16 September 2011, 24 hours. Given as coming from compass rose direction.*

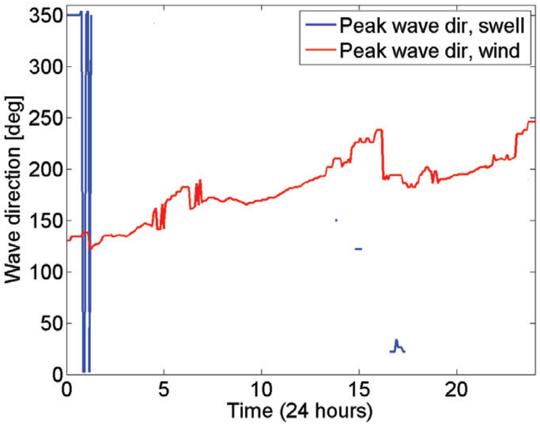

Figure A.35: *Peak wave direction for swell and wind driven component from WaMoS on 16 September 2011, 24 hours. Given as coming from compass rose direction.*

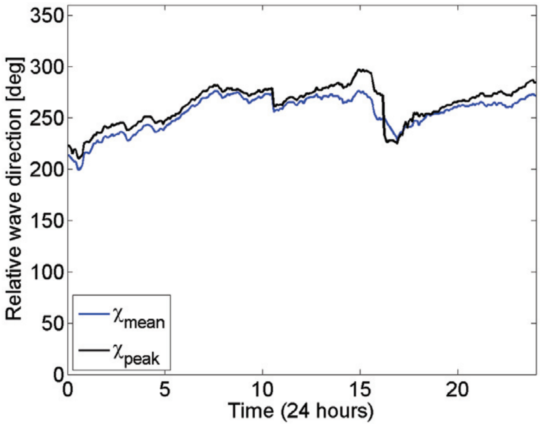

Figure A.36: *Relative mean and peak wave direction from WaMoS on 16 September 2011, 24 hours. 180 deg is head sea.*

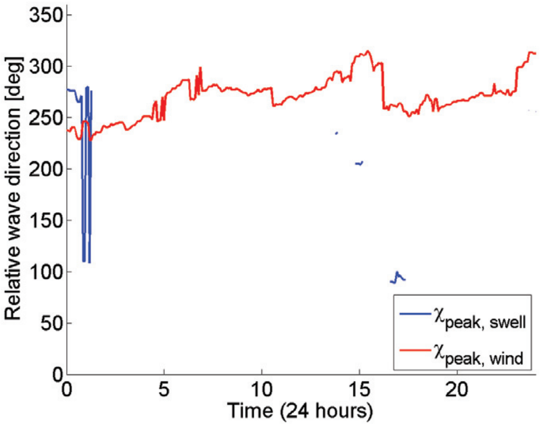

Figure A.37: *Relative peak wave directions for swell and wind components from WaMoS on 16 September 2011, 24 hours. 180 deg is head sea.*

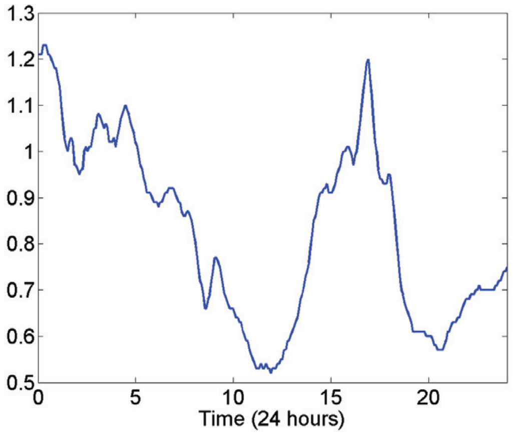

Figure A.38: *Spreading parameter for Jonswap spectrum from WaMoS for 16 September 2011, 24 hours.*

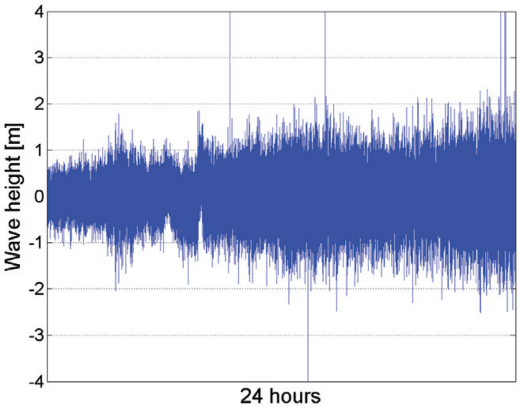

Figure A.39: *Wave height from Radac for 16 September 2011, 24 hours.*

20 September 2011

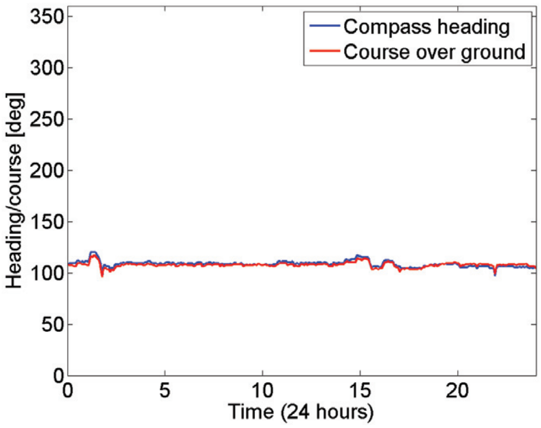

Figure A.40: *Ship true heading from gyro compass and course over ground from GPS on 20 September 2011.*

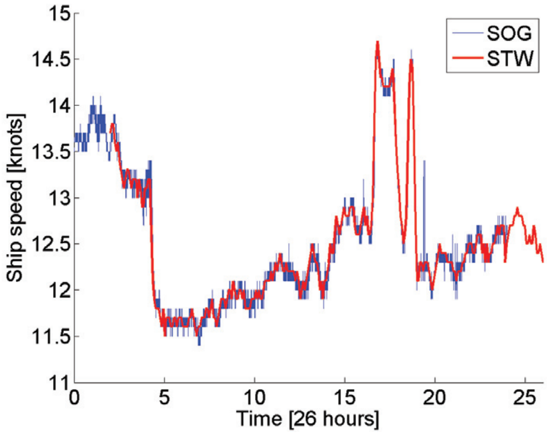

Figure A.41: *Ship speed through water (STW) and over ground (SOG) on 20 September 2011.*

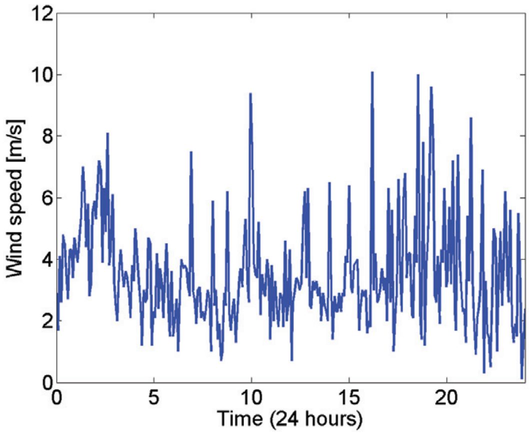

Figure A.42: *Wind speed on 20 September 2011.*

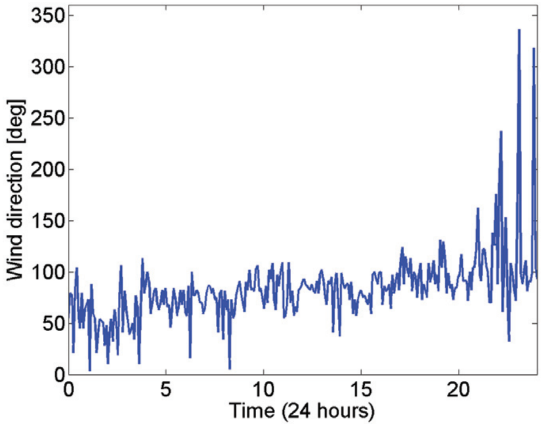

Figure A.43: *Wind direction on 20 September 2011.*

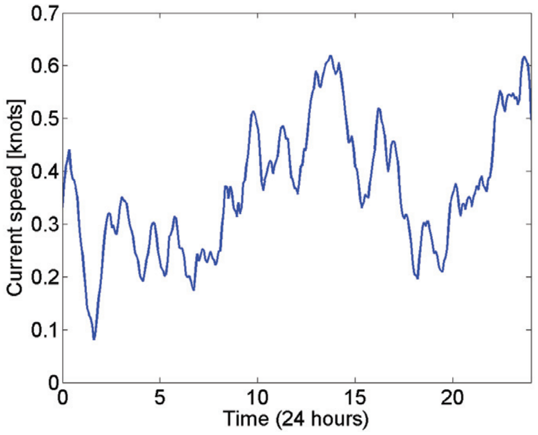

Figure A.44: *Current speed for 20 September 2011.*

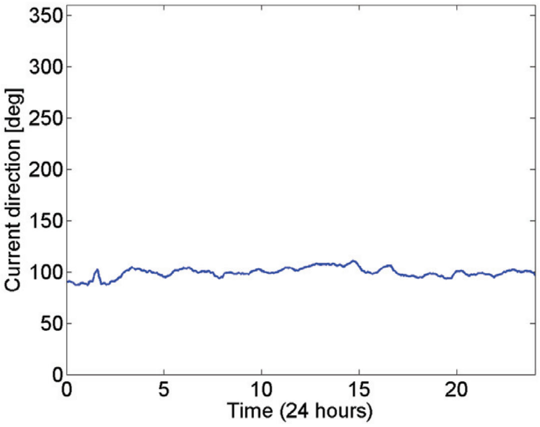

Figure A.45: *Current direction for 20 September 2011.*

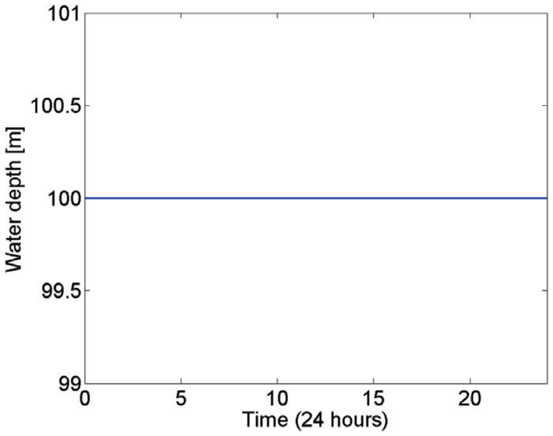

Figure A.46: *Logged water depth on 20 September 2011. Depths above 100 m cannot be measured.*

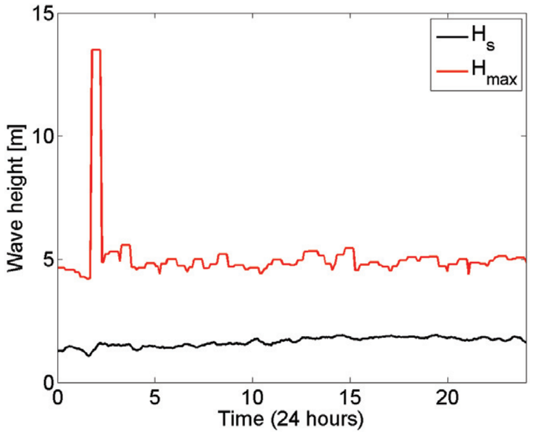

Figure A.47: *Significant and maximum wave height from WaMoS on 20 September 2011, 24 hours.*

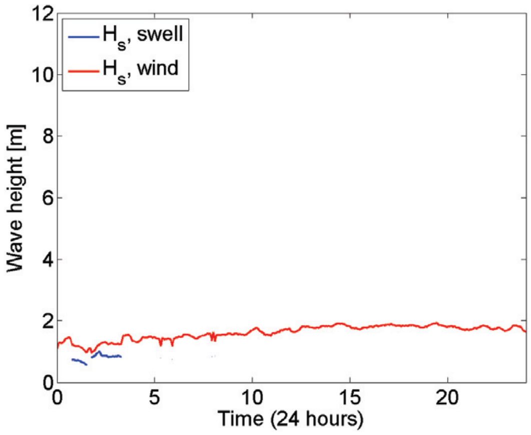

Figure A.48: *Significant wave height for swell and wind driven component from WaMoS on 20 September 2011, 24 hours.*

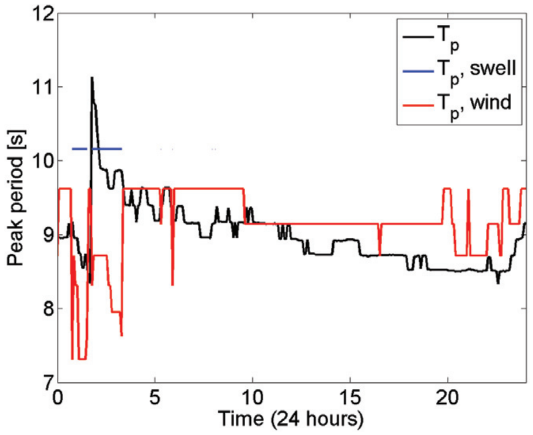

Figure A.49: *Peak periods from WaMoS on 20 September 2011, 24 hours.*

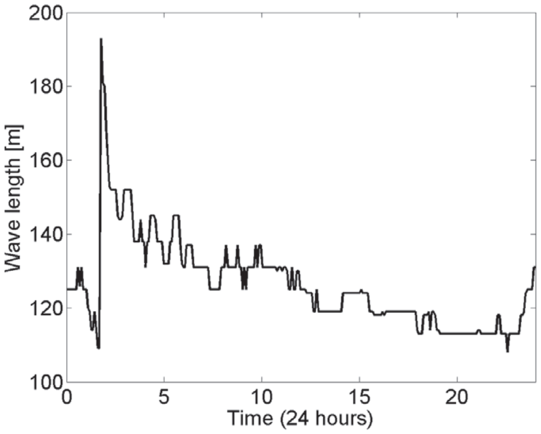

Figure A.50: *Wave length with respect to T_p from WaMoS on 20 September 2011, 24 hours.*

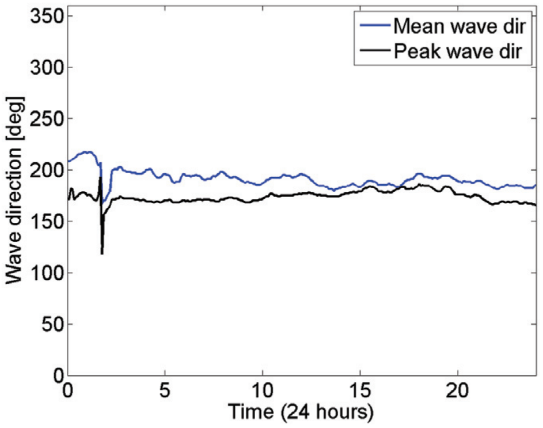

Figure A.51: *Mean and peak wave direction from WaMoS on 20 September 2011, 24 hours. Given as coming from compass rose direction.*

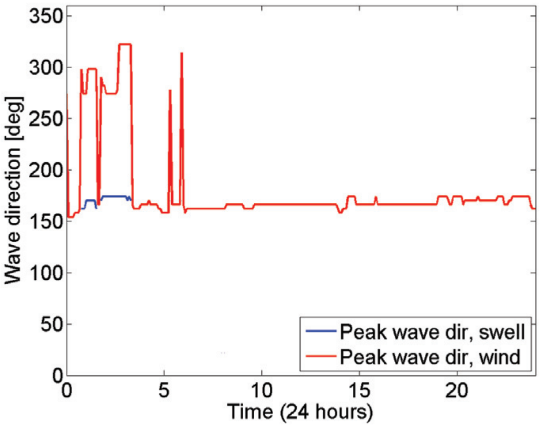

Figure A.52: *Peak wave direction for swell and wind driven component from WaMoS on 20 September 2011, 24 hours. Given as coming from compass rose direction.*

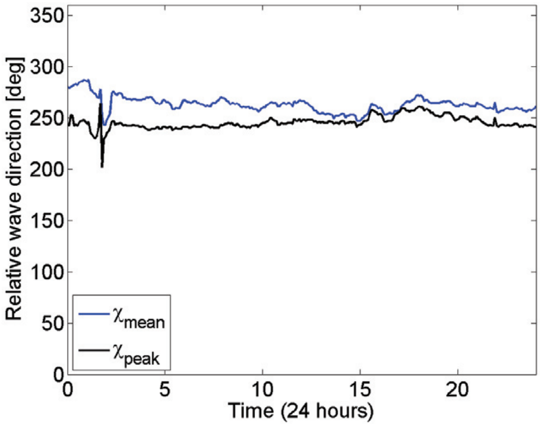

Figure A.53: *Relative mean and peak wave direction from WaMoS on 20 September 2011, 24 hours. 180 deg is head sea.*

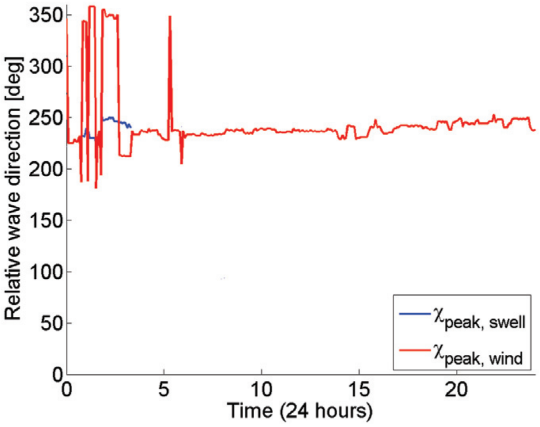

Figure A.54: *Relative peak wave directions for swell and wind components from WaMoS on 20 September 2011, 24 hours. 180 deg is head sea.*

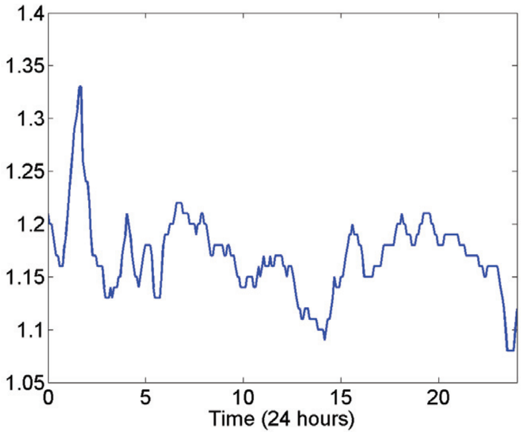

Figure A.55: *Spreading parameter for Jonswap spectrum from WaMoS for 20 September 2011, 24 hours.*

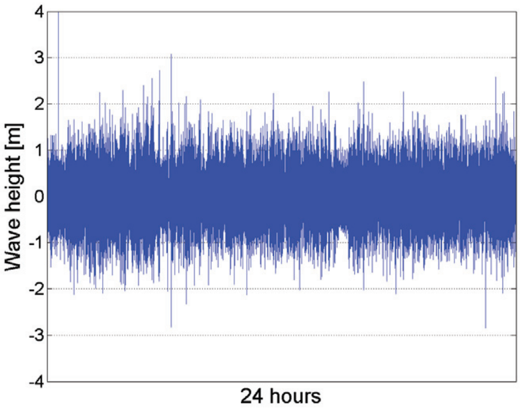

Figure A.56: *Wave height from Radac for 20 September 2011, 24 hours.*

02 October 2011

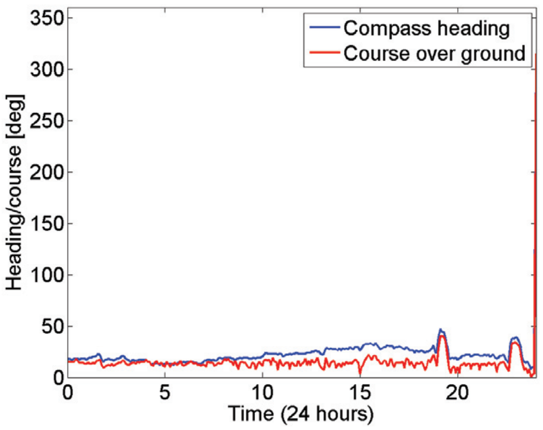

Figure A.57: *Ship true heading from gyro compass and course over ground from GPS on 02 October 2011.*

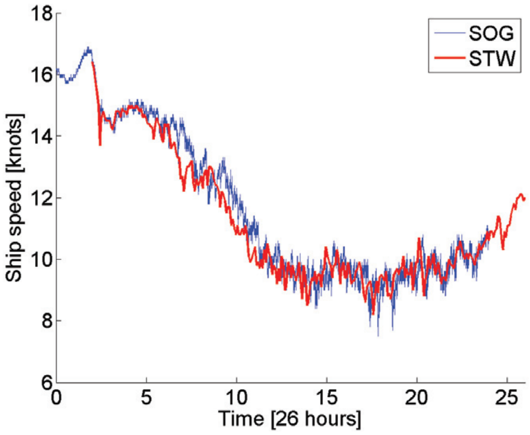

Figure A.58: *Ship speed through water (STW) and over ground (SOG) on 02 October 2011.*

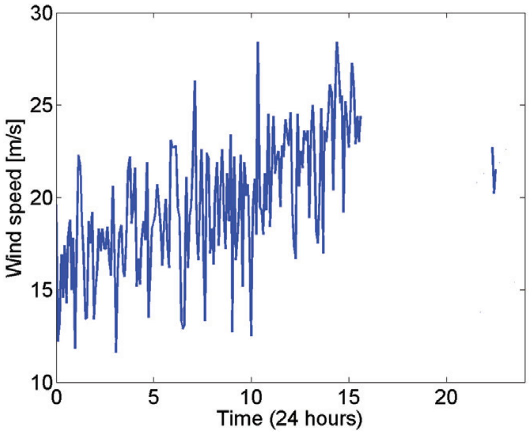

Figure A.59: *Wind speed on 02 October 2011.*

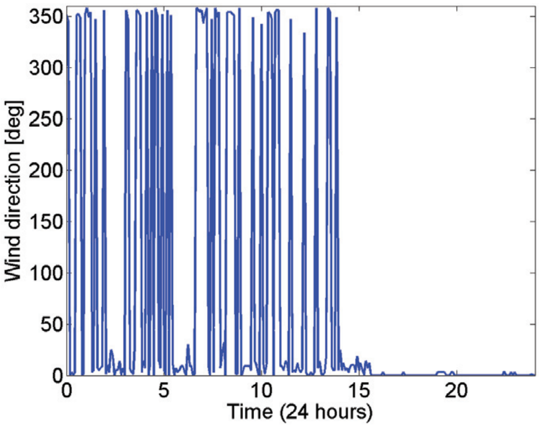

Figure A.60: *Wind direction on 02 October 2011.*

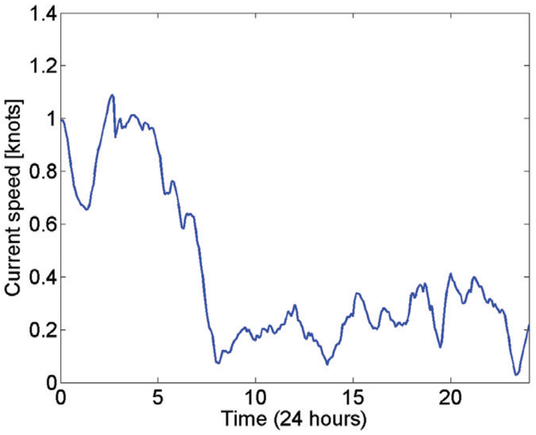

Figure A.61: *Current speed for 02 October 2011.*

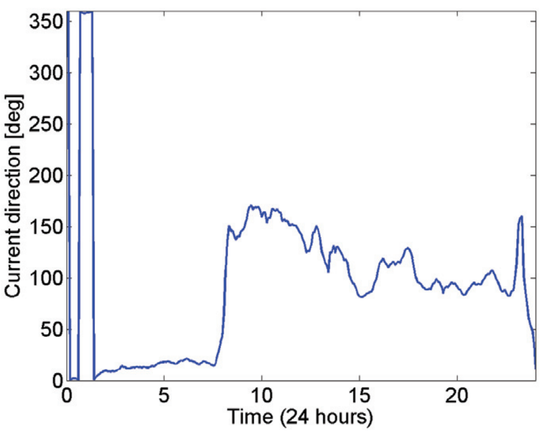

Figure A.62: *Current direction for 02 October 2011.*

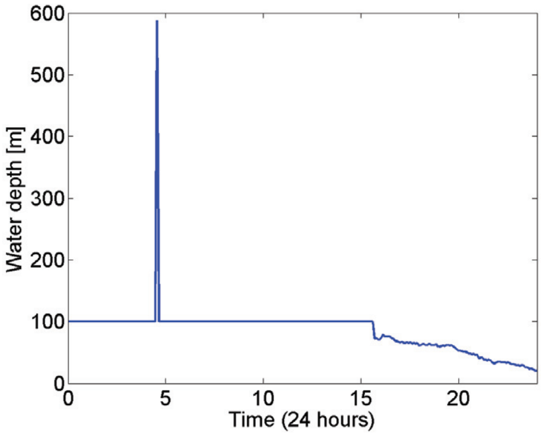

Figure A.63: *Logged water depth on 02 October 2011. Depths above 100 m cannot be measured.*

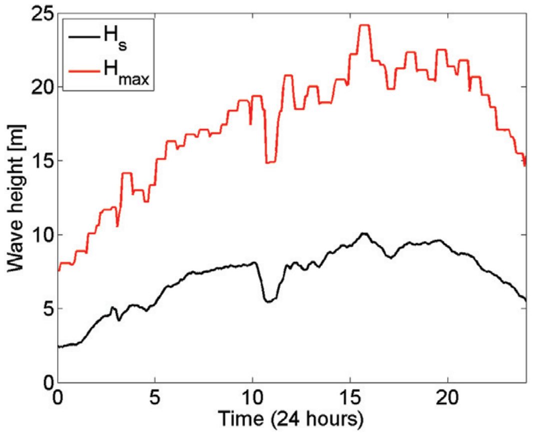

Figure A.64: *Significant and maximum wave height from WaMoS on 02 October 2011, 24 hours.*

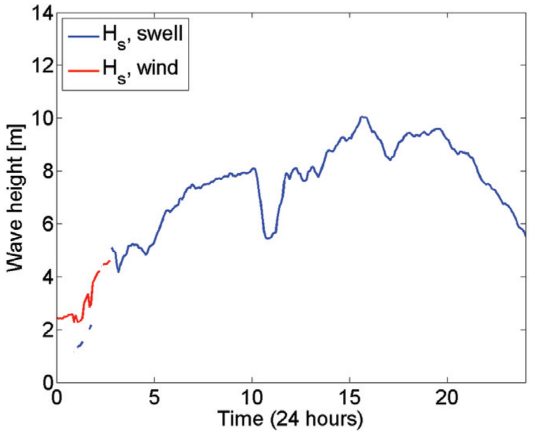

Figure A.65: *Significant wave height for swell and wind driven component from WaMoS on 02 October 2011, 24 hours.*

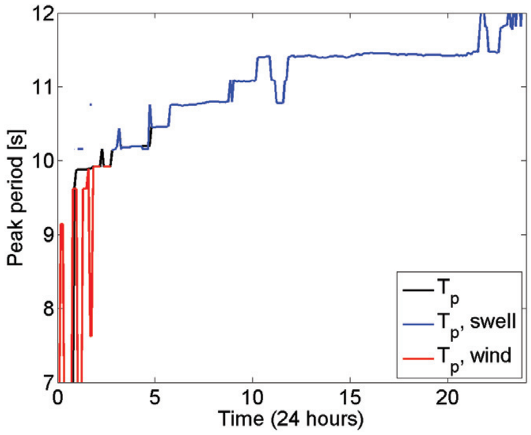

Figure A.66: *Peak periods from WaMoS on 02 October 2011, 24 hours.*

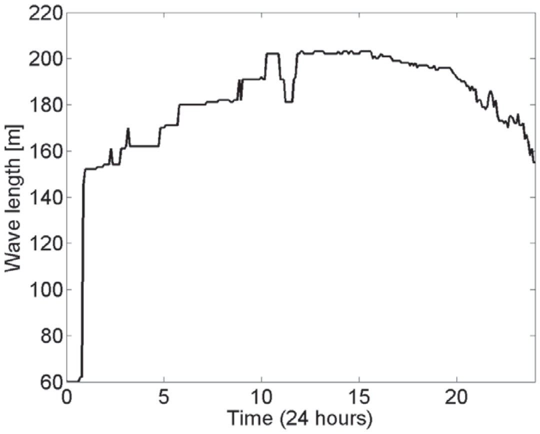

Figure A.67: *Wave length with respect to T_p from WaMoS on 02 October 2011, 24 hours.*

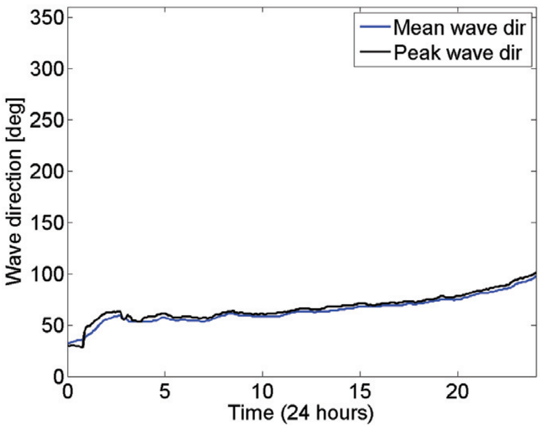

Figure A.68: *Mean and peak wave direction from WaMoS on 02 October 2011, 24 hours. Given as coming from compass rose direction.*

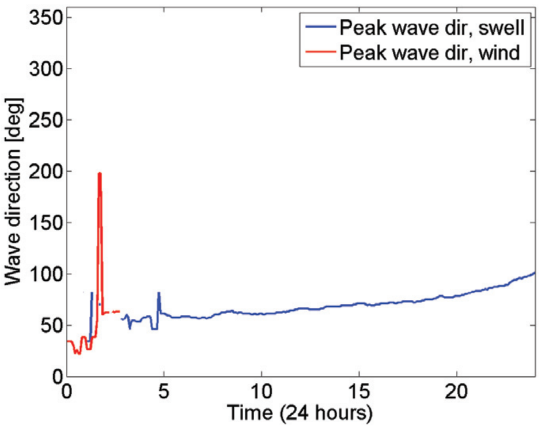

Figure A.69: *Peak wave direction for swell and wind driven component from WaMoS on 02 October 2011, 24 hours. Given as coming from compass rose direction.*

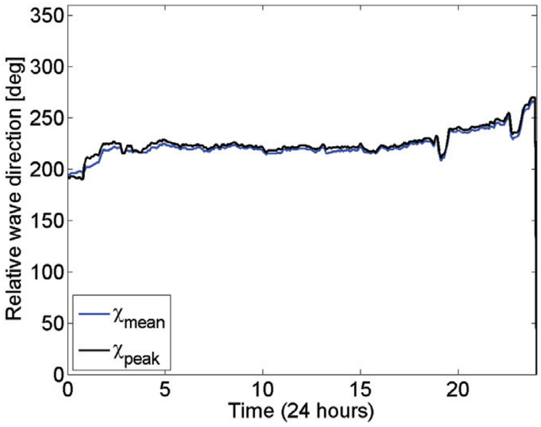

Figure A.70: *Relative mean and peak wave direction from WaMoS on 02 October 2011, 24 hours. 180 deg is head sea.*

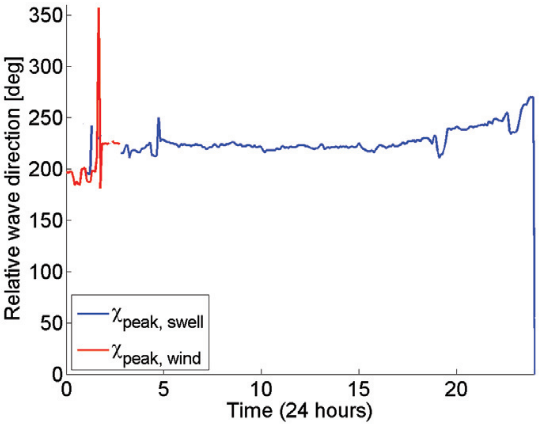

Figure A.71: *Relative peak wave directions for swell and wind components from WaMoS on 02 October 2011, 24 hours. 180 deg is head sea.*

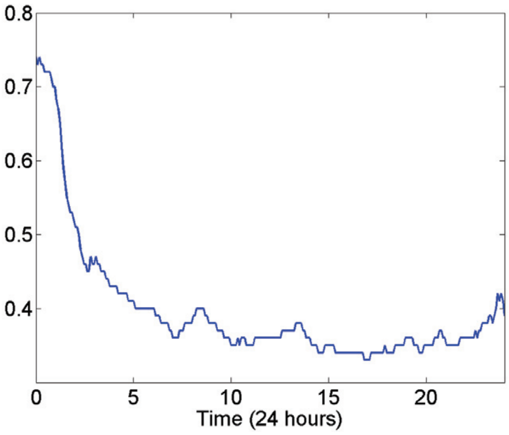

Figure A.72: *Spreading parameter for Jonswap spectrum from WaMoS for 02 October 2011, 24 hours.*

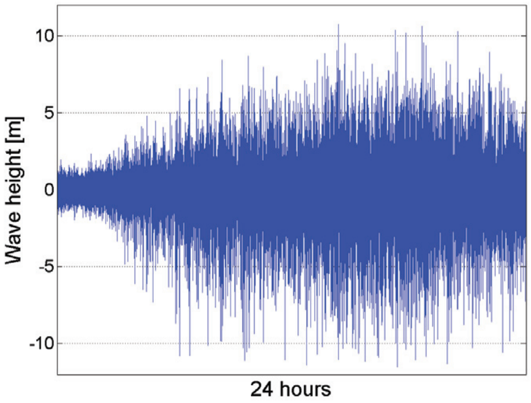

Figure A.73: *Wave height from Radac for 02 October 2011, 24 hours.*

17 December 2011

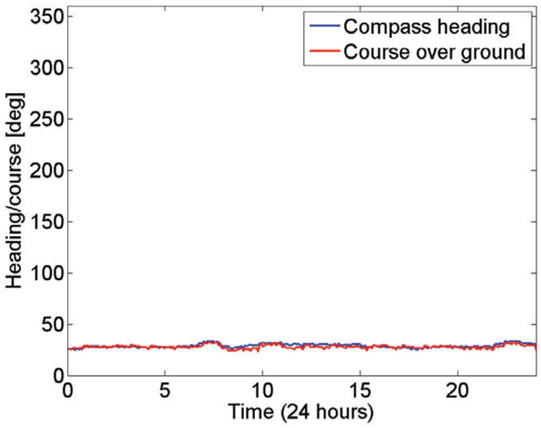

Figure A.74: *Ship true heading from gyro compass and course over ground from GPS on 17 December 2011.*

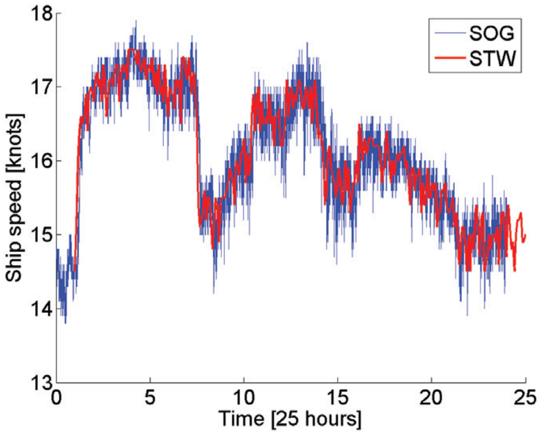

Figure A.75: *Ship speed through water (STW) and over ground (SOG) on 17 December 2011.*

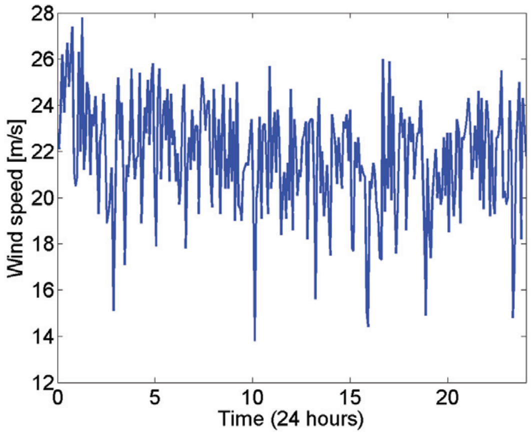

Figure A.76: *Wind speed on 17 December 2011.*

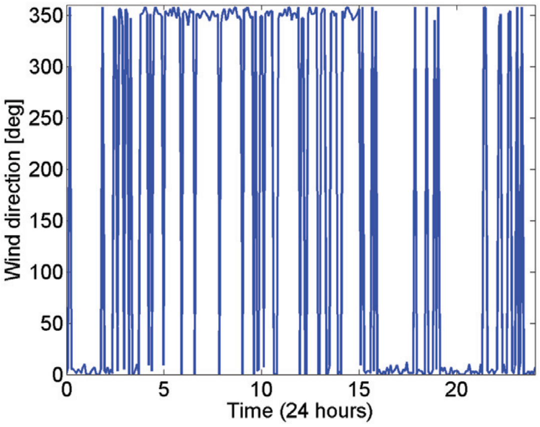

Figure A.77: *Wind direction on 17 December 2011.*

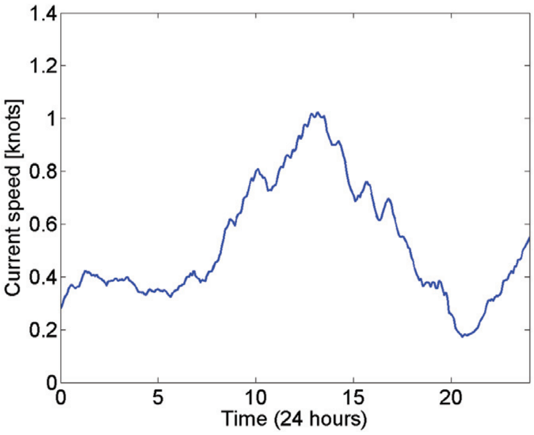

Figure A.78: *Current speed for 17 December 2011.*

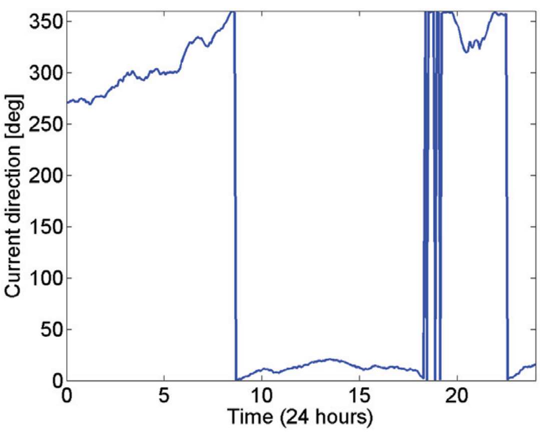

Figure A.79: *Current direction for 17 December 2011.*

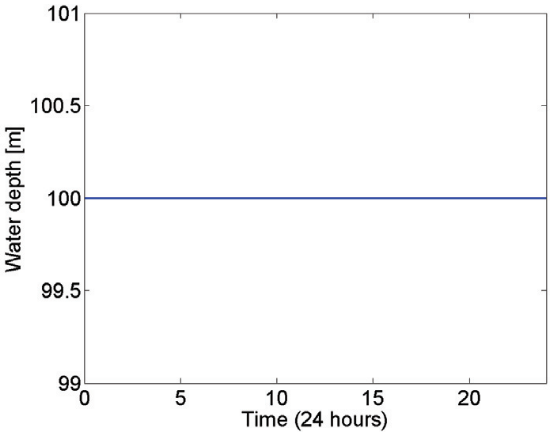

Figure A.80: *Logged water depth on 17 December 2011. Depths above 100 m cannot be measured.*

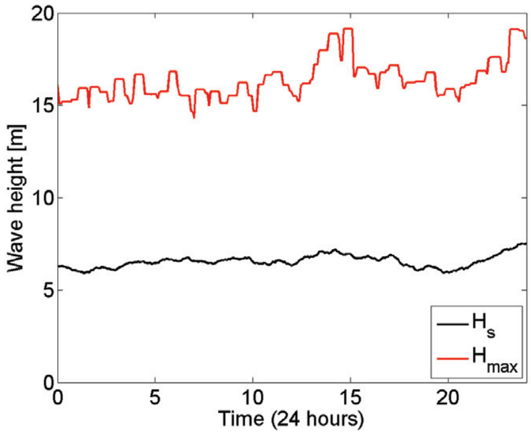

Figure A.81: *Significant and maximum wave height from WaMoS on 17 December 2011, 24 hours.*

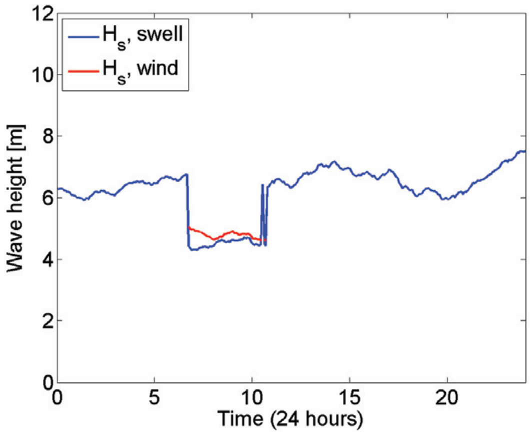

Figure A.82: *Significant wave height for swell and wind driven component from WaMoS on 17 December 2011, 24 hours.*

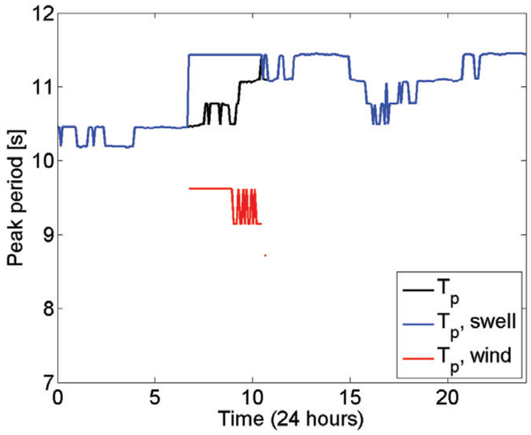

Figure A.83: *Peak periods from WaMoS on 17 December 2011, 24 hours.*

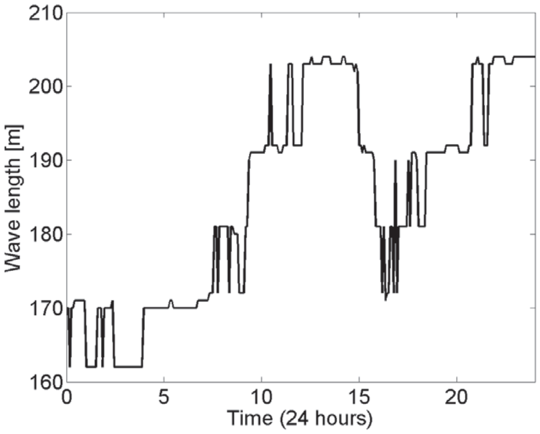

Figure A.84: *Wave length with respect to T_p from WaMoS on 17 December 2011, 24 hours.*

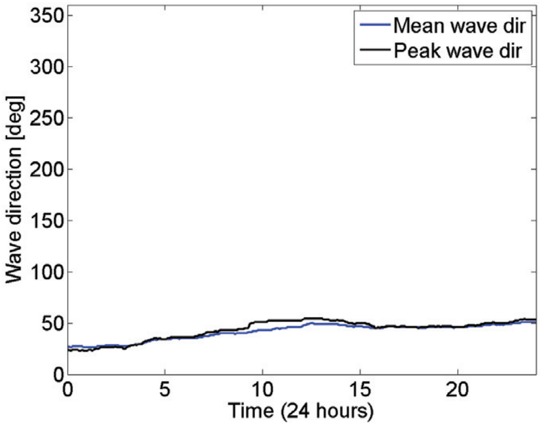

Figure A.85: *Mean and peak wave direction from WaMoS on 17 December 2011, 24 hours. Given as coming from compass rose direction.*

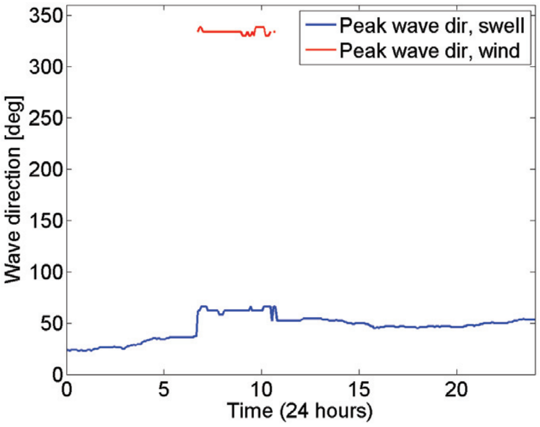

Figure A.86: *Peak wave direction for swell and wind driven component from WaMoS on 17 December 2011, 24 hours. Given as coming from compass rose direction.*

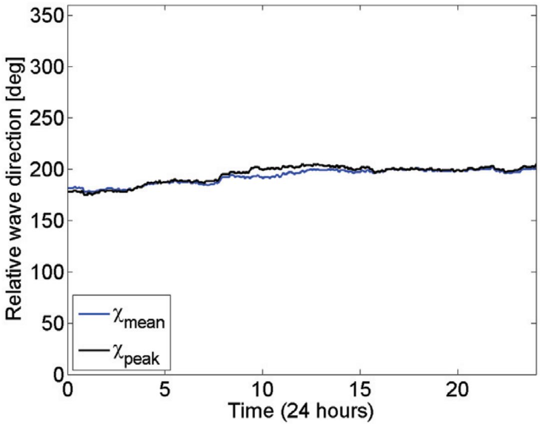

Figure A.87: *Relative mean and peak wave direction from WaMoS on 17 December 2011, 24 hours. 180 deg is head sea.*

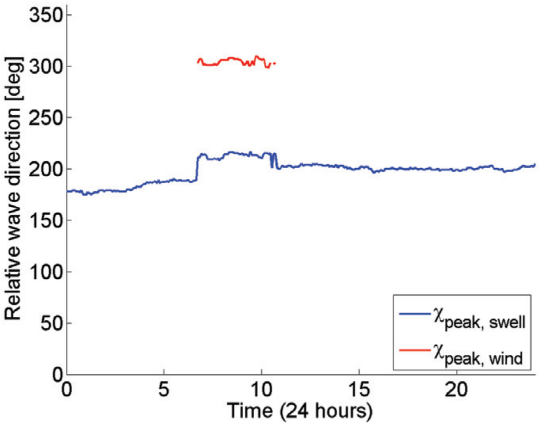

Figure A.88: *Relative peak wave directions for swell and wind components from WaMoS on 17 December 2011, 24 hours. 180 deg is head sea.*

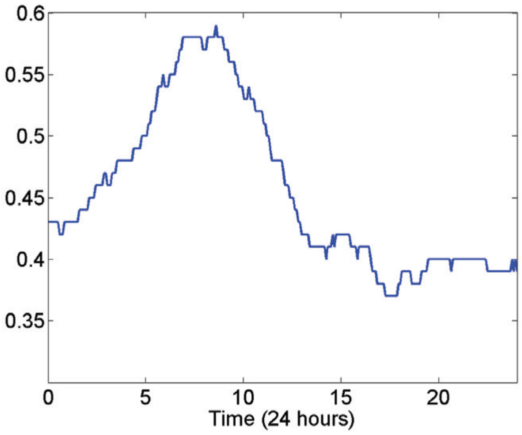

Figure A.89: *Spreading parameter for Jonswap spectrum from WaMoS for 17 December 2011, 24 hours.*

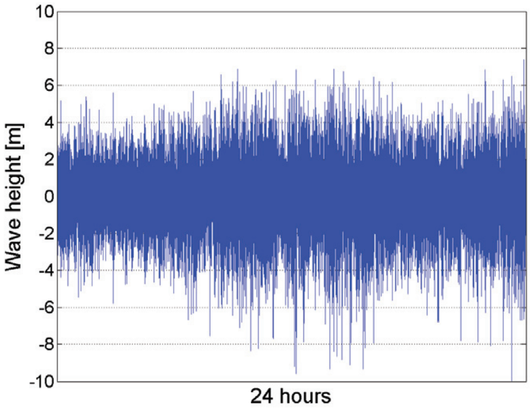

Figure A.90: *Wave height from Radac for 17 December 2011, 24 hours.*

A.1.3 Hindcast wind and wave data

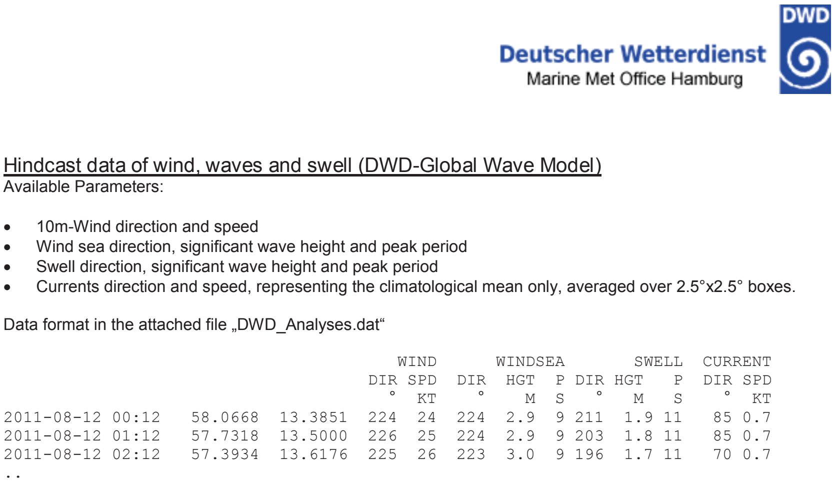

Deutscher Wetterdienst
Marine Met Office Hamburg

Hindcast data of wind, waves and swell (DWD-Global Wave Model)
Available Parameters:

- 10m-Wind direction and speed
- Wind sea direction, significant wave height and peak period
- Swell direction, significant wave height and peak period
- Currents direction and speed, representing the climatological mean only, averaged over 2.5°x2.5° boxes.

Data format in the attached file „DWD_Analyses.dat“

```
                                        WIND      WINDSEA       SWELL  CURRENT
                                     DIR SPD  DIR  HGT  P DIR HGT   P  DIR SPD
                                        ° KT     °   M  S    °  M   S    °  KT
2011-08-12 00:12   58.0668  13.3851  224  24  224  2.9  9 211  1.9 11   85 0.7
2011-08-12 01:12   57.7318  13.5000  226  25  224  2.9  9 203  1.8 11   85 0.7
2011-08-12 02:12   57.3934  13.6176  225  26  223  3.0  9 196  1.7 11   70 0.7
..
```

```
                                      DWD_Analyses
                                          WIND       WINDSEA        SWELL   CURRENT
                                        DIR SPD  DIR  HGT  P DIR HGT    P   DIR SPD
                                          °  KT    °    M  S   °   M    S     °  KT
2011-08-12 00:12    58.0668   13.3851   224  24  224  2.9  9 211  1.9 11    85 0.7
2011-08-12 01:12    57.7318   13.5000   226  25  224  2.9  9 203  1.8 11    85 0.7
2011-08-12 02:12    57.3934   13.6176   225  26  223  3.0  9 196  1.7 11    70 0.7
2011-08-12 03:12    57.0568   13.7371   224  26  223  3.1  9 187  1.5 11    70 0.7
2011-08-12 04:12    56.7229   13.8566   223  27  221  3.2  9 181  1.4 11    70 0.7
2011-08-12 05:12    56.3923   13.9692   221  27  218  3.3  9 179  1.4 11    70 0.7
2011-08-12 06:12    56.0721   14.0825   219  26  217  3.3  9 180  1.5 11    70 0.7
2011-08-12 07:12    55.7440   14.1977   217  25  216  3.1  9 182  1.7 11    70 0.7
2011-08-12 08:12    55.3882   14.2500   216  24  216  3.0  9 183  1.8 11    70 0.7
2011-08-12 09:12    55.0227   14.2837   219  25  216  3.0  9 179  1.8 11    70 0.7
2011-08-12 10:12    54.6587   14.3175   221  25  215  2.8  9 178  1.8 11    80 0.7
2011-08-12 11:18    54.2505   14.3507   217  24  211  2.7  9 175  1.8 10    80 0.7
2011-08-12 12:18    53.8720   14.3821   214  23  208  2.4  9 177  2.0 10    80 0.7
2011-08-12 13:18    53.5030   14.4135   210  21  206  2.0  8 182  2.3  9    80 0.7
2011-08-12 14:18    53.1374   14.4106   205  20  204  1.6  7 183  2.4  9    80 0.7
2011-08-12 15:18    52.7894   14.3730   202  18  202  1.3  7 181  2.4  9    80 0.7
2011-08-12 16:12    52.4443   14.2724   197  16  197  1.1  6 179  2.3  9    90 1.0
2011-08-12 17:18    52.0852   14.1681   195  15  195  0.8  5 177  2.2 10    90 1.0
2011-08-12 18:18    51.7211   14.0646   188  15  188  0.7  5 176  2.2 10    90 1.0
2011-08-12 19:18    51.3464   13.9634   198  13  198  0.6  5 178  1.9 10    90 1.0
2011-08-12 20:18    50.9757   13.8368   197  11  200  0.4  4 177  1.7 10    90 1.0
2011-08-12 21:12    50.5986   13.7115   207  11  210  0.4  4 178  1.5 10    90 1.0
2011-08-12 22:12    50.2191   13.5983   218  11  224  0.3  4 178  1.4 10    90 1.0
2011-08-12 23:12    49.8384   13.4734   222  11  227  0.3  3 175  1.2 10    90 1.1

                                          WIND       WINDSEA        SWELL   CURRENT
                                        DIR SPD  DIR  HGT  P DIR HGT    P   DIR SPD
                                          °  KT    °    M  S   °   M    S     °  KT
2011-09-16 00:12    49.9296   13.3982   223   9  228  0.0  / 146  1.1 11    90 0.7
2011-09-16 01:12    50.2234   13.4776   219   9  270  0.0  / 148  1.2 11    55 1.1
2011-09-16 02:12    50.5112   13.5661   204   9  180  0.0  / 150  1.3 11    55 1.1
2011-09-16 03:12    50.7925   13.6606   196  10  184  0.1  / 152  1.4 10    55 1.1
2011-09-16 04:12    51.0769   13.7455   193   9  184  0.1  / 154  1.5 10    55 1.1
2011-09-16 05:12    51.4167   13.8520   193  11  186  0.2  3 164  1.8 10    55 1.1
2011-09-16 06:12    51.7411   13.9512   192  12  188  0.2  4 169  2.1 10    55 1.1
2011-09-16 07:12    52.0394   14.0438   198  13  196  0.3  4 171  2.1 10    55 1.1
2011-09-16 08:12    52.3349   14.1362   201  15  198  0.6  4 175  2.1  9    55 1.1
2011-09-16 09:12    52.6625   14.2392   205  17  201  0.7  5 177  2.1  9    65 0.6
2011-09-16 10:18    52.9549   14.3278   205  17  203  0.9  5 178  2.1  9    65 0.6
2011-09-16 11:12    53.2551   14.3430   206  18  204  1.0  6 180  2.1  9    65 0.6
2011-09-16 12:12    53.5619   14.3443   210  18  209  1.0  5 182  2.1  9    65 0.6
2011-09-16 13:12    53.8675   14.3447   216  18  214  1.0  6 183  2.1  9    65 0.6
2011-09-16 14:12    54.1755   14.3464   217  17  216  0.9  5 186  2.1  9    65 0.6
2011-09-16 15:12    54.4895   14.3427   216  15  217  0.7  5 189  2.2  9    65 0.6
2011-09-16 16:12    54.7826   14.2742   212  15  214  0.6  5 191  2.3  9    65 0.6
2011-09-16 17:12    55.0667   14.1774   207  17  207  0.8  5 191  2.2  9    75 0.4
2011-09-16 18:12    55.3452   14.0835   207  20  206  1.3  7 189  2.1  9    75 0.4
2011-09-16 19:12    55.6276   13.9853   210  22  207  1.7  7 186  1.9 10    75 0.4
2011-09-16 20:12    55.9158   13.8866   214  25  212  2.1  8 181  1.7 10    75 0.4
2011-09-16 21:12    56.2125   13.7911   216  26  215  2.4  8 175  1.6 11    75 0.4
2011-09-16 22:12    56.5014   13.6909   217  26  217  2.4  8 175  1.6 11    75 0.4
2011-09-16 23:18    56.8210   13.5790   219  26  219  2.3  8 178  1.7 10    75 0.4

                                          WIND       WINDSEA        SWELL   CURRENT
                                        DIR SPD  DIR  HGT  P DIR HGT    P   DIR SPD
                                          °  KT    °    M  S   °   M    S     °  KT
2011-09-20 00:12    73.5021    7.8441   259  10  270  0.0  / 178  1.6  9   130 0.5
2011-09-20 01:12    73.7128    7.7734   260  12  262  0.0  / 177  1.6  9   130 0.5
2011-09-20 02:12    73.9198    7.7082   260  13  260  0.1  / 177  1.6  9   130 0.5
2011-09-20 03:12    74.1094    7.6522   261  13  259  0.1  / 177  1.6  9   130 0.5
2011-09-20 04:12    74.2947    7.5926   265  13  261  0.2  3 178  1.6  9   130 0.5
2011-09-20 05:12    74.4804    7.5351   268  13  261  0.3  3 179  1.6  9   130 0.5
2011-09-20 06:12    74.6684    7.4767   270  13  260  0.4  3 180  1.6  9   135 0.7
2011-09-20 07:12    74.8596    7.4174   270  13  263  0.4  3 181  1.6  9   135 0.7
2011-09-20 08:12    75.0492    7.3579   271  13  266  0.4  4 182  1.6  9   130 0.7
                                        Page 1
```

```
                                  DWD_Analyses
2011-09-20 09:12   75.2423   7.2969  273  14  269  0.3  4 182  1.6  9  130 0.7
2011-09-20 10:12   75.4370   7.2365  269  14  265  0.4  4 181  1.5  9  130 0.7
2011-09-20 11:18   75.6465   7.1695  265  14  261  0.4  4 182  1.5  9  130 0.7
2011-09-20 12:12   75.8407   7.1087  264  15  260  0.5  4 182  1.6  9  130 0.7
2011-09-20 13:18   76.0434   7.0432  263  14  262  0.5  4 183  1.6  9  130 0.7
2011-09-20 14:18   76.2456   6.9783  263  14  264  0.6  4 185  1.6  9  130 0.7
2011-09-20 15:18   76.4605   6.8923  264  14  265  0.6  4 187  1.6  9  130 0.7
2011-09-20 16:18   76.6764   6.8292  263  15  265  0.6  4 187  1.6  9  130 0.7
2011-09-20 17:18   76.8853   6.7669  261  16  263  0.7  5 187  1.6  9  130 0.7
2011-09-20 18:18   77.0841   6.7185  262  16  263  0.7  5 187  1.6  9  130 0.7
2011-09-20 19:12   77.2793   6.6577  266  16  265  0.8  5 186  1.6  9  130 0.7
2011-09-20 20:12   77.4758   6.5927  268  17  266  0.8  5 185  1.6  9  130 0.7
2011-09-20 21:12   77.6737   6.5294  268  17  267  0.8  5 185  1.6  9  125 0.7
2011-09-20 22:18   77.8755   6.4686  265  18  265  0.8  5 186  1.6  9  125 0.7
2011-09-20 23:18   78.0769   6.4037  265  18  265  0.8  5 185  1.6  9  125 0.7

                                        WIND      WINDSEA       SWELL  CURRENT
                                     DIR SPD  DIR  HGT  P DIR HGT   P  DIR SPD
                                       °  KT    °    M  S   °   M   S    °  KT
2011-10-02 00:12  113.3181  17.7788   23  21   31  1.2  5  67  1.6  9  275 0.8
2011-10-02 01:12  113.3839  18.0352   25  22   32  1.4  6  66  1.7  9  275 0.8
2011-10-02 02:12  113.4435  18.2758   27  23   34  1.6  7  68  1.8  9  275 0.8
2011-10-02 04:12  113.5597  18.7315   25  29   36  2.6  9  80  1.6 10  275 0.8
2011-10-02 05:12  113.6205  18.9606   25  33   37  3.0  9  86  1.5 11  275 0.8
2011-10-02 06:12  113.6720  19.1739   25  36   38  3.4  9  90  1.5 11  275 0.8
2011-10-02 07:12  113.7250  19.3781   27  37   40  3.8  9  92  1.5 12  275 0.8
2011-10-02 08:12  113.7717  19.5763   28  39   41  4.2 10  92  1.5 12  275 0.8
2011-10-02 09:12  113.8185  19.7550   30  40   42  4.4 10  94  1.5 12  275 0.8
2011-10-02 10:12  113.8574  19.9183   31  40   42  4.5 10  94  1.5 12  275 0.8
2011-10-02 11:12  113.8975  20.0758   32  39   43  4.4 10  93  1.5 12  265 0.7
2011-10-02 12:12  113.9364  20.2294   33  38   44  4.4 10  92  1.5 12  265 0.7
2011-10-02 13:12  113.9765  20.3798   36  37   45  4.4 10  91  1.6 12  265 0.7
2011-10-02 14:12  114.0151  20.5393   39  36   46  4.3 10  91  1.7 13  265 0.7
2011-10-02 15:12  114.0535  20.6935   42  36   49  4.4 10  93  1.7 13  265 0.7
2011-10-02 16:12  114.0952  20.8363   43  38   51  4.6 10  96  1.5 13  265 0.7
2011-10-02 17:12  114.1330  20.9858   44  38   52  4.8 10  99  1.5 13  265 0.7
2011-10-02 18:12  114.1722  21.1411   44  38   52  4.7 10  99  1.5 13  265 0.7
2011-10-02 19:12  114.2217  21.2964   43  38   52  4.6 10  98  1.5 13  265 0.7
2011-10-02 20:12  114.2673  21.4468   42  37   53  4.4 10  97  1.7 13  265 0.7
2011-10-02 21:12  114.3030  21.6131   42  36   54  4.0 10  95  1.8 13  265 0.7
2011-10-02 22:12  114.3414  21.7842   42  35   54  3.9 10  95  1.7 13  265 0.7
2011-10-02 23:18  114.4166  21.9671   42  34   54  3.4 10  94  1.5 13  265 0.7
```

A.1.4 Ship response spectra and RAOs

In the following, the response spectra for five different ship responses are given together with the corresponding transfer functions (RAOs). The response spectra are derived from one hour of data from 02 October 2011 at 11 hours. FFT with smoothing is applied using the WAFO package.

All RAOs are calculated for a draft of 14.5 m and speed of 15 knots roughly corresponding to the operation conditions on 02 October 2011. 180 deg is head sea for the RAOs. The RAOs for the motions are determined by Bureau Veritas and the RAO for the VBM amidships is determined using linear strip theory. The FFT of the time derivatives of the same response (except the VBM) are also given but without the RAOs.

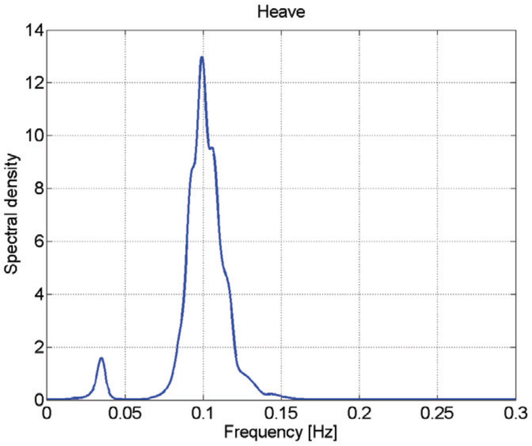

Figure A.91: *FFT of the heave response (measured in m). Smoothing using a Parzen window function is applied.*

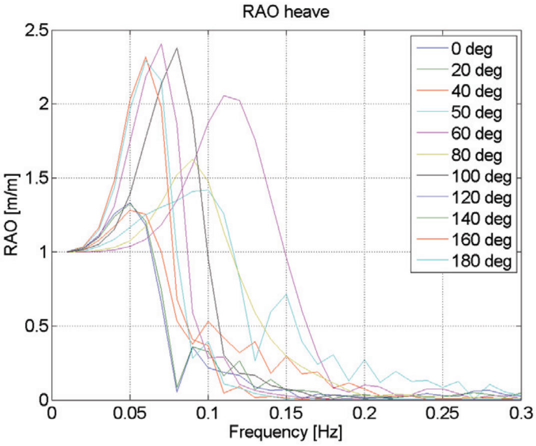

Figure A.92: *RAO for heave. 180 deg is head sea.*

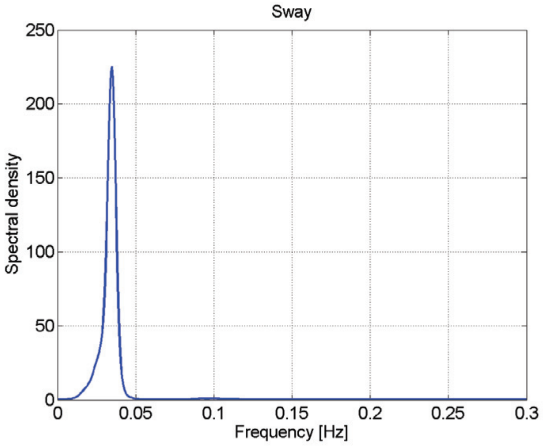

__Figure A.93:__ FFT of the sway response (measured in m). Smoothing using a Parzen window function is applied.

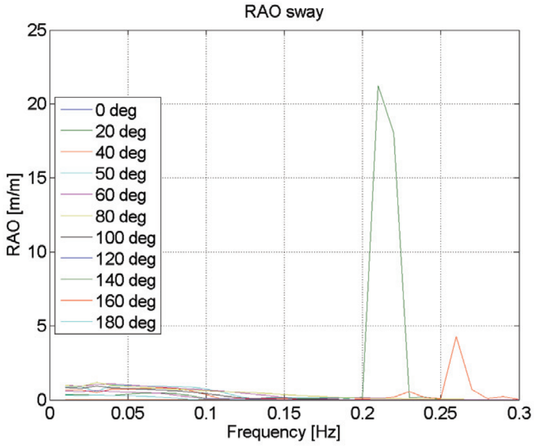

__Figure A.94:__ RAO for sway. 180 deg is head sea.

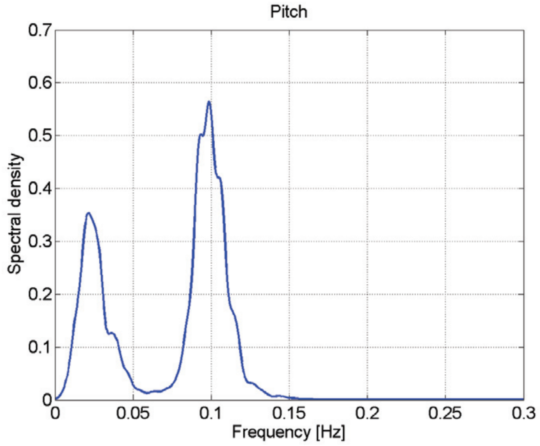

__Figure A.95:__ FFT of the pitch response (measured in deg). Smoothing using a Parzen window function is applied.

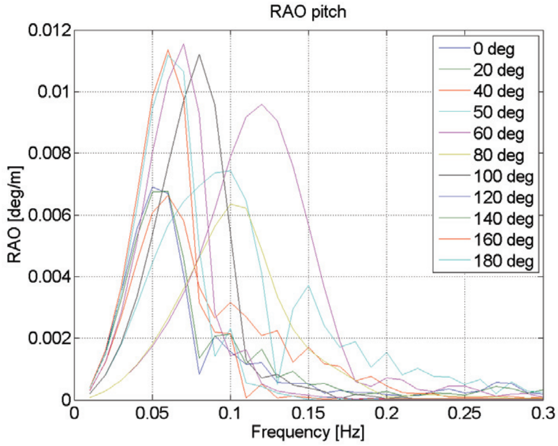

__Figure A.96:__ RAO for pitch. 180 deg is head sea.

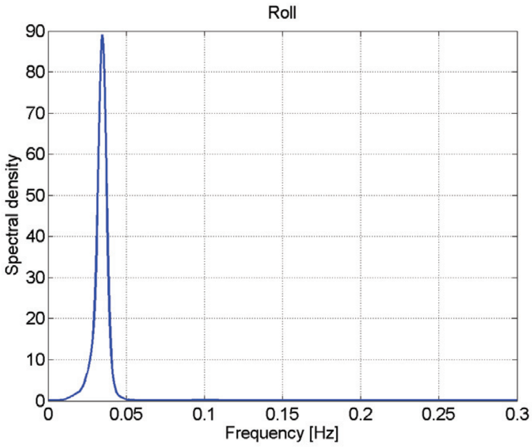

Figure A.97: *FFT of the roll response (measured in deg). Smoothing using a Parzen window function is applied.*

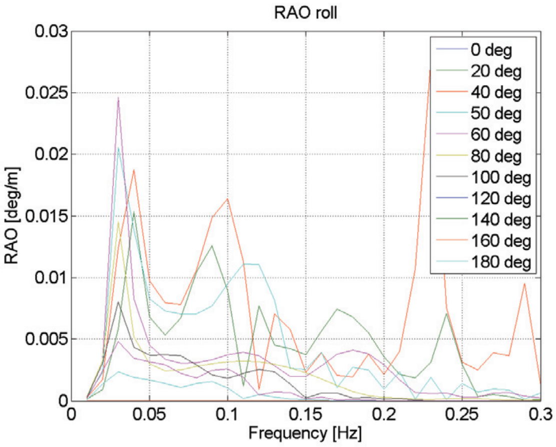

Figure A.98: *RAO for roll. 180 deg is head sea.*

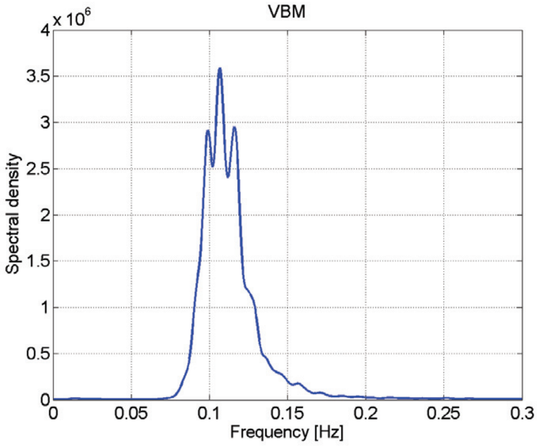

Figure A.99: *FFT of the vertical bending moment amidships (measured in MNm). Smoothing using a Parzen window function is applied.*

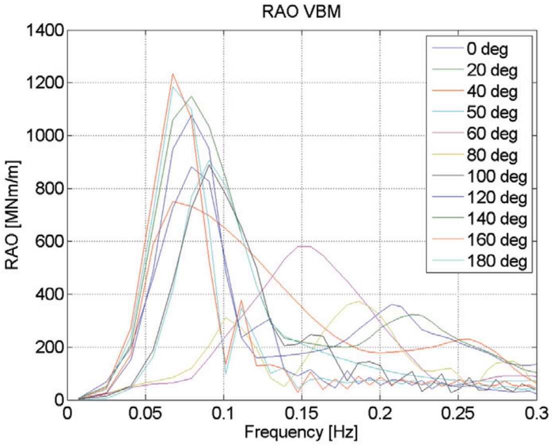

Figure A.100: *RAO of the vertical bending moment amidships. 180 is head sea.*

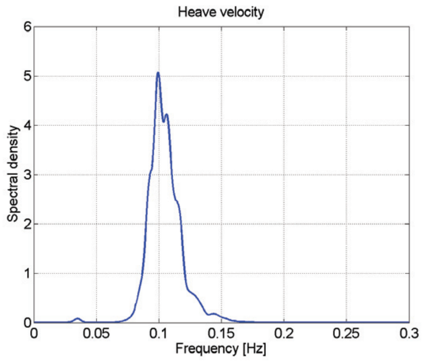

Figure A.101: *FFT of the vertical velocity. Smoothing using a Parzen window function is applied. One hour of data from 02 October 2011 at 11 hours.*

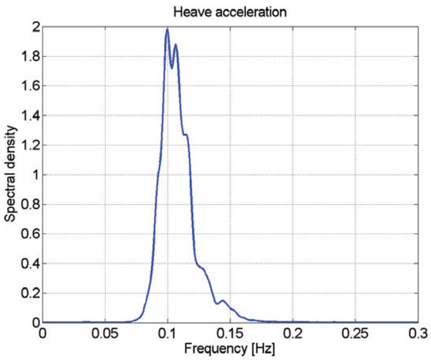

Figure A.102: *FFT of the vertical acceleration. Smoothing using a Parzen window function is applied. One hour of data from 02 October 2011 at 11 hours.*

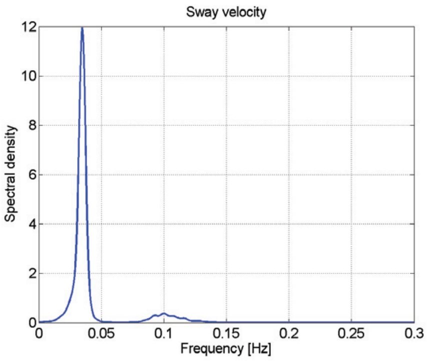

Figure A.103: *FFT of the transverse velocity. Smoothing using a Parzen window function is applied. One hour of data from 02 October 2011 at 11 hours.*

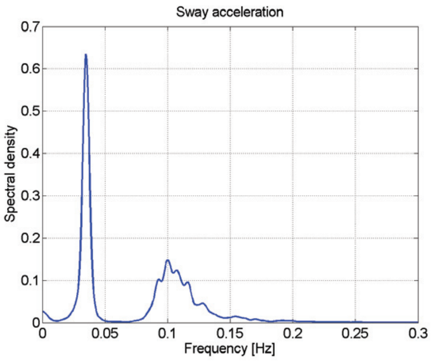

Figure A.104: *FFT of the transverse acceleration. Smoothing using a Parzen window function is applied. One hour of data from 02 October 2011 at 11 hours.*

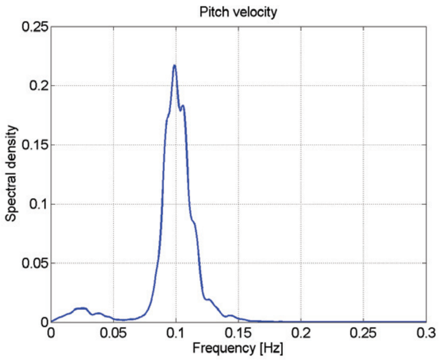

Figure A.105: *FFT of the pitch rate. Smoothing using a Parzen window function is applied. One hour of data from 02 October 2011 at 11 hours.*

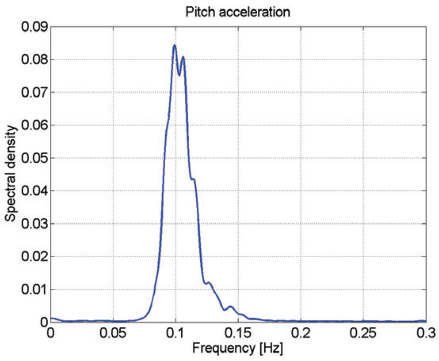

Figure A.106: *FFT of the pitch acceleration. Smoothing using a Parzen window function is applied. One hour of data from 02 October 2011 at 11 hours.*

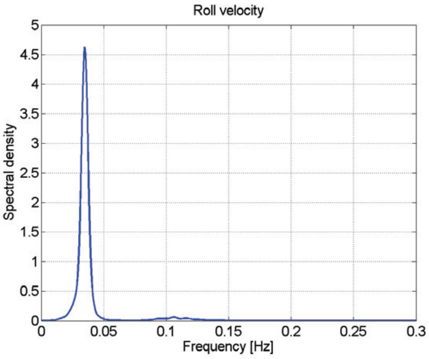

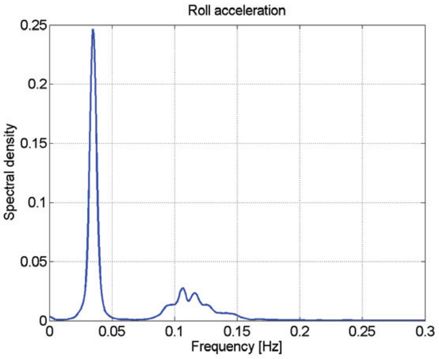

Figure A.107: *FFT of the roll rate. Smoothing using a Parzen window function is applied. One hour of data from 02 October 2011 at 11 hours.*

Figure A.108: *FFT of the roll acceleration response. Smoothing using a Parzen window function is applied. One hour of data from 02 October 2011 at 11 hours.*

A.1.5 Wave buoy analogy

In the figures below 180 deg is head sea. The results from the Bayesian and parametric modelling are average values from the two different response combinations {sway, heave, roll} and {sway, heave, pitch}.

For the Radac system the peak and upcrossing periods, T_p and T_z are derived from the spectral analysis of the wave elevation in the encounter frequency domain using WAFO. In order to transform the Radac results into the wave frequency domain for comparisons with the WaMoS and wave buoy analogy results, the knowledge of the ship speed and the relative wave direction from WaMos is used. For 02 October, the estimated directional wave spectra are also given using the parametric and the Bayesian method based on one hour of data.

12 August 2011

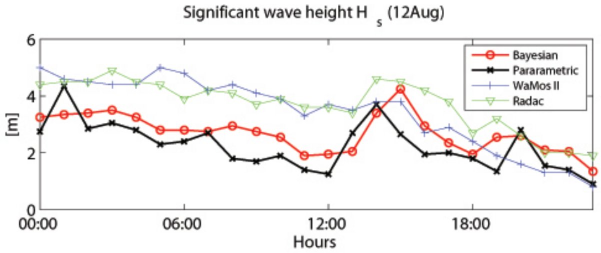

Figure A.109: *Significant wave height from Bayesian and parametric modelling, from directional wave radar (WaMoS) and the down-looking wave radar in the bow (Radac). Figure from Nielsen et al. (2013). 12 August 2011.*

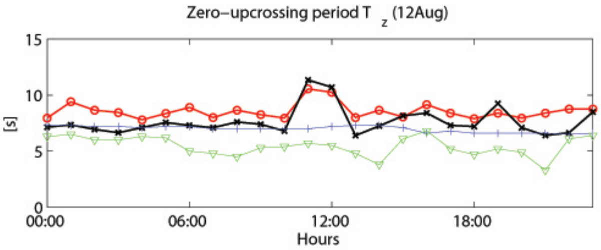

Figure A.110: *Zero-upcrossing wave period T_z from Bayesian and parametric modelling, from directional wave radar (WaMoS) and the down-looking wave radar in the bow (Radac). Figure from Nielsen et al. (2013). 12 August 2011.*

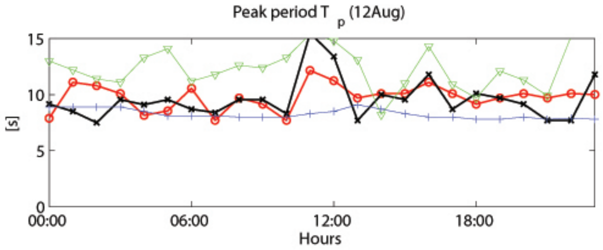

Figure A.111: *Peak wave period T_p from Bayesian and parametric modelling, from directional wave radar (WaMoS) and the down-looking wave radar in the bow (Radac). Figure from Nielsen et al. (2013). 12 August 2011.*

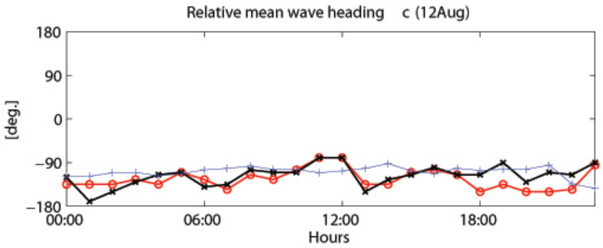

Figure A.112: *Relative wave direction χ from Bayesian and parametric modelling and from directional wave radar (WaMoS). The down-looking wave radar system (Radac) cannot estimate the relative wave direction). Figure from Nielsen et al. (2013). 12 August 2011.*

16 September 2011

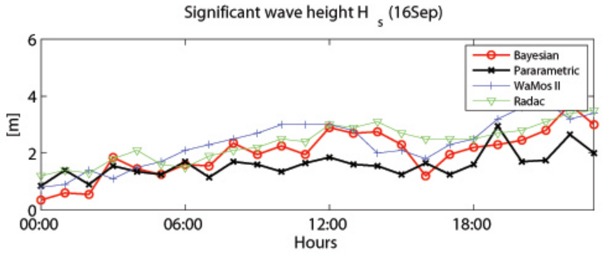

Figure A.113: *Significant wave height from Bayesian and parametric modelling, from directional wave radar (WaMoS) and the down-looking wave radar in the bow (Radac). Figure from Nielsen et al. (2013). 16 September 2011.*

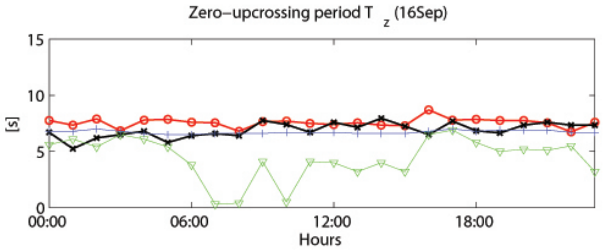

Figure A.114: *Zero-upcrossing wave period T_z from Bayesian and parametric modelling, from directional wave radar (WaMoS) and the down-looking wave radar in the bow (Radac). Figure from Nielsen et al. (2013). 16 September 2011.*

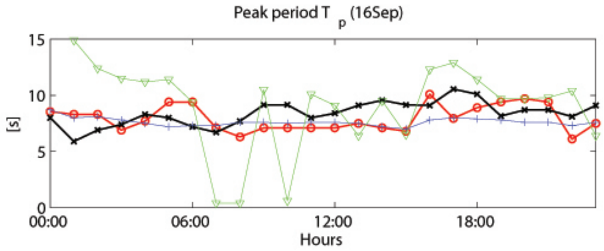

Figure A.115: *Peak wave period T_p from Bayesian and parametric modelling, from directional wave radar (WaMoS) and the down-looking wave radar in the bow (Radac). Figure from Nielsen et al. (2013). 16 September 2011.*

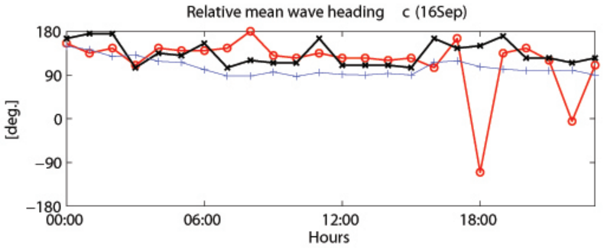

Figure A.116: *Relative wave direction χ from Bayesian and parametric modelling and from directional wave radar (WaMoS). The down-looking wave radar system (Radac) cannot estimate the relative wave direction). Figure from Nielsen et al. (2013). 16 September 2011.*

20 September 2011

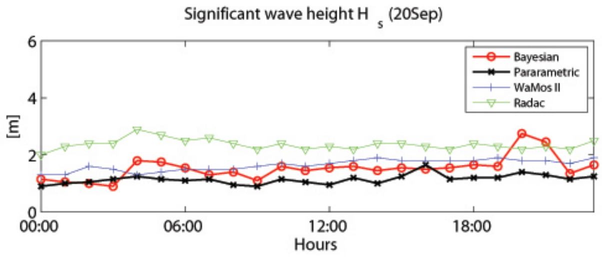

Figure A.117: *Significant wave height from Bayesian and parametric modelling, from directional wave radar (WaMoS) and the down-looking wave radar in the bow (Radac). Figure from Nielsen et al. (2013). 20 September 2011.*

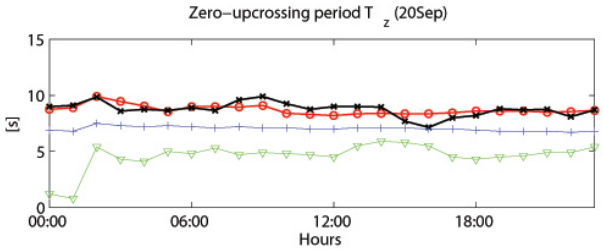

Figure A.118: *Zero-upcrossing wave period T_z from Bayesian and parametric modelling, from directional wave radar (WaMoS) and the down-looking wave radar in the bow (Radac). Figure from Nielsen et al. (2013). 20 September 2011.*

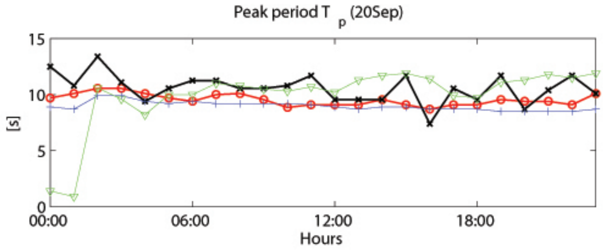

Figure A.119: *Peak wave period T_p from Bayesian and parametric modelling, from directional wave radar (WaMoS) and the down-looking wave radar in the bow (Radac). Figure from Nielsen et al. (2013). 20 September 2011.*

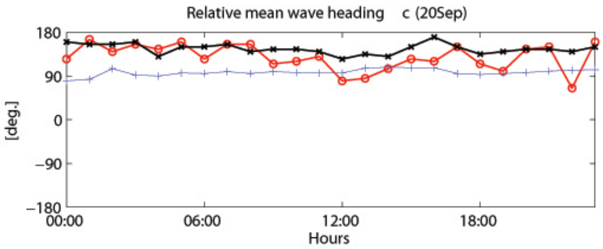

Figure A.120: *Relative wave direction χ from Bayesian and parametric modelling and from directional wave radar (WaMoS). The down-looking wave radar system (Radac) cannot estimate the relative wave direction). Figure from Nielsen et al. (2013). 20 September 2011.*

02 October 2011

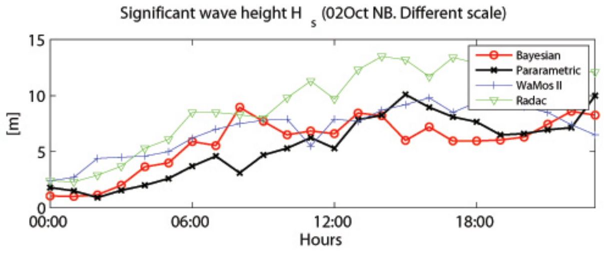

Figure A.121: *Significant wave height from Bayesian and parametric modelling, from directional wave radar (WaMoS) and the down-looking wave radar in the bow (Radac). Figure from Nielsen et al. (2013). 02 October 2011.*

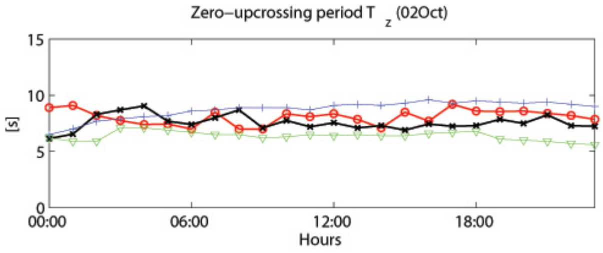

Figure A.122: *Zero-upcrossing wave period T_z from Bayesian and parametric modelling, from directional wave radar (WaMoS) and the down-looking wave radar in the bow (Radac). Figure from Nielsen et al. (2013). 02 October 2011.*

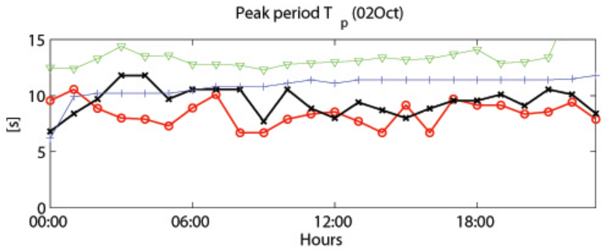

Figure A.123: *Peak wave period T_p from Bayesian and parametric modelling, from directional wave radar (WaMoS) and the down-looking wave radar in the bow (Radac). Figure from Nielsen et al. (2013). 02 October 2011.*

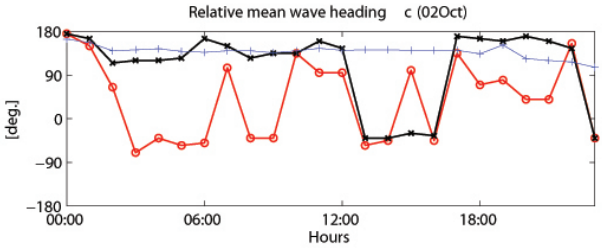

Figure A.124: *Relative wave direction χ from Bayesian and parametric modelling and from directional wave radar (WaMoS). The down-looking wave radar system (Radac) cannot estimate the relative wave direction). Figure from Nielsen et al. (2013). 02 October 2011.*

A.2 8,600 TEU Container Ship

A.2.1 Plots of 8,600 TEU ship tracks

For 07-08 November 2010 the GPS was offline. According to Heggelund et al. (2011) the ship was most likely somewhere between Gibraltar and northern Europe.

For 17-18 November 2010 the GPS was offline. According to Mondher (2012) the ship was bound for Asia sailing in the English Channel.

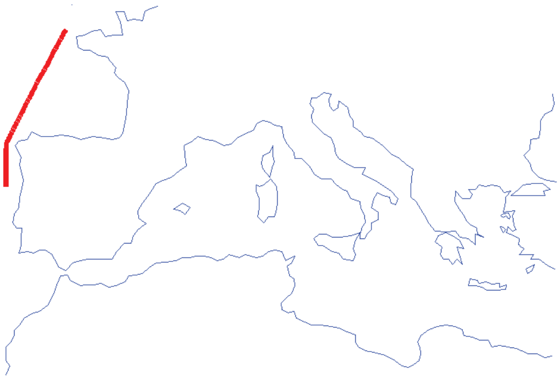

Figure A.125: *Vessel track on 05 February 2010 (Going north, 24 hours).*

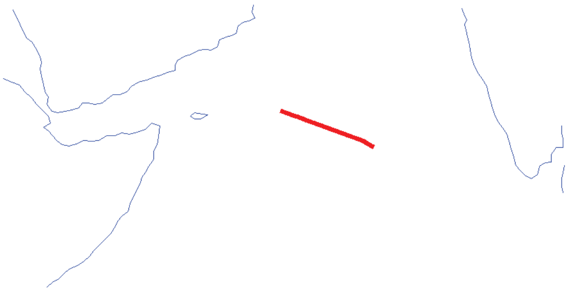

Figure A.126: *Vessel track on 01 December 2010 (Going east, 24 hours).*

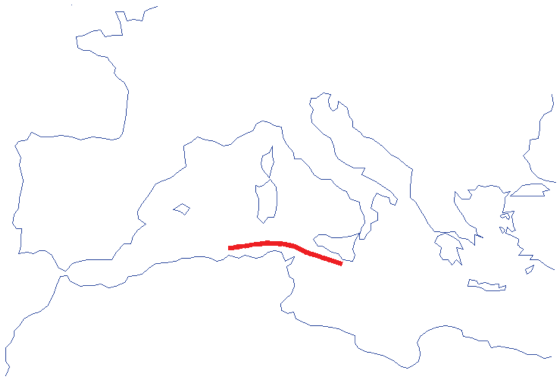

Figure A.127: *Vessel track on 30 December 2011 (Going west, 24 hours).*

A.2.2 Navigational Information

05 February 2010

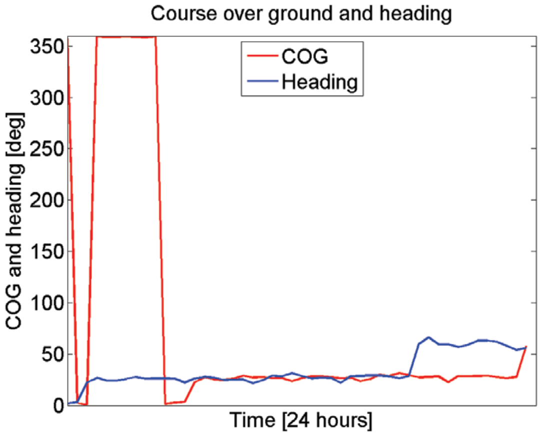

Figure A.128: *Ship course over ground (COG) compass heading on 05 February 2010.*

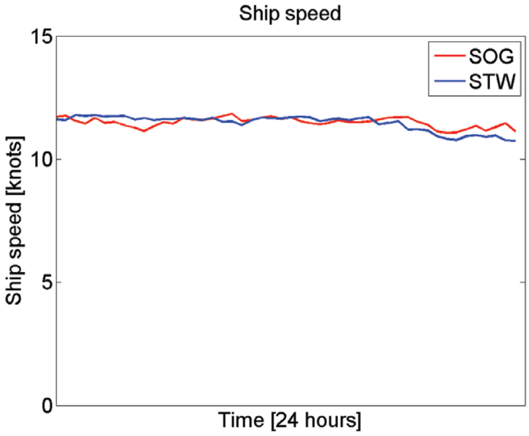

Figure A.129: *Ship speed over ground (SOG) and speed through water (STW) on 05 February 2010.*

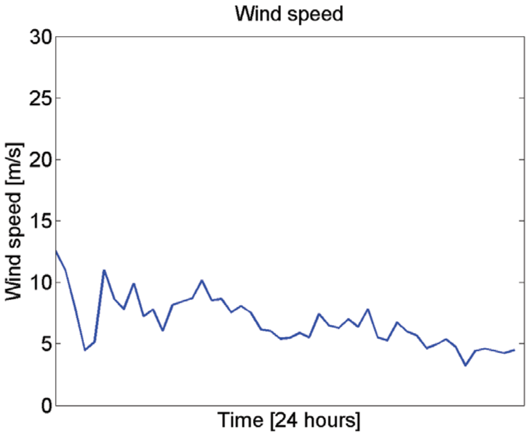

Figure A.130: *Wind speed on 05 February 2010. Not corrected for ship speed.*

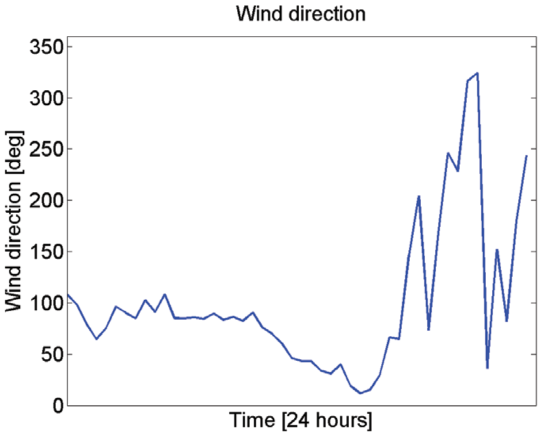

Figure A.131: *Wind direction relative to ship on 05 February 2010. 0 deg is head wind.*

07 November 2010

Ship speed and wind speed unavailable.

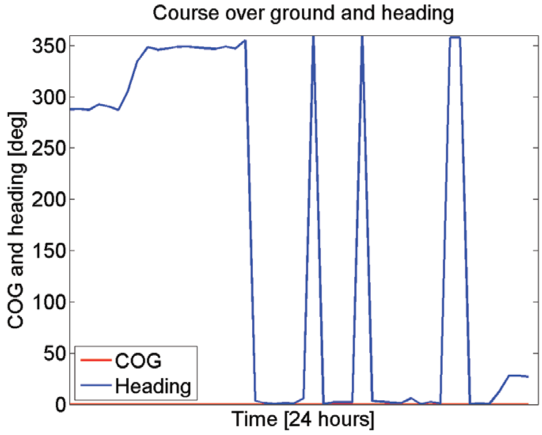

Figure A.132: Ship course over ground (COG) compass heading on 07 November 2010.

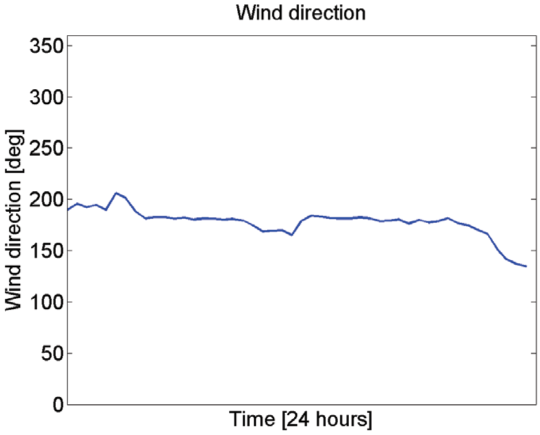

Figure A.133: Wind direction relative to ship on 07 November 2010. 0 deg is head wind.

08 November 2010

Ship speed and wind speed unavailable.

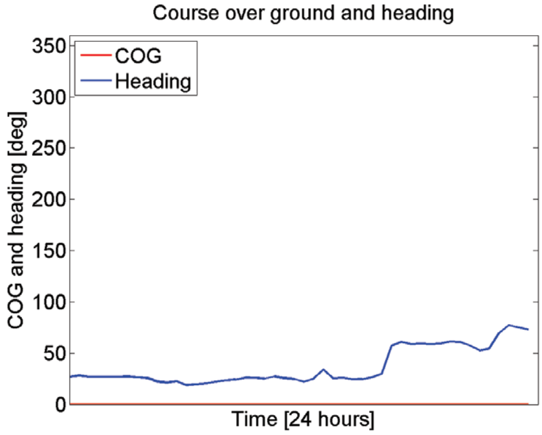

Figure A.134: Ship course over ground (COG) compass heading on 08 November 2010.

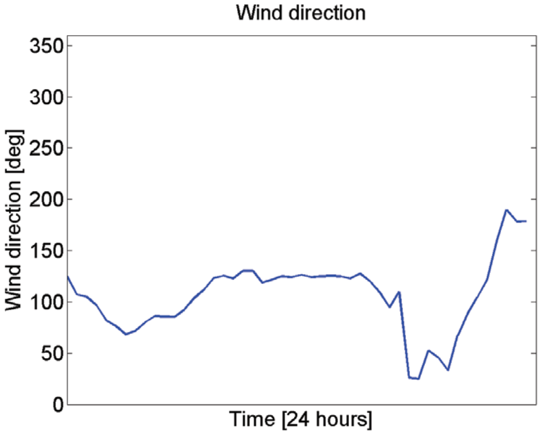

Figure A.135: Wind direction relative to ship on 08 November 2010. 0 deg is head wind.

17 November 2010

Ship speed and wind speed unavailable.

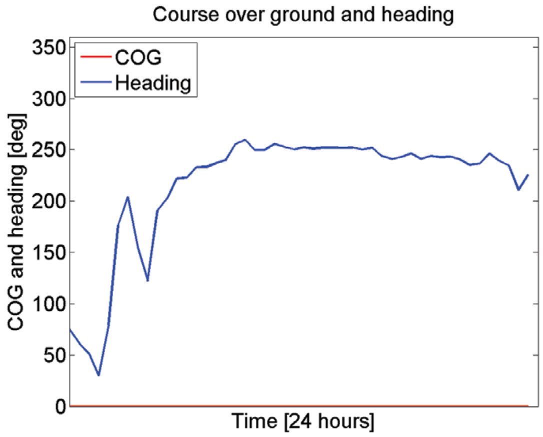

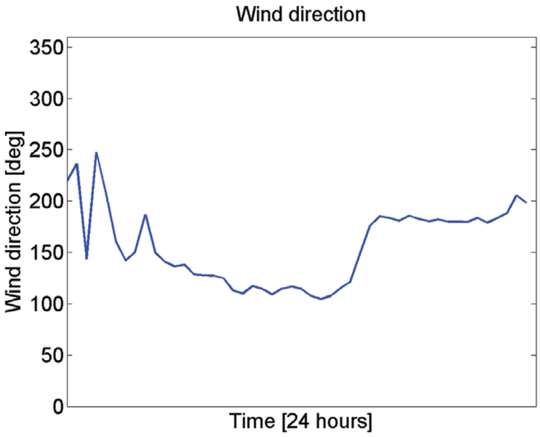

Figure A.136: *Ship course over ground (COG) compass heading on 17 November 2010.*

Figure A.137: *Wind direction relative to ship on 17 November 2010. 0 deg is head wind.*

18 November 2010

Ship speed and wind speed unavailable.

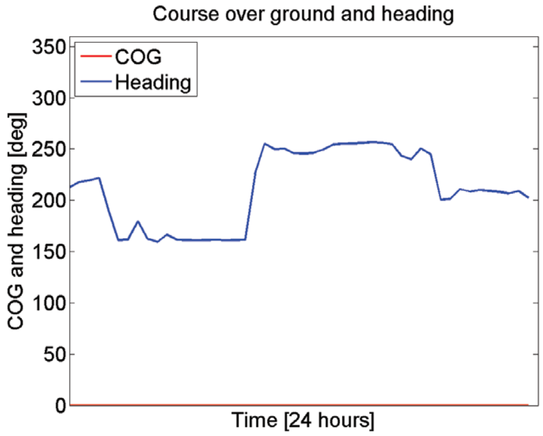

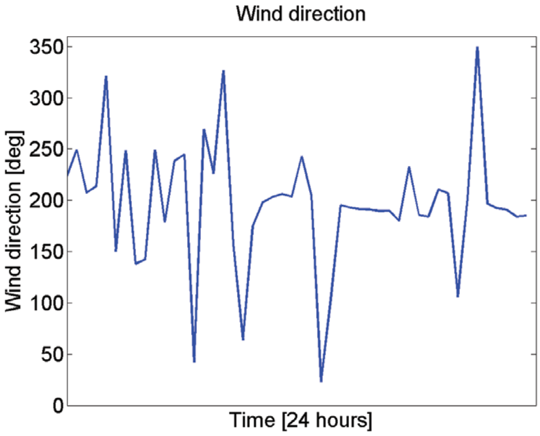

Figure A.138: *Ship course over ground (COG) compass heading on 18 November 2010.*

Figure A.139: *Wind direction relative to ship on 18 November 2010. 0 deg is head wind.*

01 December 2010

No wind speed available.

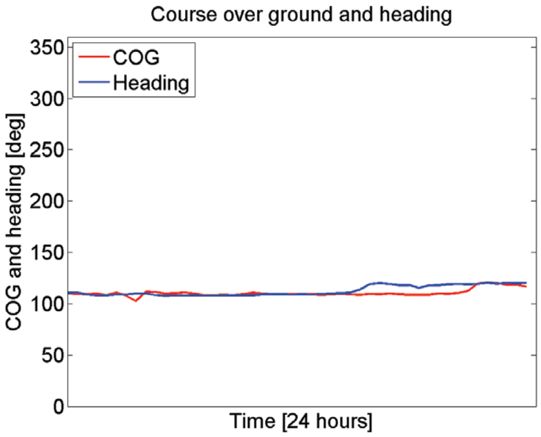

Figure A.140: *Ship course over ground (COG) compass heading on 01 December 2010.*

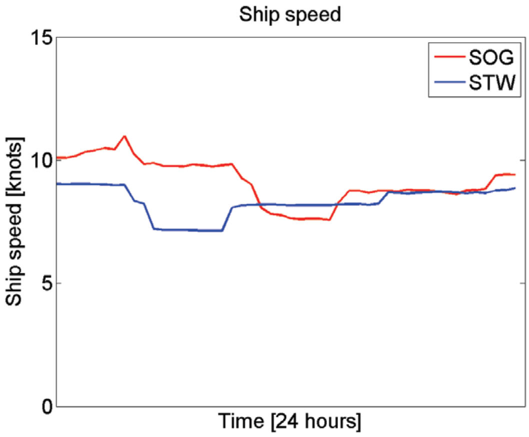

Figure A.141: *Ship speed over ground (SOG) and speed through water (STW) on 01 December 2010.*

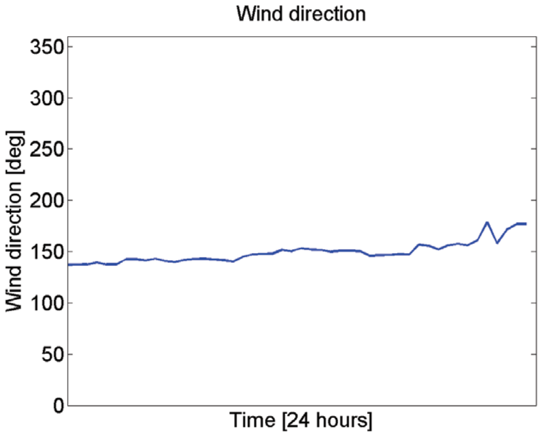

Figure A.142: *Wind direction relative to ship on 01 December 2010. 0 deg is head wind.*

30 December 2011

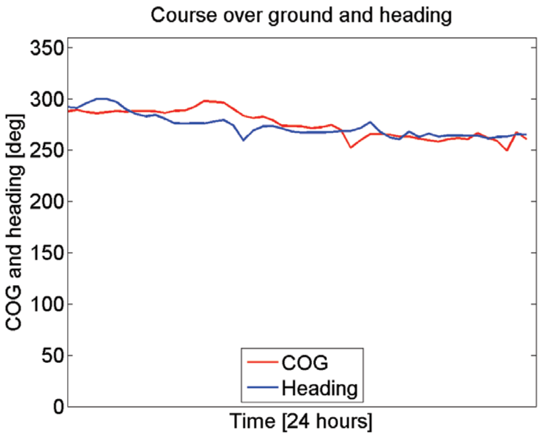

Figure A.143: *Ship course over ground (COG) compass heading on 30 December 2011.*

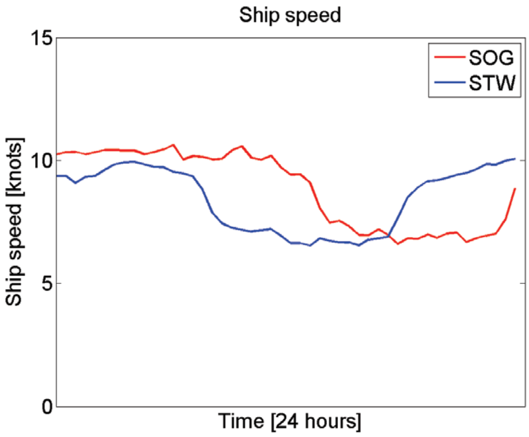

Figure A.144: *Ship speed over ground (SOG) and speed through water (STW) on 30 December 2011.*

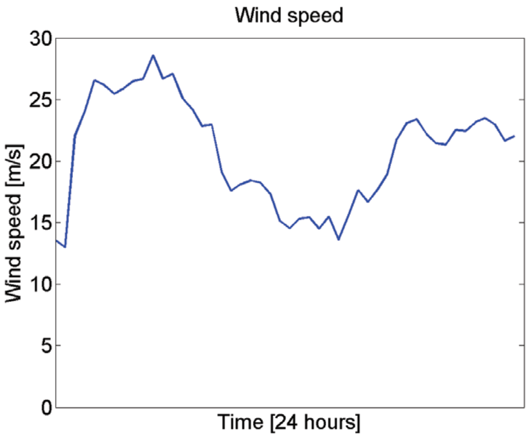

Figure A.145: *Wind speed on 30 December 2011. Not corrected for ship speed.*

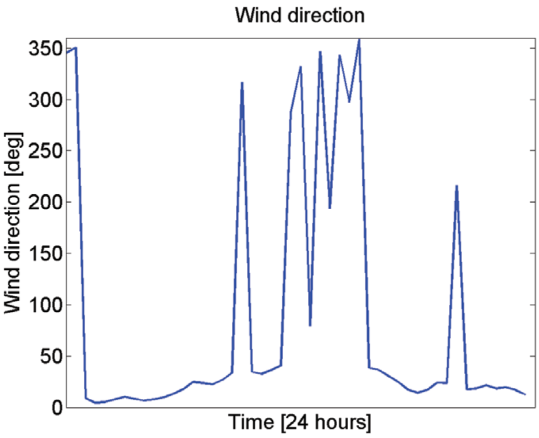

Figure A.146: *Wind direction relative to ship on 30 December 2011. 0 deg is head wind.*

A.2.3 Hull girder loads

Maximum hull girder stress per 30 minutes in Figure A.147 for 2010 and A.148 for 2011.

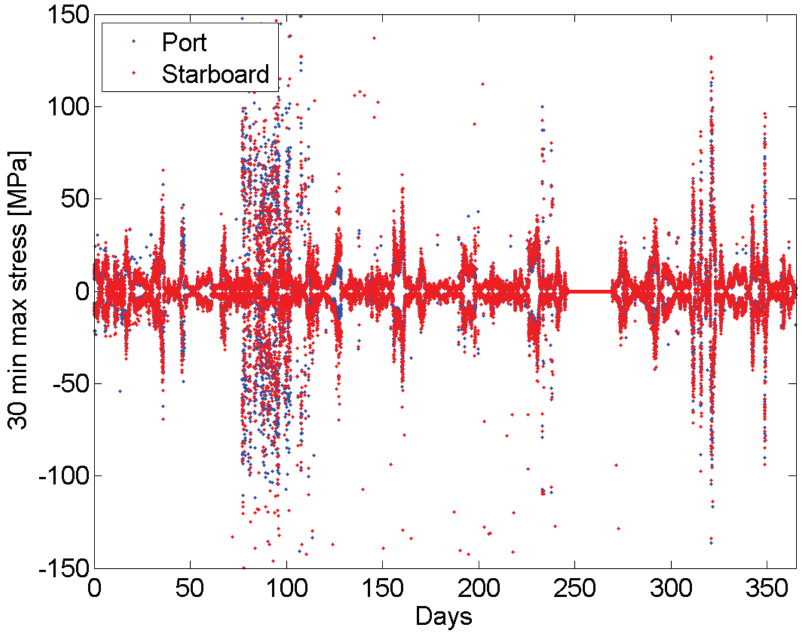

Figure A.147: *One year stress measurement (2010), port and starboard side, from 30 minute statistical file from 8,600 TEU container ship. Data from 50-150 days is regarded unreliable.*

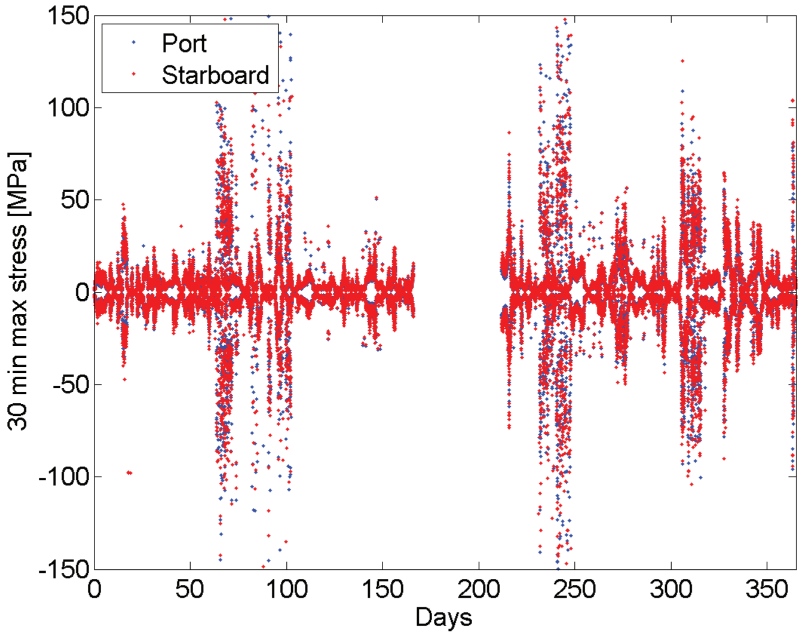

Figure A.148: *One year stress measurement (2011), port and starboard side, from 30 minute statistical file from 8,600 TEU container ship.*

A.3 14,000 TEU Container Ship

A.3.1 Navigational information

21 July 2011

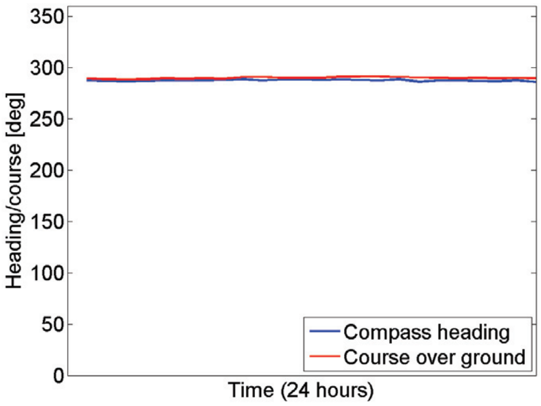

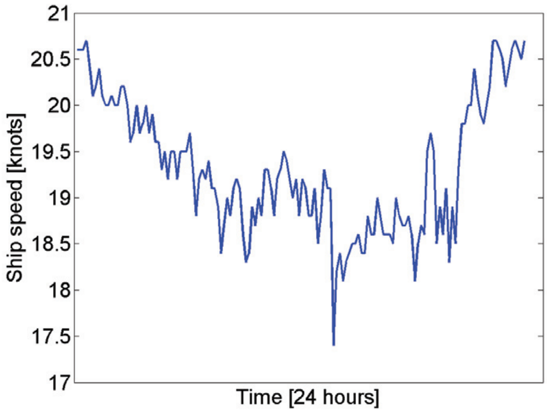

Figure A.149: *Ship course over ground (COG) and compass heading on 21 July 2011.*

Figure A.150: *Ship speed over ground on 21 July 2011.*

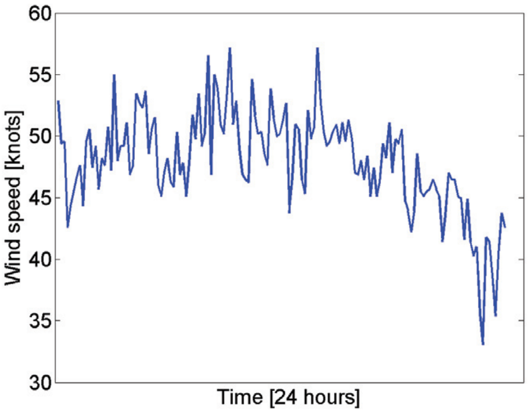

Figure A.151: *Wind speed on 21 July 2011. Not corrected for ship speed and heading.*

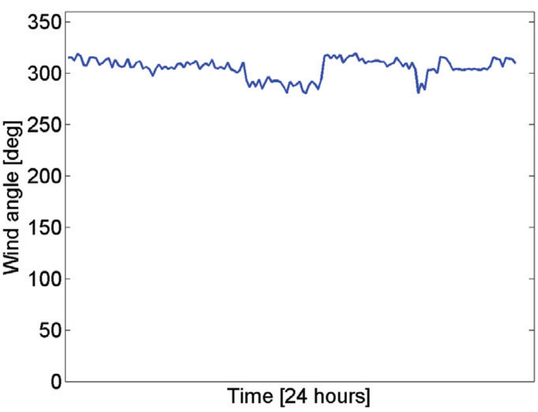

Figure A.152: *Wind direction relative to ship on 21 July 2011. 0 deg is head wind. Not corrected for ship speed and heading.*

Appendix B

Specification and Illustrations of Measurement Equipment

B.1 9,400 TEU Container Ship

B.1.1 *Directional wave radar*

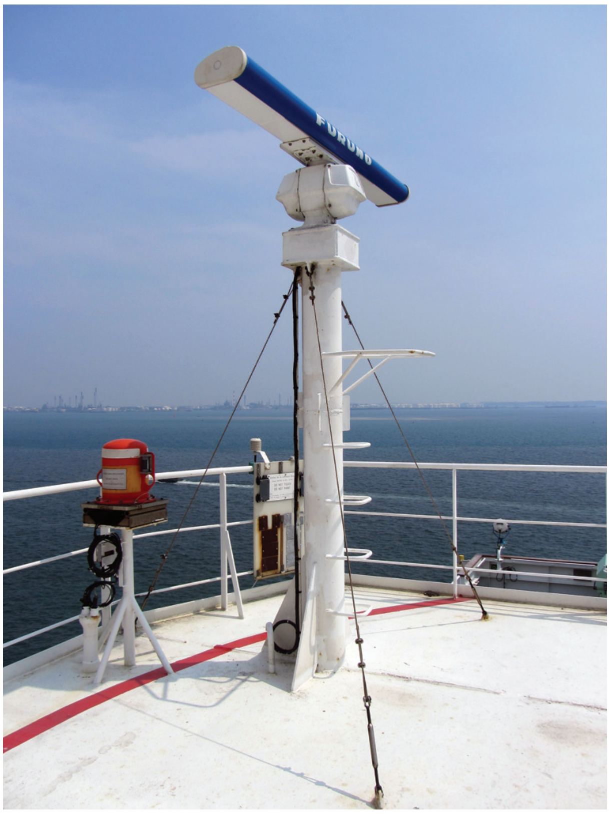

Figure B.1: *WaMoS II wave radar installed on board the 9,400 TEU container ship. Photo by the author.*

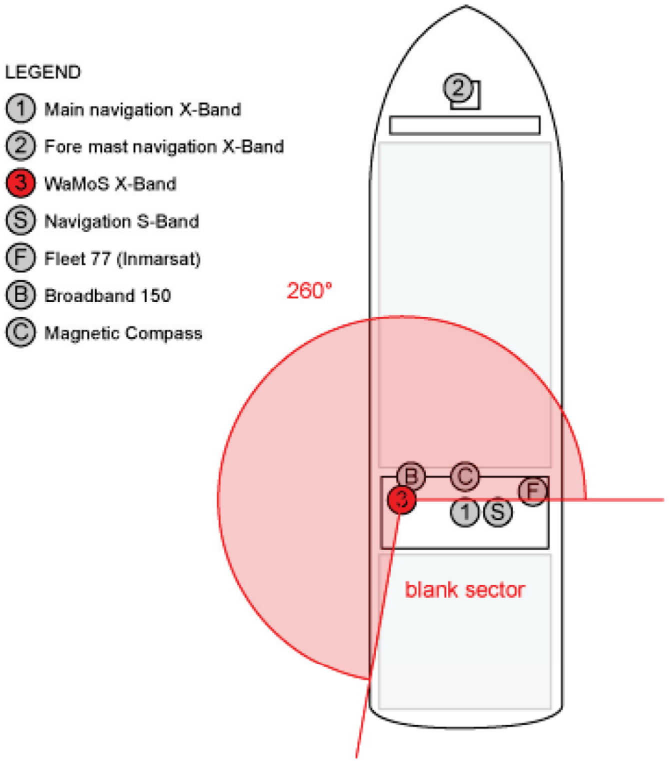
LEGEND
1 Main navigation X-Band
2 Fore mast navigation X-Band
3 WaMoS X-Band
S Navigation S-Band
F Fleet 77 (Inmarsat)
B Broadband 150
C Magnetic Compass
260°
2
B
C
F
3
1
S
blank sector

Figure B.2: *Location of the WaMoS radar with possible sources of interference. Illustration from Fresser (2011)*

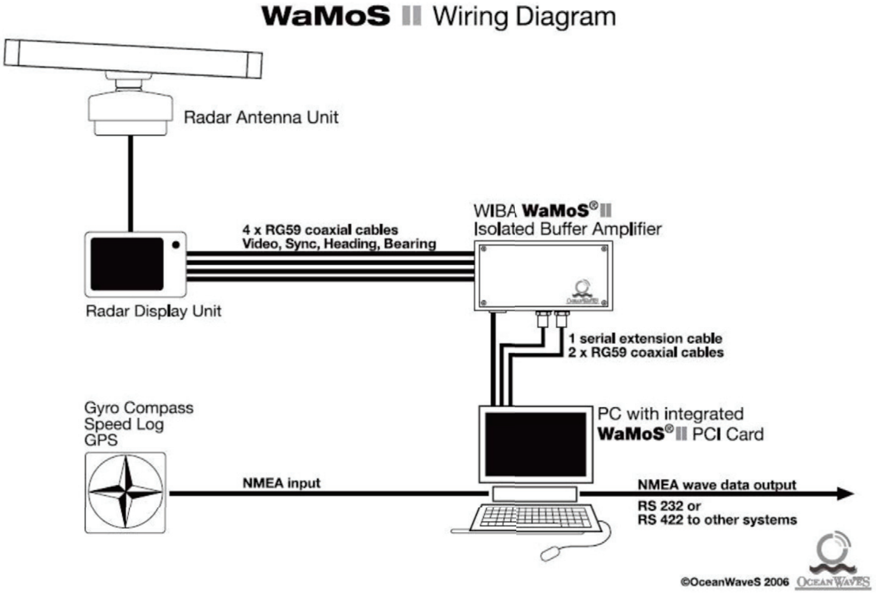
WaMoS II Wiring Diagram
Radar Antenna Unit
4 x RG59 coaxial cables
Video, Sync, Heading, Bearing
WIBA WaMoS® II
Isolated Buffer Amplifier
Radar Display Unit
1 serial extension cable
2 x RG59 coaxial cables
Gyro Compass
Speed Log
GPS
PC with integrated
WaMoS® II PCI Card
NMEA input
NMEA wave data output
RS 232 or
RS 422 to other systems
©OceanWaveS 2006
OceanWaveS

Figure B.3: *Wiring Diagram for the WaMoS II wave radar. Illustration from Fresser (2011)*

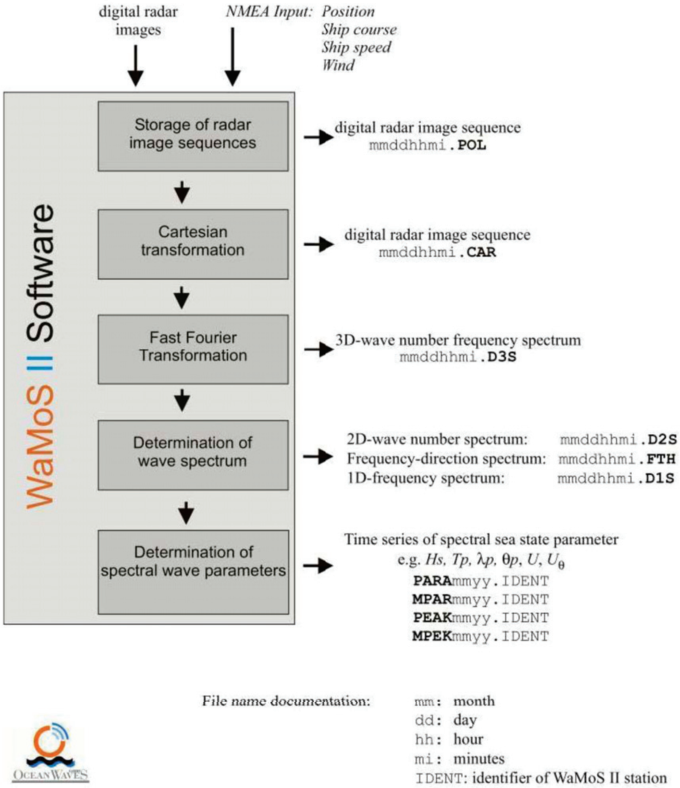
digital radar images
NMEA Input: Position
Ship course
Ship speed
Wind
WaMoS II Software
Storage of radar image sequences
digital radar image sequence
mmddhhmi.POL
Cartesian transformation
digital radar image sequence
mmddhhmi.CAR
Fast Fourier Transformation
3D-wave number frequency spectrum
mmddhhmi.D3S
Determination of wave spectrum
2D-wave number spectrum: mmddhhmi.D2S
Frequency-direction spectrum: mmddhhmi.FTH
1D-frequency spectrum: mmddhhmi.D1S
Determination of spectral wave parameters
Time series of spectral sea state parameter
e.g. Hs, Tp, λp, θp, U, Uθ
PARAmmyy.IDENT
MPARmmyy.IDENT
PEAKmmyy.IDENT
MPEKmmyy.IDENT
File name documentation:
mm: month
dd: day
hh: hour
mi: minutes
IDENT: identifier of WaMoS II station
OCEANWAVES

Figure B.4: *WaMoS II data processing flow chart. From Fresser (2011)*

B.1.2 *Down-looking wave radar*

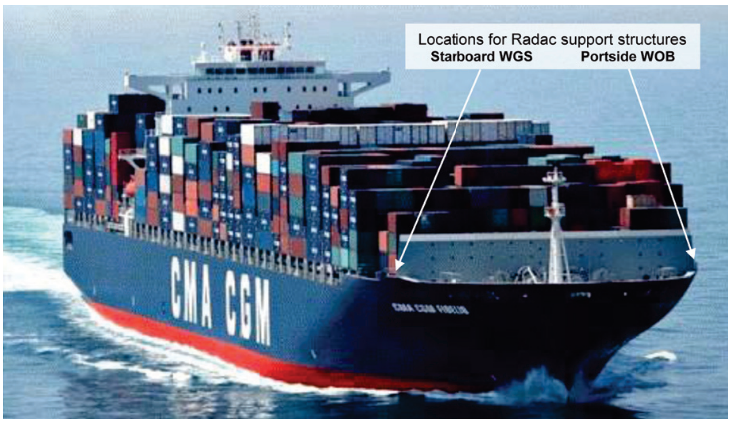
Locations for Radac support structures
Starboard WGS
Portside WOB
CMA CGM

Figure B.5: *Location of the two Radac sensors on board the 9,400 TEU ship. Illustration from Fresser (2011)*

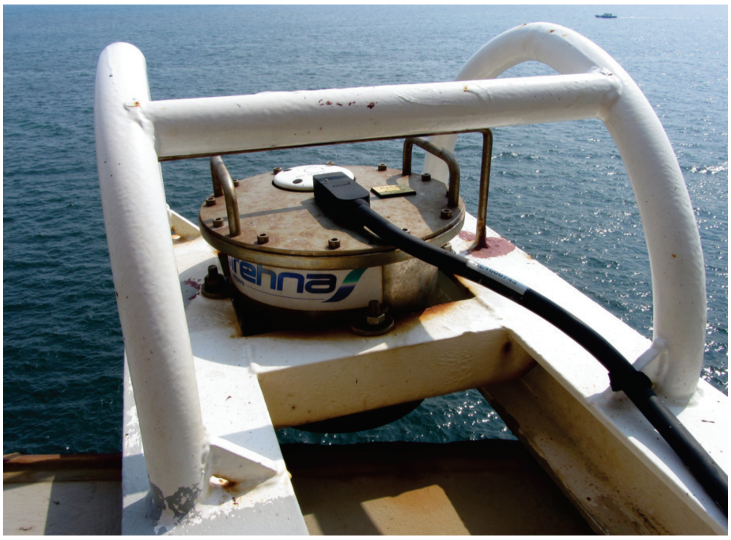

Figure B.6: *Port side Radac sensor on board the 9,400 TEU ship. Photo by the author.*

B.1.3 *Accelerations*

The accelerometers are calibrated for ± 5g and the rate of turn sensors for ± 150 deg/s.

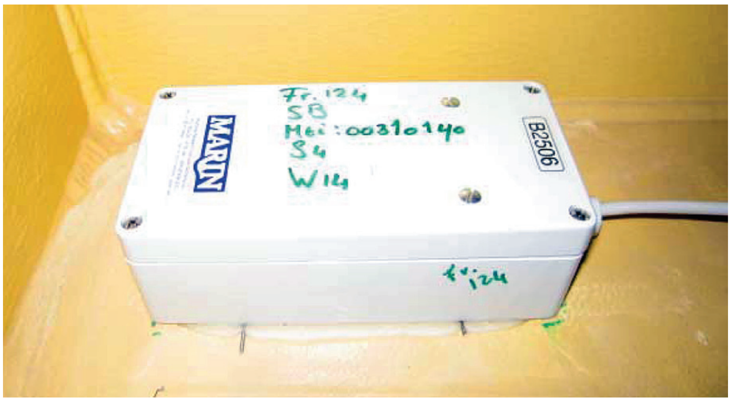

Figure B.7: *Acceleration sensor at frame 124 on board the 9,400 TEU ship. Illustration courtesy of MARIN.*

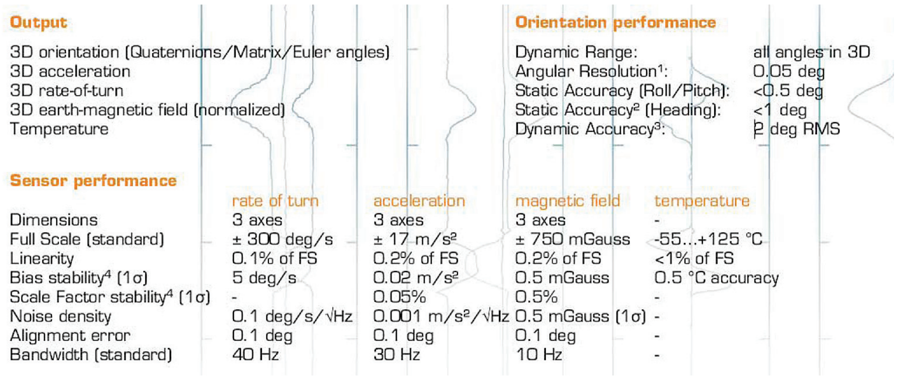

Output

- 3D orientation (Quaternions/Matrix/Euler angles)
- 3D acceleration
- 3D rate-of-turn
- 3D earth-magnetic field (normalized)
- Temperature

Orientation performance

Dynamic Range:	all angles in 3D
Angular Resolution[1]:	0.05 deg
Static Accuracy (Roll/Pitch):	<0.5 deg
Static Accuracy[2] (Heading):	<1 deg
Dynamic Accuracy[3]:	2 deg RMS

Sensor performance

	rate of turn	acceleration	magnetic field	temperature
Dimensions	3 axes	3 axes	3 axes	-
Full Scale (standard)	± 300 deg/s	± 17 m/s^2	± 750 mGauss	-55...+125 °C
Linearity	0.1% of FS	0.2% of FS	0.2% of FS	<1% of FS
Bias stability[4] (1σ)	5 deg/s	0.02 m/s^2	0.5 mGauss	0.5 °C accuracy
Scale Factor stability[4] (1σ)	-	0.05%	0.5%	-
Noise density	0.1 deg/s/$\sqrt{Hz}$	0.001 $m/s^2/\sqrt{Hz}$	0.5 mGauss (1σ)	-
Alignment error	0.1 deg	0.1 deg	0.1 deg	-
Bandwidth (standard)	40 Hz	30 Hz	10 Hz	-

Figure B.8: *Specifications of acceleration sensors on board the 9,400 TEU ship. Courtesy of MARIN.*

Designation	**Unit**	**Positive direction**
Surge	m	Forward
Sway	m	Port
Heave	m	Upwards
Longitudinal velocity	m/s	Forward
Transverse velocity	m/s	Port
Vertical velocity	m/s	Upwards
Longitudinal acceleration	m/s^2	Forward
Transverse acceleration	m/s^2	Port
Vertical acceleration	m/s^2	Upwards
Roll	deg	Starboard turning down
Pitch	deg	Bow down
Yaw	deg	Bow turning to port
Roll rate	deg/s	Starboard turning down
Pitch rate	deg/s	Bow down
Yaw rate	deg/s	Bow turning to port
Roll acceleration	deg/s^2	Starboard turning down
Pitch acceleration	deg/s^2	Bow down
Yaw acceleration	deg/s^2	Bow turning to port

Table B.1: *Definitions and sign conventions for the motion measurements on board the 9,400 TEU ship. Table reproduced from Koning (2007).*

B.1.4 *Hull girder loads*

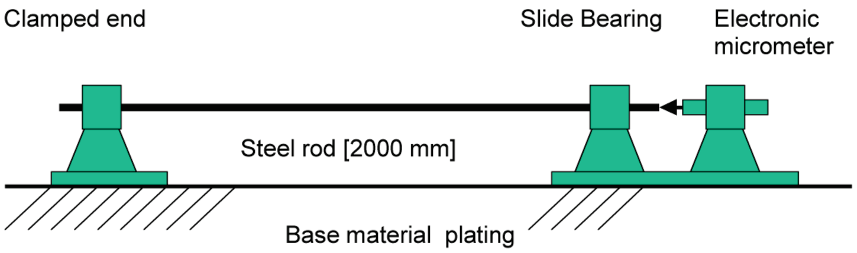
Clamped end
Slide Bearing
Electronic micrometer
Steel rod [2000 mm]
Base material plating

Figure B.9: *Principle of the long base strain gauges used on board the 9,400 TEU ship. Illustration from Koning (2007).*

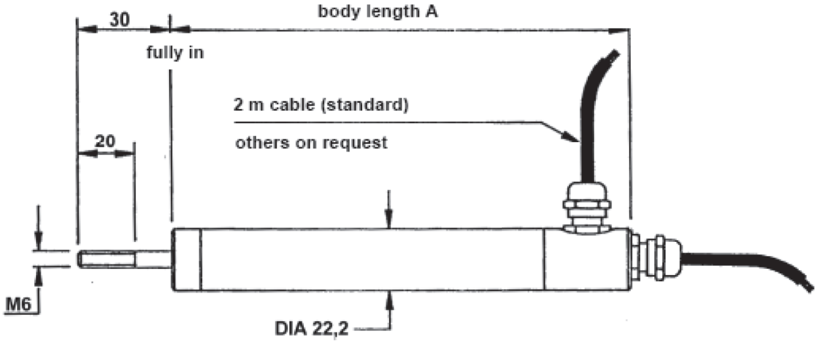

+/- 550	1460	1410	430	10	550	1530
+/- 500	1460	1410	390	10	550	1530
+/- 400	1200	1150	460	20	450	1010
+/- 300	970	920	400	5	690	770
+/- 250	860	810	350	10	290	560
+/- 200	750	700	300	10	250	430
+/- 175	665	615	310	2	230	360
+/- 150	610	560	330	5	210	290
+/- 125	550	500	300	2	180	320
+/- 100	500	450	190	5	150	150
+/- 75	440	390	350	20	260	460
+/- 50	370	320	320	2	200	270
+/- 25	285	235	240	5	130	210
+/- 15	225	175	230	20	90	190
+/- 12,5	210	160	300	15	120	190
+/- 10	180	130	280	10	70	170
+/- 5	165	115	80	5	100	110
+/- 2,5	140	90	90	5	180	460
+/- 0,5	130	80	50	20	40	1800
range (mm)	body length A (mm) internal electronics	body length A (mm) external electronics	sensitivity at 3 kHz (mV/V)	null (mV)	primary resistance (Ω)	secondary resistance (Ω)

internal electronics - technical data

±2,5 VDC
supply: 10...30 VDC
current consumption: 35 mA (at 12 VDC)
ripple: max. 30 mV
output bandwidth: 300 Hz
zero temperature coefficient: 0,01% /°C
span temperature coefficient: 0,03% /°C
temperature range: -50...+85°C

0...10 VDC
supply: 15...30 VDC
current consumption: 35 mA (at 15 VDC)
ripple: max. 30 mV
output bandwidth: 300 Hz
zero temperature coefficient: 0,01% /°C
span temperature coefficient: 0,03% /°C
temperature range: -50...+85°C

4...20 mA
supply: 14...24 VDC
ripple: max. 0,1% at 20 mA
null: 12 mA ± 0,5%
temperature range: -20...+95°C

Figure B.10: *Specifications of the long base strain gauges used on board the 9,400 TEU ship. Courtesy of MARIN.*

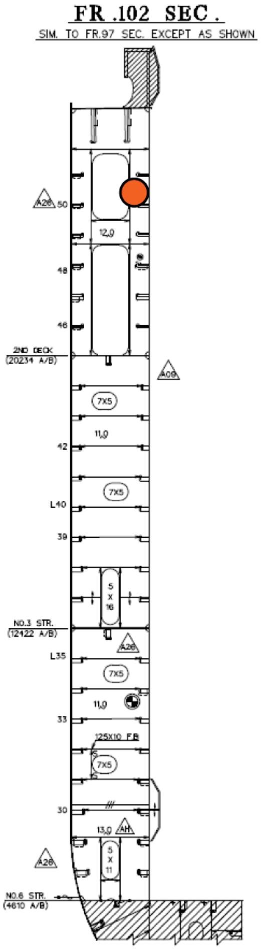
FR .102 SEC.
SIM. TO FR.97 SEC. EXCEPT AS SHOWN
A26
50
12,0
48
46
2ND DECK
(20234 A/B)
A09
7X5
11,0
42
7X5
L40
39
5
X
16
NO.3 STR.
(12422 A/B)
A26
L35
7X5
11,0
33
125X10 FB
7X5
30
13,0
AH
A26
5
X
11
NO.6 STR.
(4610 A/B)

Figure B.11: *Location of strain gauges at frame 102 on board the 9,400 TEU ship. Illustration from Koning (2010).*

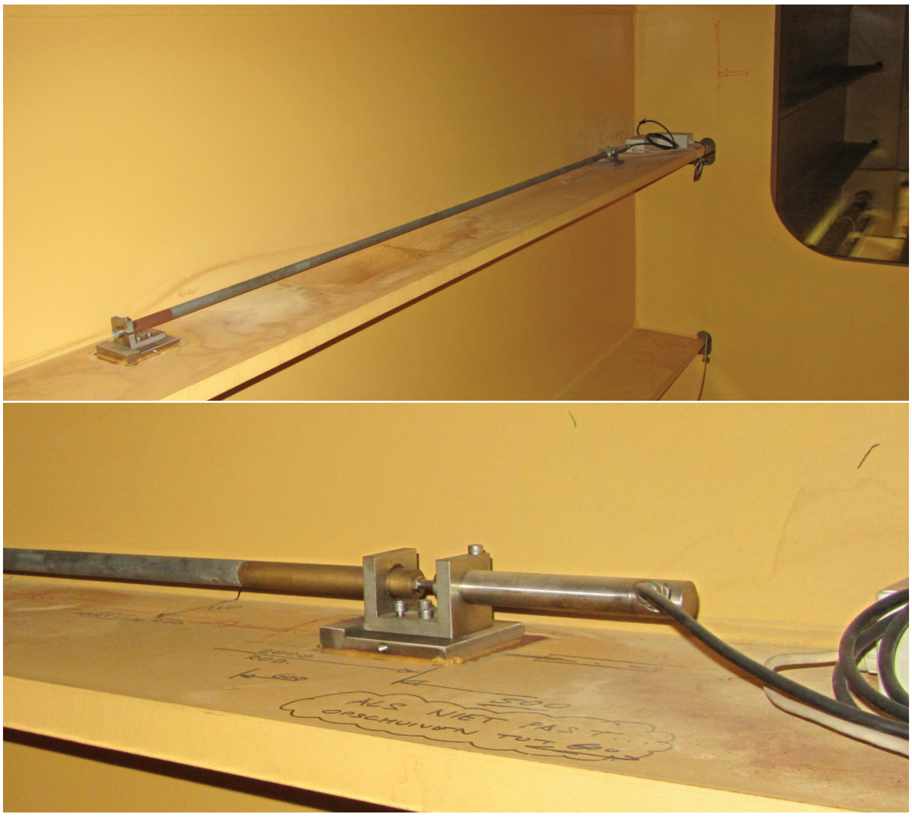
2000
ROD.
1500
ALS NIET PAST.
OPSCHUIVEN TOT 800

Figure B.12: *Strain gauge amidships at the location illustrated in Figure B.11. Photo by Gregoire Wencesla Guitard.*

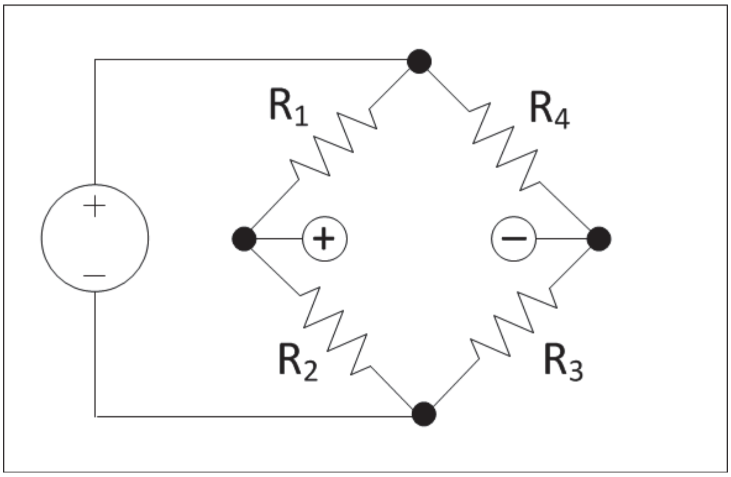

Figure B.13: *Principle of the Wheatstone bridge-type strain gauge mounted in the bow of the 9,400 TEU ship.*

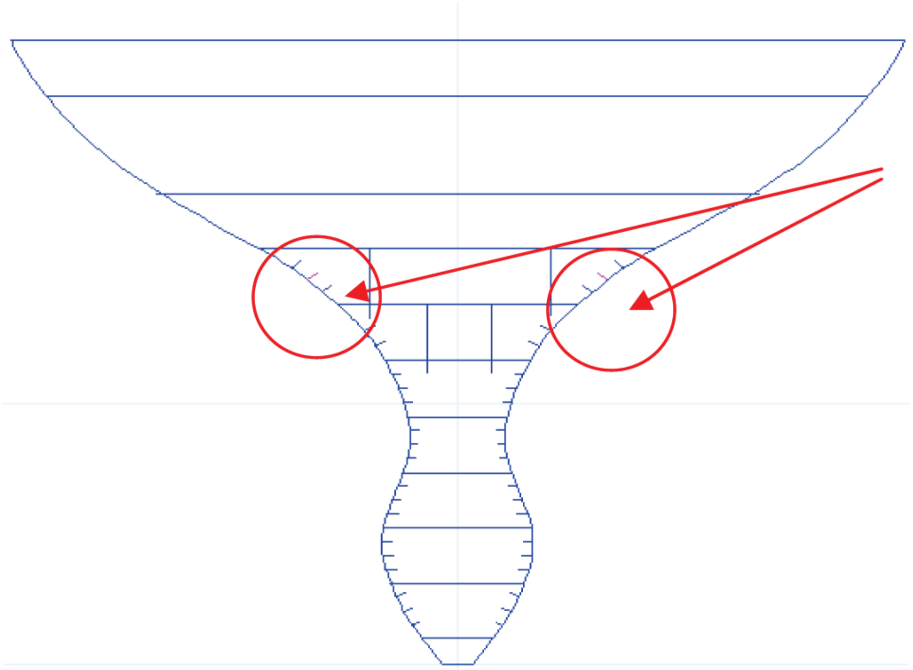

Figure B.14: Location of strain gauges at frame 154/155 in the bow of the 9,400 TEU ship. Illustration from Koning (2010).

B.2 8,600 TEU Container Ship

B.2.1 *Hull girder loads*

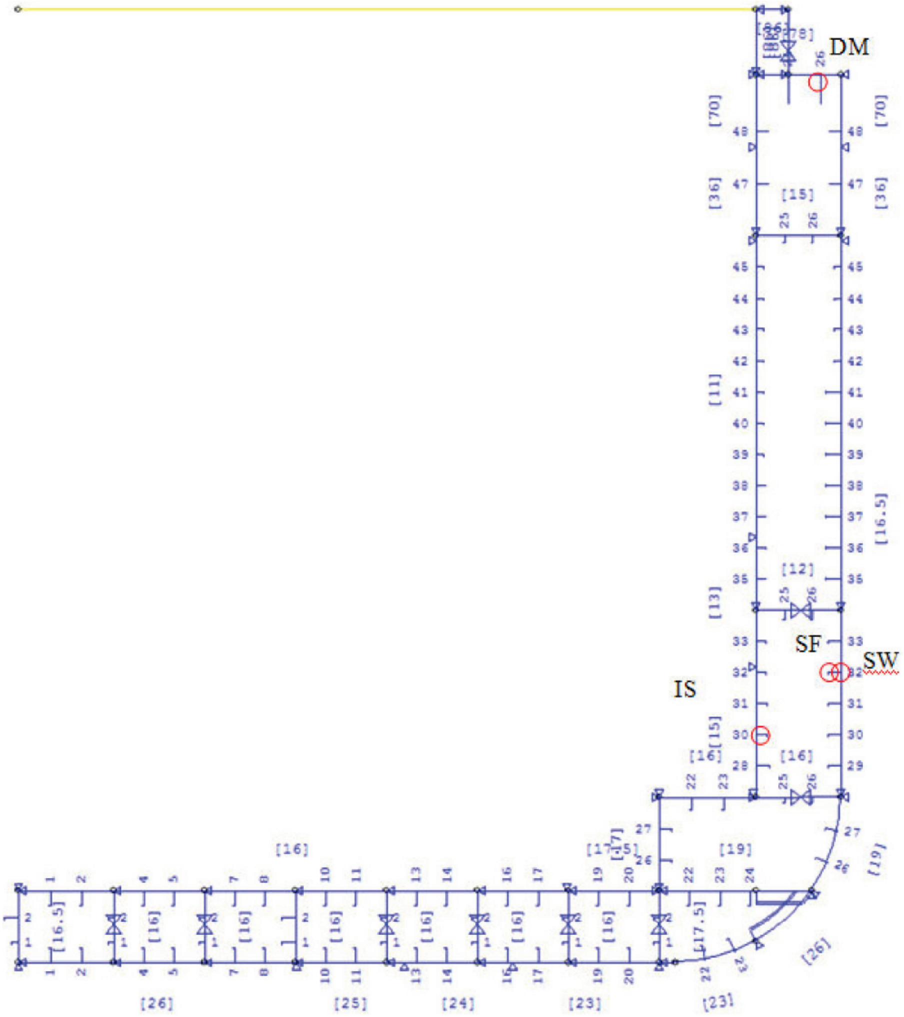
DM
[70]
[36]
[15]
[11]
[16.5]
[12]
[13]
SF
SW
IS
[15]
[16]
[16]
[19]
[19]
[16]
[17.5]
[16.5]
[16]
[16]
[16]
[16]
[16]
[16]
[17.5]
[26]
[26]
[25]
[24]
[23]
[23]

Figure B.15: *Location of strain sensors at frame 101/102 (amidships) the 8,600 TEU container ship. Illustration from Heggelund et al. (2011).*

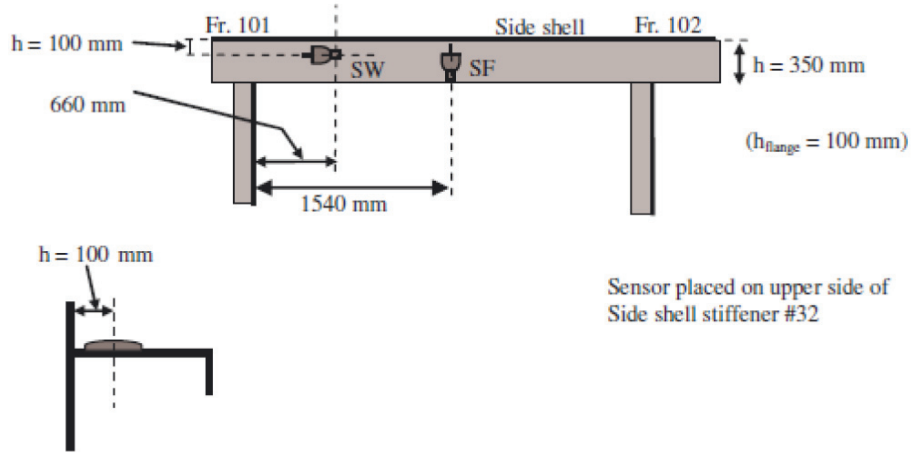
h = 100 mm
Fr. 101
Side shell
Fr. 102
SW
SF
h = 350 mm
660 mm
(h$_{flange}$ = 100 mm)
1540 mm
h = 100 mm
Sensor placed on upper side of
Side shell stiffener #32

Figure B.16: *Location of strain sensors at frame 101/102 (amidships) in the deck of the 8,600 TEU container ship. Illustration from Heggelund et al. (2011).*

Appendix C

Estimated Fatigue Damage

C.1 9,400 TEU Container Ship

C.1.1 *12 August 2011*

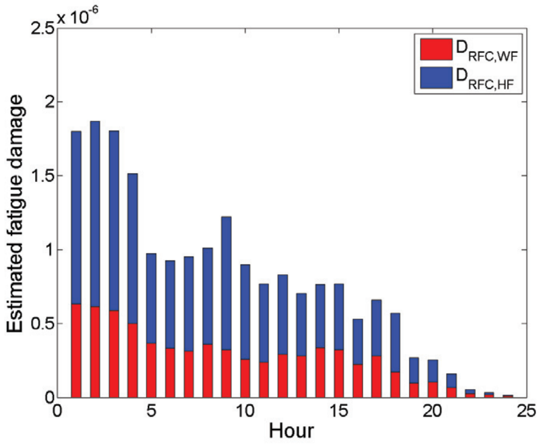

Figure C.1: *Fatigue damage per hour during 24 hours on 12 August 2011 estimated using rainflow counting and the Palmgren-Miner rule.*

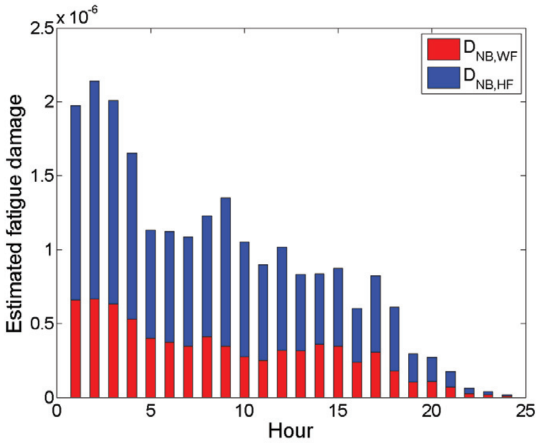

Figure C.2: *Fatigue damage during 24 hours on 12 August 2011 estimated using narrow-banded spectral analysis (one narrow-banded process).*

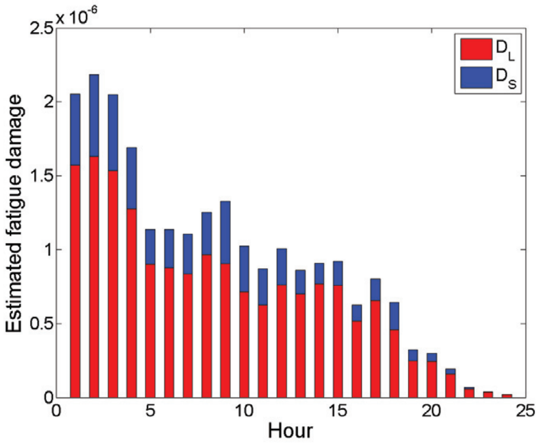

Figure C.3: *Fatigue damage during 24 hours on 12 August 2011 estimated using narrow-banded spectral analysis assuming two Gaussian narrow-banded processes (Jiao and Moan (1990)).*

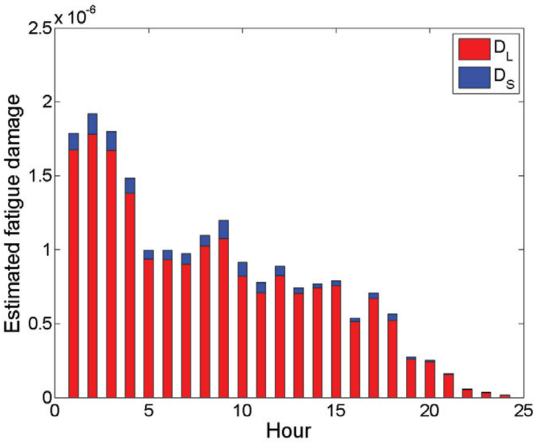

Figure C.4: *Fatigue damage during 24 hours on 12 August 2011 estimated using narrow-banded spectral analysis assuming two Gaussian, narrow-banded processes (Low (2010)).*

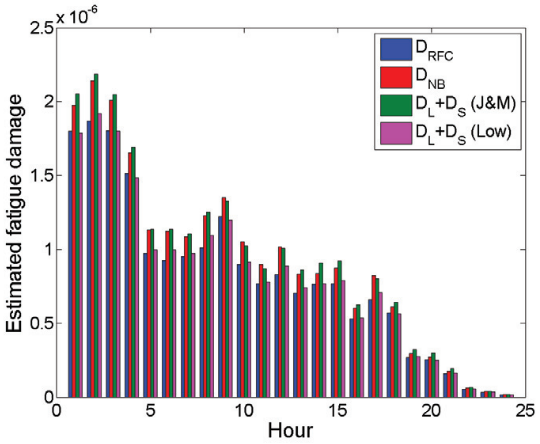

Figure C.5: *Comparison of total estimated fatigue damage per hour during 24 hours on 12 August 2011.*

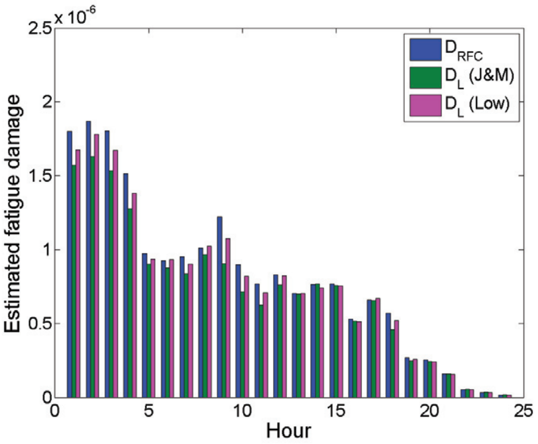

Figure C.6: *Comparison of estimated fatigue damage for the two envelope processes (Eq. (6.4) and Eq. (6.20)) with the total estimate from RFC for 12 August 2011.*

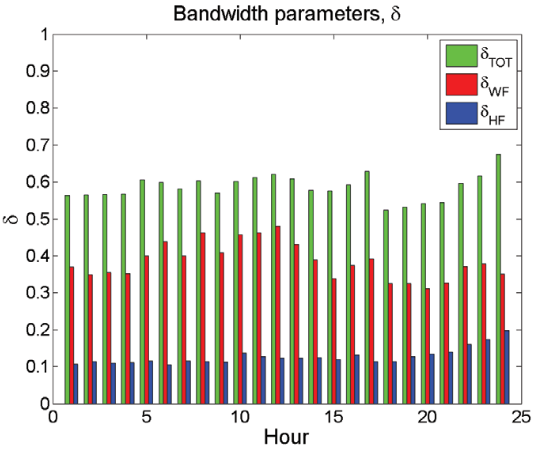

__Figure C.7:__ Bandwidth parameters, δ (Eq. (6.10)), for the total, WF and HF part of the process for 12 August 2011.

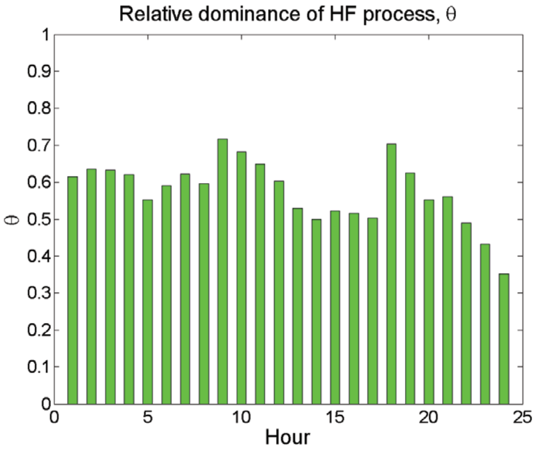

__Figure C.8:__ Relative dominance of the HF process, θ (Eq. (6.8)), for 12 August 2011.

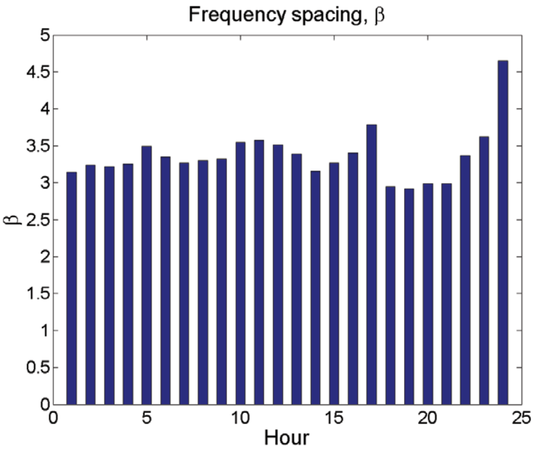

__Figure C.9:__ Spacing between low and high frequency parts, β (Eq. (6.9)), for 12 August 2011.

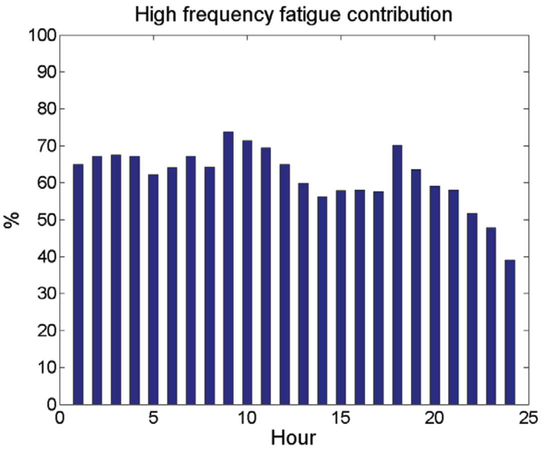

__Figure C.10:__ High frequency (HF) contribution to the total estimated fatigue damage per hour for 12 August 2011 using RFC.

C.1.2 *16 September 2011*

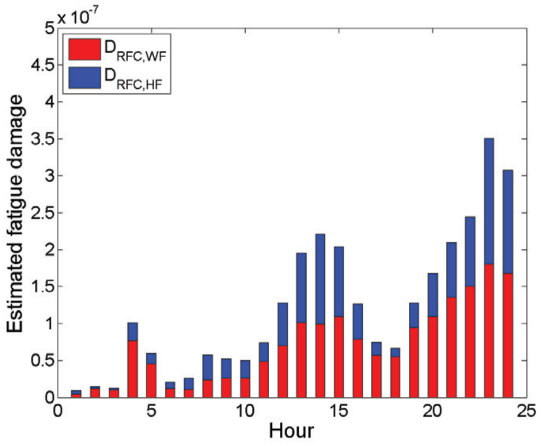

Figure C.11: *Fatigue damage per hour during 24 hours on 16 September 2011 estimated using rainflow counting and the Palmgren-Miner rule.*

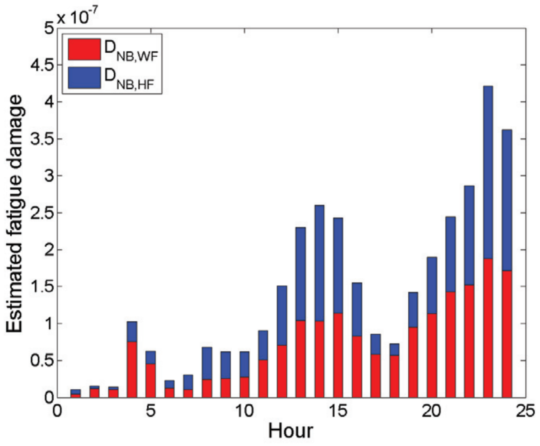

Figure C.12: *Fatigue damage during 24 hours on 16 September 2011 estimated using narrow-banded spectral analysis (one narrow-banded process).*

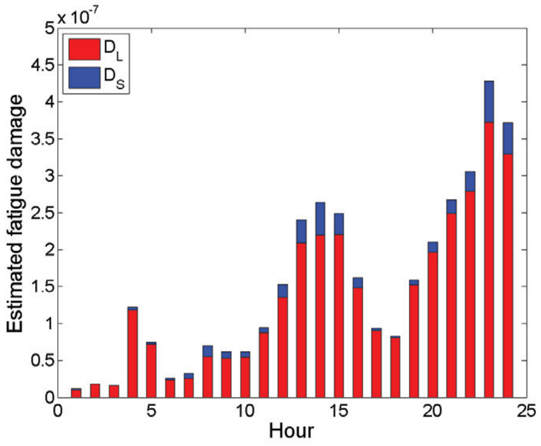

Figure C.13: *Fatigue damage during 24 hours on 16 September 2011 estimated using narrow-banded spectral analysis assuming two Gaussian narrow-banded processes (Jiao and Moan (1990)).*

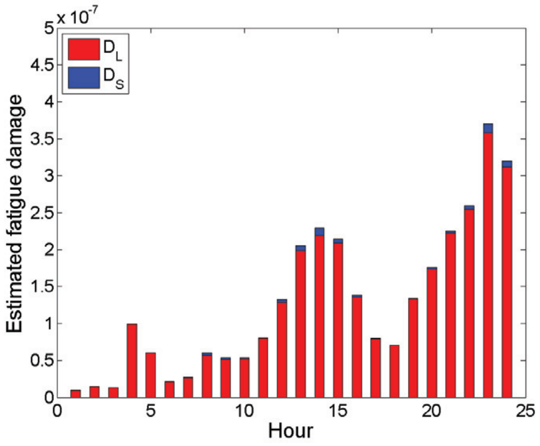

Figure C.14: *Fatigue damage during 24 hours on 16 September 2011 estimated using narrow-banded spectral analysis assuming two Gaussian, narrow-banded processes (Low (2010)).*

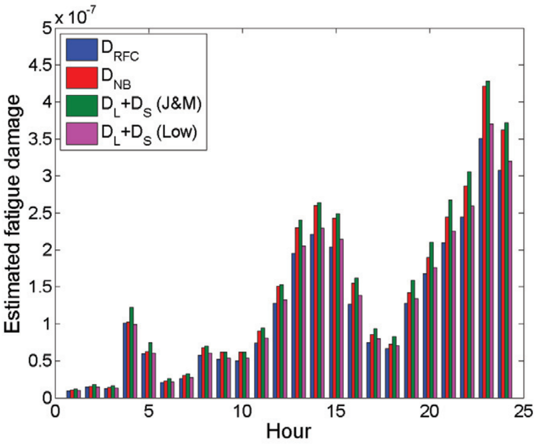

Figure C.15: *Comparison of total estimated fatigue damage per hour during 24 hours on 16 September 2011.*

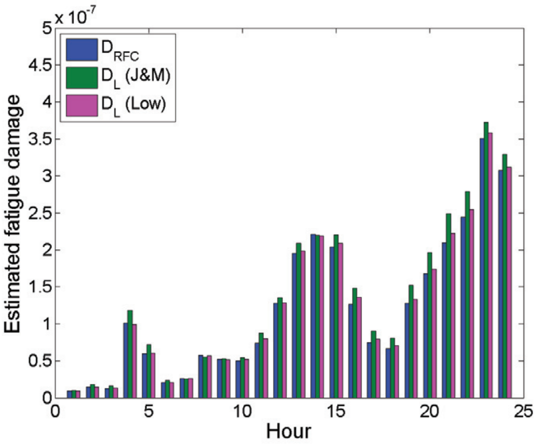

Figure C.16: *Comparison of estimated fatigue damage for the two envelope processes (Eq. (6.4) and Eq. (6.20)) with the total estimate from RFC for 16 September 2011.*

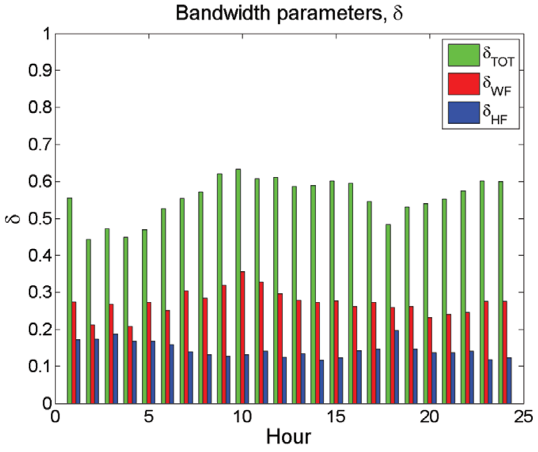

Figure C.17: *Bandwidth parameters, δ (Eq. (6.10)), for the total, WF and HF part of the process for 16 September 2011.*

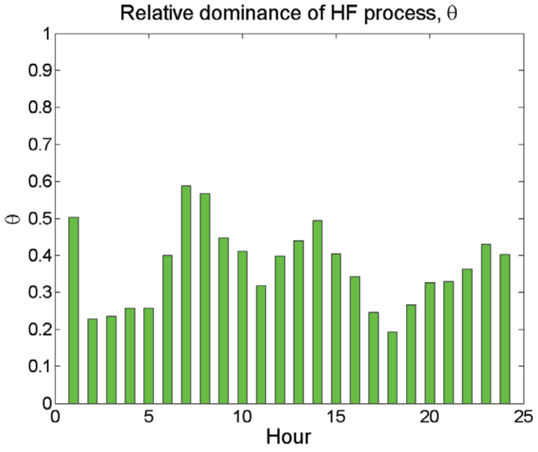

Figure C.18: *Relative dominance of the HF process, θ (Eq. (6.8)), for 16 September 2011.*

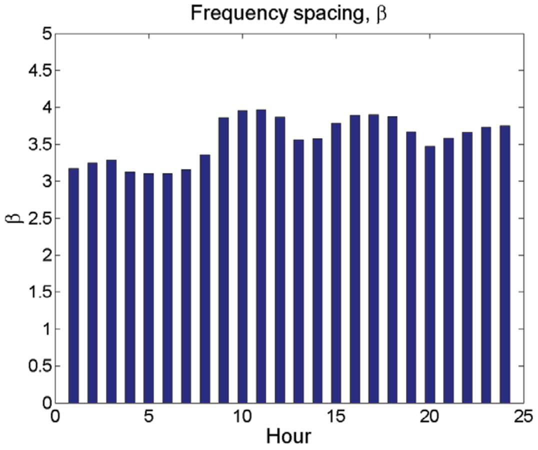

Figure C.19: *Spacing between low and high frequency parts, β (Eq. (6.9)), for 16 September 2011.*

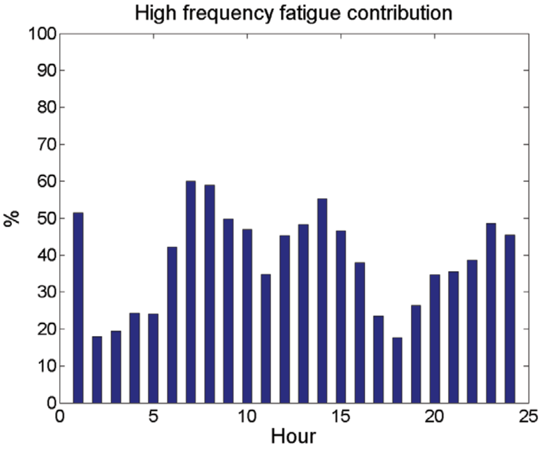

Figure C.20: *High frequency (HF) contribution to the total estimated fatigue damage per hour for 16 September 2011 using RFC.*

C.1.3 *20 September 2011*

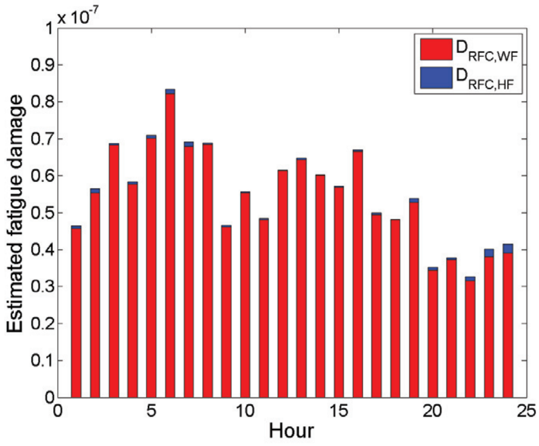

Figure C.21: *Fatigue damage per hour during 24 hours on 20 September 2011 estimated using rainflow counting and the Palmgren-Miner rule.*

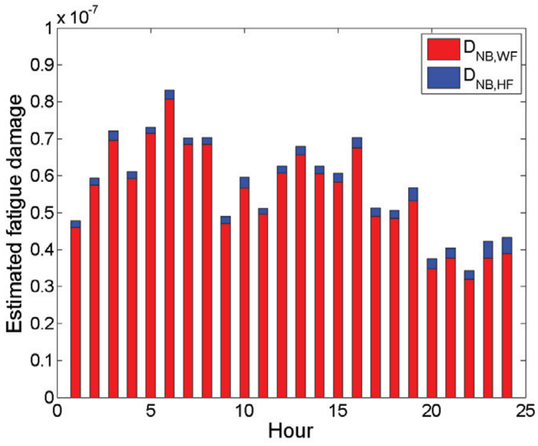

Figure C.22: *Fatigue damage during 24 hours on 20 September 2011 estimated using narrow-banded spectral analysis (one narrow-banded process).*

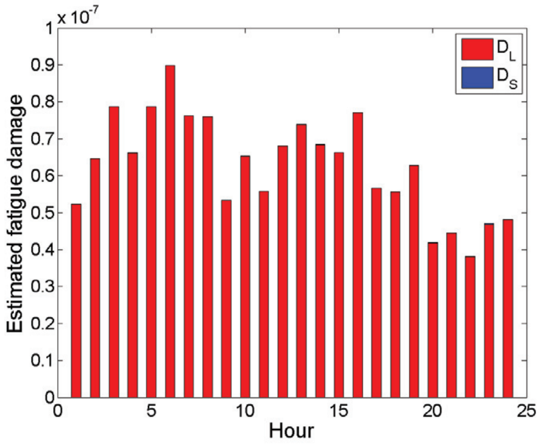

Figure C.23: *Fatigue damage during 24 hours on 20 September 2011 estimated using narrow-banded spectral analysis assuming two Gaussian narrow-banded processes (Jiao and Moan (1990)).*

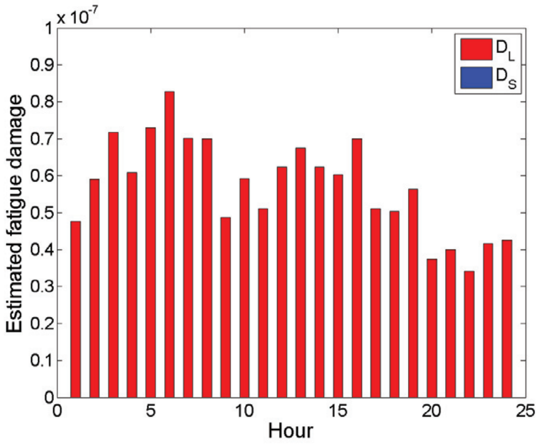

Figure C.24: *Fatigue damage during 24 hours on 20 September 2011 estimated using narrow-banded spectral analysis assuming two Gaussian, narrow-banded processes (Low (2010)).*

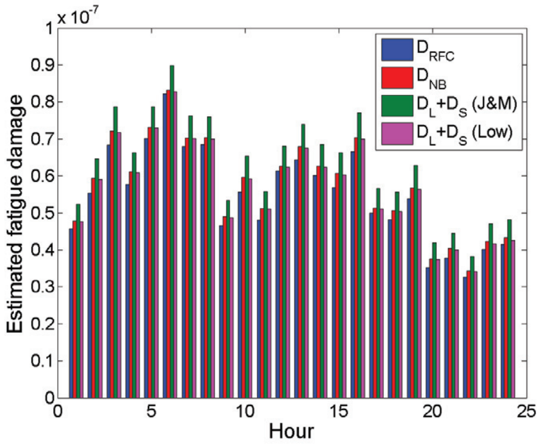

Figure C.25: *Comparison of total estimated fatigue damage per hour during 24 hours on 20 September 2011.*

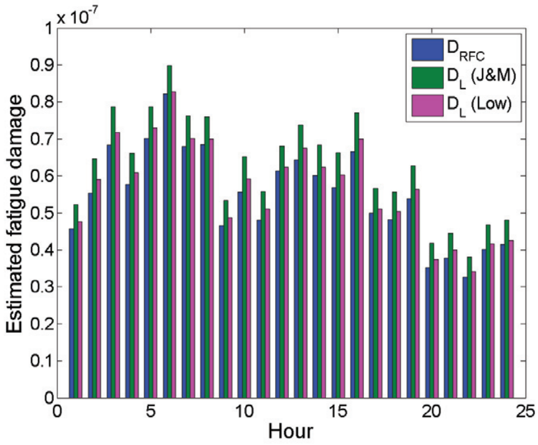

Figure C.26: *Comparison of estimated fatigue damage for the two envelope processes (Eq. (6.4) and Eq. (6.20)) with the total estimate from RFC for 20 September 2011.*

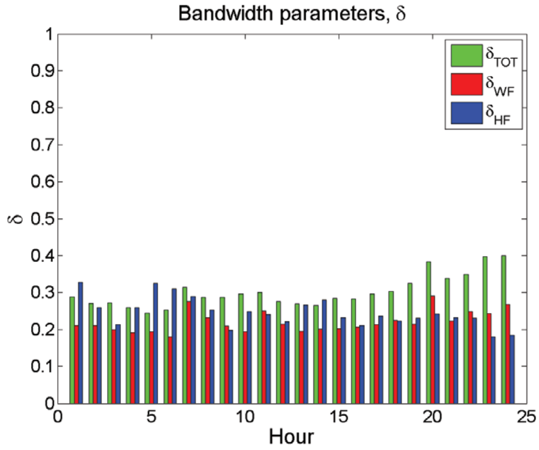

Figure C.27: *Bandwidth parameters, δ (Eq. (6.10)), for the total, WF and HF part of the process for 20 September 2011.*

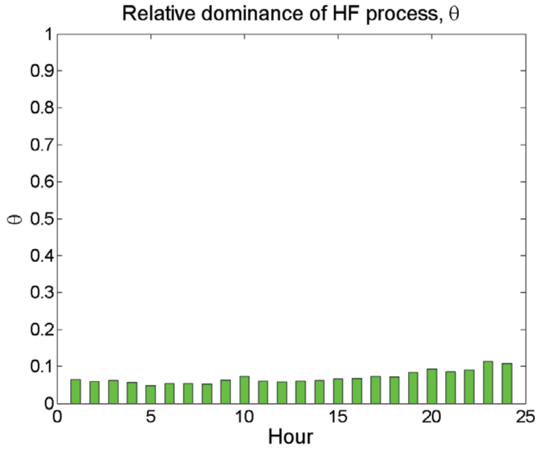

Figure C.28: *Relative dominance of the HF process, θ (Eq. (6.8)), for 20 September 2011.*

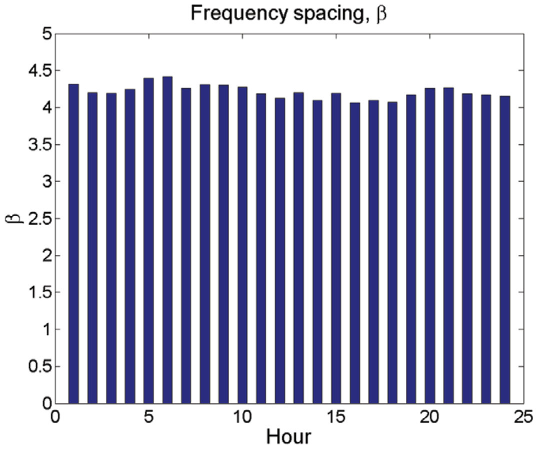

Figure C.29: *Spacing between low and high frequency parts, β (Eq. (6.9)), for 20 September 2011.*

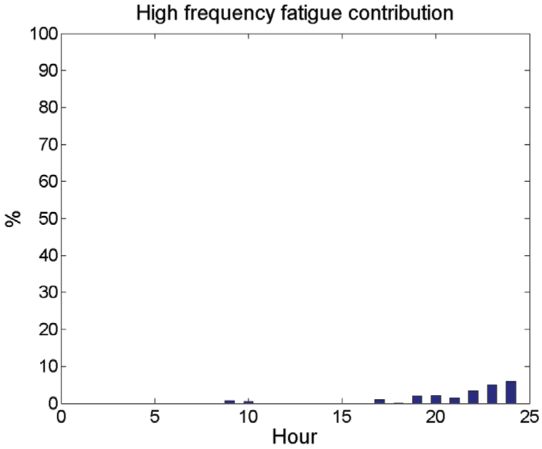

Figure C.30: *High frequency (HF) contribution to the total estimated fatigue damage per hour for 20 September 2011 using RFC.*

C.1.4 *02 October 2011*

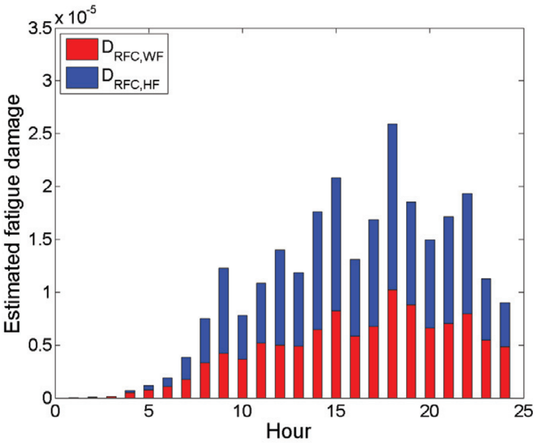

Figure C.31: *Fatigue damage per hour during 24 hours on 02 October 2011 estimated using rainflow counting and the Palmgren-Miner rule.*

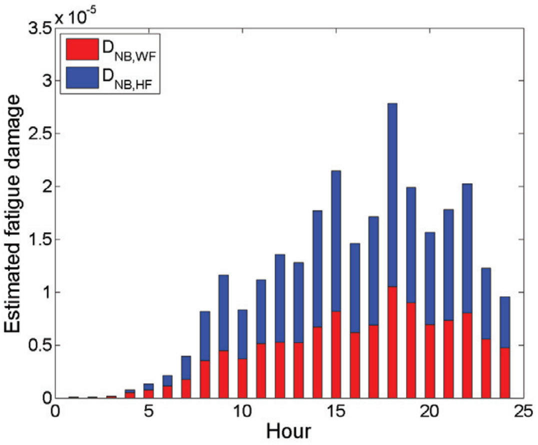

Figure C.32: *Fatigue damage during 24 hours on 02 October 2011 estimated using narrow-banded spectral analysis (one narrow-banded process).*

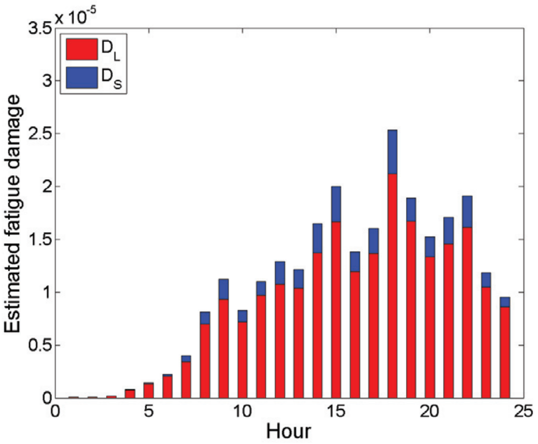

Figure C.33: *Fatigue damage during 24 hours on 02 October 2011 estimated using narrow-banded spectral analysis assuming two Gaussian narrow-banded processes (Jiao and Moan (1990)).*

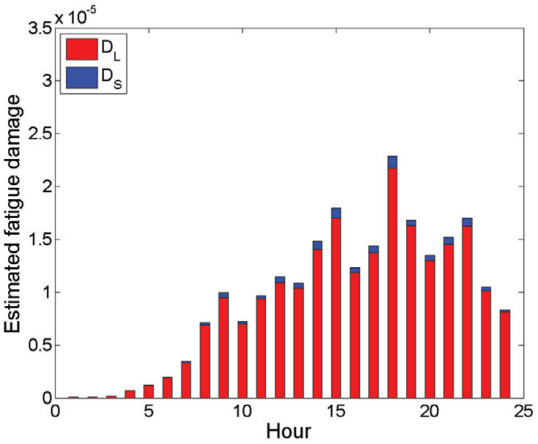

Figure C.34: *Fatigue damage during 24 hours on 02 October 2011 estimated using narrow-banded spectral analysis assuming two Gaussian, narrow-banded processes (Low (2010)).*

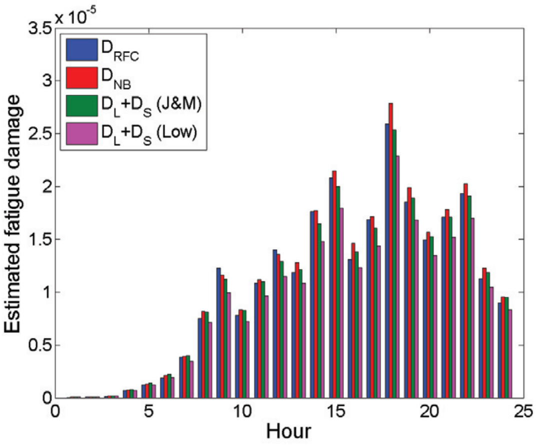

Figure C.35: *Comparison of total estimated fatigue damage per hour during 24 hours on 02 October 2011.*

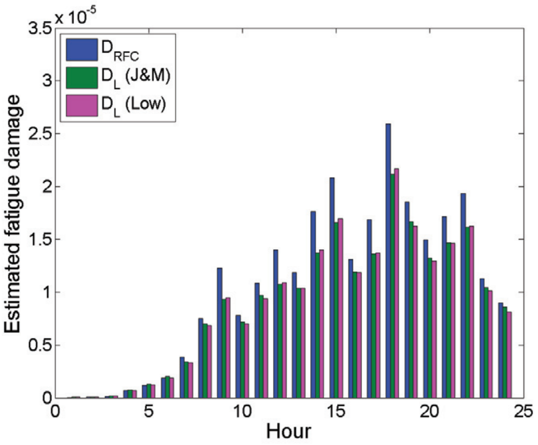

Figure C.36: *Comparison of estimated fatigue damage for the two envelope processes (Eq. (6.4) and Eq. (6.20)) with the total estimate from RFC for 02 October 2011.*

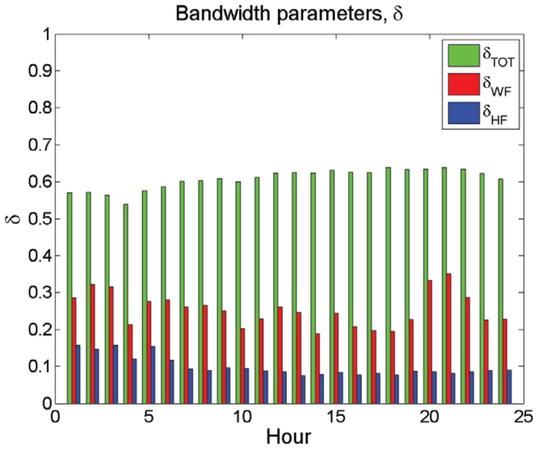

Figure C.37: *Bandwidth parameters, δ (Eq. (6.10)), for the total, WF and HF part of the process for 02 October 2011.*

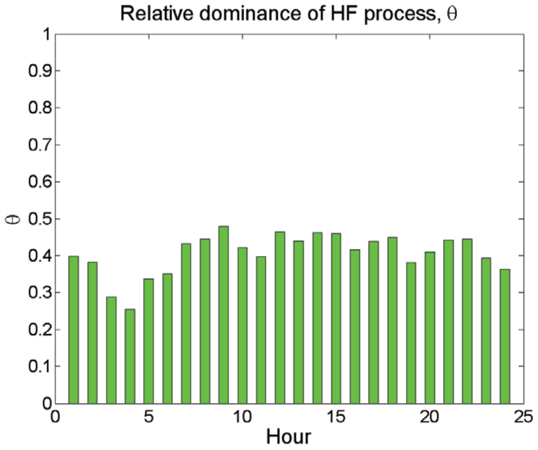

Figure C.38: *Relative dominance of the HF process, θ (Eq. (6.8)), for 02 October 2011.*

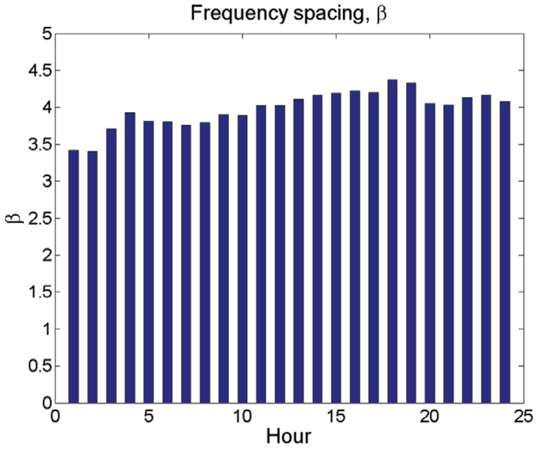

Figure C.39: *Spacing between low and high frequency parts, β (Eq. (6.9)), for 02 October 2011.*

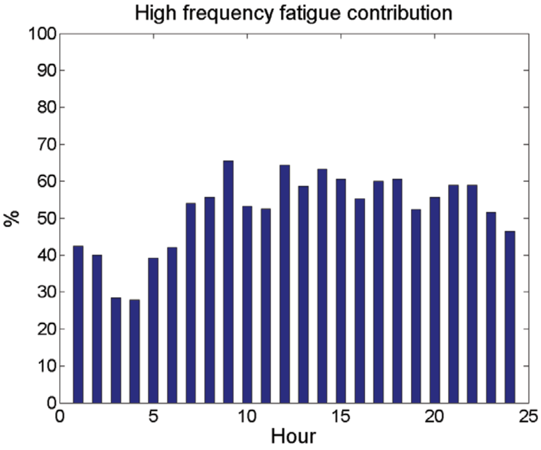

Figure C.40: *High frequency (HF) contribution to the total estimated fatigue damage per hour for 02 October 2011 using RFC.*

C.2 8,600 TEU Container Ship

C.2.1 *05 February 2010*

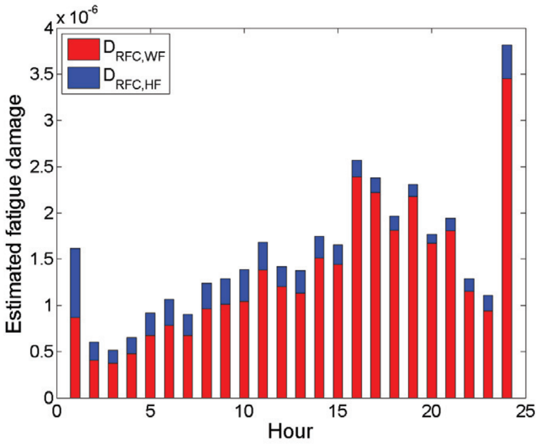

Figure C.41: *Fatigue damage per hour during 24 hours on 05 February 2010 estimated using rainflow counting and the Palmgren-Miner rule.*

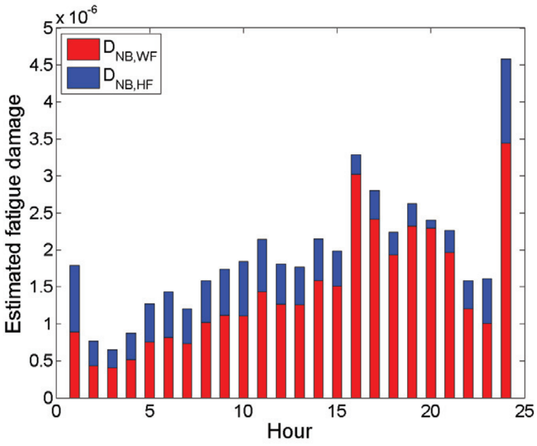

Figure C.42: *Fatigue damage during 24 hours on 05 February 2010 estimated using narrow-banded, spectral analysis (one narrow-banded process).*

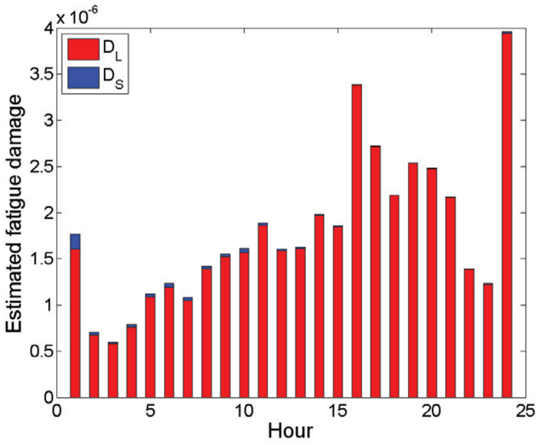

Figure C.43: *Fatigue damage during 24 hours on 05 February 2010 estimated using narrow-banded spectral analysis assuming two Gaussian narrow-banded processes (Jiao and Moan (1990)).*

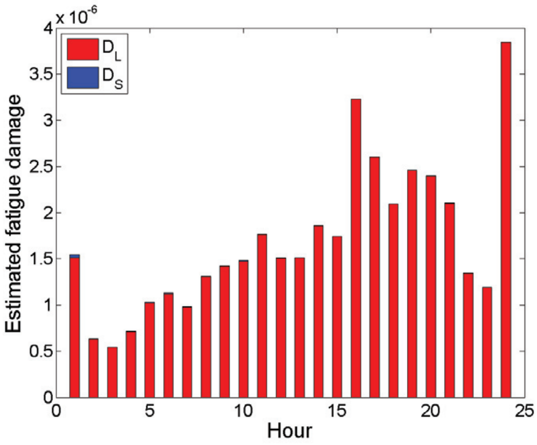

Figure C.44: *Fatigue damage during 24 hours on 05 February 2010 estimated using narrow-banded spectral analysis assuming two Gaussian, narrow-banded processes (Low (2010)).*

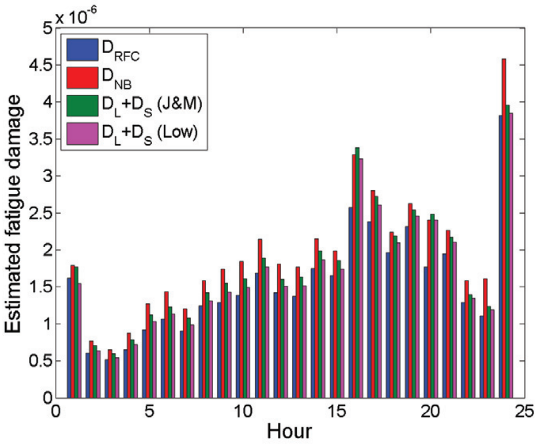

Figure C.45: *Comparison of total estimated fatigue damage per hour during 24 hours on 05 February 2010.*

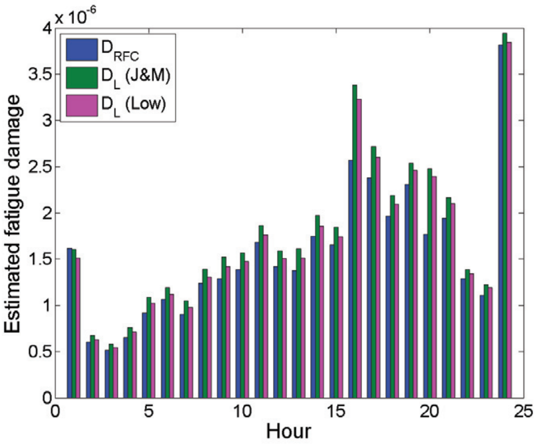

Figure C.46: *Comparison of estimated fatigue damage for the two envelope processes (Eq. (6.4) and Eq. (6.20)) with the total estimate from RFC for 05 February 2010.*

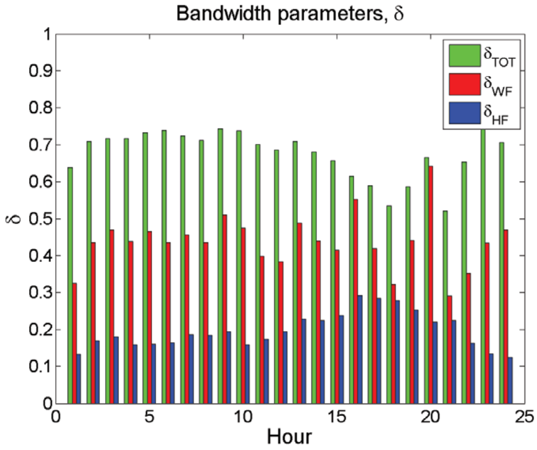

Figure C.47: *Bandwidth parameters, δ (Eq. (6.10)), for the total, WF and HF part of the process for 05 February 2010.*

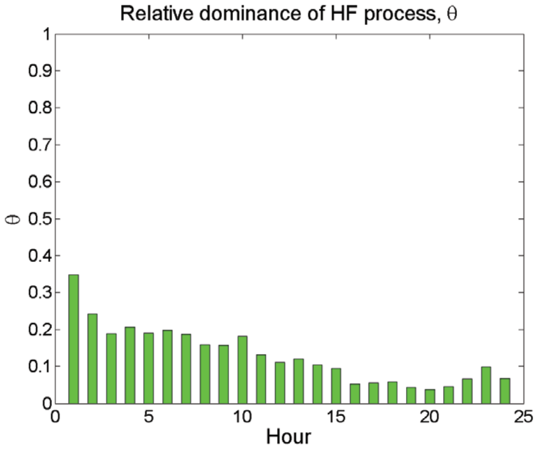

Figure C.48: *Relative dominance of the HF process, θ (Eq. (6.8)), for 05 February 2010.*

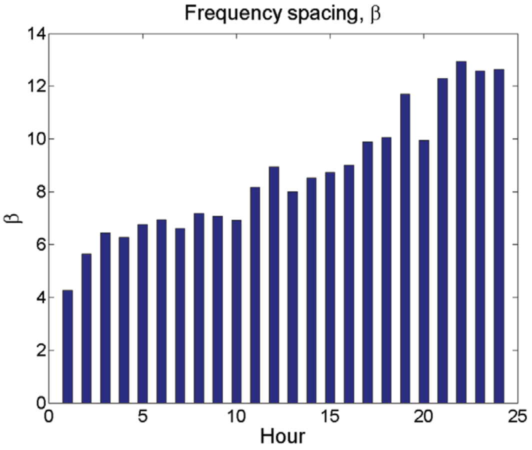

Figure C.49: *Spacing between low and high frequency parts, β (Eq. (6.9)), for 05 February 2010.*

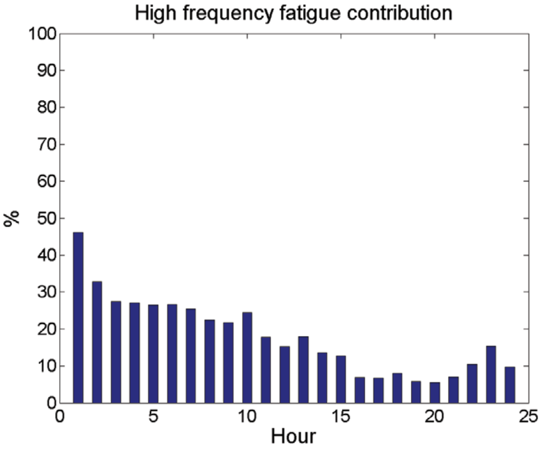

Figure C.50: *High frequency (HF) contribution to the total estimated fatigue damage per hour for 05 February 2010 using RFC.*

C.2.2 *07 November 2010*

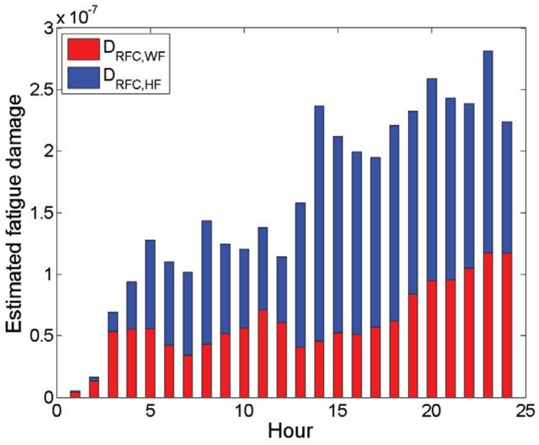

Figure C.51: *Fatigue damage per hour during 24 hours on 07 November 2010 estimated using rainflow counting and the Palmgren-Miner rule.*

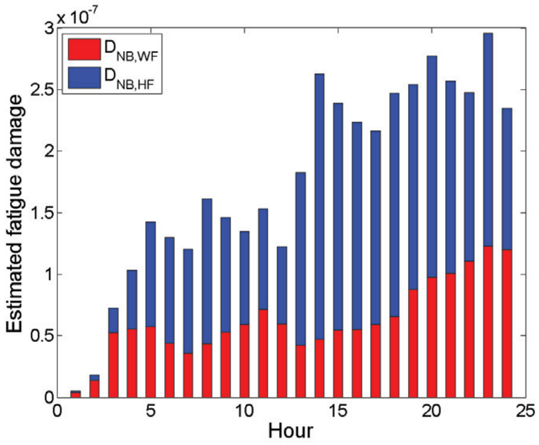

Figure C.52: *Fatigue damage during 24 hours on 07 November 2010 estimated using narrow-banded, spectral analysis (one narrow-banded process).*

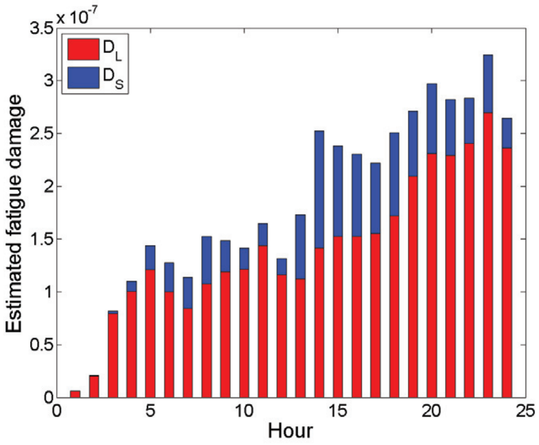

Figure C.53: *Fatigue damage during 24 hours on 07 November 2010 estimated using narrow-banded spectral analysis assuming two Gaussian narrow-banded processes (Jiao and Moan (1990)).*

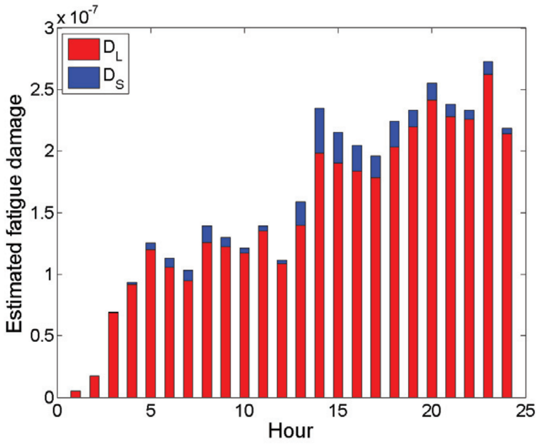

Figure C.54: *Fatigue damage during 24 hours on 07 November 2010 estimated using narrow-banded spectral analysis assuming two Gaussian, narrow-banded processes (Low (2010)).*

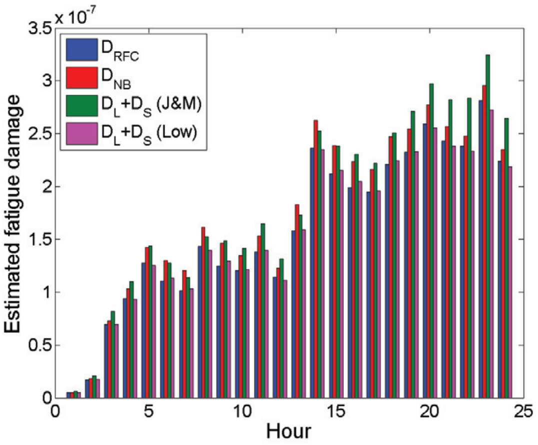

Figure C.55: *Comparison of total estimated fatigue damage per hour during 24 hours on 07 November 2010.*

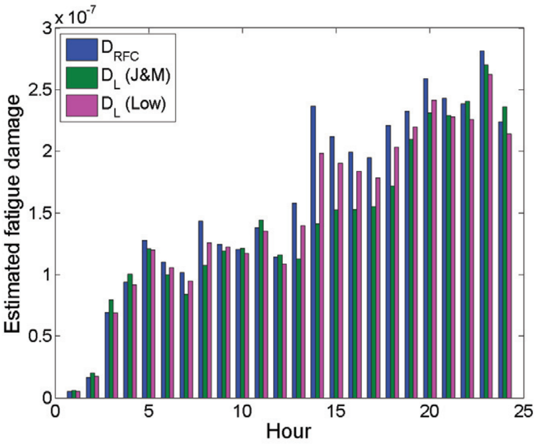

Figure C.56: *Comparison of estimated fatigue damage for the two envelope processes (Eq. (6.4) and Eq. (6.20)) with the total estimate from RFC for 07 November 2010.*

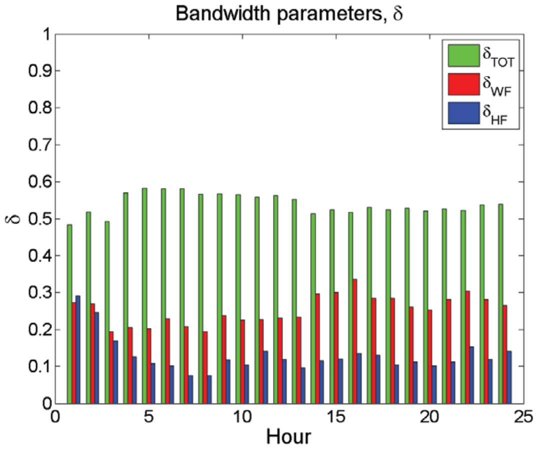

Figure C.57: *Bandwidth parameters, δ (Eq. (6.10)), for the total, WF and HF part of the process for 07 November 2010.*

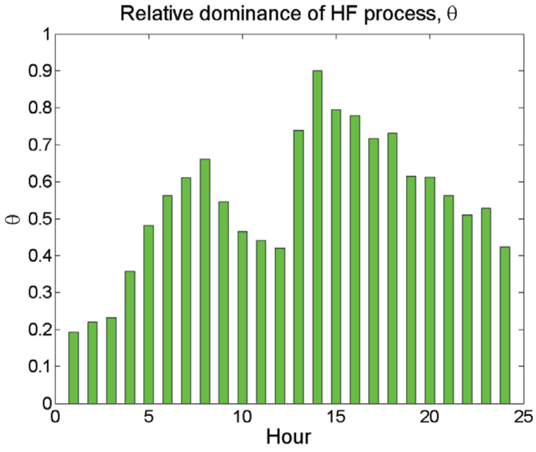

Figure C.58: *Relative dominance of the HF process, θ (Eq. (6.8)), for 07 November 2010.*

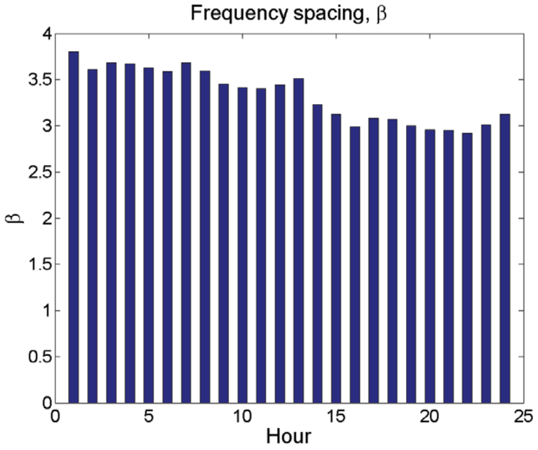

Figure C.59: *Spacing between low and high frequency parts, β (Eq. (6.9)), for 07 November 2010.*

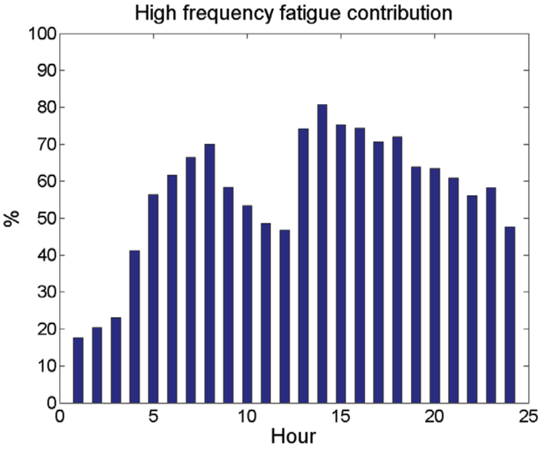

Figure C.60: *High frequency (HF) contribution to the total estimated fatigue damage per hour for 07 November 2010 using RFC.*

C.2.3 *08 November 2010*

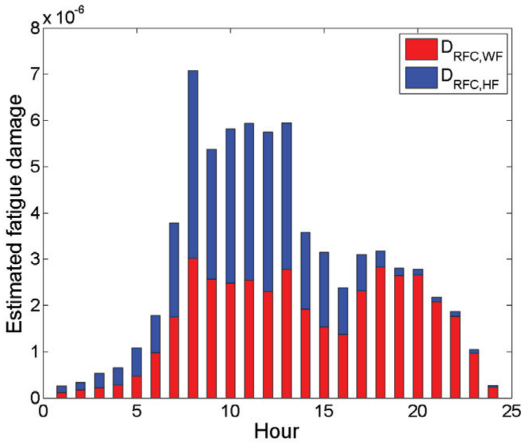

Figure C.61: *Fatigue damage per hour during 24 hours on 08 November 2010 estimated using rainflow counting and the Palmgren-Miner rule.*

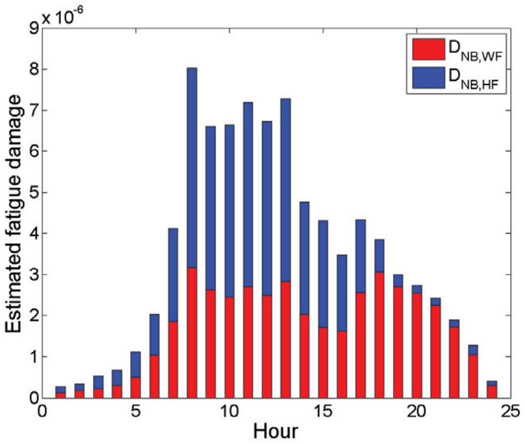

Figure C.62: *Fatigue damage during 24 hours on 08 November 2010 estimated using narrow-banded, spectral analysis (one narrow-banded process).*

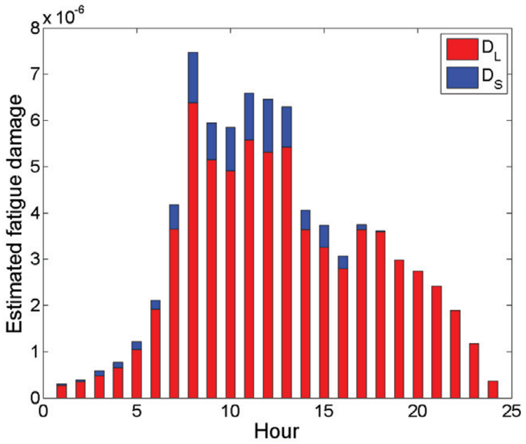

Figure C.63: *Fatigue damage during 24 hours on 08 November 2010 estimated using narrow-banded spectral analysis assuming two Gaussian narrow-banded processes (Jiao and Moan (1990)).*

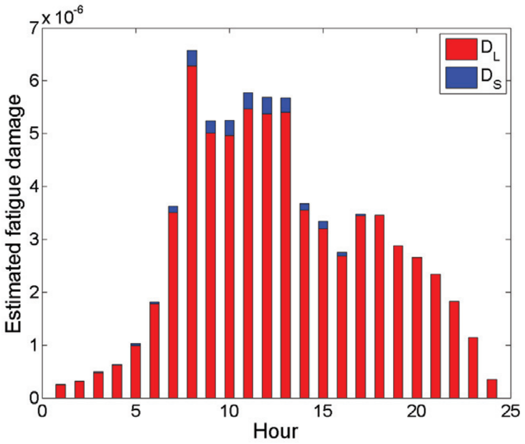

Figure C.64: *Fatigue damage during 24 hours on 08 November 2010 estimated using narrow-banded spectral analysis assuming two Gaussian, narrow-banded processes (Low (2010)).*

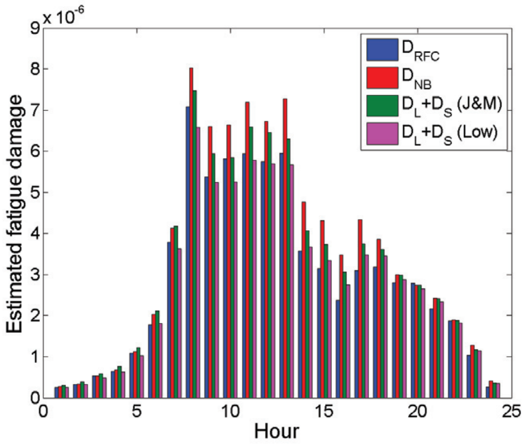

Figure C.65: *Comparison of total estimated fatigue damage per hour during 24 hours on 08 November 2010.*

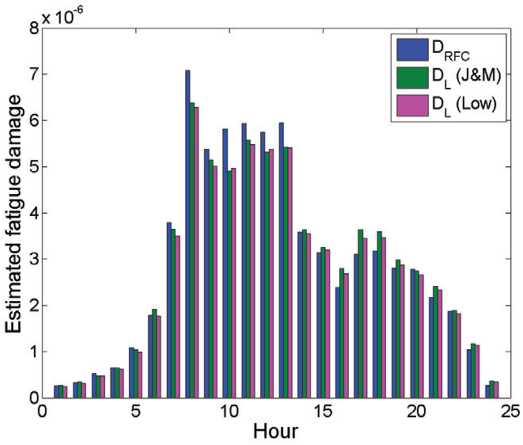

Figure C.66: *Comparison of estimated fatigue damage for the two envelope processes (Eq. (6.4) and Eq. (6.20)) with the total estimate from RFC for 08 November 2010.*

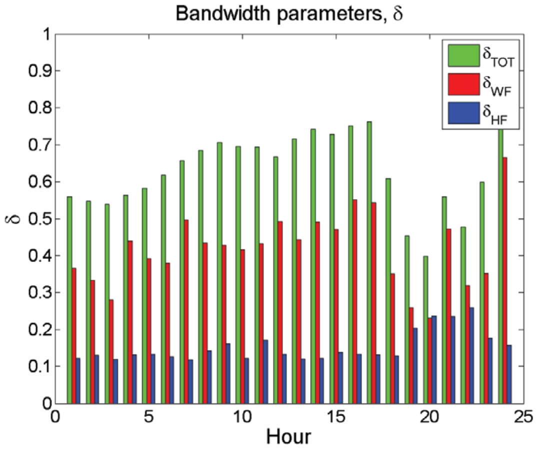

Figure C.67: *Bandwidth parameters, δ (Eq. (6.10)), for the total, WF and HF part of the process for 08 November 2010.*

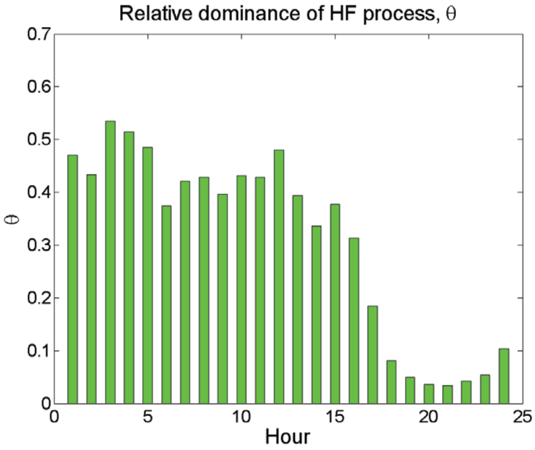

Figure C.68: *Relative dominance of the HF process, θ (Eq. (6.8)), for 08 November 2010.*

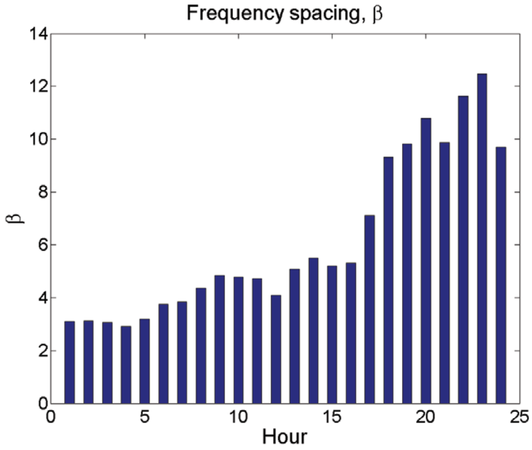

Figure C.69: Spacing between low and high frequency parts, β (Eq. (6.9)), for 08 November 2010.

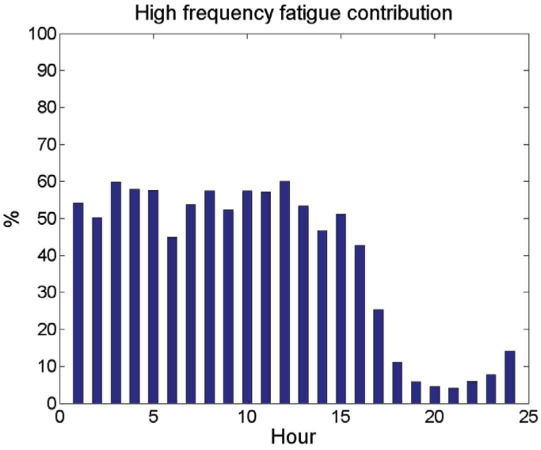

Figure C.70: High frequency (HF) contribution to the total estimated fatigue damage per hour for 08 November 2010 using RFC.

C.2.4 *17 November 2010*

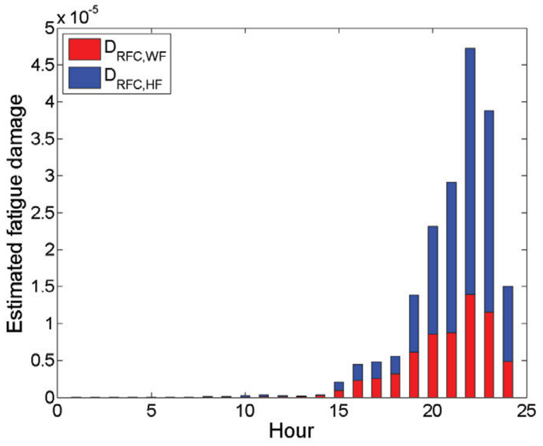

Figure C.71: *Fatigue damage per hour during 24 hours on 17 November 2010 estimated using rainflow counting and the Palmgren-Miner rule.*

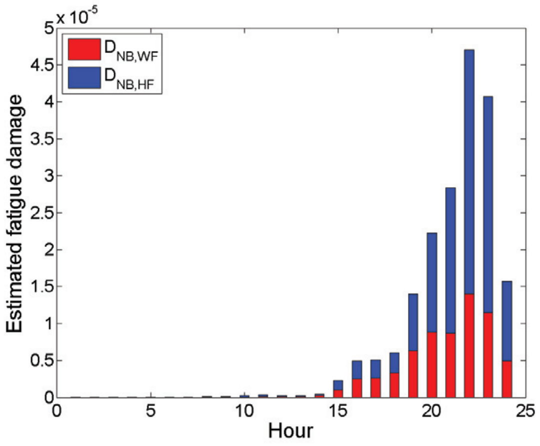

Figure C.72: *Fatigue damage during 24 hours on 17 November 2010 estimated using narrow-banded, spectral analysis (one narrow-banded process).*

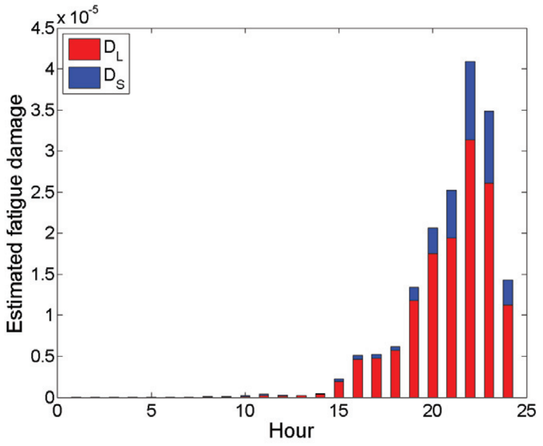

Figure C.73: *Fatigue damage during 24 hours on 17 November 2010 estimated using narrow-banded spectral analysis assuming two Gaussian narrow-banded processes (Jiao and Moan (1990)).*

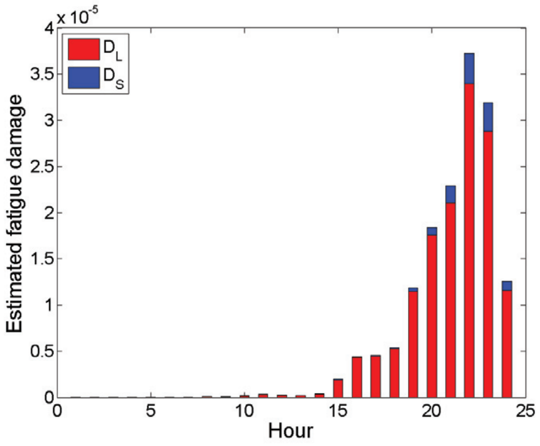

Figure C.74: *Fatigue damage during 24 hours on 17 November 2010 estimated using narrow-banded spectral analysis assuming two Gaussian, narrow-banded processes (Low (2010)).*

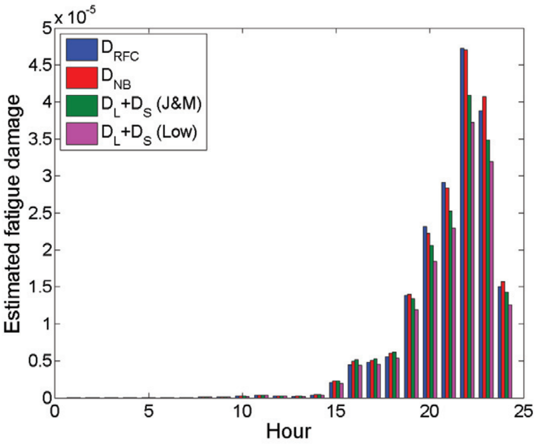

Figure C.75: *Comparison of total estimated fatigue damage per hour during 24 hours on 17 November 2010.*

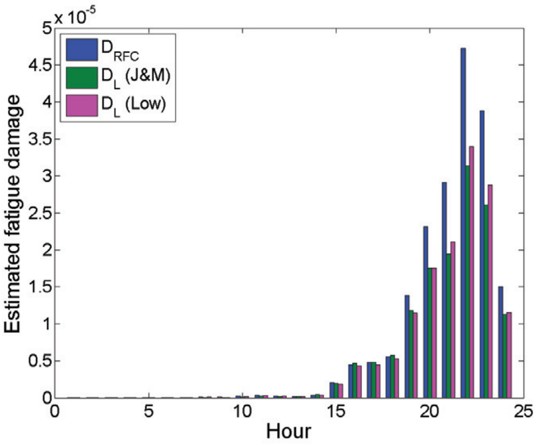

Figure C.76: *Comparison of estimated fatigue damage for the two envelope processes (Eq. (6.4) and Eq. (6.20)) with the total estimate from RFC for 17 November 2010.*

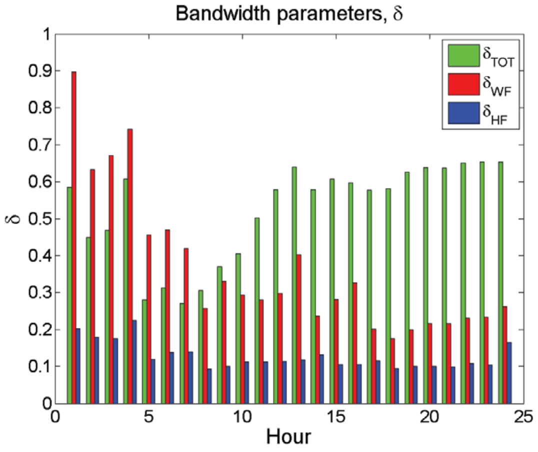

Figure C.77: *Bandwidth parameters, δ (Eq. (6.10)), for the total, WF and HF part of the process for 17 November 2010.*

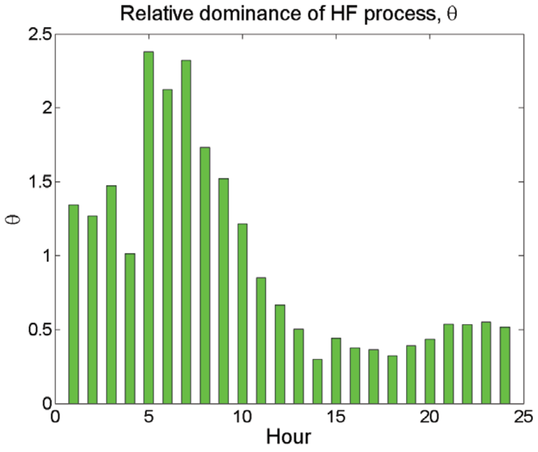

Figure C.78: *Relative dominance of the HF process, θ (Eq. (6.8)), for 17 November 2010.*

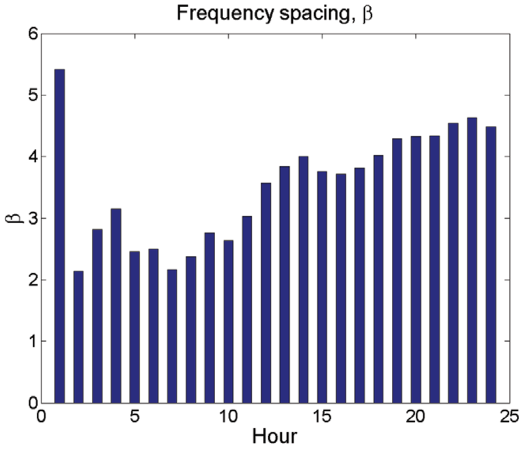

Figure C.79: Spacing between low and high frequency parts, β (Eq. (6.9)), for 17 November 2010.

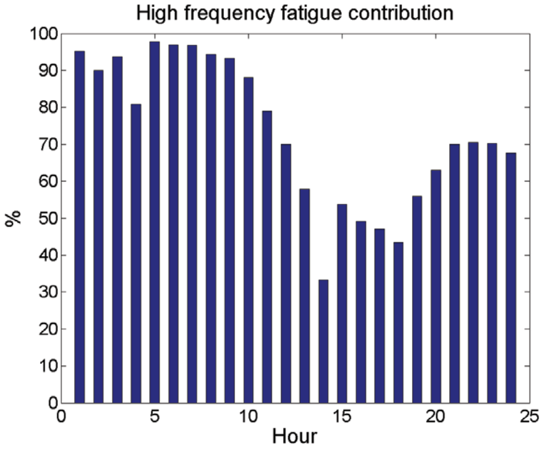

Figure C.80: High frequency (HF) contribution to the total estimated fatigue damage per hour for 17 November 2010 using RFC.

C.2.5 *18 November 2010*

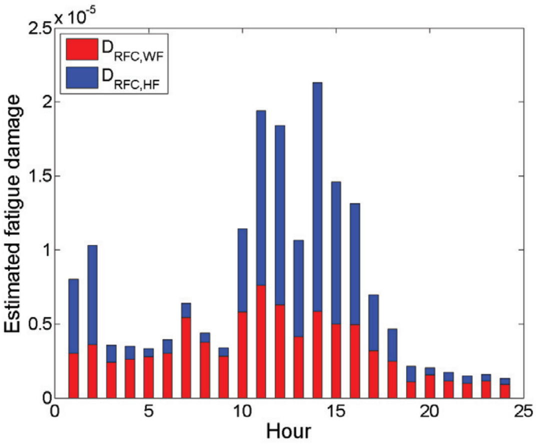

Figure C.81: *Fatigue damage per hour during 24 hours on 18 November 2010 estimated using rainflow counting and the Palmgren-Miner rule.*

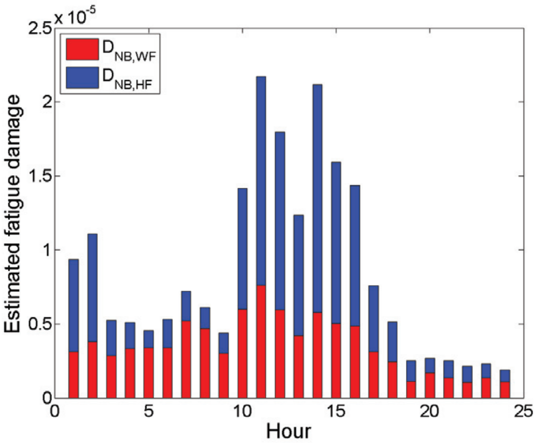

Figure C.82: *Fatigue damage during 24 hours on 18 November 2010 estimated using narrow-banded, spectral analysis (one narrow-banded process).*

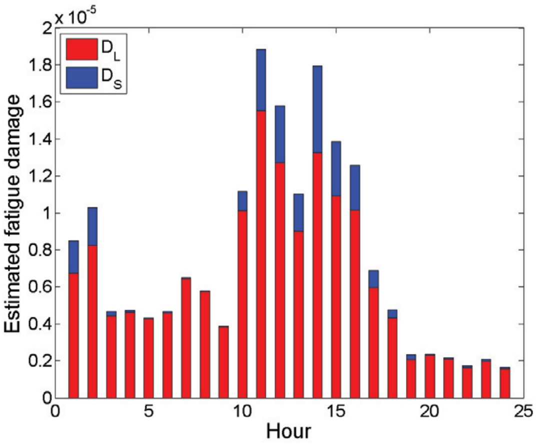

Figure C.83: *Fatigue damage during 24 hours on 18 November 2010 estimated using narrow-banded spectral analysis assuming two Gaussian narrow-banded processes (Jiao and Moan (1990)).*

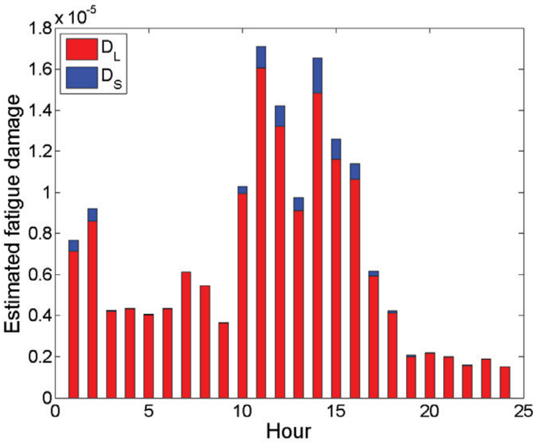

Figure C.84: *Fatigue damage during 24 hours on 18 November 2010 estimated using narrow-banded spectral analysis assuming two Gaussian, narrow-banded processes (Low (2010)).*

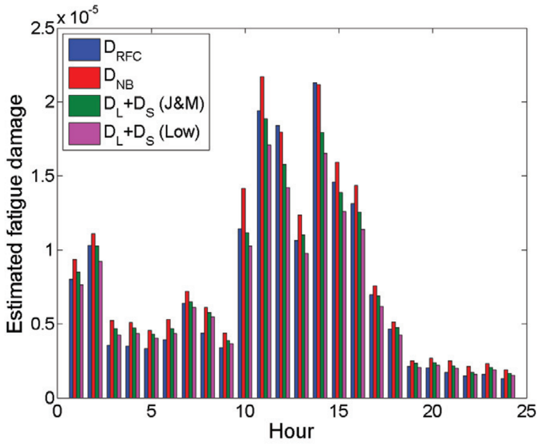

Figure C.85: *Comparison of total estimated fatigue damage per hour during 24 hours on 18 November 2010.*

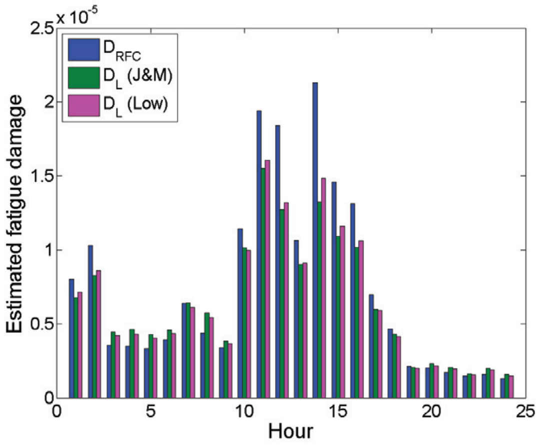

Figure C.86: *Comparison of estimated fatigue damage for the two envelope processes (Eq. (6.4) and Eq. (6.20)) with the total estimate from RFC for 18 November 2010.*

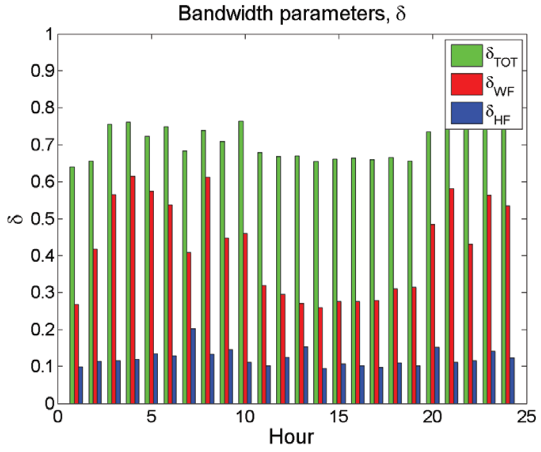

Figure C.87: *Bandwidth parameters, δ (Eq. (6.10)), for the total, WF and HF part of the process for 18 November 2010.*

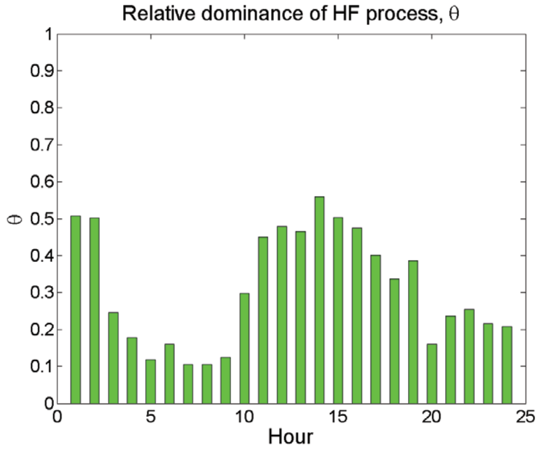

Figure C.88: *Relative dominance of the HF process, θ (Eq. (6.8)), for 18 November 2010.*

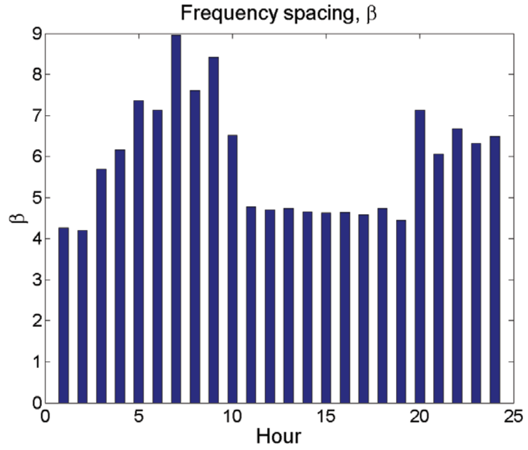

Figure C.89: *Spacing between low and high frequency parts, β (Eq. (6.9)), for 18 November 2010.*

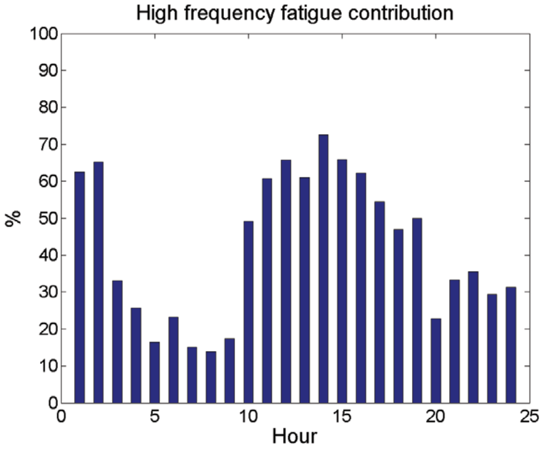

Figure C.90: *High frequency (HF) contribution to the total estimated fatigue damage per hour for 18 November 2010 using RFC.*

C.2.6 *01 December 2010*

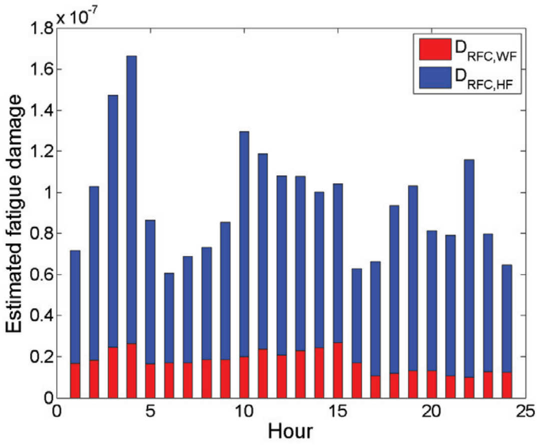

Figure C.91: *Fatigue damage per hour during 24 hours on 01 December 2010 estimated using rainflow counting and the Palmgren-Miner rule.*

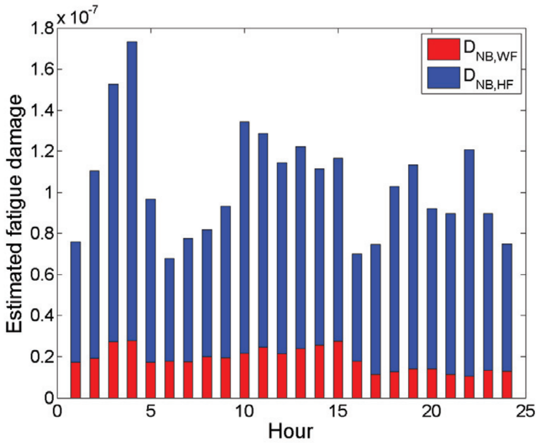

Figure C.92: *Fatigue damage during 24 hours on 01 December 2010 estimated using narrow-banded, spectral analysis (one narrow-banded process).*

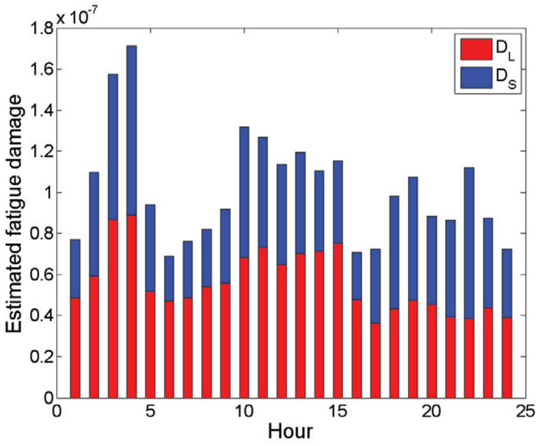

Figure C.93: *Fatigue damage during 24 hours on 01 December 2010 estimated using narrow-banded spectral analysis assuming two Gaussian narrow-banded processes (Jiao and Moan (1990)).*

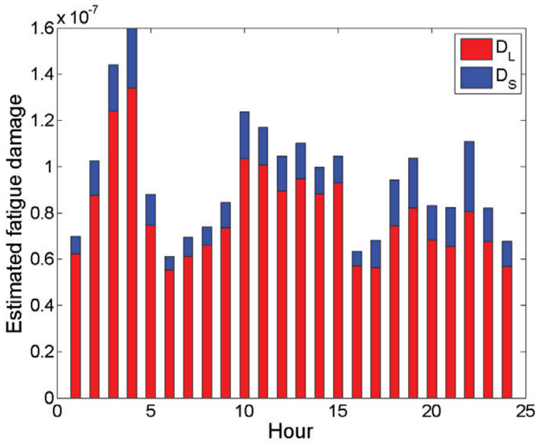

Figure C.94: *Fatigue damage during 24 hours on 01 December 2010 estimated using narrow-banded spectral analysis assuming two Gaussian, narrow-banded processes (Low (2010)).*

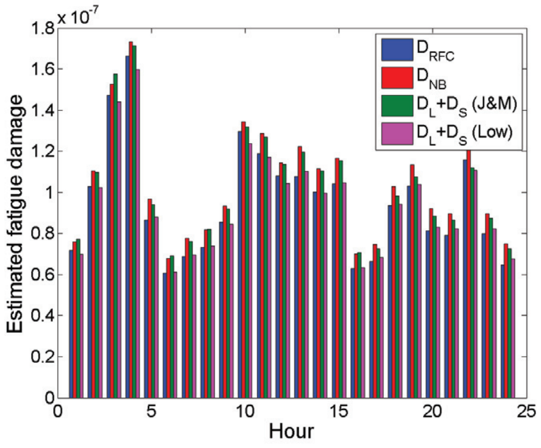

Figure C.95: *Comparison of total estimated fatigue damage per hour during 24 hours on 01 December 2010.*

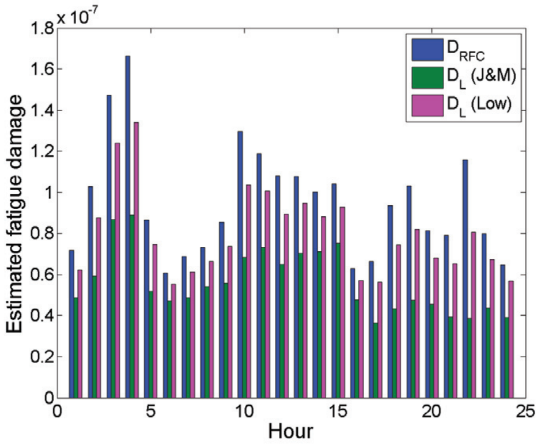

Figure C.96: *Comparison of estimated fatigue damage for the two envelope processes (Eq. (6.4) and Eq. (6.20)) with the total estimate from RFC for 01 December 2010.*

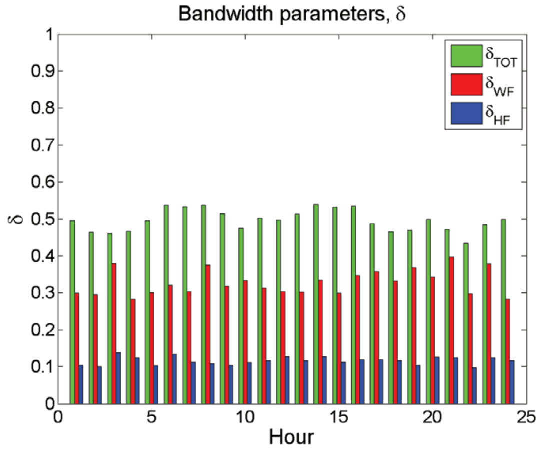

Figure C.97: *Bandwidth parameters, δ (Eq. (6.10)), for the total, WF and HF part of the process for 01 December 2010.*

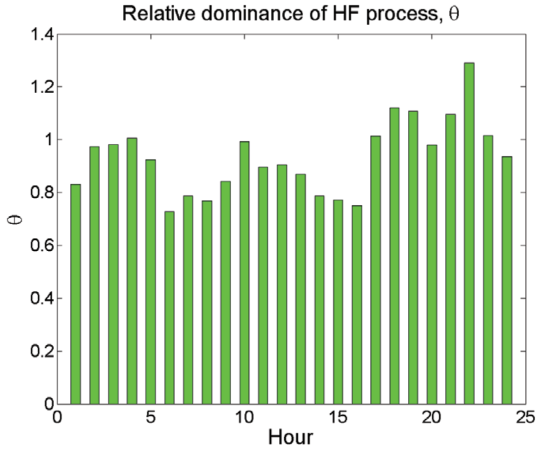

Figure C.98: *Relative dominance of the HF process, θ (Eq. (6.8)), for 01 December 2010.*

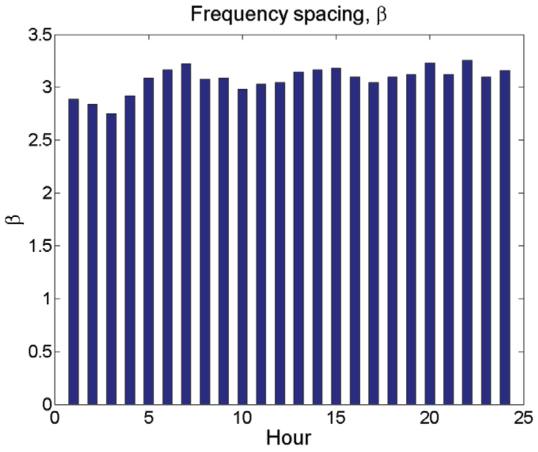

Figure C.99: *Spacing between low and high frequency parts, β (Eq. (6.9)), for 01 December 2010.*

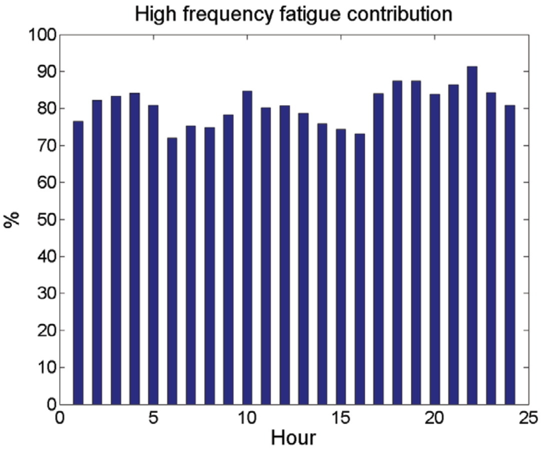

Figure C.100: *High frequency (HF) contribution to the total estimated fatigue damage per hour for 01 December 2010 using RFC.*

C.2.7 *30 December 2011*

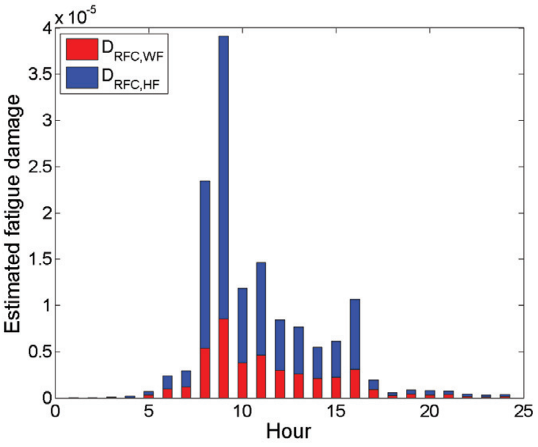

Figure C.101: *Fatigue damage per hour during 24 hours on 30 December 2011 estimated using rainflow counting and the Palmgren-Miner rule.*

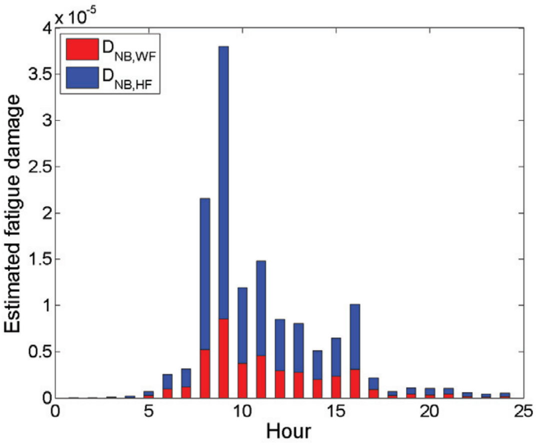

Figure C.102: *Fatigue damage during 24 hours on 30 December 2011 estimated using narrow-banded, spectral analysis (one narrow-banded process).*

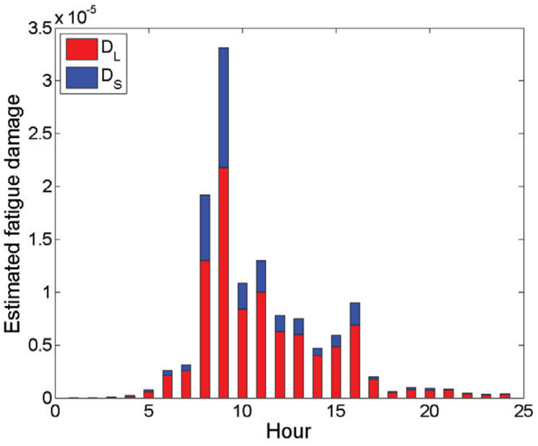

Figure C.103: *Fatigue damage during 24 hours on 30 December 2011 estimated using narrow-banded spectral analysis assuming two Gaussian narrow-banded processes (Jiao and Moan (1990)).*

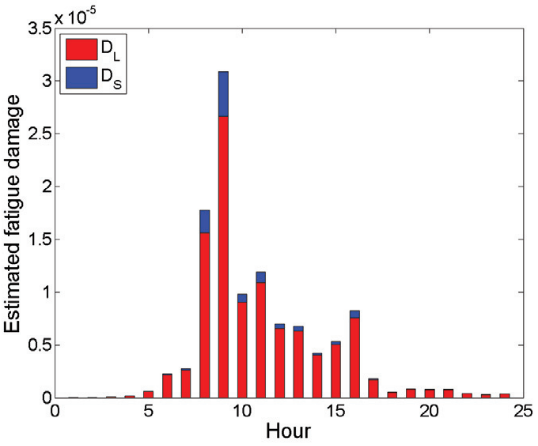

Figure C.104: *Fatigue damage during 24 hours on 30 December 2011 estimated using narrow-banded spectral analysis assuming two Gaussian, narrow-banded processes (Low (2010)).*

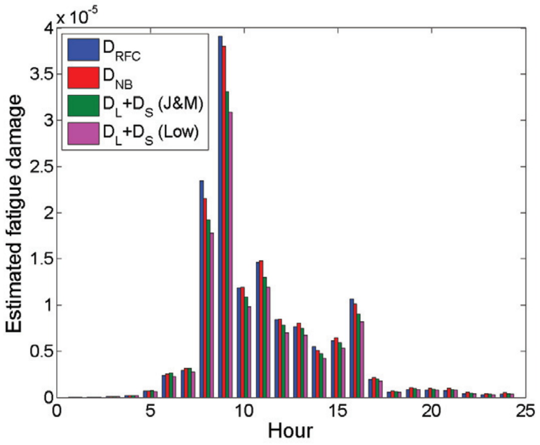

Figure C.105: *Comparison of total estimated fatigue damage per hour during 24 hours on 30 December 2011.*

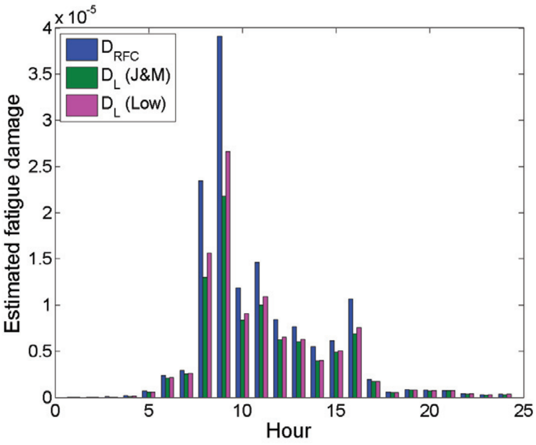

Figure C.106: *Comparison of estimated fatigue damage for the two envelope processes (Eq. (6.4) and Eq. (6.20)) with the total estimate from RFC for 30 December 2011.*

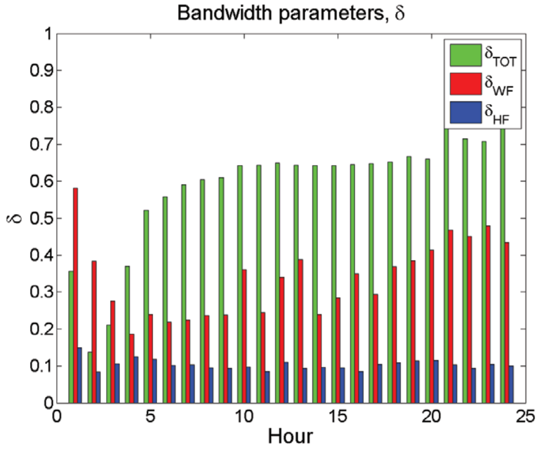

Figure C.107: *Bandwidth parameters, δ (Eq. (6.10)), for the total, WF and HF part of the process for 30 December 2011.*

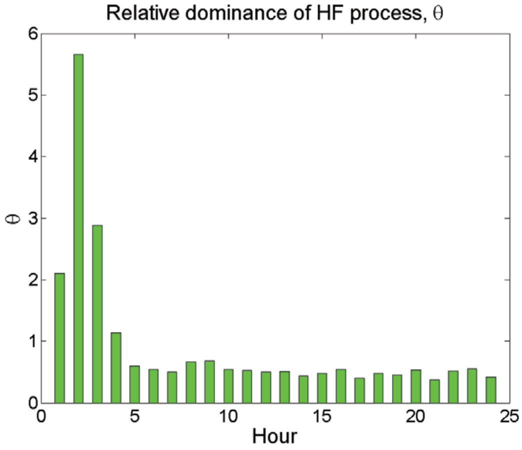

Figure C.108: *Relative dominance of the HF process, θ (Eq. (6.8)), for 30 December 2011.*

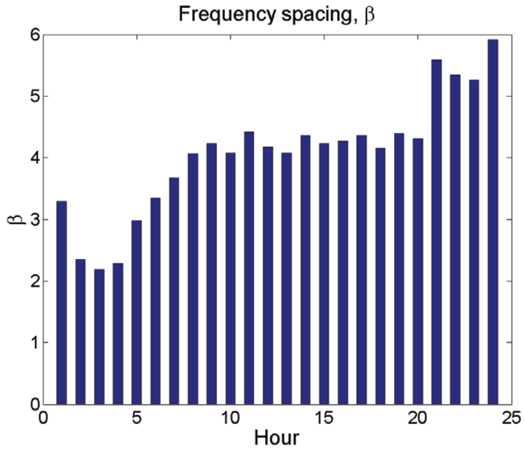

Figure C.109: *Spacing between low and high frequency parts, β (Eq. (6.9)), for 30 December 2011.*

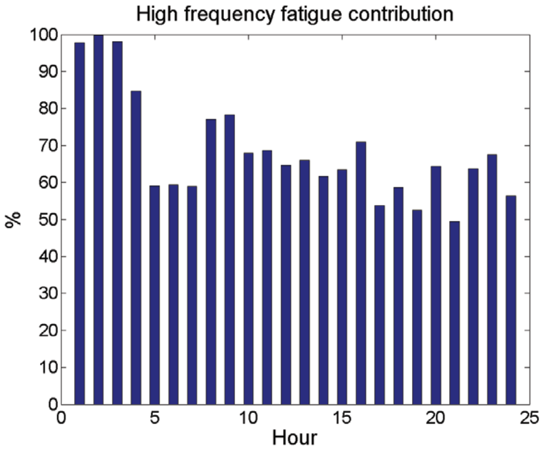

Figure C.110: *High frequency (HF) contribution to the total estimated fatigue damage per hour for 30 December 2011 using RFC.*

C.3 Fatigue Damage Estimation using a Combination of a Stationary Gaussian Process and a Non-Gaussian Transient Process

In the approach proposed by Jiao and Moan (1990) the total process is modelled as a combination of a narrow-banded Gaussian WF process and a transient HF part. The inter-arrival time between each transient event T_0 can be adjusted to the nature of the signal. Small T_0 would thus correspond to a more or less constant high-frequency vibration response (springing) while large T_0 would correspond to slamming induced whipping vibrations and thus the method could, in theory, treat both springing and whipping induced fatigue damage.

The estimate of the fatigue damage depends on T_0 and the sensitivity to the value of T_0 is investigated here. The variation of the inter-arrival time of transient events is carried out for the two roughest sea states for the 9,400 TEU container ship on 12 August and 02 October 2011 and compared to the outcome of the RFC analysis in Figures C.113 to C.122.

For small T_0 (in the order of 10-20 s) the damage due to the small cycles, D_2, is found the play a considerable role for two of the days (12 August and 02 October) and the contribution from the transient process D_2 cannot generally be neglected contrarily to findings in Nielsen et al. (2011).

For the data from 12 August it appears that $T_0 = 20$ s is gives the best fit to the RFC results whereas $T_0 = 10$ s gives better agreement for 02 October. In both cases the inter-arrival time T_0, which should be interpreted as the time between mean return period between slams, is considerably shorter than expected since the vessel is not expected to encounter a slam every 10-20 seconds on average. However, as was also found by Nielsen et al. (2011) a relatively small T_0 seems to give best agreement with RFC.

According to Jiao and Moan (1990) the Gaussian and the transient part are assumed being statistically independent, which is not generally the case for a ship, since the transient vibration is usually initiated by a slam which occurs together with a large sagging response.

Furthermore, the structural damping ξ enters into the equations for the envelope process (Eq. (6.23)) and the transient process (Eq. (6.24)). Here, $\xi = 0.01$ is used, but the uncertainty connected with the estimate of ξ is large.

Compared to the other spectral methods compared in Chapter 6 this method by Jiao and Moan (1990) is considered too sensitive to the two extra input parameters ξ and T_0 compared to the other discussed methods and does not improve accuracy of the fatigue damage estimation.

C.3.1 *12 August 2011*

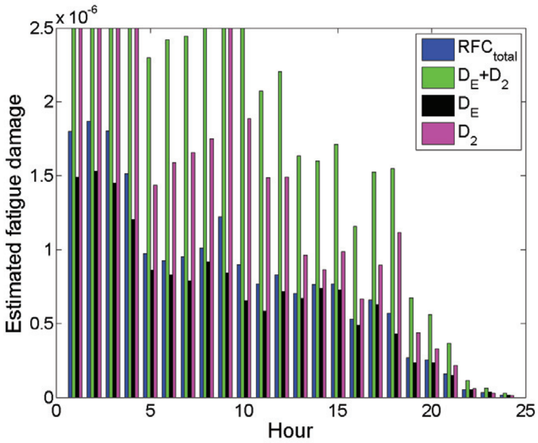

Figure C.111: *Fatigue damage during 24 hours on 12 August 2011.* $T_0 = 2$ *s.*

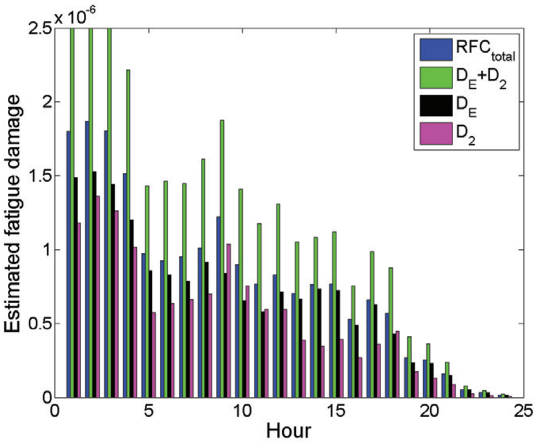

Figure C.112: *Fatigue damage during 24 hours on 12 August 2011.* $T_0 = 5$ *s.*

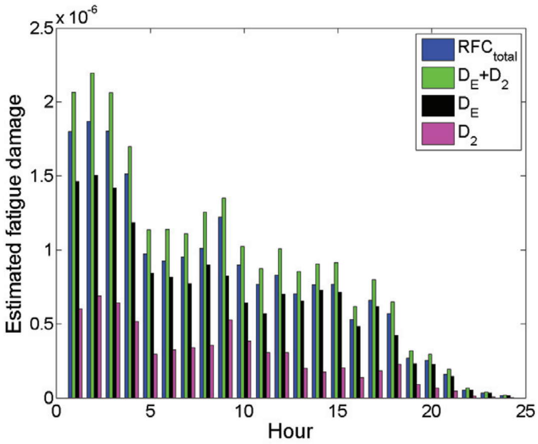

Figure C.113: *Fatigue damage during 24 hours on 12 August 2011.* $T_0 = 10$ *s.*

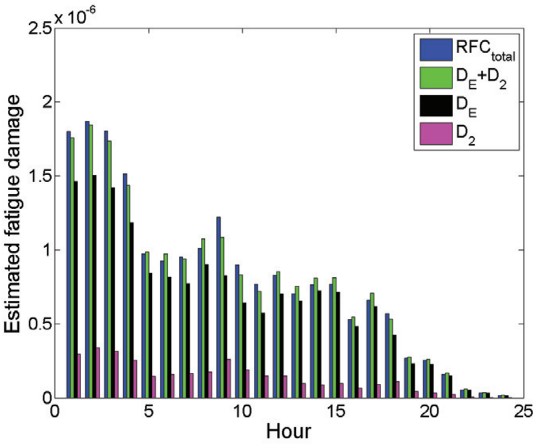

Figure C.114: *Fatigue damage during 24 hours on 12 August 2011.* $T_0 = 20$ *s.*

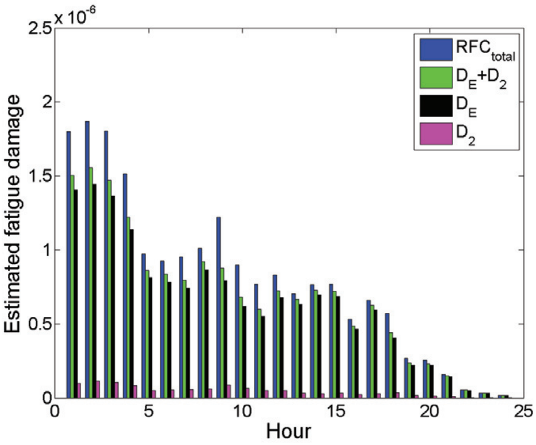

Figure C.115: *Fatigue damage during 24 hours on 12 August 2011.* $T_0 = 60$ *s.*

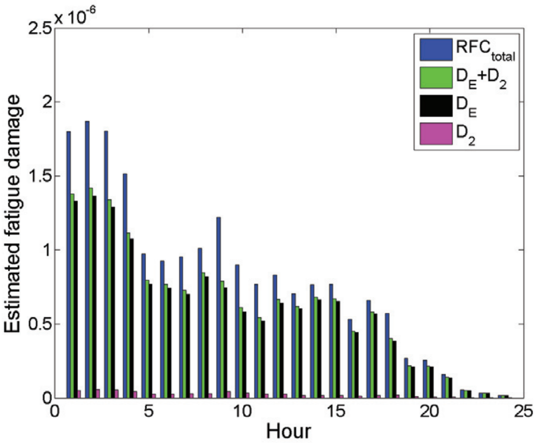

Figure C.116: *Fatigue damage during 24 hours on 12 August 2011.* $T_0 = 120$ *s.*

C.3.2 *02 October 2011*

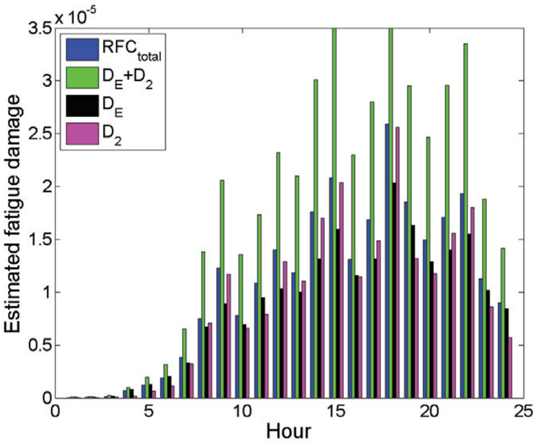

Figure C.117: *Fatigue damage during 24 hours on 02 October 2011.* $T_0 = 2$ *s.*

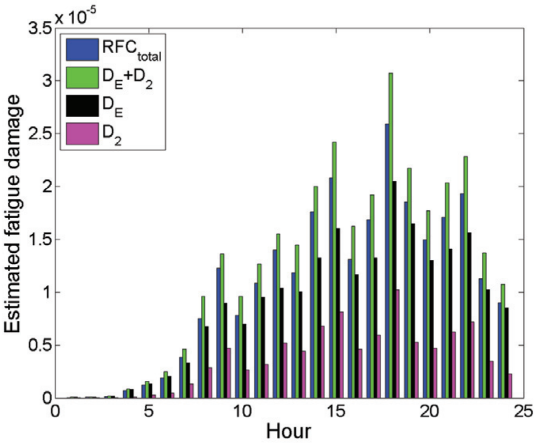

Figure C.118: *Fatigue damage during 24 hours on 02 October 2011.* $T_0 = 5$ *s.*

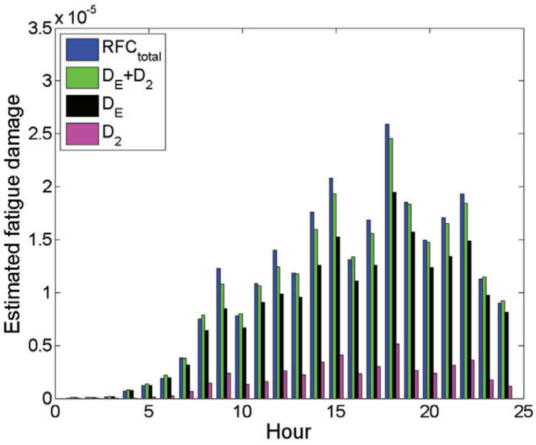

Figure C.119: *Fatigue damage during 24 hours on 02 October 2011.* $T_0 = 10$ *s.*

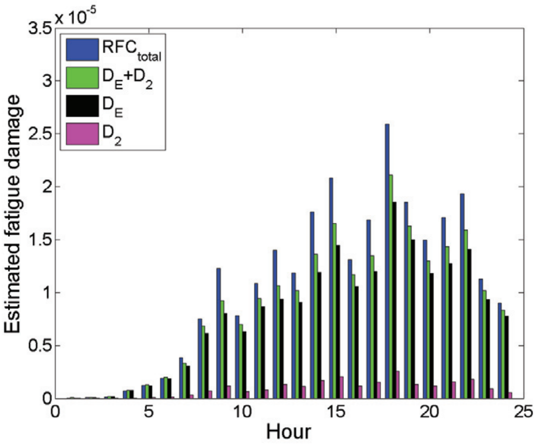

Figure C.120: *Fatigue damage during 24 hours on 02 October 2011.* $T_0 = 20$ *s.*

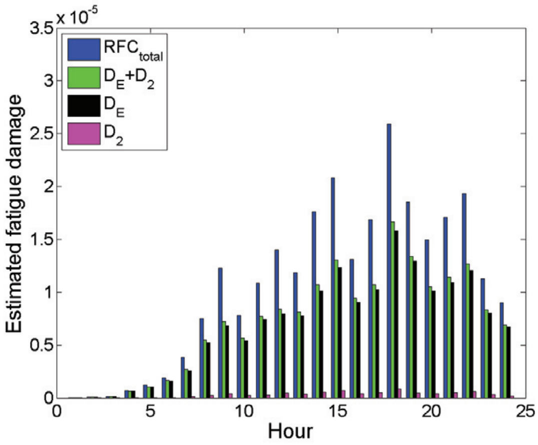

Figure C.121: *Fatigue damage during 24 hours on 02 October 2011.* $T_0 = 60$ *s.*

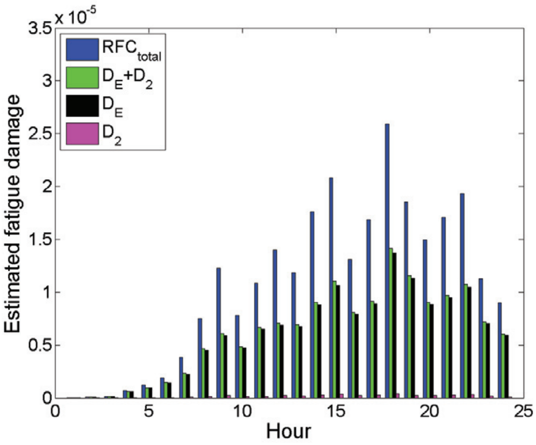

Figure C.122: *Fatigue damage during 24 hours on 02 October 2011.* $T_0 = 120$ *s.*

Appendix D

Measurements of Large Hull Girder Stresses

D.1 9,400 TEU Container Ship, 02 October 2011

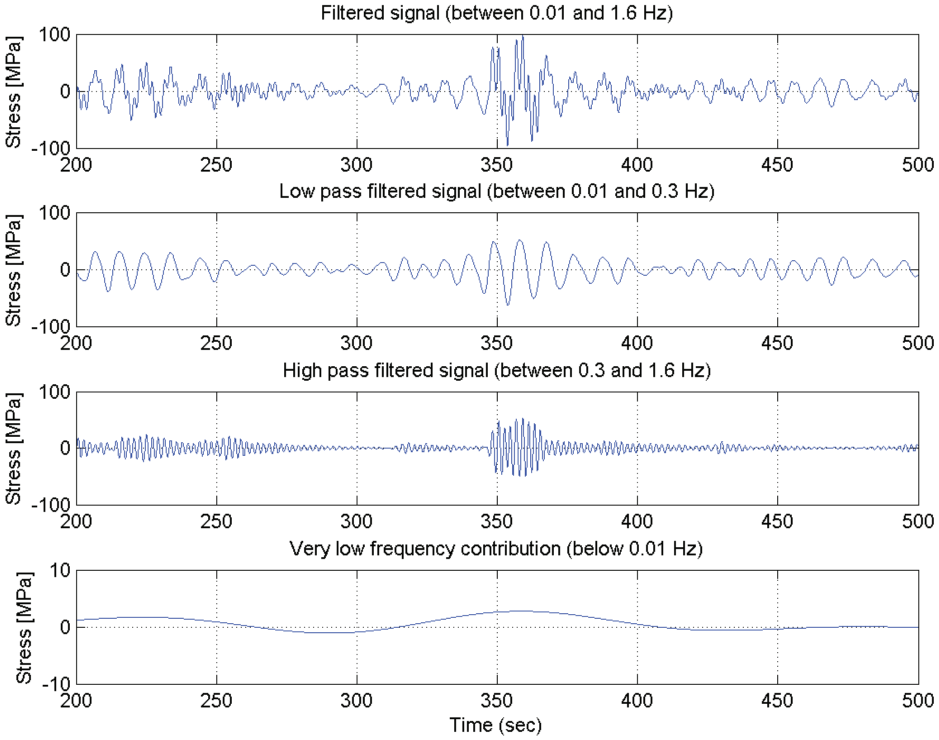

Figure D.1: *Filtered time series signal of stress (average of port and starboard side) from 9,400 TEU ship. Extract of data from 02 Oct 2011 at 16 hours.*

D.2 9,400 TEU Container Ship, 12 August 2011

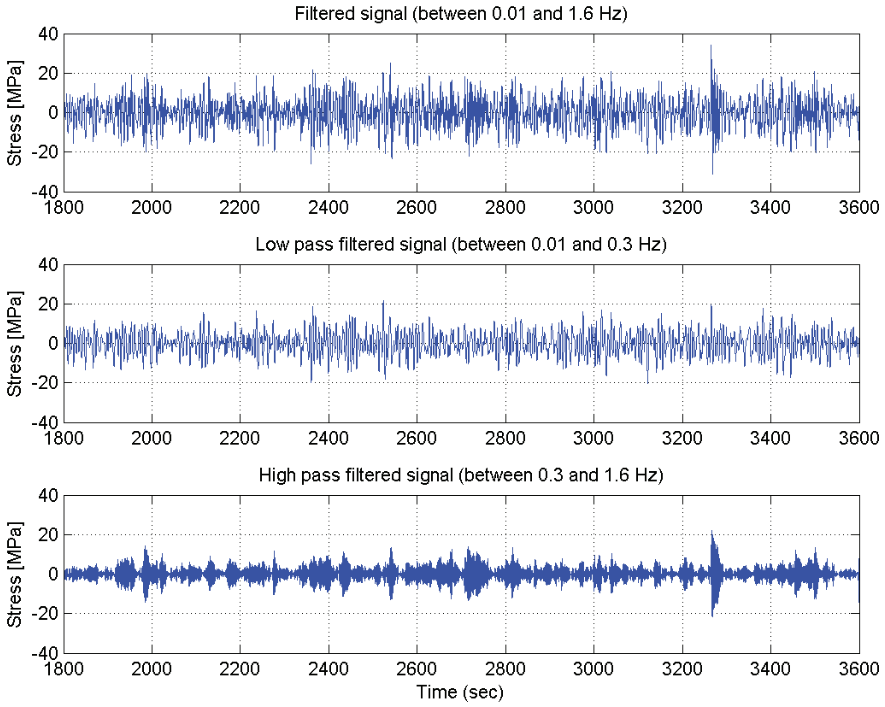

Figure D.2: *Filtered time series signal of stress (average of port and starboard side) from 9,400 TEU ship. Half an hour of data from 12 August 2011 starting at 01 hours. The largest stresses are found at about 3,300 s.*

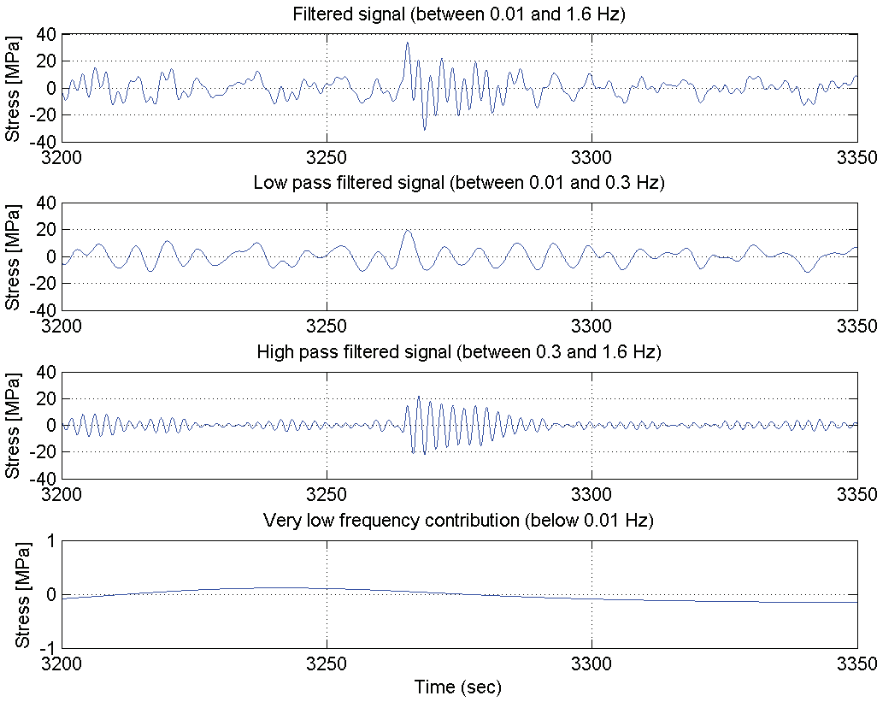

Figure D.3: *Filtered time series signal of stress (average of starboard and port side) from 9,400 TEU ship. 150 s of data from 12 August 2011 at 01 hours.*

D.3 9,400 TEU Container Ship, 17 December 2011

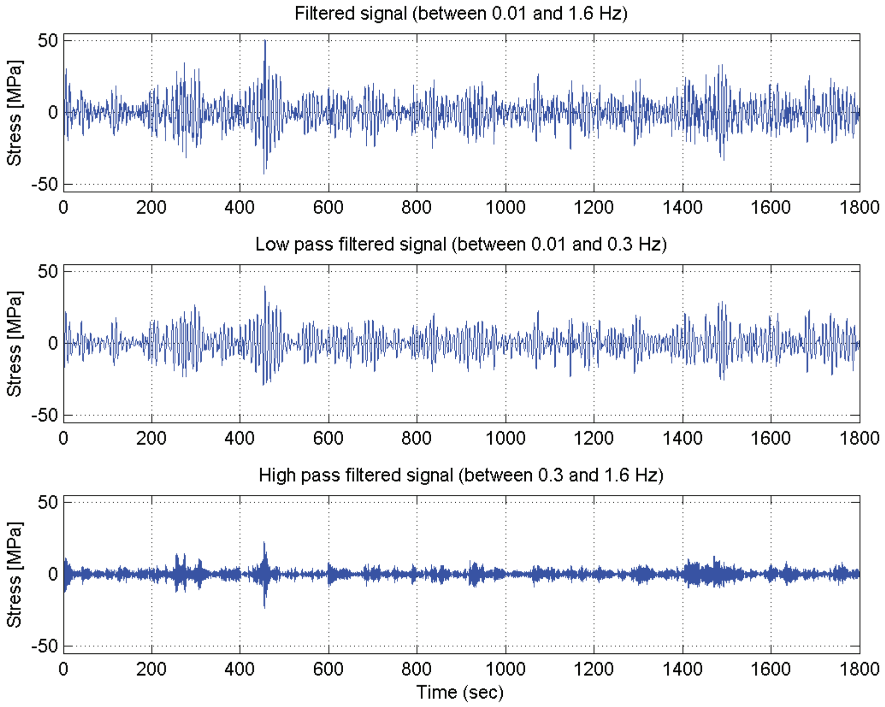

Figure D.4: *Filtered time series signal of stress from 9,400 TEU ship. Half an hour of data from 17 December 2011 starting at 14 hours. The largest stresses are found at about 455 s.*

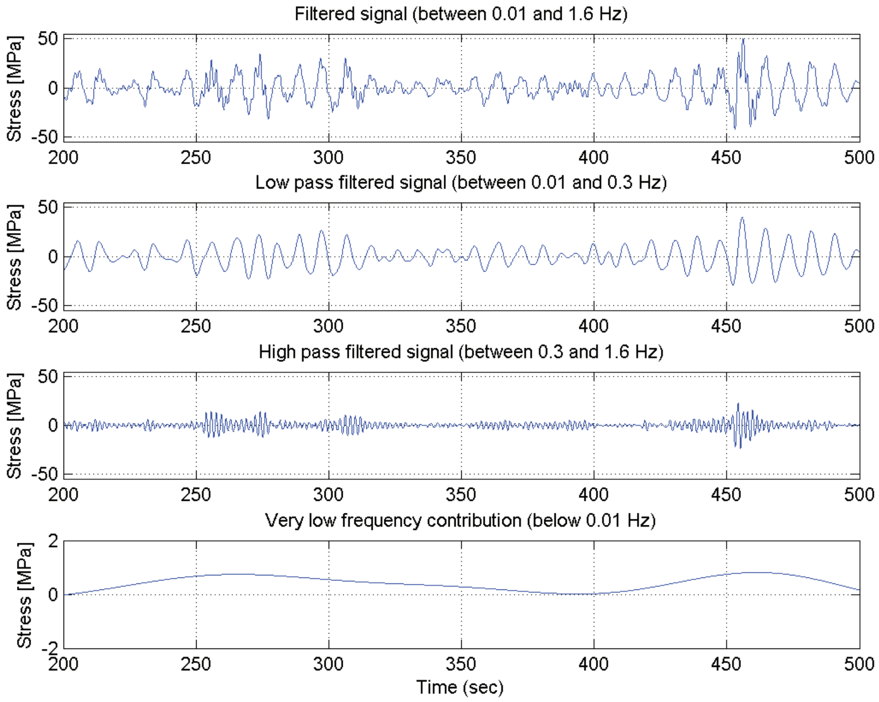

Figure D.5: *Filtered time series signal of stress from 9,400 TEU ship. 300 s of data from 17 December 2011 at 14 hours.*

D.4 8,600 TEU Container Ship, 17 November 2010

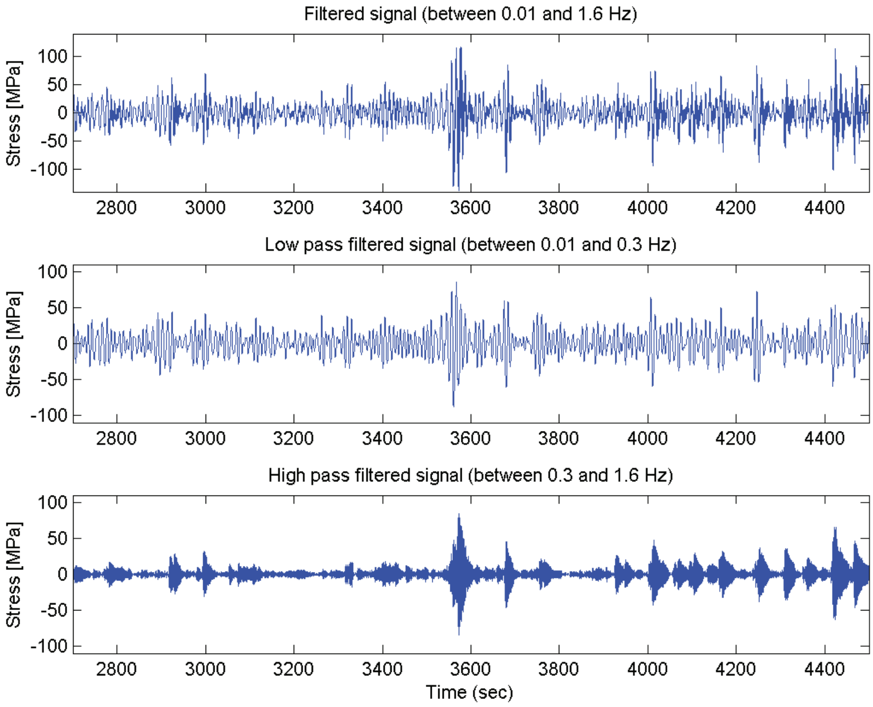

Figure D.6: *Unfiltered, low-pass and high-pass filtered time series signal of stress (average of port and starboard side) for 8,600 TEU ship. Half an hour of data from 17 November 2010 between 21 and 22 hours.*

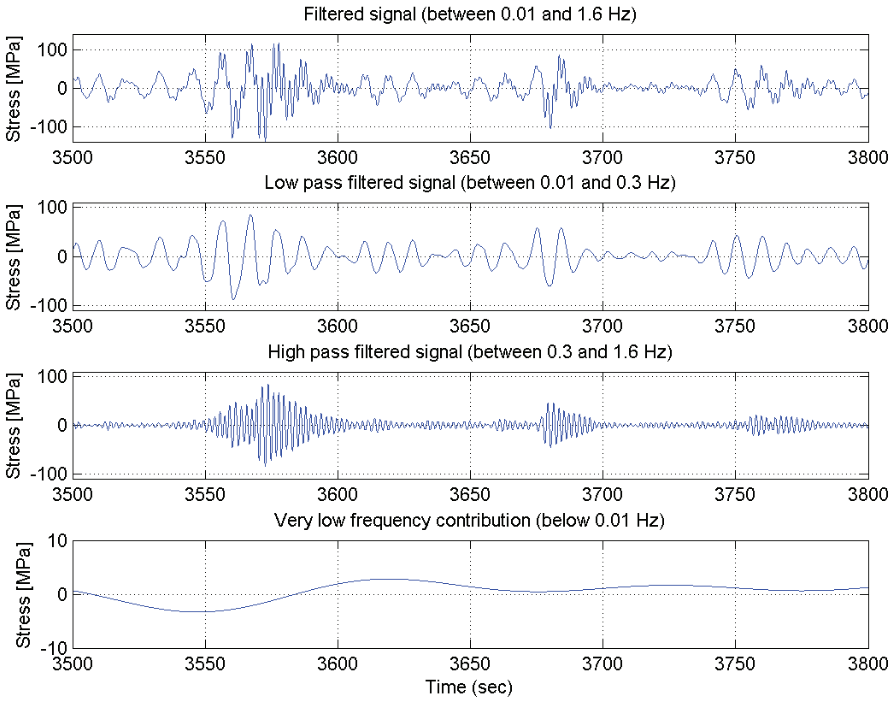

Figure D.7: *Filtered time series signal of stress (average of port and starboard side) from the 8,600 TEU vessel. Extract of data from 17 November 2010 at 21-22 hours.*

D.5 8,600 TEU Container Ship, 30 December 2011

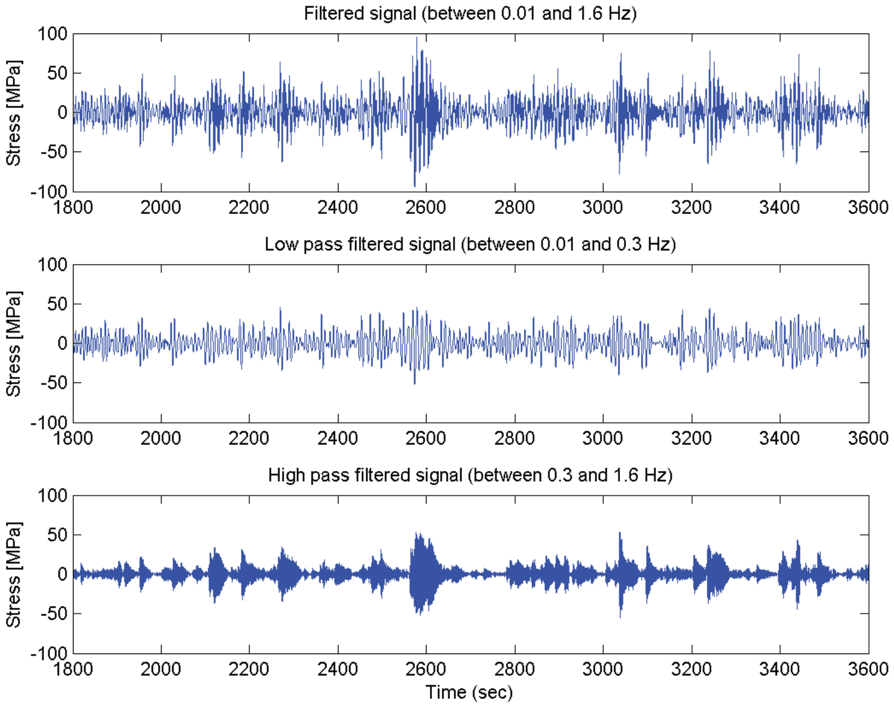

Figure D.8: *Unfiltered, low-pass and high-pass filtered time series signal of stress (average of port and starboard side) for 8,600 TEU ship. Half an hour of data from 30 December 2011 at 7 hours.*

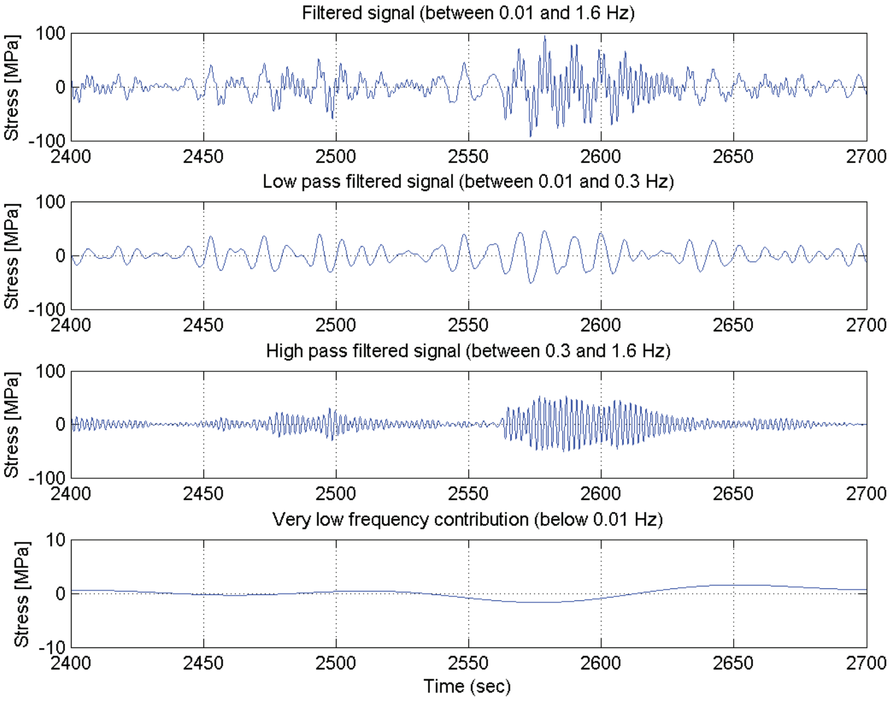

Figure D.9: *Filtered time series signal of stress (average of port and starboard side) from the 8,600 TEU vessel. Extract of data from 30 December 2011 at 7 hours.*

D.6 14,000 TEU Container Ship, 29 September 2011

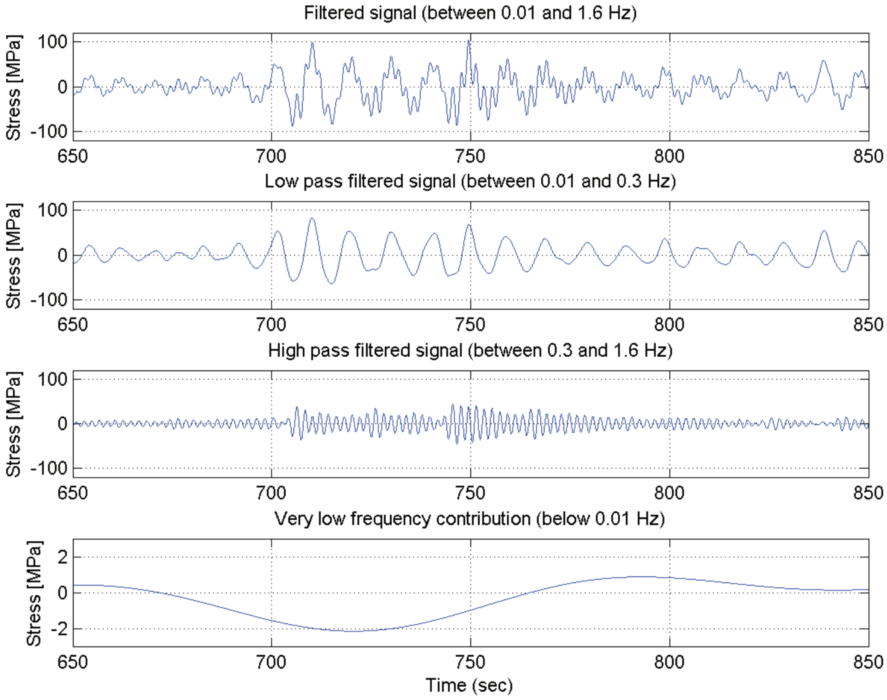

Figure D.10: *Filtered time series signal of stress (average of port and starboard side) from the 14,000 TEU vessel. Extract of data from 29 September 2011 around 10 hours.*

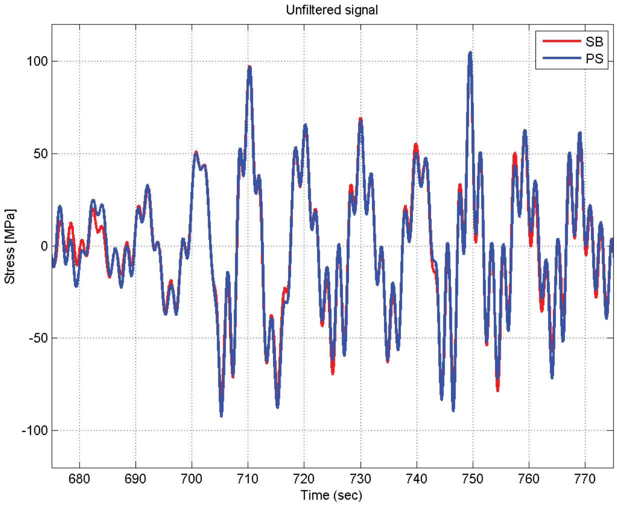

Figure D.11: *Unfiltered time series signal of stress from port and starboard side from 14,000 TEU vessel. Extract of data from 29 September 2011.*

D.7 14,000 TEU Container Ship, 21 July 2011

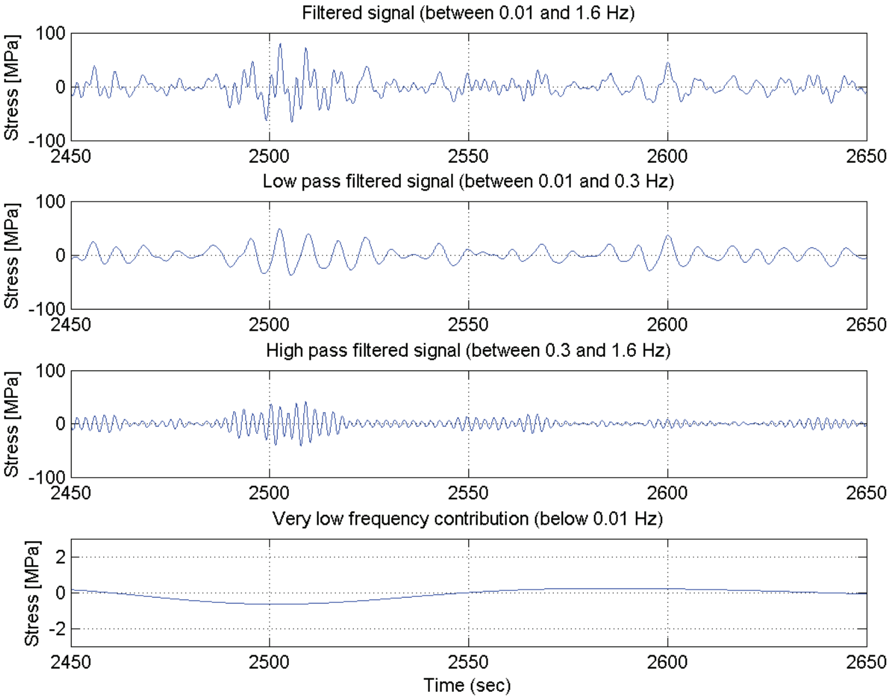

Figure D.12: *Filtered time series signal of stress (average of port and starboard side) from the 14,000 TEU vessel. Extract of data from 21 July 2011.*

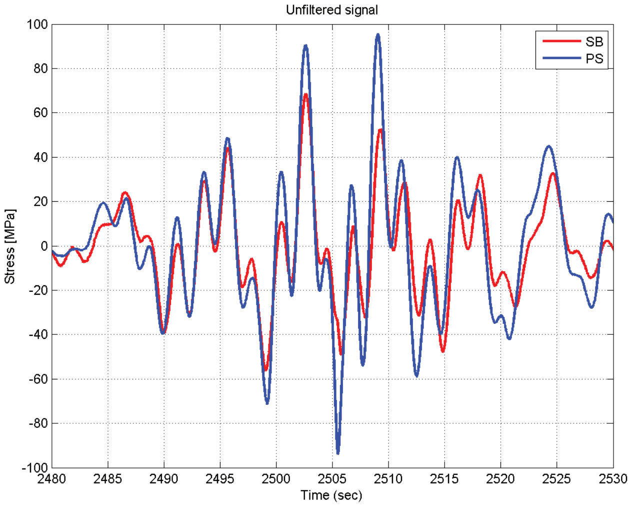

Figure D.13: *Unfiltered time series signal of stress from port and starboard side from 14,000 TEU vessel. Extract of data from 21 July 2011.*

D.8 4,400 TEU Container Ship, 02 November 2007, 11-13 hours

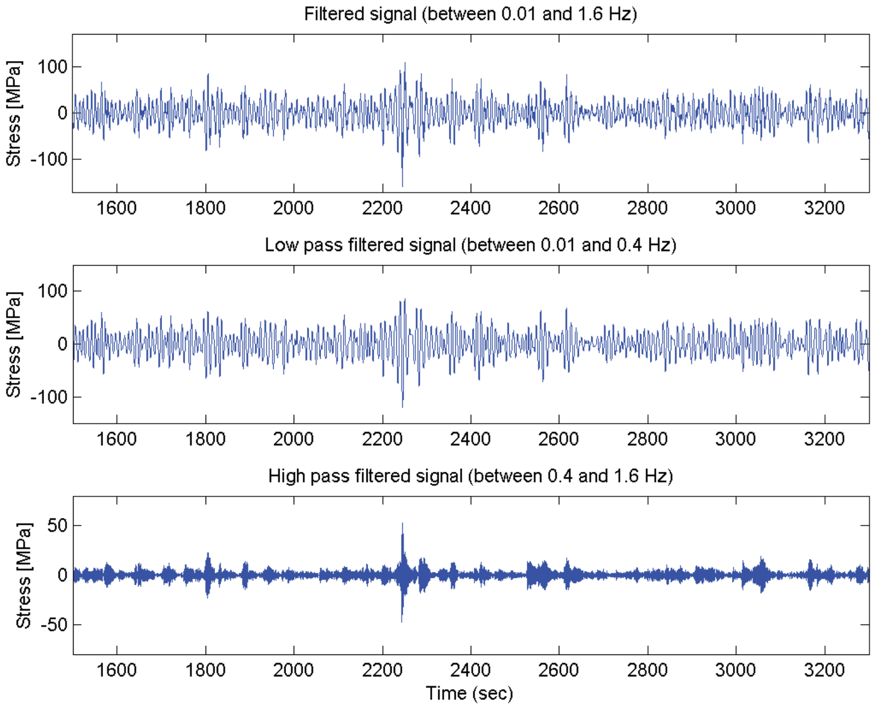

Figure D.14: *Filtered time series signal of stress (average of port and starboard side) from 4,400 TEU ship. Half an hour of data from 02 November 2007 at 11 hours.*

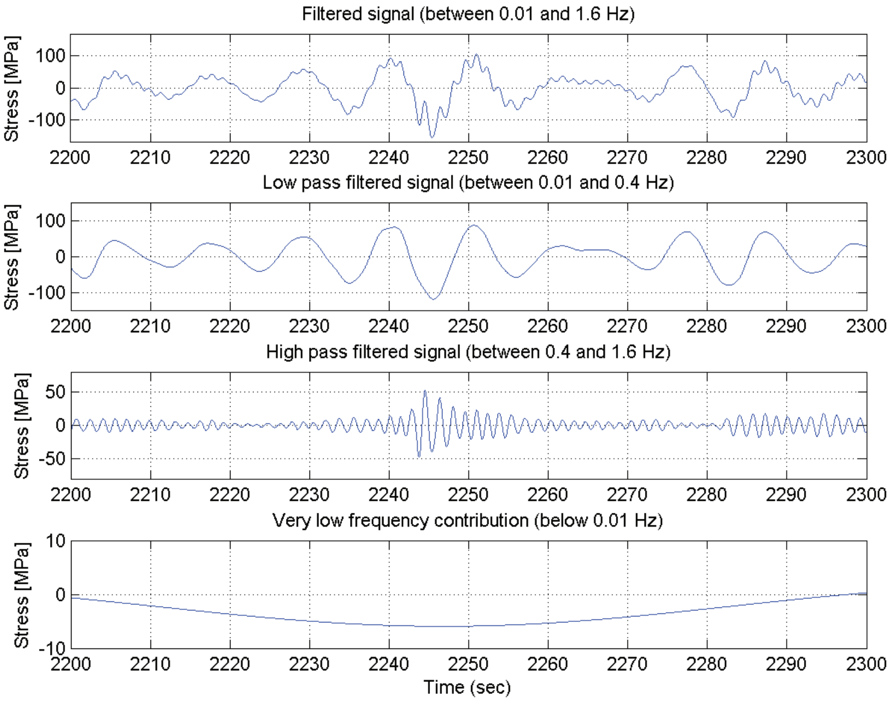

Figure D.15: *Filtered time series signal of stress (average of port and starboard side) from 4,400 TEU ship on 02 November 2007 at 11 hours.*

D.9 4,400 TEU Container Ship, 02 November 2007, 16-18 hours

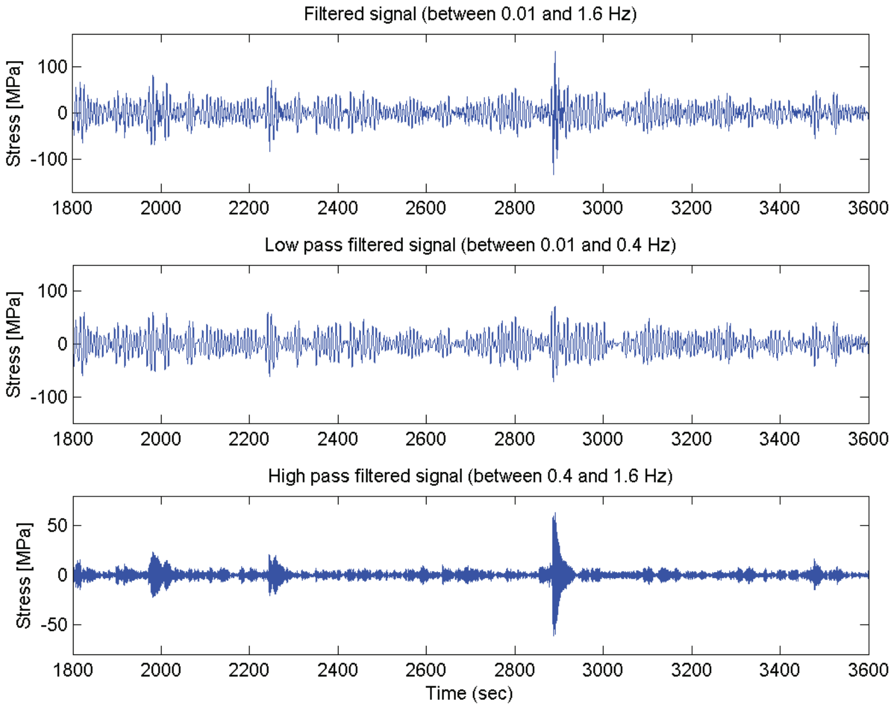

Figure D.16: *Filtered time series signal of stress (average of port and starboard side) from 4,400 TEU ship. Half an hour of data from 02 November 2007 at 16 hours.*

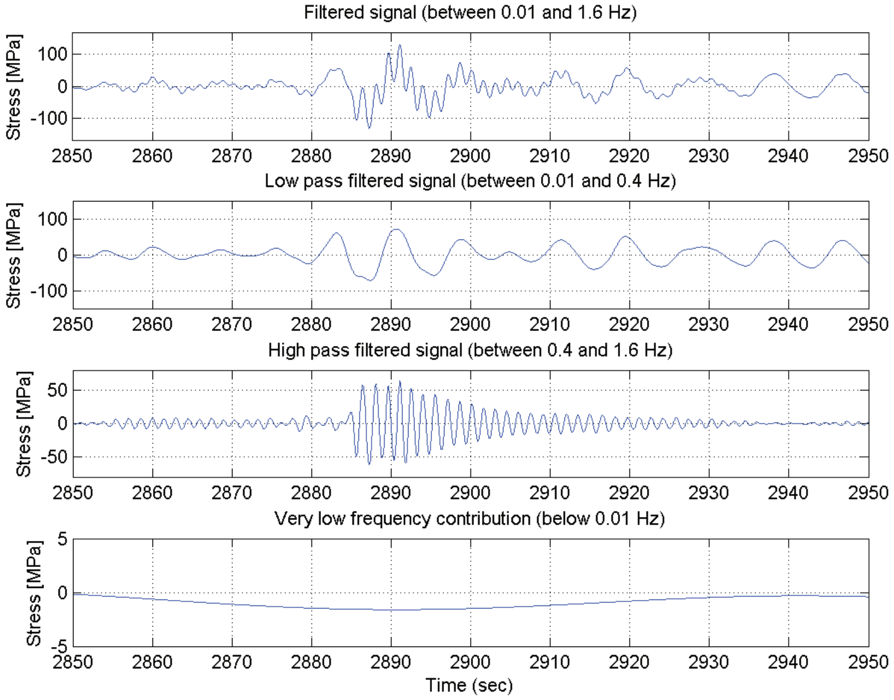

Figure D.17: *Filtered time series signal of stress (average of port and starboard side) from 4,400 TEU ship on 02 November 2007 at 16 hours.*

D.10 4,400 TEU Container Ship, 01 July 2008

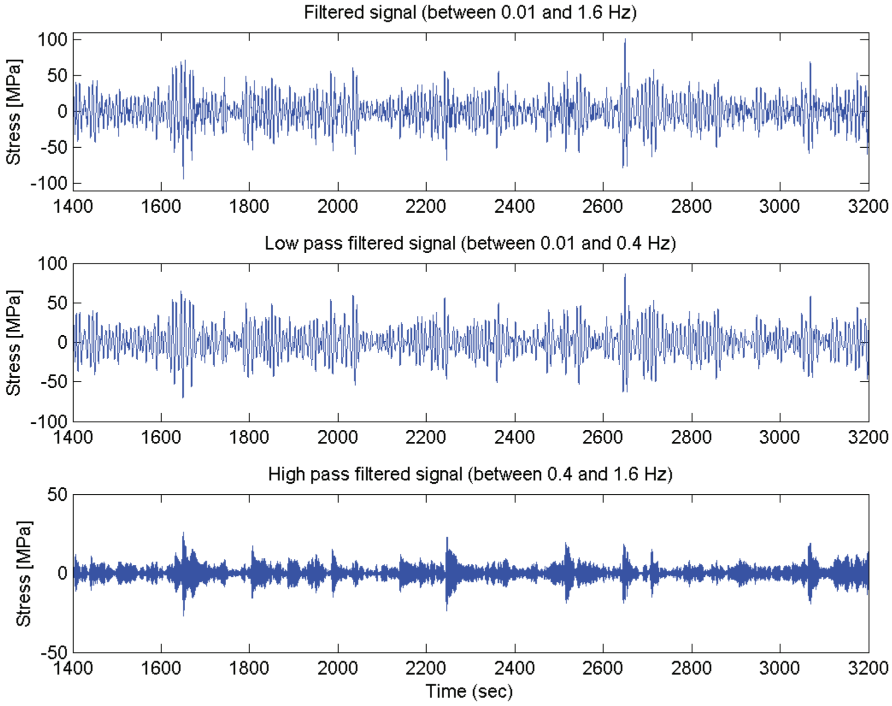

Figure D.18: *Filtered time series signal of stress (average of port and starboard side) from 4,400 TEU ship. Half an hour of data from 01 July 2008 at 19 hours.*

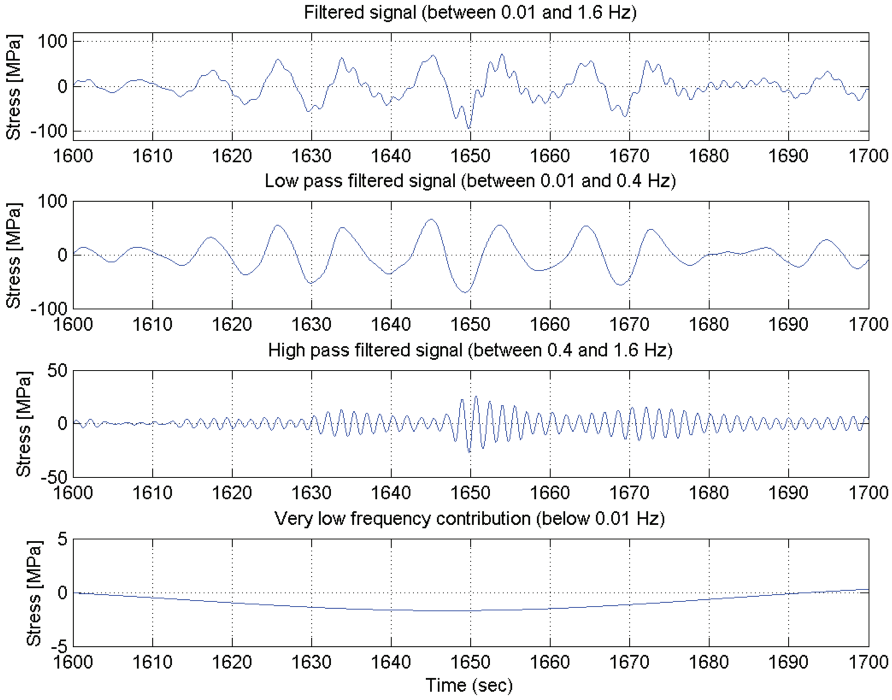

Figure D.19: *Filtered time series signal of stress (average of port and starboard side) from 4,400 TEU ship.*

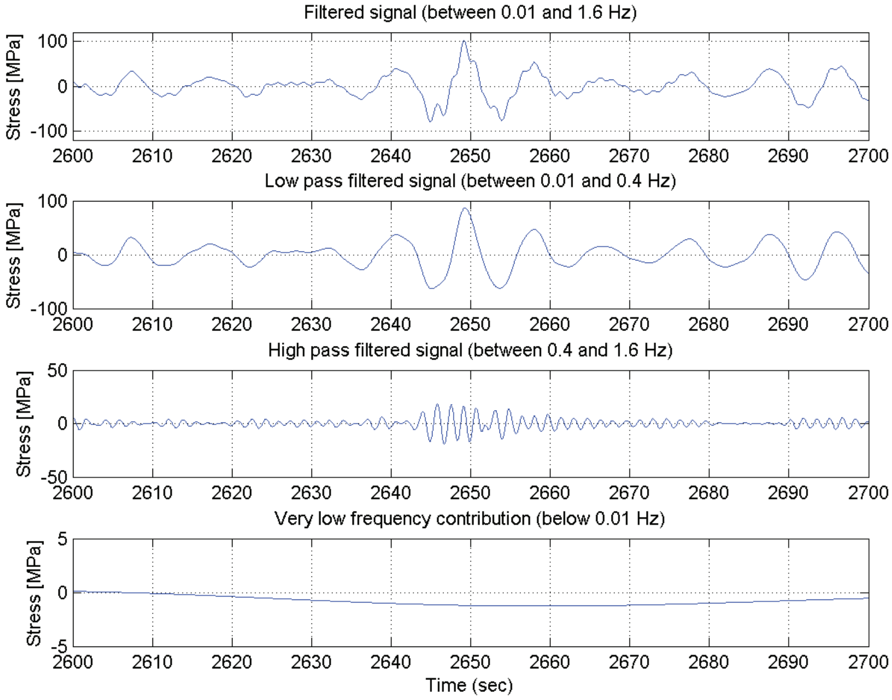

Figure D.20: *Filtered time series signal of stress (average of port and starboard side) from 4,400 TEU ship.*

D.11 High-Frequency Vibrations

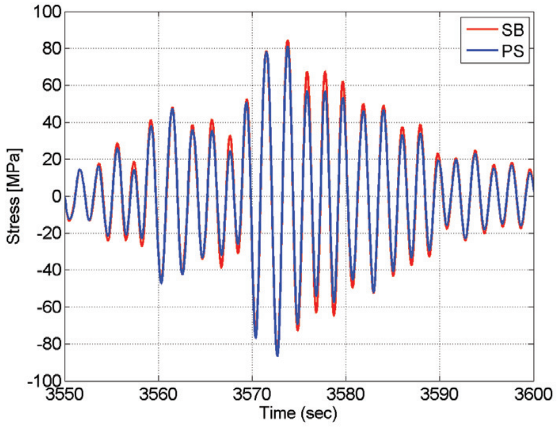

Figure D.21: *High-frequency component (high-pass filtered) of stress measurements on starboard and port side. Data from 8,600 TEU container ship on 17 November 2010 (same time series as in Figure 8.13).*

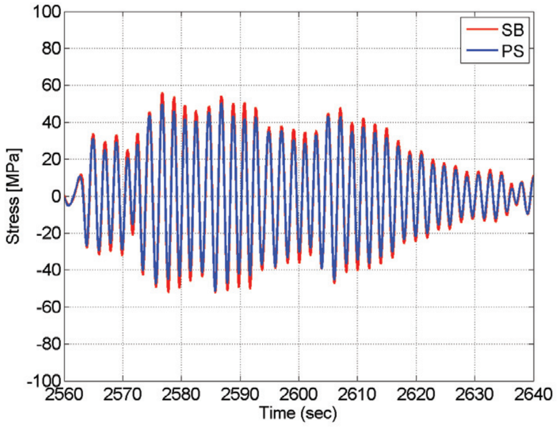

Figure D.22: *High-frequency component (high-pass filtered) of stress measurements on starboard and port side. Data from 8,600 TEU container ship on 30 December 2011 (same time series as in Figure 8.14).*

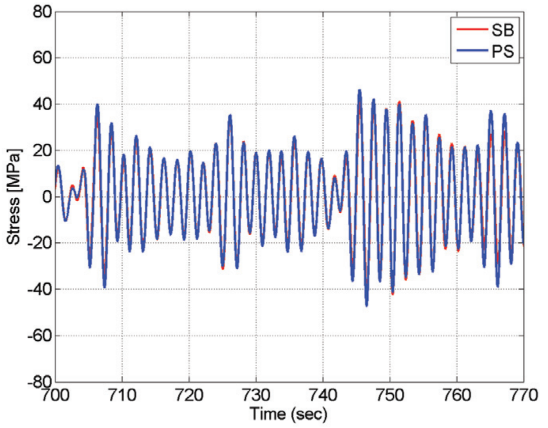

Figure D.23: *High-frequency component (high-pass filtered) of stress measurements on starboard and port side. Data from 29 September 2011 for 14,000 TEU ship. (same time series as in Figure 8.15).*

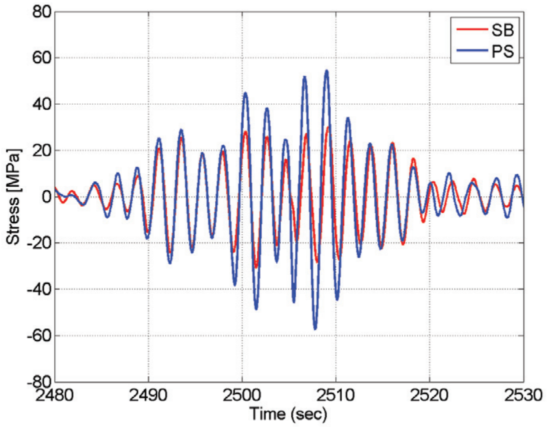

Figure D.24: *High-frequency component (high-pass filtered) of stress measurements on starboard and port side. Data from 21 July 2011 for 14,000 TEU ship. (same time series as in Figure 8.16).*

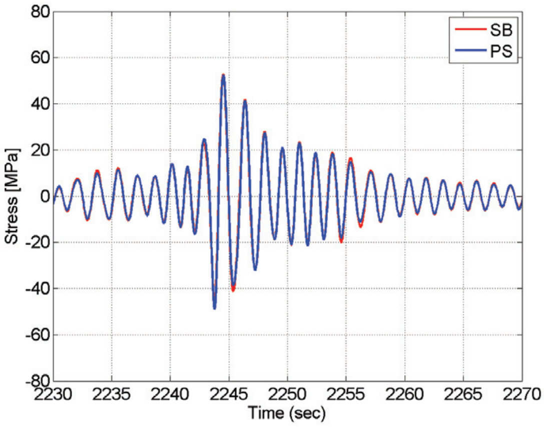

Figure D.25: *High-frequency component (high-pass filtered) of stress measurements on starboard and port side. Data from 02 November 2007 for 4,400 TEU ship. (same time series as in Figure 8.17).*

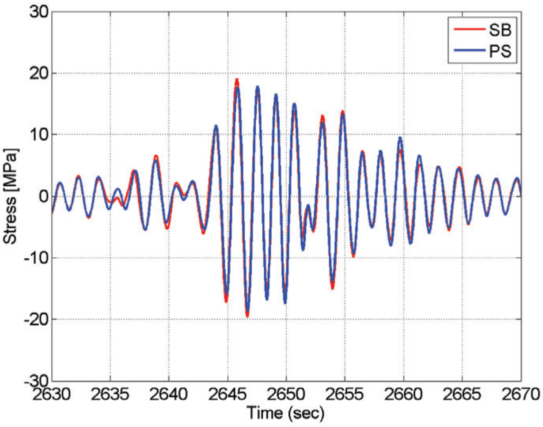

Figure D.26: *High-frequency component (high-pass filtered) of stress measurements on starboard and port side. Data from 01 July 2008 for 4,400 TEU ship. (same time series as in Figure 8.19).*

Appendix E

Extreme Value Prediction

E.1 9,400 TEU Container Ship, 02 October 2011

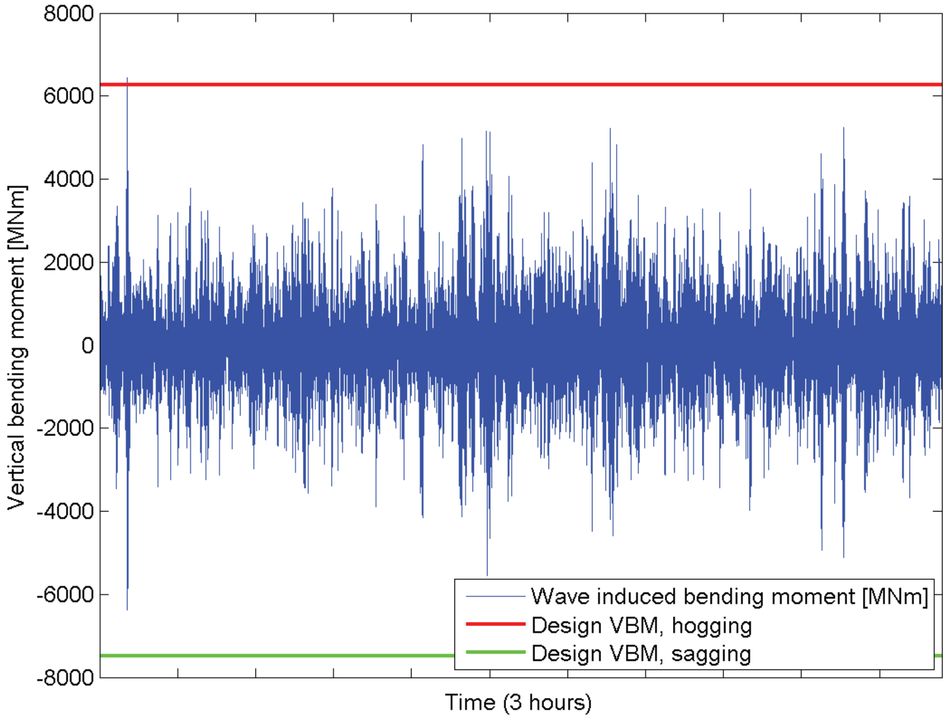

Figure E.1: *Wave-induced vertical bending moment amidships compared to the minimum design wave-induced vertical bending moment in hogging and sagging from International Association of Classification Societies (2010a) for the 9,400 TEU ship on 02 October 2011 at 16-18 hours.*

E.1.1 *ACER functions, 9,400 TEU ship, 02 October 2011*

Plots of the ACER functions for six different k from the ACER programme (Eq. (9.15)) illustrating the removal of adjacent peaks before the optimisation is carried out.

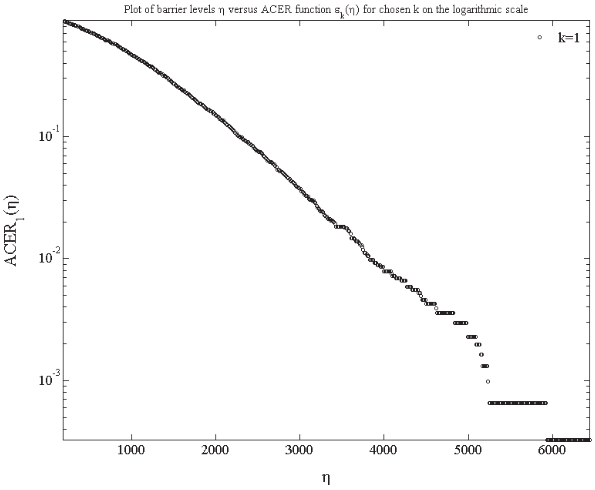

Figure E.2: *ACER function $\epsilon_k(\eta)$ for $k = 1$. Hogging, flexible 9,400 TEU ship on 02 October 2011.*

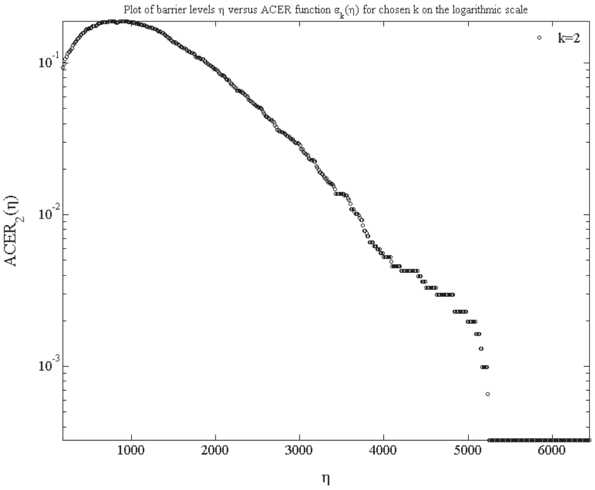

Figure E.3: *ACER function $\epsilon_k(\eta)$ for $k = 2$. Hogging, flexible 9,400 TEU ship on 02 October 2011.*

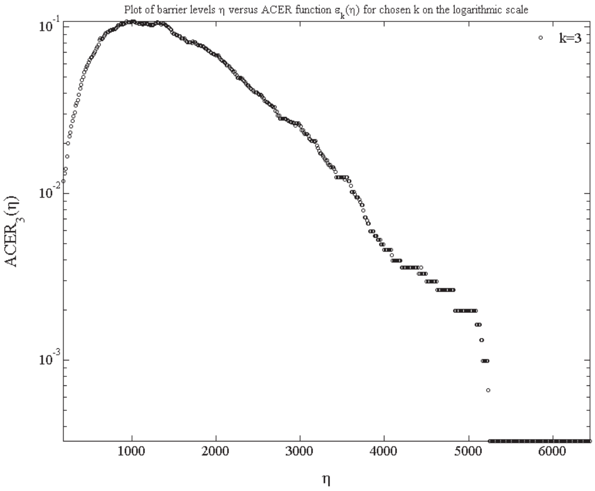

Figure E.4: *ACER function $\epsilon_k(\eta)$ for $k = 3$. Hogging, flexible 9,400 TEU ship on 02 October 2011.*

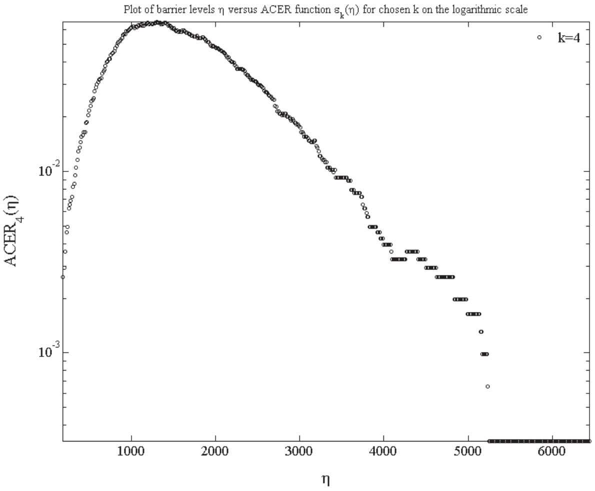

Figure E.5: *ACER function $\epsilon_k(\eta)$ for $k = 4$. Hogging, flexible 9,400 TEU ship on 02 October 2011.*

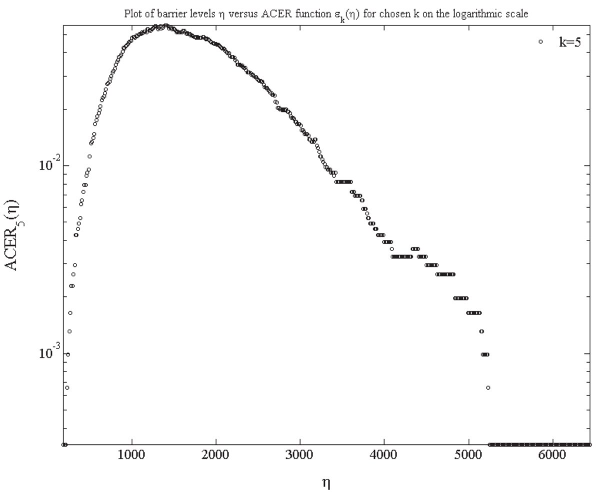

Figure E.6: *ACER function $\epsilon_k(\eta)$ for $k = 5$. Hogging, flexible 9,400 TEU ship on 02 October 2011.*

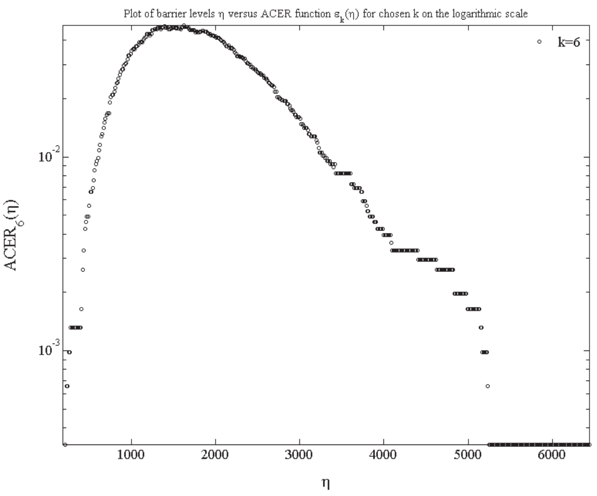

Figure E.7: *ACER function $\epsilon_k(\eta)$ for $k = 6$. Hogging, flexible 9,400 TEU ship on 02 October 2011.*

E.1.2 *Optimised ACER functions, 9,400 TEU ship, 02 October 2011*

Illustration of the outcome of the ACER optimisation for six different k (Eq. (9.16)).

	$k = 1$	$k = 2$	$k = 3$	$k = 4$	$k = 5$	$k = 6$
q	0.974	0.178	0.107	0.068	0.058	0.050
s	10.7	1,135	1,218	1,303	1,419	1,625
r	$7.2 \cdot 10^{-5}$	$11 \cdot 10^{-5}$	$5 \cdot 10^{-5}$	$4.7 \cdot 10^{-5}$	$4.9 \cdot 10^{-5}$	$10.7 \cdot 10^{-5}$
t	1.34	1.29	1.38	1.38	1.38	1.29

Table E.1: *ACER parameters, hogging, for 02 October 2011, 16-18 hours.*

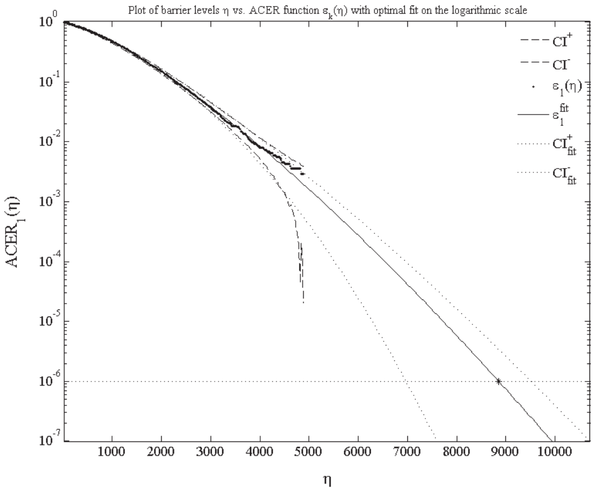

Figure E.8: *Optimised curve from ACER, $k = 1$. 9,400 TEU ship on 02 October 2011 at 16-18 hours.*

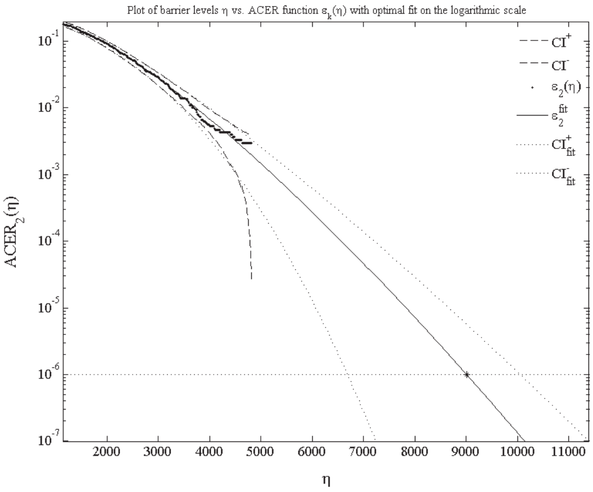

Figure E.9: *Optimised curve from ACER, $k = 2$. 9,400 TEU ship on 02 October 2011 at 16-18 hours.*

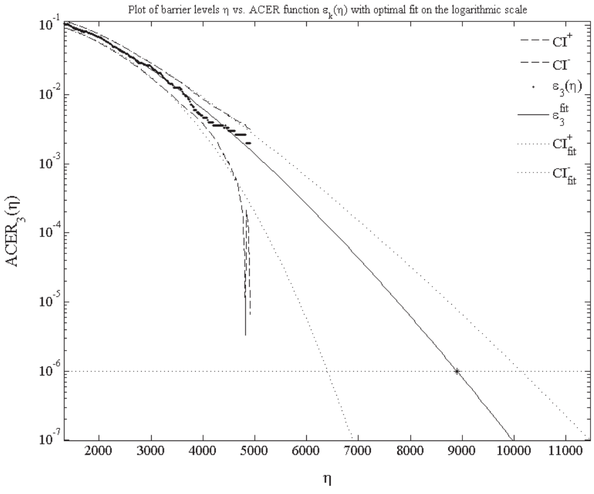

Figure E.10: *Optimised curve from ACER, $k = 3$. 9,400 TEU ship on 02 October 2011 at 16-18 hours.*

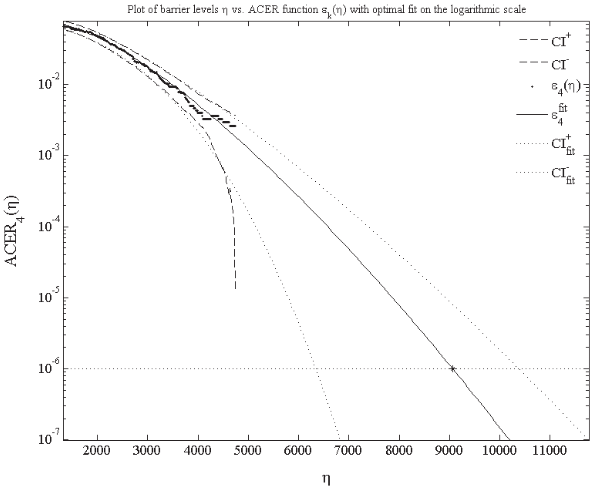

Figure E.11: *Optimised curve from ACER, $k = 4$. 9,400 TEU ship on 02 October 2011 at 16-18 hours.*

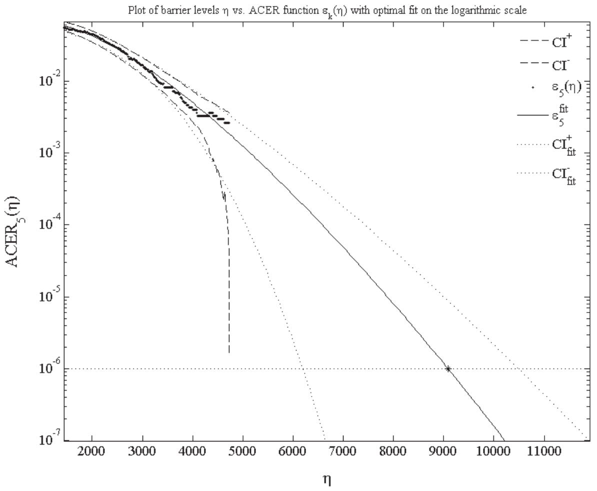

Figure E.12: *Optimised curve from ACER,* $k = 5$. *9,400 TEU ship on 02 October 2011 at 16-18 hours.*

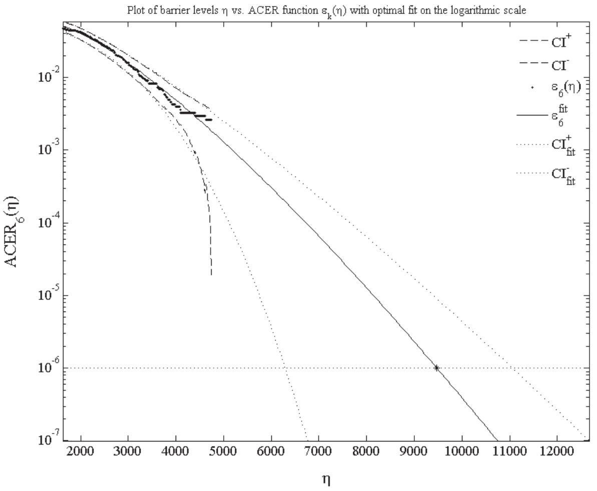

Figure E.13: *Optimised curve from ACER,* $k = 6$. *9,400 TEU ship on 02 October 2011 at 16-18 hours.*

E.2 9,400 TEU Container Ship, 12 August 2011

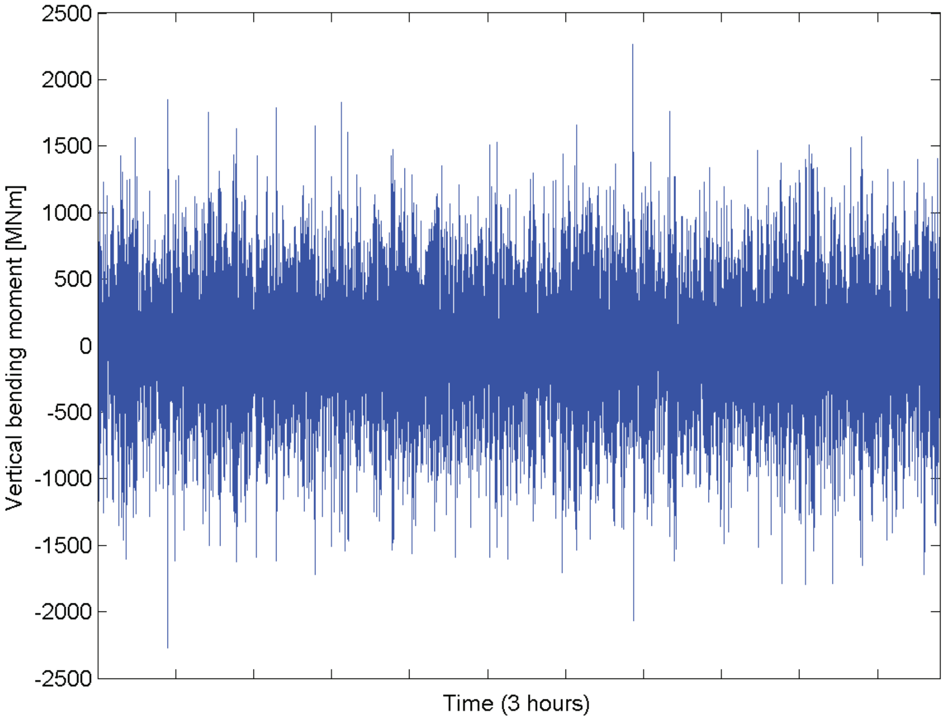

Figure E.14: *Wave-induced vertical bending moment amidships for the 9,400 TEU ship on 12 August 2011 at 00-02 hours.*

E.2.1 *Gumbel fit from Weibull parameters*

The peak value distribution for the flexible and rigid-body wave hogging VBM is fitted with the Weibull distribution in Figures E.15 and E.16.

For the hogging condition the Weibull parameters estimated for the flexible and the rigid-body response are given in Table E.2.

	a	c
Flexible response	528	1.31
Rigid-body response	502	1.54

Table E.2: *Weibull parameters for hogging for the WF and WF+HF response. Estimated from Figures E.15 and E.16. 9,400 TEU ship on 12 August 2011.*

The most probable largest value from Gumbel fit to the full data set using the Weibull parameters in Table E.2 is 2,649 MNm. The resulting Gumbel density function is shown

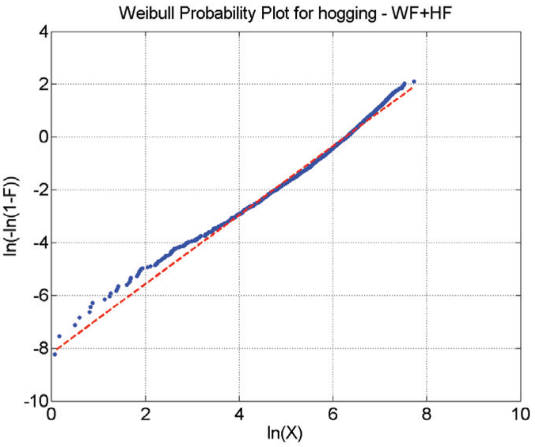

Figure E.15: Weibull probability plot for the hogging bending moment - WF+HF response. 9,400 TEU ship on 12 August 2011.

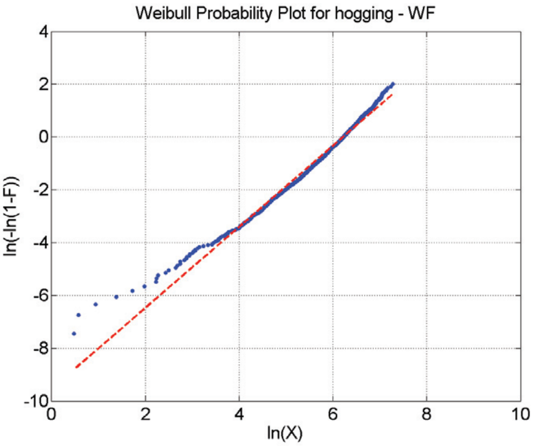

Figure E.16: Weibull probability plot for the hogging bending moment - WF response. 9,400 TEU ship on 12 August 2011.

in Figure E.17.

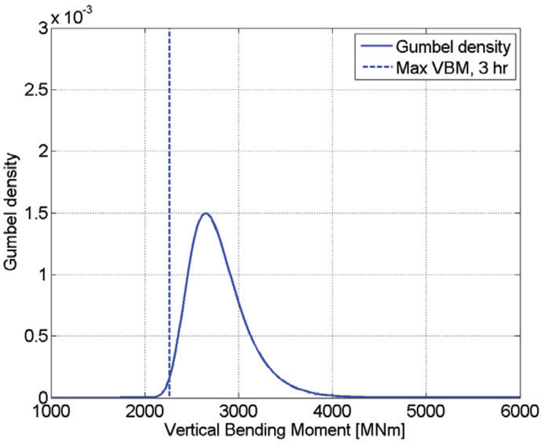

Figure E.17: Gumbel density function for the hogging VBM based on Weibull parameters for the individual peak for the flexible-body response in Table E.2. The maximum measured hogging VBM during the three hours is included for comparison. 9,400 TEU ship on 12 August 2011.

E.2.2 *Peak-over-threshold*

Again, for the Peak-Over-Threshold analysis, six different threshold values are chosen as 30%, 40%, 50%, 60%, 70% and 80% of the average of the three largest hogging VBM measured for the three hour time series. For each threshold the Weibull distribution is fitted to the excess. The resulting Weibull parameters are found in Table E.3 together with the threshold levels. Similarly the Gumbel parameters b and d are determined from the exponential fit to the peaks over the threshold. The Gumbel parameters determined

Threshold, u	a	c
594	271	1.11
792	245	1.05
990	198	0.79
1,188	160	0.83
1,387	185	0.86
1,585	215	0.97

Table E.3: *Weibull parameters a and c for for the excess of the hogging VBM for different threshold values. 9,400 TEU ship on 12 August 2011.*

Threshold, u	d	b
594	257	2,413
792	230	2,250
990	193	2,065
1,188	163	1,947
1,387	182	2,004
1,585	195	2,003

Table E.4: *Gumbel parameters b and d from an exponential fit to the excess. 9,400 TEU ship on 12 August 2011.*

from the exponential fit to the different threshold levels are given in Table E.4.

E.2.3 *Average Conditional Exceedance Rate (ACER) function*

The ACER functions for $k = 1-6$ are illustrated in Figure E.18 and the optimised ACER parameters are given in Table E.5.

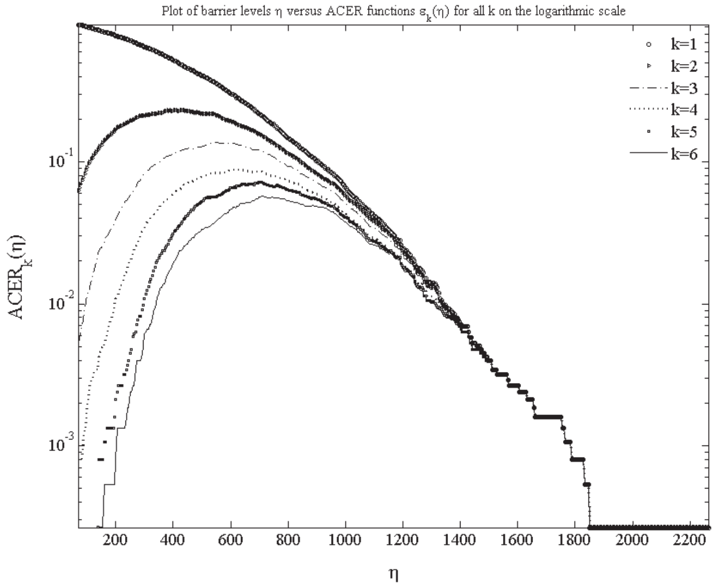

Figure E.18: *ACER function $\epsilon_k(\eta)$ for six different values of k for the hogging VBM. 9,400 TEU ship on 12 August 2011.*

The corresponding Gumbel parameters b and d derived from the optimised ACER parameters using Eq. (9.19) and (9.21) are given in Table E.6 and the Gumbel density functions for $k = 1-6$ are plotted in Figure E.19.

	$k=1$	$k=2$	$k=3$	$k=4$	$k=5$	$k=6$
q	1.08	0.226	0.140	0.090	0.072	0.059
s	-199	468	545	613	704	708
r	$29 \cdot 10^{-5}$	$6.4 \cdot 10^{-5}$	$3.7 \cdot 10^{-5}$	$3.1 \cdot 10^{-5}$	$6.7 \cdot 10^{-5}$	$2.8 \cdot 10^{-5}$
t	1.94	1.59	1.67	1.70	1.60	1.72

Table E.5: *Optimised ACER parameters for 9,400 TEU ship on 12 August 2011.*

	$k=1$	$k=2$	$k=3$	$k=4$	$k=5$	$k=6$
b	1,900	1,919	1,904	1,901	1,916	1,902
d	130	135	130	130	136	129

Table E.6: *Gumbel parameters b and d from the optimised ACER functions for hogging for six different k. 9,400 TEU ship on 12 August 2011.*

It is clearly seen from Figures E.18 and E.19 that clustering is not important for this case and that the ACER method yield almost the same result for all k.

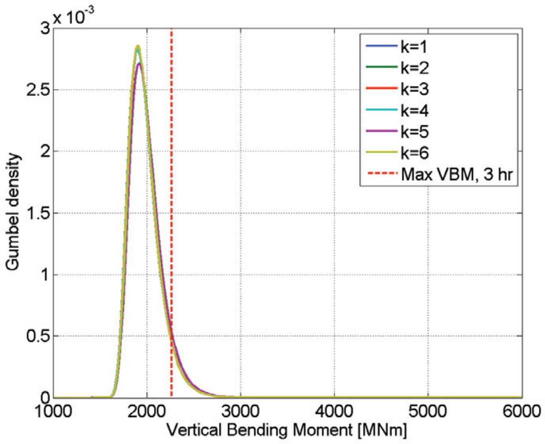

Figure E.19: *Gumbel density function from the parameters derived from the optimised ACER functions for six different values of k (Table 9.6). The maximum measured hogging VBM during the three hours is included for comparison. 9,400 TEU ship on 12 August 2011.*

E.3 9,400 TEU Container Ship, 17 December 2011

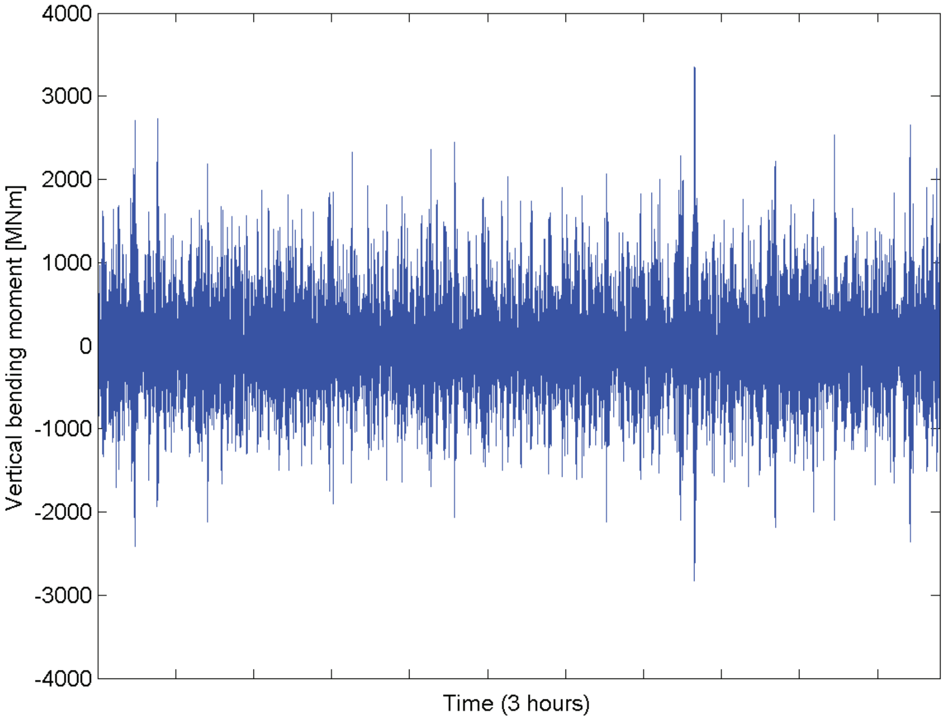

Figure E.20: *Wave-induced vertical bending moment amidships for the 9,400 TEU ship on 17 December 2011 at 12-14 hours.*

E.3.1 *Gumbel fit from Weibull parameters*

The peak value distribution for the flexible and rigid-body wave hogging VBM is fitted with the Weibull distribution in Figures E.21 and E.22.

For the hogging condition the Weibull parameters estimated for the flexible and the rigid-body response are given in Table E.7.

	a	c
Flexible response	602	1.21
Rigid-body response	722	1.43

Table E.7: *Weibull parameters for hogging for the WF and WF+HF response. Estimated from Figures E.21 and E.22. 9,400 TEU ship on 17 December 2011.*

The resulting Gumbel density function is shown in Figure E.23.

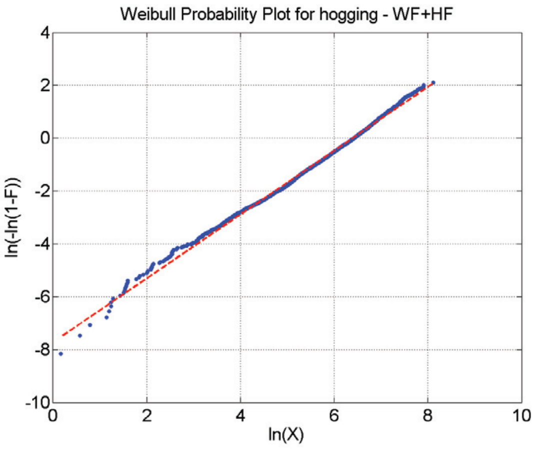

Figure E.21: *Weibull probability plot for the hogging bending moment - WF+HF response. 9,400 TEU ship on 17 December 2011.*

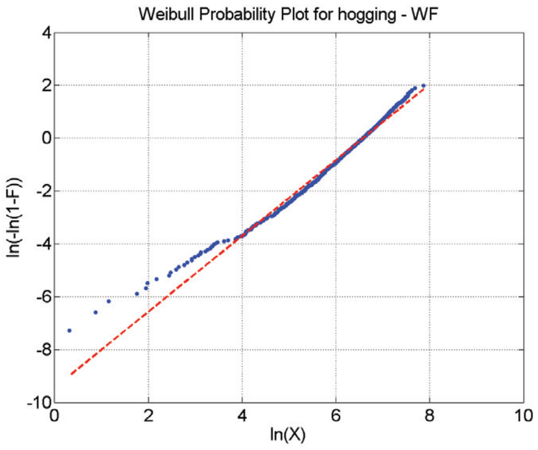

Figure E.22: *Weibull probability plot for the hogging bending moment - WF response. 9,400 TEU ship on 17 December 2011.*

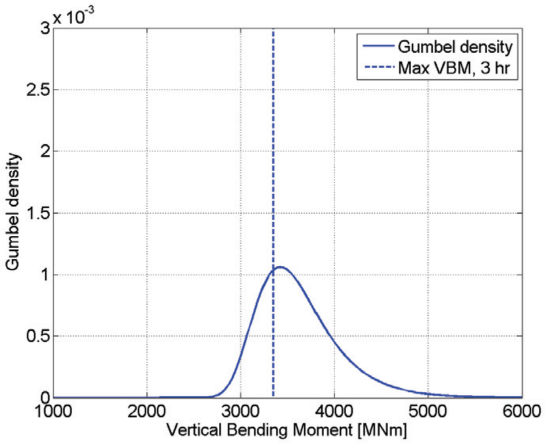

Figure E.23: *Gumbel density function for the hogging VBM based on Weibull parameters for the individual peak for the flexible-body response in Table E.7. The maximum measured hogging VBM during the three hours is included for comparison. 9,400 TEU ship on 17 December 2011.*

E.3.2 *Peak-over-threshold*

Again, for the Peak-Over-Threshold analysis, six different threshold values are chosen as 30%, 40%, 50%, 60%, 70% and 80% of the average of the three largest hogging VBM measured for the three hour time series. For each threshold the Weibull distribution is fitted to the excess. The resulting Weibull parameters are found in Table E.8 together with the threshold levels. Similarly, the Gumbel parameters b and d are determined from the exponential fit to the peaks over the threshold. The Gumbel parameters determined from the exponential fit to the different threshold levels are given in Table E.9.

Threshold, u	a	c
879	356	1.00
1,173	336	1.03
1,466	312	1.21
1,759	338	0.71
2,052	343	0.83
2,345	330	0.76

Table E.8: *Weibull parameters a and c for for the excess of the hogging VBM for different threshold values. 9,400 TEU ship on 17 December 2011.*

Threshold, u	d	b
879	345	3,142
1,173	329	3,057
1,466	304	2,953
1,759	327	3,002
2,052	316	2,999
2,345	304	3,002

Table E.9: *Gumbel parameters b and d from an exponential fit to the excess. 9,400 TEU ship on 17 December 2011.*

E.3.3 *Average Conditional Exceedance Rate (ACER) function*

The ACER functions for $k = 1-6$ are illustrated in Figure E.24 and the optimised ACER parameters are given in Table E.10.

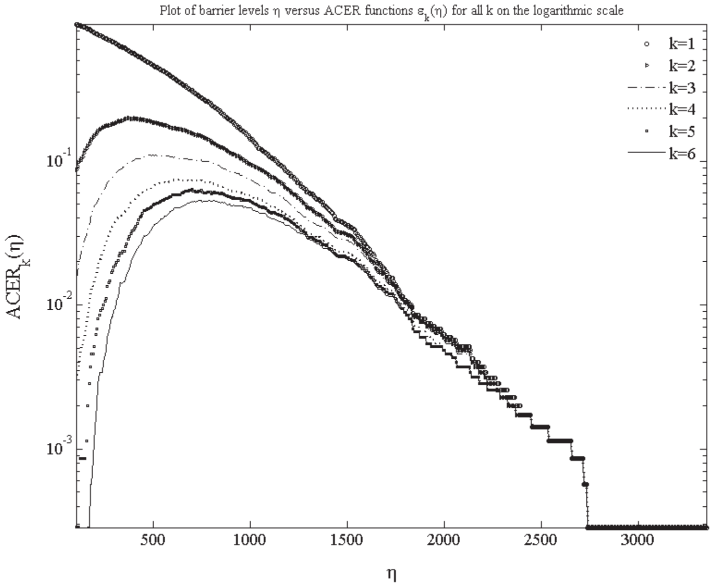

Figure E.24: *ACER function $\epsilon_k(\eta)$ for six different values of k for the hogging VBM. 9,400 TEU ship on 17 December 2011.*

The corresponding Gumbel parameters b and d derived from the optimised ACER parameters using Eq. (9.19) and (9.21) are given in Table E.11 and the Gumbel density functions for $k = 1 - 6$ are plotted in Figure E.25.

	$k = 1$	$k = 2$	$k = 3$	$k = 4$	$k = 5$	$k = 6$
q	1.096	0.176	0.110	0.076	0.064	0.054
s	-147	558	571	612	699	746
r	$5.5 \cdot 10^{-5}$	$9.0 \cdot 10^{-5}$	$2.3 \cdot 10^{-5}$	$1.6 \cdot 10^{-5}$	$2.4 \cdot 10^{-5}$	$2.2 \cdot 10^{-5}$
t	1.49	1.45	1.62	1.66	1.61	1.62

Table E.10: *Optimised ACER parameters for 9,400 TEU ship on 17 December 2011.*

	$k = 1$	$k = 2$	$k = 3$	$k = 4$	$k = 5$	$k = 6$
b	2,799	2,825	2,801	2,794	2,804	2,816
d	239	244	232	235	241	243

Table E.11: *Gumbel parameters b and d from the optimised ACER functions for hogging for six different k. 9,400 TEU ship on 17 December 2011.*

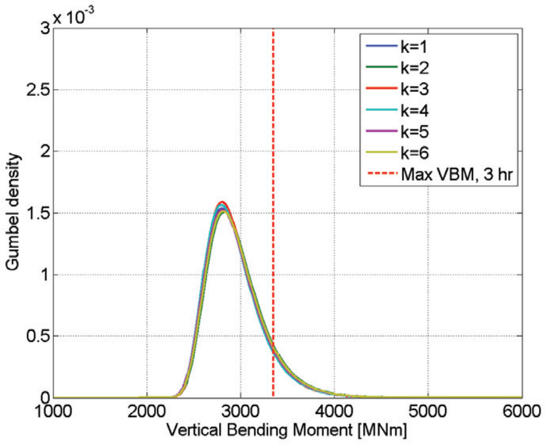

Figure E.25: *Gumbel density function from the parameters derived from the optimised ACER functions for six different values of k (Table 9.6). The maximum measured hogging VBM during the three hours is included for comparison. 9,400 TEU ship on 17 December 2011.*

E.4 8,600 TEU Container Ship, 17 November 2010

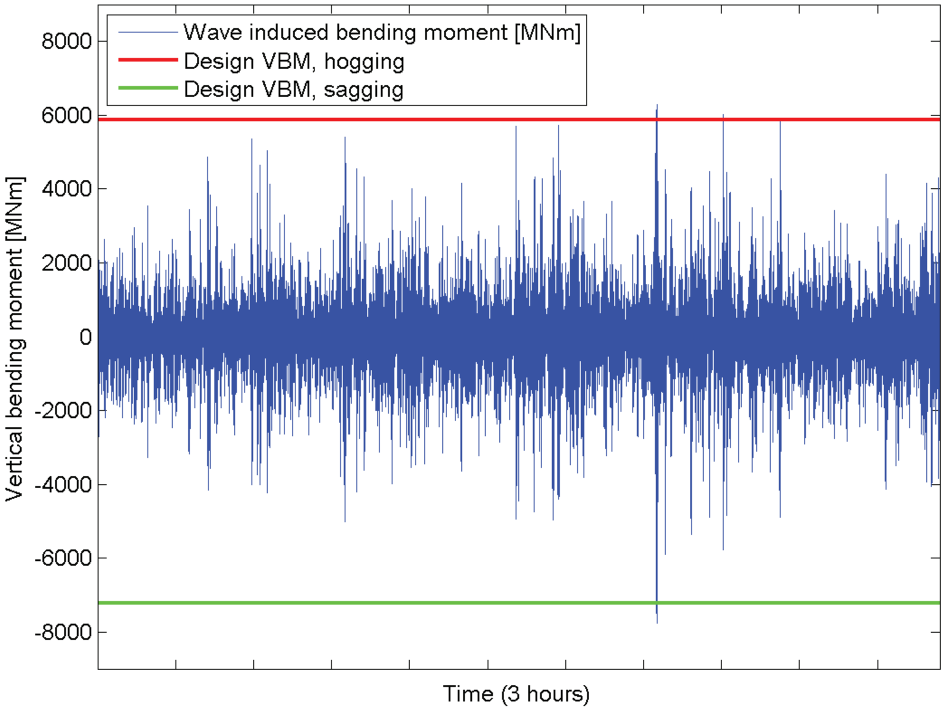

Figure E.26: *Wave-induced vertical bending moment amidships compared to the minimum design wave-induced vertical bending moment in hogging and sagging from International Association of Classification Societies (2010a) for the 8,600 TEU ship on 17 November 2010 at 20-22 hours.*

E.4.1 *Gumbel fit from Weibull parameters*

The peak value distribution for the flexible and rigid-body wave hogging VBM is fitted with the Weibull distribution in Figures E.27 and E.28.

For the hogging condition the Weibull parameters estimated for the rigid-body and the flexible response are given in Table E.12.

	a	c
Flexible response	1,137	1.20
Rigid-body response	1,276	1.57

Table E.12: *Weibull parameters for hogging for the WF and WF+HF response. Estimated from Figures E.27 and E.28. 8,600 TEU ship on 17 November 2010.*

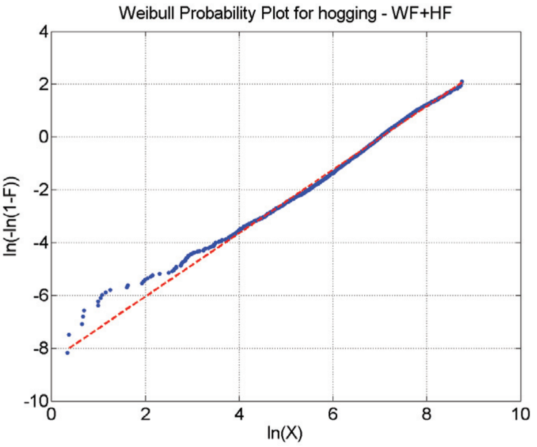

Figure E.27: *Weibull probability plot for the hogging bending moment - WF+HF response. 8,600 TEU ship on 17 November 2010.*

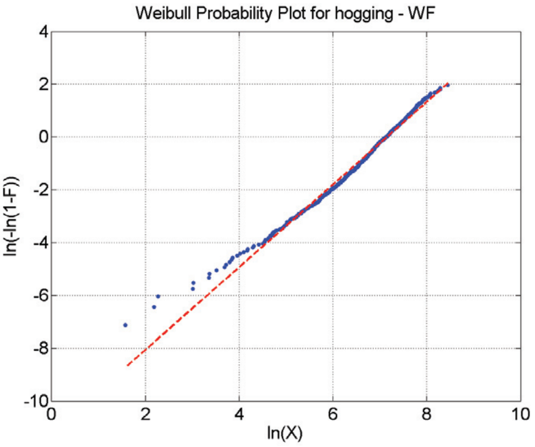

Figure E.28: *Weibull probability plot for the hogging bending moment - WF response. 8,600 TEU ship on 17 November 2010.*

The resulting Gumbel density function is shown in Figure E.29.

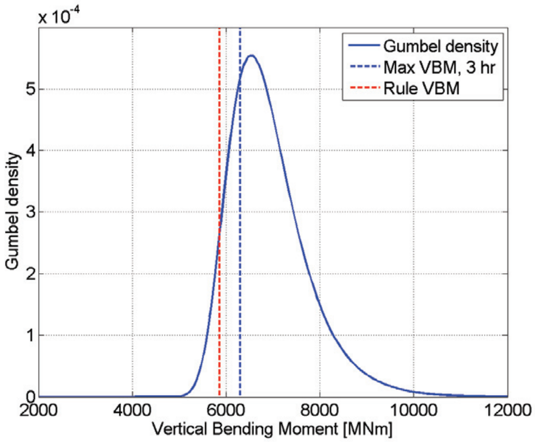

Figure E.29: *Gumbel density function for the hogging VBM based on Weibull parameters for the individual peak for the flexible-body response in Table E.12. The maximum measured hogging VBM during the three hours and the rule wave VBM are included for comparison. 8,600 TEU ship on 17 November 2010.*

E.4.2 *Peak-over-threshold*

Six different threshold values are chosen as 30%, 40%, 50%, 60%, 70% and 80% of the average of the three largest hogging VBM measured for the three hour time series. The corresponding Weibull parameters are given in Table E.13 together with the threshold levels. The Gumbel parameters b and d are determined from the exponential fit to the peaks over the threshold and are given in Table E.14.

Threshold, u	a	c
1,859	777	0.96
2,478	881	1.00
3,098	896	1.02
3,717	824	1.00
4.337	840	0.87
4,956	752	0.72

Table E.13: *Weibull parameters a and c for for the excess of the hogging VBM for different threshold values. 8,600 TEU ship on 17 November 2010.*

Threshold, u	d	b
1,859	794	6,794
2,478	876	7,186
3,098	864	7,144
3,717	793	6,911
4.337	761	6,817
4,956	648	6,909

Table E.14: *Gumbel parameters b and d from an exponential fit to the excess. 8,600 TEU ship on 17 November 2010.*

E.4.3 *Average Conditional Exceedance Rate (ACER) function*

The same analysis as for the 9,400 TEU ship is carried out for the 8,600 TEU ship. The ACER functions $\epsilon_k(\eta)$ for six different values of k are given in Figure E.30. The optimised ACER parameters for the six different k are given in Table E.15.

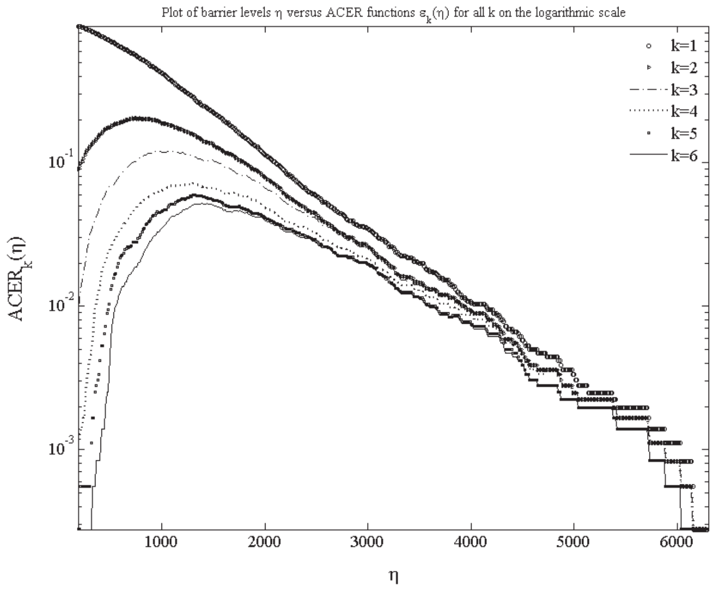

Figure E.30: *ACER function $\epsilon_k(\eta)$ for six different values of k for the hogging VBM. 8,600 TEU ship on 17 November 2010.*

The corresponding Gumbel parameters are given in table E.16.

The Gumbel density functions from the parameters in Table E.16 are plotted in Figure E.31. Some de-clustering is visible as the distribution with $k = 1$ (uppermost line) is

	$k = 1$	$k = 2$	$k = 3$	$k = 4$	$k = 5$	$k = 6$
q	1.06	0.197	0.127	0.073	0.06	0.052
s	10	1,049	1,087	1,301	1,295	1,390
r	$36 \cdot 10^{-5}$	$58 \cdot 10^{-5}$	$18 \cdot 10^{-5}$	$14 \cdot 10^{-5}$	$7.3 \cdot 10^{-5}$	$5.6 \cdot 10^{-5}$
t	1.14	1.08	1.21	1.22	1.30	1.33

Table E.15: *Optimised ACER parameters for 8,600 TEU ship on 17 November 2010.*

	$k = 1$	$k = 2$	$k = 3$	$k = 4$	$k = 5$	$k = 6$
b	6,495	6,899	6,843	7,033	6,803	6,730
d	688	829	780	842	789	765

Table E.16: *Gumbel parameters b and d from the optimised ACER functions for hogging for six different k. 8,600 TEU ship on 17 November 2010.*

somewhat different from the distributions with $k > 1$.

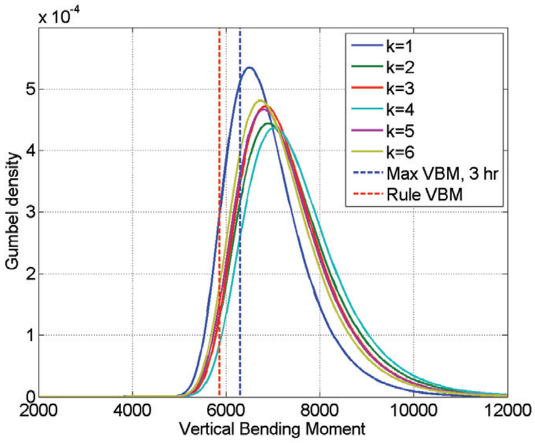

Figure E.31: *Gumbel density function from the parameters derived from the optimised ACER functions for six different values of k (Table E.16). The maximum measured hogging VBM during the three hours is included for comparison. 8,600 TEU ship on 17 November 2010.*

E.5 8,600 TEU Container Ship, 30 December 2011

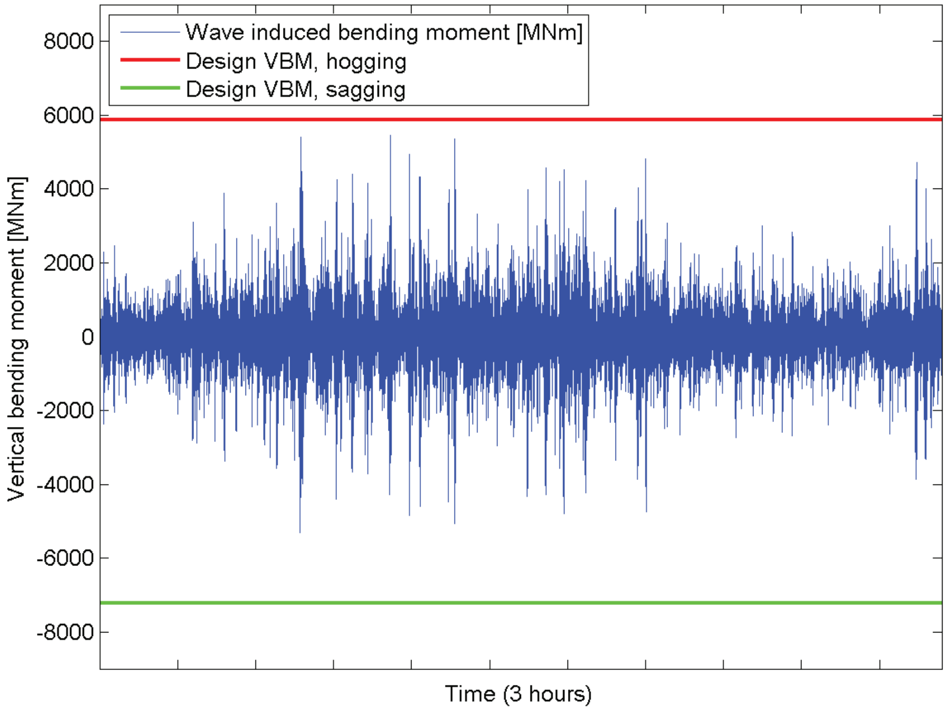

Figure E.32: *Wave-induced vertical bending moment amidships compared to the minimum design wave-induced vertical bending moment in hogging and sagging from International Association of Classification Societies (2010a) for the 8,600 TEU ship on 30 December 2011 at 07-09 hours.*

E.5.1 *Gumbel fit from Weibull parameters*

The peak value distribution for the flexible and rigid-body wave hogging VBM is fitted with the Weibull distribution in Figures E.33 and E.34.

For the hogging condition the Weibull parameters estimated for the flexible and rigid-body response are given in Table E.17.

	a	c
Flexible response	923	1.20
Rigid-body response	977	1.43

Table E.17: *Weibull parameters for hogging for the WF and WF+HF response. Estimated from Figures E.33 and E.34. 8,600 TEU ship on 30 December 2011.*

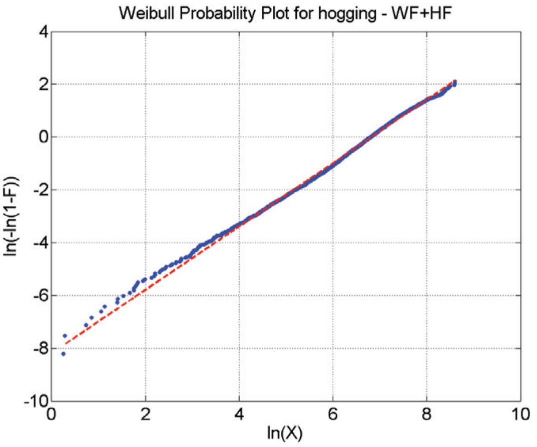

Figure E.33: *Weibull probability plot for the hogging bending moment - WF+HF response. 8,600 TEU ship on 30 December 2011.*

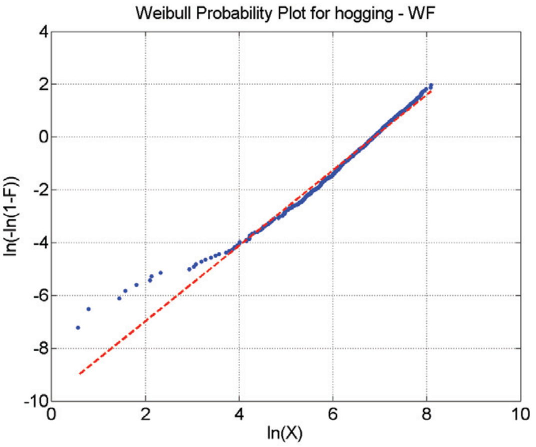

Figure E.34: *Weibull probability plot for the hogging bending moment - WF response. 8,600 TEU ship on 30 December 2011.*

The resulting Gumbel density function is shown in Figure E.35.

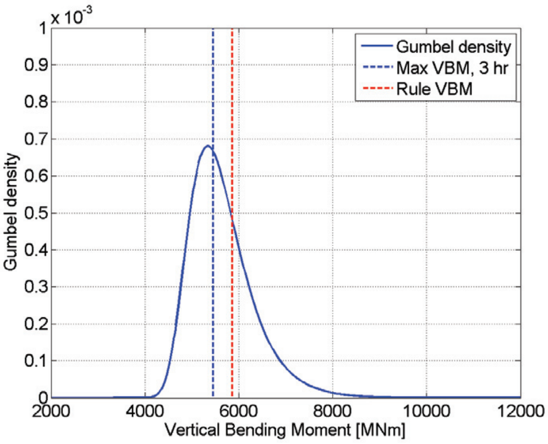

Figure E.35: *Gumbel density function for the hogging VBM based on Weibull parameters for the individual peak for the flexible-body response in Table E.17. The maximum measured hogging VBM during the three hours and the rule wave VBM are included for comparison. 8,600 TEU ship on 30 December 2011.*

E.5.2 *Peak-over-threshold*

Six different threshold values are chosen as 30%, 40%, 50%, 60%, 70% and 80% of the average of the three largest hogging VBM measured for the three hour time series. The corresponding Weibull parameters are given in Table E.18 together with the threshold levels. The Gumbel parameters b and d are determined from the exponential fit to the peaks over the threshold and are given in Table E.19.

Threshold, u	a	c
1,621	704	1.01
2,161	783	1.01
2,702	810	0.95
3,242	943	0.99
3,783	680	1.53
4,323	428	0.49

Table E.18: *Weibull parameters a and c for for the excess of the hogging VBM for different threshold values. 8,600 TEU ship on 30 December 2011.*

Threshold, u	d	b
1,621	712	5,964
2,161	765	6,198
2,702	790	6,281
3,242	805	6,343
3,783	610	5,836
4,323	401	5,933

Table E.19: *Gumbel parameters b and d from an exponential fit to the excess. 8,600 TEU ship on 30 December 2011.*

E.5.3 *Average Conditional Exceedance Rate (ACER) function*

The ACER functions $\epsilon_k(\eta)$ for six different values of k are given in Figure E.36. The optimised ACER parameters for the six different k are given in Table E.20.

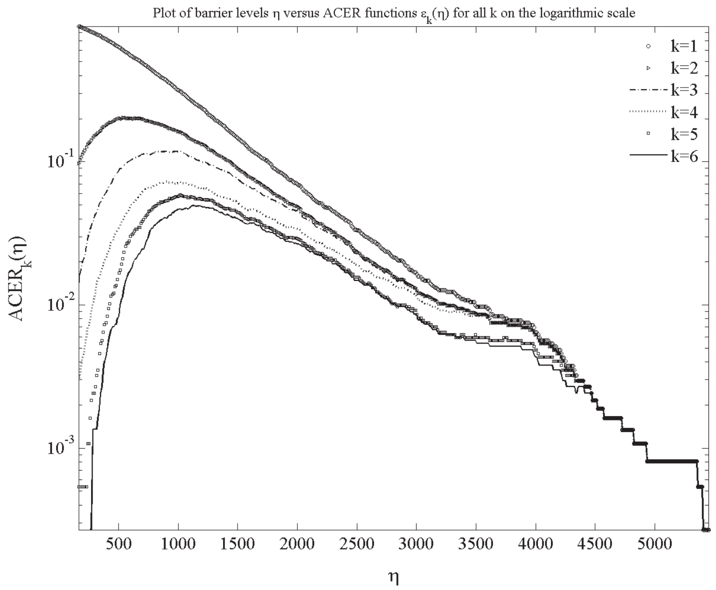

Figure E.36: *ACER function $\epsilon_k(\eta)$ for six different values of k for the hogging VBM. 8,600 TEU ship on 30 December 2011.*

The corresponding Gumbel parameters are given in table E.21.

The Gumbel density functions from the parameters in Table E.21 are plotted in Figure E.37. Here, clustering effects are clearly visible.

	$k = 1$	$k = 2$	$k = 3$	$k = 4$	$k = 5$	$k = 6$
q	1.07	0.21	0.13	0.08	0.06	0.05
s	10	750	897	897	1,017	1,126
r	$64 \cdot 10^{-5}$	$110 \cdot 10^{-5}$	$69 \cdot 10^{-5}$	$40 \cdot 10^{-5}$	$57 \cdot 10^{-5}$	$49 \cdot 10^{-5}$
t	1.10	1.01	1.06	1.10	1.06	1.08

Table E.20: *Optimised ACER parameters 8,600 TEU ship on 30 December 2011.*

	$k = 1$	$k = 2$	$k = 3$	$k = 4$	$k = 5$	$k = 6$
b	5,669	6,320	6,481	6,810	6,557	6,426
d	623	826	855	945	952	926

Table E.21: *Gumbel parameters b and d from the optimised ACER functions for hogging for six different k. 8,600 TEU ship on 30 December 2011.*

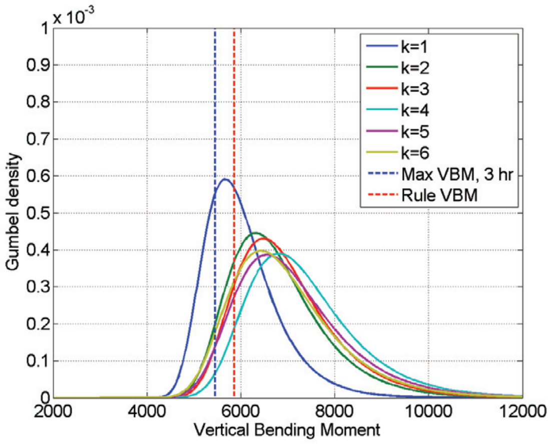

Figure E.37: *Gumbel density function from the parameters derived from the optimised ACER functions for six different values of k (Table E.21). The maximum measured hogging VBM during the three hours is included for comparison. 8,600 TEU ship on 30 December 2011.*

E.6 14,000 TEU Container Ship, 29 September 2011

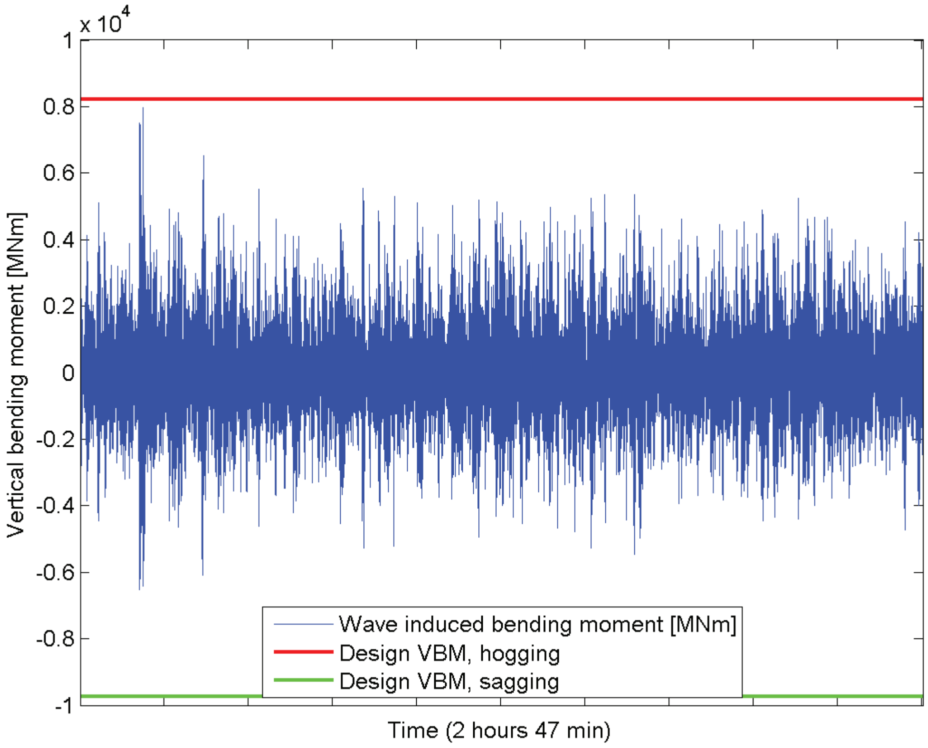

Figure E.38: *Wave-induced vertical bending moment amidships compared to the minimum design wave-induced vertical bending moment in hogging and sagging from International Association of Classification Societies (2010a) for the 14,000 TEU ship on 29 September 2011.*

Series	Time start	length [s]	s_M
1	10:11	1,020	1,572
2	11:19	1,800	1,544
3	13:04	7,200	1,478
Total		10,020	1,500

Table E.22: *Time series information, 14,000 TEU ship, 29 November.*

E.6.1 *Gumbel fit from Weibull parameters*

The peak value distribution for the flexible and rigid-body wave hogging VBM is fitted with the Weibull distribution in Figures E.39 and E.40.

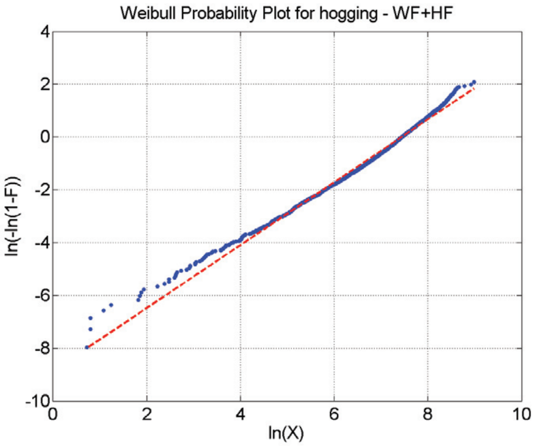

Figure E.39: *Weibull probability plot for the hogging bending moment - WF+HF response. 14,000 TEU ship on 29 September 2011.*

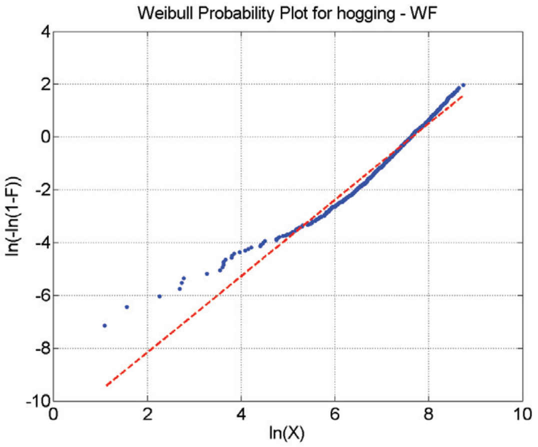

Figure E.40: *Weibull probability plot for the hogging bending moment - WF response. 14,000 TEU ship on 29 September 2011.*

For the hogging condition the Weibull parameters estimated for the flexible and rigid-body response are given in Table E.23.

	a	c
Flexible response	1,709	1.19
Rigid-body response	2,105	1.45

Table E.23: *Weibull parameters for hogging for the WF and WF+HF response. Estimated from Figures E.39 and E.40. 14,000 TEU ship on 29 September 2011.*

The resulting Gumbel density function is shown in Figure E.41.

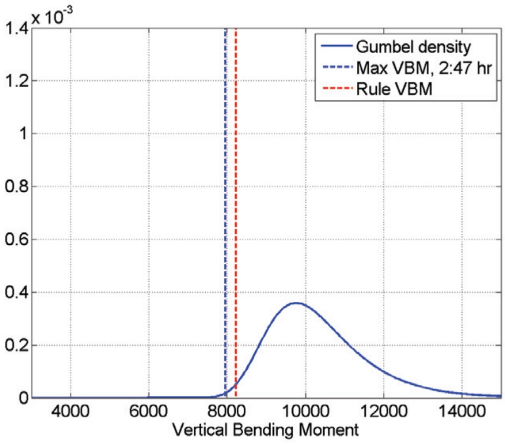

Figure E.41: *Gumbel density function for the hogging VBM based on Weibull parameters for the individual peak for the flexible-body response in Table E.23. The maximum measured hogging VBM during the period and the rule wave VBM are included for comparison. 14,000 TEU ship on 29 September 2011.*

E.6.2 *Peak-over-threshold*

Six different threshold values are chosen as 30%, 40%, 50%, 60%, 70% and 80% of the average of the three largest hogging VBM measured for the three hour time series. The corresponding Weibull parameters are given in Table E.24 together with the threshold levels. The Gumbel parameters b and d are determined from the exponential fit to the peaks over the threshold and are given in Table E.25.

Threshold, u	a	c
2,198	993	1.06
2,930	868	1.04
3,662	720	1.02
4,395	513	0.96
5,127	521	0.68
5,860	1,852	1.24

Table E.24: *Weibull parameters a and c for for the excess of the hogging VBM for different threshold values. 14,000 TEU ship on 29 September 2011.*

Threshold, u	d	b
2,198	943	8,387
2,930	822	7,757
3,662	674	7,113
4,395	531	6,593
5,127	616	6,795
5,860	1,465	6,536

Table E.25: *Gumbel parameters b and d from an exponential fit to the excess. 14,000 TEU ship on 29 September 2011.*

E.6.3 *Average Conditional Exceedance Rate (ACER) function*

The ACER functions $\epsilon_k(\eta)$ for six different values of k are given in Figure E.42. The optimised ACER parameters for the six different k are given in Table E.26.

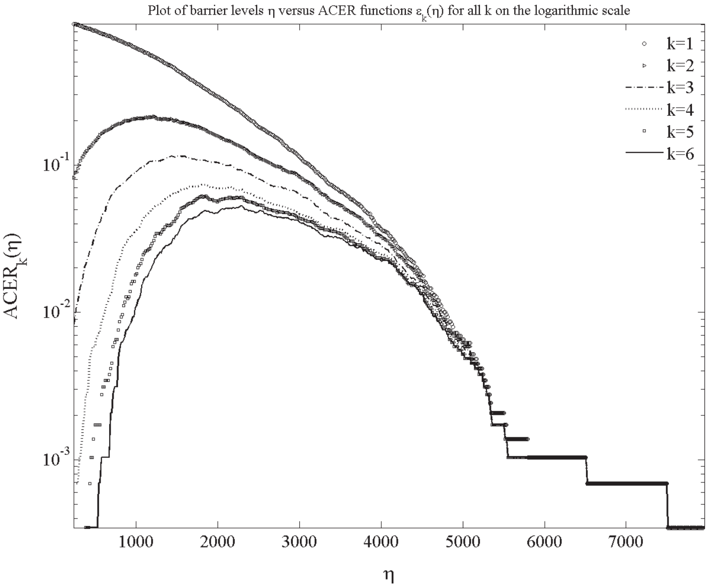

Figure E.42: *ACER function $\epsilon_k(\eta)$ for six different values of k for the hogging VBM. 14,000 TEU ship on 29 September 2011.*

The corresponding Gumbel parameters are given in table E.27.

The Gumbel density functions from the parameters in Table E.27 are plotted in Figure E.43.

	$k=1$	$k=2$	$k=3$	$k=4$	$k=5$	$k=6$
q	1.37	0.18	0.13	0.078	0.06	0.05
s	-1,625	10.0	2.14	2.12	703	1,183
r	$1.14 \cdot 10^{-7}$	$7.09 \cdot 10^{-12}$	$8.19 \cdot 10^{-11}$	$8.39 \cdot 10^{-13}$	$1.66 \cdot 10^{-12}$	$9.27 \cdot 10^{-12}$
t	2.00	3.16	2.86	3.37	3.35	3.18

Table E.26: *Optimised ACER parameters for 14,000 TEU ship on 29 September 2011.*

	$k=1$	$k=2$	$k=3$	$k=4$	$k=5$	$k=6$
b	6,804	6,000	6,343	6,246	6,111	6,107
d	508	303	377	342	313	311

Table E.27: *Gumbel parameters b and d from the optimised ACER functions for hogging for six different k. 14,000 TEU ship on 29 September 2011.*

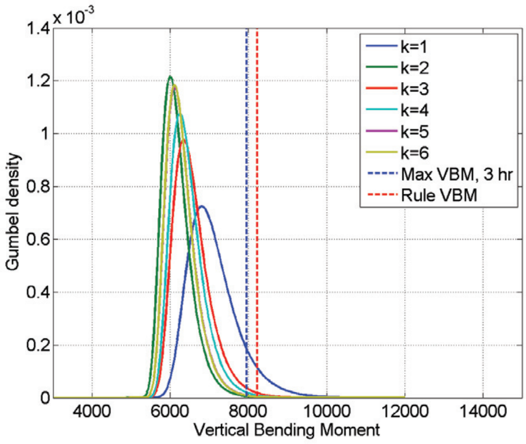

Figure E.43: *Gumbel density function from the parameters derived from the optimised ACER functions for six different values of k (Table E.27). The maximum measured hogging VBM during the three hours is included for comparison. 14,000 TEU ship on 29 September 2011.*

E.7 14,000 TEU Container Ship, 21 July 2011

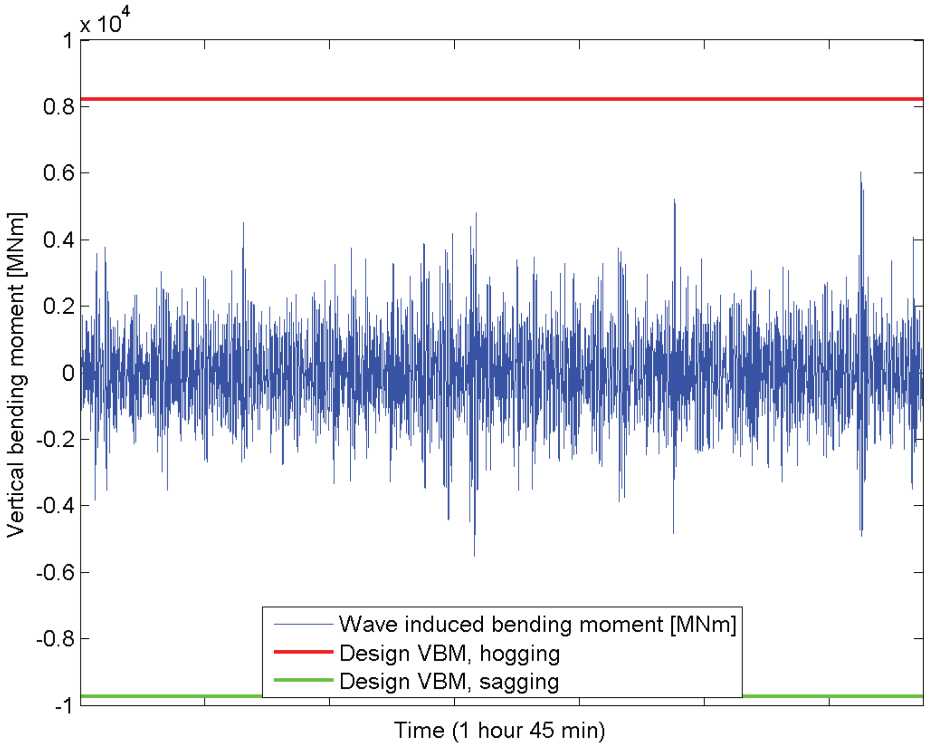

Figure E.44: *Wave-induced vertical bending moment amidships compared to the minimum design wave-induced vertical bending moment in hogging and sagging from International Association of Classification Societies (2010a) for the 14,000 TEU ship on 21 July 2011.*

Series	Time start	length [s]	standard deviation
1	04:32	3,600	1,089
2	07:32	2,700	1,164
Total		6,300	1,122

Table E.28: *Time series information, 14,000 TEU ship, 21 July 2011.*

E.7.1 *Gumbel fit from Weibull parameters*

The peak value distribution for the flexible and rigid-body wave hogging VBM is fitted with the Weibull distribution in Figures E.45 and E.46.

For the hogging condition the Weibull parameters estimated for the flexible and rigid-body response are given in Table E.29.

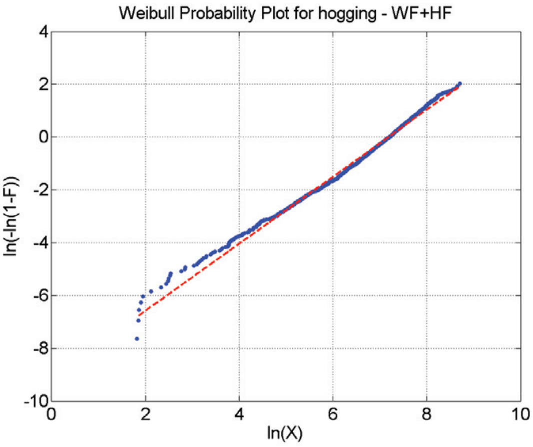

Figure E.45: *Weibull probability plot for the hogging bending moment - WF+HF response. 14,000 TEU ship on 21 July 2011.*

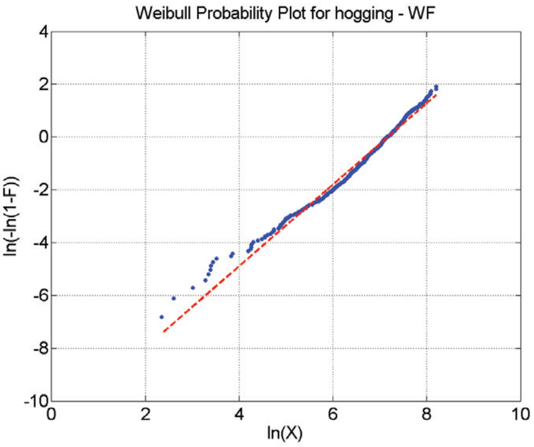

Figure E.46: *Weibull probability plot for the hogging bending moment - WF response. 14,000 TEU ship on 21 July 2011.*

	a	c
Flexible response	1,328	1.27
Rigid-body response	1,303	1.54

Table E.29: *Weibull parameters for hogging for the WF and WF+HF response. Estimated from Figures E.45 and E.46. 14,000 TEU ship on 21 July 2011.*

The resulting Gumbel density function is shown in Figure E.47.

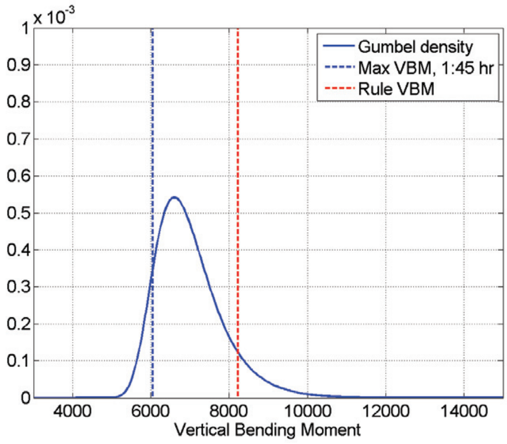

Figure E.47: *Gumbel density function for the hogging VBM based on Weibull parameters for the individual peak for the flexible-body response in Table E.29. The maximum measured hogging VBM during the period and the rule wave VBM are included for comparison. 14,000 TEU ship on 21 July 2011.*

Threshold, u	a	c
1,741	718	1.04
2,322	684	1.10
2,902	631	1.03
3,483	667	0.84
4,063	994	0.68
4,643	943	1.21

Table E.30: *Weibull parameters a and c for for the excess of the hogging VBM for different threshold values. 14,000 TEU ship on 21 July 2011.*

Threshold, u	d	b
1,741	702	6,072
2,322	662	5,872
2,902	643	5,775
3,483	670	5,865
4,063	848	6,237
4,643	776	6,293

Table E.31: *Gumbel parameters b and d from an exponential fit to the excess. 14,000 TEU ship on 21 July 2011.*

E.7.2 *Peak-over-threshold*

Six different threshold values are chosen as 30%, 40%, 50%, 60%, 70% and 80% of the average of the three largest hogging VBM measured for the three hour time series. The corresponding Weibull parameters are given in Table E.30 together with the threshold levels. The Gumbel parameters b and d are determined from the exponential fit to the peaks over the threshold and are given in Table E.31.

E.7.3 *Average Conditional Exceedance Rate (ACER) function*

The ACER functions $\epsilon_k(\eta)$ for six different values of k are given in Figure E.48. The optimised ACER parameters for the six different k are given in Table E.32.

	$k = 1$	$k = 2$	$k = 3$	$k = 4$	$k = 5$	$k = 6$
q	0.98	0.25	0.14	0.09	0.07	0.06
s	10	1205	1301.7	1568.08	1616.51	1810.23
r	$3.07 \cdot 10^{-5}$	$14 \cdot 10^{-5}$	$3.38 \cdot 10^{-5}$	$2.98 \cdot 10^{-5}$	$1.70 \cdot 10^{-5}$	$4.80 \cdot 10^{-5}$
t	1.45	1.28	1.45	1.46	1.53	1.40

Table E.32: *Optimised ACER parameters for 14,000 TEU ship on 21 July 2011.*

The corresponding Gumbel parameters are given in table E.33.

The Gumbel density functions from the parameters in Table E.33 are plotted in Figure E.49. Clustering is seen not to be important in this case.

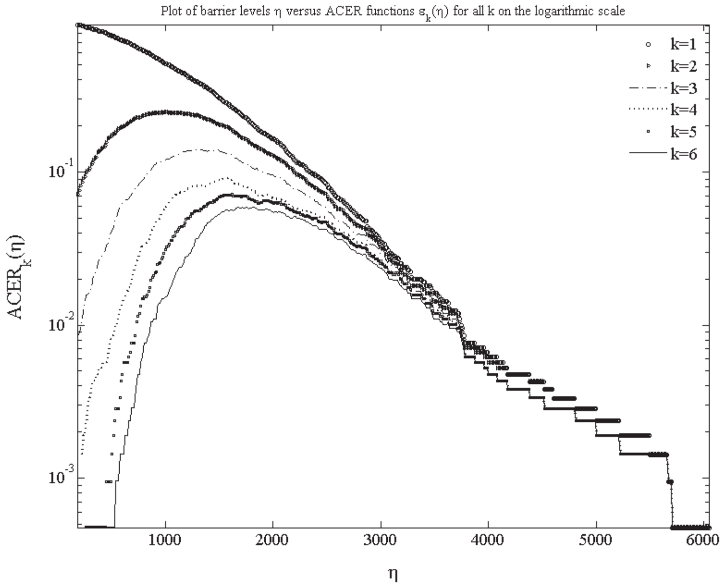

Figure E.48: *ACER function $\epsilon_k(\eta)$ for six different values of k for the hogging VBM. 14,000 TEU ship on 21 July 2011.*

	$k = 1$	$k = 2$	$k = 3$	$k = 4$	$k = 5$	$k = 6$
b	5,424	5,607	5,415	5,501	5,466	5,562
d	491	551	498	520	502	552

Table E.33: *Gumbel parameters b and d from the optimised ACER functions for hogging for six different k. 14,000 TEU ship on 21 July 2011.*

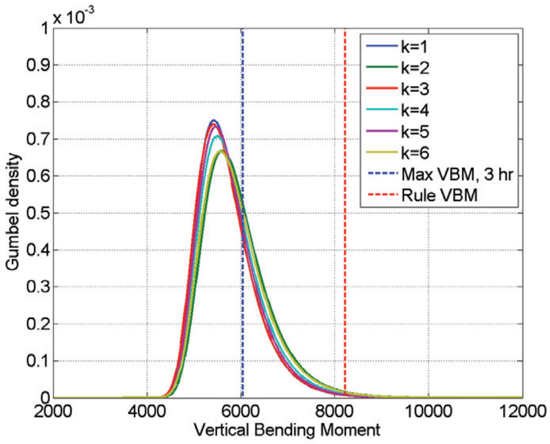

Figure E.49: *Gumbel density function from the parameters derived from the optimised ACER functions for six different values of k (Table E.33). The maximum measured hogging VBM during the three hours is included for comparison. 14,000 TEU ship on 21 July 2011.*

E.8 4,400 TEU Container Ship, 02 November 2007, 11-13 hours

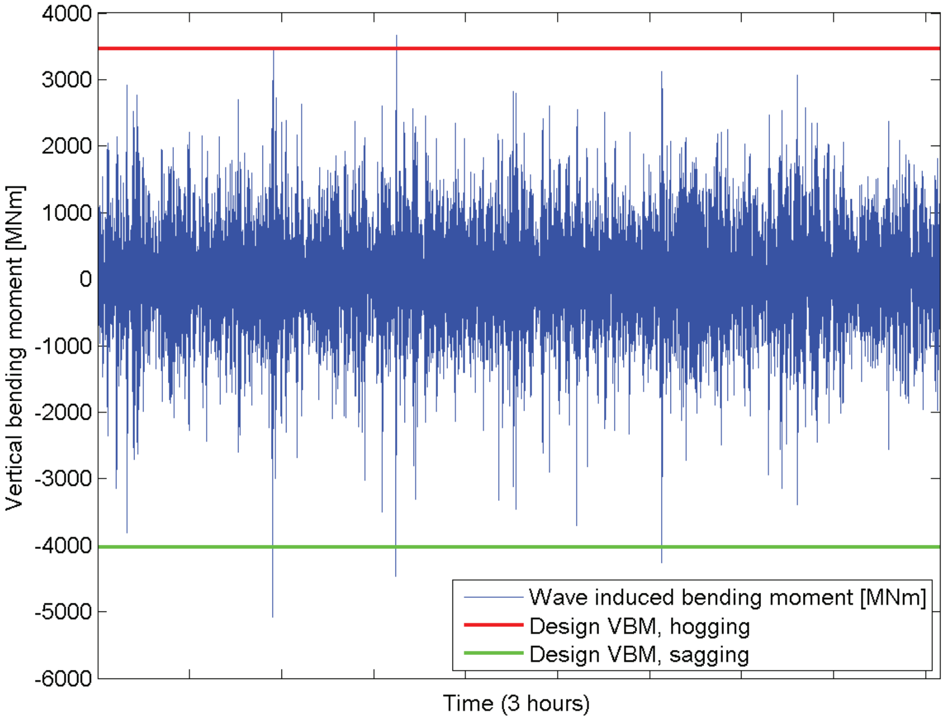

Figure E.50: *Wave-induced vertical bending moment amidships compared to the minimum design wave-induced vertical bending moment in hogging and sagging from International Association of Classification Societies (2010a) for the 4,400 TEU ship on 02 November 2007 at 11-13 hours.*

E.8.1 *Gumbel fit from Weibull parameters*

The peak value distribution for the flexible and rigid-body wave hogging VBM is fitted with the Weibull distribution in Figures E.51 and E.52.

For the hogging condition the Weibull parameters estimated for the flexible and rigid-body response are given in Table E.34.

The resulting Gumbel density function is shown in Figure E.53.

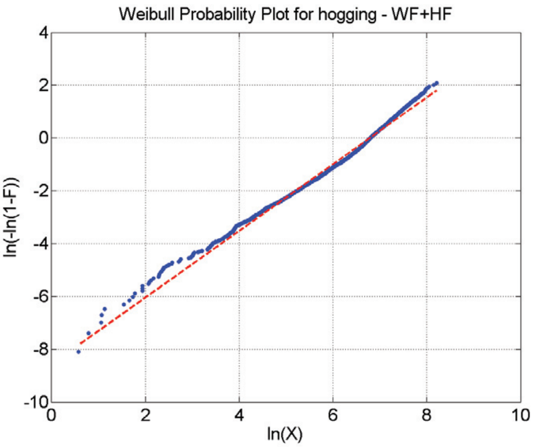

Figure E.51: *Weibull probability plot for the hogging bending moment - WF+HF response. 4,400 TEU ship on 02 November 2007, 11-13 hours.*

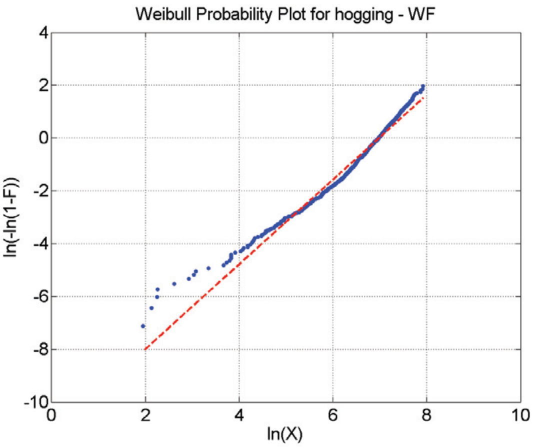

Figure E.52: *Weibull probability plot for the hogging bending moment - WF response. 4,400 TEU ship on 02 November 2007, 11-13 hours.*

	a	c
Flexible response	889	1.26
Rigid-body response	1,077	1.61

Table E.34: *Weibull parameters for hogging for the WF and WF+HF response. Estimated from Figures E.51 and E.52. 4,400 TEU ship on 02 November 2007, 11-13 hours.*

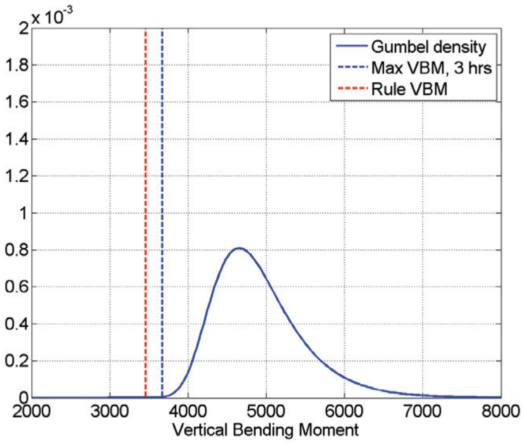

Figure E.53: *Gumbel density function for the hogging VBM based on Weibull parameters for the individual peak for the flexible-body response in Table E.44. The maximum measured hogging VBM during the three hours and the rule wave VBM are included for comparison. 4,400 TEU ship on 02 November 2007, 11-13 hours.*

E.8.2 *Peak-over-threshold*

Six different threshold values are chosen as 30%, 40%, 50%, 60%, 70% and 80% of the average of the three largest hogging VBM measured for the three hour time series. The

Threshold, u	a	c
1,026	477	1.03
1,368	444	0.95
1,710	379	0.95
2,052	353	0.94
2,394	377	1.07
2,736	289	1.07

Table E.35: *Weibull parameters a and c for for the excess of the hogging VBM for different threshold values. 4,400 TEU ship on 02 November 2007, 11-13 hours.*

Threshold, u	d	b
1026	453	4,134
1368	412	3,903
1710	370	3,698
2052	346	3,609
2394	337	3,581
2736	272	3,600

Table E.36: *Gumbel parameters b and d from an exponential fit to the excess. 4,400 TEU ship on 02 November 2007, 11-13 hours.*

corresponding Weibull parameters are given in Table E.35 together with the threshold levels. The Gumbel parameters b and d are determined from the exponential fit to the peaks over the threshold and are given in Table E.36.

E.8.3 *Average Conditional Exceedance Rate (ACER) function*

The ACER functions $\epsilon_k(\eta)$ for six different values of k are given in Figure E.54. The optimised ACER parameters for the six different k are given in Table E.37.

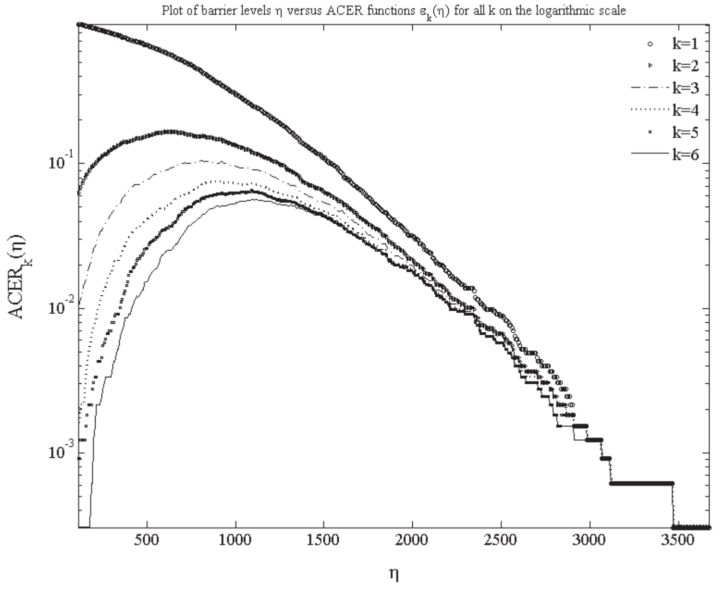

Figure E.54: *ACER function $\epsilon_k(\eta)$ for six different values of k for the hogging VBM. 4,400 TEU ship on 02 November 2007, 11-13 hours.*

	$k = 1$	$k = 2$	$k = 3$	$k = 4$	$k = 5$	$k = 6$
q	0.98	0.25	0.14	0.09	0.07	0.06
s	10	1205	1301.7	1568.08	1616.51	1810.23
r	$3.07 \cdot 10^{-5}$	$14 \cdot 10^{-5}$	$3.38 \cdot 10^{-5}$	$2.98 \cdot 10^{-5}$	$1.70 \cdot 10^{-5}$	$4.80 \cdot 10^{-5}$
t	1.45	1.28	1.45	1.46	1.53	1.40

Table E.37: *Optimised ACER parameters for the 4,400 TEU ship on 02 November 2007, 11-13 hours.*

The corresponding Gumbel parameters are given in table E.38.

	$k = 1$	$k = 2$	$k = 3$	$k = 4$	$k = 5$	$k = 6$
b	2,689	2,924	2,748	2,676	2,915	2,699
d	343	345	340	338	343	337

Table E.38: *Gumbel parameters b and d from the optimised ACER functions for hogging for six different k. 4,400 TEU ship on 02 November 2007, 11-13 hours.*

The Gumbel density functions from the parameters in Table E.38 are plotted in Figure E.55. Clustering is seen not to be important in this case.

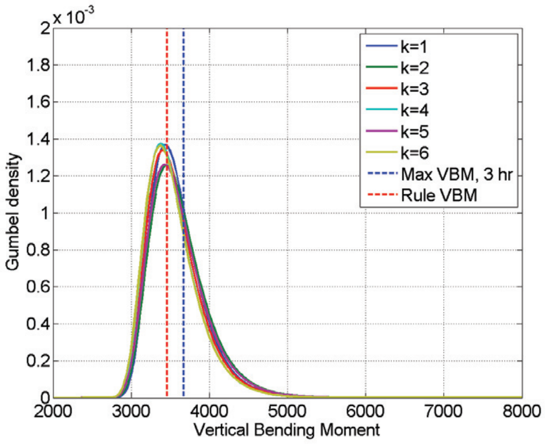

Figure E.55: *Gumbel density function from the parameters derived from the optimised ACER functions for six different values of k (Table E.38). The maximum measured hogging VBM during the three hours is included for comparison. 4,400 TEU ship on 02 November 2007, 11-13 hours.*

E.9 4,400 TEU Container Ship, 02 November 2007, 16-18 hours

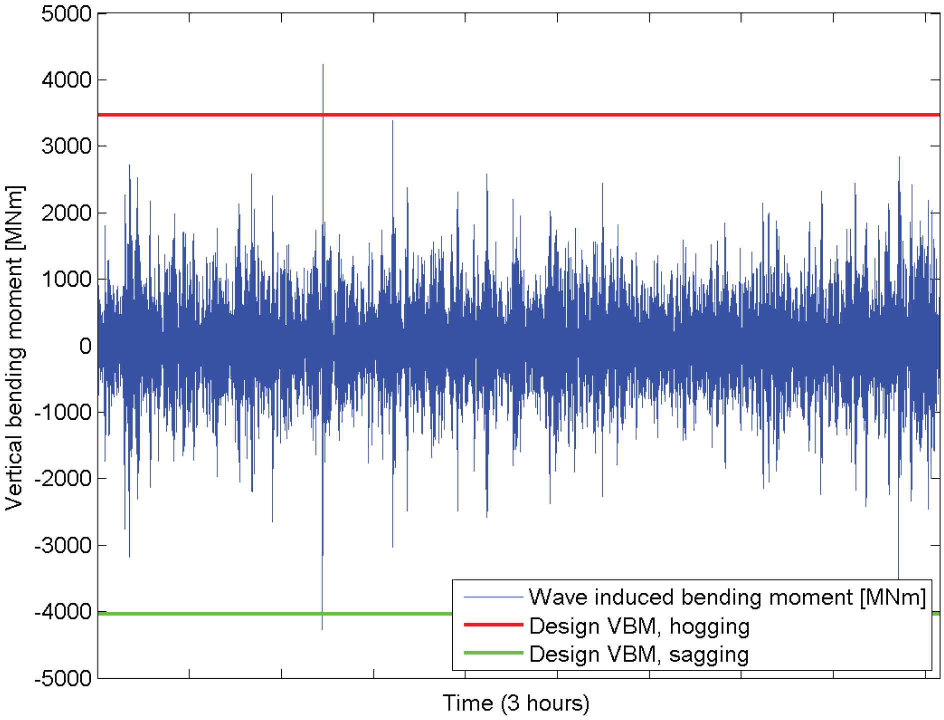

Figure E.56: *Wave-induced vertical bending moment amidships compared to the minimum design wave-induced vertical bending moment in hogging and sagging from International Association of Classification Societies (2010a) for the 4,400 TEU ship on 02 November 2007 at 16-18 hours.*

E.9.1 *Gumbel fit from Weibull parameters*

The peak value distribution for the flexible and rigid-body wave hogging VBM is fitted with the Weibull distribution in Figures E.57 and E.58.

For the hogging condition the Weibull parameters estimated for the flexible and rigid-body response are given in Table E.39.

The resulting Gumbel density function is shown in Figure E.59.

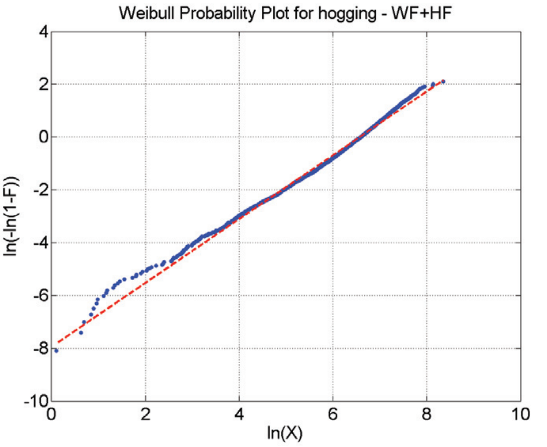

Figure E.57: *Weibull probability plot for the hogging bending moment - WF+HF response. 4,400 TEU ship on 02 November 2007, 16-18 hours.*

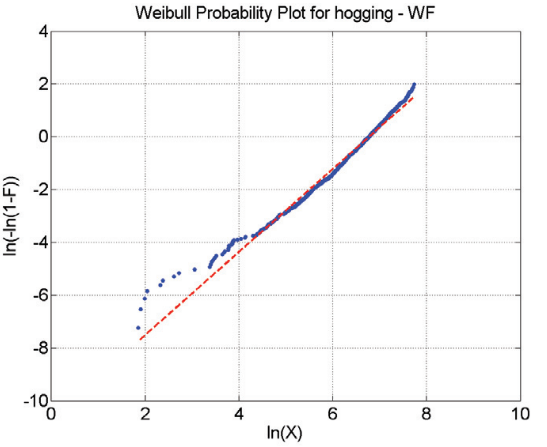

Figure E.58: *Weibull probability plot for the hogging bending moment - WF response. 4,400 TEU ship on 02 November 2007, 16-18 hours.*

	a	c
Flexible response	718	1.21
Rigid-body response	878	1.57

Table E.39: *Weibull parameters for hogging for the WF and WF+HF response. Estimated from Figures E.57 and E.58. 4,400 TEU ship on 02 November 2007, 16-18 hours.*

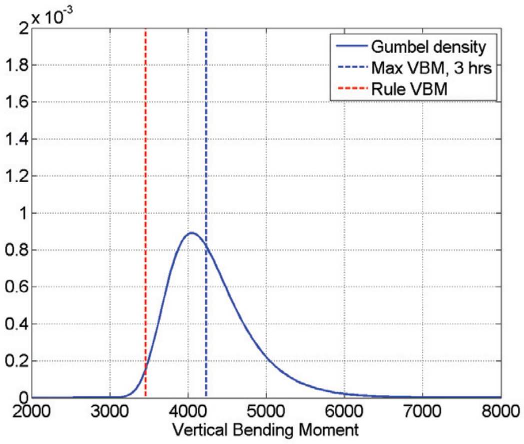

Figure E.59: *Gumbel density function for the hogging VBM based on Weibull parameters for the individual peak for the flexible-body response in Table E.44. The maximum measured hogging VBM during the three hours and the rule wave VBM are included for comparison. 4,400 TEU ship on 02 November 2007, 16-18 hours.*

E.9.2 *Peak-over-threshold*

Six different threshold values are chosen as 30%, 40%, 50%, 60%, 70% and 80% of the average of the three largest hogging VBM measured for the three hour time series. The

Threshold, u	a	c
1,104	392	1.06
1,472	359	1.04
1,840	373	0.79
2,207	384	1.10
2,575	746	0.04
2,943	943	1.14

Table E.40: *Weibull parameters a and c for for the excess of the hogging VBM for different threshold values. 4,400 TEU ship on 02 November 2007, 16-18 hours.*

Threshold, u	d	b
1,104	379	3,484
1,472	355	3,364
1,840	359	3,376
2,207	384	3,426
2,575	620	3,687
2,943	736	3,625

Table E.41: *Gumbel parameters b and d from an exponential fit to the excess. 4,400 TEU ship on 02 November 2007, 16-18 hours.*

corresponding Weibull parameters are given in Table E.40 together with the threshold levels. The Gumbel parameters b and d are determined from the exponential fit to the peaks over the threshold and are given in Table E.41.

E.9.3 *Average Conditional Exceedance Rate (ACER) function*

The ACER functions $\epsilon_k(\eta)$ for six different values of k are given in Figure E.60. The optimised ACER parameters for the six different k are given in Table E.42.

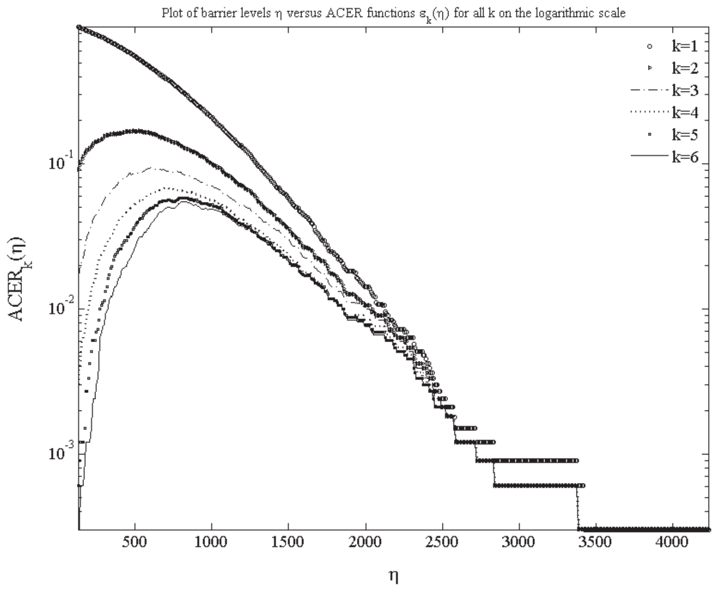

Figure E.60: *ACER function $\epsilon_k(\eta)$ for six different values of k for the hogging VBM. 4,400 TEU ship on 02 November 2007, 16-18 hours.*

	$k=1$	$k=2$	$k=3$	$k=4$	$k=5$	$k=6$
q	0.98	0.25	0.14	0.09	0.07	0.06
s	10	1205	1301.7	1568.08	1616.51	1810.23
r	$3.07 \cdot 10^{-5}$	$14 \cdot 10^{-5}$	$3.38 \cdot 10^{-5}$	$2.98 \cdot 10^{-5}$	$1.70 \cdot 10^{-5}$	$4.80 \cdot 10^{-5}$
t	1.45	1.28	1.45	1.46	1.53	1.40

Table E.42: *Optimised ACER parameters for the 4,400 TEU ship on 02 November 2007, 16-18 hours.*

The corresponding Gumbel parameters are given in table E.43.

	$k=1$	$k=2$	$k=3$	$k=4$	$k=5$	$k=6$
b	3,082	3,188	3,181	3,212	3,259	3,217
d	258	305	300	327	353	336

Table E.43: *Gumbel parameters b and d from the optimised ACER functions for hogging for six different k. 4,400 TEU ship on 02 November 2007, 16-18 hours.*

The Gumbel density functions from the parameters in Table E.43 are plotted in Figure E.61.

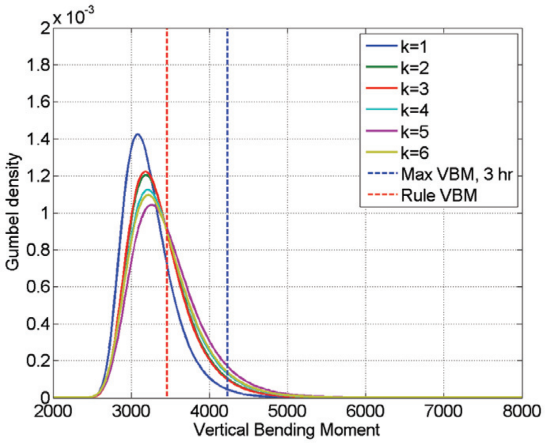

Figure E.61: *Gumbel density function from the parameters derived from the optimised ACER functions for six different values of k (Table E.43). The maximum measured hogging VBM during the three hours is included for comparison. 4,400 TEU ship on 02 November 2007, 16-18 hours.*

E.10 4,400 TEU Container Ship, 01 July 2008

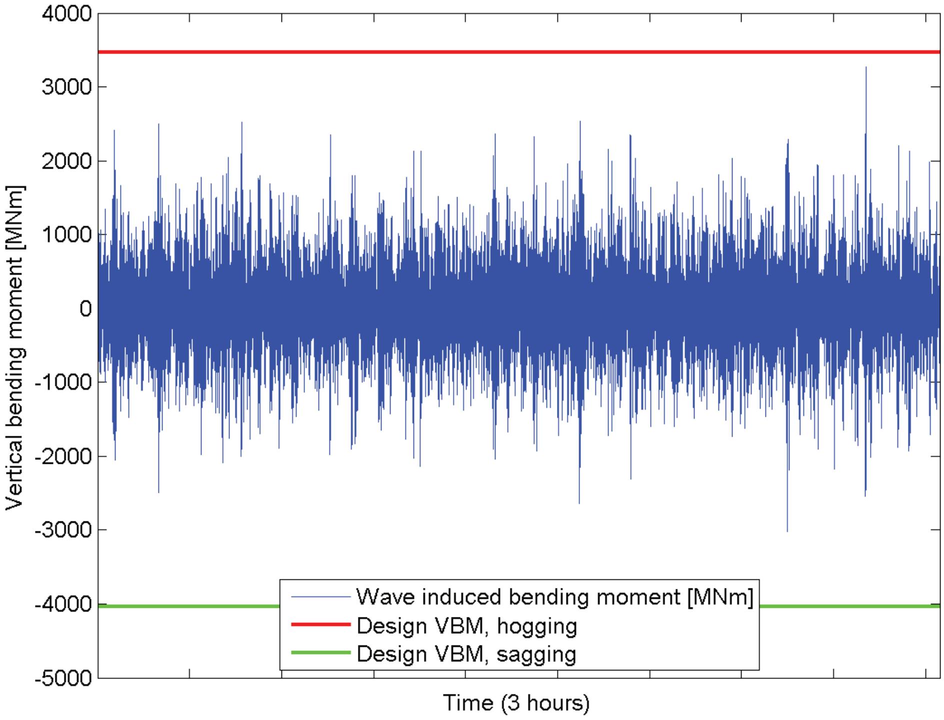

Figure E.62: *Wave-induced vertical bending moment amidships compared to the minimum design wave-induced vertical bending moment in hogging and sagging from International Association of Classification Societies (2010a) for the 4,400 TEU ship on 01 July 2008 at 17-19 hours.*

E.10.1 *Gumbel fit from Weibull parameters*

The peak value distribution for the flexible and rigid-body wave hogging VBM is fitted with the Weibull distribution in Figures E.63 and E.64.

For the hogging condition the Weibull parameters estimated for the flexible and rigid-body response are given in Table E.44.

	a	c
Flexible response	821	1.51
Rigid-body response	656	1.20

Table E.44: *Weibull parameters for hogging for the WF and WF+HF response. Estimated from Figures E.63 and E.64. 4,400 TEU ship on 01 July 2008.*

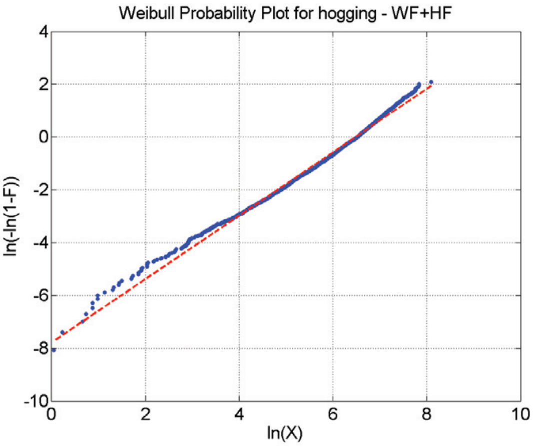

Figure E.63: *Weibull probability plot for the hogging bending moment - WF+HF response. 4,400 TEU ship on 01 July 2008.*

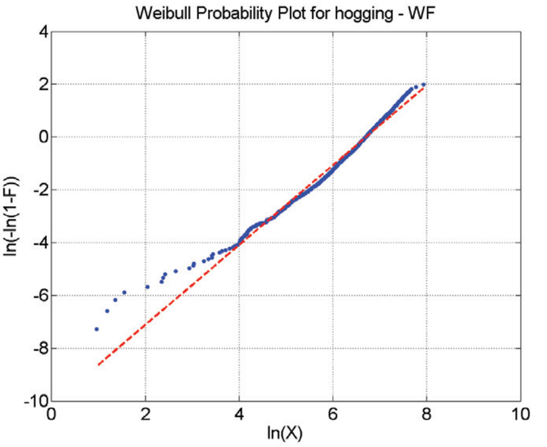

Figure E.64: *Weibull probability plot for the hogging bending moment - WF response. 4,400 TEU ship on 01 July 2008.*

The resulting Gumbel density function is shown in Figure E.65.

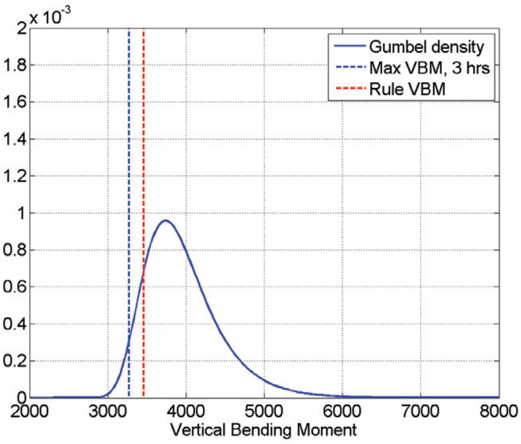

Figure E.65: *Gumbel density function for the hogging VBM based on Weibull parameters for the individual peak for the flexible-body response in Table E.44. The maximum measured hogging VBM during the three hours and the rule wave VBM are included for comparison. 4,400 TEU ship on 01 July 2008.*

E.10.2 *Peak-over-threshold*

Six different threshold values are chosen as 30%, 40%, 50%, 60%, 70% and 80% of the average of the three largest hogging VBM measured for the three hour time series. The corresponding Weibull parameters are given in Table E.45 together with the threshold levels. The Gumbel parameters b and d are determined from the exponential fit to the peaks over the threshold and are given in Table E.46.

Threshold, u	a	c
833	372	1.10
1,111	345	0.99
1,389	320	0.95
1,666	305	1.08
1,944	338	0.79
2,222	252	0.50

Table E.45: *Weibull parameters a and c for for the excess of the hogging VBM for different threshold values. 4,400 TEU ship on 01 July 2008.*

Threshold, u	d	b
833	361	3,261
1,111	332	3,103
1,389	308	2,997
1,666	298	2,957
1,944	284	2,927
2,222	210	2,970

Table E.46: *Gumbel parameters b and d from an exponential fit to the excess. 4,400 TEU ship on 01 July 2008.*

E.10.3 *Average Conditional Exceedance Rate (ACER) function*

The ACER functions $\epsilon_k(\eta)$ for six different values of k are given in Figure E.66. The optimised ACER parameters for the six different k are given in Table E.47.

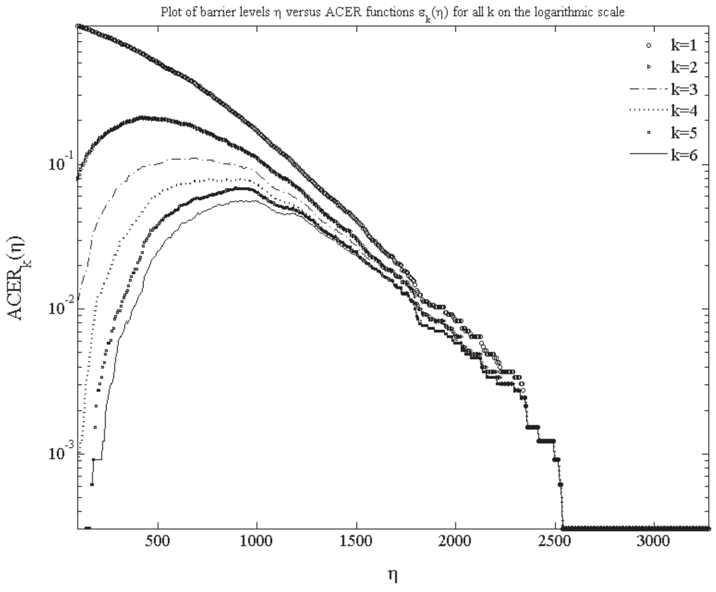

Figure E.66: *ACER function $\epsilon_k(\eta)$ for six different values of k for the hogging VBM. 4,400 TEU ship on 01 July 2008.*

The corresponding Gumbel parameters are given in table E.48.

The Gumbel density functions from the parameters in Table E.48 are plotted in Figure E.67.

	$k=1$	$k=2$	$k=3$	$k=4$	$k=5$	$k=6$
q	0.98	0.25	0.14	0.09	0.07	0.06
s	10	1205	1301.7	1568.08	1616.51	1810.23
r	$3.07 \cdot 10^{-5}$	$14 \cdot 10^{-5}$	$3.38 \cdot 10^{-5}$	$2.98 \cdot 10^{-5}$	$1.70 \cdot 10^{-5}$	$4.80 \cdot 10^{-5}$
t	1.45	1.28	1.45	1.46	1.53	1.40

Table E.47: *Optimised ACER parameters for the 4,400 TEU ship on 01 July 2008.*

	$k=1$	$k=2$	$k=3$	$k=4$	$k=5$	$k=6$
b	2,813	2,812	2,778	2,782	2,850	2,824
d	233	246	231	236	259	246

Table E.48: *Gumbel parameters b and d from the optimised ACER functions for hogging for six different k. 4,400 TEU ship on 01 July 2008.*

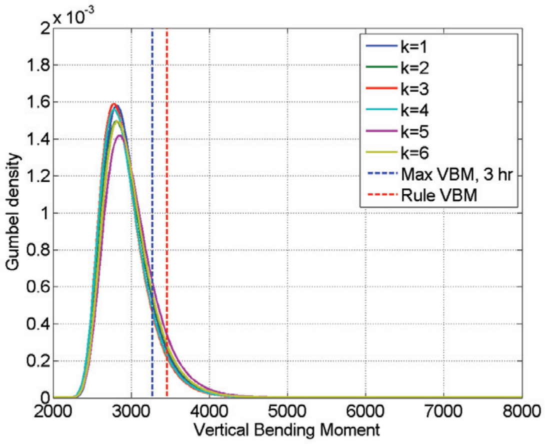

Figure E.67: *Gumbel density function from the parameters derived from the optimised ACER functions for six different values of k (Table E.48). The maximum measured hogging VBM during the three hours is included for comparison. 4,400 TEU ship on 01 July 2008.*

E.11 ACER Output Example

Output for 02 October 2011, 9,400 TEU ship, $k = 2$.

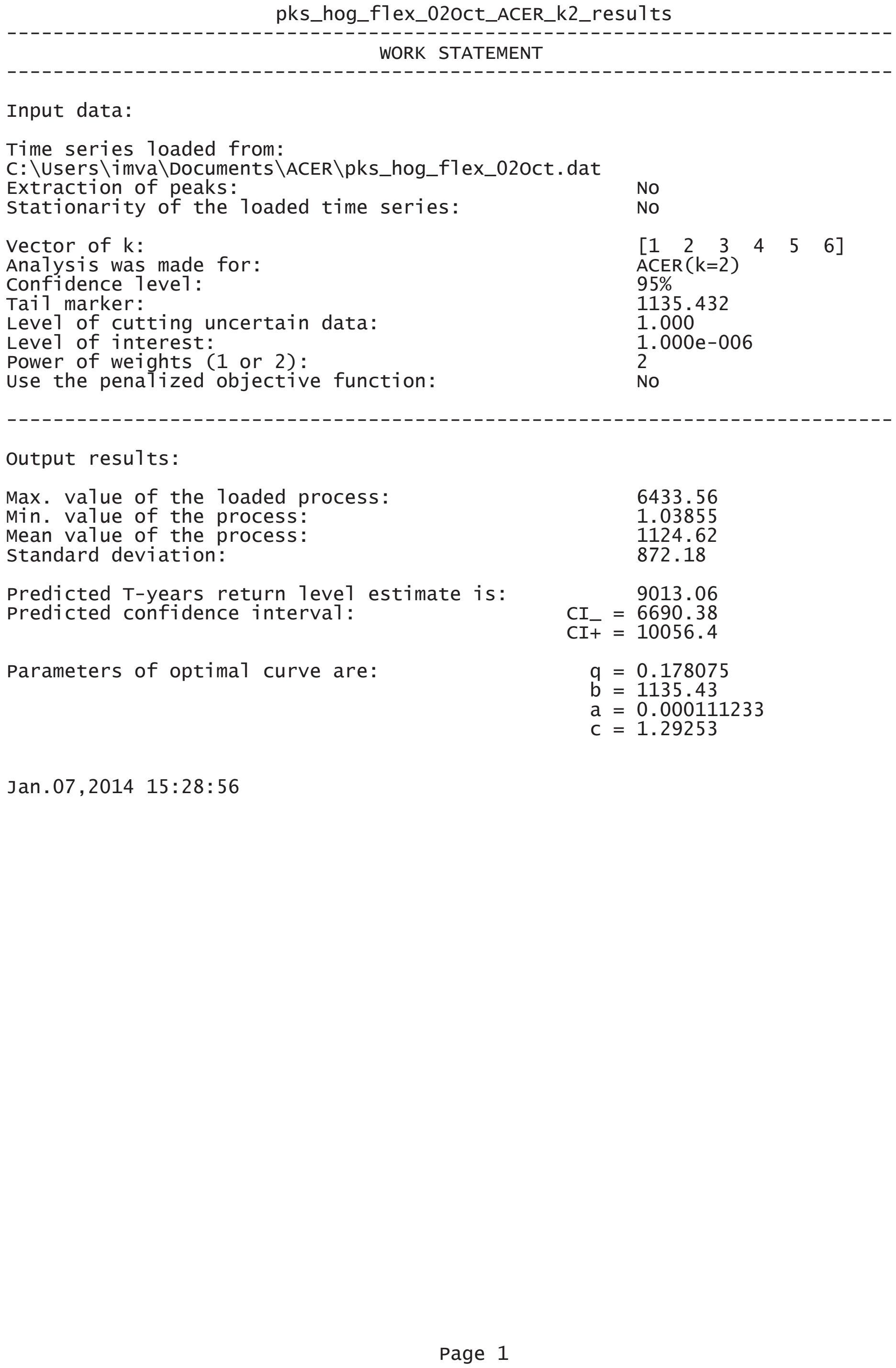

```
                       pks_hog_flex_02Oct_ACER_k2_results
----------------------------------------------------------------------------
                                WORK STATEMENT
----------------------------------------------------------------------------

Input data:

Time series loaded from:
C:\Users\imva\Documents\ACER\pks_hog_flex_02Oct.dat
Extraction of peaks:                                  No
Stationarity of the loaded time series:               No

Vector of k:                                          [1  2  3  4  5  6]
Analysis was made for:                                ACER(k=2)
Confidence level:                                     95%
Tail marker:                                          1135.432
Level of cutting uncertain data:                      1.000
Level of interest:                                    1.000e-006
Power of weights (1 or 2):                            2
Use the penalized objective function:                 No

----------------------------------------------------------------------------

Output results:

Max. value of the loaded process:                     6433.56
Min. value of the process:                            1.03855
Mean value of the process:                            1124.62
Standard deviation:                                   872.18

Predicted T-years return level estimate is:           9013.06
Predicted confidence interval:                  CI_ = 6690.38
                                                CI+ = 10056.4

Parameters of optimal curve are:                  q = 0.178075
                                                  b = 1135.43
                                                  a = 0.000111233
                                                  c = 1.29253


Jan.07,2014 15:28:56








                                     Page 1
```

Appendix F

Model Tests

F.1 $H_s = 6.5$ m

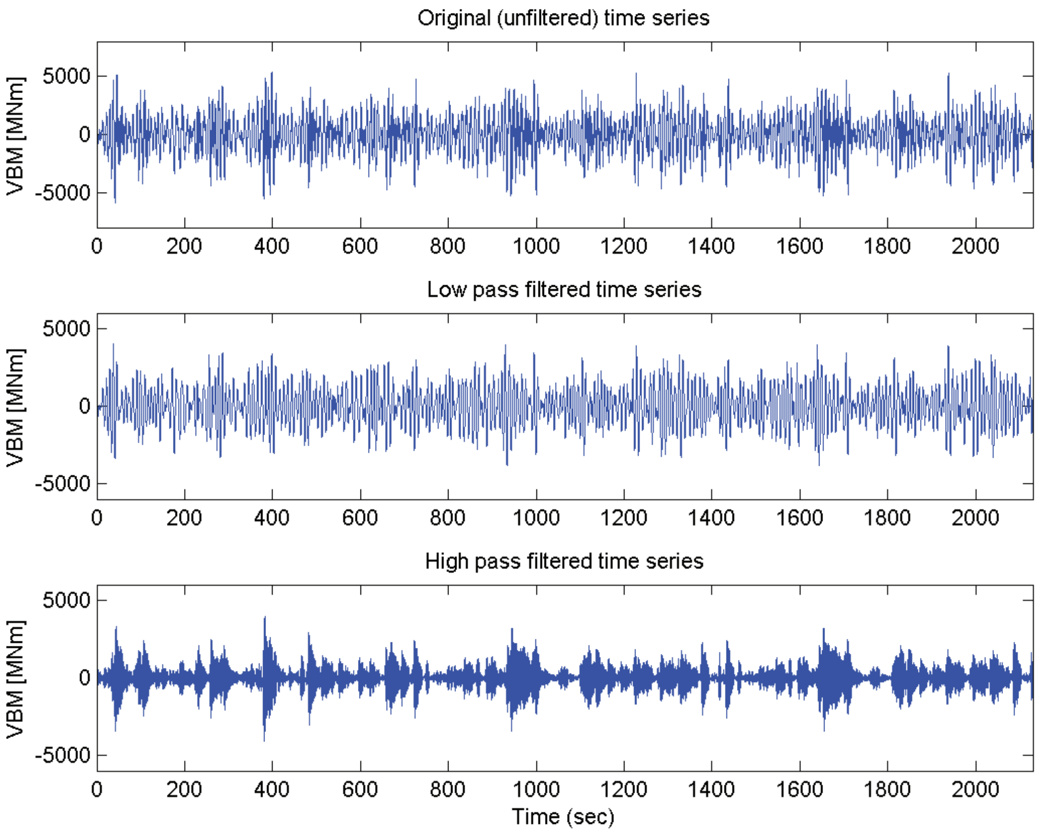

Figure F.1: *Unfiltered, low-pass and high-pass filtered time series signal of vertical bending moment for model tests in head sea and H_s of 6.5 m. Total time series is 1,420 s long and comprised of two runs.*

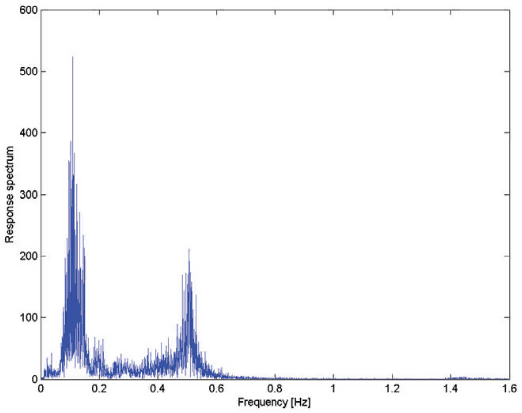

Figure F.2: *FFT of unfiltered VBM amidhips in head sea and H_s of 6.5 m. Same time series as Figure F.1.*

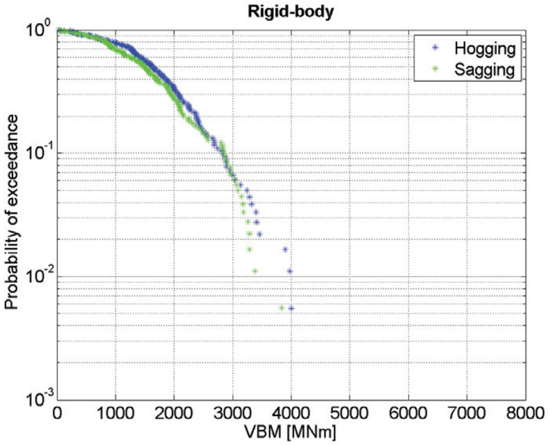

Figure F.3: *Individual peak value probability of exceedance for the rigid ship comparing hogging and sagging in head sea and H_s of 6.5 m.*

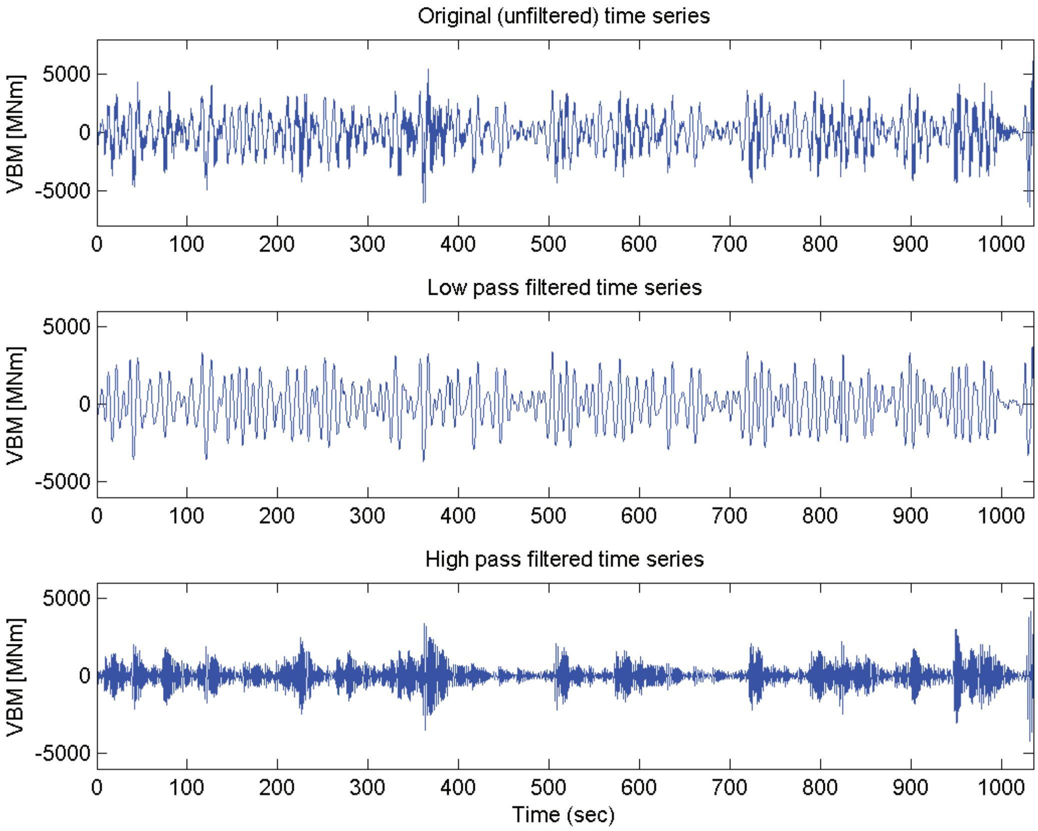

Figure F.4: *Unfiltered, low-pass and high-pass filtered time series signal of vertical bending moment for model tests in bow-quartering sea and H_s of 6.5 m. Total time series is 1,035 s long and comprised of five runs.*

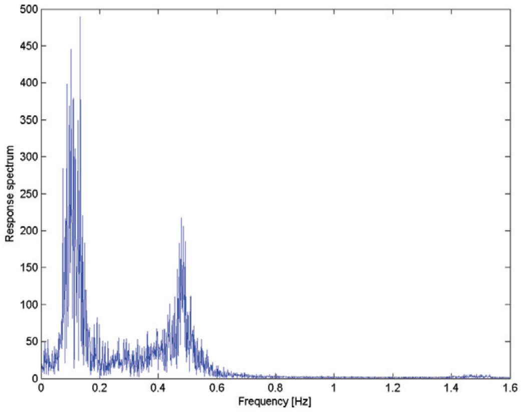

Figure F.5: *FFT of unfiltered VBM amidships in bow-quartering sea and H_s of 6.5 m. Same time series as Figure F.4.*

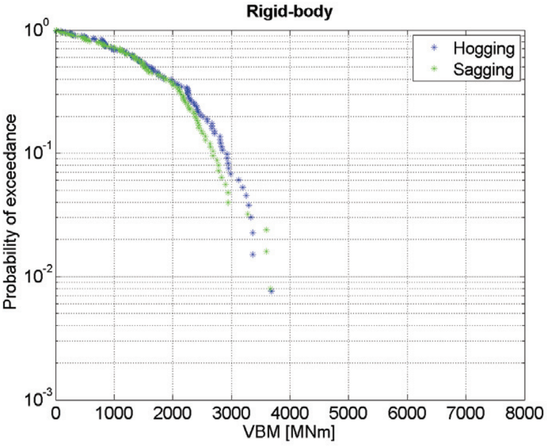

Figure F.6: *Individual peak value probability of exceedance for the rigid ship comparing hogging and sagging in bow-quartering sea and H_s of 6.5 m.*

F.2 $H_s = 9.5$ m

F.2.1 *Longer waves*

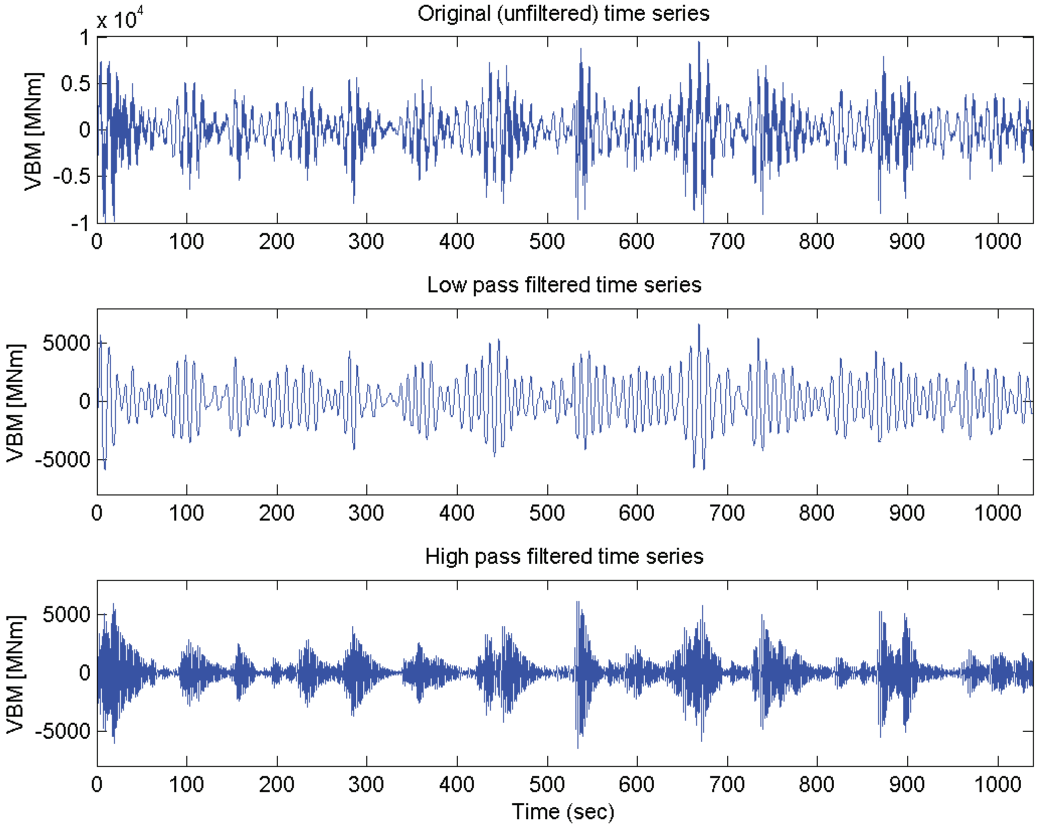

Figure F.7: *Unfiltered, low-pass and high-pass filtered time series signal of vertical bending moment for model tests in head sea, H_s of 9.5 m and T_p of 12.22 s. Total time series is 1,039 s long and comprised of one run.*

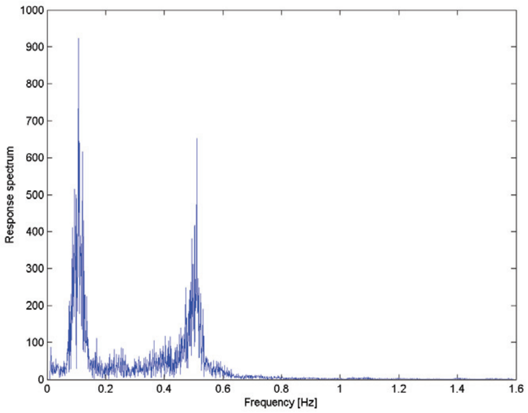

Figure F.8: FFT of unfiltered VBM amidhips in head sea, H_s of 9.5 m and T_p of 12.22 s. Same time series as Figure F.7.

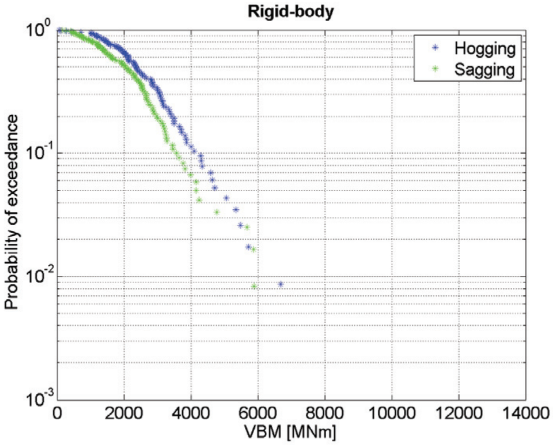

Figure F.9: Individual peak value probability of exceedance for the rigid ship comparing hogging and sagging in head sea, H_s of 9.5 m and T_p of 12.22 s.

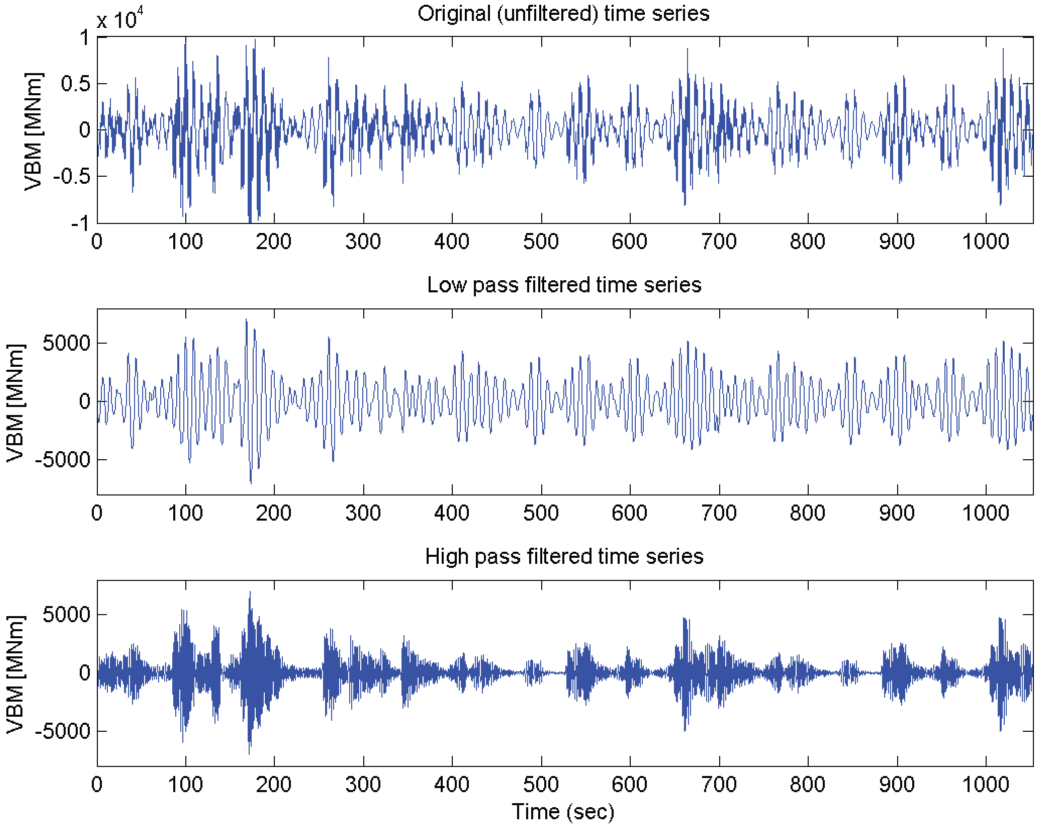

Figure F.10: Unfiltered, low-pass and high-pass filtered time series signal of vertical bending moment for model tests in bow-quartering sea, H_s of 9.5 m and T_p of 12.22 s. Total time series is 1,053 s long and comprised of three runs.

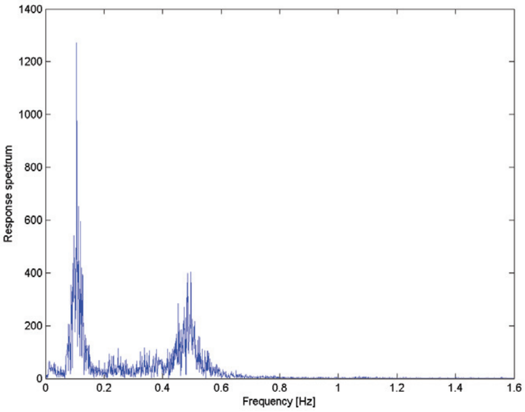

Figure F.11: *FFT of unfiltered VBM amidhips in bow-quartering sea, H_s of 9.5 m and T_p of 12.22 s. Same time series as Figure F.10.*

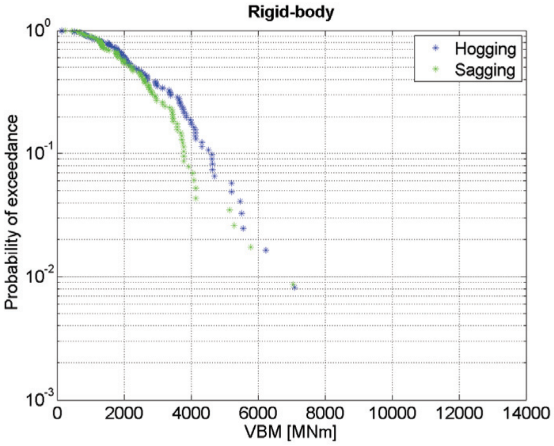

Figure F.12: *Individual peak value probability of exceedance for the rigid ship comparing hogging and sagging in bow-quartering sea, H_s of 9.5 m and T_p of 12.22 s.*

F.2.2 Shorter waves

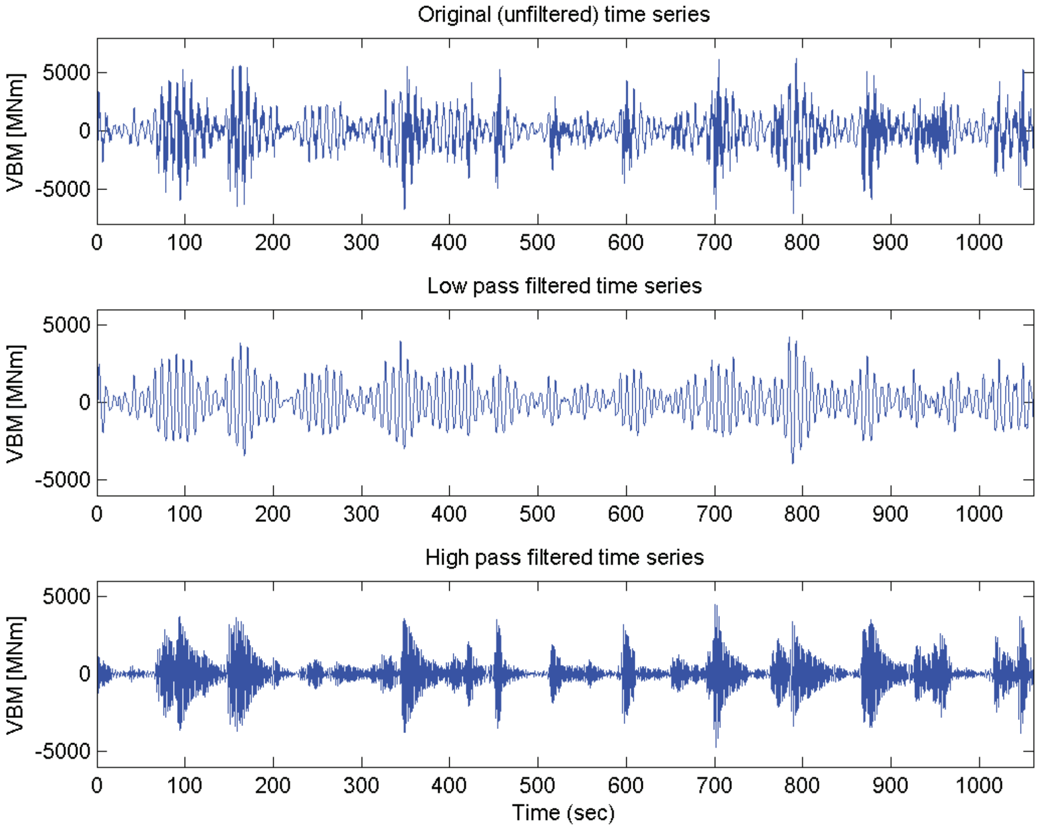

Figure F.13: *Unfiltered, low-pass and high-pass filtered time series signal of vertical bending moment for model tests in head sea,* H_s *of 9.5 m and* T_p *of 9.93 s. Total time series is 1,061 s long and comprised of one run.*

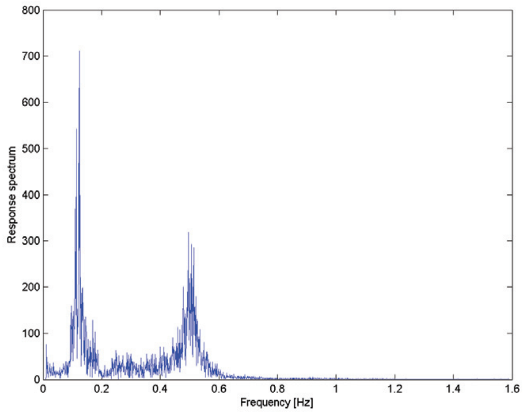

Figure F.14: *FFT of unfiltered VBM amidhips in head sea, H_s of 9.5 m and T_p of 12.22 s. Same time series as Figure F.13.*

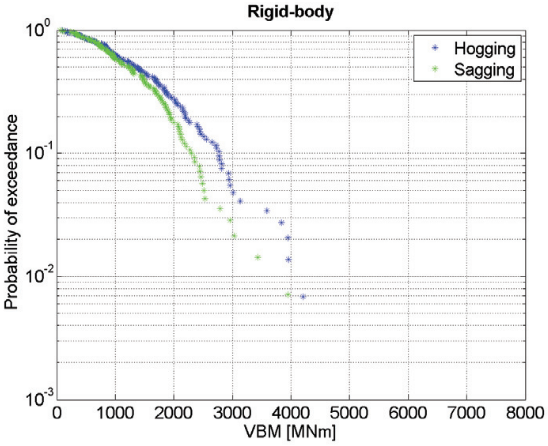

Figure F.15: *Individual peak value probability of exceedance for the rigid ship comparing hogging and sagging in head sea, H_s of 9.5 m and T_p of 9.93 s.*

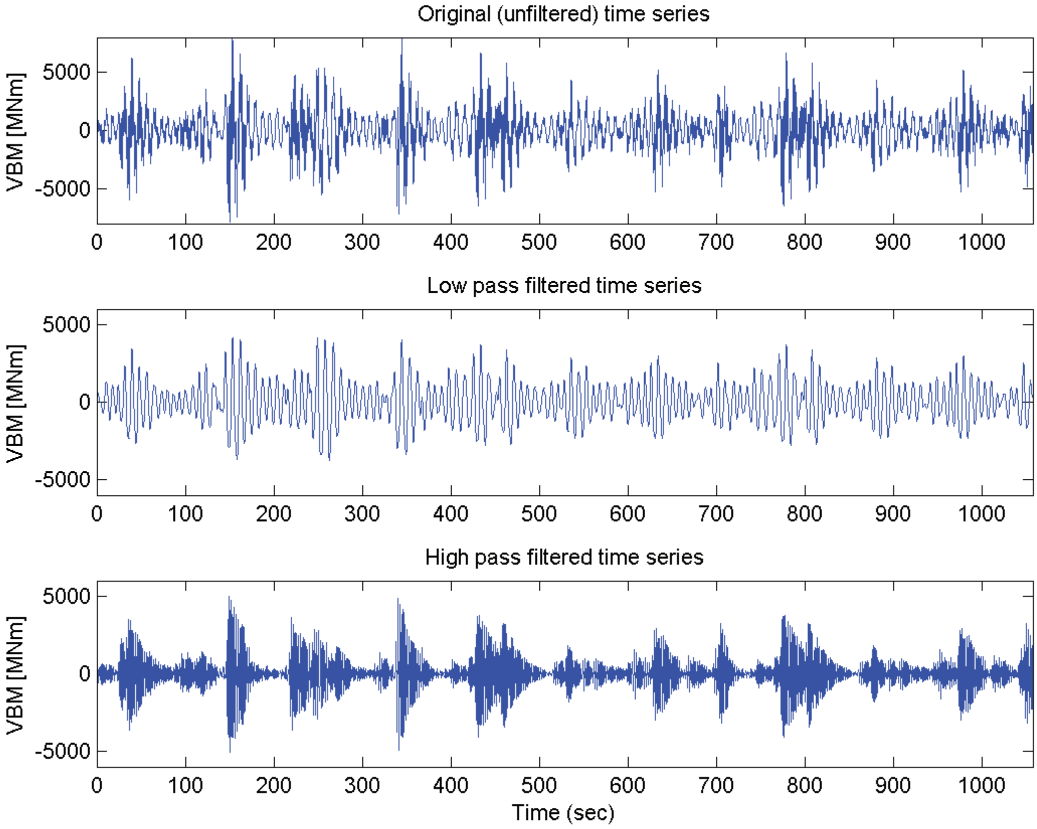

Figure F.16: *Unfiltered, low-pass and high-pass filtered time series signal of vertical bending moment for model tests in bow-quartering sea, H_s of 9.5 m and T_p of 9.93 s. Total time series is 1,057 s long and comprised of three runs.*

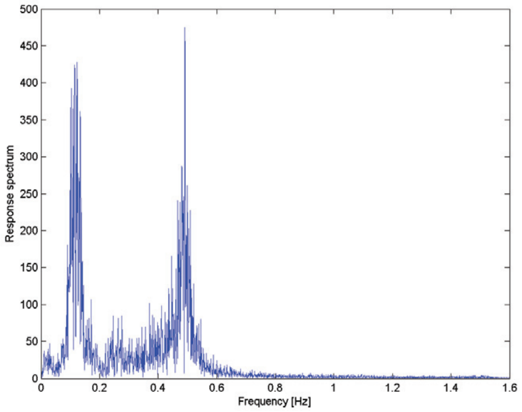

Figure F.17: *FFT of unfiltered VBM amidhips in bow-quartering sea, H_s of 9.5 m and T_p of 9.93 s. Same time series as Figure F.16.*

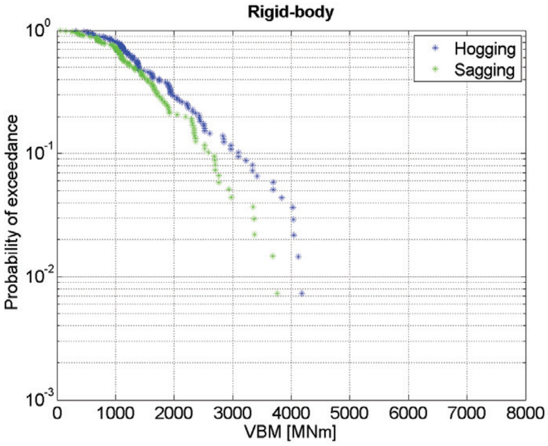

Figure F.18: *Individual peak value probability of exceedance for the rigid ship comparing hogging and sagging in bow-quartering sea, H_s of 9.5 m and T_p of 9.93 s.*

Appendix G

Basic Equations

G.1 Dynamic Response of Flexible Hulls

Basic equations for free-free Bernoulli-Euler beam.

$$EI(x)w''''(x,t) = p(x,t) - m(x)\ddot{w}(x,t) \tag{G.1}$$

$$\dot{()} = \frac{\mathrm{d}}{\mathrm{d}t} \quad \text{and} \quad ()' = \frac{\mathrm{d}}{\mathrm{d}x}$$

The vertical deflection w as function of location and time for the i'th eigenmode is given by:

$$w_i(x,t) = u_i(t)\nu_i(x)$$

where

$$u(t) = u_0 \cos(\omega_i t)$$

and $\nu_i(x)$ is the approximation to the i'th vertical vibration mode. Using modal superposition of hull girder modes the vertical deflection can be approximated as a series:

$$w(t,x) = \sum_{i_0}^{N} u_i(t)\nu_i(x) \tag{G.2}$$

The horizontal displacement (surge) is, using geometry:

$$s(x,t) = w_i'(x,t)y = u_i(t)\nu_i'(x)y$$

The surge acceleration is thus given as:

$$\ddot{s}(x,t) = \ddot{u}_i(t)\nu_i'(x)y = -u(t)\omega_i^2\nu'(x)y \tag{G.3}$$

The vertical displacement (heave) is, using geometry:

$$h(x,t) = w_i(x,t)y = u_i(t)\nu_i(x)$$

The heave acceleration, second time derivative, is thus given as:

$$\ddot{h}(x,t) = \ddot{u}_i(t)\nu_i(x) = -u_i(t)\omega_i^2\nu_i(x)$$

G.2 The Gamma Function

The gamma function is given by

$$\Gamma(x) = \int_0^\infty t^{x-1}\mathrm{exp}(-t)\mathrm{d}t$$

G.3 Probability Distribution Functions

The normal distribution

$$F(x) = \frac{1}{s\sqrt{2\pi}}\exp\left(-\frac{1}{2}\left(\frac{x-\mu}{s}\right)^2\right)$$

The Weibull distribution:

$$F(x) = 1 - \exp(-\mathrm{x}/\mathrm{a})^{\mathrm{c}} \tag{G.4}$$

The Rayleigh distribution:

$$F(x) = 1 - \exp(-\mathrm{x}/\mathrm{a})^2 \tag{G.5}$$

The exponential distribution:

$$F(x) = 1 - \exp(-\mathrm{x}/\mathrm{a}) \tag{G.6}$$

The Gumbel distribution:

$$F(x) = \exp(-\exp(-(x-b)/d)) \tag{G.7}$$

G.4 From Order Statistics to the Gumbel Distribution

The time-invariant peak distribution of a responses is the main interest for design. Extreme values in stationary stochastic processes are usually dealt with either by the Poisson model or order statistics. In both cases the basic parameter is the mean upcrossing rate ν. For upward unbounded responses, both models lead to the Gumbel distribution for the asymptotic extreme response, cf. e.g. Jensen (2009):

$$\begin{aligned} P(\max(R_p) < r) = (F_p(r))^N &= \left(1 - \frac{\nu(r)}{\nu(0)}\right)^N \\ &= \left(1 - \frac{T\nu(r)}{N}\right)^N \underset{N\to\infty}{\longrightarrow} \exp(-\nu(r)T) \end{aligned} \tag{G.8}$$

where T is the total time and $N = \nu(0)T$ is the number of peaks, respectively. $F_p(r)$ is the cumulative density function of the peaks above the level r. The ratio between level upcrossings and zero-upcrossings is assumed given by:

$$\frac{\nu(r)}{\nu(0)} = \exp(-q(r)) \tag{G.9}$$

where $q(r)$ is a monotonically increasing, positive, differential function of r.

The first step in the derivation of the extreme value distribution is to analyse the individual peak value distribution. From this distribution a Gumbel distribution of the extreme value distribution for the largest peak among N peaks can be obtained. It follows from Eq. G.8 that if the individual peak value distribution is of the form

$$F_p(r) = 1 - \exp(-q(r)) \tag{G.10}$$

then the most probable maximum value r_{mpl} i.e. the value with a return probability of $1/N$ can be found from $q(r_{mpl}) = \ln(N)$. The associated Gumbel distribution is then found by linearisation around r_{mpl}:

$$\begin{aligned} \frac{\nu(r_{mpl})}{\nu(0)} &= \frac{1}{N} \rightarrow q(r_{mpl}) = \ln(N) \rightarrow \\ P(\max(R_p) < r) &= \exp(-N\exp(-q(r))) \\ &\simeq \exp(-\exp(-q'(r_{mpl})(r - r_{mpl}))) \end{aligned} \tag{G.11}$$

It is well-known that for a narrow-banded Gaussian process the individual peaks become Rayleigh distributed. In general, broad-bandedness and non-Gaussian effects will influence the peak distribution. However, for typical wave-induced responses the Weibull distribution in Eq. (G.4) has been shown in numerous cases to be a very versatile and accurate model for measured peak distributions. For the Weibull distribution the parameters in the Gumbel distribution, Eq. (G.11), become:

$$q(r) = \left(\frac{r}{a}\right)^c \rightarrow r_{mpl} = a\sqrt[c]{\ln N} \tag{G.12}$$

$$q' \equiv \left[\frac{\mathrm{d}q}{\mathrm{d}r}\right]_{r=r_{mpl}} = \frac{c}{a}(\ln N)^{1-1/c} \tag{G.13}$$

where r_{mpl} corresponds to the Gumbel parameter b and q' corresponds to the Gumbel parameter d.

DTU Mechanical Engineering
Section of Fluid Mechanics, Coastal and Maritime Engineering
Technical University of Denmark

Nils Koppels Allé, Bld. 403
DK- 2800 Kgs. Lyngby
Denmark
Phone (+45) 4525 1360
Fax (+45) 4588 4325
www.mek.dtu.dk
ISBN: 978-87-7475-385-8

DCAMM
Danish Center for Applied Mathematics and Mechanics

Nils Koppels Allé, Bld. 404
DK-2800 Kgs. Lyngby
Denmark
Phone (+45) 4525 4250
Fax (+45) 4593 1475
www.dcamm.dk
ISSN: 0903-1685